Retinal structure and function in Age-related Maculopathy

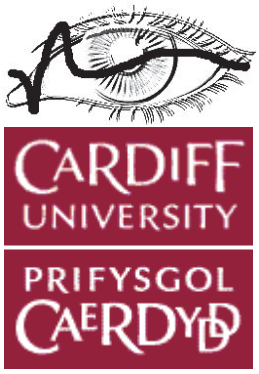

Ashley Wood
September 2011

Supervisors
Alison Binns, Nik Sheen & Tom Margrain

DECLARATION

This work has not previously been accepted in substance for any degree and is not concurrently submitted in candidature for any degree.

Signed …… (candidate) Date ……

STATEMENT 1

This thesis is being submitted in partial fulfillment of the requirements for the degree of PhD

Signed …… (candidate) Date ……

STATEMENT 2

This thesis is the result of my own independent work/investigation, except where otherwise stated. Other sources are acknowledged by explicit references.

Signed …… (candidate) Date ……

STATEMENT 3

I hereby give consent for my thesis, if accepted, to be available for photocopying and for inter-library loan, and for the title and summary to be made available to outside organisations.

Signed …… (candidate) Date ……

Summary

Age-related macular degeneration (AMD) is the principle cause of visual loss and blindness in the developed world. As new treatments and therapies are developed the need to better diagnose and then monitor outcomes of treatment has become more important. This thesis evaluates both structural and functional changes that occur in the early stage of AMD, known as age-related maculopathy (ARM), with the aim of determining their diagnostic potential. This thesis also explores the relationship between structural and functional parameters.

Twenty four participants with ARM and 26 control participants were recruited. Retinal function was probed using four focal electroretinography (ERG) techniques: the focal cone ERG, focal flicker ERG, ERG photostress test and focal rod ERG. Long wavelength optical coherence tomography (OCT) was used to assess retinal structure, specifically retinal, choroidal and four intra-retinal layer thicknesses at 21 macular locations. These techniques were initially developed and optimised for the detection of AMD related changes. The ability of each parameter to diagnose ARM was assessed. Correlation and linear regression analyses were carried out to identify any relationships between retinal structure and function in healthy controls.

Retinal thickness was reduced in participants with ARM at parafoveal locations (~2° eccentricity), but choroid thickness was unaffected. Diagnostically, focal ERG parameters provided better sensitivity and specificity to ARM than OCT measures, with the ERG photostress test providing the best diagnostic potential. No strong relationships were shown between any ERG parameter and any retinal or choroidal layer volume in control participants. Three ERG parameters were shown to be related to specific retinal features of ARM, but the strongest associations were between ERG photostress test recovery and focal cone ERG b-wave implicit time and a diagnosis of wet AMD in the contralateral eye.

In conclusion the structural and functional parameters assessed appeared to provide independent information regarding disease status and severity. ERG parameters showed better diagnostic potential than OCT measures. The single most diagnostic parameter was the recovery time constant of the ERG photostress test.

Acknowledgement

Firstly I would like to thank my supervisors Alison Binns, Tom Margrain and Nik Sheen for all their advice, help and encouraging words throughout. I would also like to acknowledge the bravery of Hannah Moncrieff and Steven Price who have lived with me during the writing up period. A thanks also goes to all those whom I have shared an office with over the years (Jenni, Moh, Saud, Mana, Jyoti & Phil). Furthermore a special mention should go to Sue Hobbs and Leanne Morrish in the office for their help and advice. And I'd like to thank Ditipriya Mukhopadhyay for listening to my moaning and Katie Mortlock for keeping me sane whilst dealing with all the issues relating to the OCT.

Table of Contents

M. Publication: Retinal and choroidal thickness in early age-related macular degeneration (2011).

Figures

Chapter 2

Chapter 3

Tables

Chapter 5

Chapter 6

Chapter 7

Abbreviations

AGE	Advance glycation end products
AMD	Age-related macular degeneration
ANOVA	Analysis of variance
AO	Adaptive optics
APB	L-2-amino-4-phosphonobutyric acid
AREDS	Age-related eye disease study
ARM	Age-related maculopathy
AUC	Area under the curve
CFF	Critical flicker frequency
CoR	Coefficient of repeatability
CS	Contrast sensitivity
CSF	Contrast sensitivity function
DTL	Dawson, Trick & Litzkow fibre electrode
ELM	External limiting membrane
ERG	Electroretinogram
ETDRS	Early treatment in diabetic retinopathy study
FD-OCT	Frequency domain OCT
GA	Geographic atrophy
GCL	Ganglion cell layer
HRT	Heidelberg Retinal Tomograph
ILM	Inner limiting membrane
INL	Inner nuclear layer
IPL	Inner plexiform layer
IPM	Inter-photoreceptor matrix
IR	Infra red
IRPB	Interphotoreceptor retinoid binding protein
ISCEV	International society for electrophysiology in vision
LGN	Lateral Geniculate Nucleus
LogMAR	Log minimum angle of resolution
NHS	National health service
NICE	National Institute for Clinical Excellence
NMDA	N-methyl-D-aspartate
OCT	Optical coherence tomography
OLM	Outer limiting membrane
ONL	Outer nuclear layer
OPL	Outer plexiform layer;
PDA	Cis-2,3-piperidine dicarboxylic acid
PDT	Photodynamic therapy
PED	Pigment epithelial detachment
PEDF	Pigment epithelial derived factor
PhNR	Photopic negative response
RGC	Retinal ganglion cells

RMSE	Root mean square error
RNFL	Retinal nerve fibre layer
ROC	Receiver operating characteristics
SD	Standard deviation
SEM	Standard error
SLD	Super luminescent diode
SLO	Scanning laser ophthalmoscope
SNR	Signal to noise ratio
STR	scotopic threshold response
TCS	Temporal contrast sensitivity
TD-OCT	Time domain OCT
TTX	Tetrodotoxin
UHR-OCT	Ultra high resolution OCT
UV	Ultra violet
VA	Visual acuity
VDU	Visual display unit
VEGF	Vascular endothelial growth factor

Chapter 1: Introduction

1.1 Outline

This thesis describes a series of studies into the retinal structure and function of people with the early stage of age-related macular degeneration (AMD). Age-related macular degeneration is a condition that principally involves the outer retina, Bruch's membrane and the choroid, which predominantly affects people over the age of 55. The early stage of AMD is also known as age-related maculopathy (ARM) and is characterised by soft drusen and focal pigmentary changes (Bird et al., 1995), but eventually progresses to either wet or dry AMD, characterised by choroidal neovascularisation or geographic atrophy respectively.

AMD is associated with a significant socio-economic burden and, in the United Kingdom, AMD is responsible for more visual impairment than all the other ocular conditions combined (Bunce and Wormald, 2006). Continuing improvements in medicine, living standards and, therefore, life expectancy mean that the prevalence of AMD will continue to rise. Between 2005 and 2050 there is predicted to be a 3 fold increase in the global number of people aged 60 years and over (UN, 2005).

Currently, treatment is limited to the wet type of AMD which is commonly and successfully treated by anti-angiogenic pharmacotherapy (Mitchell et al., 2010). No successful treatments currently exist for either dry AMD or ARM, although evidence suggests that nutritional supplements may help slow disease progression in some cases (AREDS, 2001b; Sangiovanni et al., 2007; Sangiovanni et al., 2009). There is consequently a strong research drive to develop therapeutic strategies for AMD. In order to assess outcomes of interventions, biomarkers for disease progression are needed which are sensitive to subtle changes in macular structure and function. The objective of this thesis is to explore structural and functional changes in ARM in order to enhance the understanding of disease progression and the development of tests capable of diagnosing and monitoring the condition.

This thesis starts by providing relevant background information on the healthy eye, AMD and different methods of ophthalmic imaging and assessment of retinal function in AMD. The following chapters discuss the development of protocols for this study. Results will be presented for structural and functional tests separately, where their diagnostic potential will be considered; these test results are then compared to look at the relationship between retinal structure and function.

The specific aims of this thesis are:

- To identify functional and structural changes which are diagnostic for ARM and to compare the diagnostic ability of structural and functional parameters.
- To determine if variations in macular structure are associated with macular function in healthy eyes.
- To determine if a relationship exists between macular structural and functional changes associated with ARM and to identify the nature of the relationship.

1.2 The healthy eye

1.2.1 General Structure

The gross anatomy of the eye is summarised in figure 1.2.1. Age-related macular degeneration primarily affects the outer retina, choroid and Bruch's membrane at the macula, a region covering an area approximately 6 mm in diameter centred on the fovea. The following pages will describe these and related structures in more detail.

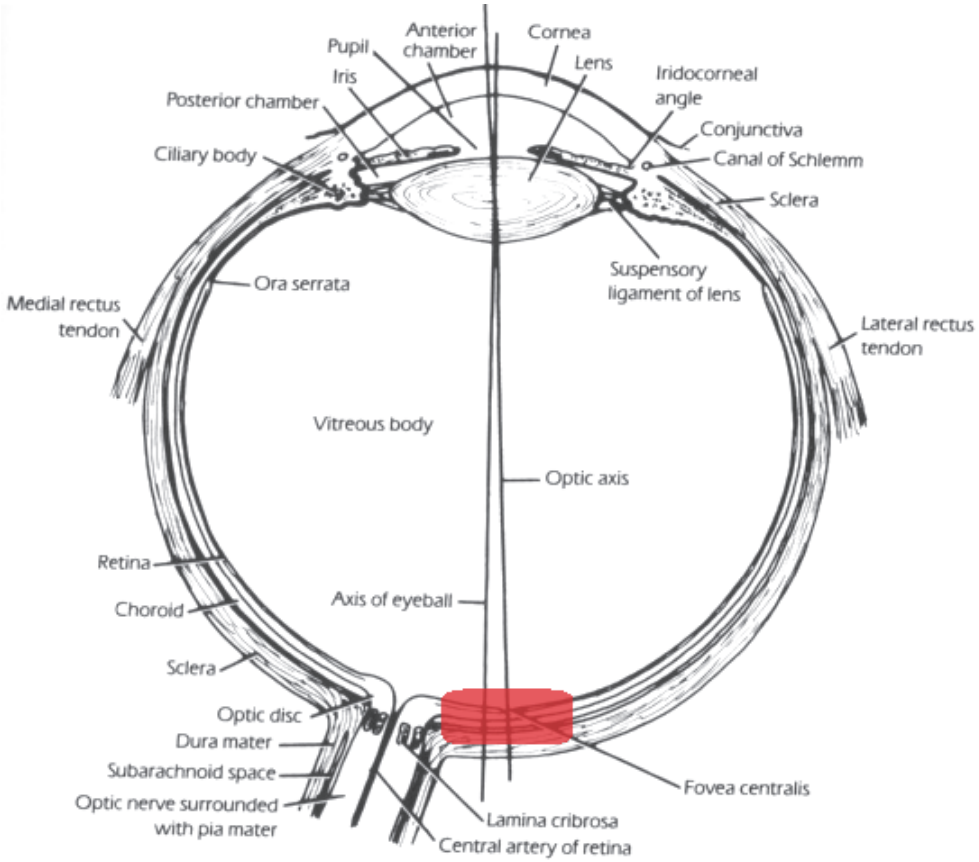

Figure 1.2.1: Diagram of the human eye, with anatomical structures and axes labelled. The macular region is highlighted in red. Image adapted from Snell and Lemp (1998).

1.2.2 Macula

The macula is a region of the retina centred on the fovea (see figure 1.2.2), located temporally to the optic nerve head, which is specialised for high acuity vision facilitated by the high spatial density of cone photoreceptors at the fovea. The macular region is encircled by the retinal vascular arcades passing from the optic nerve head, superior and inferior to the macula, and extending into the temporal retina. Anatomically, the macula is defined as the region in which the ganglion cell layer is greater than 1 cell thick; however, many clinical grading systems define the macula as a circular region 6 mm in diameter centred on the foveal pit (Klein et al., 1991; Bird et al., 1995; AREDS, 2001a). This represents approximately 20° of the visual field (Drasdo and Fowler, 1974).

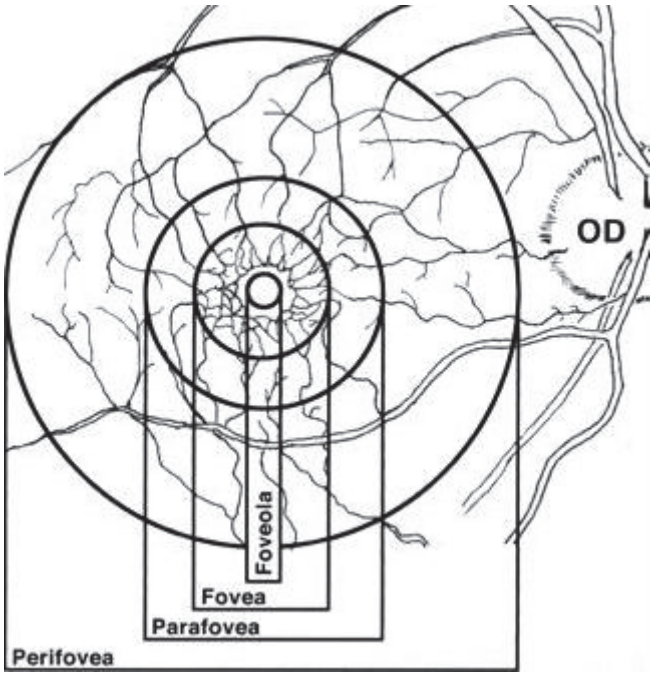

Figure 1.2.2: Diagrammatic representation of the human macula showing anatomical divisions centred on the foveal pit, or foveola. The foveola is 250-350μm in diameter and represents 1°20' of the visual field. The fovea is 1.85mm diameter and represents 5.5° of the visual field. Image from Hendrickson (2005).

1.2.3 The Choroid

The choroid is part of the uveal tract, which also includes the iris and ciliary body. The choroid is a vascular layer between the sclera and retina which is organised into 3 distinct layers; the Haller layer, the Sattler layer and the choriocapillaris (from outer to innermost). The choriocapillaris comprises the smallest and densest capillaries within the choroid, and is adjacent to Bruch's membrane; the greatest density is reached beneath the

macula where the capillaries have the widest bore (Fryczkowski and Sherman, 1988). These capillaries are fenestrated, allowing entry and exit of molecules from the vessels. The choriocapillaris is fed by and drains into the vasculature of the outer Sattler and Haller layers. The Sattler and Haller layers comprise connective tissues with predominantly medium and large sized blood vessels respectively; the choroidal blood supply feeds into these outer layers and is predominately supplied by the short posterior cilliary arteries (offshoots of the ophthalmic artery) and drained by vorticose veins into the ophthalmic vein (Snell and Lemp, 1998).

The retina has a very high metabolic rate and oxygen consumption is high (Sickel, 1972; Beatty et al., 2000; Nowak, 2006), this is supported by a combination of both the retinal and choroidal circulations, with the former predominantly supplying the inner and the latter predominantly supplying the outer retina. The major function of the choroid is to supply the outer retina with metabolites and remove the waste products, this is particularly important at the macula, where the inner retinal circulation is absent. It has been suggested that the choroidal circulation is only barely adequate for its purpose. A study in primates has shown that, dependant on lighting conditions, between 90 to 100% of oxygen delivered by the choroid is consumed by the photoreceptors (Ahmed et al., 1993). It has also been suggested that the structure of the fovea has been optimised to account for a "meagre" metabolic supply from the choroidal circulation (Provis, Diaz and Dreher, 1998). This limited availability of metabolites is also hypothesized to make the macula more susceptible to age related changes (Penfold et al., 2001; Provis et al., 2005) than the rest of the retina, which receives a dual blood supply.

Ageing has been associated with a variety of changes to the choroidal structure, including increased intercapillary spacing, and a reduction in the number and diameters of vessels (Ramrattan et al., 1994). The use of non-invasive techniques such as Doppler flowometry (Riva et al., 1994) has expanded knowledge of the human choroidal circulation, with this technique showing that choroidal blood flow and volume decreases with age (Grunwald, Hariprasad and DuPont, 1998).

1.2.4 Bruch's membrane

Bruch's membrane is a homogenous layer located between the choriocapillaris and the retinal pigment epithelium (RPE). Bruch's membrane consists of 5 layers; the basement membranes of both the choriocapillaris and RPE, an outer and inner collagenous layer, and a central elastic layer (Sumita, 1961; Del Priore, Tezel and Kaplan,

2006; Booij et al., 2010) (see figure 1.2.3). The choriocapillaris and RPE basement membranes are approximately 0.14 μm thick in the young and are predominantly comprised of collagen type IV, laminin, fibronectin, heparan sulphate and chondroitin and dermatan sulphates (Booij et al., 2010), although type VI collagen is far more abundant in the choriocapillaris than the RPE basement membrane (Guymer, Luthert and Bird, 1999). The choriocapillaris adjacent to the choriocapillaris basement membrane contains endothelial fenestrations that are permeable to macromolecules and are believed to aid the diffusion of metabolites across Bruch's membrane (Altunay, 2007; Booij et al., 2010). The inner and outer collagenous layers are composed of fibres of collagen types I, III and V (Guymer et al., 1999; Booij et al., 2010). Although both layers are similar in structure, the inner collagenous layer is approximately 1.4 μm thick whilst the outer layer is approximately 0.7 μm thick in the young (Marmor and Wolfensberger, 1998; Booij et al., 2010). Finally the elastin layer is comprised of linear elastin fibres, in addition to type VI collagen and fibronectin, with an approximate thickness of 0.8 μm in the young (Marmor and Wolfensberger, 1998; Booij et al., 2010), although this layer has been shown to be thinner at the macula compared to the periphery of the eye (Chong et al., 2005).

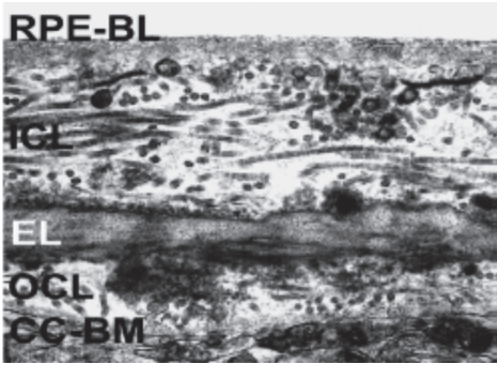

Figure 1.2.3: An electron micrograph of Bruch's membrane. Layers are as labelled: RPE-BL = basal lamina of the retinal pigment epithelium; ICL = inner collagen layer; EL = elastin layer; OCL = outer collagen layer; CC-BM = basal lamina of the choriocapillaris. Image from Del Priore et al. (2006).

1.2.5 The retinal pigment epithelium (RPE)

The retinal pigment epithelium (RPE) is a monolayer of regularly arranged cells, generally hexagonal in shape, which are located between the outer neural retina and Bruch's membrane. The RPE cells are bound together by tight junctions (zonulae occludentes), forming a blood retinal barrier with a high resistance to the passage of substances (Hudspeth and Yee, 1973). The inward facing apical surface is in contact with

the inter-photoreceptor matrix (IPM). From the apical surface microvilli extend into the IPM encompassing the rod and cone outer segments whilst simultaneously increasing the surface area.

Recent reviews by Simó et al. (2010) and Strauss (2005) have identified the main function of the RPE as (see figure 1.2.4):

- The transport of water, nutrients and ions in addition to the maintenance of the ion composition within the sub retinal space
- Absorption of stray light and protection against photo-oxidation
- The isomerisation of all-trans-retinal to 11-cis-retinal
- Phagocytosis of photoreceptor membranes
- Secretion of factors for the maintenance of retinal integrity
- Constituting part of the blood retinal barrier

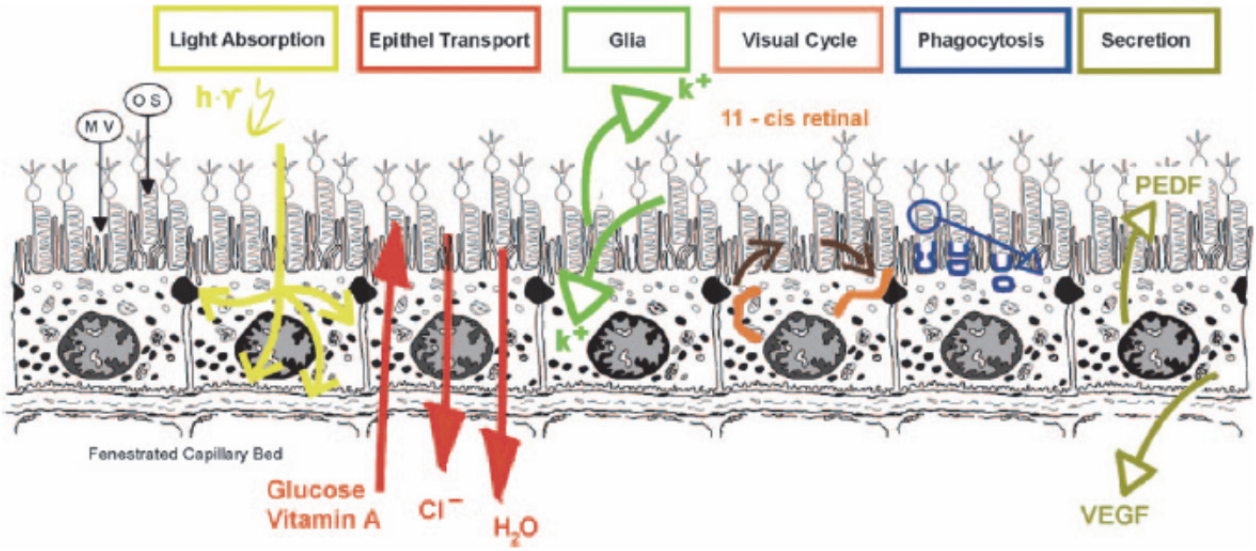

Figure 1.2.4: A summary of retinal pigment epithelium functions. Abbreviations include PEDF, pigment epithelium-derived growth factor; VEGF, vascular epithelium growth factor; MV, microvilli; OS, outer segment. Image from Strauss (2005).

The RPE is involved with transport of metabolites from the choroidal vasculature to the sub-retinal space and photoreceptors; these include electrolytes and water to the sub-retinal space and glucose to the photoreceptors (Strauss, 2005; Simo et al., 2010). An important part of this transport function is the exchange associated with the visual cycle, involving the intake of all-trans-retinal from, and delivery of 11-cis-retinal to, the photoreceptors (Baehr et al., 2003; Lamb and Pugh, 2004). The transport of the retinoid is

facilitated by the presence of inter-photoreceptor retinoid binding protein (IRBP) that originates in the RPE cells and extends into the sub-retinal space (Gonzalez-Fernandez, 2003; Wu et al., 2007). In addition, the isomerisation of all-trans-retinal to 11-cis-retinal is an essential component of the visual cycle (Lamb and Pugh, 2004) and is dependent on the protein RPE65 found within the RPE cells (Redmond et al., 1998).

Another important function of the RPE is the absorption of stray light, and protection of the retina from photo-oxidative damage (Strauss, 2005; Simo et al., 2010), the build up of which has been associated with the development of AMD (see section 1.3.2.4) (Beatty et al., 2000). The phagocytosis of shed photoreceptor outer segments, another important function of the RPE (Strauss, 2005; Simo et al., 2010), has been implicated in the susceptibility of the RPE to photo-oxidative damage, as have the high levels of polyunsaturated fatty acids within the outer segment membranes, which are easily oxidised (Beatty et al., 2000). The accumulation of the pigment lipofuscin with increasing age within the RPE and is thought to result from the incomplete digestion of this membranous material during phagocytosis. Lipofuscin itself renders the RPE prone to further oxidative damage (Margrain et al., 2004). To limit photo-oxidative damage, the RPE contains many light absorbing pigments, including melanin, and high levels of antioxidants such as dismutase and catalase (Miceli, Liles and Newsome, 1994; Simo et al., 2010). Additionally the adjacent photoreceptors also contain high levels of carotenoids, including lutein and zeaxanthin at the macula, which also act to limit photo-oxidative damage (Beatty et al., 2000; Beatty et al., 2001).

The RPE produces a range of growth and other factors for the maintenance of the retina and adjacent structures (Strauss, 2005; Simo et al., 2010). Of these factors the pigment epithelial derived factor (PEDF) and vascular endothelial growth factor (VEGF) are known to have anti-angiogenic and pro-angiogenic properties respectively and are associated with the manifestation of wet (neovascular) AMD (Frank et al., 1996; Witmer et al., 2003).

1.2.6 Retina

When observed using light microscopy the retina can be divided into distinct layers (see figure 1.2.5). The layered appearance betrays a highly organised neural retinal structure comprising many different types of cell (see figure 1.2.6).

The primary purpose of the retina is that of light detection, enabled by the light sensitive photoreceptors. The absorption of photons of light by photopigments results in

hyperpolarisation of the photoreceptors, and a reduction in release of the neurotransmitter glutamate at the synapse with second order neurones within the retina. This conversion of light to a neural signal is known as phototransduction. This visual information is transmitted and modified by a complex neuroretinal structure that includes bipolar, horizontal and amacrine cells, and eventually retinal ganglion cells. The structures comprising the retina will be described in further detail.

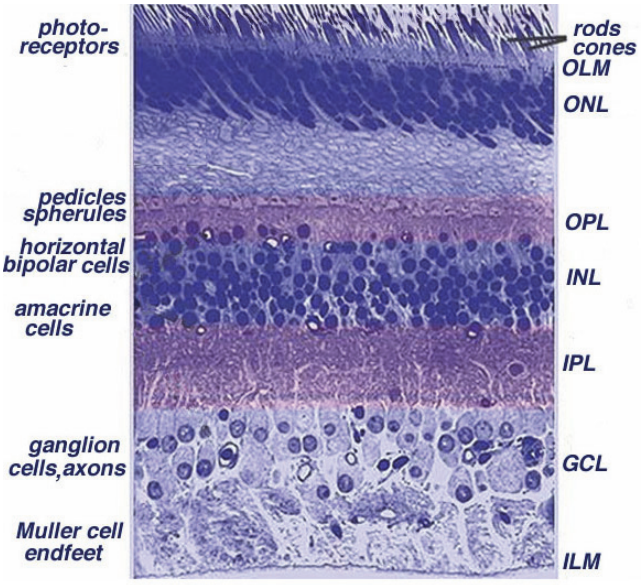

Figure 1.2.5: A light micrograph of the peripheral retina with location of retinal layers and cell types identified. OLM, outer limiting membrane; OPL, outer plexiform layer; INL, inner nuclear layer; IPL, inner plexiform layer; GCL, ganglion cell layer; ILM, inner limiting membrane. Image from Kolb, Fernandez and Nelson (2003b).

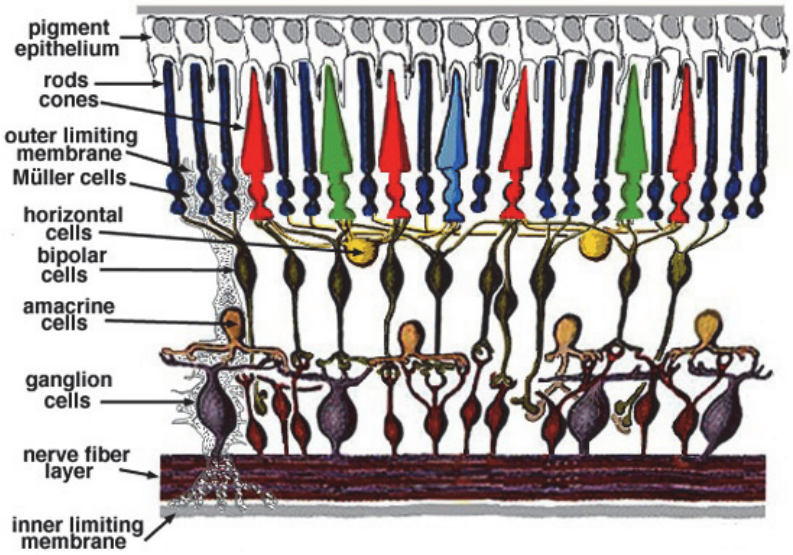

Figure 1.2.6: A schematic drawing of the neural retina showing major retinal cell types and interconnections. Image from Kolb, Fernandez and Nelson (2003b).

1.2.6.1 Retinal blood supply

The inner retina is supplied by an offshoot of the ophthalmic artery, called the central retinal artery, which enters the orbit via the optic canal. The central retinal artery enters the optic nerve approximately 1.25 cm behind the eye ball and runs forward within the optic nerve with its accompanying vein (Snell and Lemp, 1998). Upon entering the eyeball through the lamina cribrosa, the artery divides first into superior and inferior branches, before further dividing into additional nasal and temporal branches, allowing supply of all 4 retinal quadrants. The centre of the macula contains an avascular zone, centred on the fovea, which is not served by the retinal circulation and is therefore entirely dependent on the choroidal circulation (Provis et al., 2005).

The retinal circulation is drained by the central retinal vein, whose tributaries approximately correspond to those of the central retinal artery. The central retinal vein follows the path of the central retinal artery and exits the globe via the lamina cribrosa emerging from the optic nerve approximately 10 mm posterior to the globe (Snell and Lemp, 1998).

1.2.6.2 The photoreceptors

The photoreceptors comprise two types in the human retina, rods and cones, of which the latter can be divided into 3 sub-types based on their spectral sensitivity. Rod derived vision is monochromatic and optimised to lower levels of illumination, providing low visual acuity. Cone derived vision, however, is optimised for higher levels of illumination, and provides high acuity vision, enabled by the high cone density at the macula, and colour vision, due to different and overlapping spectral sensitivity curves within the cone population.

All types of photoreceptor share a similar structure: an outer segment, an inner segment, a cell body and synaptic tuft (see figure 1.2.7). The outer segment contains stacks of membranous discs which are embedded with the photopigments that are responsible for visual transduction. These membranous discs are generated at the base of the outer segment, slowly migrating along its length until they are shed at the apex; the shed membranous discs then undergo phagocytosis by RPE cells (Young and Bok, 1969; Strauss, 2005). The inner segment is connected to the outer by a thin cilium and contains numerous mitochondria, endoplasmic reticulum and the Golgi apparatus for cell energy and protein production. The cell body is where the cell nucleus is located, with the photoreceptor cell bodies forming the retinal outer nuclear layer (ONL). The synaptic tufts

extend interiorly to make connections with bipolar and horizontal cells, within the retinal outer plexiform layer (OPL).

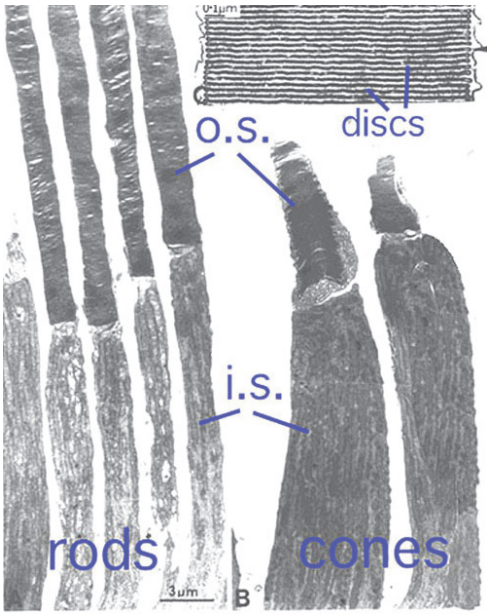

Figure 1.2.7: Electron micrograph of rod and cone photoreceptor structure, the outer segment (o.s.) and inner segments (i.s.) are labelled. A magnified section (top right) shows the distribution of membranous discs within the rod outer segments. Image from Anderson and Fisher (1976).

Rod Photoreceptors

Rods have slim “rod” shaped outer segments stretching into the sub-retinal space towards the RPE cells. There are estimated to be 78-107 million rod photoreceptors within a healthy retina (Curcio et al., 1990). There are no rod photoreceptors present within a central zone centred on the fovea (covering approximately 1.25° or 0.35 mm), however beyond this, rod density increases rapidly reaching a peak at an annulus roughly corresponding to the eccentricity of the optic disc, before declining slowly across the peripheral retina towards the ora serrata (Curcio et al., 1990) (see figure 1.2.8).

The rod photoreceptors contain the visual pigment rhodopsin, with a peak spectral absorbance at 498 nm (Bowmaker and Dartnall, 1980). The regeneration of rhodopsin following light exposure occurs within the RPE as part of the retinoid cycle (Redmond et al., 1998; Lamb and Pugh, 2004). Functionally, rod photoreceptors are known to light adapt to a background intensity range of approximately 2 log units, and with further processing within the visual system rod dominated vision can adapt to a range of up to 5

log units (Yau, 1994), this range of vision mediated by rod function is known as 'scotopic' vision.

Cone Photoreceptors

Cones have a "conical" structure, the cell bodies of which are located below the outer limiting membrane (OLM), with the inner and outer segments extending into the sub retinal space towards the pigment epithelium. There are estimated to be 4.6 million cone photoreceptors within a healthy retina (Curcio et al., 1990). The 3 types of cone are the S-cone (blue), M-cone (green) and L-cone (red) which are spectrally most sensitivity at 419 nm, 531 nm and 558 nm respectively in healthy human retinas (Gouras, 1984) (see figure 1.2.9). The range of vision mediated by the cone system is known as 'photopic' vision and extends over a brightness range starting from a point just beyond the upper limit of rod sensitivity, with the intermediate intensity range where both rod and cone systems are active known as 'mesopic' vision.

All 3 cone types increase in density towards the macular centre, and pass a parity with the rods at approximately 500µm from the centre (Curcio et al., 1990). Although s-cones make up 6-12% of total retinal cones they are absent within the central 100µm of the fovea (Curcio et al., 1991), resulting in 'small field tritanopia'. A peak cone density is found at the fovea, where the density averages 199,000 cones/mm², however, the density rapidly falls off with increasing eccentricity from the fovea (Curcio et al., 1990) (see figure 1.2.8).

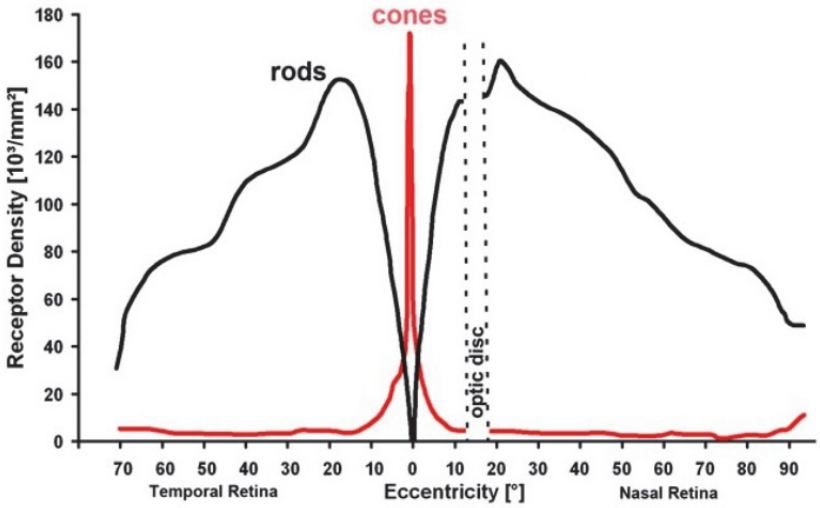

Figure 1.2.8: Graph to show the relative densities of rod and cone photoreceptors along the horizontal meridian of the retina. Image adapted from Kolb, Fernandez and Nelson (2003a) and Osterberg (1935).

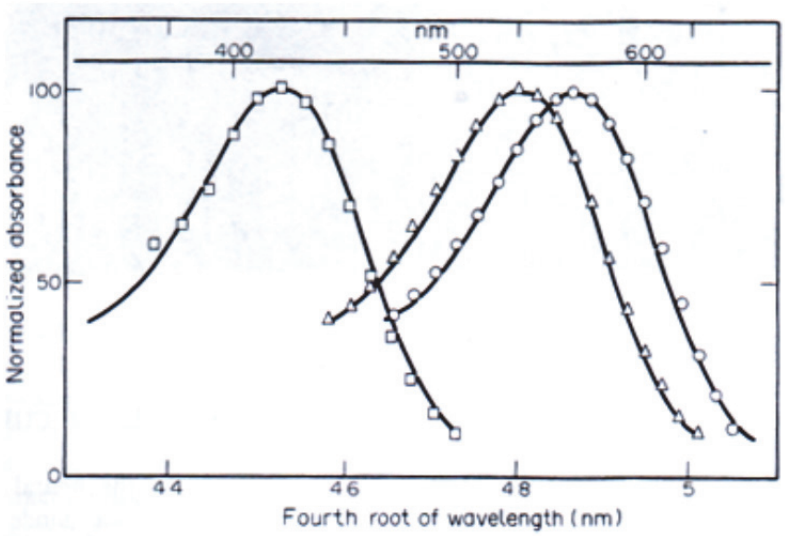

Figure 1.2.9: Absorption spectra of the human cone photoreceptors. S cone (Squares) maximum absorbance at 419 nm, M cone (Triangles) maximum absorbance at 530.8 nm and L cone (Circles) maximum absorbance at 558.4 nm. Image from Gouras (1984).

1.2.6.3 Inter-photoreceptor matrix (IPM)

The inter-photoreceptor matrix (IPM), or sub retinal space, is a region bordered by the apical RPE surface, the photoreceptor outer segments and the outer limiting membrane. The composition of the IPM is maintained by the RPE, and contains a variety of components including proteins and enzymes, such as interphotoreceptor retinoid-binding protein (IRBP), which aids in the primary function of the IPM i.e. to transport and exchange of metabolites between the photoreceptors and the RPE (Strauss, 2005).

1.2.6.4 External limiting membrane (ELM)

The external limiting membrane (ELM) is not considered a true membrane; it consists of adhesions between Müller cells and the inner segments of the photoreceptors. The ELM provides a separation between the IPM and the rest of the neural retina and is believed to act as a molecular sieve (Bunt-Milam et al., 1985).

1.2.6.5 Bipolar cells

The retina contains many different types of bipolar cells, whose cells bodies are located in the INL, from which dendrites extend into the OPL where they synapse with photoreceptors and horizontal cells. Bipolar cells also synapse in the IPL onto retinal ganglion cells (RGCs), either directly or indirectly via amacrine cells. Eleven bipolar cell

types have been identified using Golgi staining, of which only 1 type is known to synapse with rod photoreceptors whilst the remaining 10 synapse with cone photoreceptors (Kolb, Linberg and Fisher, 1992; Nelson and Connaughton, 2003).

Bipolar cells axons either terminate in sublamina **a** or sublamina **b** of the inner plexiform layer. Nelson et al. (1978) demonstrated that in the cat retina bipolar cells were of two types, either with an ON-centre (centre depolarising), which synapsed with the RGCs in sublamina **b**, or of an OFF centre (centre hyperpolarising) type which synapsed with the RGCs in sublamina **a**; this is also believed to be the case in the human retina (Kolb et al., 1992).

As the human retina is rod dominated, the rod bipolar cell type predominates in the human retina (Kolb, 2006). The rod bipolar is an ON-bipolar cell, there being no OFF rod bipolar cell. The rod bipolar cells do not make any direct synapses with the RGCs, but synapse with AII amacrine cells, which then pass this information on by a number of methods, including direct innervations or chemical synapses with OFF cone bipolar cells and RGCs, or by gap junctions between AII dendrites and ON cone bipolar cells (Kolb and Famiglietti, 1974).

The ten types of bipolar cell that synapse with cone photoreceptors consist of 7 which have a convergence function (known as diffuse and giant bistratisfied bipolar cells) that are connected to multiple cones, and 3 types which have a one to one relationship with the cone to which they synapse (consisting of 2 midget and 1 blue cone specific bipolar) (Nelson and Connaughton, 2003).

1.2.6.6 Horizontal cells

Horizontal cells are laterally interconnecting neurons within the OPL; there are 3 types designated as HI, HII and HIII (Kolb et al., 1992; Kolb et al., 1994). Horizontal cells receive input from cone photoreceptors, and are thought to be involved with the processing of light and dark adaptation within the retina and the integration of visual stimuli, enhancing spatial resolution of the retina. Specifically, the horizontal cells are thought to introduce centre-surround antagonism to the bipolar cell receptive fields (Kolb, 2006).

1.2.6.7 Müller Cells

Müller cells are a type of glial cell, with nuclei located in the inner nuclear layer, which span almost the entire neural retina, extending from the inner limiting membrane to

the photoreceptors at the level of the inner segments. Müller cells have been identified as having many roles within the retina, including maintaining retinal potassium level, contributing to the composition of the inter-photoreceptor matrix, participation in the retinal carbohydrate metabolism as a source of glycogen (Newman, 1985) and the transport and degradation of neurotransmitters (Sarthy et al., 2005). Müller cells have also been implicated in a cone only retinoid cycle (Mata et al., 2002; Lamb and Pugh, 2004); this is discussed further in section 1.2.8.

1.2.6.8 Amacrine cells

Amacrine cells synapse with both bipolar and ganglion cell types within the IPL, providing lateral connections. Amacrine cells consist of many types with different morphologies and functions which are not fully understood, although many are thought to have a role in the modulation of the retinal response to visual stimuli. The role of the AII subtype, however, is known to be pivotal in the retinal structure by providing a link from the rod bipolar cells to the cone bipolar cells, providing onward access to the cone ganglion cell pathways (Kolb and Famiglietti, 1974).

1.2.6.9 Retinal ganglion cells and their axons

The ganglion cell layer is the retina's innermost cellular layer and is comprised of RGCs whose purpose is to receive modified neurological signals from the retina and forward this visual information along the visual pathway towards the brain. Retinal ganglion cells are larger than most other retinal cells and pass the visual information they receive, in the form of transient electrical spikes (action potentials), along large axons which pass across the retinal surface forming the retinal nerve fibre layer (RNFL) and exit the globe via the optic nerve. The majority of RGC axons extend along the visual pathway and synapse at the Lateral Geniculate Nucleus (LGN) (Perry and Cowey, 1984; Perry, Oehler and Cowey, 1984).

Boycott and Wassle (1974) divided the RGCs of the cat retina into different groups depending on their morphology; these were termed alpha (α), beta (β), gamma (γ) and delta (δ). Within the cat retina the α cell type comprised ~ 3% whilst the β comprised ~ 45-50 % of the RGC population (Fukuda and Stone, 1974; Stone and Fukuda, 1974). The classification of RGCs could be refined further depending on the level of the inner plexiform layer in which the RGCs synapse. OFF-centre receptive field RGCs synapse in sublamina **a**, whilst ON-centre receptive field RGCs synapse in sublamina **b**. Kolb et al.

(1981) further classified RGC types by numbering, from G1 to G23, based on cell body size and dendritic appearance.

Within the primate retina at least 18 types of RGC have been identified, with varying size and type of receptive field (Kolb et al., 1992). These RGC types have been given the same G number as the equivalent cells in the cat retina. The human RGCs which are considered correlates of the cat α and β RGC are called P (midget) and M (parasol) cells, and project to the parvocellular and magnocellular layers of the LGN respectively (Leventhal, Rodieck and Dreher, 1981; Perry and Cowey, 1981 ; 1984; Perry et al., 1984). The majority of RGCs in the primate retina are P (midget) cells, comprising ~80% of the total, with the M (parasol) cell type comprising ~10% (Perry et al., 1984). Bistratified RGCs synapse at the koniocellular layer of the LGN, and are known as K-cells (Szmajda, Grunert and Martin, 2008).

The axons arising from the RGCs form the retinal nerve fibre layer (RNFL), the innermost layer of the retina. These axons are unmyelinated in normal individuals and extend towards the optic nerve. The RNFL is thickest at the rim of the optic nerve head, particularly at the superior and inferior border due to the path taken by the axons; those originating at or near the macula follow an arcuate path so as not to overly the photoreceptors at the fovea.

1.2.7 The visual pathway

The visual pathway consists of a series of neurological structures which convey the visual information from the retina to the brain (figure 1.2.10). Each neurone within the visual pathway has a receptive field and will respond to selected stimuli presented within this region. The visual pathway has a topographical distribution which is maintained throughout; this structural organisation enables a point to point correspondence to be maintained from any position in the visual pathway to an individual retinal location.

The visual pathway begins at the retinal photoreceptors, with the information passing successively through the retinal neurones on to the RGCs, which convey the information within their long axons through the optic nerve head and into the optic nerve. The axons then reach the optic chiasm where the axons arising from the nasal retina decussate to the opposite sides of the brain, before passing into the optic tracts; thus ensuring that each hemisphere of the visual field is carried by only the contralateral optic tract. Beyond the optic chiasm approximately 90% of the axons will continue to travel through the optic tract and synapse at the LGN (Perry et al., 1984), whilst approximately

10% will follow a “retinotectal pathway” and synapse at the superior colliculus and pretectum (Perry and Cowey, 1984), which are believed to help coordinate and control eye movements.

The LGN has a role to play in visual processing, receiving input from other areas of the brain and visual cortex (Lachica and Casagrande, 1993), before ultimately relaying the visual information forward via the optic radiations to the primary visual cortex located at the occipital pole of the brain.

A full description of the visual pathway is beyond the scope of this thesis, the anatomy and physiology of the visual pathway has been described in detail elsewhere (Snell and Lemp, 1998; Bruce, Green and Georgeson, 2003).

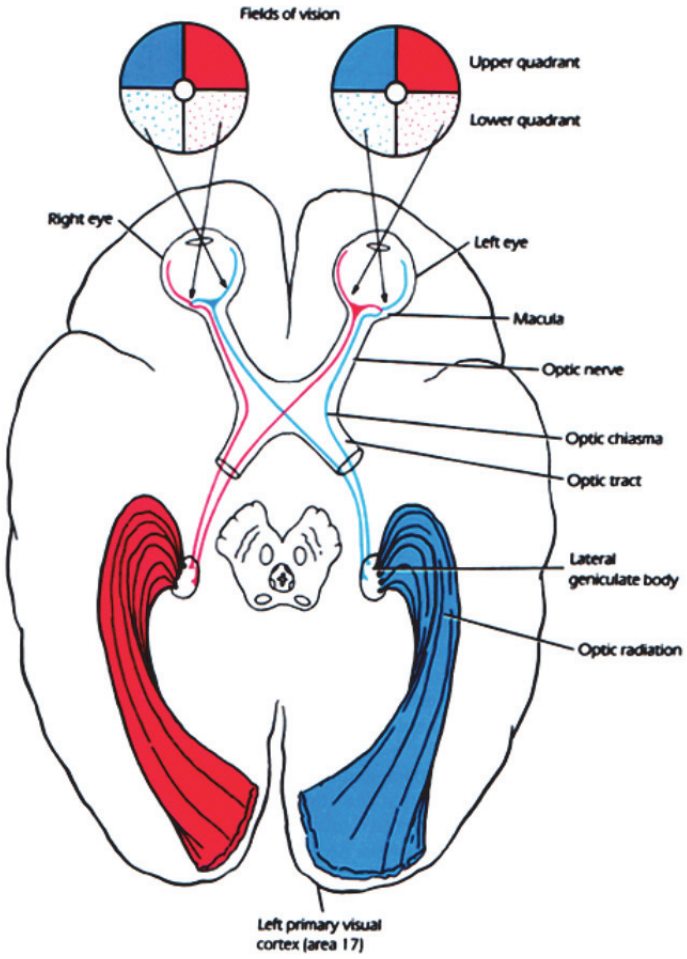

Figure 1.2.10: Schematic diagram of the visual pathway. Image adapted from Snell and Lemp (1998).

1.2.8 Visual transduction and the retinoid cycle

Photopigment molecules comprise a protein, opsin, which is covalently bound to the chromophore 11-cis-retinal (Schertler, Villa and Henderson, 1993). The photopigments are

embedded into the membranous discs of the photoreceptor outer segments (see figure 1.2.11).

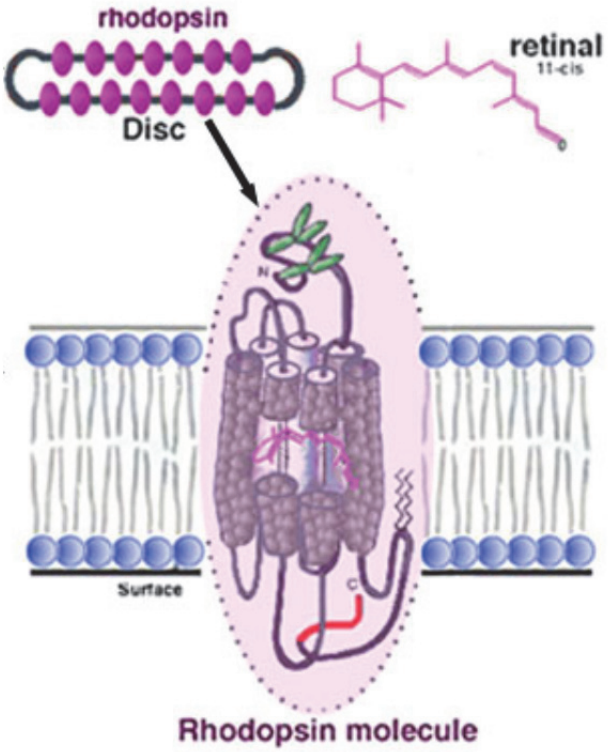

Figure 1.2.11: Diagram showing photoreceptor structure and the location of rhodopsin molecules within the phospholipid bi-layer membranes of the outer segment discs. Image adapted from Kolb & Fernandez (2003b) and Hargrave & McDowell (1992).

The absorption of light by a photopigment (e.g. rhodopsin) triggers the 11-cis-retinal to be photoisomerised into all-trans retinal. The pigment molecule (comprising the all-trans retinal and bound opsin) now becomes known as “metarhodopsin”, which may consist of a number of interchangeable forms (m_1, m_2 & m_3, see figure 1.2.12). This process results in the photopigment becoming enzymatically active turning the protein transducin into an active form, thus triggering the phototransduction cascade (Lamb and Pugh, 2004). Active transducin in turn activates phosphodiesterase enzyme, which catalyses the degredation of intracellular messenger cGMP (see Luo, Xue and Yau (2008) for a review of the literature identifying this relationship).

In the absence of light (i.e. dark adapted conditions) the plasma membrane of the outer segments allows a flow of ions into the photoreceptor through cGMP gated ion channels (Fesenko, Kolesnikov and Lyubarsky, 1985), resulting in the photoreceptor becoming depolarised. The depolarised state triggers the release of neurotransmitter

(glutamate) from the photoreceptor to second order neurones in the retina (i.e. bipolar & horizontal cells) (Copenhagen and Jahr, 1989). In the dark adapted state Na^+ and Ca^{2+} ions flow in through the cGMP gated channels (Hagins, Penn and Yoshikami, 1970; Fesenko et al., 1985), depolarising the photoreceptor, although complete depolarisation is prevented by an ion exchanger in the outer segment moving Ca^{2+}/K^+ out, and Na^+ in along the concentration gradient (Cervetto et al., 1989; Bauer, 2002). The Na^+ gradient is maintained by an ATP (adenosine triphosphate, cellular energy source) dependent channel within the photoreceptor inner segments which pumps Na^+ out in exchange for moving K^+ ions in (Stirling and Lee, 1980). This organisation enables a flow of ions between the inner and outer segments under dark adapted conditions, known as the "dark current" (Hagins et al., 1970).

Following exposure to light, the cGMP gated ion channels within the photoreceptor plasma membrane close as a result of the reduction in cytoplasmic concentration of cGMP (Fesenko et al., 1985). The altered ion flow resulting from channel closure leads to the dark current reducing and hyperpolarisation of the photoreceptor, and a consequential decrease in the release of glutamate to the second order neurones.

Following light exposure, activated photopigment molecules bind with the protein arrestin (Wilden et al., 1986), which enables the separation of all-trans chromophore from the opsin molecule. At this stage, the photopigment is said to be "bleached" and cannot absorb any further photons of light until it has been regenerated into its pre-bleach form of opsin and bound 11-cis-retinal.

The retinoid cycle is the name given to the biochemical process of removing the products of light absorption from the photoreceptors and the regeneration of visual photopigments. The sequence of events involved in the retinoid cycle has been described by Pugh and Lamb (2004), see figure 1.2.12 and table 1.2.1.

In order for the activated photopigment to become photosensitive again, the all-trans retinal needs to be replaced with 11-cis retinal, this requires the removal of the retinoid from the photoreceptor. A series of biochemical processes occur within the outer segments which separate the all-trans-retinal from the opsin molecule. The opsin remains within the outer segment, whilst the separated all-trans retinol is transported by the inter-photoreceptor binding protein (IRBP) chaperone across the inter-photoreceptor matrix to the RPE (Gonzalez-Fernandez, 2003; Wu et al., 2007). Within the RPE the all-trans retinol is converted to 11-cis retinal via one of two pathways. The major pathway involves a series of steps within the RPE cell cytoplasm, with the isomerisation of all-trans to the 11-cis form

carried out by the enzyme retinyl ester isomerohydrolase, whilst chaperoned by the protein RPE65 (Redmond et al., 1998; Mata et al., 2004). This reaction derives energy from the hydrolysis of the ester bond to create 11-cis retinol, which in turn is oxidised to11-cis retinal (Lamb and Pugh, 2004).

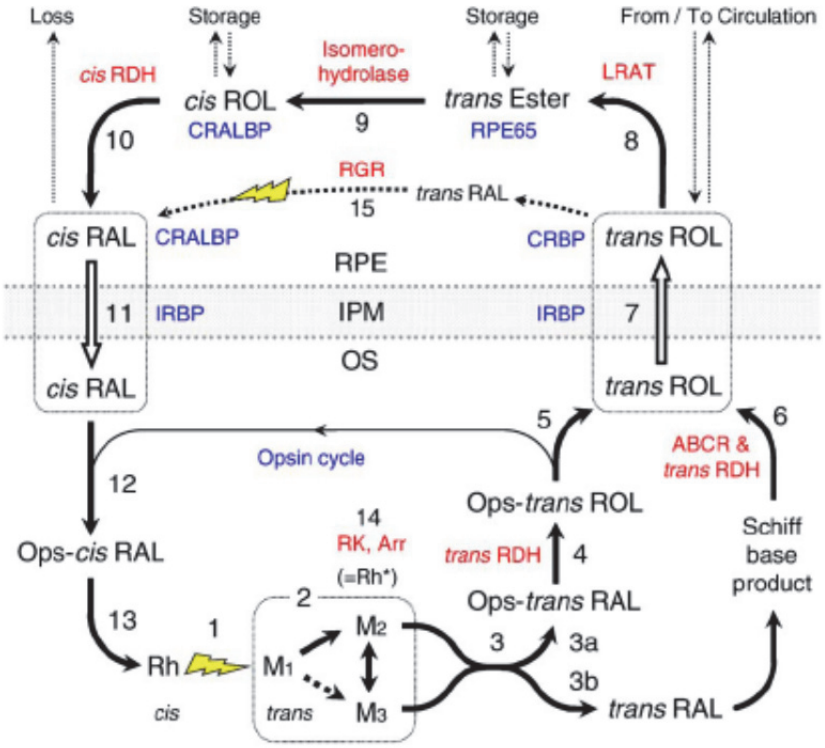

Figure 1.2.12: The retinoid cycle as a biochemical representation. Abbreviations and numbered steps are shown in table 1.2.1. Image from Lamb and Pugh (2004).

The minor pathway involves the direct photoisomerisation of all-trans retinal back to 11-cis retinal by the enzyme retinal G-protein-coupled receptor (RGR), but is thought to make only a limited contribution, even in the presence of light (Lamb and Pugh, 2004). A supply of vitamin A derived from the choroidal circulation is required to maintain the retinoid levels of the retina (Dowling and Wald, 1960; Chen and Heller, 1977).

Substrate (in black)	Chaperone protein (in blue)	Step/reaction (arrows)	Enzyme (in red)	Abbreviation	Gene
(A) *Primary steps*					
11-*cis* Retinal (*cis* RAL)	Opsin (rhodopsin)	1. Photoactivation	[Light]	Rh	*RHO*
all-*trans* Retinal (*trans* RAL)	Opsin (metarhodopsin)	2. Protein re-arrangement	—	M1, M2, M3	
	Opsin (metarhodopsin)	3. Hydrolysis of Schiff base bond	—		
	Opsin (Ops-*trans* RAL)	4. Reduction of aldehyde	all-*trans* Retinol dehydrogenase	*trans* RDH	*RDH8= prRDH*
all-*trans* Retinol (*trans* ROL)	Opsin (Ops-*trans* ROL)	5. Release of all-*trans* retinol	—		
Condensation product (NrPE)	—	6. Flippase	ATP-binding cassette, retina	ABCR	*ABCA4*
all-*trans* Retinol (*trans* ROL)	Inter-photoreceptor retinol binding protein	7. Transport across IPM and within RPE	—	IRBP	*RBP3*
	Cellular retinol binding protein		—	CRBP	*CRBP-I*
		8. Esterification	Lecithin retinol acyl transferase	LRAT	*LRAT*
all-*trans* Retinyl ester (*trans* Ester)	RPE65		—	RPE65	*RPE65*
		9. Isomerization	Retinyl ester isomerohydrolase	Isomerase	—
11-*cis* Retinol (*cis* ROL)		10. Oxidation of alcohol	11-*cis* Retinol dehydrogenase	*cis* RDH	*RDH5*
11-*cis* Retinal (*cis* RAL)	Cellular retinal binding protein	11. Transport within RPE and across IPM	—	CRALBP	*RLBP1*
	Inter-photoreceptor retinol binding protein		—	IRBP	*RBP3*
	Opsin (Ops-*cis* RAL)	12. Non-covalent binding	—		
	Opsin (rhodopsin)	13. Schiff base formation	—	Rh	*RHO*
(B) *Subsidiary steps*					
MII (= Rh*)		14a. Phosphorylation	Rhodopsin kinase	RK	*GRK1*
MII-P		14b. Arrestin binding	Arrestin	Arr	*ARR*
all-*trans* Retinal (*trans* RAL)		15. Photoisomerization	Retinal G-protein-coupled receptor	RGR	*RGR*

Table 1.2.1: Biochemical components of the retinoid cycle, numbered steps related to retinoid cycle stages as shown in Figure 1.9. Table from Lamb and Pugh (2004).

The final stage of the retinoid cycle is the return of the regenerated 11-cis retinal to the photoreceptor; the 11-cis-retinal diffuses across the interphotoreceptor space, probably with the aid of the chaperone protein IRBP (see figure 1.2.12). Upon reaching the

photoreceptor disc membranes the 11-cis-retinal forms a bond with an available opsin yielding a molecule of regenerated rhodopsin (or iodopsin in cones).

Wang and Kefalov (2011) highlight several key factors which are suggestive that a separate pathway exists for iodopsin regeneration, evidence includes the rapid sensitivity recovery (dark adaptation) of cones following exposure to bright light (Hecht, Haig and Chase, 1937), the rate of pigment regeneration being limited by the supply of chromophore (Lamb and Pugh, 2004), and that the RPE visual cycle alone is too slow to support cone function under high illumination (Mata et al., 2002). The identification of the final enzymes in the retinoid cycle within the cone inner segments and the Müller cells, allowing the production of 11-cis-retinol from all-trans retinal, suggests that Müller cells could act as a separate pathway for photopigment regeneration (Mata et al., 2002). It was also suggested that this pathway is exclusively available to the cones, as the Müller cells return the all-trans retinal to its penultimate form 11-cis-retinol, with only the cones containing the enzymes capable of the final transformation into 11-cis-retinal (Mata et al., 2002; Wang and Kefalov, 2011).

1.3 Age-related macular degeneration

Age-related macular degeneration (AMD) is a condition which manifests in later life and affects the macular region of the retina, usually bilaterally, ultimately leading to severe central vision loss. Affected individuals lose the visual abilities associated with high acuity central vision, most notably the abilities to read and write, drive and recognise faces (Mitchell and Bradley, 2006). For individuals with AMD the associated visual impairment can mean loss of independence and income, and depression (Rovner, Casten and Tasman, 2002; Berman and Brodaty, 2006).

1.3.1 Risk factors for AMD

Many risk factors for AMD have been identified as a result of epidemiological studies (Klaver et al., 2004), the most important being: age, smoking, previous cataract surgery, a genetic predisposition, racial background, diet and light exposure. For further information about the risk factors for AMD see the excellent reviews by Klein et al. (2004), Evans (2001) and Chakravarthy et al. (Chakravarthy et al., 2010).

1.3.2 Aetiology & Pathogenesis of AMD

The pathogenesis of AMD is complex and still not fully understood. The current literature indicates a multi-factorial process involving oxidative stress, metabolic insufficiency, chronic inflammation and choroidal vascular changes, all of which contribute to a greater or lesser extent to the development and progression of AMD (see Donoso et al. (2006) & Zarbin et al. (2004) for extensive discussion). Histology reveals that the first AMD-related pathological changes occur within the outer retina, retinal pigment epithelium, choriocapillaris and adjacent structures (Sarks et al., 1999; Provis et al., 2005; Donoso et al., 2006). As ageing is closely associated with AMD, the following sections will outline both age and AMD-related changes to these structures as well as considering some key aetiological factors in the disease process.

1.3.2.1 Bruch's membrane

Bruch's membrane undergoes a series of age-related changes which are closely associated with AMD pathology and are difficult to separate. Age-related Bruch's membrane changes and their relationship to AMD pathology are summarised in figure 1.3.1.

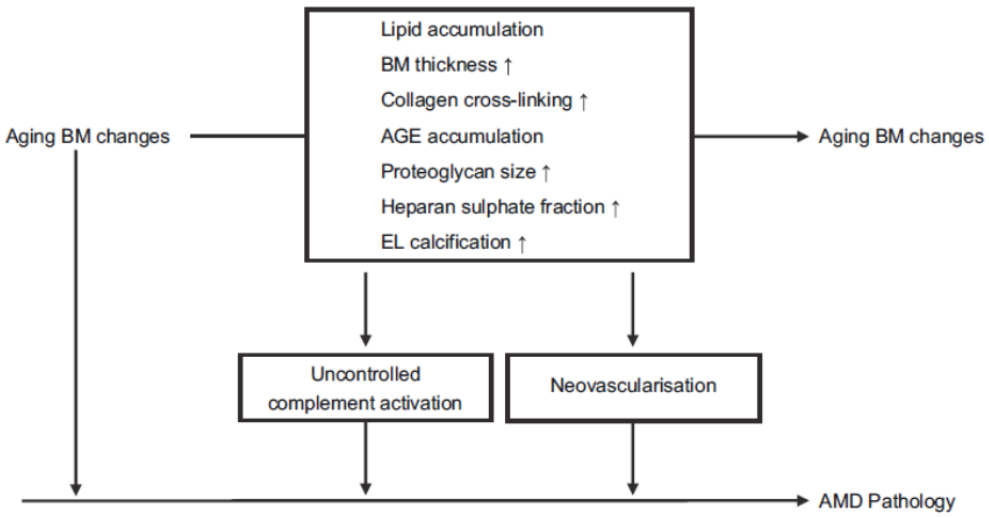

Figure 1.3.1: Changes in Bruch's membrane associated with ageing and the relationship with AMD pathology. The upper component of the image identifies changes that occur within Bruch's membrane associated with ageing, the lower component of the image shows the potential progress of AMD pathology associated with these changes, which includes either complement system activation or stimulus to neovascularisation. Image from Booij (2010).

Ramratten et al. (1994) was able to identify a thickening of Bruch's membrane in line with age, reporting an increase from 2.0 μm to 4.7 μm over 10 decades, with the greatest increase at the posterior pole. Booij et al. (2010) attribute this age-related membrane thickening to increased deposition and cross-linking of collagen fibres and increased deposition of biomolecules and oxidized metabolic waste.

An increase in collagen cross-linking is known to occur with age and is thought to contribute to a reduced permeability of the membrane (Guymer et al., 1999). An age-related linear decline in the solubility of the collagen which comprises Bruch's membrane has also been reported (Karwatowski et al., 1995). Age-related changes to the elastin layer include an increased density and calcification, with a consequential reduction in flexibility (Loffler and Lee, 1986). The integrity of the elastin layer has additionally been shown to be significantly reduced in both early and end stage AMD compared to age matched controls in a study of 121 eyes (Chong et al., 2005). Similarly the presence and accumulation of advanced glycation end products (AGE) have been associated with age and AMD (Yamada et al., 2006).

Light and electron microscopy has also identified diffuse accumulation of extraneous material, termed "basal laminar deposits" and "basal linear deposits", at the inner aspect of Bruch's membrane (Guymer et al., 1999). Basal laminar deposits are composed of granular material located between the plasma membrane and basal laminar of the RPE cells, whereas basal linear deposits are granular deposits within the inner collagenous zone of Bruch's membrane, but external to the basal lamina of the RPE (Green, 1999). The progressive accumulation of hydrophobic lipids and lipoprotein like particles within Bruch's membrane has also been linked with altering the permeability of the membrane (Huang, Curcio and Johnson, 2008; Wang et al., 2009; Booij et al., 2010). These age-related changes to Bruch's membrane are thought to act as a barrier to the normal metabolic exchange between the choriocapillaris and RPE/photoreceptor complex (Bird and Marshall, 1986; Moore, Hussain and Marshall, 1995; Guymer et al., 1999; Moore and Clover, 2001).

1.3.2.2 Choroid

The choroid also undergoes ageing changes, including a decrease in overall thickness and reductions in both the density and diameter of the choriocapillaris vessels (Sarks, 1976; Ramrattan et al., 1994). Although there is strong evidence for the occurrence of age-related thinning of the choroid (Sarks, 1976; Ramrattan et al., 1994;

Margolis and Spaide, 2009), and for changes in choroidal perfusion in ARM (Friedman et al., 1995; Ciulla et al., 1999; Harris et al., 1999), evidence for thinning of the choroid specific to ARM is not apparent in the literature. However, choroidal thinning may occur in end-stage AMD (Sarks, 1976; McLeod et al., 2009). McLeod et al. (2009) examined the post-mortem choroid in 3 aged control eyes, 5 with GA, and 3 with neovascular AMD and reported a linear relationship between the loss of RPE and choriocapillaris in GA, and a 50% reduction in choroidal vascular cross-sectional area in eyes with wet AMD, even in the absence of RPE atrophy. Sarks (1976) carried out a histological study on 378 eyes from patients aged 43-97 years, who had either a normal retina or some degree of AMD. They reported thinning of the choroid, resulting in a 'tigroid' retinal appearance. Thinning was associated with increasing age both in aged eyes classified as clinically normal and in those with all stages of AMD, but was especially prevalent in eyes with advanced AMD.

1.3.2.3 Retina

A study by Curcio et al. (1993) investigated photoreceptor topography with regard to ageing in 27 healthy retinas from donors aged 27 to 90. In these eyes there was no consistent relationship between cone density and age; however a 30 % loss in rod density was reported with preferential loss in an annulus 0.5 to 3 mm in eccentricity. Following on from these findings, Curcio at al. (1996) investigated the photoreceptor mosaic in eyes with AMD, theorising that the preferential rod loss previously shown in ageing may be a sign of subclinical AMD. Five eyes with dry AMD demonstrated loss of rods and cones in the parafovea but sparing of foveal cones, whilst in cases of wet AMD where the retina overlies disciform scarring remaining photoreceptors were predominantly cones. Given these findings, it is proposed that rods are preferentially susceptible to the pathological changes in AMD, whilst it is also proposed that loss of rods may indirectly lead to eventual cone loss given evidence that rods support cone function and survival (Hicks and Sahel, 1999).

1.3.2.4 Oxidative stress

Oxidative stress has been implicated in RPE and possible choriocapillaris injury in ageing and AMD (Beatty et al., 2000; Roth, Bindewald and Holz, 2004; Zarbin, 2004). The macula is prone to photo-oxidative damage due to the high oxygen demand of the tissue, a high exposure to visible light and the high concentration of polyunsaturated fatty acids within the outer segments of the photoreceptors (Beatty et al., 2000). A decrease in

antioxidant and macular pigment density with age further increases the risks of photo-oxidative damage; the cumulative oxidative stress could lead to the formation and accumulation of non-degradable lipofuscin, contributing to the impairment of RPE function (Roth et al., 2004). Additionally, Roth et al. (2004) suggested that increasing the presence of antioxidants at the macula could help protect against oxidative damage, a view supported by the Age-Related Eye Disease Study group (AREDS) finding that high doses of antioxidants, when taken with zinc, demonstrated a prophylactic effect on AMD progression (AREDS, 2001b).

1.3.2.5 Lipofuscin

The accumulation of lipofuscin results from incomplete phagocytosis within the RPE and is thought to play an important role in the pathogenesis of AMD (Kennedy, Rakoczy and Constable, 1995; Holz et al., 2001). The full composition of lipofuscin is not known, but it is known to contain toxic molecules such as N-retinylidene-N-retinylethanolamine (A2-E) which are thought to compromise lysosomal activity (Beatty et al., 2000). Holz et al. (2001) used autofluorescence imaging to identify lipofuscin accumulation in RPE cells as being directly associated with the development of geographic atrophy. However, it remained unclear whether high levels of lipofuscin cause RPE cell dysfunction and loss, or if the lipofuscin accumulation is a symptom of RPE dysfunction preceding eventual cell loss. In areas of geographic atrophy the loss of RPE cells is thought to precede eventual loss of both the adjacent photoreceptors and choriocapillaris (Sunness, 1999; Roth et al., 2004).

1.3.2.6 Chronic inflammation

Chronic inflammation related to the complement system has been associated with AMD, with evidence of inflammatory proteins being reported within drusen (Johnson et al., 2001; Anderson et al., 2002). There is also growing evidence of a genetic predisposition in AMD for particular polymorphisms of the Complement Factor H gene, which codes for proteins within the complement immune response (Donoso, Vrabec and Kuivaniemi, 2010). Fragments of complement system proteins (C3 and C5), which are often found in drusen of AMD patients, have been linked to the expression of vascular endothelial growth factors (VEGF) with the implication that these fragments may contribute to the process resulting in choroidal neovascularisation (CNV) (Nozaki et al., 2006).

1.3.2.7 Hypoxia and metabolism

Abnormalities identified in the choroidal circulation and vasculature structure have been suggested to be the primary insult in AMD (Sarks, 1976; Friedman et al., 1995; Ciulla et al., 1999; Friedman, 2008). The increased prevalence of AMD with ageing (Klein, Klein and Linton, 1992) mirrors age-related changes in the choriocapillaris (Sarks, 1976; Ramrattan et al., 1994). Functional abnormalities in measures such as scotopic thresholds (Chen et al., 1992) and flicker ERG implicit times (Remulla et al., 1995) have been associated with reductions in choroidal blood flow in AMD (Chen et al., 1992; Remulla et al., 1995), and are similar to those reported under conditions of experimental hypoxia (Feigl, Stewart and Brown, 2007; Feigl et al., 2008). This provides further evidence that hypoxic changes may be a factor in the aetiology of AMD.

The high cone density at the fovea, and limited retinal blood supply within the macula and foveal avascular zone are evolutionary compromises to enable high acuity vision (Provis et al., 2005). Provis et al. (2005) proposed that the anatomy of the macula make it highly susceptible to age-related degenerative changes. It is argued that the macular neurones are adapted to a limited blood supply that just meets the significant metabolic demands under normal conditions (Provis et al., 2005). However, age-related changes to Bruch's membrane (Ramrattan et al., 1994; Karwatowski et al., 1995; Guymer et al., 1999) and reductions in choroidal blood flow (Sarks, 1976; Ramrattan et al., 1994; Grunwald et al., 1998) further reduce the already limited supply of metabolites. Additionally, although the choroidal blood flow is controlled by sympathetic innervations, it does not include a regulatory system responsive to local metabolic demand (Delaey and Van De Voorde, 2000), making the blood flow independent of demand. These age-related changes are thought to eventually impact on the provision of oxygen and nutrients to the macular region, which in turn would characteristically result in increased hypoxic stress and inflammation (Provis et al., 2005). Stefansson, Geirsdottir and Sigurdsson (2011) have recently reviewed the literature, and proposed that retinal changes associated with early AMD and ageing, including retinal elevation, drusen and choroid ischemia, all increase retinal hypoxia. They suggested that the hypoxia may have a positive feedback effect, progressively exacerbating the situation. The resulting chronic hypoxia would eventually provide a stimulus for VEGF expression and neovascularisation (Witmer et al., 2003).

1.3.2.8 Summary

It is apparent that AMD is a multi factorial condition, with underlying ageing changes within Bruch's membrane (Ramrattan et al., 1994; Karwatowski et al., 1995; Green, 1999) and the choroid (Sarks, 1976; Ramrattan et al., 1994; Grunwald et al., 1998; Margolis and Spaide, 2009) occurring at an early stage. These underlying processes appear to be the catalyst for a series of pathogenic processes within the outer retina, resulting in reduced metabolic supply and chronic hypoxia (Moore et al., 1995; Guymer et al., 1999; Moore and Clover, 2001; Feigl, 2009; Stefansson et al., 2011). A series of interrelated processes have been identified which include localised inflammation (Donoso et al., 2006), with a strong association with the CFH gene (Donoso et al., 2010), oxidative stress (Beatty et al., 2000), lipofuscin and membranous deposition (Kennedy et al., 1995; Holz et al., 2001; Roth et al., 2004) and loss of choroidal perfusion (Friedman et al., 1995; Ciulla et al., 1999; Harris et al., 1999; Ciulla et al., 2002; Feigl, 2009). The ultimate outcome of these processes is geographic atrophy (non-exudative / dry AMD) and/or choroidal neovascularisation (exudative / wet AMD) resulting in severe central vision loss. The progression to an exudative end point is determined by the expression of VEGF (Frank et al., 1996; Witmer et al., 2003).

1.3.3 Clinical features of AMD

AMD does not typically develop before the age of 55 (Klein et al., 2004). The earliest associated changes are within the photoreceptors, RPE, Bruch's membrane and the choriocapillaris (Sarks et al., 1999; Provis et al., 2005; Coleman et al., 2008). The following section will discuss the clinical features commonly associated with the various stages of AMD.

1.3.3.1 Drusen

Drusen are discrete deposits located between the RPE and Bruch's membrane (Maguire, 1999), generally occurring prior to other clinical features of AMD (Gass, 1972). The development of drusen has been associated with the sub clinical presence of extracellular material deposits, known as basal linear and basal laminar deposits (see Green (1999) for a histopathology review). Drusen may regress over time, which can be associated with degeneration and atrophy of the RPE, choriocapillaris or outer retina but can occur without overt evidence of atrophy (Sarks et al., 1999). Drusen can vary greatly in their size, shape, composition, colour and border definition; however the most

commonly occurring types can be broadly classified as either hard or soft drusen. Different sources have attempted to categorise drusen appearance and features; given the variability in clinical presentation there are some variations in definition between sources (Bird et al., 1995; Maguire, 1999; AREDS, 2001a). The following section discusses the most common clinically identifiable drusen types.

Hard drusen

Hard drusen are defined as small (<63μm), round, flat deposits with a yellow to white colour (Bird et al., 1995; Maguire, 1999; AREDS, 2001a). Hard drusen consist of hyaline material deposited between the inner collagenous layer of Bruch's membrane and the RPE (Sarks, 1976). The presence of drusen at the macula is common and not in itself an indication of AMD, with hard drusen being regarded as a normal change associated with ageing (Sarks et al., 1999). It has been reported that over 90% of the white population over the age of 40 may have hard drusen present in either eye (Klein et al., 1992).

Soft drusen

Soft drusen (see figure 1.3.2) are larger than hard drusen (>63μm) and similarly consist of hyaline deposits located between Bruch's membrane and the RPE. Clinically they appear to have a yellow or grey colour, and may have a distinct or indistinct border. For the purposes of classification, soft drusen are often subdivided into distinct (characterised by a uniform density and defined borders) and indistinct (characterised by varying density and fuzzy borders) subtypes (Bird et al., 1995; Maguire, 1999; AREDS, 2001a). The presence of soft drusen within the macular region is classified as a sign of AMD (Bird et al., 1995; AREDS, 2001a), in addition the presence of a large number is a risk factor for progression to advanced AMD (Klein et al., 1997).

Confluent drusen

The borders of multiple large soft drusen can merge; these coalescent drusen are referred to as confluent drusen (Maguire, 1999). Confluent drusen can result in a significant detachment of the overlying RPE and are therefore commonly associated with drusenoid pigment epithelial detachments (Zayit-Soudry, Moroz and Loewenstein, 2007). Drusen confluence has also been identified as a high risk factor for progression to advanced AMD (Smiddy and Fine, 1984).

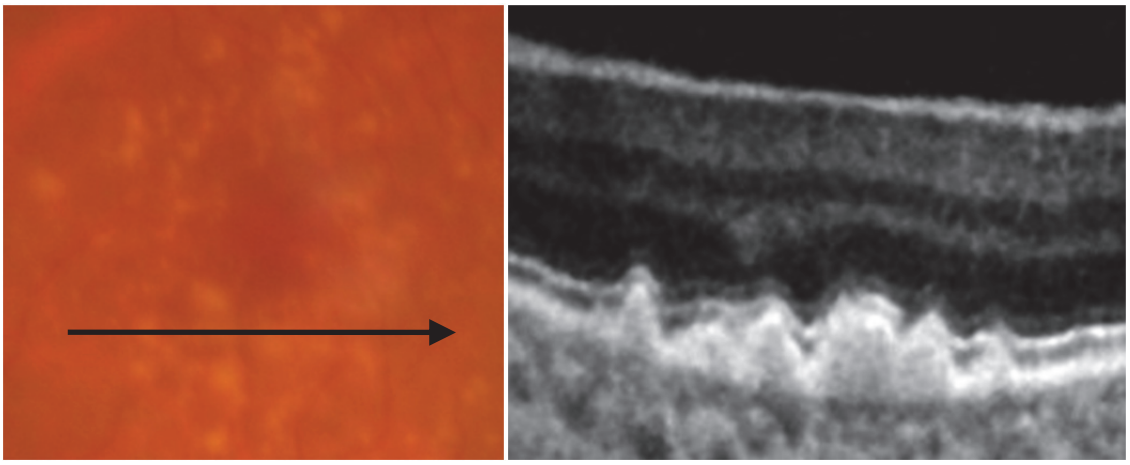

Figure 1.3.2: Retinal photograph (Left) showing a macula with multiple soft drusen. OCT cross-sectional image (Right) corresponding to the black arrow on the retinal photograph, drusen appear as localised elevation in the RPE layer with underlying reflective material.

Other drusen types

Basal laminar drusen represent hyalinised nodular thickening of the RPE basement membrane and are not associated with AMD. Reticular, or pseudo-drusen, are yellow lobular or ribbon like areas often seen in the outer macular area (Maguire, 1999). Calcified drusen appear to glisten and are associated with RPE atrophy (Bird et al., 1995; Maguire, 1999; AREDS, 2001a).

1.3.3.2 Pigment abnormalities

Pigment abnormalities, focal areas of hyperpigmentation and hypopigmentation within the RPE, are a common sign of early AMD. Hyperpigmentation represents areas of pigment clumping within the macula, and is often associated with the presence of both hard and soft drusen (Bressler et al., 1990). The hyperpigmentation has been attributed to a combination of RPE cell proliferation, RPE cell migration and increased levels of melanin expression (Bressler et al., 1994). Hypopigmentation is believed to result from reduced RPE melanin pigment density and is associated with RPE atrophy or thinning (Pauleikhoff et al., 2004). Focal hyperpigmentation is also a risk factor for progression to advanced AMD (Smiddy and Fine, 1984; Bressler et al., 1990; Klein et al., 1997).

1.3.3.3 Geographic atrophy

Geographic atrophy is the end stage of dry (non-exudative) AMD. Its presence is considered a feature of advanced AMD and, in the absence of CNV, is the defining feature

of dry AMD (Bird et al., 1995; AREDS, 2001a). Geographic atrophy is identified as sharply demarcated depigmented areas, with increased visualisation of choroidal vessels and decreased retinal thickness (see figure 1.3.3). There are often areas of retinal sparing within regions of atrophy. Areas of geographic atrophy are usually associated with surrounding areas of pigmentary disturbance. Initially geographic atrophy spares fixation, beginning with localised areas of atrophy in the parafovea, which coalesce eventually affecting the fovea and fixation (Sarks, Sarks and Killingsworth, 1988). On fluoroscein angiography geographic atrophy usually appears as a hyperfluorescent region (Sunness, 1999).

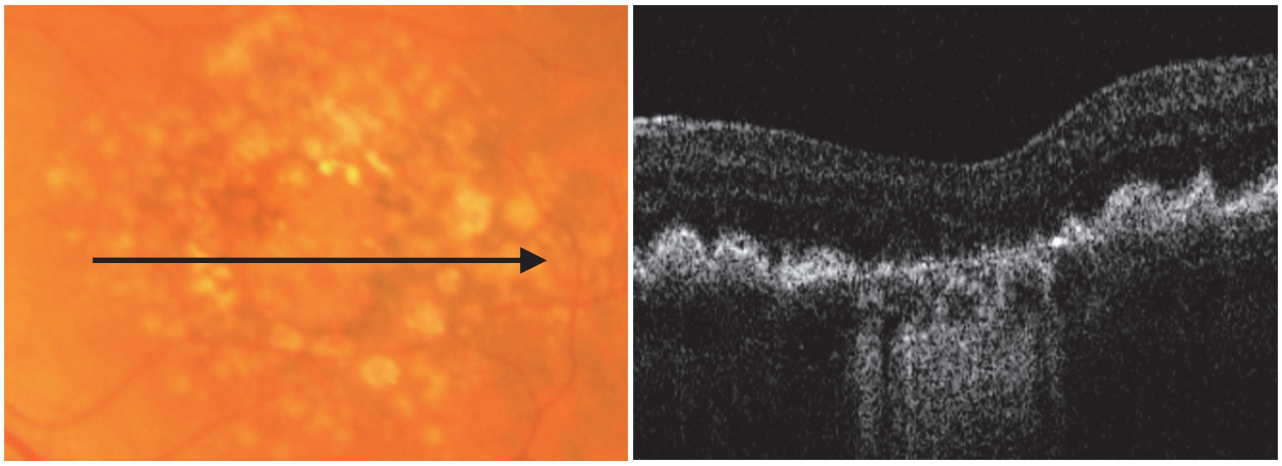

Figure 1.3.3: Retinal photograph (Left) showing central area of atrophy with surrounding pigmentary disturbance and extensive soft drusen. OCT cross-sectional image (Right) corresponding to the black arrow on the retinal photograph, demonstrates retinal thinning overlying a region of RPE atrophy, note the reflectivity of sub-RPE structures facilitated by the loss of RPE. Soft drusen are apparent as extensive undulation of the RPE adjacent to the atrophic region.

1.3.3.4 Choroidal neovascularisation (CNV)

Light microscopy reveals that the new vessels originate from the choroid, extending through breaks in Bruch's membrane (Sarks, 1980). The growth of these vessels is thought to result from a local imbalance of growth factors (Roth et al., 2004), specifically VEGF (angioproliferative) and PEDF (angiogenesis antagonist), which usually ensure the non-vascular nature of Bruch's membrane.

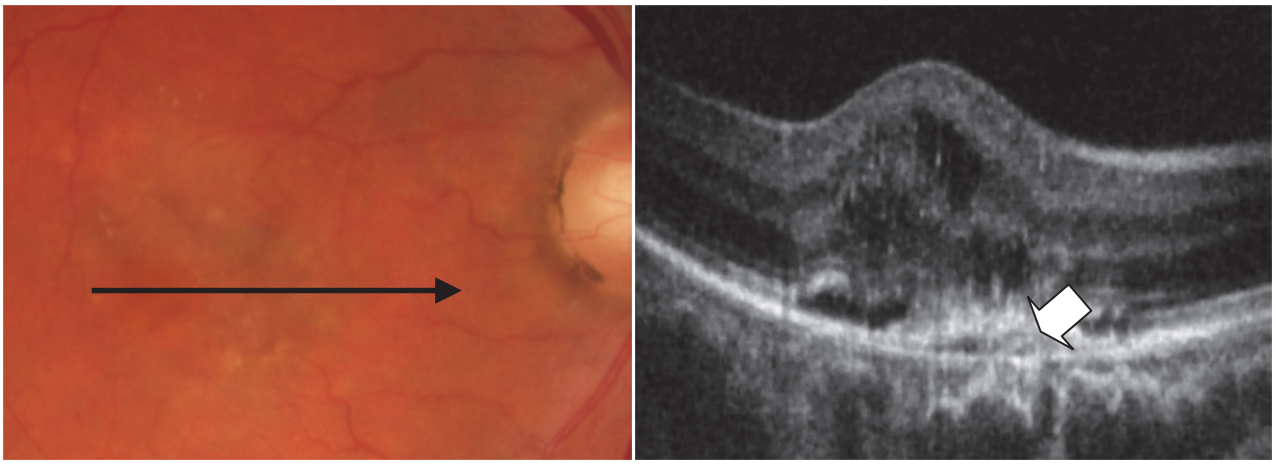

Figure 1.3.4: Retinal photograph (Left) showing an active choroidal neovascular lesion in wet AMD. OCT cross-sectional image (Right) corresponding to the black arrow on the retinal photograph, CNV highlighted (white arrow) as a highly reflective structure at the level of the RPE with associated retinal oedema.

Clinically the presence of CNV may appear as a greenish brown lesion at the macula (see figure1.3.4); however, due to the fragile nature of the vasculature, extensive haemorrhage, oedema, exudates and pigment epithelial detachments are common. Accompanying symptoms usually include metamorphopsia and reduced visual acuity. Recurrent haemorrhage of these new vessels ultimately leads to fibrovascular tissue and the development of disciform scarring (Penfold et al., 2001). This scarring results from the persistent presence of CNV, associated retinal oedema, haemorrhage and other structural abnormality within the retina and adjacent structures, which leads to widespread fibrosis and atrophy across the affected area. Clinical appearance of the scar tissue is varied on ophthalmoscopic investigation, with the lesion ranging in elevation and in colour from white-yellow to black. Optical coherence tomography (see figure 1.3.5) classically reveals a highly reflective structure corresponding to the disciform scar.

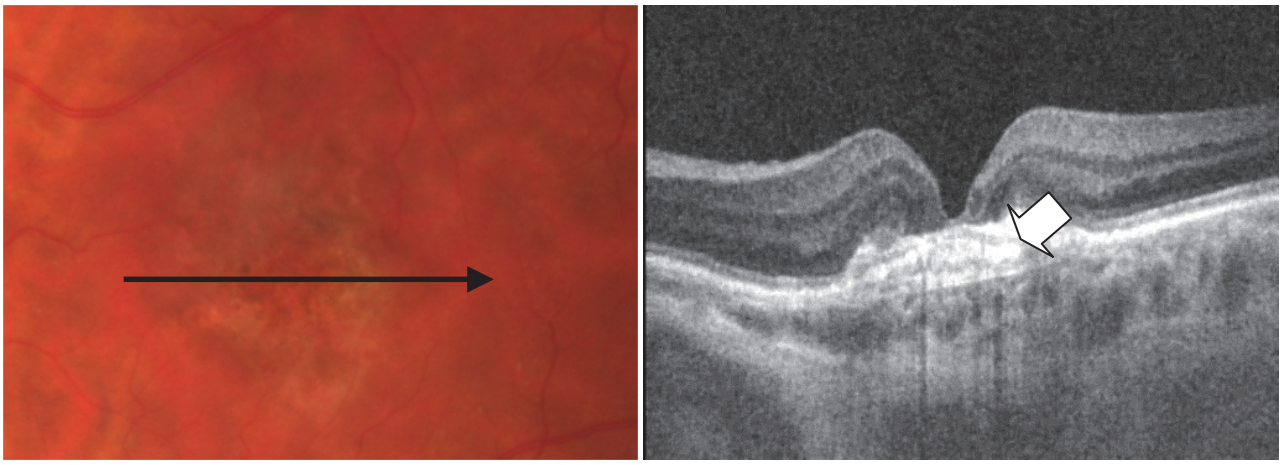

Figure 1.3.5: Retinal photograph (Left) showing an inactive choroidal neovascular lesion in wet AMD undergoing treatment with monthly ranibizumab (lucentis; Novartis) injections. OCT cross-sectional image (Right), corresponding to the black arrow on the retinal photograph, showing subfoveal CNV and extensive localised scarring (white arrow) appearing as a thickened and highly reflective structure at the level of the RPE.

1.3.3.5 Pigment epithelial detachment (PED)

Pigment epithelial detachment (PED) is a feature of AMD which may or may not be associated with choroidal neovascularisation. The adhesion between Bruch's membrane and the RPE is thought to be maintained by a vector force created by the limited hydraulic conductivity of the RPE to the flow of fluid from the vitreous to the choroid (Kirchhof and Ryan, 1993). RPE detachments occur between the inner collagenous layers of Bruch's membrane and the basal lamina of the RPE (Murphy et al., 1985). Pigment epithelial detachments associated with AMD are divided into 3 types depending on the clinical appearance: drusenoid, serous and fibrovascular (see figure 3.1.6). Pigment epithelial detachments are mostly asymptomatic but those involving the fovea may result in blurred vision, distortion, metamorphopsia or micropsia (Zayit-Soudry et al., 2007).

Drusenoid PEDs (see figure 1.3.6) are characterised by an irregular surface, often with overlying orange/grey hyperpigmentation, with a typically slow rate of enlargement. On fluoroscein angiography they are characterised by delayed hyperfluorescence due to the gradual staining of the sub RPE with no leakage and possible irregular density (Zayit-Soudry et al., 2007). The impediment to fluid outflow towards the choroid, caused by ageing changes to Bruch's membrane and the presence of soft drusen/basal linear deposits, is thought to result in a build up of fluid in the sub-RPE space and leads to PED (Casswell, Kohen and Bird, 1985; Bird and Marshall, 1986). A study by Roquet et al.

(2004) followed 61 eyes for an average of 4 to 6 years and found progression to geographic atrophy (dry AMD) in 49%, CNV (wet AMD) in 13% and persistent drusenoid PED in 38% of eyes followed.

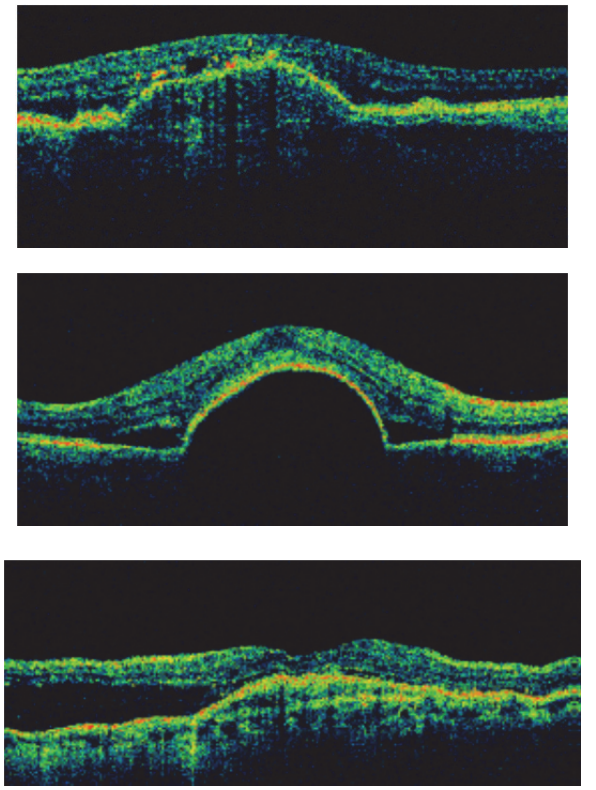

Drusenoid PED, with adjacent RPE elevation associated with drusenoid changes, resulting from solid hyper reflective material. No sub-retinal fluid is present.

A smooth sub foveal serous PED. Internal to the PED, the absence of reflectivity indicates the presence of fluid.

Fibrovascular PED with thickening of the RPE and continuity breaks associated with underlying CNV. Large areas of sub-retinal and intra-retinal fluid accumulation are seen adjacent to the PED.

Figure 1.3.6: OCT image showing drusenoid (top), serous (middle) and fibrovascular (bottom) PEDs. Images from Zayit-Soudry et al. (2007).

A serous PED is defined as an area of smooth, sharply demarcated dome shaped and regular PED, it characteristically has sharply demarcated margins due to firm adherence of the RPE to Bruch's membrane (Zayit-Soudry et al., 2007). Diagnosis of serous PED is primarily made using fluoroscein angiography, which shows rapid, bright, and uniform filling of the lesion, delayed compared to the background fluorescence without leakage (Zayit-Soudry et al., 2007), but can also be identified using OCT (Mavrofrides et al., 2004). Serous PED is often, but not always, associated with the presence of CNV (Elman et al., 1986).

A fibrovascular PED is considered a subtype of CNV which has an irregular appearance. The PED has breaks in the RPE where the underlying CNV is exposed, and there are often large sub retinal fluid accumulations adjacent to the PED. The irregular elevations of the PED demonstrate a granular or stippled hyperfluorescence within 1 to 2

minutes on fluoroscein angiography; late frames often demonstrate leakage beyond the elevated boundaries of the PED (Zayit-Soudry et al., 2007).

1.3.3.6 Retinal thickness changes

A number of studies have evaluated *in vivo* retinal thickness, using OCT, in eyes with advanced dry or wet AMD (Yamaguchi, Otani and Kishi, 2000; Joeres et al., 2007; Kashani et al., 2009; Blair et al., 2010; Yuda et al., 2010), and ARM (Kaluzny et al., 2009; Malamos et al., 2009; Schuman et al., 2009).

There is evidence that OCT is an effective technique for the imaging and quantitative evaluation of retinal thickness in advanced AMD (Kashani et al., 2009; Blair et al., 2010; Yuda et al., 2010). For example, Kashani et al. (2009) were able to associate increased ONL thickness with reduced visual acuity in 53 participants with wet AMD, using a technique that successfully allowed manual segmentation of images including PED and intraretinal fluid. Yuda et al. (2010) were able to compare peripapillary RNFL thickness in eyes with wet AMD to non-exudative fellow eyes (n=100); the finding that that RNFL thickness was is not different between these eyes suggests that the inner retinal thickness was relatively unaffected in wet AMD. Blair et al. (2010) found a significant positive correlation ($r=0.7$, $p=0.003$) between maximum retinal thickness and PED height in participants with wet AMD and PED. This demonstrates that even in the presence of PED retinal thickness measurements may be obtained and, furthermore, that there is a relationship between the two.

Those studies that have used OCT to investigate early AMD reported finding localised reductions in retinal thickness only overlying drusen and PEDs (Kaluzny et al., 2009; Malamos et al., 2009; Schuman et al., 2009). This localised reduction in retinal thickness has been ascribed to the outer retina, with Schuman et al. (2009) finding inner retinal thickness to be almost unchanged over drusen.

1.3.4 AMD treatments and prevention

The treatments for AMD are primarily for wet AMD, with no effective treatments available for dry AMD, although nutritional and lifestyle advice has been shown to reduce the risk of progression (Mares-Perlman et al., 1995; Klein, Klein and Moss, 1998; AREDS, 2001b; Seddon et al., 2001; Mitchell et al., 2002; Chong et al., 2007; Tan et al., 2007; Tan et al., 2009). The following sections outline the current approaches to treatment and prevention of AMD.

1.3.4.1 Lifestyle and nutrition

A diet high in anti-oxidants and zinc has been shown to slow the progression of AMD in some instances (AREDS, 2001b; Chong et al., 2007), but there is insufficient evidence to indicate that this has a primary preventative effect (Chong et al., 2007). The Age-Related Eye Disease Study (AREDS) in the United States looked at ~5000 men and women with AMD over a 7 year period. The study showed that taking a formulation of antioxidants and zinc significantly reduced the progression of AMD compared to a placebo group; with a 25% risk reduction in progression to late AMD over 5 years (AREDS, 2000 ; 2001b). However, the intake of antioxidants and zinc has not been shown to prevent the initial development of AMD (Chong et al., 2007) and the AREDS formulation was only recommended for those with at least 1 large drusen, multiple intermediate sized drusen, parafoveal geographic atrophy or unilateral advanced AMD. It should be noted that individuals with a history of smoking are unable to benefit from the supplement beta-carotene due to the increased risk of developing lung cancer (Evans, 2006). Those individuals who smoke tobacco should be advised to quit, with those who quit appearing to benefit from a reduced risk of progression and incidence of AMD compared to current smokers (Klein et al., 1998; Mitchell et al., 2002; Tan et al., 2007).

Increased risks are associated with high levels of dietary fat intake, but a reduced risk is associated with dietary intake of fish, omega 3 fatty acids (Mares-Perlman et al., 1995; Seddon et al., 2001; Sangiovanni et al., 2009; Tan et al., 2009) and carotenoids, including luetin and zeaxanthin (Seddon et al., 1994). Therefore, reasonable dietary advice to at risk individuals could include a reduced fat intake, but increased consumption of fish, nuts and green leafy vegetables such as kale and spinach. However, a lack of randomised control trial evidence means there is no conclusive evidence for such advice. There is also evidence to suggest that those exposed to high levels of sunlight may benefit from protection such as sun hats and sunglasses (Tomany et al., 2004).

1.3.4.2 Anti-VEGF therapies

There are several anti-VEGF drugs, which can deactivate the angioproliferative effect of VEGF. Currently available anti-VEGF drugs include Ranibizumab (Lucentis; Novartis), Pegaptanib sodium (Macugen;Pzifer) and Bevacizumab (Avastin; Genentech Inc). Recent studies have shown Ranibizumab and Bevacizumab to be effective in halting

the progression of wet AMD and they even improve the visual outcome for patients in some cases (Bhatnagar et al., 2007; Bashshur et al., 2008).

A recent review of the current literature by Chiang and Regillo (2011) identifies Ranibizumab as the treatment of choice for wet AMD. However, Bevacizumab has been shown to provide similar clinical outcomes in a large (n=1208) multicentre trial. Those treated with monthly intravitreal injections of Ranibizumab or Bevacizumab demonstrated an average gain of 8.5 and 8.0 letters respectively on a logMAR grading at 1 year, whilst those on an "as needed" treatment regime gained 6.8 and 5.9 letters respectively (Martin et al., 2011). Currently within the United Kingdom, the National Institute for Clinical Excellence (NICE) has only approved Ranibizumab, and not Bevacizumab, for the treatment of wet AMD.

1.3.4.3 Laser photocoagulation & photodynamic therapy (PDT)

Laser photocoagulation was shown to limit vision loss people with CNV compared to no treatment in randomised controlled trials by the Macular Photocoagulation Study Group (1993). Laser photocoagulation utilises laser burns to destroy the CNV membrane whilst sparing the fovea, and was developed to reduce the risk of severe vision loss. However this approach does not restore vision, and can only be applied in cases where the CNV lesion is well defined and does not involve the fovea, due to the risk of laser induced visual loss (MPSG, 1996; Virgili and Bini, 2007).

Photodynamic therapy involves the intravenous injection of the photosensitive dye "Verteporfin". Verteporfin diffuses into the blood stream and is selectively taken up by the CNV. A diode laser, of 689nm, is then focused into the CNV, activating the verteporfin dye which destroys and seals the CNV. However PDT is only recommended by NICE guidelines for a very specific group of patients with wet AMD who have a predominantly 'classic' lesion not larger than 5400µm, and demonstrate a visual acuity of 6/60 or better (Kanski, 2003). Although Barnes et al. (2004) reported a reduction of less than 15 letters of acuity in 73% of all wet AMD eyes (n=170) treated with PDT within the NHS at 12 months, it should be noted that treatment with newer anti-VEGF therapies is associated with better visual outcomes (Lazic and Gabric, 2007).

1.3.4.4 Surgical intervention & other novel therapies

Sub macular surgery to remove sub foveal CNV is an option available in cases of sub macular haemorrhage, however this approach has shown only modest improvements

in visual acuity, and suffers from a high rate of recurrence (Falkner et al., 2007). Other techniques that have been used to treat wet AMD include transpupillary thermotherapy (Newsom et al., 2001) and prophylactic laser treatment, which was intended to reduce progression to advanced AMD in eyes with high risk drusen (Choroidal Neovascularization Prevention Trial Research, 1998) but appeared to have had the opposite effect.

1.4 Retinal imaging

Retinal imaging is a diverse field, with many different techniques providing a range of qualitative and quantitative information. This section considers the advantages and disadvantages of different techniques suitable for imaging the macula and provides a rationale for the use of OCT in this thesis.

1.4.1 Retinal photography

Retinal photography uses a principle similar to ophthalmoscopy. The first retinal photographs were produced in the 1880's, however the first commercial camera was not produced until 1925 by Zeiss (Van Cader, 1978).

Traditionally retinal photography utilised photographic film but now it predominantly uses digital imaging. Retinal cameras typically have a field of view limited to a range between 30 and 60°, although new technologies are capable of more extensive imaging (Csutak et al., 2010). Retinal photography is still principally used to image the posterior pole for the purposes of detection, monitoring or diagnosis of retinal disease. Retinal photographs have been shown to be effective for these purposes in many retinal conditions including AMD (Sperduto et al., 1986; AREDS, 2001a), diabetic retinopathy (Hutchinson et al., 2000), and glaucoma (Detry-Morel et al., 2004).

Additional filters may be used to enhance the types of images produced, e.g. a red-free filter to improve contrast when assessing vasculature. Retinal photography is also used for angiography, where filters are used to enable excitation and imaging of intravenously administered dye (commonly fluorescein or indocyanine green) as it enters and drains from the retinal/ choroidal circulation (Novotny and Alvis, 1961).

1.4.2 Stereo photography

Stereo retinal photography is an adaptation of standard retinal photography where two disparate images are taken of the eye, either simultaneously or sequentially (Van Cader, 1978). These images when viewed binocularly, often with the aid of polarising

filters, provide a stereoscopic view of the retina. Stereo imaging allows an appreciation of depth and height of retinal features, not obtained from standard 2-D photographs. Stereoscopic photography was used for grading in the AREDS (AREDS, 2001a) and International (Bird et al., 1995) AMD grading scales, because it provided depth information which enabled improved identification of specific retinal features.

1.4.3 Scanning laser ophthalmoscopy (SLO)

Scanning laser ophthalmoscopes (SLO) were first described in the 1980's by Webb & Hughes (1981), and later a pinhole aperture was incorporated within the optics to create the confocal SLO (Webb, Hughes and Delori, 1987). The SLO uses a tightly focused laser beam which scans across the retina in a raster pattern, with the laser focused on each spot sequentially. The light reflected or emitted from the laser spot is detected electronically and coded allowing the retinal image to be generated on a computer system. The advantage of this point-by-point system is that it allows imaging through small pupils and media opacities, and requires low levels of illumination.

Commercially available ophthalmic SLO systems include the Heidelberg Retinal Tomograph (HRT, Heidelberg Engineering GmbH, Heidelberg, Germany) and the ultra-wide field Optomap (Optos PLC, Dunfermline, Fife, Scotland, UK). The HRT is intended for detailed assessment of the optic nerve head and macula, producing high contrast topographic images with an axial resolution of ~300 μm and a transverse resolution of ~10μm (Soares and LeBlanc, 2006). The Optomap is capable of imaging into the peripheral retina with a reported field of view of 200°. Unlike the HRT, the Optomap does not enable direct appreciation of depth, although the use of two different wavelength lasers (red and green) provides improved colour contrast and additional depth clues for retinal features based on the relative absorption by these structures of the different wavelength lasers (Kernt et al., 2010).

1.4.4 Optical coherence tomography (OCT)

Optical coherence tomography is a non-invasive optical technique first reported in 1991 (Huang et al., 1991), which utilises low coherence light to measure backscattered (reflected) light from within the imaged structure. The sampling depth is determined by an optical equivalent of the echo time delay in ultrasound, utilising the principles of interferometry, thus allowing depth-reflectivity data points to be obtained longitudinally from within the imaged structure to provide an axial (a) scan. Lateral movement of the

scanning system across the imaged structure enables construction of both 2 (b-scan) and 3 (c-scan) dimensional images comprising multiple adjacent a-scans.

Major advances in the technology since 1991 include the use of broad bandwidth light sources and Frequency Domain (FD) OCT technology. This has made OCT technology a promising imaging technique for the monitoring and diagnosis of retinal disease including AMD (Drexler, 2004). Commercially many ophthalmic OCT systems are available, with the most recent generation capable of axial resolutions of ~5μm and transverse resolutions of ~20 μm (Drexler and Fujimoto, 2008).

Although SLO imaging systems are capable of obtaining better transverse resolutions than OCT, they do not provide a high axial resolution. The OCT was chosen for use in this thesis because it allows high resolution, layer by layer analysis of the retinal structure, which should readily facilitate comparisons with electrophysiological functional parameters. The following sub-sections will consider the principles and characteristics of OCT imaging in more detail.

1.4.4.1 Basic principles

There have been many reviews of OCT in the literature at various stages of its development (Huang et al., 1991; Schmitt, 1999; Drexler, 2004; Brezinski, 2006; Drexler and Fujimoto, 2008). Optical coherence tomography is a complex and rapidly developing technology; the following is an overview of the fundamental principles of OCT imaging.

The basic principles of OCT can be explained with reference to a Michelson interferometer. The interferometer splits light into two equal components using a semi-transparent mirror. Each component is guided along a separate path to a mirror or other reflecting surface, where it is directed back towards the semi-transparent mirror. At the mirror the light is recombined and undergoes interference. The light will have the exact same phase and amplitude when it returns to the mirror provided that both paths are identical in length and optical conditions. Should one or both of the paths be different, for example undergoing a change in amplitude, phase or spectral composition, then the optical properties of the recombined light will also have changed.

In a Michelson interferometer (see figure 1.4.1), assuming that all other properties are equal, increasing or decreasing the distance of one of the mirrors from the light source will change the phase of the light within a given path in relation to the other. Therefore, when the two paths are recombined at the semi-reflecting mirror there will be a phase difference, and the resulting interference will affect the amplitude of the recombined light.

When considering the rules of interference, should the length of the paths be the same, or differ by a whole number of wavelengths, then constructive interference will occur. But when the difference in path length is a multiple of half the wavelength, then total destructive interference will occur. The resulting amplitude will either be a maximum or minimum, when these two conditions are met, or an intermediate value, depending on the phase difference between each path.

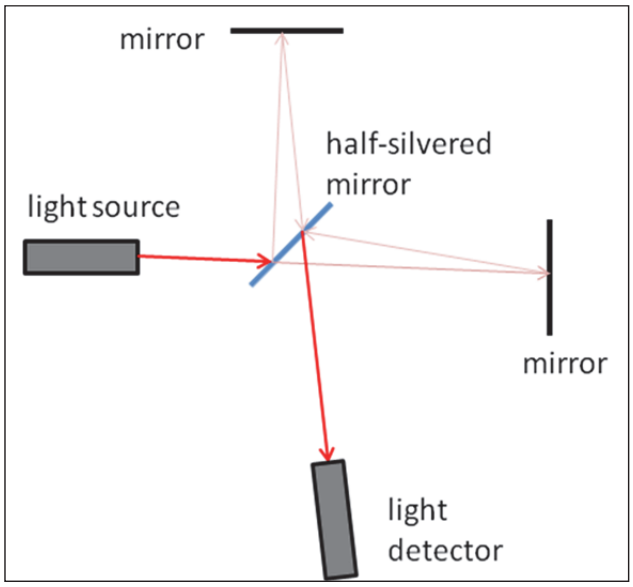

Figure 1.4.1: Schematic diagram of a Michelson interferometer.

If a photodetector is introduced to measure the intensity of the recombined light it is possible to deduce the phase difference between each path of light, caused by increased or decreased distance to one of the mirrors. Additionally, if both mirrors are at a fixed path length, but the reflectivity of one of these mirrors is reduced, the intensity of the recombined light measured by the photodetector would similarly be reduced, and therefore it is possible to calculate the reflectance of this new mirror.

If a pulse of light is now passed through the system, rather than a beam, then the pulse will only coincide and recombine at the semi-reflecting mirror if the difference in path lengths is less than the length of the light pulse. In these circumstances, changing the position of one mirror requires that the location of the second must be changed by the same amount so that the pulses coincide, otherwise only a maximum of 50% of the light will reach the photodetector at one time. As a pulse of light will only coincide when the path lengths are equal, we can determine the distance to a reflecting object of unknown distance by moving the mirror (the so called “reference mirror”) in the second path until a maximum intensity is found at the photo-detector (i.e. over 50%).

For a semi-reflecting sample whose reflectivity changes with depth (for example the retina), it is possible to assess the reflectivity at different depths within the sample (Huang et al., 1991). If the reference mirror is at the correct distance that a pulse of light reflected from a certain layer of the sample coincides at the semi-reflecting mirror we get a signal at the photodetector greater than 50% intensity, corresponding to that layer. All light reflected from material at different optical distances will not coincide with the reference pulse. By moving the reference mirror, the distance at which the light will need to be reflected from within the sample to coincide with the reference pulse will change; this enables the reflectivity to be assessed at different depths. However, the loss of light intensity due to backscattering and absorption within the sample ultimately limits the depth at which the OCT is able to image successfully (Huang et al., 1991).

1.4.4.2 Broad bandwidth light & axial resolution

The coherence length is a finite distance over which light maintains a degree of coherence, i.e. where different wavelengths remain together and interfere (see figure 1.4.2). Within OCT systems a shorter coherence length enables higher axial resolutions to be achieved, as a greater number of depth-reflectivity measurements can be obtained from a sample without them overlapping. The coherence length is inversely proportional to the spectral bandwidth of the OCT light source used (Drexler, 2004), with the axial resolution being related to the spectral bandwidth of the light source as shown by equation 1.4.1.

Equation 1.4.1: $\Delta z = 2\ln(2)\lambda^2/(\pi\Delta\lambda)$

Where:
Δz is the axial resolution,
$\Delta\lambda$ is the spectral bandwidth of the light source,
λ is the centre wavelength of the light source used for imaging (assuming a Gaussian spectrum).

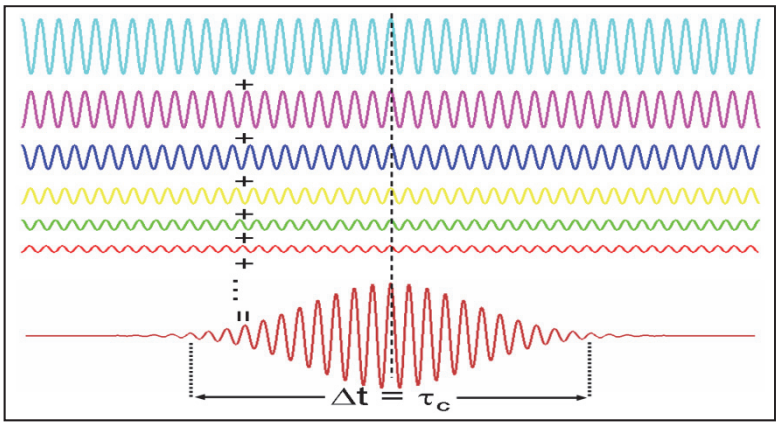

*Figure1.4.2: Representation of a broadband laser and the resulting coherence length (shown as **Δt**) of the pulse produced. Image from Lundeen (2008).*

Therefore, the use of a broader bandwidth light source enables a proportionally higher axial resolution which has facilitated the development of Ultra-High Resolution Optical Coherence Tomography (UHR-OCT) with axial resolutions of 2-3μm (Drexler, 2004; Drexler and Fujimoto, 2008).

Schmitt (1999) identifies “emission in the near infrared”, a “short temporal coherence length” and a “high irradiance” as requirements for an ideal OCT light source. Super luminescent diodes (SLD) are a commonly used OCT light source. SLDs are available with output in the near infrared, a high irradiance and are relatively cheap to manufacture, although suffer from a wide coherence length, limiting the axial resolution (Schmitt, 1999). The UHR-OCT requirement for short coherence lengths has led to the use of femtosecond titanium-sapphire lasers (Drexler, 2004; Drexler and Fujimoto, 2008). These light sources, however, require greater power and are less portable than the traditional SLD (Schmitt, 1999). The advances in SLD light sources, such as multiplexed SLD (multiple spectrally displaced SLD’s which are combined to produce a broad bandwidth output) (Drexler and Fujimoto, 2008), have enabled imaging approaching the resolution of femtosecond lasers (Adler et al., 2004; Ko et al., 2004).

1.4.4.3 Frequency domain OCT (FD-OCT)

OCT systems where the individual reflectivity data points are collected by manual adjustment of the reference mirror is known as Time Domain OCT (TD-OCT). The need for mechanical movement within the system means acquisition speeds are limited (Drexler, 2004) and as a result the acquisition of enough data points to construct UHR images or 3D

constructs is restricted. This represented one of biggest limitations in the early commercial OCT systems.

An alternative to TD-OCT is a technique known as Frequency Domain OCT (FD-OCT) which has a significant speed and sensitivity advantage compared to the older technique (Drexler and Fujimoto, 2008). Frequency domain OCT uses a stationary reference mirror and measures an entire a-scan simultaneously rather than sequentially. The depth resolved reflectivity profile of the a-scan can be determined from interferometric information obtained by either using a spectrometer and high speed charged coupled device (Spectral/Fourier Domain OCT) or a frequency swept light source with a photodetector (Swept Source OCT). The interferometric information obtained by both of these techniques is processed by computer systems using Fourier transforms (Van Velthoven et al., 2007) to produce the a-scans which comprise the OCT images. The utilisation of FD-OCT acquisition techniques has resulted in much improved acquisition speeds (Drexler, 2004; Povazay et al., 2007b; Van Velthoven et al., 2007; Drexler and Fujimoto, 2008) and has led to the realisation of clinically useful three dimensional scans (Drexler, 2004; Schmidt-Erfurth et al., 2005; Drexler and Fujimoto, 2008).

1.4.4.4 Adaptive optics

Optical coherence tomography achieves a high axial image resolution which, unlike traditional microscopy, is independent of transverse resolution (Drexler and Fujimoto, 2008). The transverse resolution in OCT is determined by the focal spot size, as in traditional microscopy, however this is limited in ophthalmic imaging due to dispersion and aberrations in the eye (Drexler, 2004; Drexler and Fujimoto, 2008).

Adaptive optics (AO) can correct for aberrations, such as those in the eye (e.g. coma, spherical aberration), which has the effect of decreasing the focal spot size in OCT, improving transverse resolution. This process is achieved by monitoring the returning wave front electronically in real time with computer manipulation of a deformable mirror correcting for the aberrations in the wave front, thus allowing a tighter point focus and a reduced point spread function (Van Velthoven et al., 2007).

The first reported use of AO in OCT technology was made by Hermann et al.(2004), who used an adaptive optics technique within an UHR-OCT. The AO UHR-OCT demonstrated an improvement in transverse resolution from ~15-20 μm to 5-10 μm in retinal imaging, without an associated loss in axial resolution. Adaptive optics in combination with UHR-OCT is still in its infancy with the potential for near cellular

resolution making it a promising development. The balance between the clinical benefits and technical complexities of this technology has not yet been fully assessed (Drexler and Fujimoto, 2008), and no commercial OCT has incorporated AO at this time.

1.4.4.5 OCT Wavelength

Traditionally, OCT imaging has been undertaken using near infra-red light sources, with a bandwidth based around 800 nm having been used in most FD-OCT systems (Drexler and Fujimoto, 2008). When imaging using an 800 nm light source, the presence of ocular opacities can degrade the image quality (an important factor to consider when imaging elderly individuals), whilst the high levels of light scatter within the retinal tissue and absorption of light by the RPE results in limited visualisation of sub RPE layers, such as the choriocapillaris (Unterhuber et al., 2005; Povazay et al., 2007a; Povazay et al., 2009).

Recent developments have seen the use of light sources in the 1060 nm region, which have been shown to allow deeper penetration into the choroidal tissue and a better signal-to-noise ratio in the presence of media opacities (Povazay et al., 2003; Unterhuber et al., 2005; Povazay et al., 2007a; Povazay et al., 2009).

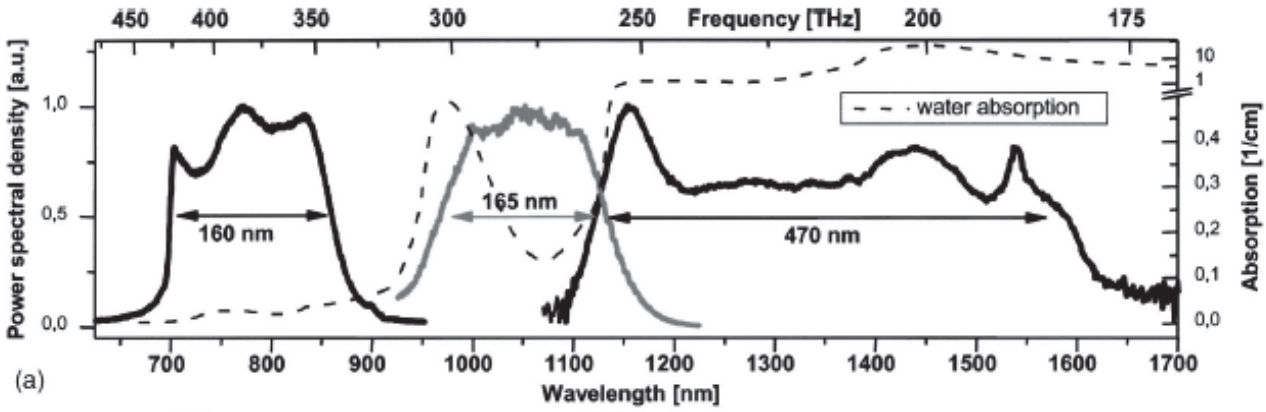

Figure 1.4.3: Output spectra of a ~800 nm Ti:sapphire laser (thin black line left), ~ 1050 nm PCF-based light source (gray line), and a long wavelength MenloSystems laser (black line, right), overlaid with a water absorption spectrum (dashed line). Image from Drexler (2004).

In order to image the retina of a human eye the imaging beam has to pass twice through the cornea, lens and vitreous which, given the increased absorption of water at longer wavelengths, limits the available wavelengths for ophthalmic imaging (Unterhuber

et al., 2005). The water absorption spectrum has two regions where the absorption is low, the first includes the visible range up to ~950 μm, and the second is a narrow band between ~1000 μm and ~1100 μm (Drexler and Fujimoto, 2008). Figure 1.4.3 (Drexler, 2004) shows 3 different lasers with the water absorption overlaid, it can be seen that only two of the 3 lasers would be suitable for ophthalmic imaging, those corresponding to water absorption minima with wavelengths of ~800 μm and ~1050 μm.

1.4.4.6 Imaging terminology

The increasing use of OCT systems, particularly for ophthalmic purposes, has led to the evolution of common terminology to describe types of image and their components; some of the most commonly used terms are described in table 1.4.1. The terms and definitions described have been used throughout this thesis. It should be noted that the data points which comprise the retinal volumes are termed voxels due to their location in three dimensional spaces, in this thesis images were all analysed and measured in two dimensions on a visual display unit (VDU) and have, therefore, been referred to as pixels throughout.

Imaging Term (s)	Definition
Pixel	A pixel represents an individual data point within an OCT image, comprising location and reflectivity (backscatter intensity) information, commonly based on either a colour or black/white value scale. A pixel technically represents location in only 2 dimensions (an x & y axis scale) and is usually used to describe OCT data points as viewed on a VDU. The minimum dimensions of each individual pixel (or Voxel) are determined by the axial and transverse resolution of the OCT system.
Voxel	A Voxel is the same as a pixel with the exception that the location is represented in 3 dimensions (an x, y & z axis scale).
a-scan	The a-scan is analogous to an ultrasound a-scan. It is a representation of reflectivity (backscatter intensity) with depth, comprising a series of adjacent pixels at increasing depth within the sample (i.e. the retina).
b-scan (cross section / 2D section)	The b-scan is analogous to an ultrasound b-scan and is comprised of adjacent a-scans to produce a 2-D cross-section through the sample.
c-scan (retinal volume / 3D volume)	A c-scan is stack of adjacent b-scans, which can be viewed as a 3D volume.

Table 1.4.1: Definitions of terms commonly used to describe ophthalmic OCT images and their composition.

Less common terms are also encountered in the literature, for example a temporal scan (m-scan), is one in which a single image is repeatedly acquired at the same location, in order to track changes over time (Bizheva et al., 2006).

1.4.4.7 OCT imaging and histology

Optical coherence tomography images comprise tomograms with various bands of high and low reflectivity, depending on the reflectivity of the structure the imaging laser interacts with as the image is produced. As a clinical tool it is necessary to identify what structures these reflective bands represent in the retina. Studies have been carried out which have directly compared OCT images to histology (Huang et al., 1991; Toth et al., 1997; Huang et al., 1998; Chauhan and Marshall, 1999; Gloesmann et al., 2003; Anger et al., 2004).

Gloesmann et al. (2003) and Anger et al. (2004) conducted studies which compared UHR-OCT tomograms directly to histology in pig and monkey retinas respectively. Although previous studies compared histology to OCT (Huang et al., 1991; Toth et al., 1997; Chauhan and Marshall, 1999), these used older TD-OCT systems where the axial resolution made comparison of intra-retinal layers to histology ambiguous at best (Anger et al., 2004).

Anger et al. (2004) conducted a systematic comparison of histological sections to OCT tomograms from *Macaca Fascicularis* monkeys. In order to overcome non-linear distortions which originate from the dehydration and sectioning stress involved in histology preparation, a 'metamorphosis' computer program was used to correct for these distortions and to make images comparable to the UHR-OCT tomograms in the study. To ensure these "morphing" procedures scaled the histological images correctly, a series of unequivocal points were selected to correspond on both the UHR-OCT and histology images, for example blood vessels or the inner limiting membrane. This study was able to directly relate the hyper-reflective bands from the OCT tomograms to the retinal layers identified by histology. Figure 1.4.4 demonstrates the relationship between individual retinal layers at the macula from histology and UHR-OCT.

1060 nm OCT enables a greater depth of imaging and improved penetration through media opacity due to the reduced reflectivity of ocular media to 1060 nm light (Povazay et al., 2003; Drexler, 2004; Unterhuber et al., 2005; Povazay et al., 2007a; Drexler and Fujimoto, 2008; Povazay et al., 2009). The difference in reflectivity of the retinal structures to the 1060 nm laser compared to the traditional 800 nm may affect the identification of the structures in 1060 nm OCT images. Chen et al. (2009) compared images obtained from 1060 nm and 845 nm OCT systems. This study found that the visible layers in the images were comparable to the histological retinal layers for both systems; however the relative intensity of the individual retinal layers was different

between the two OCT systems. For retinal layers anterior to the RPE the contrast was reduced in 1060 nm images relative to 845 nm, however those located posterior to the RPE underwent an increase in contrast with the longer wavelength system, improving their visibility (see figure 1.4.5).

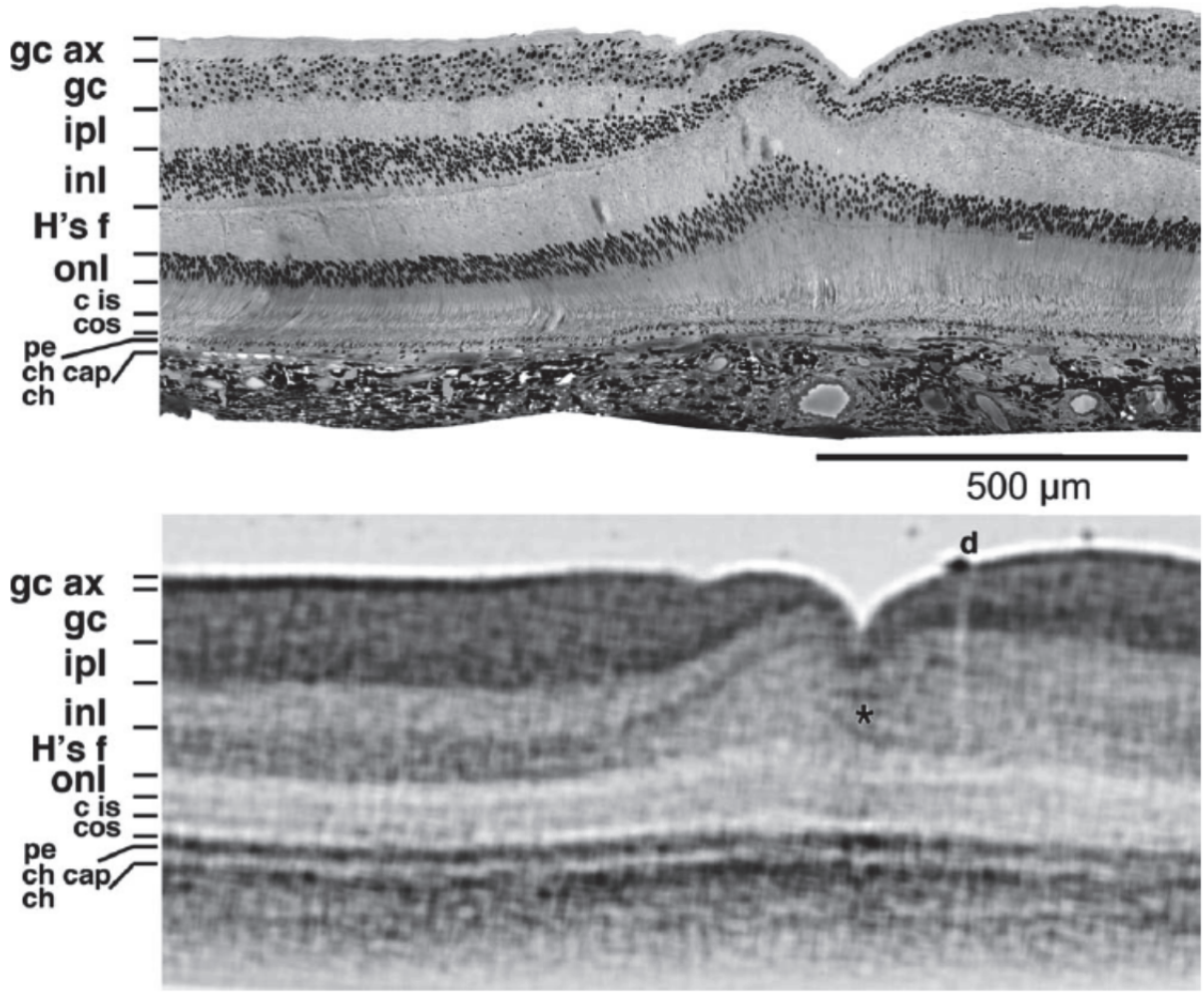

Figure 1.4.4: A comparison of a foveal semi-thin histological section (top) and corresponding UHR-OCT b-scan (bottom, note reverse contrast to traditional OCT greyscale to facilitate comparison). Major retinal sublayers are distinguishable and are labelled as follows: ***gc ax****, ganglion cell axon layer;* ***gc****, ganglion cells;* ***ipl****, inner plexiform layer;* ***inl****, inner nuclear layer;* ***H's f****, Henle's fibres;* ***onl****, Outer nuclear layer;* ***cis/cos****, photoreceptor inner/outer segments;* ***pe****, Pigment epithelial layer;* ***ch cap****, choriocapillaris;* ***ch****, choroid; asterisk (****), darker faults in foveal floor indicative of foveal strain;* ***d****, epi-retinal debris producing negative shadow. Image from Anger et al. (2004).*

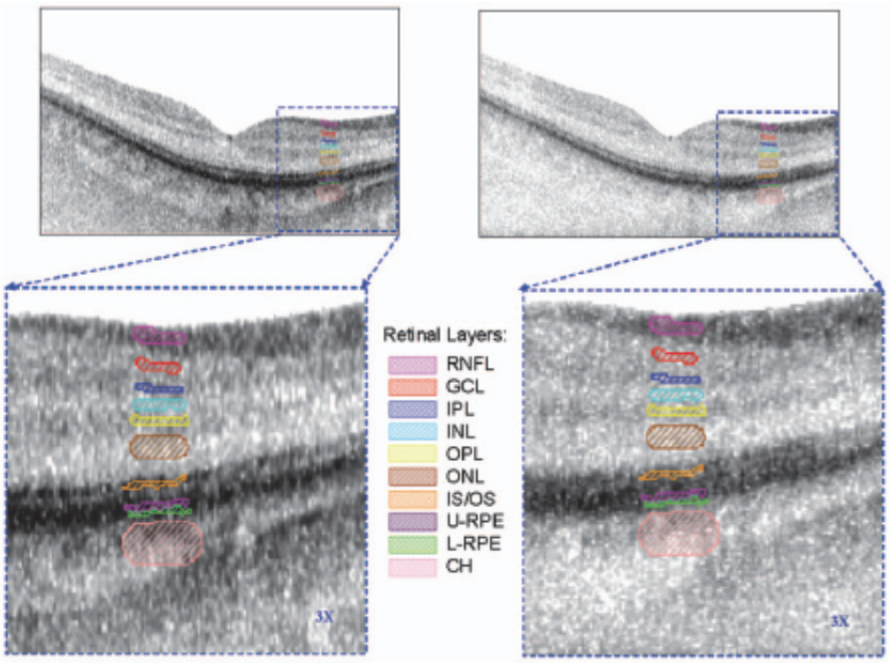

Figure 1.4.5: A pointwise matched frame of a 1060 nm OCT b-scan (Left) and a 845 nm OCT b-scan (Right) with corresponding retinal layers identified. Image from Chen et al. (2009).

1.4.4.8 Commercial OCT and analysis software

The first commercially available OCT system was a TD-OCT released in 1996 by Zeiss with a 10 μm resolution and scan rate of 100 a-scans/s (Drexler and Fujimoto, 2008). Since 1996, OCT technology has advanced, for example with the advent of FD-OCT which has eventually become available as part of newer commercially available OCT systems. The latest generation of OCT comprises a range of competing systems, which share similar axial resolutions of 5-7 μm and imaging speeds of ~25,000 a-scans/s, based on ~800 nm light sources (Drexler and Fujimoto, 2008), for example the Cirrus OCT system (Carl Zeiss, Meditec Inc, CA).

Commercially available systems, unlike research based systems, are required to be easy to use and to allow speedy presentation of clinically relevant data to the clinician. As a result, commercial systems contain software designed to aid the clinician in image acquisition and processing. The software provided with these commercial devices is able to provide the clinician with both qualitative data, through image viewing tools, and quantitative information derived from automated segmentation of the OCT images.

Automated segmentation is an important feature of commercial OCT systems, allowing rapid identification of the boundaries between retinal layers so that thicknesses,

areas and volumes may be calculated. Automated segmentation of the ILM and RPE layers allows retinal thickness to be calculated and is a standard feature of most commercial OCT systems. Although automated segmentation has been shown to be a reliable and accurate method of rapidly assessing macular thickness in healthy eyes, the evidence suggests that automated segmentation is less accurate in diseases such as AMD, where retinal structures become disorganised, than manual segmentation techniques (Menke and Feke, 2005; Sadda et al., 2006; Krebs et al., 2008; Ghazi et al., 2009; Keane et al., 2009; Taban et al., 2009; Sadda et al., 2010).

Study & participant details	OCT system and measurement type	Reported retinal thickness values
Ikuno et al. 2009 Myopic eyes (n=31), 51.7 ± 11.4 years (-6 to -23 D)	Cirrus HD-OCT (Carl Zeiss Meditec, Inc.). Manual	Fovea 201.2 ± 40.6 µm
Legaretta et al 2008 Normal eyes (n=50), 22 to 68 years.	Cirrus HD-OCT (Carl Zeiss Meditec, Inc.) Automated Stratus TD-OCT (Carl Zeiss Meditec, Inc.) Automated	Foveal (500µm)* 258.2 ± 23.5 µm Foveal (500µm)* 212 ± 20 µm
Grover et al. 2010 Normal eyes (n=36), 20 to 69 years.	Spectralis SD-OCT (Heidelberg Engineering, Heidelberg, Germany) Automated Stratus TD-OCT (Carl Zeiss Meditec, Inc.) Automated	Foveal (500µm)* 271.4 µm Foveal (500µm)* 202.3 µm
Kakinoki et al. 2008 Normal eyes (n=50), 49.9 ±18 years.	Cirrus HD-OCT (Carl Zeiss Meditec, Inc.) Automated Stratus TD-OCT (Carl Zeiss Meditec, Inc.) Automated	Foveal (500µm)* 257.6 ± 19.6 µm Foveal (500µm)* 197.2 ± 17.8 µm
Cheng et al. 2010 Myopic (n=30; -6.00 to -13.63 DS, mean age 22.73) and non-myopic eyes (n=31; +2,75 to -0.50 DS, mean age 23.26),	Stratus TD-OCT (Carl Zeiss Meditec, Inc.) Automated	Myopic Fovea 162 ± 19.21 µm Myopic Fovea (500 µm)* 199 ± 17.27 µm Normal Fovea 149 ± 11.80 µm Normal Fovea (500 µm)* 191 ± 12.37 µm

*Table 1.4.2: Comparison of normal foveal thickness values from recent literature. * 500 µm refers to radius of ETDRS grid central subfield.*

Automated segmentation applied by different commercially available systems has been shown to produce different thickness values. Retinal thickness assessed using the older Stratus (TD-OCT; Carl Zeiss, Meditec Inc, CA) has been shown to produce lower values (~50 μm) than the newer Cirrus (FD-OCT; Carl Zeiss, Meditec Inc, CA) system in healthy subjects (Legarreta et al., 2008; Kakinoki et al., 2009). Legaretta et al. (2008) identified the inclusion of the photoreceptor layer within the retinal thickness measurement as the determining factor for this difference, facilitated by the increased resolution of the Cirrus. Kakinoki et al. (2009) drew attention to the potential pitfalls of comparing thickness values between different OCT systems. Table 1.4.2 describes a number of recent studies which have produce normative retinal thickness values using commercially available OCT systems. A more extensive list of OCT derived normative values including eccentric retinal locations, and intra-retinal and choroid layer thicknesses are given in Appendix F.

1.5 Assessment of visual function

Visual function can be assessed using psychophysical or electrophysiological methods. This section considers a range of psychophysical and electrophysiological approaches to the assessment of retinal function, with an emphasis on those techniques which assess macular function.

1.5.1 Visual psychophysics

The most common type of psychophysical tests carried out is where a detection threshold is determined for a specific visual stimulus. Because the responses are subjective, the threshold levels are usually calculated using probabilistic methods. A range of methods to estimate visual perception thresholds exist, which vary in the control of the stimulus properties, the method of presentation and type of subjective response required (Kalloniatis and Luu, 2005).

The psychophysical tests used to assess visual function in AMD may be divided into five broad categories, which comprise spatial vision, temporal vision, visual adaptation, visual field testing and chromatic function (Neelam et al., 2009); the following sections will discuss psychophysical tests within these categories.

1.5.1.1 Spatial vision

Spatial vision is concerned with how patterned stimuli are interpreted by the visual system. It is commonly assessed by way of visual acuity (VA), contrast sensitivity (CS) and reading speed or accuracy.

Visual acuity is the highest spatial frequency that can be detected by the visual system at 100% contrast (Owsley, 2003). Visual acuity is considered to be the standard test of visual function, and is most commonly assessed using a Snellen chart (Neelam et al., 2009). Visual acuity is commonly expressed as a Snellen fraction, comprising the test distance as the numerator, and the distance at which a just resolvable optotype should be positioned to subtend 5' arc at the eye as the denominator. Visual acuity is now commonly recorded using LogMAR notation, which expresses the VA as the logarithm of the minimum angle of resolution. Test charts using the LogMAR notation, for example, the Bailey-Lovie and the early treatment diabetic retinopathy study (ETDRS) acuity charts, have additionally been designed to avoid problems associated with the traditional Snellen charts such as unequal visual tasks, i.e. varying number of letters per line and crowding between letter on each line and truncation of high and low acuity tasks (Bailey and Lovie, 1976), resulting in better reproducibility and sensitivity (Ferris et al., 1982; Lovie-Kitchin, 1988).

Contrast is defined as the difference in luminance between a target and its background expressed as a percentage of mean background luminance. The amount of contrast required to identify an object or border is the contrast threshold, in the human visual system it is often referred to as the contrast sensitivity (reciprocal of threshold) (Owsley, 2003). Contrast sensitivity varies according to the spatial frequency of the object or border being observed. The typical contrast sensitivity function, which describes the relationship between contrast sensitivity and spatial frequency, is shown for a normal subject in figure 1.5.1. Contrast sensitivity can be assessed using sine wave gratings, presented on a VDU, where the contrast and spatial properties of the alternating stripes (gratings) presented can easily be varied. However, clinical optotype charts, such as the Pelli-Robson chart (Pelli, Robson and Wilkins, 1988), are more practical and provide a test method likely to be more familiar to the patient.

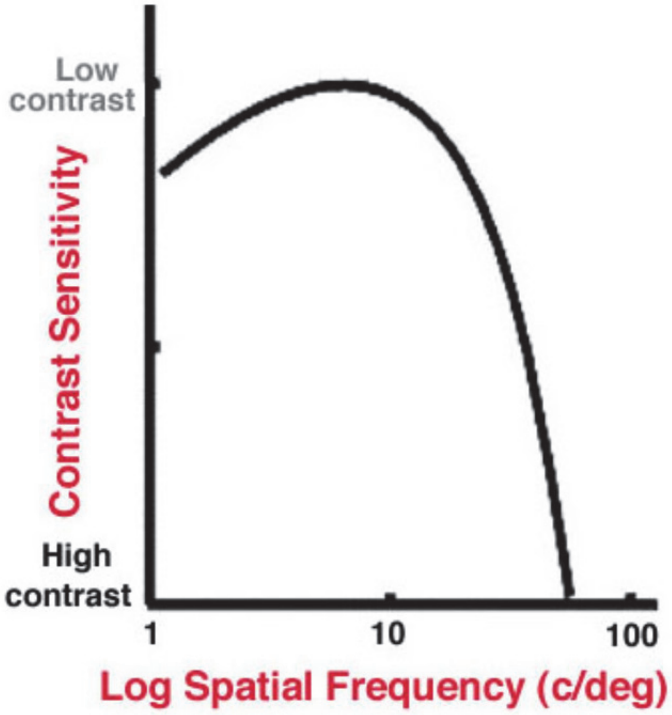

Figure 1.5.1: The photopic spatial contrast sensitivity function (CSF) showing a peak in sensitivity for the mid spatial frequency range, with a rapid fall off towards high spatial frequencies and mild roll off towards low spatial frequencies. Image from Kalloniatis and Luu (2005).

1.5.1.2 Temporal vision

Temporal vision is concerned with how a flickering stimulus, which may be non-periodic, is interpreted by the visual system. Intermittent stimuli are perceived by the eye as flicker; however when the temporal frequency reaches the 'critical flicker frequency' (CFF) the visual system is no longer able to perceive the flickering. The temporal contrast sensitivity (TCS) function described the modulation depth (temporal contrast) required to detect flicker at different temporal frequencies (see figure 1.5.2). It can be thought of as analogous to the spatial CSF, where the function describes the limits of the visual system with respect to contrast and frequency. The CFF is equivalent to visual acuity in the spatial domain, i.e. the maximum temporal frequency detectable at maximum contrast (Neelam et al., 2009).

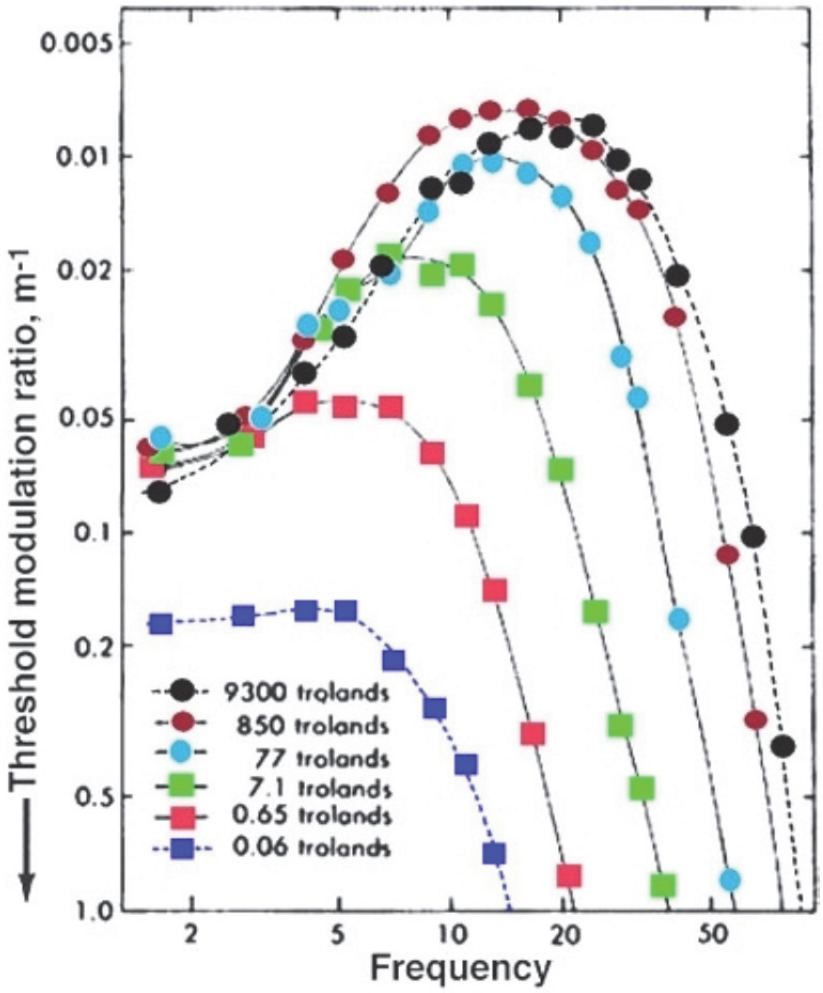

Figure 1.5.2: The Temporal Contrast Sensitivity (TCS) function where the "threshold modulation ratio" is a measure of stimulus contrast, smaller values indicating a lower stimulus contrast, and "frequency" refers to the temporal frequency (Hz) of the stimulus. At photopic luminances, sensitivity is greatest at stimulus frequencies of 15 to 20 Hz, whilst the upper temporal frequency cut off is approximately 60 Hz at maximum contrast. Lower luminance levels (scotopic) show a shift in the upper temporal frequency cut off towards a lower temporal frequency and a reduction in the overall height of the function. Image adapted from Hart (1987).

The TCS function demonstrates that the eye is capable of responding to flicker at temporal frequencies of up to 80 Hz (Brown and Lovie-Kitchin, 1987). The detection of frequencies below ~25 Hz is mediated by both the rod and cone photoreceptors whilst responses to higher frequencies are dominated by the cone photoreceptors (Skottun, Nordby and Magnussen, 1981).

Flickering stimuli are known to increase the neural activity and metabolic demand within the stimulated retina, requiring an increase in retinal blood flow (Kiryu et al., 1995). The changes at the outer retina associated with AMD, which include the loss of choriocapillaris, the thickening, and deposition of lipids in Bruch's membrane with resultant reduction in hydraulic conductivity (see section 1.3), and the consequential inhibition of metabolic supply suggest that aspects of temporal vision may be particularly sensitive to AMD (Phipps et al., 2004).

1.5.1.3 Visual adaptation

Visual adaptation is concerned with the eyes ability to adapt to a range of luminances and can be assessed by monitoring dark adaptation.

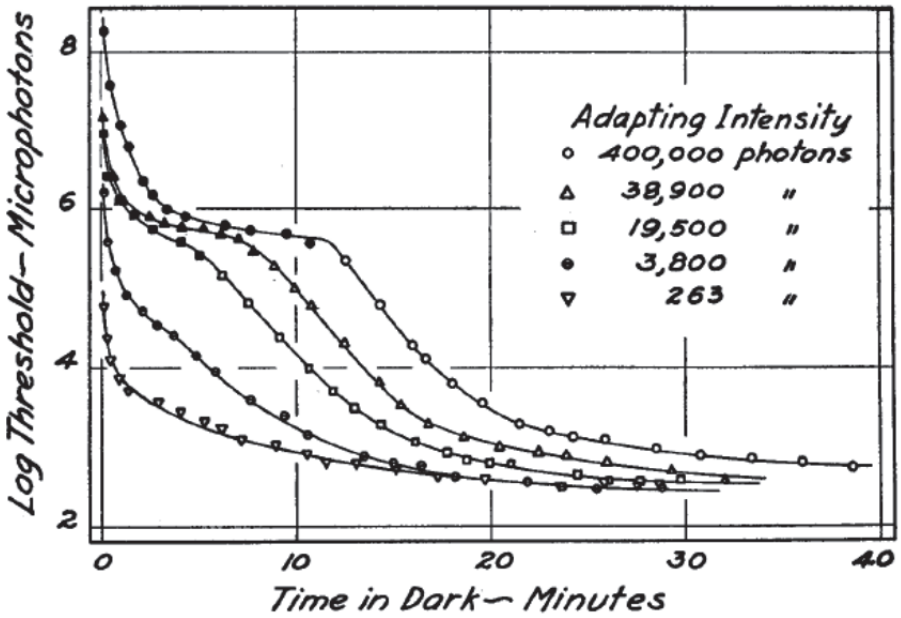

Figure 1.5.3: Dark adaptation functions for a normal subject measured with a violet light following different levels of light adaptation. The solid symbols indicate that a violet colour was apparent at the threshold representing cone mediated sensitivity, whilst empty symbols indicate absence of colour appreciation representing rod mediated sensitivity. Figure from Hecht, Haig and Chase (1937).

Dark adaptation is the slow recovery of retinal sensitivity following exposure of the retina to a light that bleaches a significant proportion of visual pigment (Lamb and Pugh, 2004) (see section 1.2.8 for overview of kinetics of photopigment regeneration). The dark adaptation function describes the drop in threshold which occurs over time in the dark after cessation of a bleaching light (see figure 1.5.3). Classically, there are two distinct periods

of sensitivity recovery, cone and rod, separated by a transition known as the rod-cone break. The recovery of rod sensitivity begins at light cessation, but the cone system shows a faster recovery, and initially has lower thresholds than the rod system and therefore dominate the subjective response at early time points (Lamb and Pugh, 2004).

1.5.1.4 Visual field testing

Visual field testing is concerned with the eyes' ability to detect the presence of stimuli at different retinal locations. The visual field normally extends to ~ 110° temporally, ~65° nasally, ~60° superiorly and ~75° inferiorly (Henson, 2000). Visual field assessment usually takes the form of visual threshold testing at a range of distinct retinal locations (commonly called perimetry).

Amsler grids are a series of grid patterns presented monocularly to patients at a fixed viewing distance. The patient is asked a series of questions, the answers of which describe the perceived integrity of the grid and therefore subjectively identify the location and extent of any central visual field abnormalities (Elliott, 2007). Amsler grids are commonly used clinically to identify visual field abnormalities in the macular region, although evidence suggests that they are relatively insensitive to many central visual field defects (Schuchard, 1993).

1.5.1.5 Chromatic function

This type of psychophysical assessment is concerned with the eye's ability to discriminate between stimuli with different spectral (colour) composition regardless of other visual attributes. Colour vision can be assessed by various methods including colour matching, discrimination arrangement and sensitivity (Neelam et al., 2009). Tests of colour discrimination and arrangement include the Farnsworth-Munsell 100 Hue test and the D-15 saturated and desaturated tests. Isochromatic plates are used as part of the Ishihara colour vision test but this approach is limited to the detection of red-green defects.

1.5.2 Electrophysiology

The visual system comprises many different cell types from the retina to the visual cortex, which carry out different functional roles. Electrophysiological techniques can be used to record the electrical changes these cells undergo in response to different visual stimuli. Although external sensors are only able to measure the summed activity of cells, for example in the retina, different groups of cells in the visual pathway become active at

different times after a stimulus is presented. Experimental techniques can be used to identify the underlying physiological processes which produce different components of the electrophysiological responses, for example by using pharmacological agents to block activity of different neurone types. The components of these responses can often then be attributed to specific cell types within the visual system (Granit, 1933; Bush and Sieving, 1994; Frishman, 2006) and hence can be used to as a means to assess visual function on a 'layer by layer' basis.

The International Society for Clinical Electrophysiology of Vision (ISCEV) was established to promote global comparability and standardisation of electrodiagnostic techniques, for which it has developed and published standards for the recording of a range of electrodiagnostic tests. These electrodiagnostic techniques are commonly used within the Hospital Eye Service for the assessment and diagnosis of a range of conditions including congenital stationary night blindness, retinitis pigmentosa, Bests disease, rod and cone dystrophies and albinism (Weisinger, Vingrys and Sinclair, 1996). Standards or guidelines currently exist for electroretinograms (ERG) (Marmor et al., 2009), multi-focal electroretinograms (mfERGs) (Hood et al., 2008), electro-oculograms (EOG) (Brown et al., 2006), pattern electroretinograms (PERG) (Holder et al., 2007) and cortical visual evoked potentials (VEP) (Odom et al., 2010). Guidelines for equipment setup and calibration have also been published (Brigell et al., 2003).

1.5.2.1 Electro-oculogram (EOG)

The electro-oculogram (EOG) is an electrophysiological technique used to assess the slow changes in the standing potential of the eye during light and dark adaptation, which are attributable to changes in voltage across the RPE basal membrane (the trans-epithelial potential). The normal EOG relies on the integrity of both the RPE and the photoreceptors, as it is a reduction in sub retinal potassium (K+) due to a light evoked closure of the cation channels in photoreceptor outer segments which is indirectly responsible for changes in the transepithelial potential recorded by the EOG (Joseph and Miller, 1992). The most common use of this technique is for the diagnosis of Best's vitelliform dystrophy (Marmor and Zrenner, 2006).

1.5.2.2 Visual evoked potential (VEP)

The visual evoked potential (VEP) and multi-focal visual evoked potential (mfVEP) record electrical potentials generated by the occipital cortex. The VEP is recorded in

response to stimulation of the central 15 – 20° of the visual field whereas the mfVEP enables simultaneous recording from different regions within the visual field. The VEPs can show the integrity of the whole visual system; as the signals from the stimulated retina are required to travel the length of the visual pathway to the occipital cortex, any defects within the visual pathway may change the waveform or latency of the VEP response (Fahle and Bach, 2006). Conversely, the localisation of an abnormal response may be complicated as the causative lesion may exist at any point along the visual pathway. Furthermore, due to the disproportionate representation of the macula in the primary visual cortex (cortical magnification) the response is dominated by signals originating from the central retina. The VEP is recorded by electrodes placed on the scalp overlying the occipital cortex, guidelines have been published regarding stimulus and recording protocols for standard VEPs (Odom et al., 2010).

1.5.2.3 Multi-focal electroretinogram (mfERG)

Conventional ERG waveforms represents the summed electrical potentials from across the entire stimulated retina, whereas multi-focal electroretinograms (mfERGs) use a complex display system in combination with a selective extraction process to isolate localised retinal activity (Bearse and Sutter, 1996).

The stimulus used for mfERGs typically comprise an array of 61 or 103 hexagons with each hexagon scaled in size to produce an approximately equivalent amplitude response from each retinal area stimulated. The hexagons are presented in a pseudo-random stimulus pattern (called an M-sequence), with each hexagon being either white or black at any one time and starting at a different point in the m-sequence (Hood et al., 2012). A continuous ERG is recorded, using a similar setup as for recording standard full field ERGs. Computer analysis is used to isolate the individual responses elicited by each hexagonal stimulus region, based on the cross-correlation of the stimulus sequence and the recorded ERG. The mfERG is a cone driven response, without a rod contribution, and typically is recorded for a central retinal area of between 20 and 30° (Hood et al., 2012).

The extracted waveform for each hexagonal stimulus is called the basic mfERG response (or first-order kernel) and comprises 3 peaks, the first a negative wave, followed by a positive then a second negative referred to as N1, P1 and N2, respectively (see figure 1.5.4). The peak N1 is understood to be derived from the same cells that contribute to the a-wave of the full-field cone ERG, whilst P1 receives contributions from the cells attributed to the cone b-wave and oscillatory potentials (Hood et al., 2008).

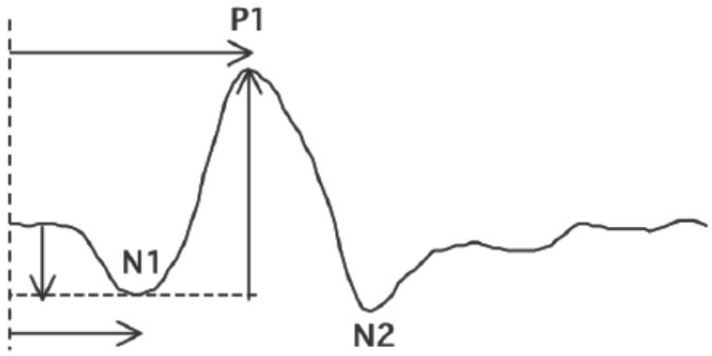

Figure 1.5.4: A basic mfERG waveform (first-order kernel) with peaks N1, P1 and N2 shown. Image from Hood et al. (2008).

1.5.2.4 Electroretinogram (ERG)

The ERG is an electrophysiological signal derived from the retina in response to light stimulation. Electroretinograms are usually recorded using an electrode (active) placed in contact with the test eye and a second electrode (reference) attached to the head or the non-test eye. Differential amplification is then used to isolate the light evoked response from the test eye. A single flash of light will evoke a transient ERG, which is highly repeatable. The ERG waveform comprises a series of major subcomponents known as the a, b and d waves, the photopic negative response (PhNR) and oscillatory potentials (OPs) (see figure1.5.5 and 1.5.6), however, not all subcomponents are visible in all flash ERGs. The waveform characteristics depend on the stimulus used and the state of retinal adaptation, with stimulus, duration, luminance, wavelength, location and extent all known to affect the resultant waveform by affecting the response of different cell types within the stimulated retina (Frishman, 2006).

A flickering stimulus evokes a flicker ERG (sometimes called a steady state ERG) which has a characteristic repeating waveform comprising positive to negative oscillations that match the temporal frequency of the stimulus. Patterned stimuli may also be used, often a reversing black and white checker board, to evoke a pattern electroretinogram (Holder et al., 2007).

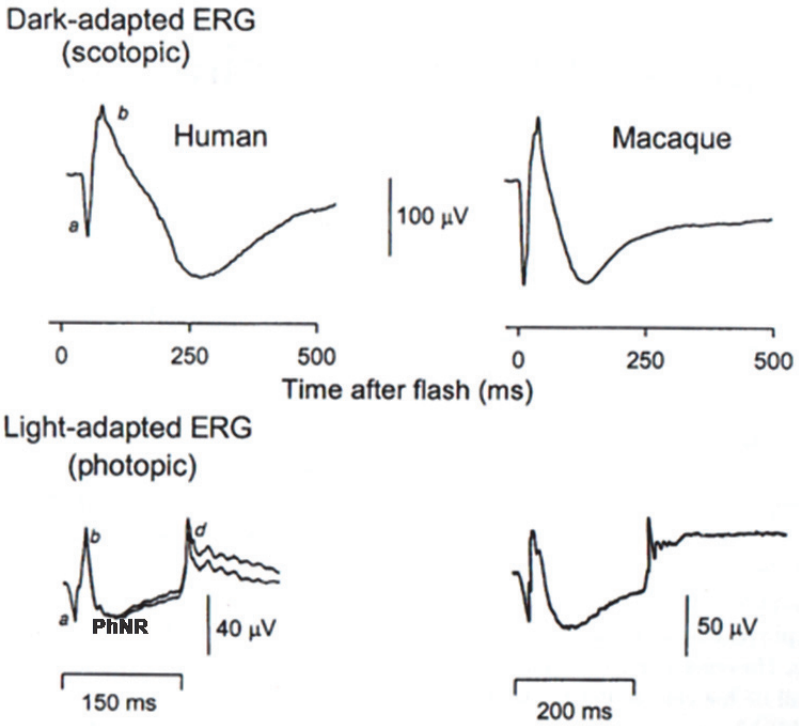

Figure 1.5.5: Diagrammatic representation of ERGs recorded from human (left) and macaque monkeys (right). Dark adapted (scotopic) ERGs recorded in response to a brief flash, with a and b waves labelled (top). Light adapted (photopic) ERGs recorded in response to a 150 ms and 200 ms duration flash (human and macaque respectively) with a, b, PhNR and d wave labelled (bottom). Image adapted from Frishman (2006).

ISCEV have published standards for the recording of 5 standard ERG responses, including a combination of full field transient and flicker ERGs, the characteristic responses are described in figure 1.5.6 (Marmor et al., 2009).

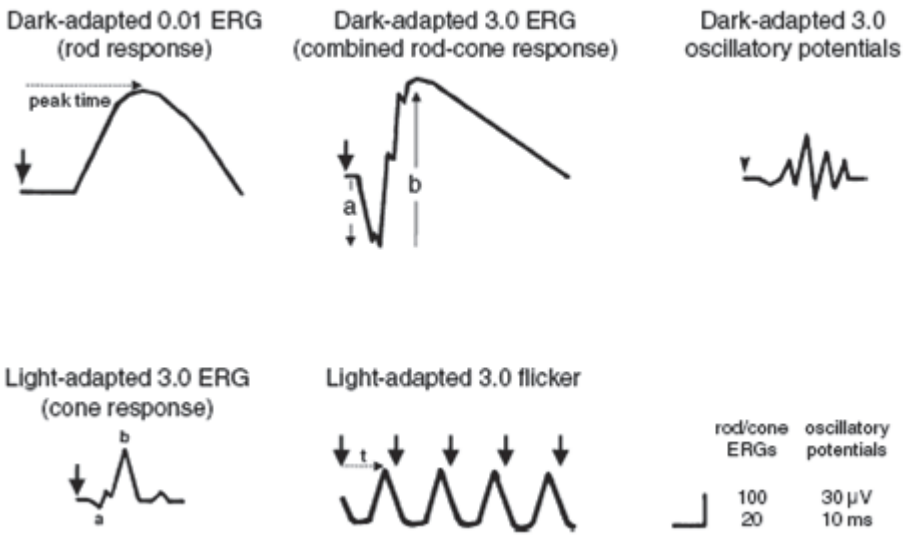

Figure 1.5.6: Diagrammatic representations of the standard ISCEV ERG responses. Large arrow heads indicate the stimulus flash, dotted arrows exemplify how to measure time-to-peak (t = implicit time), a-wave amplitude and b-wave amplitude. (1) Dark-adapted 0.01 ERG "rod response" recorded to a weak flash in the dark-adapted eye. (2) Dark-adapted 3.0 ERG "maximal or standard combined rod–cone response" recorded to a strong flash in the dark-adapted eye. (3) Dark-adapted 3.0 oscillatory potentials "oscillatory potentials" recorded to strong flashes in the dark adapted eye with the signal isolated using a 100-1000 Hz band pass filter. (4) Light-adapted 3.0 ERG "single-flash cone response" recorded to a strong flash in the light-adapted eye. (5) Light-adapted 3.0 flicker ERG "30 Hz flicker" recorded to a rapidly repeated stimulus. Image adapted from Marmor et al. (2009).

1.5.3 The Flash Electroretinogram (ERG)

The ERG is a sum combination of all electrical activity within the retina; this activity can be divided into distinct components (peaks and troughs) of different cellular origin that can aid the analysis of the response. Granit (1933) was one of the pioneers in the isolation of the processes underlying the scotopic ERG, with work conducted on the rod dominated cat retina. Granit (1933) used ether, with increasing potency, to sequentially knock out the physiological processes contributing to the scotopic ERG. This approach revealed 3 distinct processes, PI, PII and PIII, numbered according to which disappeared from the ERG waveform first (see figure 1.5.7). PIII has since been subdivided into fast and slow components (Frishman, 2006). The measureable sub-components of ERG are shaped by

these underlying processes. Although PI, PII and PIII are summed to produce the transient ERG, different processes dominate at different times following stimulation.

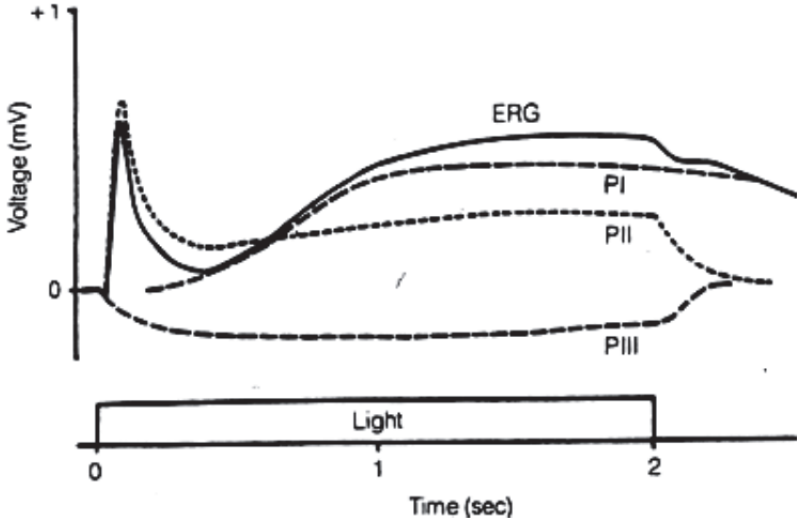

Figure 1.5.7: The scotopic ERG and the three components identified by Granit (1933), PI, PII and PIII. Image adapted from Granit (1933).

1.5.3.1 a-wave

The a-wave is the initial negative deflection of the transient ERG with the leading edge being dependent on the component fast PIII (Granit, 1933; Frishman, 2006). The a-wave amplitude and latency are dependent on the adaptional state of the eye and the strength of the flash stimulus, with scotopic (rod dominated) responses being larger and slower than photopic (cone dominated) responses; however, under both light and dark adapted conditions the amplitude is truncated by the rising b-wave (Frishman, 2006).

It has been shown that the a-wave (and the fast PIII component) predominately reflect the rod and cone photocurrent, with current source density analysis showing a comparable time course and waveform to the rod photoreceptor extracellular current in response to light stimuli (Penn and Hagins, 1969 ; 1972). Pharmacological techniques have further reinforced the photoreceptoral origin of the a-wave. Aspartate, an agonist for the neurotransmitter glutamate, can be used to eliminate synaptic transmission from the photoreceptor cells; when used in monkey retina this was shown to abolish all but a negative going deflection corresponding to the a-wave and comparable to Granit's PIII component (see figure 1.5.8) (Bush and Sieving, 1994). Bush and Sieving (1994) used the more specific L-2-amino-4-phosphonobutyric acid (APB) which blocked the ON-bipolar neurotransmitters, and Cis-2,3-piperidine dicarboxylic acid (PDA) which blocked synaptic transmission to OFF bipolar, horizontal, amacrine and ganglion cells when eliciting ERGs

from the monkey retina. The use of these more specific synaptic inhibitors however, indicated a post-receptoral contribution to the photopic a-wave, this can be appreciated in figure 1.5.8 where the APB only response shows an initially larger negative going response than the Aspartate response in which all post-receptor activity is eliminated.

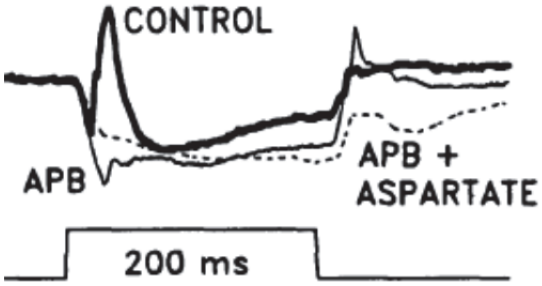

Figure 1.5.8: Comparison of effects intravitreal injection of APB and APB + Aspartate on the monkey ERG in response to a 200 ms flash stimulus. Image from Bush and Sieving (1994).

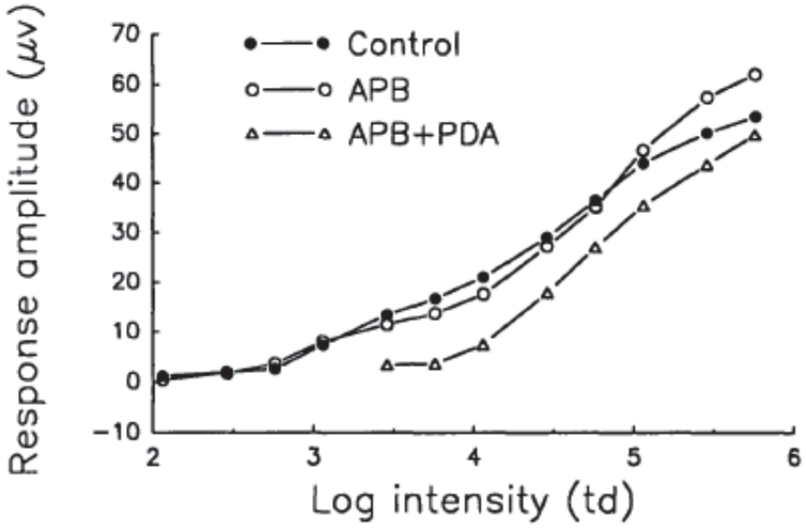

Figure 1.5.9: The photopic a-wave response amplitude plotted against stimulus luminance for a monkey retina with intravitreal injection of APB and APB+PDA up until maximal a-wave amplitude in the control responses. Image from Bush and Sieving (1994).

Bush and Sieving (1994) also investigated the stimulus-response relationship of the photopic a-wave over an intensity range extending up to the maximum response amplitude in the control monkey retina, and compared this to a APB and APB+PDA treated retina. A relative increase in amplitude of the response treated with APB+PDA indicated a reducing influence of inner retinal contributions on the a-wave amplitude at high stimulus levels (see

figure 1.5.9). These findings suggest that the photopic a-wave reflects both cone photoreceptor activity and a component of the cone inner retinal pathway. It has been suggested that this inner retinal contribution originates in the OFF-pathway (Bush and Sieving, 1994), in particular the amacrine and retinal ganglion cells, as NMDA (N-methyl-D-aspartate) treated retina, which selectively blocks these neurones, demonstrates similarly reduced photopic a-wave responses (Frishman, 2006).

1.5.3.2 b-wave

The b-wave is the dominant positive deflection within the transient ERG, with the peak being dependent upon the PII process (Granit, 1933). It is generally accepted that the b-wave reflects the activity of depolarising bipolar cells (Knapp and Schiller, 1984; Stockton and Slaughter, 1989; Gurevich and Slaughter, 1993; Xu and Karwoski, 1994; Robson and Frishman, 1995; Karwoski and Xu, 1999; Shiells and Falk, 1999).

Pharmacological techniques have been used to demonstrate the depolarising (ON) bipolar cell origin of PII and the b-wave. Shiells and Falk (1999) recorded dark adapted ERGs from dog fish retina in eyes with and without APB. By subtracting the pre from the post APB responses it was possible to separate the b-wave from the negative photoreceptor response and thus demonstrate the depolarising bipolar cell origin of the b-wave (PII component). In addition, a stimulus-response series for the isolated b-wave showed agreement with that of rod bipolar cell function measured using intracellular recordings.

A contribution to the b-wave by the Müller cells has also been suggested (Miller and Dowling, 1970; Xu and Karwoski, 1994; Jamison et al., 2001). However, a study using barium chloride to block the activity of the Müller cells, was not able to demonstrate an effect on the size of the b-wave (Lei and Perlman, 1999), thus suggesting that the b-wave (& PII) may be directly attributable to bipolar cell activity.

1.5.3.3 Oscillatory potentials (OP)

Oscillatory potentials (OP) are a series of small wavelets that are present on the ascending limb of the ERG b-wave, which occur in response to a bright stimulus and are maximal in mesopic conditions. Oscillatory potentials have been shown to be present under both light and dark adapted conditions (Peachey, Alexander and Fishman, 1987). These can be isolated by the use of filters, i.e. a high pass filter between 75 and 100 Hz

and a low pass filter set at 300 Hz or above, as described in the ISCEV standard (Marmor et al., 2009).

The evidence suggests that OPs are post receptoral in origin, with pharmacological blocking of post receptoral signals eliminating the response (Yonemura et al., 1974). Although the exact origin has not been confirmed, evidence suggests that both retinal ganglion cells and amacrine cells may contribute depending on whether photopic or scotopic stimulus parameters are used to elicit the OPs (Frishman, 2006).

1.5.3.4 Photopic negative response (PhNR)

The photopic negative response (PhNR) is a negative wave that occurs following the b-wave under photopic conditions, originating from the retinal ganglion cells. The PhNR has been shown to be reduced in cases of glaucoma (Colotto et al., 2000; Drasdo et al., 2001; Viswanathan et al., 2001). Monkeys with induced glaucoma have demonstrated reductions in the PhNR when a and b wave parameters were unaffected. The same study also demonstrated that eyes treated with Tetrodotoxin (TTX), which blocks RGC action potentials, had massively reduced or eliminated PhNR responses, both these findings strongly suggesting an RGC origin (Viswanathan et al., 1999).

1.5.3.5 Scotopic threshold response (STR)

The scotopic threshold response (STR) is apparent after exposure to very weak stimuli, resulting in a slow negative response (Sieving, Frishman and Steinberg, 1986; Wakabayashi, Gieser and Sieving, 1988). The STR may simulate the a-wave response, but has been shown to be an independent response by pharmacological methods; in aspartate treated retina the STR was eliminated, but the a-wave remained (Wakabayashi et al., 1988) suggesting a postreceptoral origin. Frishman (2006) suggests that the STR originates in either the amacrine or retinal ganglion cell function within the rod pathway, based on the assessment of pharmacological studies.

1.5.3.6 c-wave

The c-wave is a positive wave which develops slowly when a short, bright flash is presented to the dark adapted eye. The c-wave is the sum of two processes, PI and PII (Granit, 1933). A positive component (PI) has been attributed to the RPE by Noell (1953) (cited by Rodieck (1972)) who used sodium iodate to remove the RPE contribution in the rabbit retina. The positive potential attributable to the RPE is thought to result from a

decrease in the extra cellular potassium indirectly associated with the light-evoked closure of potassium channels in the photoreceptor outer segments (Weisinger et al., 1996). The negative contribution to the c-wave (Slow PIII) has been attributed to hyperpolarisation of the Müller cells, also caused by the decrease in extracellular potassium following light exposure (Witkovsky, Dudek and Ripps, 1975).

1.5.3.7 d-wave

This sub-component of the ERG is a positive response to the cessation of light stimulation of the cone photoreceptors, under light adapted conditions. The d-wave is only detected when long duration stimuli are used, as it merges with the b-wave for short flashes. The d-wave has been attributed to the transient depolarisation of OFF-bipolar cells of the retina (Weisinger et al., 1996).

1.5.4 The flicker ERG

The flicker ERG (photopic fast flicker ERG) is generated in response to a flickering stimulus, usually at a temporal frequency of about 30 Hz (Frishman, 2006; Marmor et al., 2009), which produces a repeatable waveform. As rods are insensitive to temporal frequencies above around 20 Hz, this response is dominated by the cone pathway (Sharpe, Stockman and MacLeod, 1989). Bush and Seiving (1996) used pharmacological dissection to demonstrate the origins of the flicker ERG in monkeys, recording both transient (15-ms single flash) and flicker ERGs (33 Hz). Glutamate analogues (APB & PDA) were used to selectively block the ON (APB) and OFF (PDA) pathways. Blocking the ON pathway delayed the time to peak of both the transient ERG b-wave and the flicker ERG. The application of both APB and PDA (blocking both ON and OFF pathways) virtually eliminated the flicker ERG, indicating that the fast flicker ERG originates post receptorally.

By assessing the first and second harmonic of the Fourier analysed focal flicker ERGs, Falsini et al. (1995) were able to demonstrate deficits in both the first and second harmonic responses in participants with outer retinal disease, for example AMD. In contrast, those with only post receptoral disease (i.e. central artery occlusion) had normal first harmonic responses. These findings suggested an outer retinal origin for the first harmonic of the flicker ERG. However, other studies have shown this response to be post receptoral in origin (Kondo and Sieving, 2002), and have suggested that the first harmonic

of the flicker ERG appears to be dominated by bipolar cell activity (Kondo and Sieving, 2001; Hare and Ton, 2002; Viswanathan, Frishman and Robson, 2002).

1.5.5 The focal cone ERG

Because full field ERGs are a sum of the total retinal response, they are likely to be insensitive to macular diseases such as early AMD (Sunness et al., 1985; Holopigian et al., 1997), which may only affect up to ~2% of the total retinal area. A focal ERG allows selective stimulation of a particular area of the retina, so facilitating identification of localised defects. The focal stimulus requires a desensitising surround to prevent stimulation of the peripheral retina by scattered light. A common approach to obtaining focal cone ERGs has been the use of a stimulator ophthalmoscope, which utilises a 4° stimulus operating at 42Hz, with a 12° white surround (Weiner and Sandberg, 1991; Sandberg, Miller and Gaudio, 1993; Remulla et al., 1995). Falsini et al. (1999b) similarly used a focal 32 Hz flicker stimulus (9° diameter) presented against a light adapting background.

The focal flicker ERG technique used by Binns and Margrain (2005) utilised a circular stimulus which was positioned such that it stimulated the central 20° of visual field. The stimulus was an amber (595 nm) colour designed to provide effective stimulation of the L and M cones. A ganzfeld adapting surround was used to suppress any response from the peripheral retina, luminance matched to the time averaged luminance of the stimulus (Binns and Margrain, 2005).

Although ISCEV standards recommend a 30 Hz stimulus frequency for full field flicker ERG recording (Marmor et al., 2009), a frequency of 41Hz is used by Binns and Margrain (2005; 2007). Both of these frequencies are above the rod flicker detection threshold (~20Hz) ensuring a cone dominated response (Sharpe et al., 1989). The literature shows that stimuli flickering at around 40 Hz have been used successfully for studies of macular function, for example by Falsini et al. (2000) and Sandberg et al. (1993), using temporal frequencies of 41 and 42 Hz respectively. Work by Seiple, Greenstein and Carr (1989) on 6 normal subjects investigated the response amplitude as a function of temporal frequency, and demonstrated a maximum response at 40Hz .

Although many focal ERGs are based on eliciting a focal flicker ERG (Weiner and Sandberg, 1991; Sandberg et al., 1993; Remulla et al., 1995; Falsini et al., 1999b), Miyake et al. (1988; 1989) utilised a 5 degree focal target with a time averaged luminance of 29.46 $cd.m^{-2}$ presented at 4.5 Hz within a uniform adapting background of 2.84 $cd.m^{-2}$ (> 40

degrees diameter) to elicit a transient focal ERG response. Miyake et al. (1988) was able to show that the transient ERG was elicited from the macula and did not contain any contributions from the peripheral retina.

More recently transient focal macular ERG responses have been successfully used to assess retinal function in AMD (Terasaki et al., 2002; Terasaki et al., 2004; Nishihara et al., 2008). The focal ERGs in these studies were elicited from a larger 15° (diameter) stimulus presented against a 45° light adapting background. The ERG was evoked by a 5-Hz rectangular stimulus consisting of alternating 100 ms light-on and 100 ms light-off periods with a mean luminance of 29.46 $cd.m^{-2}$ (Terasaki et al., 2004).

Binns and Margain (2007) used an identical 5 Hz rectangular stimulus to elicit transient ERG responses from the macula. However an even larger 20° (diameter) amber stimulus, with an average luminance of 30 $cd.m^{-2}$, was used. This was presented within a luminance-matched ganzfeld surround, to suppress the response of the peripheral retina whilst avoiding any differential light adaptation between stimulated and suppressed retina. The transient focal cone ERG provided the characteristic response with demonstrable a and b waves, however, the amplitude of these components were reduced compared to a full field stimulus due to the reduced retinal area stimulated. Furthermore, Binns and Margrain (2007) were able to demonstrate that any rod contribution to the transient focal cone ERG was minimal.

1.5.6 The ERG photostress test

Recovery of function following adaptation to a bright light is largely dependent on the speed of photopigment regeneration (Binns and Margrain, 2005). Diseases which compromise the integrity of the choriocapillaris, RPE and/or photoreceptor layers are likely to interrupt or limit the supply of metabolites to the photoreceptors thus affecting the speed of their functional recovery after a photopigment bleach. The literature clearly indicates that diseases affecting the outer retina, such as AMD, prolong recovery (Smiddy and Fine, 1984; Sandberg and Gaudio, 1995; Midena et al., 1997; Phipps, Guymer and Vingrys, 2003; Binns and Margrain, 2007; Dimitrov et al., 2008), indicating the clinical potential for a dynamic assessment of photostress recovery.

The ERG photostress test assesses the rate of recovery of the focal flicker ERG amplitude following exposure to a bright white adapting light (Binns and Margrain, 2005; Binns and Margrain, 2007). The test was developed to provide an objective measure of photostress recovery.

Binns and Margain (2005) showed that the greatest limitation with previous photostress techniques was their subjective nature and that, by using an ERG measure of outer retinal function, it was possible to avoid this potential problem. Alternative objective techniques have been based on the VEP (Lovasik, 1983; Parisi, 2001), but have a reliance on a healthy inner retina and visual pathway, which makes them less suitable for assessing outer retinal disease. Although the flicker ERG (see section 1.5.4) is dominated by the bipolar response, i.e. is not directly a photoreceptoral response, this more directly reflects outer retinal recovery than the psychophysical or VEP alternatives (Binns and Margrain, 2005). The rate of ERG recovery is thought to reflect the regeneration of cone photopigment (Binns and Margrain, 2005). An additional benefit of using the flicker ERG to monitor photostress recovery, compared to a transient response, is that it enables significant rapid signal averaging, improving the signal to noise ratio of the ERG post-bleach.

Binns and Margrain (2005) were able to successfully model the ERG recovery data using two models, a “first order” and “rate limited” model, which have been proposed to describe photopigment regeneration kinetics (Paupoo et al., 2000; Mahroo and Lamb, 2004). However the residual standard deviation of both models, an indication of goodness of fit, did not indicate a significant difference between the models, therefore given the smaller number of parameters, the first order exponential was deemed most appropriate.

1.5.7 The focal rod ERG

Focal scotopic ERGs normally produce a double b-wave, the first from the direct stimulation of the central retina, the second as a result of light scatter stimulating the peripheral retina (Sandberg, Pawlyk and Berson, 1996). Removing the scattered light response is more problematic in scotopic conditions, because of the lack of directional sensitivity in rods (Alpern, Ching and Kitahara, 1983). The current ISCEV standards therefore only include a method for full field rod assessment (Marmor et al., 2009).

Various approaches have been used to try and overcome the scattered light response, these include a subtraction technique developed by Sandberg et al. (1996), a background adaptation technique based on work by Hood et al. (1998), and finally the use of a very dim light stimulus (Choshi, Matsumoto and Nakatsuka, 2003).

The subtraction technique assumes that a full field signal of a similar amplitude and implicit time to that produced by scattered light can be produced by presenting a low

luminance flash to the whole retina, and then subtracting this from the double-peaked ERG leaving the isolated contribution from the focal stimulus (Sandberg et al., 1996).

The background adaptation technique proposed by Hood et al. (1998) works on the principle that the peripheral retina, not exposed to the focal stimulus, can be desensitised by a low luminance suppressing surround and therefore the suppressed peripheral retina should not be able to produce a signal in response to the scattered light.

Finally, the approach advocated by Choshi et al. (2003) to elicit a pure focal rod ERG was based upon a stimulus which was bright enough to produce a focal ERG, but dim enough to avoid a scattered light response. The ERGs were elicited using a 5° diameter blue stimulus. The luminance that would produce no scattered response was determined by projecting the stimulus onto the optic nerve head and identifying the maximum luminance that did not produce an ERG (1.5 scotopic $cd.m^{-2}$).

Binns and Margrain (2006) considered the 3 different methods described above to isolate the focal rod response in the development of a focal rod ERG protocol. The approach taken by Choshi et al. (2003) was capable of producing a measurable focal rod ERG but the averaging required and the minimal size of the b-wave produced was considered to be a major disadvantage by the investigators for a clinically viable protocol and was not considered for further evaluation. However the subtraction (Sandberg et al., 1996) and background adaptation (Hood et al., 1998) techniques were directly compared. The subtraction technique produce larger and slower b-waves compared to the adaptation technique but only 4 of the 10 subjects assessed demonstrated an a-wave. This finding would limit the usefulness of this technique for investigating the function of the outer retinal complex, as the photoreceptor function is reflected in the a-wave component of the ERG. In contrast, the background adaptation technique produced a smaller b-wave amplitude, however the resulting ERG waveforms demonstrated a-waves in more cases. Additionally, Binns and Margain (2006) reported that the background adaptation approach was simpler and quicker to conduct, a significant benefit for a potential clinical protocol.

1.6 Functional changes in age-related macular degeneration

Sections 1.4 and 1.5 discussed how retinal structure and visual function may be assessed, with particular regard to the macula. This section will consider the functional deficits which occur in AMD and how these relate to structural changes.

The effect of geographic atrophy on visual acuity, the most commonly used assessment of visual function, is largely dependent on the extent of foveal and adjacent

retinal involvement (Sarks et al., 1988). Choroidal neovascularisation and retinal scarring associated with the wet form of AMD usually result in severe central field loss and reduced visual acuity, the severity again being dependent on the extent of the lesion and foveal involvement (MPSG, 1994; Hogg et al., 2003).

Functional losses are also associated with the early stages of AMD. Affected visual functions include, but are not limited to, contrast sensitivity (Kleiner et al., 1988; Owsley et al., 1990; Stangos et al., 1995; Midena et al., 1997; Feigl et al., 2005b), flicker sensitivity (Mayer et al., 1994; Mayer, Dougherty and Hu, 1995), photostress recovery (Smiddy and Fine, 1984; Sandberg and Gaudio, 1995; Midena et al., 1997; Phipps et al., 2003; Binns and Margrain, 2007), dark adaptation (Eisner et al., 1991; Eisner et al., 1992; Steinmetz et al., 1993; Owsley et al., 2001; Haimovici et al., 2002; Owsley et al., 2007; Dimitrov et al., 2008) and foveal ERG parameters (Sandberg et al., 1993; Remulla et al., 1995; Sandberg et al., 1998; Falsini et al., 1999b; Falsini et al., 2000; Li, Tso and Lam, 2001; Chen et al., 2004; Binns and Margrain, 2007; Falsini et al., 2007; Piccardi et al., 2009).

These impairments are often apparent in individuals whose visual acuity remains near normal. For example, Midena et al. (1997) assessed macular function in participants with early AMD with good visual acuity, with (n=13) and without (n=47) wet AMD in the fellow eye, and compared them to age matched healthy subjects (n=36). In comparison with the ‘normal’ group, central visual field sensitivity and contrast sensitivity were reduced in the diseased group. Additionally, there was a positive relationship between the functional impairment and the extent of the retinal lesions. Other studies have also compared / correlated functional losses with ophthalmoscopically visible retinal features in AMD (Smiddy and Fine, 1984; Eisner et al., 1987; Collins and Brown, 1989; Eisner et al., 1991; Cheng and Vingrys, 1993; Sandberg et al., 1998). However, recent research has begun to take advantage of modern imaging techniques such as OCT: for example studies have been published showing a relationship between photoreceptor layer integrity and visual acuity in different pathologies (Aizawa et al., 2009; Forooghian et al., 2010; Maheshwary et al., 2010; Oster et al., 2010), including AMD (Hayashi et al., 2009; Landa et al., 2011; Shin, Chung and Kim, 2011).

1.6.1 Visual acuity and contrast sensitivity

Visual acuity is often used as the primary clinical measure of visual function, however, the association with structural changes at the macula are variable. Advanced AMD is usually associated with a significant reduction in acuity, whereas those lesions

associated with early AMD, such as drusen and pigmentary changes, may only be associated with negligible changes (Klein et al., 1995).

Beirne et al. (2006) evaluated short wavelength sensitive (SWS) grating acuity with regard to different stages of AMD in 88 adults between the ages of 51 and 87 years. The study participants were graded using the Wisconsin Age-Related Maculopathy Grading System (WARMGS) (Klein et al., 1991), and assigned a severity grade (stages 0 to 6). Beirne et al. (2006) found that there was a statistically significant reduction in SWS acuity in those with AMD compared to normal participants ($p<0.002$). However, there was no evidence of a significant relationship between functional deficit and disease severity using ANOVA and general linear models, with considerable overlap between severity grades. When the data was reassessed following reallocation of individuals into new groups of healthy (stage 0), early AMD (stages 1 to 4) and advanced AMD (stage 5) participants, the analysis revealed statistically significant differences between all the revised groupings. This may suggest that only a gross relationship exists between retinal appearance and function.

Whilst recent evidence suggests that retinal thickness, assessed using OCT, was not a good predictor of visual function in people with wet AMD (Moutray et al., 2008) there are reports that the IS/OS junction is affected in AMD (Drexler et al., 2003; Ko et al., 2005). Hence, Hayashi et al. (2009) decided to investigate the relationship between the structural integrity of the IS/OS junction and visual acuity. The study used OCT to image 51 eyes with wet AMD following successful treatment with PDT. The integrity of the IS/OS junction was graded at the fovea as either complete, discontinuous or absent. Twenty eight eyes were graded as having no visible IS/OS junction and were shown to have a statistically poorer visual acuity than those with continuous or discontinuous IS/OS junctions ($p<0.001$). Landa et al. (2011) was also able to identify a correlation between visual acuity and integrity of the IS/OS junction at the fovea in participants (n=55 eyes) with both wet ($r=-0.6$, $p<0.02$) and dry ($r=-0.58$, $p<0.02$) AMD. This study also compared microperimetry measurements on a point by point basis to IS/OS integrity, and retinal sensitivity was shown to provide a stronger correlation than visual acuity to integrity in both wet and dry AMD. Pappuru et al. (2011) demonstrated that there are also mild correlations between acuity and ONL and photoreceptor inner segment thickness ($r=-0.49$ and -0.59 respectively) in participants with dry AMD (n=100 eyes), however, given the weakness of these correlations and variability in acuity measurements they concluded that these OCT parameters could not fully explain the acuity levels achieved. The relationship between

visual acuity and parameters of outer retinal structure, particularly the photoreceptors, has also been shown in other conditions including diabetic eye disease (Forooghian et al., 2010; Maheshwary et al., 2010), retinitis pigmentosa (Aizawa et al., 2009) and in the presence of epiretinal membranes (Arichika, Hangai and Yoshimura, 2010; Oster et al., 2010).

Contrast sensitivity has also been shown to be affected in AMD (Kleiner et al., 1988; Owsley et al., 1990; Stangos et al., 1995; Midena et al., 1997; Feigl et al., 2005b). Midena et al. (1997) were able to associate a loss in high spatial frequency sensitivity with confluence of drusen, hyperpigmentation and RPE atrophy, although not absolute number of drusen. Losses in high spatial frequency sensitivity and peak contrast sensitivity have also been demonstrated in a study involving participants with drusen (n=52) and healthy controls (n=27) all with good acuity (6/6). The drusen within this study were categorised based on severity into 4 groups, which were assessed using one way analysis of variance techniques, and demonstrated worsening contrast sensitivity with increasing severity of drusen ($p<0.001$) (Kleiner et al., 1988). Studies by Midena et al. (1997) and Stangos et al. (1995) also attempted to establish if contrast sensitivity was a predictor for wet AMD by comparing participants with bilateral early AMD to those with a contralateral wet AMD eye; however, in both studies contrast sensitivity measures were not found to be predictors of wet AMD.

High spatial frequency contrast sensitivity and visual acuity are dependent on the cone density of the photoreceptor mosaic at the fovea (Curcio et al., 1990), but a significant reduction in photoreceptor density or function is required before reductions in VA become apparent (Geller, Sieving and Green, 1992). Therefore, it seems likely that other measures of visual function may be more sensitive to early AMD (Landa et al., 2011).

1.6.2 Colour vision

Midena at al. (1997) reported that colour vision (assessed using the Farnsworth-Munsell 100) was not significantly impaired in participants with early AMD (with good acuity), however, colour vision defects have frequently been linked to AMD in the literature (Bowman, 1978; Eisner et al., 1991; Holz et al., 1995; Elsner, Burns and Weiter, 2002; Feigl et al., 2005b; Mitrut et al., 2010), with early AMD predominantly associated with tritan (blue-yellow) defects (Feigl et al., 2005b).

Eisner et al. (1991) investigated cone dark adaptation, absolute cone sensitivity, s-cone mediated sensitivity and colour matching in participants with AMD in the test eye and unilateral wet AMD in the fellow eye (n=41). The eyes assessed were sub divided into high and low risk of progression by assessing drusen confluence, drusen size and focal hyperpigmentation, and visual function was compared between these groupings. In this study, test eyes with abnormal colour matching (n=16), were all found to express retinal features associated with a high risk of AMD progression. Elsner et al. (2002) also assessed colour matching in 53 participants with ARM and not only demonstrated that colour matching was abnormal in these participants, but was able to attribute this to a reduced density of cone photopigment, based on a modelling technique which assessed how the colour matching changed over a range of retinal illuminance. Recently, Mitrut et al. (2010) reported a correlation between colour vision deficiency, (red-green and blue-yellow) assessed using a computerized optotype test, and total drusen area within a 3000 µm diameter centred on the fovea.

1.6.3 Visual fields and retinal sensitivity

Various studies have attempted to correlate retinal sensitivity with disease severity in terms of drusen characteristics, pigmentary abnormalities and atrophy (Eisner et al., 1991; Midena et al., 1994; Tolentino et al., 1994; Midena et al., 1997). Midena et al. (1994) evaluated retinal sensitivity (central 10°) in participants with drusen (n=35 eyes) and age matched controls (n=16 eyes) and detected a reduction in mean retinal sensitivity which was associated with the presence of large and soft drusen, these findings were supported by similar findings reported in a later study (Midena et al., 1997) but contradicted by Tolentino et al. (1994) who was unable to find a relationship with drusen extent. Eisner et al. (1991) was able to identify deficits in absolute sensitivity in eyes with early AMD and identified a greater reduction in absolute sensitivity in eyes deemed “high risk” compared to “low risk” eyes ($p<0.001$), although the author cautioned whether this finding could have been influenced by the greater age of participants within the “high risk” group.

More recently Iwama et al. (2010) used microperimetry in 22 eyes to investigate the relationship between retinal sensitivity overlying soft drusen (with and without disruption of the inner and outer photoreceptor segment (IS/OS) junction), and that overlying apparently normal adjacent retina. The retinal structure was assessed using images produced by the Topcon 3D-OCT 1000 (Topcon medical systems Inc., Tokyo). The retinal sensitivity was measured at 57 locations in each eye, and each point was classified as above or below 14

decibel sensitivity. The study found that 68.1% of non-drusen locations achieved this sensitivity, however, for locations overlying soft drusen this dropped to 38.9%, and in the presence of disruption to the IS/OS junctions only 15.2% of the locations tested had a sensitivity greater than 14 dB. These findings revealed a significant reduction in sensitivity overlying the drusen and locations with disrupted IS/OS junctions ($p<0.0001$), indicating a clear association between early AMD changes and retinal function. A previous study by Sunness et al. (1988) had also investigated retinal sensitivity overlying drusen but suggested that sensitivity loss was diffuse and not directly related to the presence of drusen, however, this study only tested a total of 54 points in 8 patients, with comparison between drusen and non-drusen retinal points made for only 12 pairs. The smaller number of patients assessed may mean that the study was not sufficiently powered to detect the difference between drusen and non-drusen locations.

In addition to retinal features being associated with retinal sensitivity, a study by Chen et al. (1992) was able to associate changes in choroidal perfusion to localised reduction in dark adapted sensitivity. Eight eyes with abnormal choroidal filling phases, identified by fluoroscein angiography, were compared to 6 eyes matched for retinal appearance but with normal choroidal filling phases. Areas of scotopic threshold elevation (of up to 3.4 log units) were shown to correspond to areas of abnormal choroidal filling.

1.6.4 Dark adaptation and the macular photostress test

Dark adaptation is the slow recovery in visual sensitivity following exposure to a bright adapting light (often called a photobleach). The dynamics of dark adaptation have been shown to be abnormal in AMD (Eisner et al., 1991; Eisner et al., 1992; Steinmetz et al., 1993; Owsley et al., 2001; Haimovici et al., 2002; Owsley et al., 2007; Dimitrov et al., 2008). The macular photostress test provides a more rapid measure of dark adaptation kinetics by assessing cone adaptation following exposure to a bright adapting light. This is commonly carried out clinically by timing the recovery of visual acuity following a photobleach to a line above the pre-bleach level (Margrain and Thomson, 2002). The macular photostress test has been shown to be sensitive to AMD and associated retinal features (Smiddy and Fine, 1984; Sandberg and Gaudio, 1995; Midena et al., 1997; Phipps et al., 2003; Binns and Margrain, 2007).

Eisner et al. (1991) investigated rates of dark adaptation and showed that “high risk” eyes tended to have longer time constants of recovery than “low risk” eyes ($P<0.01$), furthermore, all 21 eyes in the study with a time constant greater than 200s (considered to

be the upper limit of normal) were “high risk” eyes, with slow dark adaptation being considered a very specific marker of high risk retinal features in this study. The study showed that a combination of dark adaptation and colour matching assessment was very sensitive to “high risk” eyes ($P<0.001$), in fact 30 out of 32 high risk eyes demonstrated abnormal colour matching or dark adaptation in the study.

Owsley et al. (2001) investigated rod dark adaptation in participants with ARM (n=20) and healthy age matched controls (n=16). They showed that participants with ARM had abnormal dark adaptation parameters. Later work by Owsley et al. (2007) again investigated parameters of dark adaptation in participants with ARM (n=83) and once more identified a significant abnormality in rod-mediated parameters of dark adaptation including the rod-cone break, rod slope and rod sensitivity ($P<0.0001$), when compared with normal age matched participants (n=43). Additionally they showed that these parameters worsened with increased disease severity (participants were categorised into early, intermediate and advanced AMD based on retinal photograph grading).

Cone parameters were also assessed by Owsley et al. (2007), who reported that cone mediated time constants and cone sensitivity were not impaired compared to control participants in this study. This may be expected given the reported preferential loss of rod photoreceptors over cones in early AMD (Curcio et al., 1996), however other studies have found delayed cone adaptation to be highly sensitive to early AMD (Dimitrov et al., 2008; Gaffney, Binns and Margrain, 2011). This may reflect differences in the bleach and stimulus parameters used e.g. the retinal location tested.

Furthermore, Sandberg et al. (Sandberg and Gaudio, 1995; Sandberg et al., 1998), using a macular photostress test technique, have shown cone mediated adaptation to be associated with AMD in studies assessing fellow eyes of participants with wet AMD. In a longitudinal follow-up they showed a slowed photostress recovery time to be an independent risk factor for the development of wet AMD (Sandberg et al., 1998). Midena et al. (1997) were similarly able to show that a slowed photostress recovery time was associated with AMD, and related this to disease severity, with slower recovery associated with increased extent of drusen, pigmentary changes and atrophy in test eyes. Other studies have failed to identify a relationship between photostress recovery and drusen confluence or AMD severity, despite finding significant delays in photostress recovery (Smiddy and Fine, 1984; Cheng and Vingrys, 1993).

A study by Binns and Margrain (2007) used an ERG photostress test (see section 1.5.6) to provide an objective measure of cone recovery. In this study, participants with

ARM (n=31) were shown to have a reduced rate of recovery, compared to age-matched controls (n=27; p<0.001). Additionally, 9 individuals did not demonstrate any recovery during the testing period; 5 of these participants had a fellow eye with wet AMD, again suggesting photostress recovery as having a prognostic role for wet AMD.

Dark adaptation and photostress recovery parameters may be particularly sensitive to AMD related changes given the relationship between the dynamics of photopigment regeneration upon which these parameters depend, and the health of the outer retina. The retinoid cycle requires constant exchange of retinoid across the inter-photoreceptor space between the RPE and rods to regenerate rod photoreceptor photopigments (Lamb and Pugh, 2004). During retinal adaptation the outer retina requires a constant supply of metabolites derived from the choroidal circulation which must be transported across Bruch's membrane. Structural changes related to ageing and AMD, such as deposition of hydrophobic material and the thickening of Bruch's membrane and loss of choriocapillaris (see section 1.3.2), are likely to impede the rate and supply of metabolites to the outer retina and therefore, slow the rate of retinal adaptation in AMD (Owsley et al., 2001).

1.6.5 Electrophysiology

The electroretinogram (ERG) objectively assesses visual function at the level of the retina and through modifying the state of adaptation and the stimulus parameters used can elicit responses which reflect different aspects of retinal function (see section 1.5). There are numerous reports of abnormal ERG parameters in people with ARM and AMD. However, whilst many authors identify statistically significant differences, only a fraction of these describe the diagnostic potential of the techniques. The Appendix G identifies those publications where statistically significant differences in ERG parameters are reported. This section will therefore concentrate on studies where the diagnostic potential or a relationship with retinal structure has been assessed. Studies evaluating treatment outcomes using the ERG have not been included.

1.6.5.1 Ageing and ERG parameters

Electroretinogram parameters have been shown to be affected by normal ageing independent of AMD-related changes (Weleber, 1981; Birch and Fish, 1988; Birch and Anderson, 1992; Freund et al., 2011). For example, Birch & Anderson (1992) reported a reduction in full field photopic and scotoptic ERG amplitudes whilst b-wave implicit times lengthened with increasing age in a study comprising healthy adults (n=269). More

recently Freund et al. (2011), cited two similar studies which investigated the effect of age on the cone ERG, one reported no change (Chiti et al., 2003), the other a reduction in b-wave amplitude with age (Weleber, 1981). Prompted by the contradictory evidence within the literature Freund et al. (2011) investigated the effect of normal ageing on a series of transient ERGs over range of adaptation states and for a series of ISCEV standard ERG techniques (Marmor et al., 2009). ERGs were recorded from healthy participants with good visual acuity (>6/6) and the ERG parameters compared between 3 age groups, 20-39 (n=27), 40-59 (n=20) and 60-82 (n=18) years. Bilateral full field ERGs were recorded using an active DTL fibre electrode and reference and earth gold skin electrodes. Standard ISCEV responses (Marmor et al., 2009) were recorded in addition to a photopic (11 increments, -1.63 to 2.86 photopic log $cd.m^{-2}.s$) and scotopic (16 increments, -5.22 to 1.37 scotopic log $cd.m^{-2}.s$) luminance response series. The older participant group in this study demonstrated increased photopic a and b wave amplitude and implicit times for high luminance flashes (>7.6 photopic $cd.s.m^{-2}$), delayed dark adaptation, reduced dark adapted a wave amplitudes (although b wave amplitudes were unaffected) and prolonged scotopic a and b wave implicit times.

This evidence would suggest that ageing can be expected to influence ERG parameters. Weleber et al. (1981) suggested that a correction to ERG parameters should be made for age related changes using age-corrected values derived from linear or multiple regression coefficients.

1.6.5.2 Full field techniques

The effect of AMD on full field ERG and EOG responses is unclear. For example, Walter et al. (1999) investigated participants with AMD (n=122 eyes) and compared these to age matched controls (n=47 eyes) for a range of full field responses and found deficits in both rod and cone driven ERG parameters. Findings included delayed and reduced amplitude a and b waves of the rod dominated ERG, and reduced amplitude a and b waves of the cone dominated ERG, although the 30 Hz ERG was unaffected. Only 42 of the 122 eyes that Walter et al. (1999) assessed could be classified as ARM, whilst the remainder had advanced AMD. In contrast, Sunness et al. (1985) and Holopigian et al. (1997) found a range of full-field ERGs to be unaffected by earlier stage AMD, which might be expected given that macular disease only affects up to ~2% of the total retinal area. Full field ERGs are therefore unlikely to provide measures of value in the diagnosis of ARM.

1.6.5.3 Focal techniques

Falsini et al. (1999b) assessed cone mediated macular function using a focal flicker ERG (32 Hz; 9° diameter) in non-exudative AMD. Twenty-five participants with bilateral dry AMD were compared to 10 age matched controls, and the participants with AMD demonstrated a reduced ERG amplitude (57% reduction, $p<0.001$), whilst those with minimal AMD related lesions and normal acuity had a relatively smaller reduction in ERG amplitude (47% reduction, $p<0.01$). The amplitudes were also found to correlate with grading scores ($r=-0.63$, $p<0.001$), based on the Wisconsin AMD grading scale (Klein et al., 1991), and the percentage area of hyperflourescence ($r=-0.70$, $p<0.01$). Falsini et al. (1999b) suggested that the focal flicker response may be a suitable measure for assessing disease severity (Falsini et al., 1999b; Falsini et al., 2000).

Piccardi et al. (2009) compared perimetry and focal electroretinography (ERG), to morphological changes in people with ARM (n=26) and age matched controls (n=12). A series of focal flicker ERGs (41 Hz) were recorded to central (4.5° diameter) and paracentral (4.5 to 18° diameter annulus) stimuli. Both stimuli showed a statistically significant reduction in amplitude in the group with ARM ($p<0.01$), and a phase delay was identified for the paracentral stimuli ($p<0.01$). It was reported that ERG delays and morphological lesions associated with ARM were most evident in the paracentral region tested, but they concluded that ERG responses were linked to eccentricity and not retinal morphology.

Sandberg et al. (1993) reported delayed implicit time in responses obtained using a focal flicker (4°, 42 Hz) ERG technique, in fellow eyes of participants with unilateral wet AMD (n=73) when compared to normal eyes (n=28). Remulla et al. (1995) similarly utilised a focal flicker ERG (4°, 42 Hz) to investigate 67 fellow eyes of participants with unilateral wet AMD. In this study fluoroscein angiography identified 28 eyes with abnormal choroidal perfusion, which demonstrated delayed implicit times of 1 ms ($p<0.02$) compared to eyes with normal perfusion, and were more likely to have delayed implicit times ($p<0.01$). These studies suggest a link between choroidal circulation / metabolic supply in AMD and the focal flicker ERG implicit time, however, the small difference in implicit time between groups suggests that this is unlikely to be clinically useful. In addition, when 127 participants with unilateral wet AMD were followed up over a 4.5 year period, the focal flicker ERG implicit time of the fellow eye was not found to be an independent risk factor for neovascular changes, although the interval to CNV manifestation was inversely related

to flicker ERG implicit time in those participants who progressed. This later study did report that the extent of macular abnormalities (e.g drusen confluence and pigmentary abnormalities) and the glare recovery time were independent risk factors for progression (Sandberg et al., 1998).

Binns and Margrain (2007) demonstrated not only delayed implicit time ($p<0.001$ & AUC=0.73) and reduced amplitude ($p<0.003$ & AUC=0.73) of the focal flicker ERG (20°, 41 Hz) in participants with ARM (n=31) compared to age matched controls (n=27), but also deficits in transient focal cone ERG parameters. The focal cone ERG elicited by a photopic (20°, 5 Hz) stimulus demonstrated delayed implicit times for both a ($p<0.002$ & AUC=0.74) and b ($p<0.001$ & AUC=0.77) waves. These findings were in addition to the slowed ERG photostress recovery previously discussed. As can be seen by the area under ROC curves, these parameters all had relatively good diagnostic potential for the detection of ARM.

Chen et al. (2004) investigated cone and rod function using an mfERG technique in both light and dark adapted conditions. They showed that rod N1 and P1 mfERG components were significantly reduced in AMD participants (n=24) compared to normals (n=16) in a ring at 5° eccentricity, corresponding to a deficit in scotopic sensitivity assessed using a perimetry technique. However, this finding was in isolation, and both rod and cone mfERG amplitude and latencies for other retinal regions and the summed responses were not found to be significantly different between groups.

The literature clearly shows that cone ERGs can be used to investigate AMD. Although, there is relatively little literature on focal rod techniques, psychophysical evidence suggests that electrophysiological measures of rod function are likely to be impaired in early AMD (Owsley et al., 2000; Owsley et al., 2001; Owsley et al., 2007).

1.7 Project overview and aims

A combination of the advent of anti-VEGF therapy and the recent advances in OCT technology (Drexler and Fujimoto, 2008), has meant that imaging techniques have become much more important as a method of diagnosis and monitoring of AMD. Optical coherence tomography has been shown to be a reliable technique for retinal imaging, being able to clearly image the structural changes which occur within the eye as a result of AMD (Pieroni et al., 2006; Chen and Lee, 2007; Zayit-Soudry et al., 2007). The literature indicates that there are many functional changes associated with AMD, some of which are

apparent at even the earliest stages of the disease, even when visual acuity remains normal (see section 1.6).

Clinically, the detection and diagnosis of AMD is made based on a combination of both structural and functional changes of the eye. Within a primary care, setting functional assessment of visual acuity, Amsler chart and structural assessment, by way of routine ophthalmoscopic examination of the macula, have been considered enough for a preliminary diagnosis. It is clear that there exists the possibility of extending the current clinical protocol for AMD assessment to increase the sensitivity to mild structural and functional changes. As the intensive effort invested in the research and development of new treatments and therapies for AMD comes to fruition the ability to accurately diagnose the onset of AMD and to monitor disease progression is vital for the early identification of patients suitable for therapy, and in evaluating the outcomes of the treatment.

Therefore, the first aim of this thesis was to determine and compare the diagnostic potential of a range of structural (provided by OCT imaging), and functional (provided by electrophysiological tests) parameters. This was achieved by carrying out a case control study using participants with ARM (early AMD) and comparing these with age matched healthy controls.

The evidence to date for relationships between structural changes within the retina or choroid and ARM have largely considered the presence and extent of retinal lesions associated with AMD, such as drusen (see section 1.6). However, advances in OCT imaging have enabled the accurate identification and measurement of features such as intra-retinal layer thickness, which were not accessible using traditional techniques (Loduca et al., 2010). Optical coherence tomography retinal images are comprised of hyper-reflective bands; which have been shown to reflect the underlying retinal histology. Correspondence between the different cellular layers within the retina and OCT images has been well documented (Chauhan and Marshall, 1999; Gloesmann et al., 2003; Anger et al., 2004; Chen et al., 2009).

Electrophysiological techniques have been shown to be capable of isolating and assessing the function of individual cell types within the retina (Bush and Sieving, 1994; Frishman, 2006). Section 1.5 describes how the subcomponents of the ERG are dominated by the activity of different cell types within the retina, many of which may be found within specific retinal layers. Therefore with the ability to identify, delineate and quantify many of the intra-retinal cellular layers using OCT images this provides an excellent opportunity to directly compare retinal and choroidal structure to retinal function.

The second aim of this thesis was to investigate the relationship between retinal structure and function. This was achieved by imaging the retina using OCT and measuring the thickness of the intra-retinal layers and the choroid and then comparing the thickness of these individual layers to retinal function as determined by focal ERG parameters.

The final aim of this study was to determine if retinal appearance was related to focal ERG parameters in participants with ARM.

Ultimately this information will be of value in understanding the development and progress of AMD, and will aid in the development of clinical tests suitable for the detection and monitoring of AMD.

Chapter 2: Development of imaging techniques

This chapter describes the OCT system used for this thesis, the imaging protocols and image processing methods selected, and the evaluation of a novel segmentation method. In addition, the system used for grading and classifying age-related macular degeneration in this thesis is described.

2.1 1060 nm FD-OCT system

The 1060 nm FD-OCT, also known as the Enhanced Choroidal Penetration OCT, was a prototype system capable of an imaging rate of 47,000 a-scans/s allowing 512 x 512 a-scan raster patterns to be acquired in a clinically viable timescale (Esmaeelpour et al., 2010). The 1060 nm light source allows the system to achieve greater penetration of media opacities such as cataract, and increased imaging depth i.e. to the level of the choroid-scleral junction (Povazay et al., 2007a). The 1060 nm FD-OCT has an axial resolution of ~8μm, less than the equivalent 800 nm system (Povazay et al., 2007a).

The 1060 nm FD-OCT system used for this thesis lacked several clinically important features. Firstly, the software did not provide a 'review' image facility to allow assessment of image quality following acquisition. Secondly, the use of a 'fixed' fixation target within the imaging system required accurate patient instruction to image eccentric locations. Consequently to ensure that accurate and usable images were obtained from participants, multiple images were acquired so that the best images could be used for analysis.

Dimensions (X by Y by Z)	Angular Extent	Imaging Wavelength	Details
512x512x1024	20°x20°	1060 nm	
512x512x1024	36°x36°	1060 nm	Imaged area exceeds the central 20° giving more allowance for poor fixation and centration.

Table 2.1.1: OCT scan parameters used in this thesis for the 1060 nm FD-OCT system.

The 1060 nm FD-OCT system, in contrast to commercial systems such as the Cirrus OCT (Carl Zeiss, Meditec Inc, CA), had no pre-defined imaging protocols, but was able to capture images which exceeded 20° of visual angle. However, for a given b-scan, a larger visual angle results in a proportional reduction in a-scan density and therefore a reduced transverse resolution of the resulting image. The scan protocols selected for use in this thesis are shown in table 2.1.1. The protocols selected were based on equal spacing of a-scans in each image dimension, highest achievable image resolution and

coverage of the 3 macula subfields used for the international ARM grading system (Bird et al., 1995) assuming central (foveal) fixation.

2.2 Post processing and quantification

2.2.1 Transverse image magnification

The axial component of an OCT image is unaffected by magnification effects, however, the transverse parameters are subject to magnification effects in the same way as retinal photographs. The magnification is derived from both the optics of the imaging system and the eye being imaged. A method of correcting for magnification in retinal imaging was first proposed by Littmann (1982) and has since been modified by Bennett et al. (1994). Thus, a correction can be made to length and area measurements obtained from retinal images using equations 2.1 & 2.2 respectively.

Equation 2.1: $t = pqs$

Equation 2.2: $t^2 = (pqs)^2$

Where:
"t" is the true size of retinal feature
"s" is the size of the feature on the photograph
"q" is a value based on the optical dimensions of the eye
"p" is a value based on the optics of the imaging device

The factor q is directly related to the optical properties of the eye being imaged and can be calculated based upon the ametropia, keratometry, lens curvature and refractive indices of the media in the eye being imaged. However, Bennett et al. (1994) compared 12 different methods for calculating q and found that axial length was the most important contributing factor to determining the value q. Accordingly, this study determined that the most effective method for calculation "q" was using equation 2.3, called the "adjusted axial length method".

Equation 2.3: $q = 0.01306(x-1.82)$

Where:
“q” = eye correction factor,
“x” = axial length of imaged eye (mm).

In order to calculate the correction factor for OCT images the value “p” is needed for the system. Studies have calculated the value “p” for OCT systems using a telecentric optical setup (Leung et al., 2007; Kang et al., 2010); these systems have no magnification effect when the axial length of the eye is 24.46mm. Therefore, using equation 2.3 it is possible to produce a correction factor for the magnification effect in OCT, as shown below:

When the axial length is 24.46 mm there is no magnification effect, therefore t = s and it follows from equation 2.1 that, p.q = 1 and therefore:

$p = 1/q$

The value p is calculated as:
$p = 1/ (0.01306. (24.46-1.82)) =$ **3.3822**

Thus, transverse OCT dimensions should be corrected for axial length using equation 2.4 (Littmann, 1982).

Equation 2.4: $t = 3.3822 . (0.01306.(x-1.82)).s$

Where:
t = true size of retinal feature (μm)
x = axial length of imaged eye (mm)
s = measured size of retinal feature (μm)

To reflect the effect axial length may have on the transverse dimensions of an OCT image the magnification factor for a 20 and 27mm axial length eye have been calculated below:

20 mm axial length magnification factor: 0.80x

27 mm axial length magnification factor: 1.11x

To summarise, where OCT measurements are made in the transverse plane then these measurements should be corrected for the magnification. The adjusted axial length method (Bennett et al., 1994) was used for calculating the eye correction factor "q" whilst the factor "p" is fixed at 3.3822 for the OCT system used in this thesis.

2.2.2 Image enhancement techniques

Optical coherence tomography images are usually recorded using a raster scan pattern, the individual a-scans that comprise the b-scans and full image are therefore recorded sequentially. Although the a-scans are collected at high speed, minimising the potential for adjacent a-scans to be misaligned, the numbers required for large images (e.g. 262144 a-scans for a 512x512 image) make it increasingly likely that the acquisition will be affected by movements or fixation artefacts in the images. Additionally, the pupil margins or a poorly timed blink may obstruct imaging of part, or the entire retina, during image acquisition. The optics of the eye may also degrade the image due to media opacities and aberrations resulting in universal or localised reductions in image quality, whilst the eyes' pigmentation may reduce the laser penetration limiting the visibility of retinal/ choroidal features.

Some factors that affect image quality may be reduced or eliminated by good imaging technique, for example good patient alignment and instruction. Other factors, however, require correction by 'post processing' techniques following image acquisition. The techniques may be both objective and subjective in nature, with the application of each technique dependent upon both the quality of the image and the clinical features of interest to the observer. The following is an overview of the post-processing techniques used in this thesis, all of which were carried out using 'ImageJ' (Rasband, 1997), the descriptions given are based on information available from the ImageJ website (http://rsbweb.nih.gov/ij/index.html, as accessed 27th August 2010).

2.2.2.1 Brightness and contrast

The brightness adjustment adds or subtracts a bias to every pixel within the image, increasing or decreasing the absolute luminance. The contrast applies a scale factor to all the pixels, proportional to the original intensity of each. The adjustment of the brightness and contrast of an image can help improve the visualisation of the individual retinal layers.

However adjustments can lead to blurring of the intra-retinal boundaries, possibly changing the interpretation of their exact location. The brightness and contrast of images were adjusted manually, using ImageJ (Rasband, 1997), until the retinal layers were subjectively identifiable.

2.2.2.2 Stack registration

B-scans within a newly acquired OCT image are not necessarily aligned with their neighbour, for example when motion artefacts occur during image acquisition. Stack registration aligns adjacent b-scans based on common features between adjacent scans. Stack registration sequentially assesses each b-scan from a predefined starting point within the image (for the purposes of this study the b-scan corresponding to the foveal pit was used).

2.2.2.3 Spatial convolution blur

Spatial convolution allows the introduction of controlled blur into the OCT image with the pattern described by a ‘kernel’. The kernel is a matrix whose centre corresponds to the source pixel and the other elements correspond to the adjacent pixels, the adjusted pixel intensity is obtained by multiplying each source pixel by its corresponding kernel coefficient and adding the results. ‘Convolving blur’ was applied to the OCT images to enhance the retinal layers by reinforcing features common to adjacent b-scans whilst also reducing noise.

2.2.2.4 Gaussian blur

Gaussian blur blurs each pixel according to the shape of the Gaussian function. A 'Radius' can be specified which describes radius of decay to exp(-0.5) ~ 61% (i.e. the standard deviation sigma of the Gaussian). The radius value specified for each OCT image was determined subjectively with the intention of producing a blur that improved the visibility of the retinal layers and choroid.

2.2.2.5 Reslice

Reslicing is a function which enables the reconstruction of one or more orthogonal slices through the image. The reconstruction can be specified to start at any edge of the image, and the number slices and orientation of the new image can be specified. This function was used to produce enface views (viewable from the top or bottom of the image),

or to view horizontal or vertical cross-sections (b-scans) through the OCT image.

2.2.2.6 Radial reslice

Radial reslice is an adaptation of the 'reslice' function, which creates an orthogonal reconstruction of the image stack by consecutively rotating a line around a central point (in this case the foveal pit), each successive image in the new stack represents a section from the fovea to the periphery, at regular intervals (1° per image) over 360°. These images were used in this thesis to produce a series of 'annular' images comprising rings of a-scans with increasing eccentricity from the fovea by applying the reslice function. Each consecutive annular image represented an increase in eccentricity from the foveal pit of 1 pixel. This technique was used in section 2.3 only.

2.2.2.7 Z-project

The Z-project function enables adjacent images (usually b-scans) to be merged into a single image, effectively producing an averaged b-scan. The Z-project function can improve OCT image quality by reducing noise. That is, noise is reduced whilst the appearance of common features such as intra-retinal boundaries is enhanced. This type of image processing is achieved at the loss of spatial localisation relative to the number of adjacent scans combined.

The Z-project may merge multiple images using a variety of techniques, the most useful approaches involve averaging the intensity or summing the intensity across merged images. This technique was used to combine adjacent b-scans during analysis to improve the localisation of faint or poorly defined retinal layers.

2.3 OCT measurement techniques

Clinically, quantitative analysis of OCT images is carried out manually using a digital calliper to measure retinal structure at specific locations or, more commonly, by automated segmentation. Segmentation works by delineating specific layers within each b-scan (for example, the ILM and RPE for retinal thickness) and then calculating the volume, area and thickness of the structures contained within the delineated area. Commercial OCT systems usually contain specifically designed and calibrated software for this purpose.

The advantage of manual segmentation is that it allows the observer to ensure that the retinal layers are correctly identified in the potentially disordered diseased retina. The

processes used in automated segmentation do not necessarily follow retinal morphology, but do allow images to be analysed in such a way that any value (for example retinal thickness) can be recalled for any point within the imaged area. When carried out by computer software this approach can be very effective, allowing a wide range of analyses to be conducted. In contrast, manual segmentation of an entire OCT image is time consuming and labour intensive, with FD-OCT images often comprising 256 or 512 individual b-scans that need to be segmented by hand. Manual segmentation often only involves a subsection of b-scans within an OCT image; however, each reduction in sample density reduces the reliability of thickness maps and other data produced.

Given the difficulties associated with manual segmentation, consideration was given to a novel approach involving the selective segmentation of 'annular' OCT scans corresponding to specific retinal eccentricities. This study investigated structural and functional changes in ARM participants and, therefore, it seemed reasonable to concentrate the analytical effort on retinal locations where AMD related changes had been previously identified. Structural and functional changes have both been shown to occur preferentially in an annular region within the parafovea (Curcio et al., 1993; Curcio et al., 1996; Owsley et al., 2000). Therefore, by concentrating manual segmentation measurement of retinal and choroidal thickness to locations at specific eccentricities within this region (up to 10° eccentricity) it was hoped to provide an efficient method for the detection of AMD related changes.

The following study compared two methods of analysing OCT images obtained using the 1060 nm FD-OCT system. The first method utilised a manual segmentation approach which produced an average retinal and choroidal thickness for a series of annular rings centred on the fovea. The second method utilised manual measurements, at pre-determined points of increasing eccentricities along the horizontal and vertical planes intersecting the fovea. Measurements using these two approaches were compared to each other and to retinal thickness values from established analysis techniques in the literature.

2.3.1 Methods

21 healthy elderly participants were recruited (age 56-76 years). Each participant was imaged using the 1060 nm FD-OCT system, with a 512x512 scan (20°x20°) protocol. All OCT images were post processed using the techniques described in section 2.2 to improve image quality and allow identification of the ILM, RPE and choroid-scleral boundaries. The following sections describe both the 'manual measurement' (section

2.3.1.1) and 'annular segmentation' (section 2.3.1.2) techniques applied to each image. The agreement between techniques was assessed using a technique proposed by Bland and Altman (1999) and the thickness values produced were compared to equivalent values reported in the literature.

2.3.1.1 Manual measurement

The post processed OCT images were resliced (see section 2.2) to isolate b-scans that provided a horizontal and vertical cross section that intersected at the foveal pit. Thickness measurements were obtained at 21 locations, corresponding to the foveal pit and at 0.4 mm intervals temporally and nasally on the horizontal image, and superiorly and inferiorly on the vertical image extending to an eccentricity of 2.0mm (~7°) in each direction.

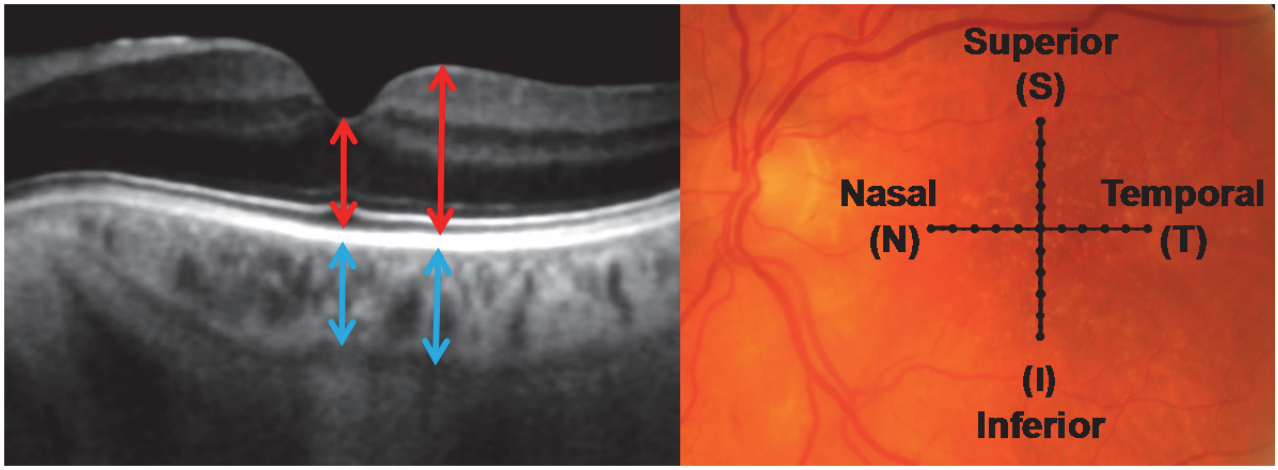

Figure 2.3.1: OCT b-scan (Left) with arrows indicating example calliper measurements for retinal (red arrows) and choroidal (blue arrow) thickness at 2 locations. Retinal thickness was measured between the ILM (the most anterior hyper-reflective line) and the RPE (inner edge of the brightest hyperreflective line). Choroid thickness was measured between the RPE/choriocapillaris boundary (outer edge of the brightest hyper-reflective line) and the choroid-scleral boundary, identified by a combination of a visible sclera reflectivity band and the limit of visible choroidal vessels. Retinal photograph (right) indicates measurement location at 0.4 mm intervals (black spots) along the vertical and horizontal meridians (black lines).

The calliper function within ImageJ (Rasband, 1997) was used to measure the retinal and choroidal thickness at each location (see figure 2.3.1). The calliper was orientated vertically to avoid introducing a transverse component to the measurement. The

measurement was returned in pixels, and converted into microns (μm) using the conversion factor of 2.43μm per pixel. To aid comparison with the annular segmentation technique a mean of the 4 manual measurements at each eccentricity was determined.

2.3.1.2 Annular segmentation

The post processed OCT images were radially resliced to obtain annular rings centred on the foveal pit with each ring spaced in pixel steps from the fovea (see figure 2.3.2). The rings were separated by 0.4 mm with the outer ring being 2 mm from the fovea. These were manually segmented using bespoke software called 'Manseg 4'. The four boundaries corresponding to the borders of the retina and choroid were manually delineated (see figure 2.3.1). Manseg 4 used the boundaries to calculate an area for each image representing the total number of pixels within each segmented area. This area was then divided by the circumference (circumference = 2.π.r) to provide an average thickness for each ring.

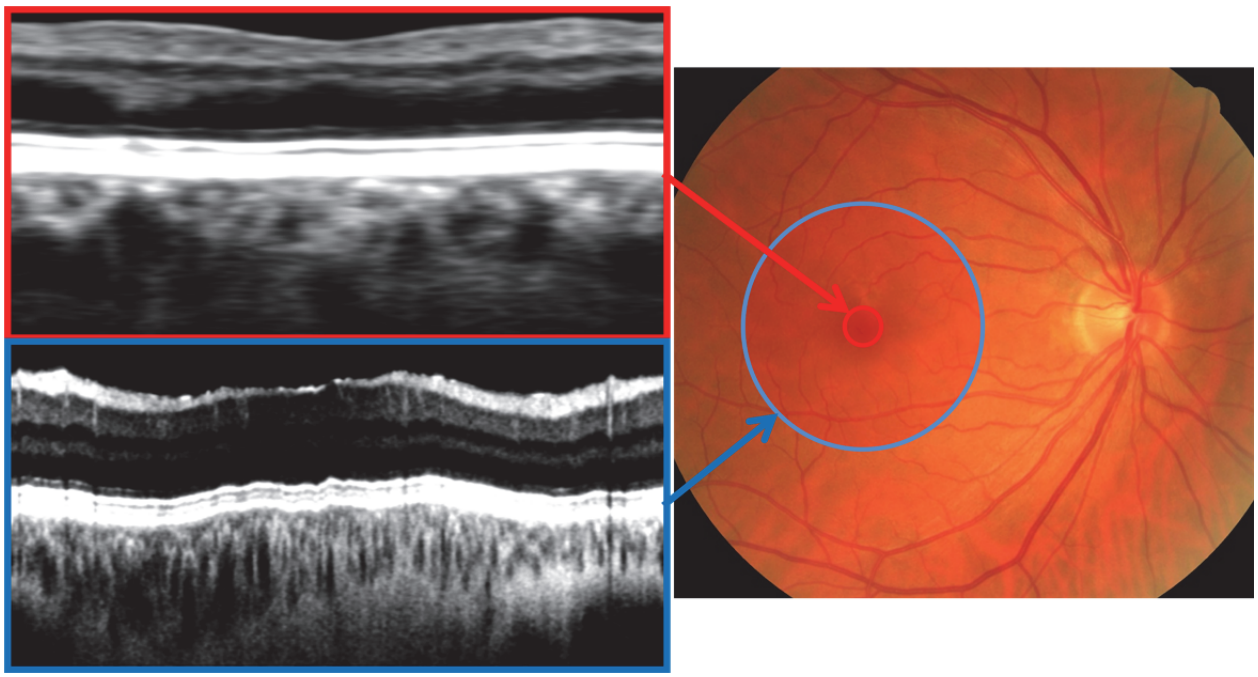

Figure 2.3.2: Example annular images for ~0.4 mm (outlined in red) and ~2.0 mm (outlined in blue) eccentricity.

2.3.2 Results

Retinal thickness measurements for both manual and annular techniques demonstrated an increase in retinal thickness from the thinnest point at the fovea reaching a peak at ~0.8 mm eccentricity before declining towards the periphery (see figure 2.3.3).

The annular technique produced a slightly smaller mean of between 8 and 14 μm at each retinal eccentricity compared to the manual approach, this difference was statistically significant at every eccentricity ($p<0.05$; paired t-tests).

Choroidal thickness appeared to be less affected with increasing eccentricity, although both techniques demonstrated a small decline with increasing eccentricity (see figure 2.3.3). Both the variability of the measurements and the difference between the groups was larger for choroidal compared to retinal measurements with the manual technique providing thicker measurements. However, the choroidal measurements were only statistically different between methods at the fovea and 0.8 mm eccentricity ($p<0.05$; paired t-tests).

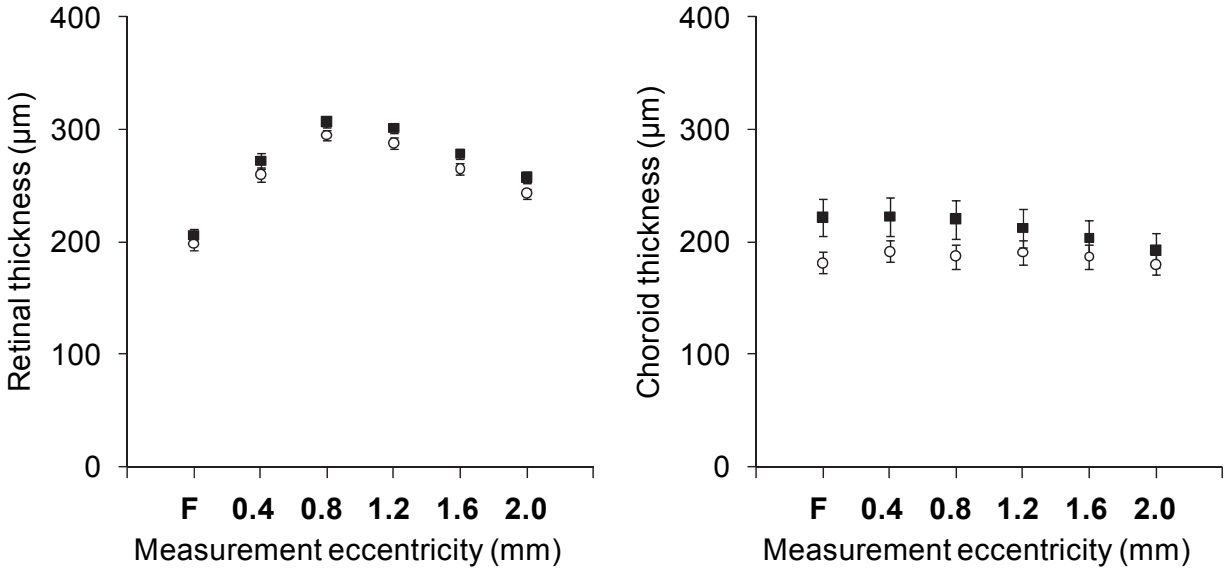

Figure 2.3.3: Comparison of retina (left) and choroid (right) thickness measurements at 0 (Foveal pit; denoted as F) 0.4, 0.8, 1.2, 1.6 and 2 mm retinal eccentricity for healthy participants (n=21) for the manual (solid) and annular segmentation (open) techniques. Error bars shown the standard error of the mean. The difference between techniques was assessed using a paired t-test at each eccentricity, these differences were significant (P<0.05) for all retinal eccentricities, and choroidal measurements at the fovea and 0.8 mm eccentricity for the choroid.

Figure 2.3.4 shows Bland and Altman plots of agreement between techniques at the fovea, 1.2 mm and 2 mm eccentricity. The small bias towards thicker values using the manual technique is clear at all eccentricities. The agreement between techniques is clearly poorer for the choroidal than retinal measurements, as evidenced by the wider

limits of agreement.

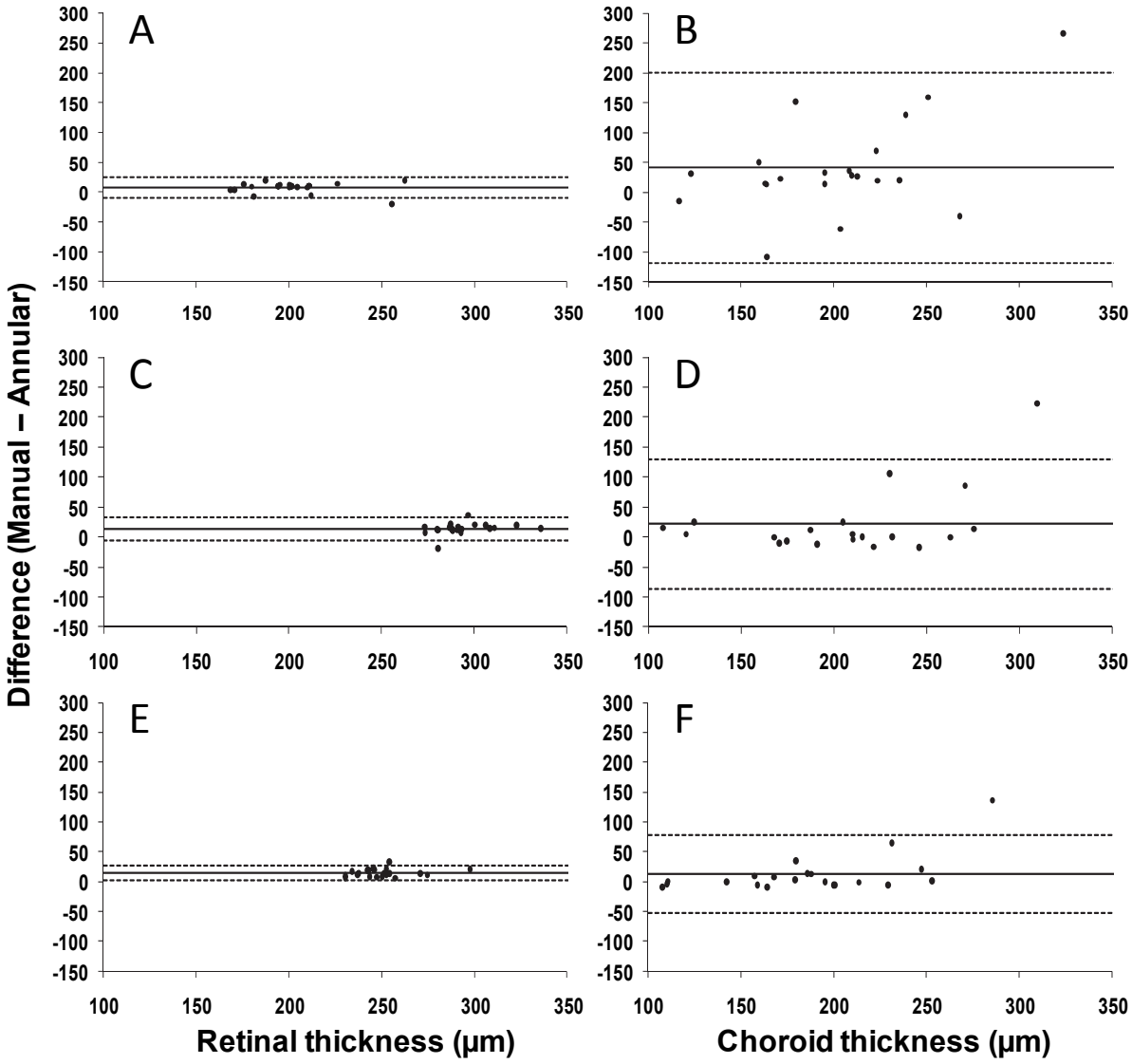

Figure 2.3.4: A comparison between manual measurement and annular segmentation for retinal thickness (Left; A, C & E) and choroidal thickness (Right; B, D, F) measurements at the fovea (top; A & B), at 1.2 mm (middle; C & D) and at 2 mm (bottom; E & F) eccentricity. The difference between methods is plotted against the average of both methods providing a graphical comparison between methods, as advocated by Bland and Altman (1986). The solid horizontal line represents the mean difference between methods (the bias), whilst the dotted lines indicate the 95% limits of agreement; a narrower interval between these lines indicates better agreement.

The relatively constant bias of between 8 and 14 microns for retinal thickness across eccentricities measured, although small, may suggest an underlying systematic

difference between each methodology. The narrowing limits of agreement for the choroidal thickness with increasing eccentricity suggests an increased variability for measurements obtained closer to the fovea.

2.3.3 Conclusion

The results showed that the annular technique produced retinal thickness values that were between 8 and 14 μm thinner at each eccentricity than the corresponding manual measurement. We would expect the results to be identical as the underlying OCT images were identical and the same retinal boundaries were used. However, given that the images were measured and segmented manually, a subjective bias may have occurred when identifying the boundaries, possibly related to the difference in appearance of the annular and traditional b-scan images. This difference may also relate to the fact that the annular scan is composed of many data points, whilst the manual technique uses only 4 a-scans to determine the average thickness for each eccentricity. Although consistent, this difference between techniques was less than the standard deviation of the mean for either approach.

The choroidal thickness results also demonstrated a bias between techniques, but this decreased with increasing measurement eccentricity (see figure 2.3.4). The choroid thickness data also demonstrated a greater variability than the equivalent retinal thickness data. These findings are almost certainly attributable to the less well defined boundaries used to delineate the choroid, resulting in a greater variance amongst the data (see figure 2.3.1). The difference between the two methods for choroidal thickness measurements, however, was only statistically significant ($p<0.05$) at the fovea and 0.8 mm eccentricity (possibly due to the greater variability of the choroidal measurements), again the annular segmentation technique returned thinner values (see figures 2.3.3 and 2.3.4).

When considering the merits of each approach, the manual technique produced measurements at specific locations, whereas the annular segmentation technique returned an averaged value for all points at the eccentricity measured. The manual technique was quicker and simpler to carry out and did not require the aid of additional software to provide the results. Potential difficulties also arose using the annular segmentation techniques. These largely involved the annular rings closest to the fovea where, due to the small circumference, they comprised less a-scans than the more eccentric rings reducing the quality and clarity of the image (see figure 2.3.2). These images were therefore more difficult to measure. In contrast the manual technique presented a similar task difficulty for

all measurements. Although each manual measurement was localised to a single point within the image (a single a-scan), the adjacent b-scan image provided a contour and definition to the layer boundaries to enable accurate measurement. This was particularly helpful in poorer quality images and when identifying the less well defined boundaries such as that between the choroid and sclera (see figure 2.3.1).

Commercially available OCT systems, such as the Cirrus OCT (Carl Zeiss, Meditec Inc, CA), usually present thickness data as averages for retinal regions corresponding to an ETDRS grid configuration (see Appendix H, figure H.1) making direct comparison with published studies difficult. The results at 0.4 mm eccentricity for the annular (259 ±25μm) and manual (272 ±30μm) methods in this study are not directly comparable to those from Cirrus OCT systems, however, similarities were observed. For example, Legaretta et al. (2008), who imaged 50 healthy eyes (20 to 68 years), reported an average foveal thickness of 258.2 ± 23.5 μm whilst a similar study by Kakinoki et al.(2009) who also imaged 50 healthy eyes (49.9 ±18 years) reported an average foveal thickness of 257.6 ± 19.6 μm.

Given the lack of fully automated segmentation software which could produce comparable data analysis to commercial OCT systems, and the difficulties experienced segmenting data points nearest the fovea using the annular segmentation approach, further OCT measurements in this thesis were obtained using the manual technique described.

This study used the inner edge of the RPE to delineate the outer retinal boundary, in a similar approach to that used by the automated software on the Cirrus OCT (Carl Zeiss, Meditec Inc, CA). However, it was observed that adjustments to brightness and contrast during post-processing increased or decreased the width of this OCT feature. Therefore it was decided that the centre of the outer hyper-reflective line should be used to represent the boundary between the retina and choroid for all future measurements within this thesis. This approach has been previously used by Esmaeelpour et al. (2010) and should allow for more repeatable measurements.

2.4 AMD classification and grading

An important aspect of a study is the ability to determine the clinical classification of study participants. There are published methods for the grading of AMD, one of the earliest being the “Wisconsin Age-Related Maculopathy Grading System” (Klein et al., 1991). The Wisconsin system was developed, based on methods previously used to grade

AMD and diabetic retinopathy, to provide a reliable and consistent method for the classification of AMD in population based studies, for example the Beaver Dam Eye study (Klein et al., 1992). More recently, two further grading systems have been developed based on the original “Wisconsin” system, these are the International Classification and Grading System for AMD (Bird et al., 1995), developed in 1995 as a collaboration between six research groups to produce a universal AMD grading system, and the more recent Age Related Eye Disease Study group (AREDS) grading system (AREDS, 2001a) designed for their multicentre study of nutrition in AMD (AREDS, 2000).

All of these systems record the presence, location and frequency of clinical features (e.g. drusen and pigmentary abnormalities) attributable to AMD, within the macula, based entirely upon 30° or 35° stereoscopic retinal photographs. These systems define the macula as a 6000 μm diameter circle, centred on the fovea, which for the purposes of grading is subdivided into three distinct annular regions; central (500 μm radius), inner (500 to 1500 μm radius) and outer (1500 to 3000 μm radius). The inner and outer regions are further subdivided into quadrants representing the superior, inferior, nasal and temporal macula (see Appendix H, figure H.1). The systems also set a minimum age whereby clinical features maybe attributable to AMD, this is 50 years for the International System (Bird et al., 1995) and 55 years for the AREDS system (AREDS, 2000; 2001a). However, none of these systems take account of visual acuity or other clinical investigations such as fluorescein angiography.

For this thesis there was access to a conventional 2-D retinal camera, but not stereoscopic imaging as used for the Wisconsin (Klein et al., 1991), AREDS (2001a) or International (Bird et al., 1995) systems. This posed two problems; firstly, in the absence of stereoscopic images the established grading systems could not be directly applied, and secondly, an alternative methodology or technique was required to provide depth information regarding the retinal features associated with AMD to enable effective identification and grading.

Using a technique such as binocular indirect ophthalmoscopy would provide depth information, but has the limitation of being a subjective technique and the assessment is limited to when the participant is present. Fluorescein angiography has been considered for grading AMD, but was deemed by the AREDS study to be “too risky” due to the invasive nature of the test and risks of anaphylaxis and death (AREDS, 2001a). It should be noted that when the International (Bird et al., 1995) and AREDS (AREDS, 2001a) grading systems were developed, alternative imaging techniques such as OCT were not

available. However, OCT has since been shown to be capable of not only providing the depth information required, but also of providing *in vivo* cross-sectional imaging of the retina not possible with stereo photography. This intra-retinal imaging provides additional clinical information enabling, for example, differentiation between types of PED (Mavrofrides et al., 2004).

For this thesis the classification of participants into disease groups was based upon the appearance of both 2-D digital retinal photographs and the OCT images obtained using the 1060 nm OCT system. The definitions of AMD used were largely based on the International (Bird et al., 1995) and AREDS (AREDS, 2001a) classification system definitions. The following sections will describe and define how participants were allocated to the disease (ARM) or control (normal) groups.

2.4.1 Classifications

The following section outlines a comparison of the International (Bird et al., 1995) and AREDS (AREDS, 2001a) classification systems and describes the classification of AMD used for this study. The classification criteria were based on the ability to identify pathology using the imaging techniques available, the established grading systems and recent research on the clinical features of AMD and their aetiology.

2.4.1.1 Normal

The classification of normal for the purpose of grading varies, this is unsurprising as signs such as drusen are not only associated with AMD, but are also considered a part of normal ageing (Sarks et al., 1999). The AREDS system deemed the presence of any drusen within the macula to be indicative of AMD, although small drusen (<63μm) were graded as the lowest level of abnormality, (AREDS, 2001a). By contrast the International system (Bird et al., 1995), defines the presence of drusen of less than 125μm diameter in the absence of pigmentary changes or other signs of AMD as normal. Given the potential overlap with individuals displaying normal ageing signs (i.e. small hard drusen), the International system designation for normal was adopted.

2.4.1.2 ARM / Early AMD

This classification is what the International system (Bird et al., 1995) defines as age-related maculopathy (ARM), or early AMD. The International system characterises ARM as the presence of soft drusen and/or focal pigmentary changes within the macular

area which are not secondary to another disorder. This is similar to levels 2 and 3 on the 4 step AREDS system, which are characterised by soft drusen (>63µm), pigment changes or geographic atrophy not located at the centre of the macula. For this study ARM was defined as the presence, within the macula, of any soft drusen (>125µm), any pigment change (hyper or hypo) or drusenoid PED.

AMD Type	International system	AREDS system
Dry AMD	Any sharply delineated roughly round or oval area of hypopigmentation or depigmentation or apparent absence of the RPE in which choroidal vessels are more visible than in surrounding areas that must be at least 175µm in diameter (>=C_2) on the colour slide (using a 30° or 35° camera).	Geographic atrophy in central subfield with at least questionable involvement of centre of macula
Wet AMD	*Wet AMD is also called "neovascular" AMD,"disciform" AMD, or "exudative" AMD and is characterized by any of the following:* *RPE detachment(s), which may be associated with neurosensory retinal detachment, associated with other forms of ARM. *Subretinal or sub-RPE neovascular membrane(s). *Epiretinal (with exclusion of idiopathic macular puckers), intraretinal, subretinal, or sub-pigment epithelial scar/glial tissue or fibrin-like deposits. *Subretinal hemorrhages that may be nearly black, bright red, or whitish-yellow and that are not related to other retinal vascular disease. (Hemorrhages in the retina or breaking through it into the vitreous may also be present). *Hard exudates (lipids) within the macular area related to any of the above, and not related to other retinal vascular disease.	*Evidence of neovascular AMD:* *Fibrovascular/serous pigment epithelial detachment *Serous (or hemorrhagic) sensory retinal detachment *Subretinal/subretinal pigment epithelial hemorrhage *Subretinal fibrous tissue (or fibrin) *Photocoagulation for AMD

Table 2.4.1: Advanced AMD definitions as used for the International (Bird et al., 1995) and AREDS (AREDS, 2001a) systems, the presence of any features of wet AMD supersedes the presence of any other grading feature for both systems, resulting in a classification of wet AMD.

2.4.1.3 Advanced AMD

The definitions used for advanced AMD were generally in agreement for both grading systems (see table 2.4.1). However, the International Classification and Grading System for AMD (Bird et al., 1995) defines any serous pigment epithelial detachment (PED) as wet AMD regardless of its aetiology, as stereo retinal photographs are not

capable of differentiation between the vascular and avascular forms (Bird et al., 1995). The AREDS system (AREDS, 2001a), in the absence of angiographic information, grades PED by its stereoscopic appearance as dome shaped, shallow or irregular and does not classify the presence of drusenoid pigment epithelial detachment as advanced AMD.

For this thesis advanced AMD was graded as either dry or wet AMD. Consistent with both grading systems dry AMD was defined as the presence of geographic atrophy of at least 175μm in diameter (as in the International system), with visibility of choroidal vessels (Bird et al., 1995). Wet AMD was defined as the presence of any signs of neovascularisation, including the presence of a suspect vascular serous or fibrovascular PED, haemorrhage, serous retinal detachment, retinal oedema or disciform scarring. The eye was also classified as wet if it had been previously treated or diagnosed as wet AMD by an ophthalmologist.

The definitions used in this study, based on those shown in table 2.4.1 for the International and AREDS systems, are described in table 2.4.2.

Category	Definition
Normal	Defined as the absence within a 6000μm diameter circle centred on the fovea of any clinical feature associated with AMD. The presence of drusen less than 125μm in extent was not considered a feature of AMD
ARM (early AMD)	Defined as the presence within a 6000μm diameter circle centred on the fovea of any of the following features, in the absence of signs associated with wet or dry AMD: Drusen > 125μm in diameter Hyper or hypopigmentation Drusenoid PED
Dry AMD (advanced AMD)	Defined as the presence within a 6000μm diameter circle, centred on the fovea, of geographic atrophy (at least 175μm in diameter) without any signs of wet AMD.
Wet AMD (advanced AMD)	Defined as the presence within a 6000μm diameter circle centred on the fovea of any of the following signs attributable to AMD: Choroidal neovascularisation Haemorrhage Serous or fibrovascular PED Exudates Disciform scarring
Other	Defined as the presence within a 6000μm diameter circle centred on the fovea of any clinical feature not associated with AMD.

Table 2.4.2: Definitions of disease status for participants in this study.

2.4.2 Classification and grading methodology

The grading of participants in this thesis had two primary purposes, firstly to allow the categorisation of eyes based on disease status and secondly to provide information regarding disease severity within the disease group (ARM participants). The following describes the methodology used to categorise the participants and then provide an assessment of disease features associated with early AMD based upon the International Classification System (Bird et al., 1995).

For each eye a 37° digital retinal photograph and 1060 nm OCT image (36° in diameter) centred on the fovea were evaluated to classify the retinal appearance according to table 2.4.2. The retinal photograph was viewed within Powerpoint (Microsoft, Richmond WA), which enabled digital overlays to be used, which represented the macular anatomical divisions and sizing circles for assessment of size and location of clinical features as in Bird et al. (1995) (see Appendix H, figure H.2 and table H.1 for further detail on scaling calculations). The OCT images were viewed using ImageJ (Rasband, 1997), and were used specifically to identify the presence and nature of PED (serous, fibrovascular or drusenoid), choroidal neovascular membranes, retinal oedema and scar/ glial/ fibrous tissue (disciform scarring) associated with AMD.

In addition the severity of drusen and pigmentary abnormalities was graded according to the criteria described by the International System (Bird et al., 1995) (see Appendix H, figure H.3). This provided data to allow comparison with other studies which have investigated early AMD using the International (Bird et al., 1995), and similar grading systems (Klein et al., 1991; AREDS, 2001a) whilst also providing additional structural information relating to extent and severity of clinical features within the study group.

All the participant eyes in this study were classified and graded by the author, and then classified by two optometrists masked to all other patient data. The final classification assigned to each eye was that agreed by the author and the two optometrists, in the case of disagreement, a majority verdict was accepted.

2.4.3 Evaluation of classification system

During the course of this study a total of 104 eyes were graded using this grading approach, each eye was assigned a category based on the eyes appearance, either Normal, ARM, Wet, Dry or Other. Unanimous agreement occurred in ~89% of Normal participants, ~92 % of ARM participants and in all cases where a grade of wet was assigned. Where there was not unanimous agreement, and a majority decision was taken

in determining the final diagnosis, the category assigned by the grader in the minority is shown in Table 2.4.3. In no cases did each of the 3 graders provide 3 different categories.

Grading categories	Number of eyes	Categorisation of minority grader				
		Normal	ARM	Wet	Dry	Other
Normal	56	-	5	0	0	1
ARM	37	0	-	3	0	0
Wet	11	0	0	-	0	0
Dry	0	0	0	0	-	0
Other	0	0	0	0	0	-

Table 2.4.3: Grading categories assigned to 104 eyes assessed in this study. Final category allocated based on majority (2 out of 3 graders), in cases of disagreement the categorisation assigned by the grader in the minority is shown.

Chapter 3: Development of electrophysiology techniques

This chapter describes the development and refinement of the ERG protocols used in this thesis. All participants who took part in studies within this chapter had a corrected visual acuity of 0.2 (LogMAR) or better, clear ocular media, normal retinal / optic disc appearance, no history of retinal or systemic disease, and were not taking medication known to affect retinal function, unless otherwise stated.

3.1 Standard Techniques

This section describes the general ERG recording methods and recording protocols for the focal cone ERG, focal flicker ERG, ERG photostress test and focal rod ERG.

3.1.1 Participant preparation

The following methods were used for ERG protocols throughout this thesis unless otherwise specified.

Participants' pupils were dilated bilaterally with 1 drop of 1.0% Tropicamide prior to electrode placement. A silver-silver chloride 9mm, touchproof skin electrode (*Viasys Healthcare Ltd, Warick, UK*) was applied to the skin at a midfrontal position to act as the earth electrode. The skin electrode was attached using surgical tape (*Blenderm;3M, St.Paul, MN*) following skin preparation with abrasive gel (Nuprep;D.O. Weaver & Co., Aurora, CO). The electrode cup was filled with electrolyte electrode gel (*Teca, Pleasentville, NY*). DTL fibre electrodes (Dawson, Trick and Litzkow, 1979); (*Unimed Electrode Supplies, Surrey, UK*) were placed into the lower fornix of each eye, and connected to the Medelec Synergy evoked potential monitoring system (Medelec Synergy EP; Oxford Instruments Medical, Surrey, UK) using a holder, which was attached to the outer canthus using surgical tape (*Blenderm;3M, St.Paul, MN*) (see figure 6.1.1). The DTL electrodes acted as the active (test eye) and reference (non-test eye) electrodes, the non-test eye was patched prior to any ERG recording.

Figure 3.1.1: Participant prepared for ERG recording with DTL fibre holders adjacent to each eye (active and reference electrodes) and a skin (earth) electrode attached to the forehead.

3.1.2 General ERG recording

3.1.2.1 Filtering, averaging and artefact rejection

Filtering, averaging and artefact rejection are used to isolate the signal of interest whilst removing, or reducing, the influence of noise in ERG recordings. ISCEV guidelines recommend the use of filtering and averaging where appropriate, for example when trying to identify “very weak pathologic” signals (Marmor et al., 2009).

Signals at frequencies outside the range of interest are considered to be noise. ISCEV recommends that specific ranges of frequencies are isolated when recording particular ERG waveforms. For example, to record flicker or transient ERGs a range of 1 to 100 Hz is recommended, whilst for oscillatory potentials the suggested range is 100 to 1000 Hz (Marmor et al., 2009). Filters are used to eliminate undesirable frequencies from electrophysiological recordings, this is typically achieved using a combination of 4 main types of filter described below (see figure 3.1.2):

- A **low pass filter** allows frequencies below a preset level whilst rejecting frequencies above this level (Odom, 2006).
- A **high pass filter** allows frequencies above a preset level whilst rejecting frequencies below this level (Odom, 2006).
- A **band pass filter** works by allowing through a range of frequencies between two preset vales, and rejecting all frequencies which fall outside this range (Odom, 2006).
- A **notch filter (band reject)** works by rejecting frequencies between two preset values but allowing all others, in electrophysiology this type of filter can be applied to eliminate mains interference (50Hz) (Odom, 2006).

Ideally these filters would have a sharp cut-off between frequencies but in reality they have an attenuated roll off (see figure 3.1.2) (Odom, 2006). An attenuated roll off means that the amplitude of the response at frequencies adjacent to the cut off frequency may be altered, therefore this may distort the overall waveform recorded. In some cases the use of filters may be detrimental to recording particular electrophysiological responses.

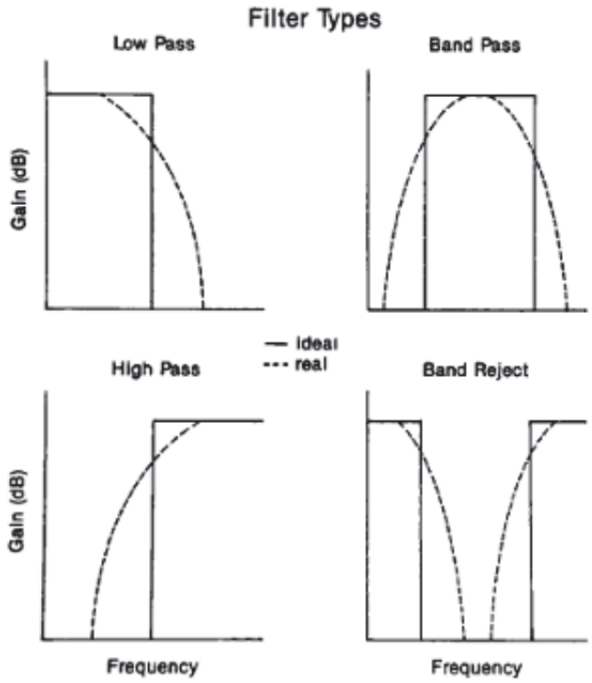

Figure 3.1.2: Schematic diagrams of the characteristics of the four filter types used in electrophysiology recordings, the "theoretical" effectiveness (bold) and "actual" effectiveness (dashed) of each filter type is shown. Image from Odom (2006).

The signal to noise ratio (SNR) describes the ratio between the size of the response and the noise created by all other signals recorded (e.g. 50 Hz electricity hum). A high SNR aids the recording of reliable and repeatable ERGs. The SNR may be improved by either reducing the noise or increasing the signal. Averaging involves the recording of multiple responses and finding the mean value of all recorded responses. Averaging improves the SNR based on the principle that noise and artefacts make a random contribution to each individual ERG, which is not time-locked to the onset of the stimulus, whilst the evoked signal remains relatively constant. This results in a progressive reduction in the noise due to destructive interference such that the SNR of the averaged data improves in proportion to the square root of the total number of traces averaged (van der Tweel and Estéves, 2006). However, from a clinical perspective averaging is time consuming and can potentially lead to fatigue and reduced patient compliance.

Artefact rejection is based on the principle that the signal of interest will not be expected to exceed a particular value in amplitude, under any circumstances, therefore any value that exceeds this amplitude must be an artefact. The artefact reject will ignore any response recorded that exceeds a pre-determined upper amplitude limit.

An evoked potential monitoring system (Medelec Synergy EP; Oxford Instruments Medical, Surrey, UK) was used to record the ERGs. Unless otherwise specified, all responses were band-pass filtered from 1 to 100 Hz and an artefact-reject setting (50 μV) applied to exclude traces contaminated with blinks or eye movements. The system digitally averaged the ERG responses, as specified in each recording protocol.

3.1.2.2 Stimulation

All stimuli were produced by a miniature LED ganzfeld stimulator (CH electronics, Kent, UK). The stimulator consisted of an array of LEDs of different wavelengths (red, amber, green and blue) set within a tube, behind a circular diffuser. The LEDs could be modulated with respect to luminance, frequency and duration of stimulation. All focal stimuli were provided by viewing the miniature ganzfeld tube from a distance of 16 cm, such that it subtended 20° of visual angle.

3.1.3 Focal cone ERG

This section describes the protocol used to record the focal cone ERG based on a previously published protocol (Binns and Margrain, 2007).

3.1.3.1 Recording protocol

An amber stimulus (λ_{max} = 595 nm, half-height bandwidth =17 nm) with an average luminance of 30 cd.m^{-2} (1500 photopic td.s) subtending 20° at the eye, was presented at a temporal frequency of 5 Hz (50 % duty cycle). A luminance matched desensitising white square surround (30 cd.m^{-2}, 118° width) was used to suppress the cones and rods of the peripheral retina. Responses were recorded on a 200 ms time base with a 20ms baseline prior to stimulus presentation. Four traces were recorded, each consisting of an average of 100 responses (recorded in blocks of 25 to minimise blink artefacts).

3.1.3.2 Data analysis

The ERG traces were exported and analysed using Excel (Microsoft. Redmond, WA). Each trace was drift corrected and Fourier analysed (Stroud, 1986). A waveform, comprising the first 9 harmonics, was reconstructed (see figure 3.1.3), this removed all frequencies above 45 Hz (previous work has indicated that higher frequencies do not contribute to the a and b waves (Binns and Margrain, 2007)). The a and b waves were identified objectively from the reconstructed trace, using Excel, and the amplitude and implicit times assessed (see table 3.1.1). The a and b waves were measured for each trace separately, and the values averaged. The traces were inspected visually to confirm the objective analysis.

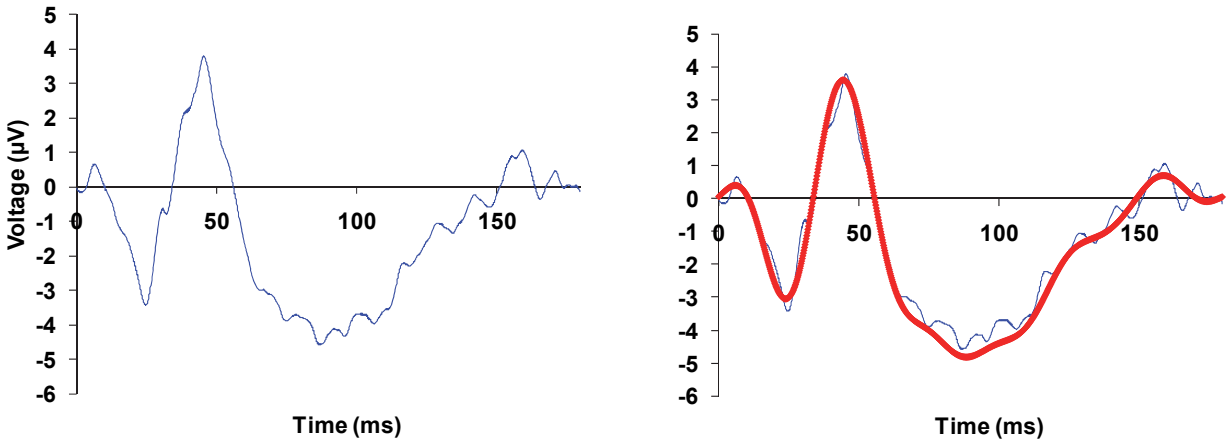

Figure 3.1.3: Raw focal cone ERG waveform for a healthy participant (left, blue trace) and the Fourier analysed focal cone ERG waveform (right, red trace).

Parameter	Selection
a-wave implicit time (ms)	The time from flash onset to the amplitude minimum between 5 to 30 ms post flash.
a-wave amplitude (μV)	The potential difference from the time of flash onset to the amplitude minimum between 5 to 30 ms post flash.
b-wave implicit time (ms)	The time from flash onset to the amplitude maximum between 30.2 to 55 ms post flash.
b-wave amplitude (μV)	The potential difference between the amplitude minimum between 5 to 30 ms post flash, and the amplitude maximum occurring between 30.2 to 55 ms post flash.

Table 3.1.1: Criteria for identification of a and b wave parameters of the focal cone ERG waveform.

3.1.4 Focal flicker ERG

This section describes the protocol used to record the focal flicker ERG based a previously published methods (Binns and Margrain, 2007).

3.1.4.1 Recording protocol

An amber stimulus (λ_{max} = 595 nm, half-height bandwidth =17 nm) with an average luminance of 30 cd.m^{-2} (1500 photopic td.s) subtending 20° at the eye, was presented at a temporal frequency of 40 Hz (50% duty cycle). A wavelength of 595 nm was selected to be a good stimulus for the l and m cones, whilst the luminance (30 cd.m^{-2}) produced a good signal to noise ratio without significantly bleaching the retina. A luminance matched (30 cd.m^{-2}) desensitising square white surround (118° width) was used to suppress responses from the peripheral retina. Each trace was recorded using a 50 ms time base and consisted of 100 averaged responses; eight traces were recorded per participant. Responses were band-pass filtered from 10 to 100 Hz.

Using a time base (= analysis interval) of 50 ms, with a stimulus of 40 Hz provided for exactly 2 response cycles. By ensuring the number of response cycles were whole integers (for the stimulus frequency used, i.e. 40Hz) within the analysis interval, the introduction of 'trends' due to aliasing or extra harmonics due to 'leakage' were avoided (Bach and Meigen, 1999).

The harmonic content of the focal flicker ERG was assessed in 5 healthy participants (age 56-75 years, median 65). The amplitude of the first 8 harmonics was calculated as a percentage of the 1st harmonic (fundamental) for each participant. This analysis showed that the 2nd Harmonic represented between 11 and 32 % (mean 21%) of the fundamental, whilst the 3rd harmonic represented between 4 and 14 % (mean 8%) of

the fundamental amplitude. All additional harmonics represented less than 10% of the fundamental in these participants.

3.1.4.2 Data analysis

The ERG traces were exported and analysed using Excel (Microsoft. Redmond, WA). The traces were drift corrected and then the first harmonic of the 40 Hz response was isolated using Fourier analysis (see figure 3.1.4) (Stroud, 1986). The amplitude and implicit time of the first harmonic were objectively determined using Excel for each trace separately then averaged. The traces were inspected visually to confirm the objective analysis.

The first harmonic was isolated for analysis as it has been shown to be dominated by bipolar cell activity, most closely reflecting outer retinal activity if interest, whilst the higher harmonics have a stronger contribution from inner retinal neurones (Kondo and Sieving, 2001; Hare and Ton, 2002; Kondo and Sieving, 2002; Viswanathan et al., 2002). Furthermore, higher harmonic noise, such as the 50 Hz 'mains hum' was also removed from analysis.

A consequence of the artefact reject (above 50 μV) setting the potential for 'trend' artefacts in the averaged data exists, therefore prior to Fourier analysis a ramp function was applied to neutralise any trend effects within the ERG trace, thus limiting the introduction of harmonic content not related to the stimulus (Bach and Meigen, 1999).

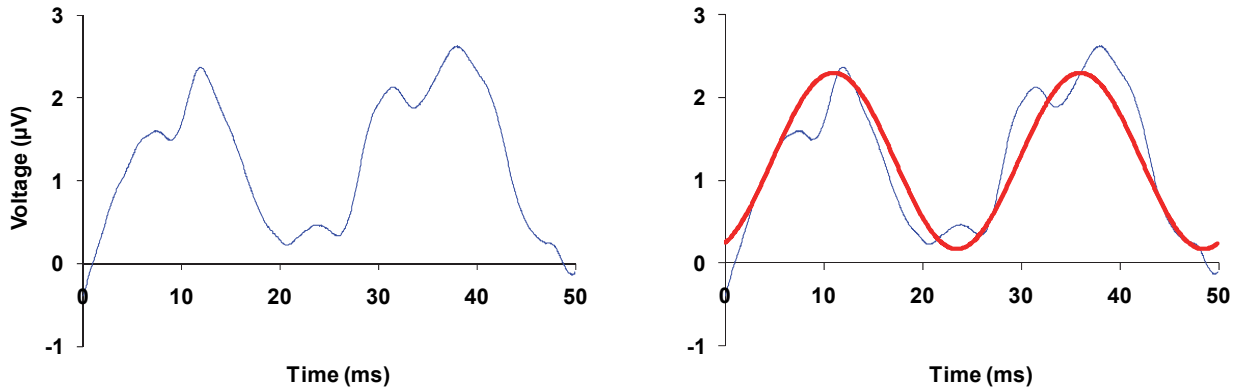

Figure 3.1.4: Raw flicker ERG (40 Hz) waveform for a healthy participant (left, blue trace) and the Fourier analysed flicker ERG waveform (right, red trace).

3.1.5 ERG photostress test

The following describes the recording of the ERG photostress test based on the previously published methods of Binns and Margrain (2005; 2007).

3.1.5.1 Recording protocol

Four focal flicker ERGs (see section 3.1.5) were recorded to provide a baseline measure. A Maxwellian view imaging system was used to provide a retinal illuminance of 144543 photopic td.s (5.16 log photopic td.s) to the central 40° of the retina for 1 minute, which produced an equilibrium bleach of approximately 80% of cone photopigment (see Appendix A & B) (Westheimer, 1966; Hollins and Alpern, 1973; Paupoo et al., 2000). Immediately after the cessation of the bleach, focal flicker ERG traces were obtained at 20 s intervals for 5 minutes.

3.1.5.2 Data analysis

The average phase of the four baseline focal flicker ERG traces was used, with a flexibility of 5 ms, to phase-lock the Fourier analysis so that only the 40 Hz component in phase with the original signal was extracted from the post-bleach recordings. This improved the SNR by eliminating all 40 Hz signals not time locked to the stimulus onset or with a different phase from the pre-bleach response.

The amplitudes of the first harmonic of the post-bleach focal flicker ERGs were then modelled using an exponential function (see equation 3.1) which has been shown to reflect photopigment regeneration (Binns and Margrain, 2005). The data were fitted using a least squares fit paradigm using the solver function within Excel (Microsoft. Redmond, WA). The modelled data returned values for the time constant of photopigment regeneration (τ), pre-bleach amplitude (μv) and initial bleach effectiveness (%).

Equation 3.1: $\text{Amplitude}(t) = a\,[1 - B * \exp(-t/\tau)]$

Where “t” is time after the photobleach in seconds (s), “a” is the pre-bleach amplitude (μv), “B” is the initial bleach effectiveness (%) and “τ” is the time constant in seconds (s). “B” was constrained to return a positive value.

3.1.6 Focal rod ERG

The following describes the protocol used to record the focal rod ERG test, based on a previously described methods (Binns and Margrain, 2006).

3.1.6.1 Recording protocol

A 1 scotopic cd.m^{-2} blue stimulus, following dark adaptation for 20 minutes, (λ_{max} = 454 nm, half-height bandwidth =67 nm, 1.7 log scotopic td.s) subtending 20° at the eye was presented to the eye at a temporal frequency of 0.5 Hz. A desensitising 0.9 scotopic cd.m^{-2} green Ganzfeld surround was used (λ_{max}= 525 nm, half-height bandwidth = 37 nm, 1.67 log scotopic td.s) to suppress responses from rods in the peripheral retina.

Each trace was recorded using a 500 ms time base with a 50 ms pre-stimulus baseline, and comprised 25 responses which were digitally averaged (recorded in blocks of 5 to minimise blink artefacts).

3.1.6.2 Data analysis

The ERG traces were exported to Excel (Microsoft. Redmond, WA) and drift corrected prior to Fourier analysis (Stroud, 1986). Fourier analysis involved the isolation of the first 9 harmonics (removing all frequencies above 45 Hz; see figure 3.1.5). The a and b waves were identified objectively from the resultant waveform using Excel, and amplitude and implicit times determined (see table 3.1.3). The objective assessment was confirmed by visual inspection.

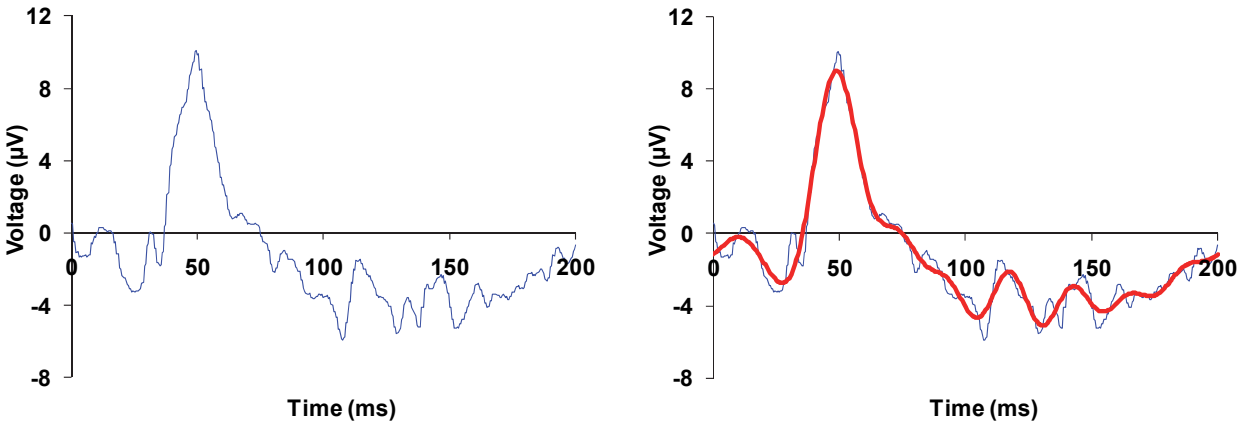

Figure 3.1.5: Raw focal rod ERG waveform for a healthy participant (left, blue trace) and the Fourier analysed focal cone ERG waveform (right, red trace).

Parameter	Selection
a-wave implicit time (ms)	The time from flash onset to the amplitude minimum between 20 to 40 ms post flash.
a-wave amplitude (μV)	The potential difference from the time of flash onset to the amplitude minimum between 20 to 40 ms post flash.
b-wave implicit time (ms)	The time from flash onset to the amplitude maximum between 40.2 to 70 ms post flash.
b-wave amplitude (μV)	The potential difference between the amplitude minimum between 20 to 40 ms post flash, and the amplitude maximum occurring between 40.2 to 70 ms post flash.

Table 3.1.3: Criteria for identification of a and b wave parameters of the focal rod ERG waveform.

3.1.7 Equipment

In the recording of all focal cone ERGs, the adapting surround was provided by a light box containing white LEDs, which were viewed through an acrylic white diffuser, to provide a wide adapting field (~118°). At the centre of this adapting surround was mounted the focal stimulus set behind a diffuser. An adjustable chin rest was mounted in front of the light box to improve patient comfort and enable more accurate patient alignment with the focal stimulus (see figure 3.1.6). The light box was connected to a direct current power supply (rather than alternating current) in an effort to reduce electromagnetic noise. This equipment was used to record all focal cone ERGs, focal flicker ERGs and ERG photostress tests in this thesis unless otherwise stated.

The ERG photostress test described by Binns and Margrain (2005; 2007), used a halogen light source positioned behind a Ganzfeld bowl to produce the photobleach. This approach was also used in the preliminary study described in section 3.6. However Maxwellian view optical systems are smaller and more efficient as they achieve uniform illumination of the retina by focusing light entering the eye at the nodal point, eliminating the effect of pupil size on retinal illumination (Westheimer, 1966). A Maxwellian view bleaching system was therefore constructed to deliver photobleaches in this thesis unless otherwise stated (see figures 3.1.7 & 3.1.8). The system utilised a LED light source, with a variable voltage power supply, which was then directed through an optical system to image the light source at a location in front of the objective lens, which was coincident with the nodal point of the eye. By varying the input voltage the light intensity could be varied and therefore used to modify the photobleach delivered. The Maxwellian view optical system calibration is described in Appendices A and B.

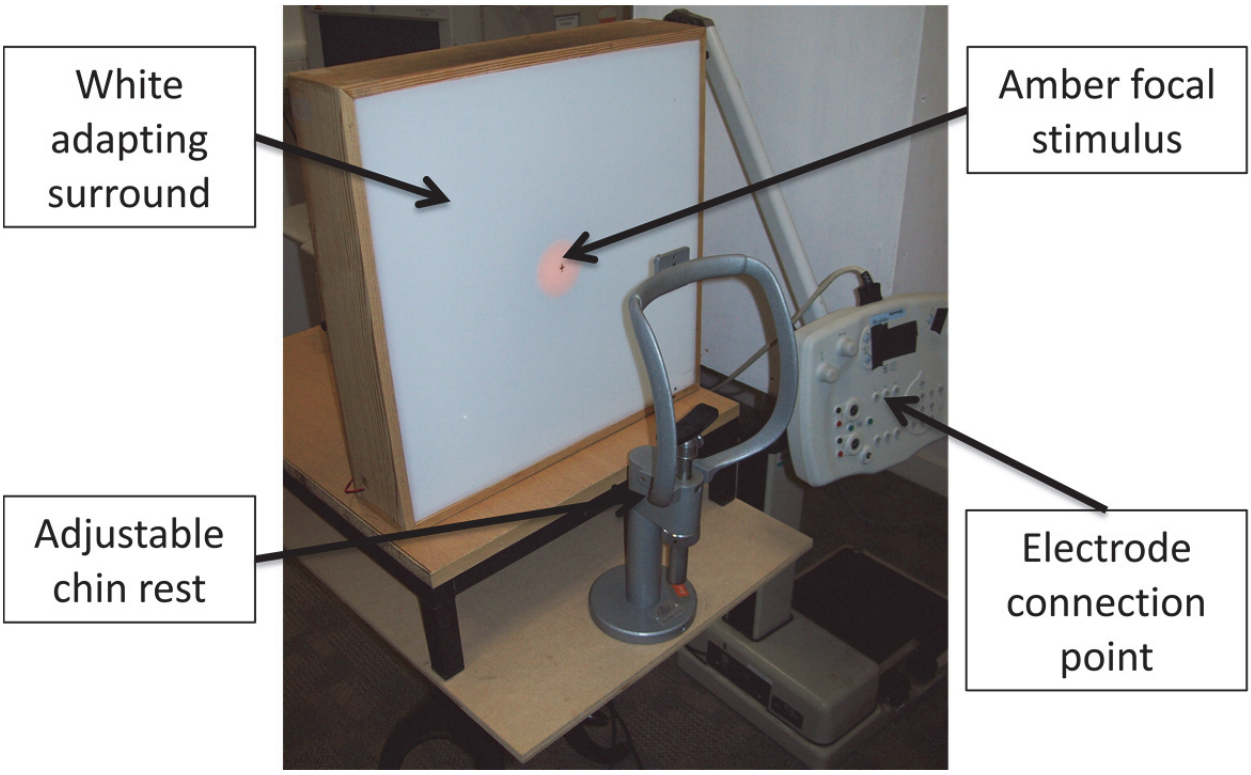

Figure 3.1.6: Photograph of the ERG photostress test "light box" with the adapting surround, focal stimulus, chin rest and the electrode connection point for the Synergy evoked potential monitoring system.

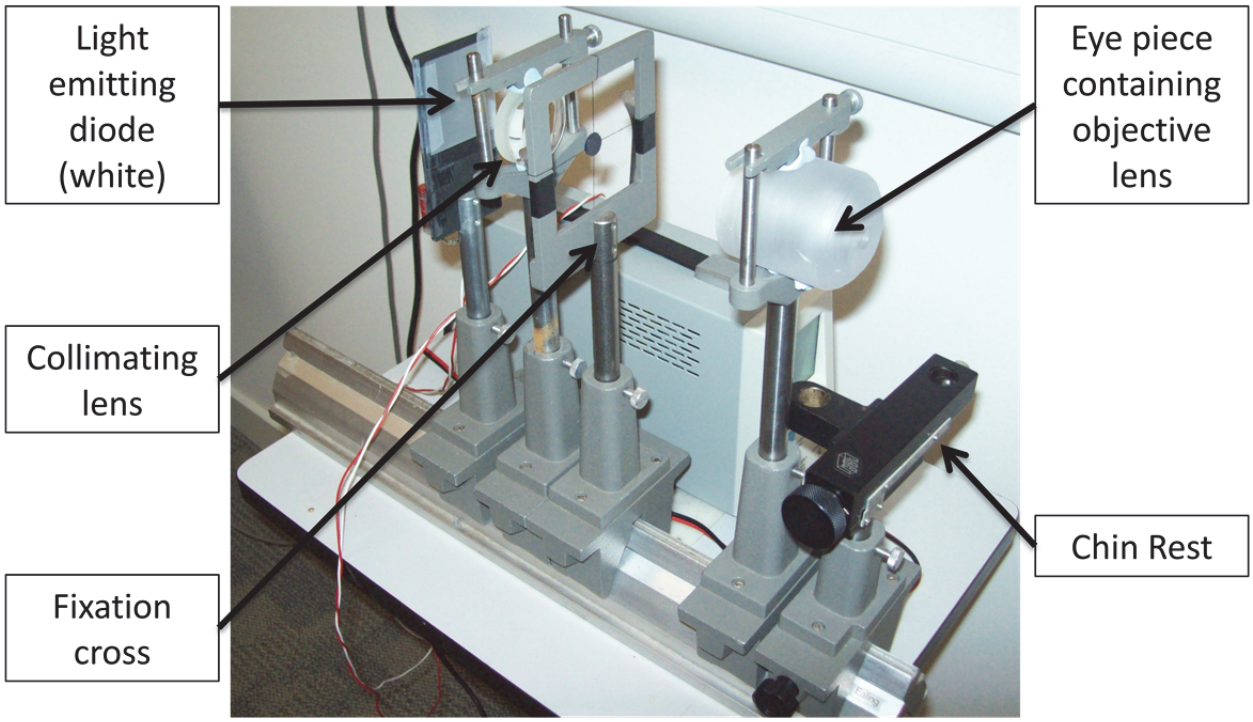

Figure 3.1.7: Photograph showing the Maxwellian view optical system with the LED, collimating and objective lenses, fixation cross and chin rest labelled.

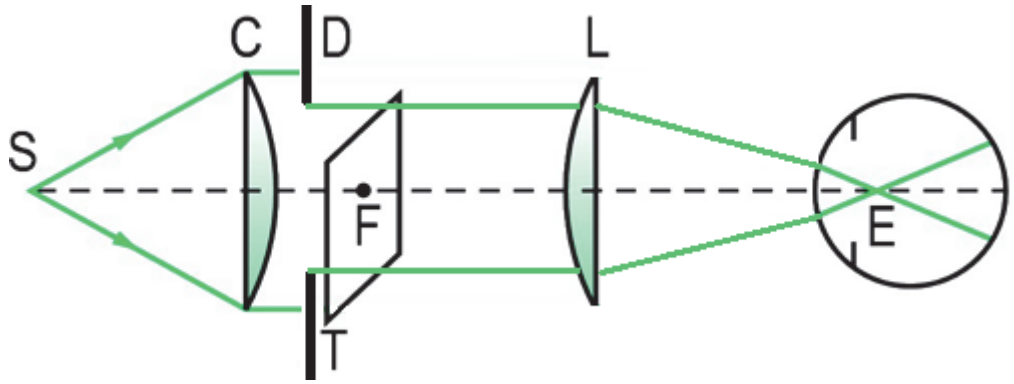

Figure 3.1.8: A diagrammatic representation of the Maxwellian view optical system showing the source of light (S); collimating lens (C); diaphragm (D); fixation target (T) in the focal plane of objective lens (L); the first focal point (F) of objective lens (L) which is conjugate of the retina of an emmetropic eye; the centre of the entrance pupil of the eye (E). Image adapted from Millodot (2009).

3.2 Establishing optimal electrode placement

Current ISCEV standards for full field ERGs recommend the use of a bipolar corneal lens or reference skin electrode for flash ERG recording, attached to the ipsilateral temple of the eye being examined (Marmor et al., 2009). However, electrode positioning has been shown to affect ERG amplitude in canines (Mentzer et al., 2005). In cases of monocular ERG recording, it is possible to use a reference electrode on the cornea of the contralateral eye, this approach has been shown to produce larger pattern ERG amplitudes than the traditional ipsilateral skin electrode for pattern ERGs (Aldebasi et al., 2001). Aldebasi et al. (2001) speculated that contralateral corneal reference electrodes produced more reliable results as artefacts due to blinking and eye movement were common to both eyes, which allowed differential amplification to give an improved SNR. Therefore, ISCEV standard for pattern ERGs suggest using a contralateral corneal reference electrode to record monocular pattern ERGs (Holder et al., 2007).

To determine the effect of reference position on the quality of ERG recordings a preliminary experiment was conducted. Specifically, ERGs were recorded with an active DTL fibre electrode and 4 different reference electrode positions. The ERG response amplitude and clinical ease of use were considered before selecting a preferred electrode setup for use in this thesis.

3.2.1 Methods

Seventeen healthy participants (ages 18-39 years) were recruited, four skin electrodes and bilateral DTL fibre electrodes (Dawson et al., 1979) were applied as shown in figure 3.2.1. This arrangement provided an active, earth and four reference electrodes (a contralateral DTL and ipsilateral skin electrodes at 3 positions). Skin reference electrodes were positioned at 1, 3 and 5 cm from the outer canthus.

Focal flicker ERGs were recorded simultaneously for each of the four reference electrodes as described in section 3.1.4. Two hundred responses were averaged for each trace. Subsequently, the ERG amplitudes were determined for each reference electrode. The ERG amplitudes for the 4 reference electrodes were compared to identify any statistically significant differences (1-way ANOVA).

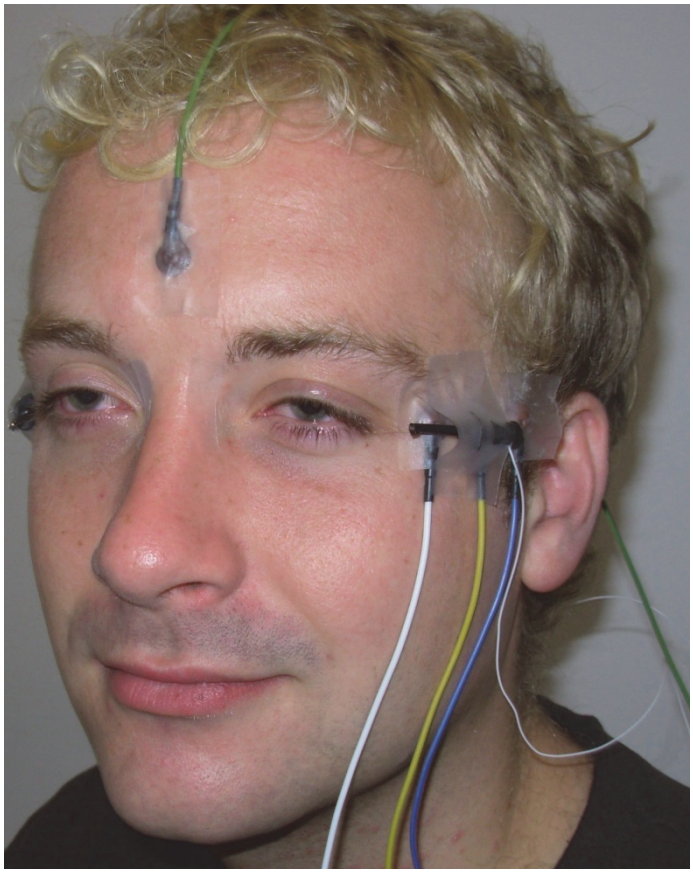

Figure 3.2.1: Electrode placement on participants. DTL fibre electrodes (black holder) were placed within the lower canthus of each eye, acting as the active electrode in the test eye (patients left eye), and reference electrode in the contralateral eye. Skin electrodes were connected to the temple, posterior to the test eye, at distances of 1 (white wire), 3 (yellow wire) and 5 cm (blue wire) to act as reference electrodes. A skin electrode attached to the forehead (green wire) acted as the earth electrode.

3.2.2 Results

The ERG amplitude data indicated an increasing amplitude with posterior displacement of the skin electrodes from the outer canthus (see figure 3.2.2), however, this was not shown to be statistically significant (P> 0.5, 1-way ANOVA). In 71% of participants the skin electrode at 3 cm (2.41 µv) demonstrated greater amplitude responses than at 1 cm (2.12 µv).

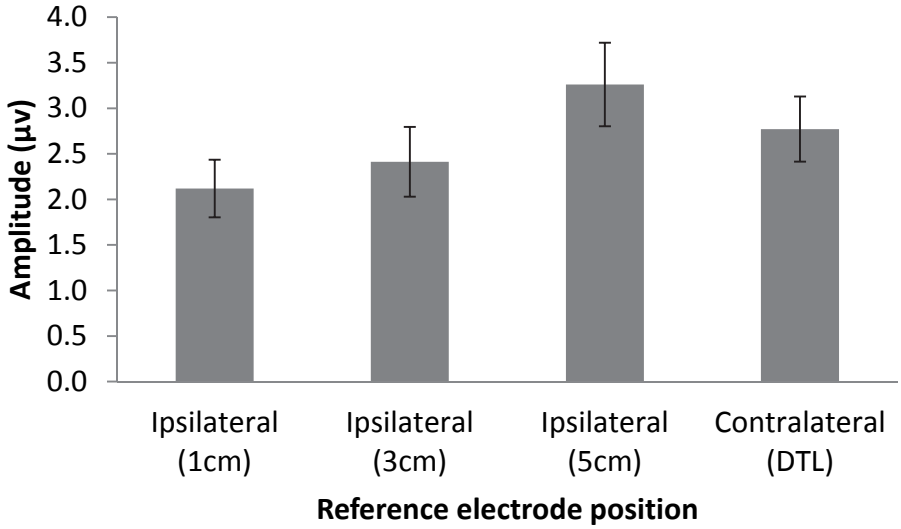

Figure 3.2.2: Graph showing average amplitude (±SEM) for each reference electrode position for 17 participants.

3.2.3 Conclusions

The skin electrode placed 5 cm posterior to the outer canthus was found not to be practical due to the anatomical position of the hair line in many participants, which made electrode attachment difficult and often resulted in high electrode impedance. The contralateral DTL electrode and the 3 cm skin electrode provided recordable responses from all 17 participants. However, the DTL electrode produced a lower contact impedance in all cases. In addition, the use of the DTL electrode enabled a rapid switch of test eye and ensured consistent electrode placement for all participants on all visits. Therefore, contralateral DTL reference electrodes were selected as reference electrodes for all monocular ERG recordings in this thesis.

3.3 Determining optimal stimulus frequency for flicker ERGs

The ERG photostress test and the focal flicker ERG both use a flickering stimulus to evoke a highly repeatable sinusoidal waveform dominated by bipolar cell activity (Bush and Sieving, 1996; Kondo and Sieving, 2002).

A range of stimulus frequencies have been used to elicit the cone flicker ERG (Miyake et al., 1987; Seiple et al., 1989; Peachey, Alexander and Fishman, 1991; Sandberg et al., 1993; Bush and Sieving, 1996; Falsini et al., 1999a; Falsini et al., 2000; Kondo and Sieving, 2002). Many studies have utilised a ~30 Hz stimulus frequency (Miyake et al., 1987; Peachey et al., 1991; Falsini et al., 1999a), this is also the recommended frequency for full field flicker ERGs given in the ISCEV standards (Marmor et al., 2009). Studies on monkeys have used similar frequencies, for example 33 Hz in the case of Bush and Sieving (1996), and 32 Hz by Kondo and Sieving (2002). However, other studies have used frequencies in the 40 Hz range, for example, Binns and Margrain (2005; 2007) and Falsini et al. (2000) used a 41 Hz, whilst Sandberg et al. (1993) used a 42 Hz stimulus frequency. In order to determine which stimulus frequency would produce the largest response, and hence contribute to obtaining the best SNR, focal flicker ERGs were recorded using a range of frequencies, and the amplitude of the responses compared.

3.3.1 Methods

Eleven healthy participants (age 18-31years) were recruited and focal flicker ERGs were recorded following the protocol set out in section 3.1.4. Each flicker ERG trace comprised 200 digitally averaged responses. Focal flicker ERGs were recorded in response to stimuli of temporal frequency between 10 and 60 Hz, at 5 Hz intervals. The timebase was adjusted depending on the temporal frequency to ensure a full response cycle (peak and trough) was included within each trace. The flicker ERG amplitudes were measured manually (peak to trough) using the calliper function of the Synergy onboard software (Medelec Synergy EP; Oxford Instruments Medical, Surrey, UK). The mean amplitudes for each stimulus frequency were then plotted for comparison.

3.3.2 Results

Data were obtained at 25, 30, 35 and 40 Hz stimulus frequencies for all participants (n=11), whilst amplitudes were determined for stimulus frequencies between 10 and 60 Hz for a smaller number of participants (n=5). The mean amplitude values (and standard errors) are shown in figure 3.3.1. The peak amplitude was seen at 10 Hz before declining

to a local minimum at 20 Hz, the amplitude recovered and reached a second maximum between 30 and 40 Hz. Frequencies above 40 Hz resulted in progressively smaller amplitudes.

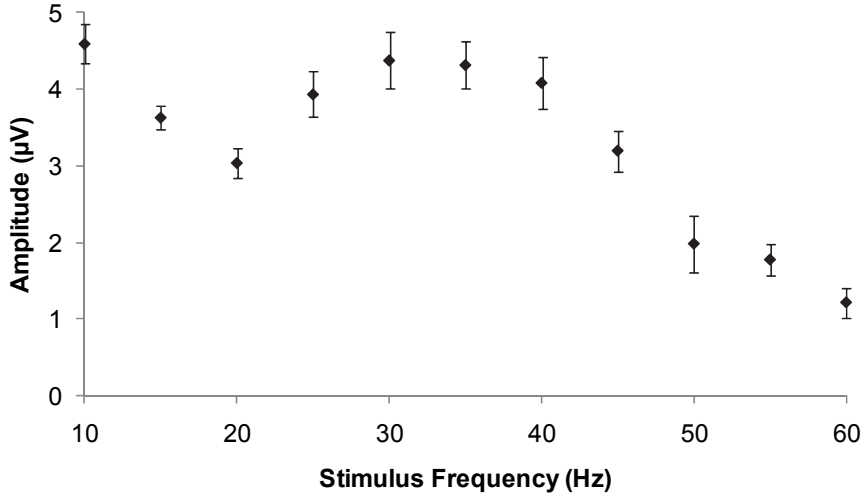

Figure 3.3.1: Graph showing ERG amplitude for a range of stimulus frequencies, error bars represent standard error.

3.3.3 Conclusions

A maximum amplitude was found at 10 Hz however, stimuli at this frequency could include a rod contribution (Sharpe et al., 1989), and therefore would not be suitable for use with the focal flicker ERG or ERG photostress tests which aim to elicit a cone response. The results also demonstrated a second peak in amplitude response to stimuli in the 30 to 40 Hz range. This finding is similar to that reported by Seiple et al. (1989) who evaluated the effect of stimulus frequency on ERG amplitude in 6 normal subjects. The results of that study showed that a stimulus frequency of 40 Hz produced the largest ERG amplitude. Falsini et al. (2007) assessed the focal (central 18°) flicker ERG amplitude over a range of stimulus frequencies for 3 groups of subjects, i.e. young (n=13), old (n=9) and people with early ARM (n=18). The young group produced a peak in amplitude at 3.7 Hz and 41 Hz, whilst a minimum was found at approximately 10Hz. The old and early ARM groups demonstrated two peaks in amplitude, the first at 14Hz and a second peak at 41Hz. Both Seiple et al. (1989) and Falsini et al. (2007) agree that peak amplitude is at ~40 Hz, in addition the results of Falsini et al. (2007) suggest that frequency sensitivity changes with age, but does not appear to be affected in early ARM.

Given these findings and the evidence in the literature, it was decided to use a 40 Hz stimulus frequency for the focal flicker ERG and ERG photostress test. The 40 Hz

stimulus frequency also allowed more data to be averaged within a fixed time period than the ISCEV standard of 30 Hz (Marmor et al., 2009). This was an important consideration when using the focal flicker ERG to monitor rapid cone recovery after a photobleach.

3.4 Assessment of stimulus size

The literature reveals that a range of stimulus sizes has been used to evoke focal ERGs from participants with macular disease; a summary of these is given in table 3.4.1. Stimuli ranging from 2.8° in diameter, to assess foveal function (Mayer et al., 1994), to as large as 20° to evaluate the whole macular region (Binns and Margrain, 2005; Binns and Margrain, 2007) have been used, although few studies have provided a rationale for the stimulus size used. However, Falsini et al. (1999b) justified the use of a 9° (diameter) stimulus based on evidence provided by Curcio et al. (1996) which showed preferential loss of photoreceptors in the parafovea of patients with AMD, and on the size of the "inner macula" as defined under the International Classification and Grading System for AMD (Bird et al., 1995).

Study	Diameter of stimulus	Condition investigated
Binns and Margrain(2007)	20°	AMD
Falsini et al.(1999b)	9°	AMD
Sandberg et al.(1993)	4°	AMD (stimulator ophthalmoscope)
Falsini et al.(2007)	18°	AMD
Mayer et al.(1994)	2.8°	AMD
Seiple et al.(1989)	9°	Retinitis Pigmentosa & Stargardt's Disease
Remulla et al.(1995)	4°	AMD
Birch and Fish(1988)	3°	AMD (stimulator ophthalmoscope)
Piccardi et al.(2009)	4.5° & 4.5 to 18° (annulus)	AMD
Miyake et al.(1988 & 89)	5°	Normals
Terasaki et al.(2002 & 04)	15°	AMD
Nishihara et al.(2008)	15°	AMD

Table 3.4.1: A comparison of focal ERG stimuli used to assess macular function in a range of studies.

Histological evidence suggests a preferential photoreceptor loss occurs within the parafoveal region, out to ~10° from fixation, as a result of ARM (Curcio et al., 1996). Functional deficits have also been shown by electrophysiology (Feigl et al., 2005a) and psychophysical findings (Owsley et al., 2000) to be present within this region. However, the effect of disease may not be uniform over this area and therefore comparison of

function in the central retina (central 5-10° diameter) to the wider macula (20° diameter) in ARM may be more sensitive to a heterogeneous functional deficit.

As the ERG is a summed response from the retinal area stimulated, a reduction in stimulus size would be expected to reduce the amplitude of the response. To determine whether this reduction in amplitude would render the SNR too low for the response to be measured, focal flicker ERGs and the ERG photostress test were carried out with different diameter stimuli on two participants prior to any further investigation of stimulus size.

3.4.1 Methods

Two healthy participants (AW age 23, AB age 30) were recruited and focal flicker ERGs recorded as described in section 3.1.4. A black paper mask was placed over the original 20° stimulus to reduce its size to 10° or 5° in diameter. Four focal flicker ERGs were recorded from each participant with a 20° and 10° diameter stimulus, the participant AW had a further 4 focal flicker ERG traces recorded with a 5° diameter stimulus. In addition, ERG photostress tests were performed using the protocol described in section 3.1.5 on participant AB with a 10° and 20° diameter stimulus. Both the focal flicker ERGs and the ERG photostress test recovery curves were assessed visually and amplitudes measured. Responses obtained using the different stimulus sizes were then compared.

3.4.2 Results

The focal flicker ERG traces are shown in figure 3.4.1. It is apparent that the biphasic waveform is diminished for the 10°, and almost extinguished for the 5° diameter stimulus. The ERG photostress test recorded using the 10° stimulus for participant AB produced a diminished amplitude recovery (see figure 3.4.2) and resulted in a considerably lengthened time constant (306 s) in comparison to the 20° stimulus (109.7 s).

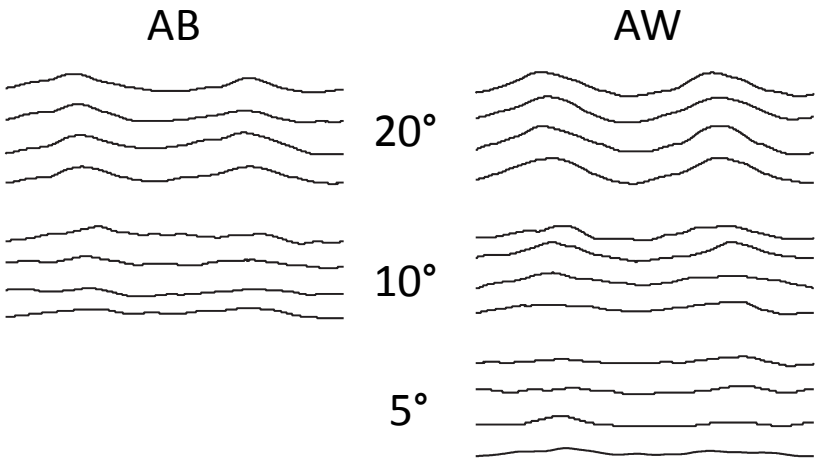

Figure 3.4.1: Pre-bleach flicker ERG traces obtained from participant AB (Left) for a 20° diameter stimulus and 10° diameter stimulus. Flicker ERG traces from participant AW (Right) using a 20°, 10°and 5° diameter stimulus.

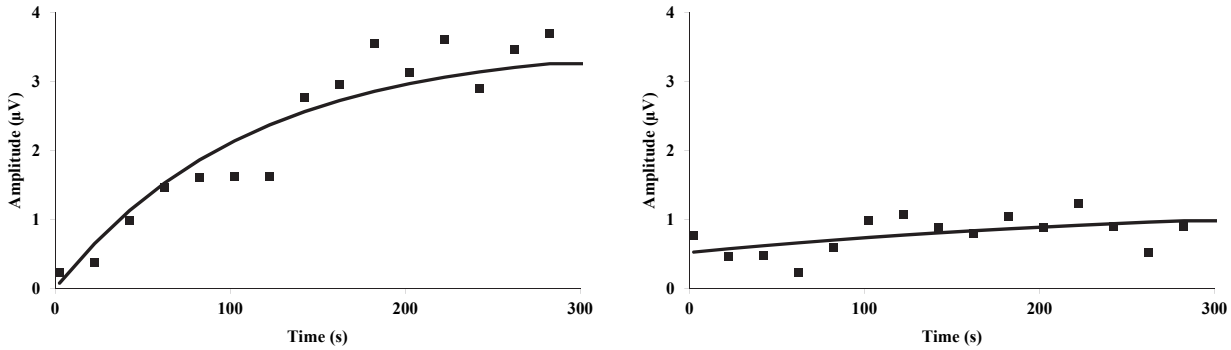

Figure 3.4.2: ERG photostress test recovery curves from participant AB for a 20° diameter stimulus (Left) with a time constant (τ) of 109.7s, and a 10° diameter stimulus (Right) with a time constant (τ) of 306s.

3.4.3 Conclusions

As was expected, the amplitude of the focal flicker ERG was diminished when elicited using a smaller stimulus size. In addition, the low amplitude responses elicited by the 10° diameter stimulus showed a more variable recovery in the ERG photostress test than those produced by the 20° diameter stimulus, presumably due to the lower SNR. Given that these results were from healthy young participants, it was deemed unlikely that a smaller stimulus size could produce reliable or repeatable results, particularly in participants with compromised retinal function, and therefore the 20° diameter was used for all further ERG recording.

3.5 Assessing adaptation to the stimulus

The ERG photostress test records consecutive focal flicker ERGs following a photobleach, and assesses the amplitude recovery. To determine if this recovery may be affected by physiological adaptation to the flickering stimulus the amplitude and implicit time of the flicker ERG was assessed over an extended period of recording, in the absence of a photobleach.

3.5.1 Methods

Two experienced participants (AB age 30 and TM age 44) were recruited and a series of flicker ERGs were recorded (using the otherwise similar protocol described in section 3.1.4) in response to a full field stimulus at regular intervals for a period of up to 1500 seconds. The interval between consecutive ERG recordings was 20 s (initially) and 40 s (after 300 s) during the period of recording, this was done to limit participant fatigue and loss of concentration during the lengthy recording session. The participants were required to maintain fixation of the flickering stimulus throughout the recording session. The amplitude and implicit time of the flicker ERGs were determined and plotted against time for each of the participants to allow qualitative assessment of any adaptation effects. Participants were adapted to the ambient room lighting prior to ERG recording.

3.5.2 Results

The data demonstrated a small increase in implicit time over consecutive recordings, that was demonstrable upon repetition for both subjects (see figure 3.5.1). This change appeared to have stabilised within 400 seconds. The amplitude data similarly appeared to show a small increase over the first 400 seconds before stabilising (see figure 3.5.2).

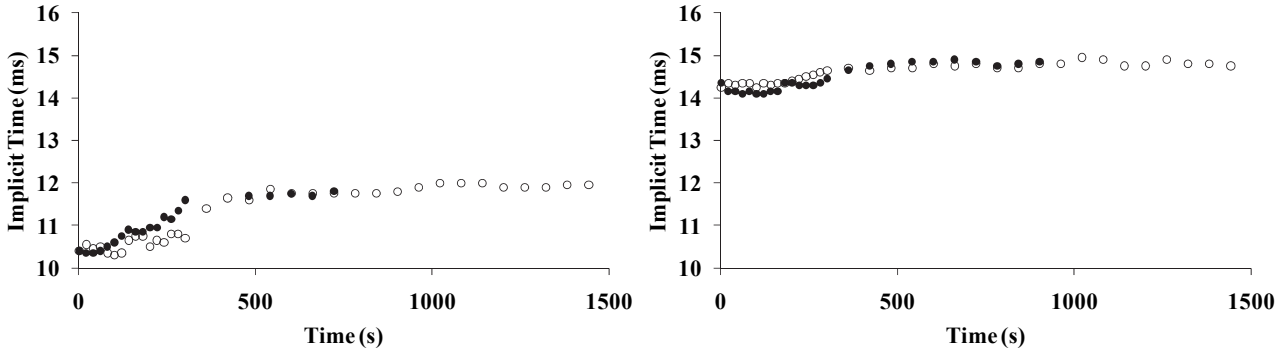

Figure 3.5.1: Implicit time plotted against time for participant TM (left) and AB (right) showing the effect of adaptation to stimuli on two separate occasions.

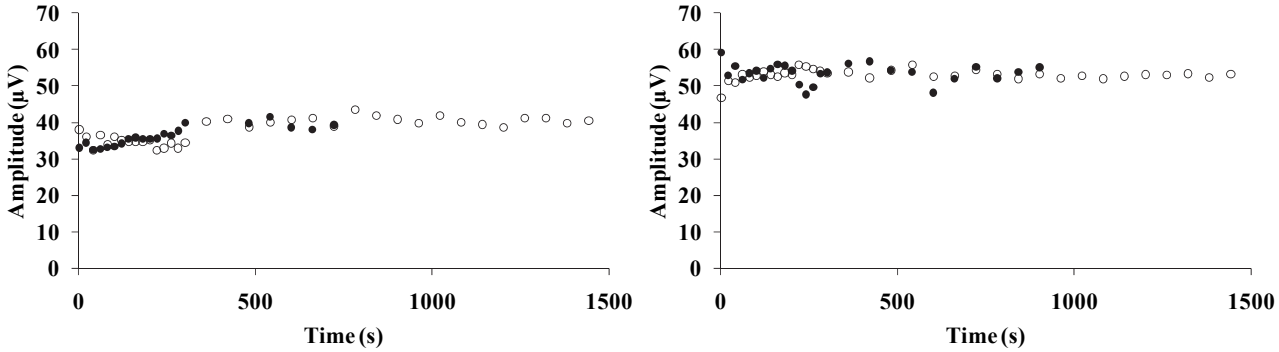

Figure 3.5.2: Amplitude plotted against time for participant TM (left) and AB (right) showing the effect of adaptation to stimuli on two separate occasions.

3.5.3 Conclusions

Given the changes in implicit time and amplitude over the first 400 seconds following exposure to the flicker stimulus, it was decided that participants should undergo a 5 minute period of adaptation to the flicker stimulus prior to the ERG photostress test and focal flicker ERG recordings.

3.6 The ERG photostress test: A comparison of bleaching techniques and the effect of age

The study described in this section has been published (Wood, Margrain and Binns, 2011b), and is presented in Appendix L.

3.6.1 Introduction

In previous dark adaptation and photostress studies, photopigment bleaches have been produced in one of two ways. The first method typically involves the use of a

photoflash unit which produces a very brief but intense flash of light (Owsley et al., 2001; Bartlett, Davies and Eperjesi, 2004; Wolffsohn et al., 2006; Owsley et al., 2007; Dimitrov et al., 2008; Newsome and Negreiro, 2009). The second method exposes the retina to a less intense but longer duration light until equilibrium is reached between photopigment bleaching and regeneration (Hollins and Alpern, 1973; Midena et al., 1997; Mahroo and Lamb, 2004; Binns and Margrain, 2005; Binns and Margrain, 2007).

The literature suggests that the kinetics of cone photopigment regeneration are different in these two situations. Following an equilibrium bleach the recovery rate is not dependent on the percentage of photopigment bleached (Hollins and Alpern, 1973). For a short duration bleach the recovery rate shortens as the percentage bleach achieved increases, furthermore even when an equivalent percentage bleach is achieved recovery is faster following a short bleach than an equilibrium bleach (Hollins and Alpern, 1973). Given that clinic time is at a premium, the use of a photoflash is an attractive alternative to the longer duration equilibrium bleach that was used by Binns and Margrain (2007).

The first aim of this study was to compare the intersession repeatability of the ERG photostress test recorded using an equilibrium and photoflash bleach. Additionally, the psychophysically determined time constant of cone dark adaptation is known to be affected by age (Coile and Baker, 1992), with a reported increase of 0.21 minutes per decade. Therefore, the second aim of this study was to determine the effect of age on the time constant of recovery determined using the ERG photostress test.

3.6.2 Methods

Twenty-three healthy participants (age 20-71 years) were recruited from staff, students and volunteers attending the Eye Clinic at the Cardiff University School of Optometry and Vision Sciences.

3.6.2.1 Bleaching techniques

A long duration ‘equilibrium’ bleach was provided by a tungsten halogen source which was presented to the subject within a Ganzfeld bowl. A central fixation cross was placed within the Ganzfeld bowl such that the bleaching source subtended 40° at the eye. The focal flicker stimulus was placed directly above this, allowing the subject to quickly take up position for ERG recording at cessation of the photobleach. Heat filters were in place, which reduced output of the bleaching light to below 5% between 800-900nm, so that excessive infra-red (IR) radiation did not reach the eye. The eye was light-adapted to

a bright white background of 19905 cd.m^{-2} for a period of 2 minutes (~5.6 log photopic td.s). The effective retinal illuminance was calculated as 5.2 log photopic td.s, when adjusted for the Stiles-Crawford effect, which bleached approximately 84% of the cone visual pigment (Hollins and Alpern, 1973).

A short duration "photoflash" bleach was provided by a Metz Mecablitz 76 MZ-5 flashgun (Metz-Werke GmbH & Co., Zirndorf, Germany), positioned such that this source also subtended 40° at the eye when centrally fixated. The eye was exposed to a bright white flash of 415445 cd.s.m^{-2} (~9.5 log photopic td.s, duration 6.6ms). The effective retinal illuminance, adjusted for the Stiles-Crawford effect, was calculated as 9.1 log photopic td.s, which bleached approximately 98% of the cone visual pigment (Paupoo et al., 2000). A higher percentage bleach was chosen for the photoflash because brief bleaches are associated with more rapid recovery times, which could be problematic when attempting to monitor recovery of sensitivity.

Heat filters were used to attenuate output to below 5% between 800-900nm, so that excessive infra-red (IR) radiation did not reach the eye. Additionally a UV filter integrated within the flash gun eliminated wavelengths below 375 nm. All luminance measurements were made using an IL1700 photometer (International Light Inc, Newburyport, MA) and exposures were within the safety guidelines set out within BS EN 15004-2 (BSI, 2007) (see appendix C for calculations).

3.6.2.2 General procedure

Both bleaching protocols were evaluated with the ERG photostress test at the same recording session. Participants were randomly assigned to one of two groups determining whether the photoflash or equilibrium bleach was to be used first. The eye with better visual acuity was chosen for testing, with the left eye chosen as default in cases of equal acuity. Prior to recording, a 5 minute period of adaptation to the flickering stimulus and surround was undertaken to avoid any flicker adaptation effects during the recording period. To prevent any carry over effects between tests, a 5 minute break was implemented. The entire protocol was repeated on a second occasion within 4 weeks of the first visit for every participant. A sequential representation of the protocol undertaken at each visit is shown in figure 3.6.1.

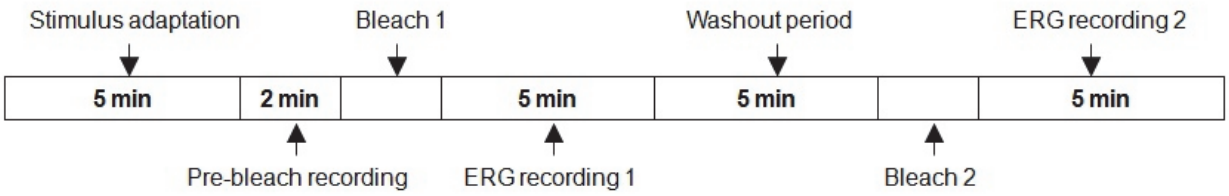

Figure 3.6.1: The timeline showing recording process for ERG photostress tests. The bleach type for tests 1 and 2 were randomly selected prior to recording for each participant, and bleach duration was either 6.6 ms or 2 minutes.

3.6.2.3 Analysis

The ERG photostress test data were analysed following the methods described in section 3.1.6, and the time constants of recovery were calculated. Inter-session repeatability of the time constant was determined by calculating the coefficient of repeatability (CoR) (determined as 1.96 x the standard deviation of differences between visits 1 and 2). The repeatability was also demonstrated graphically by plotting the difference in time constant between visits 1 and 2 against the mean time constant for both visits, a technique advocated by Bland and Altman (1986). Paired t-tests were also carried out to determine whether there was a statistically significant difference between mean data obtained at visit 1 and 2 for each technique. The time constant of recovery for the equilibrium bleach and photoflash were calculated as the average of the two visits for each participant and plotted against age. The data were then assessed for any relationship between age and the time constant of recovery (Pearson's correlation coefficient).

3.6.3 Results

Typical focal flicker ERG traces for 3 participants aged 23, 44 and 60 are shown in figure 3.6.2. The upper traces are the pre-bleach baseline and represent the expected waveform after a full recovery. The subsequent 15 traces were recorded at 20 second intervals following the bleach. The recovery in ERG amplitude post-bleach, towards the baseline level, is apparent in these participants for both bleaching modalities. Figure 3.6.3 plots ERG amplitudes as a function of time for each participant and the amplitude recovery data have been fitted with an exponential function (see equation 3.1 and section 3.1.5).

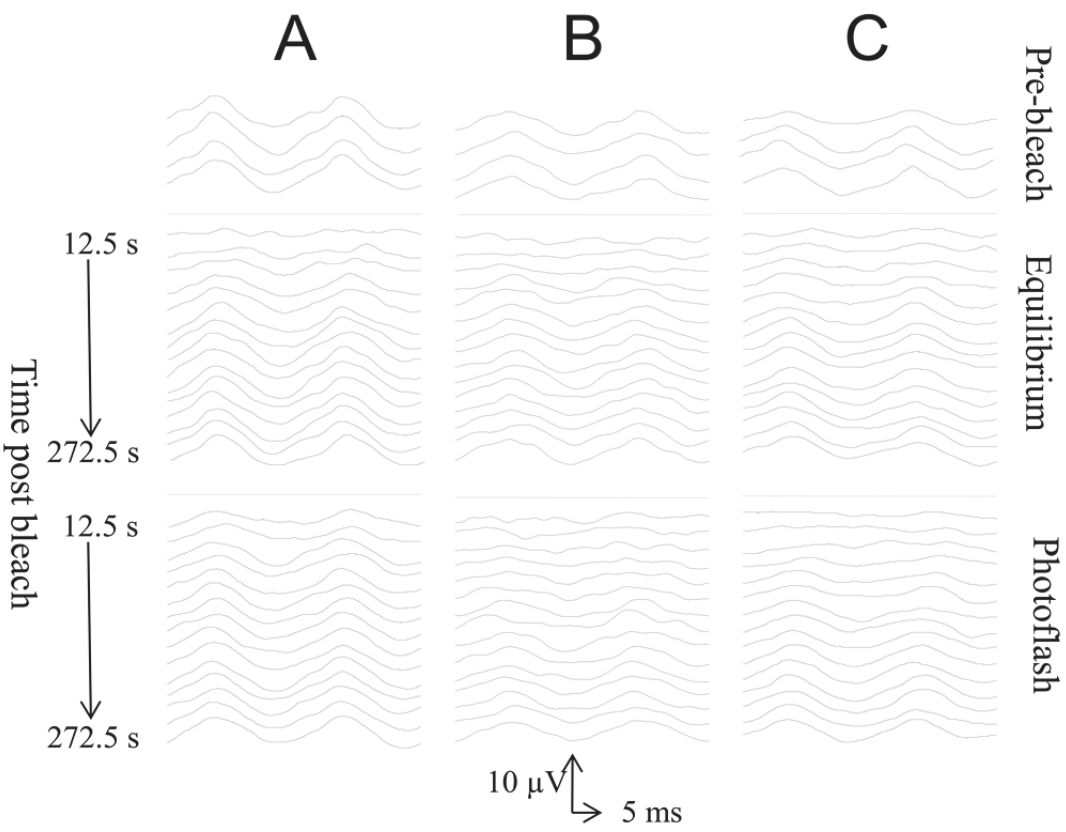

Figure 3.6.2: Focal flicker ERG traces for participant A (aged 23 years), B (aged 44 years) and C (aged 60 years). Top panel shows pre-bleach traces, middle panel shows traces following an equilibrium bleach and the bottom panel shows the traces following a photoflash bleach.

ERG photostress tests were recorded from all 23 participants on both occasions, only 1 recovery was excluded due to excessive recording noise. However, of the tests conducted using the photoflash, 8 were excluded due to ineffective bleaching i.e. the 'bleach' did not diminish the amplitude of the focal flicker ERG and hence there was no recovery. Of the 8 failed photoflash bleaches, one participant did not produce valid results on either visit. The mean time constants for the equilibrium and photoflash bleach techniques (Visits 1 and 2) were 117 (±72) s and 112 (±58) s respectively. This difference was not statistically significant ($p>0.05$; paired t-test).

Figure 3.6.4 describes the repeatability of each technique, the CoR was 85 s (n=22) for the equilibrium bleach and 184 s (n=16) for the photoflash bleach. The mean difference between visits was close to zero, indicating no overall bias for either technique (see figure 3.6.4).

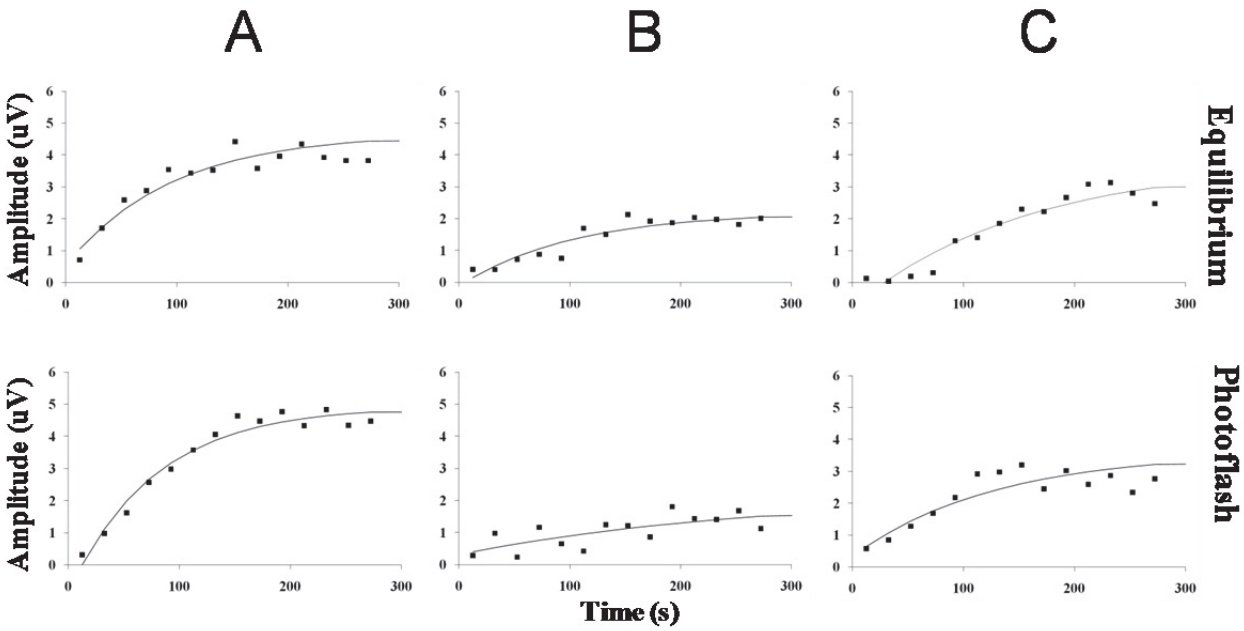

*Figure 3.6.3: ERG amplitudes for participant A, B and C plotted against time post bleach, and recovery to baseline modelled with an exponential function for the equilibrium (Participant A; **T** = 95.6, Participant B; **T** = 103.5, Participant C; **T**= 157.8) and photoflash bleach (Participant A; **T** = 77.8, Participant B; **T** = 273.2, Participant C; **T** = 127.5,).*

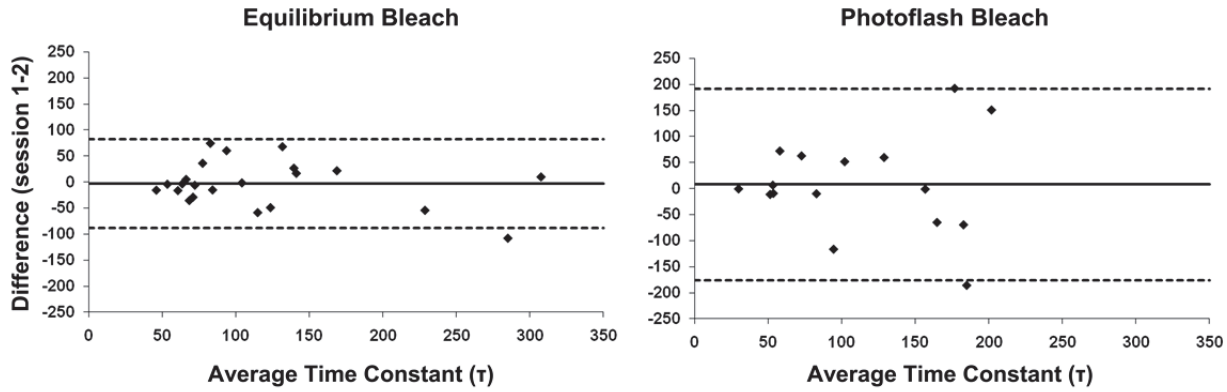

Figure 3.6.4: Intersession difference plotted against intersession average providing a graphical representation of intersession repeatability as advocated by Bland and Altman (1986). The solid horizontal line represents the mean difference between visits 1&2, whilst the dotted lines indicate the 95% limits of agreement; a narrower interval between these lines indicates better repeatability. The coefficients of repeatability (1.96 x SD of differences) for each technique were 85 s (equilibrium bleach) and 184 s (photoflash). This analysis does not include data from those participants who were excluded due to ineffective photoflash bleaching.

Figure 3.6.5 plots the time constant of recovery as a function of age for the ERG photostress test carried out using the equilibrium bleach. The time constant (**T**) of recovery increased significantly (r=0.66, p=0.0008; Pearson's correlation coefficient) with age (by 27.6 s per decade), there was also a subjectively evident increase in variability with older participants. There was no significant relationship with age for the photoflash bleach.

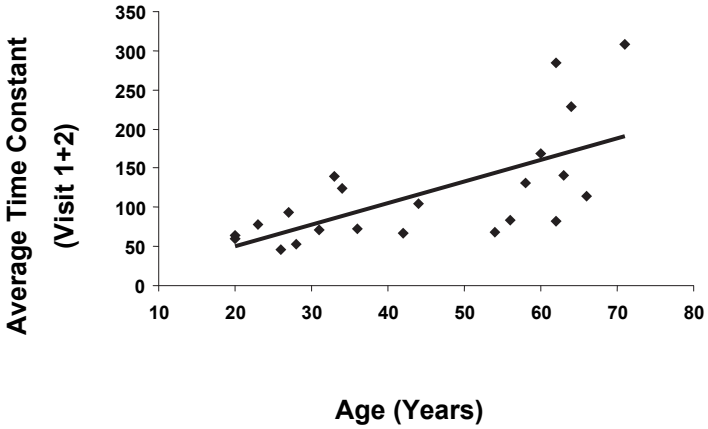

Figure 3.6.5: The relationship between mean time constant and age for the equilibrium bleach data. A statistically significant correlation was identified for the equilibrium bleach (r=0.66 p=0.0008; Pearson's correlation coefficient).

3.6.4 Conclusions

The results provide compelling evidence for the retention of the equilibrium bleach as part of the ERG photostress test. The equilibrium bleach showed relatively good repeatability (CoR 85 s) and was successfully recorded on 45 out of 46 occasions. The photoflash bleach, by comparison, was less repeatable (CoR 184 s) and did not always provide an effective bleach.

The ERG photostress test has been shown to differentiate those with ARM from age matched controls demonstrating a mean difference of 106 s in time constants between groups (Binns and Margrain, 2007). Given that the coefficient of repeatability for the photoflash technique (184 s) is larger than the difference between those with and without disease (106 s) it is apparent that the sensitivity and specificity of the ERG photostress test would be compromised by switching to the photoflash bleaching method.

It is noteworthy that this assessment of the repeatability of the photoflash bleaching method only included data from 16 out of 23 subjects for whom a post bleach recovery was available. The observation that the photoflash unit did not diminish the amplitude of

the focal flicker ERG in 7 participants suggests that blinks or gross fixation losses must have coincided with the timing of the photoflash discharge. Given the number of bleach failures, additional bleaches would need to be administered to obtain satisfactory results. In a clinical situation this would increase examination time making the technique clinically unviable. The instantaneous nature of the photoflash exposure may also have increased the potential for partial bleaches due to inaccurate patient fixation and incomplete blinks and this may have contributed to the relatively poor CoR of this technique. This renders the technique unreliable.

In contrast, the equilibrium bleach allows 2 minutes to bleach the retina, therefore transient fixation losses and blinking are unlikely to affect the photopigment bleach obtained (see figure 3.6.6).

There is also a theoretical basis for assuming that an equilibrium bleach may provide a better separation between individuals with ARM and age matched controls than a photoflash bleach. The rod photoreceptors, when bleached, obtain the retinal required to regenerate photopigment from the RPE. As a result of this, the rate of photopigment regeneration within the rods is dependent on the health and function of the RPE and the diffusion of retinoids to the RPE from the choroidal circulation via Bruch's membrane (Lamb and Pugh, 2004). The cone photoreceptors, however, are able to regenerate photopigment using a local store of retinoid derived from the Müller cells (Mata et al., 2002), and therefore do not necessarily have the same dependence on the health of the RPE, Bruch's membrane and choroidal circulation. Abnormal RPE/Bruch's function may have little or no effect on cone photopigment regeneration whilst this local retinoid store is present. Unlike photoflash bleaches, long duration bleaches are likely to deplete local stores of 11-cis-retinal (Rushton and Henry, 1968) placing a greater emphasis on the role of the RPE in photopigment regeneration. Hence long, but not short, duration bleaches may help elucidate functional delays in people with ARM.

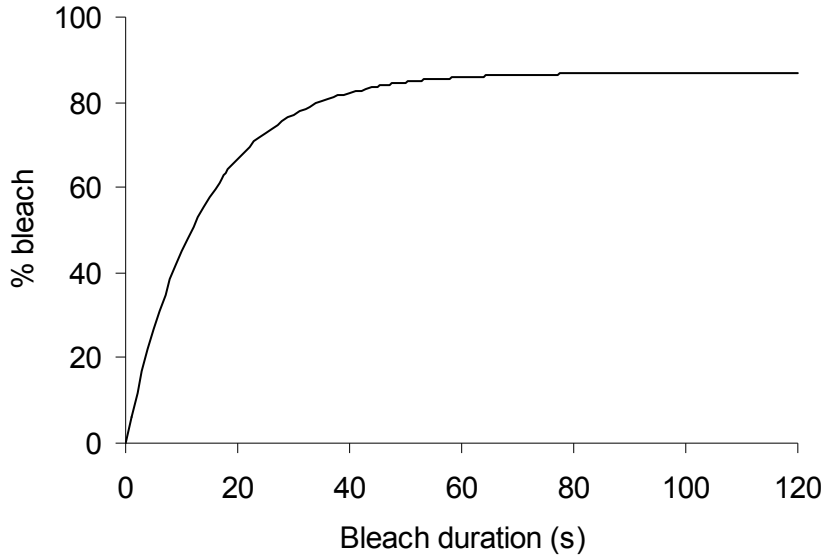

Figure 3.6.6: Percentage cone photopigment bleach achieved during exposure to a constant adapting light. Image derived from Hollins and Alpern (1973).

It has been reported that the rate of dark adaptation decreases as we get older (Jackson, Owsley and McGwinJr, 1999). The effect of age on recovery time constant in this study produced an increase of 27 seconds per decade (0.45 minutes / decade) which was comparable to the findings of Coile & Baker (1992) who showed an increase of 0.21 minutes per decade. In agreement with our findings, Coile & Baker (1992) also demonstrated greater variability in the rate of adaptation of older participants compared to younger ones. The increased variability could suggest that those apparently normal individuals with prolonged time constants may be at risk of developing ARM.

Currently ARM is identified on the basis of retinal photography, but it is possible that significant changes occur in the function of the retina prior to macroscopic changes, such as the appearance of drusen and pigmentary changes. Histological work by Sarks (1976) identified changes to Bruch's membrane and the presence of basal linear deposits beneath the retina in eyes with a normal retinal appearance and often good visual acuity. Changes in the permeability of Bruch's membrane have been suggested to be the cause of delayed dark adaptation in ARM (Steinmetz et al., 1993), so individuals with pre-clinical ARM might be expected to show abnormal time constants. Confounders such as media opacities could also be influencing the spread of data. The increase in lenticular changes with age would conceivably lead to more variability in retinal illumination, and therefore increase the variability of the results. However, this is unlikely to have played a role here

because those with marked lens opacities were excluded from the study. Hollins and Alpern (1973) also showed that equilibrium bleaches over a range of intensities produced the same time constants of recovery. This would minimise any differences in time constants (τ) due to minor media opacities.

In conclusion, the current equilibrium bleach technique was found to have intersession repeatability sufficient to be sensitive to ARM related changes. The alternative photoflash bleaching technique was found to be less repeatable and clinically unreliable. In addition the data showed that the time constant of recovery, as determined using an equilibrium bleach, was found to increase with age. Therefore the use of an equilibrium bleach with the ERG photostress test was retained, whilst the finding that time constants are affected by age means that any comparison of time constants should utilise age matched data, or should adjust for the age effect.

3.7 Recording a focal rod ERG stimulus response series

The focal rod ERG is capable of isolating a focal ERG under scotopic conditions (Binns and Margrain, 2006) (see section 1.5.7). This section investigates the relationship between luminance of the stimulus and the ERG amplitude; the so called “stimulus response relationship” and describes work that was undertaken to develop a protocol to assess the focal rod ERG intensity-response relationship.

3.7.1 Introduction - the stimulus-response relationship

The stimulus-response relationship of retinal photoreceptors, based on measurements of the photoreceptor circulating current from *in vitro* sections of fish retina, was first modelled using a function proposed by Naka and Rushton (1966b) (see equation 3.2) and will be referred to as the ‘Naka-Rushton’ function from this point onwards. This function was latterly shown to describe the human b-wave amplitude stimulus-response relationship (Fulton and Rushton, 1978). The parameters of the function have been shown to be affected in retinal diseases such as retinitis pigmentosa (Arden et al., 1983; Massof et al., 1984; Birch and Fish, 1987), diabetic retinopathy (Roecker et al., 1992) and glaucoma (Velten et al., 2001). Additionally ERG a-wave amplitudes have also been successfully modelled using the ‘Naka-Rushton’ function, with the parameters again being good predictors of retinal disease (Hood and Birch, 1990b; Holopigian et al., 2004).

The fitting of the ‘Naka-Rushton’ function to ERG stimulus-response data has been described by Severns & Johnson (1993a) (see figure 3.7.1) and demonstrated on a group

of patients with central retinal vein occlusion. The function used to describe the stimulus-response relationship between stimulus luminance, I (cd.m^{-2}.s), and ERG b-wave amplitude, R (μv), is as follows:

Equation 3.2:

$$R(I) = \frac{R_{max} I^n}{I^n + K^n}$$

Where 'R_{max}' is the maximum amplitude (μv), 'K' is the stimulus luminance at half 'R_{max}', and 'n' is an exponent which describes the slope of the curve at I=K. The parameters 'R_{max}' and 'K' are thought to reflect the "response capacity" and "sensitivity" of the retina respectively (Massof and Johnson, 1981). Hood, Shady and Birch (1994) used a computer model to predict the effect of heterogeneous photoreceptor damage on the stimulus-response function of the rod ERG b-wave and compared this with actual data from participants with retinitis pigmentosa (n = 11) and cone-rod dystrophy (n = 17). The findings demonstrated that R_{max} is decreased when an area of the retina has a reduction of sensitivity greater than 0.5 log units compared to a healthier region of the same retina. Parameter K was shown to increase in the presence of a diffuse loss of sensitivity across the retina, and/ or a substantial reduction in sensitivity (between 0.5 to 2 log units) over a large area of the retina, but to decrease once sensitivity losses exceed 2 log units. These findings suggest that R_{max} and K parameters may be sensitive to diffuse and/ or localised functional changes within the retina, and therefore are likely to be a measure sensitive to AMD related changes.

Within the literature the exponent n has often been constrained to 1, (Naka, 1969; Arden et al., 1983). Naka (1969) investigated the stimulus-response relationship for chromatically different stimuli, showing the variation of the exponent from 1 to be small and commenting that "there seemed no reason for further elaboration", suggesting that allowing n to be a free variable would add little to the goodness of fit of the model. However, Massof et al. (1984), who applied the 'Naka-Rushton' function to human ERGs and allowed the exponent 'n' to be a free variable, claimed that changes to the shape of the function determined by 'n' may "occur secondary to heterogeneous depressions of retinal sensitivity, uneven retinal illumination, or some putative neurophysiological response anomaly" (Massof et al., 1984). Therefore, given that n may vary as a result of retinal functional changes it was decided to allow 'n' to be a free variable when modelling the 'Naka-Rushton' function as part of this thesis.

The scotopic b wave ERG stimulus-response relationship comprises two limbs (see figure 3.7.1) (Peachey, Alexander and Fishman, 1989; Hood and Birch, 1990ba; Breton and Montzka, 1992), which has been attributed to an interaction of the underlying components of the ERG, with both limbs reflecting rod activity (Peachey et al., 1989). This suggests that if sufficient stimulus strength is reached, a 2nd limb will be apparent in the rod dominated focal rod ERG stimulus-response relationship. However, the 'Naka-Rushton' function only applies to, and describes, the first limb of this relationship effectively (Peachey et al., 1989; Severns and Johnson, 1993a). The first limb could be isolated by applying an upper retinal illuminance limit to the ERG stimuli, however, this may not be an effective method given the variability in the stimulus strength at which the second limb arises in different individuals (Severns and Johnson, 1993a). A second approach which has been suggested is to remove points from the second limb before modelling the data (Severns and Johnson, 1993a). Therefore, whilst developing the focal rod ERG stimulus-response series protocol, the data in this study were assessed subjectively for involvement of 2nd limb and, depending on the extent of involvement, points were removed or alterations to the protocol considered.

Simplistically, the a and b wave amplitudes and implicit times of the focal rod ERG are attributed to photoreceptor and bipolar cell function respectively. The focal rod ERG stimulus-response series may provide additional information about the integrity of scotopic visual function. This study aimed to determine the viability of recording a stimulus-response series for the scotopic b-wave and to assess the ability of the 'Naka-Rushton' function to describe the data (Naka and Rushton, 1966b).

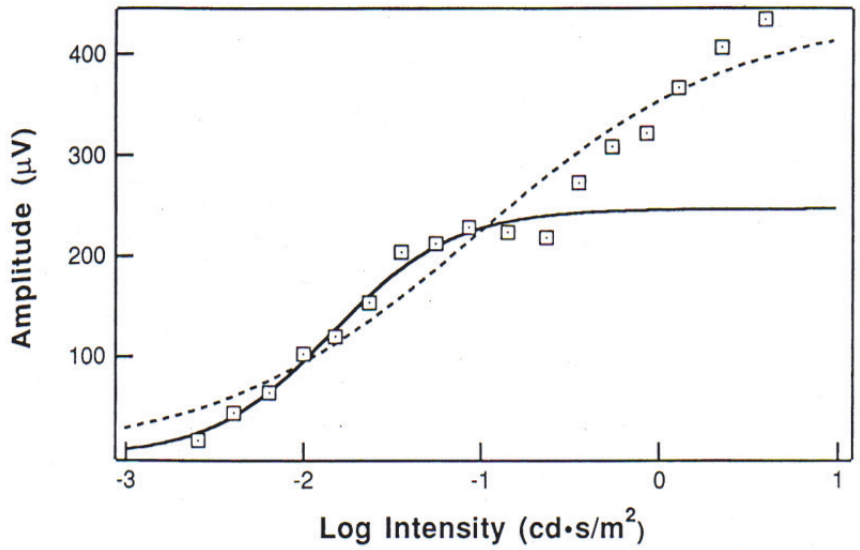

Figure 3.7.1: A scotopic ERG stimulus-response series with a pronounced second limb. The dashed curve shows the 'Naka-Rushton' function fitted to all data points comprising both the first and second limb of the series, the solid curve shows the 'Naka-Rushton' function fitted to the data points comprising the first limb only. Image from Severns & Johnson (1993a).

3.7.2 Isolation of the rod component

The first aspect of recording a focal rod ERG stimulus-response series was to ensure that the recorded ERG was rod dominated for all stimuli. Binns and Margrain (2006) determined that there would be a cone contribution to the focal rod ERG for stimuli of 50 scotopic td.s and above; the stimulus response series would exceed this stimulus strength. In order to determine the magnitude of any cone contribution to the focal rod ERG for each stimulus, Binns and Margrain (2006) presented a red stimulus to the dark adapted eye of the same photopic luminance as the blue stimulus used to elicit the focal rod ERG. On the basis that the rods are relatively insensitive to long wavelength light (Wyszeki and Stiles, 1982), any response to the red stimulus was assumed to be of cone origin. Below 50 scotopic td.s the response to the red flash was minimal, suggesting a negligible cone involvement in the focal rod ERG response. However, this approach is not ideal as rods are not completely unresponsive to the red LED (664 nm) used in the study (Wyszeki and Stiles, 1982). Therefore, the approach advocated by Hood & Birch (1996), Friedburg et al. (2001) and Birch et al. (2002) was adopted in this study whereby stimuli are presented against a rod-saturating background of 1500 scotopic td.s (30 scotopic $cd.m^{-2}$), to isolate the cone ERG component, which is then subtracted from the dark

adapted response. The first part of the study aimed to determine the luminance level at which a cone contribution must be subtracted.

3.7.2.1 Methods

A series of ERGs were recorded over a range of stimuli both with and without a rod saturating background. The participant AG (age 24) was prepared as described in Section 3.1.1. The stimulus and recording protocol outlined in section 3.1.6 was adapted as follows. The retinal illuminance of the focal stimuli were adjusted to 2.5, 5, 10, 20, 30, 40, 50, 60 and 100 scotopic td.s for successive recordings, presented dimmest to brightest. Twenty-five ERGs were averaged at each retinal illuminance, subsequently these recordings were repeated with the addition of a green (λmax 525 nm) rod saturating background (1500 scotopic td.s) to desensitise the rods; thereby isolating cone responses to the stimuli (Hood and Birch, 1996; Birch et al., 2002). The resulting ERGs were Fourier analysed and the amplitude of the b-wave measured as described in section 3.1.6.

3.7.2.2 Results

Figure 3.7.2 presents the b-wave amplitudes obtained to stimuli at each retinal illuminance. The data indicated that a cone contribution is only evident for stimuli at or above 20 scotopic td.s (0.4 scotopic cd.m^{-2}).

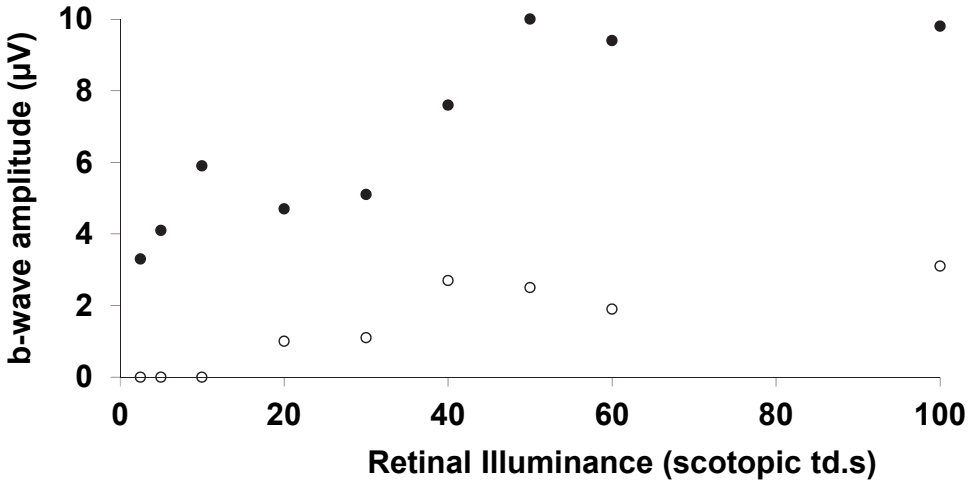

Figure 3.7.2: ERG b-wave amplitudes recorded for a range of stimuli eliciting a combined rod & cone (filled) and a cone only (open) response. The cone only response was obtained by presenting stimuli against a rod saturating background.

3.7.2.3 Conclusions

The finding of a lower retinal illuminance at which cones still contribute to the response than the 50 scotopic td.s reported by Binns and Margrain (2006) may be attributable to the different methodology employed on this occasion. To obtain a purely focal rod ERG to a stimulus above 20 scotopic td.s it is necessary to subtract the isolated cone response from the signal recorded. This subtraction technique is demonstrated in figure 3.3.4 on a focal rod ERG elicited by a stimulus of 500 scotopic td.s.

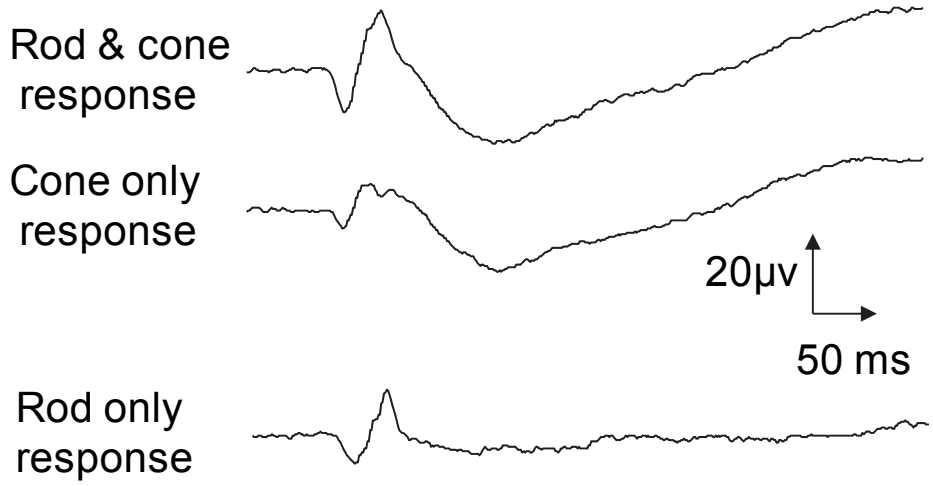

Figure 3.7.3: Subtraction technique used to isolate the Focal Rod ERG for a 500 scotopic td.s stimulus. The top trace shows the combined rod & cone response, the middle trace shows the cone only response (recorded with stimulus presented against a green rod saturating background) whilst the bottom trace shows the isolated rod response with the cone contribution subtracted.

3.7.3 Effect of the focal rod ERG recording on the adaptational state of the eye

The stimuli used to elicit the focal rod ERG may alter the adaptational state of the eye and this in turn may alter the ERG waveform. The aim of this part of the study was to ascertain whether light adaptation, produced by the ERG stimuli, could affect the focal rod ERG data by recording a series of consecutive ERG traces and assessing for changes in amplitude and implicit time.

3.7.3.1 Methods

Two participants (AW age 24 and AG age 24) were prepared as described in section 3.1.1. Focal rod ERGs were recorded following the methods described in section 3.1.6 to stimuli of 20 scotopic td.s (5 ms flash, 0.4 scotopic cd.s.m^{-2}) and 1000 scotopic

td.s (20 ms flash, 20 scotopic cd.s.m^{-2}). The subtraction of the cone component of the ERG, as described in section 3.7.2 was not undertaken on this occasion. At each retinal illuminance a series of 6 consecutive traces were recorded, with each trace comprising an average of 30 responses recorded in blocks of 5. A period of between 5 to 10 seconds, on average, for blinking was allowed between each block of 5 responses recorded, a further minute was allowed between recording with the 20 and 1000 scotopic td.s stimulus to change the stimulus intensity.

3.7.3.2 Results

The a and b wave amplitudes and implicit times for both the 20 and 1000 scotopic td.s retinal illuminance values did not show any systematic change over the 6 consecutive recordings although there was some general variability in response amplitudes (see figures 3.7.4 and 3.7.5)

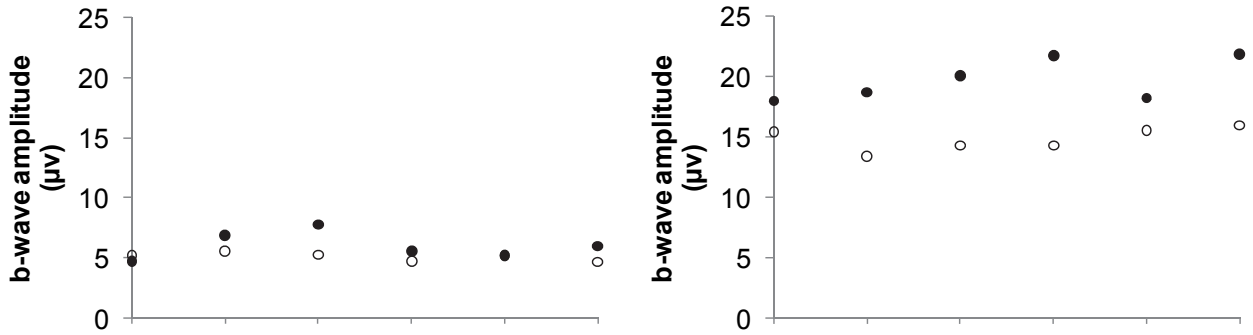

Figure 3.7.4: Consecutive focal rod ERG b-wave amplitudes for participants AG (solid) and AW (open) obtained using a 20 (Left) and 1000 (Right) scotopic td.s stimulus.

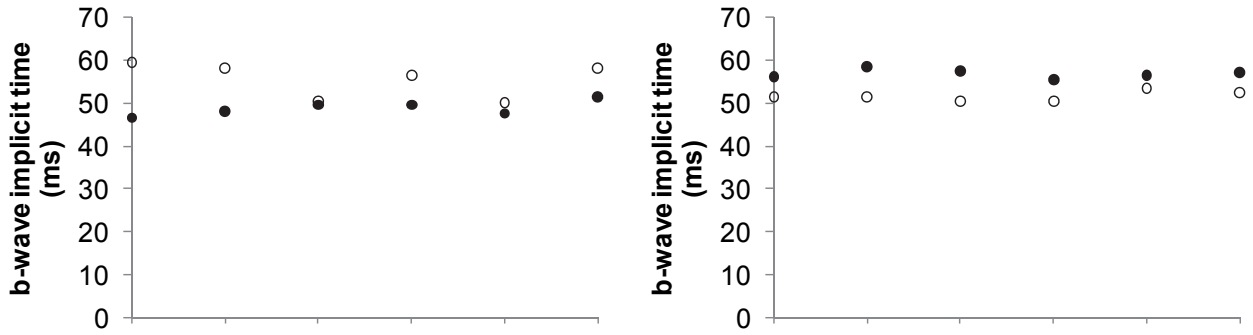

Figure 3.7.5: Consecutive focal rod ERG b-wave implicit times for participants AG (solid) and AW (open) obtained using a 20 (Left) and 1000 (Right) scotopic td.s stimulus.

3.7.3.3 Conclusion

It was concluded that adaptation due to repeated stimuli did not have an appreciable effect on the focal rod ERG parameters under normal testing conditions.

3.7.4 Determination of the luminance range for recording the stimulus-response function of the focal rod ERG

The determination of the range of stimulus luminance for a focal rod ERG stimulus-response series depends on a number of factors. The first point to consider was the number of individual data points that it was possible to obtain from a patient within a single recording session, which was then balanced against the number of data points needed to obtain a satisfactory model fit for the 'Naka-Rushton' function. The second point to consider was the lowest level at which a reliable Focal Rod ERG could be obtained. The third and final point to consider was an upper limit to the stimulus range which could minimise the involvement of the second limb of the ERG stimulus-response relationship. Previous studies which have modelled scotopic b-wave ERG stimulus-response series with the 'Naka-Rushton' function have used a range of approximately 4 log units (Arden et al., 1983; Massof et al., 1984; Birch and Fish, 1987; Severns and Johnson, 1993ab; Velten et al., 2001; Holopigian et al., 2004). The aim of this part of the study was to determine the most appropriate range of stimuli to include in the recording of the focal rod ERG stimulus-response series.

3.7.4.1 Methods

A stimulus-response series was recorded from AW (age 24) who was prepared as described in section 3.1.1. Focal rod ERGs were recorded following the methodology described in section 3.1.6 but with stimuli of 1, 4, 6, 20, 50, 100, 200, 400, 800, 1600, 3200 scotopic td.s (~0.0003, 0.60, 0.78,1.30, 1.70, 2.00, 2.30, 2.60, 2.90, 3.20 and 3.51 log scotopic td.s - presented from dimmest to brightest). These recordings were then repeated against a green (λmax 525 nm) rod saturating background (1500 scotopic td.s) to obtain a cone only response which was then subtracted from the initial response, to isolate the rod response (see section 3.7.2). All ERGs were substantially averaged (n=~50); the examiner subjectively determined the number of averages required to produce a clear ERG waveform. The focal rod ERGs were recorded over 3 recording sessions to avoid participant fatigue due to the extensive averaging required for each ERG; b-wave

amplitude data were then modelled with the 'Naka-Rushton' function using a 'least squares' paradigm in Excel (Microsoft. Redmond, WA).

3.7.4.2 Results

The stimulus-response series for participant AW is shown in figure 3.7.6, extending from 1 to 3200 scotopic td.s (0.0003 to 3.51 log scotopic td.s). The 'Naka-Rushton' function provided a good fit to the data (RMSE = 0.083). The data show a plateau of approximately 25 µv being reached with a stimulus intensity of 500 scotopic td.s (2.70 log scotopic td.s). The range of stimulus intensities shown in figure 3.3.7 appears to provide a reasonable representation of the stimulus-response relationship of the focal rod ERG b-wave, with only the 3200 scotopic td.s (3.51 log scotopic td.s) deviating substantially from the 'Naka-Rushton' model.

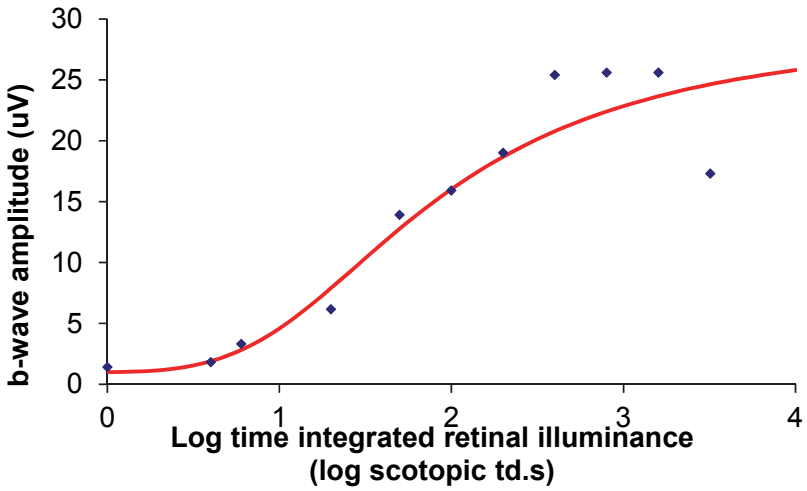

Figure 3.7.6: Focal rod ERG stimulus-response series for participant AW (blue diamond's) fitted with Naka Rushton model (red line); R_{max} = 29.27 µV, n = 2.49, LogK = 1.08 log scotopic td.s.

Given the substantial time required to produce the stimulus-response series shown in figure 3.7.6 and the intention to develop a protocol for clinical application, a revised protocol was developed. A range of 1 to 1000 scotopic td.s (0.0003 to 3 log scotopic td.s) was selected based the intensity response series shown in figure 3.7.6, which covered the full 'S' shaped curve of the stimulus-response relationship. It was determined that a maximum time frame for the completion of the protocol should be 1 hour, including 25 minutes dark adaptation. To allow for sufficient data points, whilst still allowing sufficient time for adequate averaging, 6 retinal illuminance values were selected as follows: 1, 4,

20, 100, 500, 1000 scotopic td.s (0.0003, 0.60, 1.30, 2.00, 2.70, 3.00 log scotopic td.s). Based on the recording of the previous stimulus-response series, the focal rod ERG recorded with a retinal illuminance of 1, 4 and 20 scotopic td.s (0.003, 0.60 and 1.30 log scotopic td.s) would require a minimum of 50 averaged traces. The stronger stimuli (100, 500 and 1000 scotopic td.s - 2.00, 2.70 and 3.00 log scotopic td.s), due to a better SNR, would require at least 25 averages, in addition to a further 25 averages with the rod saturating background (as these values exceeded 20 scotopic td.s it was necessary to subtract the cone only response).

The modified methods described was then assessed on two experienced participants (AW age 24 and AG age 24) and fitted with the 'Naka-Rushton' function, see figure 3.3.8. The data for each subject demonstrated the expected 'S' shape curve. The value of R_{max} in both cases was approximately equal to the b-wave amplitude for the strongest stimulus. The 'Naka-Rushton' model fit was also satisfactory, with root mean square error (RMSE) values of only 0.62 and 0.90 in the case of participants AG and AW respectively.

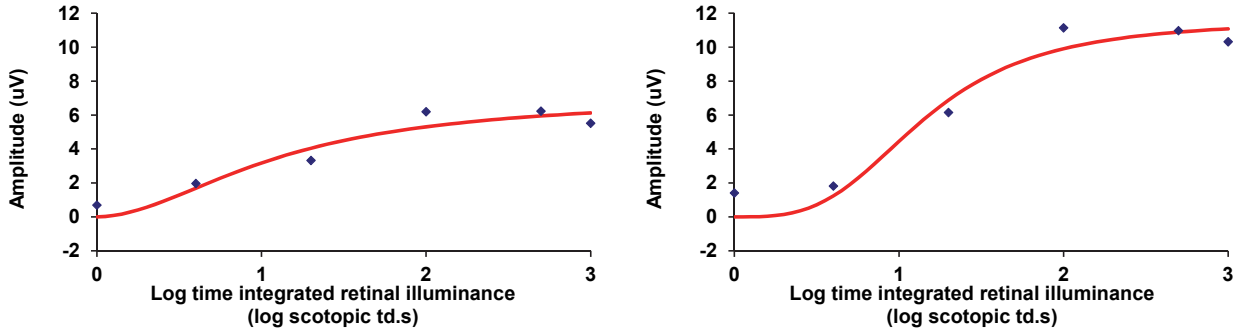

Figure 3.7.7: Focal rod ERG stimulus-response series for participant AG (Left) and AW (Right) showing ERG b-wave amplitude values (blue diamonds) fitted with the 'Naka Rushton' function (red line). Model parameters for AG (Left) R_{max} = 7.10 µV, n = 1.87, LogK = 1.12 log scot td.s and AW (Right) R_{max} = 11.59 µV, n = 3.24, LogK = 1.16 log scot td.s.

3.7.4.3 Conclusions

Given the satisfactory fit shown for the 'Naka-Rushton' function using only 6 data points over the stimulus range of 0.0003 to 3 log scotopic td.s (1 to 1000 scotopic td.s) for two experienced participants, it was decided to evaluate this methodology on a larger group of inexperienced healthy participants.

3.8 Evaluating the focal rod ERG stimulus-response function

With the aim of developing a clinical protocol to record the focal rod ERG stimulus-response series in elderly people and those with ARM it was decided to carry out a pilot feasibility study on a group of healthy participants over the age of 55 years. Data were collected on two separate occasions so that an assessment of repeatability could be made.

3.8.1 Methodology

Fourteen older participants (age 56-71 years) were recruited and the general methodology described in sections 3.1.1 and 3.1.6 were followed. Focal rod ERGs were recorded in response to the stimuli described in table 3.8.1. At least 50 responses were averaged for stimuli up to and including 20 scotopic td.s. For stimuli of more than 20 scotopic td.s, at least 25 responses were averaged. Additional responses were recorded as necessary, based on a subjective assessment of the SNR during recording. For retinal illuminance values above the cone detection threshold of 20 scotopic td.s, ERG traces were also recorded using the same focal stimuli with a constant rod suppressing green background of 1500 scotopic td.s in order to elicit a cone only response, which was then subtracted from the original mixed rod and cone ERG to leave an isolated rod response (see section 3.7.2).

scotopic td.s	(log)	Photopic cd.m^{-2}	Duration (ms)
1	(0.0003)	0.75	1
4	(0.6)	1.5	2
20	(1.3)	3	5
100	**(2.0)**	**15**	**5**
500	**(2.7)**	**18.8**	**20**
1000	**(3.0)**	**37.51**	**20**

*Table 3.8.1: Retinal illuminance values used for recording the stimulus-response series. Those values shown in **Bold** exceed the cone detection threshold and were therefore repeated with rod saturating background to isolate the cone component.*

The focal rod ERG waveforms were Fourier analysed and measured to identify the a and b-wave amplitudes and implicit times. The b-wave amplitudes were then modelled using the 'Naka-Rushton' function on a 'least squares' fit basis in Excel (Microsoft. Redmond, WA)((Naka and Rushton, 1966a; Severns and Johnson, 1993a) (see equation 4.2). The coefficient of repeatability (CoR) of the best fitting 'Naka-Rushton' functions was

calculated (1.96 x SD of differences of Visit 1 – Visit 2) for the parameters 'Rmax' and 'Log K', in addition the CoR was also calculated for the focal rod ERG b-wave amplitude for each stimulus. The CoR was also expressed as a percentage of the mean for each parameter, to allow comparison of repeatability between different stimulus levels and parameters.

3.8.2 Results

The 'Naka-Rushton' function provided a satisfactory fit to only 13 of the 28 stimulus-response series recorded. Of the remaining 15 datasets, 11 produced a fit with grossly abnormal R_{max} or LogK parameters whilst a further 4 did not return any fit (see figures 3.8.1 and 3.8.2 for examples of good and bad fits respectively). The parameters of the best fitting 'Naka-Rushton' parameters from each participant are shown in table 3.8.2. The CoR was calculated as 11.37 and 1.91 respectively for R_{max} and Log K, however, these values were calculated using only the 3 participants who provided acceptable datasets on both visits. The CoR expressed as a percentage of the mean R_{max} and Log K values was 135 and 130 % respectively.

	1st Session				2nd Session			
Participant	**Rmax**	**n**	**LogK**	**Sum of squares**	**Rmax**	**n**	**LogK**	**Sum of squares**
BA	8.51	34.89	1.30	9.24	17.42	1.48	2.47	38.72
CB	**999.11**	**1.05**	**432.28**	**0.55**	5.80	3.02	1.47	6.05
DF	**28.01**	**0.91**	**13.84**	**0.96**	**206.86**	**0.80**	**224.95**	**0.90**
RE	10.19	1.91	1.57	9.12	**24.55**	**1.41**	**4.57**	**2.23**
DFO	3.03	7.30	0.69	1.71	5.66	2.61	0.89	1.41
SA	**No Fit**				**No Fit**			
WBS	9.38	1.81	2.12	29.46	6.70	3.47	1.34	21.92
JF	**436.17**	**0.54**	**9125.77**	**1.00**	8.50	34.07	1.32	10.40
LB	**No Fit**				**1209.63**	**0.86**	**664.92**	**18.42**
LD	7.69	2.22	1.25	7.86	**No Fit**			
MF	**1868.80**	**0.73**	**3888.17**	**13.31**	**32.12**	**1.67**	**3.43**	**9.83**
ND	**610.83**	**0.69**	**1614.74**	**3.78**	6.50	29.12	1.32	2.84
PF	9.20	2.05	1.14	3.64	**352.57**	**0.71**	**776.29**	**4.92**
SD	**67.18**	**1.42**	**12.17**	**5.01**	10.27	6.58	1.66	8.52

*Table 3.8.2: 'Naka-Rushton' function parameters from modelled focal rod ERG intensity-response data. Data where no model fit was achieved are indicated whilst those with grossly abnormal parameters are highlighted in **Bold** type.*

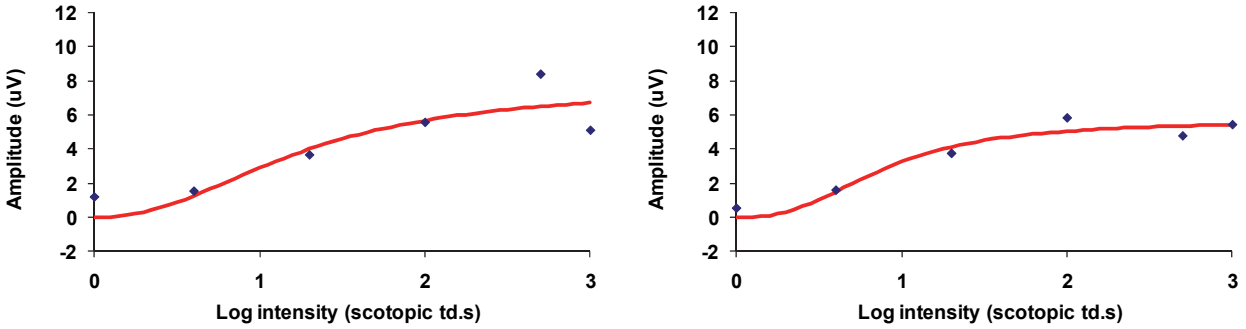

Figure 3.8.1: Examples of good Naka-Rushton data fits from participants LD session 1 (left) and DFO session 2 (right) with parameters of R_{max}=7.69, n=2.22, LogK =1.25 and R_{max}=5.66, n=2.61, LogK =0.89 respectively.

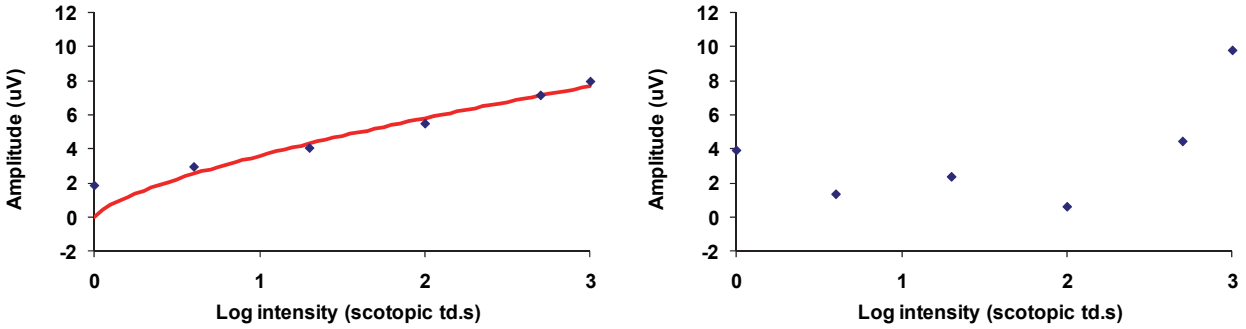

Figure 3.8.2: Examples of a poor data fit from participant ND (left) with parameters of R_{max}=610.83, n=0.69, LogK =1614.74, and data which could not be fitted using the 'Naka-Rushton' function from participant SA (right).

In addition to modelling the data with the 'Naka-Rushton' function, the repeatability of the focal rod ERG b-wave amplitude was assessed for each stimulus level (see table 3.8.3). It can be seen that the b-wave of the focal rod ERG produced larger amplitudes for stronger stimuli, with the exception of the highest level. The lowest CoR was provided by the 0.0003 log scotopic td.s (1 scotopic td.s) stimulus, although as a percentage of the b-wave amplitude the lowest CoR was provided by the 1.3 log scotopic td.s (20 scotopic td.s) stimulus. The CoR even for the most repeatable luminance was 75% of the mean b-wave amplitude, showing a high level of inter-session variability.

Retinal illuminance (scotopic td.s)	Mean b-wave amplitude (μV)	Standard deviation	Coefficient of repeatability (CoR)	CoR as percentage of Amplitude (%)
1	1.67	1.15	2.54	152
4	2.11	1.51	3.91	185
20	3.67	1.60	2.77	75
100	5.61	2.12	5.10	91
500	7.56	3.11	6.93	92
1000	6.91	2.48	5.95	86

Table 3.8.3: Mean ERG b-wave amplitudes for each retinal illuminance comprising the Focal Rod ERG intensity response series recorded, the coefficient of repeatability has been determined for each and additionally expressed as a percentage of the mean amplitude.

3.8.3 Conclusions

The recording of a focal rod ERG stimulus-response series was achieved from young healthy participants and was shown to be well described by the 'Naka-Rushton' function. However, under the reasonable clinical limitations (time and averaging) applied to the protocol the data were not found to be repeatable in a group of older adults and were also too noisy to provide a reliable fit with the Naka-Rushton function. The combination of participant fatigue limiting acquisition time and the requirement for substantial averaging to obtain reliable focal rod ERG waveforms made the recording of a stimulus-response series a challenge even in compliant healthy participants. Unless further innovations to improve the SNR of focal rod ERG data are developed it is unlikely that widespread clinical use of a focal rod ERG intensity-response series will be possible.

The results, however, did show that the focal rod ERG could be recorded effectively for stimuli with a range of different luminance levels and, with the application of the subtraction technique described in section 3.7.2, the rod response isolated. It was hoped that the stimulus-response series would provide additional information regarding rod function, over and above that of the focal rod ERG parameters (a and b wave). As this has been shown to be impractical, an alternative approach would be to record the focal rod ERG at a low and high intensity and to assess the ratio of the two. This would allow more extensive averaging due to the reduced number of ERGs recorded.

From the results, the best candidates for two stimulus levels based on the repeatability of the a and b wave parameters, and the difference in amplitudes appeared to be the 500 (2.70 log) and 20 (1.30 log) scotopic td.s stimuli. The 500 scotopic td.s stimulus produced the largest mean b-wave amplitude (7.56 μv) and was positioned towards the

higher end of the stimulus-response function, whilst the 20 scotopic td.s had a smaller amplitude and produced the smallest coefficient of repeatability as a proportion of the response amplitude.

3.9 Conclusions

As a result of the issues discussed and assessed within this chapter the following conclusions were reached with regard to the protocols described in section 3.1. The contralateral DTL reference electrode was shown to provide a reliable response of equivalent amplitude to the ipsilateral skin reference electrode for ERG recording. A 20° diameter, 40 Hz focal flicker ERG stimulus produced the largest measureable signals compared to the alternative temporal frequencies and stimulus sizes considered. The benefits of an equilibrium bleach in comparison to a potentially faster photoflash technique was shown, with better repeatability and reliability of ERG photostress test results. An ageing effect was also identified in the ERG photostress test data. The identification of an adaptational effect when recording consecutive focal flicker ERGs suggested the need for a pre-recording period of adaptation.

Although it was hoped that a focal rod ERG stimulus-response series would provide additional information regarding retinal function under scotopic conditions, it was shown to be an unfeasible approach clinically, due to difficulties related to poor SNR and collecting sufficiently averaged data within a limited clinical time frame. This work did however demonstrate that a rod dominated response could be elicited for stimuli with a range of luminance levels using a subtraction technique to remove the cone contribution from the response. An approach was also suggested whereby focal rod ERGs could be recorded using two different stimuli, and a ratio of amplitudes calculated providing additional measures of retinal function under scotopic conditions. These conclusions were used to optimise the protocols in chapter 6.

Chapter 4: Participants and baseline measurements

This section describes the selection criteria, general methodology and baseline clinical measures for the study participants in chapters 5, 6, and 7 of this thesis.

4.1 Power calculation

Power calculations were carried out representing one or more of the measurement parameters for each of the investigative techniques being compared in the final chapters (5, 6 and 7) of this thesis. For the Focal cone ERG and ERG photostress tests previously published data was used as the basis for the calculations (Binns and Margrain 2007). However, in the case of the 1060 nm OCT thickness measurements and the Focal Rod ERG parameters no previously published data was available, therefore pilot data collected from healthy participants was used to provide an expected standard deviation value, whilst the smallest clinical difference was taken to be 1 standard deviation. The power calculations and any assumptions made are shown in table 4.1.1.

It is apparent from table 4.1.1 that the target sample size is different for each parameter. The parameter requiring the largest sample size to find a clinically significant difference was the ERG photostress test. For the ERG photostress test a sample size of 120 participants (60 per group) would be required to have an 80% chance of finding a difference in means of the rate of recovery of 0.189 at the 5% significance level. Therefore the participant recruitment target was based on these values, with the aim of recruiting 60 healthy participants and 60 participants with Age-related maculopathy.

Parameter	Calculation values	Sample per group
Focal cone ERG	**Based on data from Binns & Margrain (2007)**	
'b-wave amplitude' 'b-wave implicit time'	*ARM participants (n=31)* • b-wave amplitude (μV) 3.42 (SD ±0.24) • b-wave implicit time (ms) 45.37 (SD ±0.49) *Control participants (n=27)* • b-wave amplitude (μV) 3.96 (SD ±0.28) • b-wave implicit time (ms) 42.66 (SD ±0.33) *Smallest clinical difference* Difference in means as previously found 0.54 μV (b-wave amplitude) and 2.71 ms (b-wave implicit time)	**<4** **<4**
ERG photostress test	**Based on data from Binns & Margrain (2007)**	
'rate of recovery'	*ARM participants (n=31)* • Rate of Recovery (1/T) 0.183 (SD ±0.27) *Control participants (n=27)* • Rate of Recovery (1/T) 0.372 (SD ±0.38) T = Time constant of photopigment regeneration *Smallest clinical difference* Difference in means as previously found = 0.189	**60**
Focal rod ERG	**Based on data from Chapter 3.8**	
'500 scotopic td.s b-wave amplitude'	*Healthy participants (n=14)* • b-wave amplitude (μV) 7.56 (SD ±3.11) *Smallest clinical difference* Assumed to be 1 SD (3.11 μV)	**15**
1060 nm OCT	**Based on data from Chapter 2.3**	
'Foveal retinal thickness'	*Healthy participants (n=21)* • Retinal thickness at the fovea (μm) 205.9 (SD ±23.9) *Smallest clinical difference* Assumed to be 1 SD (23.9 μm)	**15**

Table 4.1.1: Power calculations for selected study parameters based on the Altman Nomogram for unpaired t-tests. Expected group sizes are shown, all calculations assumed a power of 80% and a significance level of 95%.

4.2 Participant selection

Participants with ARM were recruited from the retinal clinic of Mr. Ayed Al-Bermani at the University Hospital of Wales. Additional participants with ARM were recruited from the Cardiff University Eye Clinic and via Optometrists within the Cardiff and Vale University Health Board area. Participants who acted as controls for this study were primarily recruited from the Cardiff University Eye Clinic and via Optometrists within the Cardiff and Vale University Health Board area.

Ethical approval was obtained from both the School of Optometry and Vision Sciences Research Ethics Committee and the South East Wales Research Ethics Committee. All participants were provided with written information regarding the study prior to attending for the first appointment, and were given the opportunity to discuss the study with the researchers prior to giving written consent. The study adhered to the tenets of the Declaration of Helsinki.

A set of eligibility criteria was specified for all participants of this study, these are outlined below (see sections 4.2.1 & 4.2.2).

4.2.1 Inclusion criteria

- Males and females aged 55 years and above.
- Participants with ARM in one or both eyes, including pigmentary changes and/or drusen within the macular area, or participants with bilateral healthy maculae (control group).

4.2.2 Exclusion criteria

- Visual acuity worse than 0.3 LogMAR (test eye).
- A visual field defect within central 30° assessed with suprathreshold automated static perimetry (test eye).
- Any of the following ocular conditions: non-AMD related fundus changes, narrow anterior angles (<grade 1 van Herick), amblyopia, congenital colour vision defects, significant cataract (LOCS III graded, above grade 4 on any criterion (Chylack et al., 1993)), central corneal/media opacity, any posterior eye condition and /or glaucoma.
- Any of the following systemic conditions: diabetes, neurological disease (for example, Parkinson's disease, Alzheimer's disease, stroke and epilepsy), any other systemic conditions known to affect ocular function.
- Taking medication known to affect retinal function (for example Chloroquine, Tamoxifen).
- Refractive error ≥ ±6.00D in the most powerful meridian.

4.3 Baseline measures and methods

4.3.1 Visual acuity

Visual acuity (VA) was assessed using an ETDRS LogMAR chart for each eye separately (the chart was calibrated to be viewed at 3m, this distance was reduced if necessary). Participants were encouraged to read down the chart until they made at least 4 errors on a line. Acuity was scored on an individual letter basis.

4.3.2 Colour vision

The colour vision was assessed for each eye using a Saturated D-15 test (Farnsworth, 1943). The caps were placed in a random order, face up, within a standard Illuminant C light box. The participant was asked, starting with the 1st cap, to place the coloured caps in an ordered sequence based on their perception of similarity. When the participant was happy with the sequence of caps, the caps were turned over and the number sequence displayed on the reverse was recorded.

Analysis was carried out using a computer based technique described by Vingrys and King-Smith (1988), with software loaded into MS-DOS (Microsoft. Redmond, WA). The D-15 cap orders were input and the program returned 6 values which describe the original D-15 cap sequence based on a vector scoring method.

The colour vision result may be described in terms of a major and minor vector (values output); the angle of the major vector is known as the confusion angle and has been shown to correspond to the type of colour vision defect present (Vingrys and King-Smith, 1988), the minor vector is perpendicular to the major axis, and represents colour confusion along vectors that deviate from the confusion angle. Normal participants were reported to have an angle of ~60°, where as protan, deutan and tritan defects had approximate angles of +3 to +17°, -4 to -11° and -70 to -90° respectively. The analysis also gives a ‘C-index’, which describes the severity of a defect, with normal participants returning values of ~ 1.0 up to 1.77, and an ‘S-index’, which provides a measure of scatter, or selectivity in cap arrangement. A low S-index (~1.09 to 1.38) may indicate a normal participant or anarchic cap arrangement, whereas a high S-index maybe suggestive of congenital colour vision defects. Acquired defects are often characterised by a high C-index, but lower S-index, thought to reflect a more generalised loss in chromatic sensitivity (achromatopsia) (Vingrys and King-Smith, 1988). The colour vision status of test eyes in

both ARM and control groups were compared with regard to group average parameters and individuals.

4.3.3 Irido-corneal angle assessment

The irido-corneal angle was assessed in each eye adjacent to the temporal limbus. This assessment was made using the Van Herick technique (Van Herick, Shaffer and Schwartz, 1969).

4.3.4 Dilation

Both pupils were dilated with 1 drop Tropicamide HCl 1%. The formulation, strength, expiry date, time of instillation and batch number were recorded for each drug administration.

4.3.5 Axial length

Axial length was assessed using the IOL master (Carl Zeiss, Meditec Inc, CA) with 5 readings from each eye recorded and a mean calculated.

4.3.6 Auto-refraction

Refraction was assessed objectively for each eye using an auto-refractor (KR-7500 Auto-kerato-refractometer, Topcon, Tokyo). Where possible, 3 individual objective refractions for each eye were obtained and mean sphero-cylinder refraction was recorded.

4.3.7 Central visual field screening

The visual field was assessed for each eye using the C 40 supra-threshold testing program on the Humphrey Field Analyser (Carl Zeiss, Meditec Inc, CA). A subjective assessment of the results was made by the researcher and, in cases of poor compliance, the test was repeated, or if suspect visual field defects were found then appropriate referral was made.

4.3.8 Lens assessment

Media clarity was assessed using a slit-lamp bio-microscope for each eye. The LOCS III grading system was used to assess the presence and extent of cataract in each eye (Chylack et al., 1993). A subjective assessment of media clarity (cornea and anterior vitreous) was also made during the slit-lamp examination.

4.3.9 Retinal photography

Retinal images were obtained for each eye using the Canon CR-DGi non-mydriatic camera (Canon medical systems, Irvine, CA). Thirty-seven degree posterior pole retinal photographs were captured and stored digitally. The retinal photographs were used to determine allocation to either the ARM or control group and to grade drusen features and pigmentary abnormalities with the International Classification and Grading System for AMD (Bird et al., 1995) using the methods described in section 2.4.

4.4 Participant characteristics

4.4.1 AMD grading

Fifty participants met the eligibility criteria for this study, comprising 24 participants graded as having ARM and 26 graded as normal. The disease characteristics of the participants graded as having ARM have been summarised in table 4.4.1. Furthermore, the grading of drusen features and pigmentary abnormalities is shown in the Appendix I , table I.1 (ARM participants) and I.2 (Control participants).

4.4.2 Age and axial length

The mean age for each group was 73.8 (±8.5) and 66.6 (±7.5) years for ARM and control groups respectively; there was a statistically significant difference between groups ($p=0.003$; independent t-test). The mean axial length for each group was 23.1 (±0.71) and 23.7 (±0.91) mm for ARM and control groups respectively, which also showed a statistically significant difference between groups ($p<0.03$; independent t-test) (see Appendix I, tables I.5 and I.6, for individual values).

Due to the difference between groups for each of these parameters, the ERG and OCT parameters measured in this thesis were assessed for significant correlations with age and axial length (Pearson's correlation coefficient for parametric data, or Spearman's rank correlation coefficient for non-parametric data). Linear regression was carried out to determine the relationship between age/axial length and ERG/OCT parameters where there was a statistically significant correlation. To avoid a confounding effect, ERG and OCT parameters were adjusted for age and axial length based on the gradient of the linear regression.

Participant	Test eye (ARM)				Contralateral eye status
	Drusen size >125µm	>10 Drusen	Pigmentary abnormalities	Drusenoid PED	
DG24	N	N	Y	N	Normal
UH38	Y	Y	N	N	ARM
MK48	Y	Y	N	N	ARM
PJ45	Y	N	N	N	Normal
JM83	Y	N	N	N	ARM
RJ95	N	N	Y	N	Wet
DR96	Y	Y	Y	Y	Wet
TO97	N	N	Y	N	Wet
BS100	Y	N	N	Y	Wet
DN82	Y	N	Y	N	Normal
DP103	Y	N	Y	N	ARM
SJ90	Y	Y	Y	N	Wet
CG101	Y	N	N	N	ARM
SO107	Y	Y	N	Y	Wet
JH108	Y	Y	N	N	Wet
AP109	N	N	Y	N	ARM
PT139	Y	N	Y	N	ARM
MT125	Y	Y	N	N	ARM
WC122	Y	Y	Y	N	Wet
JT99	N	N	Y	N	Wet
BS116	Y	N	N	N	Normal
BC92	Y	Y	Y	N	Wet
PS115	N	N	Y	N	Normal
SH93	N	N	Y	Y	Wet

Table 4.4.1: Disease characteristics for ARM participants (n=24). N= feature not present, Y = feature present.

4.4.3 Baseline

4.4.3.1 Visual Acuity

The mean visual acuity in the ARM group was 0.11 logMAR (±0.12) compared to an acuity of 0.04 logMAR (±0.11) for the control group. There was a statistically significant difference between groups ($p<0.05$ $z=-2.143$; Mann-Whitney u-test). The data from individual participants is shown in Appendix I, tables I.5 and I.6.

4.4.3.2 Gender and ethnicity

The control group contained 17 male and 9 female participants, whilst the ARM group contained 10 male and 14 female participants (χ^2= 1.952 p>0.1; Chi-squared test). All participants (n=50) within the study reported their ethnicity as white European.

4.4.3.3 Colour vision

Only 1 participant within the control group made an error on the D-15 test (see Appendix I, table I.4); the low C-index (1.44) and relatively low S-index (1.88), were suggestive of anarchic cap placement or a mild acquired defect. For the control group the mean confusion angle, C-index and S-index were 62.7°, 1.02 and 1.40 respectively. In contrast, 7 participants within the ARM group (see Appendix I, table I.3) made at least one error. For the ARM group the mean confusion angle, C-index and S-index were 65.8°, 1.16 and 1.56 respectively. All 7 ARM participants who made errors expressed a confusion angle consistent with a blue-yellow defect. The range of C-index (1.12-2.20) and S-index (1.50-3.20) scores for these 7 participants suggest that these were mild acquired defects, or a result of anarchic cap placement.

4.4.3.4 LOCS grading

The grading of the clarity of the crystalline lens of all participants using the LOCSIII system is shown in Appendix I, tables I.5 and I.6. The test eye of 4 participants within the ARM group, and 1 participant within the control group had undergone cataract extraction and had an artificial intra-ocular lens (IOL) implanted. When compared between groups, nuclear colour (NC), nuclear opalescence (NO), cortical cataract (C) and posterior sub-capsular cataract (P), were not found to be statistically different (p>0.9 z=-1.659, p>0.4 z=-0.799, p>0.1 z=-1.574,p>0.1 z=-1.545 respectively; Mann-Whitney u-test).

4.4.3.5 Refractive status

The refractive status for all participants in the study is shown in Appendix I, tables I.5 and I.6. The average mean sphere of control participants was +0.73 DS (±1.79) whilst that of the ARM group was +1.79DS (±1.65). There was a statistically significant difference in refractive error between the groups (p<0.05; independent t-test).

Chapter 5: Retinal structure

This chapter describes a study to evaluate the effect of ARM on retinal and choroidal structure using the 1060 nm OCT. As previously discussed, in section 1.4, OCT is capable of imaging and measuring retinal (Legarreta et al., 2008; Ikuno and Tano, 2009; Kakinoki et al., 2009; Ikuno et al., 2010; Wood et al., 2011a), intra-retinal (Loduca et al., 2010) and when 1060 nm wavelength OCT is used, choroidal (Ikuno and Tano, 2009; Margolis and Spaide, 2009; Ikuno et al., 2010; Manjunath et al., 2010; Hirata et al., 2011) layer thicknesses in healthy participants. However, only a few previous studies have specifically measured retinal thickness in ARM (Kaluzny et al., 2009; Malamos et al., 2009; Schuman et al., 2009), none of which have investigated choroidal thickness, or assessed the diagnostic potential of these measures. Therefore, the first aim of this chapter was to identify structural changes within the retinal, choroidal or intra-retinal layers associated with ARM. The second aim was to assess the diagnostic potential of these changes in order to determine the clinical utility of these findings and ultimately to compare the diagnostic ability with the functional measures described in chapter 6. Finally, these values provided the basis for a layer by layer comparison of retinal structure to function described in chapter 7.

The analysis described in this chapter contributed to a publication in the American Journal of Ophthalmology (Wood et al., 2011a)(see Appendix M).

5.1 Methods (OCT protocols)

OCT images were obtained after dilation of a participant's pupil (1 drop 1% Tropicamide HCl) using a 1060 nm OCT system (see figure 5.1.1). Participants were positioned comfortably and asked to fixate an internal fixation cross to ensure accurate imaging of the macula. The OCT was then aligned and focused prior to image capture. The saved images were processed by the OCT system and converted into a useable file format prior to exportation to ImageJ (Rasband, 1997) for analysis.

Figure 5.1.1: The 1060 nm OCT system; adjustable table, chin rest, imaging head and OCT system shown.

OCT images were obtained from both eyes of each participant. Two scans were carried out on each eye, both of which comprised 512x512 a-scans, (each a-scan containing 1024 individual data points). One covered a retinal area of 20°x20° and the other 36°x36°. As it was not possible to review images at the time of acquisition with this OCT system, multiple images were obtained during the imaging session, with the best images selected for post processing. In this chapter, the 36°x36° data analysis is described, as these images were better able to sample the full macular area.

5.1.1 Post processing and analysis

The visibility and definition of the intra-retinal and choroidal layers was improved using the post processing techniques described in section 2.2 (see figure 5.1.2). The post processed images were 'resliced' to create a vertical and a horizontal b-scan (see figure 5.1.3 for an example), which intersected at the foveal pit, the 'z-project' function of ImageJ (Rasband, 1997) was applied to average approximately 5 adjacent b-scans to improve image quality.

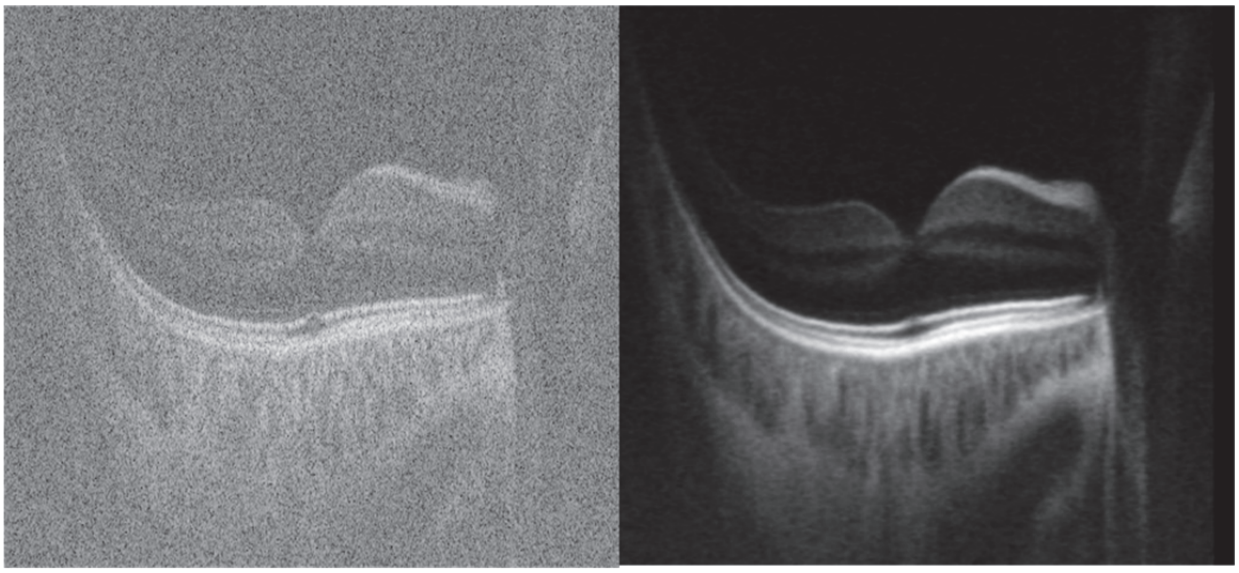

Figure 5.1.2: Image showing a raw OCT prior to post-processing (Left) and OCT after post processing techniques had been applied (Right). The image has been processed to enhance the intra-retinal and choroid-scleral boundaries.

The horizontal and vertical b-scan images were measured using the manual technique described in section 2.3.1.1. As the appearance of the intra-retinal layers in OCT images is dependent on the relative reflectivity of each component layer, the boundaries of specific retinal layers, as identified by histology, may not easily be resolved. Therefore the selection of intra-retinal layers that were measured in this study was based on using the most prominent and visible intra-retinal boundaries within the OCT image (see figure 5.1.3). The layers measured, and their histological equivalent layers, are described in table 5.1.1. The names given to the measured intra-retinal layers in this study are based upon the cell type which predominates within each layer. At the foveal pit, the retina comprises almost entirely photoreceptors (Provis et al., 2005), therefore, the retinal thickness at this location was taken to represent the photoreceptor layer thickness with the other measured intra-retinal layers being absent.

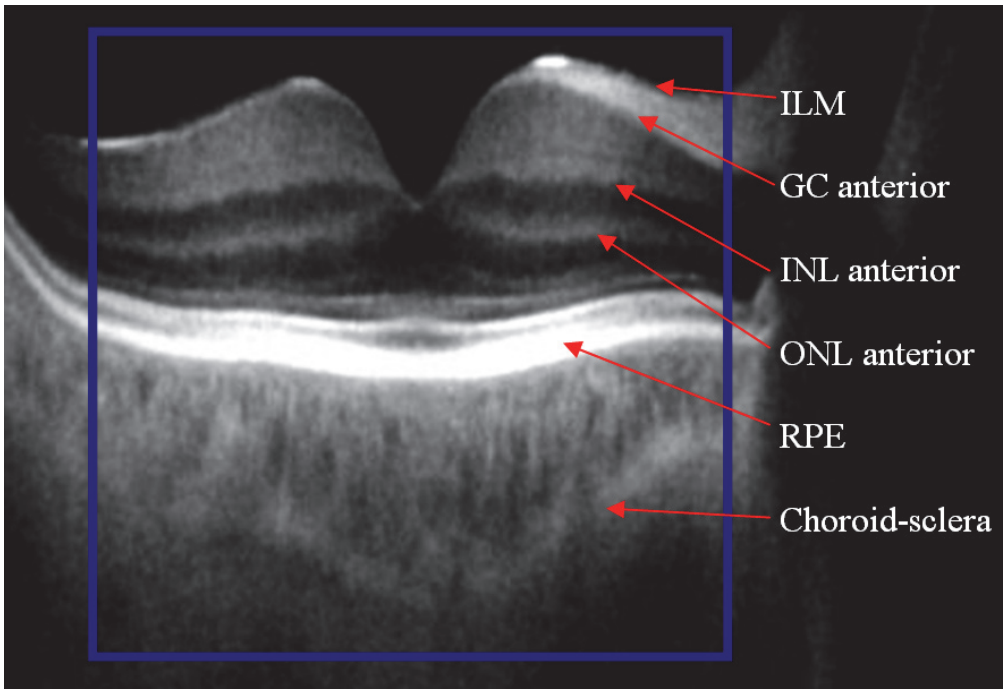

Figure 5.1.3: Image showing a post processed horizontal OCT section (36° image) from the left eye. Blue box indicates approximate 20° field that was used in this analysis. Red arrows point to the hyper-reflective boundaries which were used as reference points for the measurement of the features described in table 5.1.1. ILM (inner limiting membrane), GC anterior (anterior boundary of ganglion cell layer), INL anterior (anterior boundary of inner nuclear layer), ONL anterior (anterior boundary of outer nuclear layer), RPE (retinal pigmented epithelium) and choroid-sclera (the choroid-scleral boundary).

Thickness measurements were made at 21 individual locations, along both the vertical and horizontal b-scan intersecting at the foveal pit. The thickness measurements at the foveal pit were assessed twice i.e. once in the vertical and once in the horizontal b-scan. The position of each measurement location was determined based on the position of the foveal pit within each b-scan image, the measurement locations were then spaced at increasing eccentricity (2, 4, 6, 8 and 10 degrees) nasally, temporally, superiorly and inferiorly from this point (see figure 5.1.4). Measurement locations were determined by calculating the relative distance in pixels from the foveal pit; and were corrected for transverse image magnification using the method described in section 2.2.1.

Thicknesses were obtained whenever possible for each of the 6 layers described in table 5.1.1. Where a layer could not be visualised or where it was identifiable but not measurable (its thickness being equal to or less than the image resolution) the thickness

was recorded as ‘absent’ or as ‘0’ respectively. All measurements were recorded in pixels and converted into microns using a conversion factor of 2.43 µm per pixel.

Name	Layer (histological equivalent)	OCT boundary (see figure 5.1.3)
Retinal nerve fibre layer	Retinal nerve fibre layer	ILM to the anterior boundary of GCL
Ganglion cell layer	Retinal ganglion cells and inner plexiform layer	Anterior boundary of GCL to the anterior boundary of INL
Bipolar cell layer	Inner nuclear and outer plexiform layers	Anterior boundary of INL to the anterior boundary of ONL
Photoreceptor layer	Outer nuclear layer and the photoreceptors	Anterior boundary of the ONL to the RPE
Retina	Neural retina	ILM to the RPE
Choroid	Choroid	RPE to the choroid-sclera boundary

Table 5.1.1: Table showing the names given to the layers measured in this thesis, the histological equivalent layers and the boundaries used to delineate these layers on the OCT images.

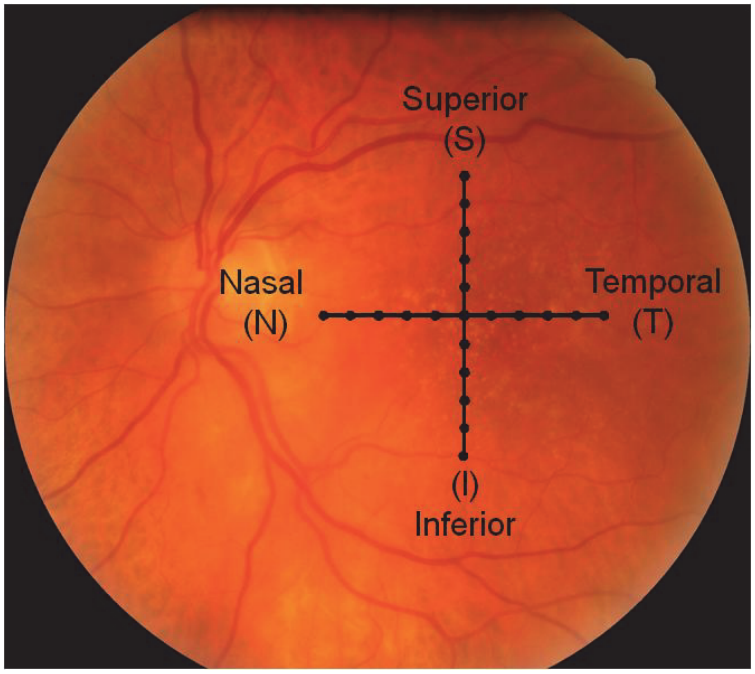

Figure 5.1.4: A retinal photograph showing the 21 OCT measurement locations (solid dots) spaced at 2° intervals from the foveal pit along a horizontal and vertical plane (black lines), retinal direction is indicated by S (Superior), I (Inferior), N (Nasal), and T (Temporal) as labelled.

In addition to layer thickness values at individual locations, a “weighted average thickness” was calculated for each of the 6 layers measured. This was intended to provide an estimate of average layer thickness across the 20° field that could be directly compared

to focal ERG results (which also originated from a 20° diameter retinal area). The weighted average volume and thickness values were calculated as described in equations 5.1 to 5.3.

The central foveal volume over the central 2° diameter region (n=1° eccentricity) was calculated as shown in equation 5.1:

Equation 5.1: $\text{Volume} = (\pi.r_n^2).(t_{(n-1)}+t_{(n+1)}/2)$

Where, t= mean thickness measurement (average of all recorded thickness measurements at each eccentricity), n= eccentricity in degrees and r= radius (μm)

The volume of each intermediate 2° wide annular rings (centred at n= 2, 4, 6 and 8° eccentricity) was calculated as shown in equation 5.1.2:

Equation 5.2: $\text{Volume} = (\pi.r_{(n+1)}^2).(t_n+t_{(n+2)}/2) - (\pi.r_{(n-1)}^2).(t_n+t_{(n+2)}/2)$

The volume of the outer annular ring 1° wide extending from 9 to 10 ° eccentricity (n=10° eccentricity) was calculated as shown in equation 5.1.3:

Equation 5.3: $\text{Volume} = (\pi.r_n^2).(t_n) - (\pi.r_{(n-1)}^2).(t_n)$

The sum of each of these volumes was then divided by the total area of the 20° diameter region ($\pi.r^2$) to produce the weighted average thickness for each retinal, intra-retinal or choroidal layer assessed.

5.1.2 Statistical analysis

All data were assessed for normality using the Shapiro-Wilk test. Thickness measurements at each location were assessed for a relationship with age and axial length (using Pearson's correlation coefficient for normally distributed data and Spearman's rank correlation coefficient for non-normally distributed data), as the control and ARM groups were not matched for these factors (see section 4.3.2). Where a statistically significant correlation was identified ($p<0.05$), linear regression was used to correct raw data.

Statistical comparison of group mean thickness values (ARM v Controls) was carried out for all 6 layers at every measurement location (Independent t-test for normally distributed data, Mann-Whitney U-test for non-normally distributed data). As the measurements obtained for different retinal locations from each individual are related variables (i.e. they are obtained from the same structure within the same eye), they show a high degree of correlation (Wood et al., 2011a). If multiple unrelated variables were compared, it would be expected that the null hypothesis would be wrongly rejected in 1 out of every 20 comparisons through chance alone (i.e. multiple testing increases the risk of a type I error). However, the risk of a type I error decreases when variables tested are correlated, such that the probability of the null hypothesis being rejected due to chance is not multiplicative of the probability of each comparison being found significant by chance alone (Bland and Altman, 1995). This means that a conservative approach to multiple statistical testing, such as Bonferroni correction, is not appropriate here.

A two way between group analysis of variance was carried out, to identify any overall difference in retinal or choroidal layer thickness between the ARM and Control groups. Measurement location and participant status (ARM or Control) were identified as categorical independent variables, whilst the thickness values were defined as the dependent continuous variable. A significance level of $p<0.05$ was used, except where the data were identified (assessed using Leverns's test of equality) as not displaying equal variance, where a more stringent significance level of $p<0.01$ was applied. The Eta squared parameter is a measure of the size of effect, ranging between 0 and 1, greater values indicates larger size of effects, a value of >0.06 is considered moderate.

In addition, the structural measures that demonstrated statistical differences between groups were assessed for diagnostic potential. Each thickness measurement was assessed using receiver operating characteristics curves (ROC). These curves describe the ability to correctly identify individuals with disease (sensitivity) and those without (specificity).

The ROC curves were assessed with regard to the area underneath the curve (AUC) which reflects the diagnostic potential of the parameter. A value of 1 indicates perfect differentiation, whilst a value of 0.5 indicates no ability to differentiate between healthy and diseased participants. Cut off values were also determined for each parameter to best distinguish between disease and healthy participants. Diagnostic tests with both a high sensitivity and specificity are those which are best at differentiating healthy

participants from those with ARM. All statistical analysis in this chapter was carried out using SPSS 19 software (IBM, Armonk NY).

5.2 Results

OCT images were obtained from all individuals, apart from 2 participants with ARM whose images were not of sufficient clarity to include in the study. The following results therefore originate from 22 participants with ARM and 26 controls. All measurements at each location were individually assessed for a relationship with age and axial length, where a statistically significant correlation was found, the individual values were adjusted by linear regression analysis. The individual thickness values for each participant are shown in Appendix J; values where adjustment for age or axial length was made are indicated.

5.2.1 Retinal thickness

The mean retinal thickness for ARM and control groups is shown as a function of eccentricity in figure 5.2.1.

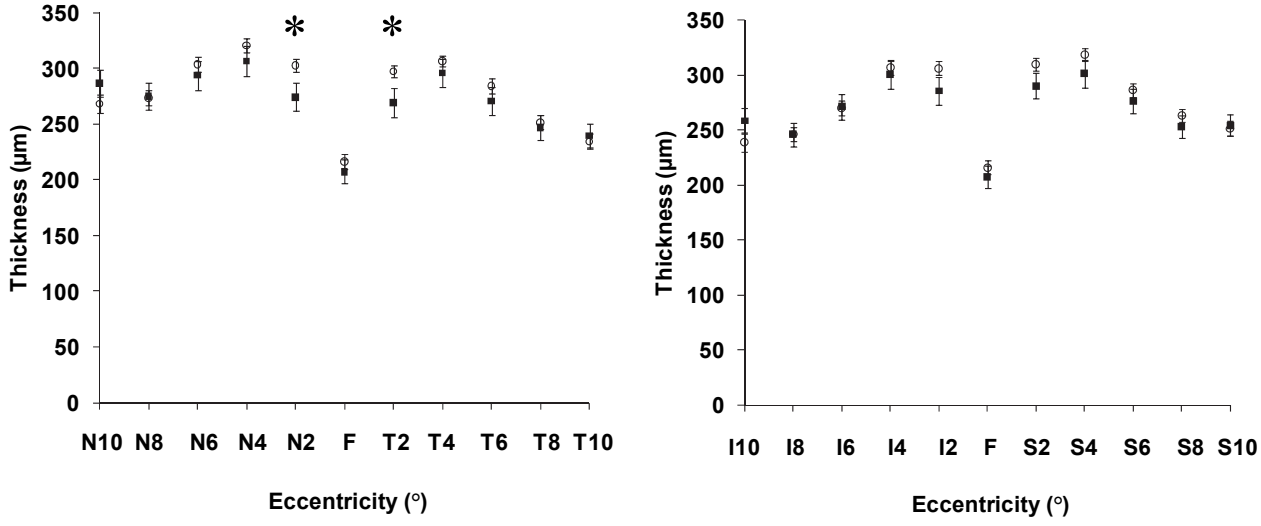

Figure 5.2.1: Retinal thickness for controls (open symbols) and participants with ARM (filled symbols). Error bars indicate standard error at each measurement location. Locations where the difference between groups was statistically significant ($p<0.05$) are denoted by a star (*).

The retina was shown to be thinnest at the foveal pit in both control (mean foveal thickness ±SD; 216 ±32 μm) and ARM (mean foveal thickness ±SD; 207 ±48 μm) participants, with thickness increasing to reach a maximum at approximately 4° in all 4 directions before decreasing towards the periphery. The ARM group tended to have thinner retinas than the control group out to 6° eccentricity in all meridians. A statistical difference in mean thickness between groups was identified at 2° nasally and temporally from the foveal pit ($p<0.05$ at both location N2 and T2; independent t-tests). Other locations did not demonstrate a statistically significant difference between groups.

5.2.2 Choroid thickness

The mean choroidal thickness for ARM and control groups is shown as a function of eccentricity in figure 5.2.2. The choroid was shown to be thinnest at the 10° nasal location (103 ±42 μm), which is the point closest to the optic nerve head. A small reduction in mean thickness was seen with increasing eccentricity from the fovea in all 4 meridians (see figure 5.2.2). The group of participants with ARM had slightly higher mean choroidal thickness at almost all locations; however, this did not reach significance for any measurement location.

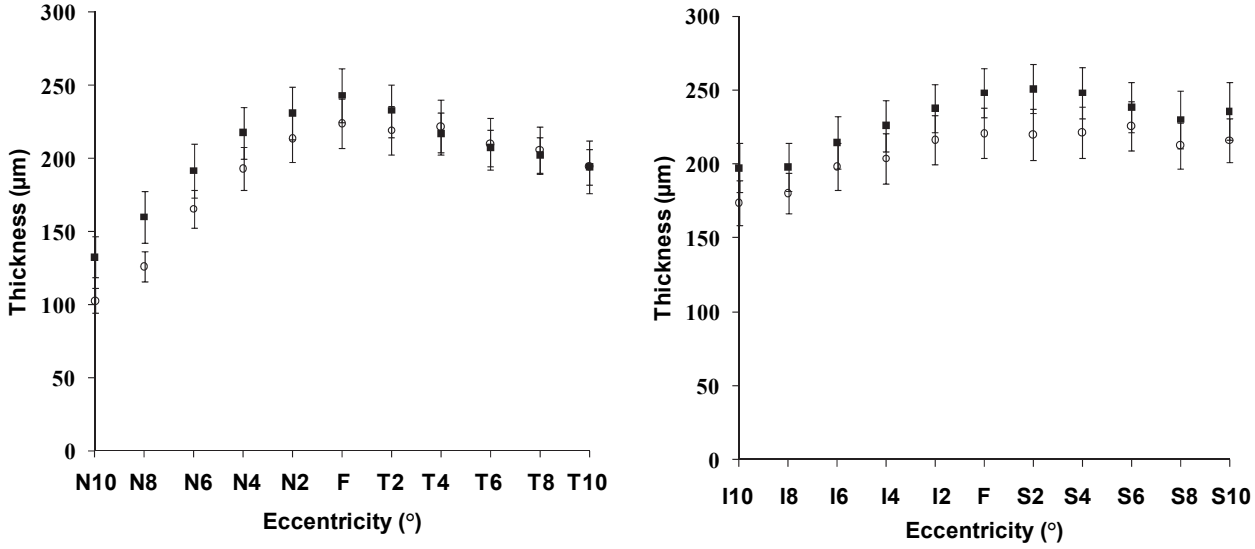

Figure 5.2.2: Choroidal thickness for controls (open symbols) and participants with ARM (filled symbols). Error bars indicate standard error at each measurement location. There were no statistically significant differences in choroidal thickness at any of the locations studied.

5.2.3 Photoreceptor layer thickness

The mean photoreceptor layer thickness for ARM and control group participants is shown as a function of eccentricity in figure 5.2.3. The photoreceptor layer was shown to be thickest at the foveal pit in both control (mean F; 216 ±32 µm) and ARM (mean F; 207 ±48 µm) participants (103 ±42 µm), and rapidly declined by 2° eccentricity before a more gradual thinning with increasing eccentricity in all directions. The mean photoreceptor layer thickness was lower for the ARM group than the control group at most locations, with those at 2° nasally and 2° and 4° superior to the fovea reaching significance ($p<0.05$; independent t-test).

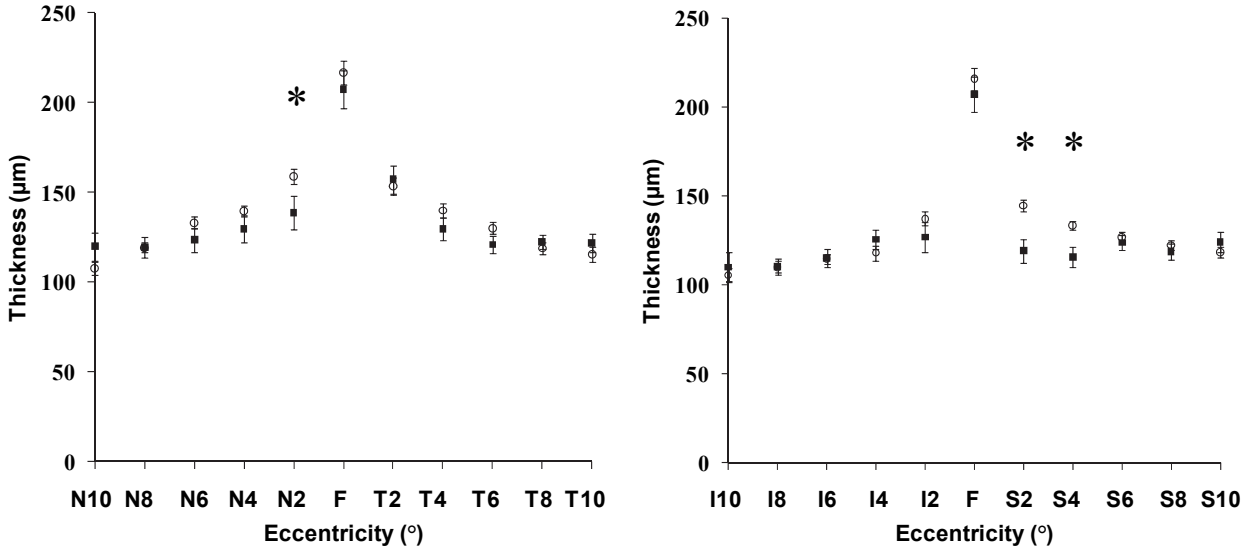

Figure 5.2.3: Photoreceptor layer thickness for controls (open symbols) and participants with ARM (filled symbols). Error bars indicate standard error at each measurement location. Locations where the difference between groups was statistically significant ($p<0.05$) are denoted by a star (*).

5.2.4 Bipolar cell layer thickness

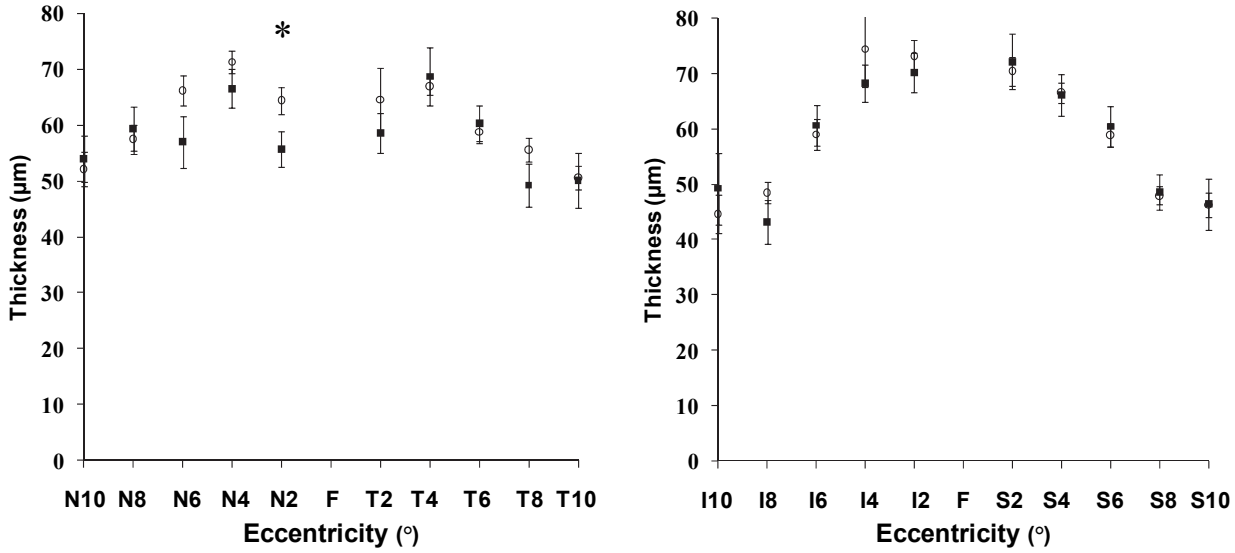

Figure 5.2.4: Bipolar layer thickness for controls (open symbols) and participants with ARM (filled symbols). Error bars indicate standard error at each measurement location. Locations where the difference between groups was statistically significant ($p<0.05$) are denoted by a star (*).

The mean bipolar cell layer thickness for ARM and control groups is shown as a function of eccentricity in figure 5.2.4. The bipolar cell layer was thickest at 2-4° eccentricity before declining gradually with increasing eccentricity. The bipolar cell layer thickness was only found to be significantly different between groups at 2° nasally ($p<0.05$; independent t-test), where the control group showed a thicker mean value.

5.2.5 Ganglion cell layer thickness

The mean ganglion cell layer thickness for ARM and control groups as a function of eccentricity is shown in figure 5.2.5. The ganglion cell layer, not present at the fovea, was thickest at 4° along all meridians before declining gradually with increasing eccentricity. The ganglion cell layer thickness was found to be significantly thinner for the ARM group at 2° nasal, temporal and superior to the fovea ($p<0.05$; independent t-test) but did not reach significance at more eccentric locations.

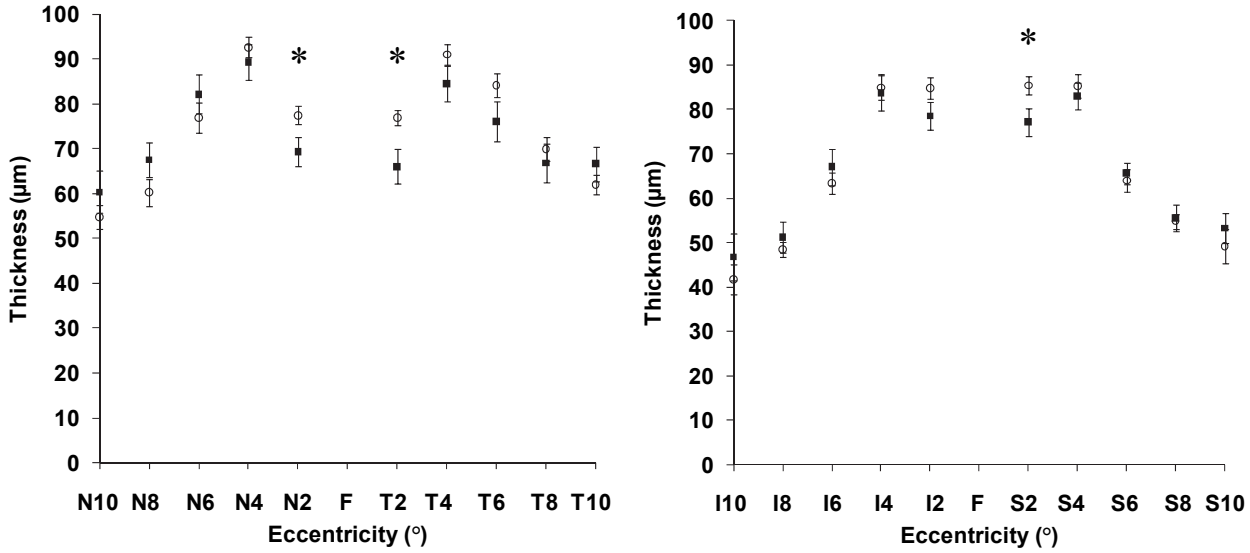

Figure 5.2.5: Ganglion cell layer thickness for controls (open symbols) and participants with ARM (filled symbols). Error bars indicate standard error at each measurement location. Locations where the difference between groups was statistically significant ($p<0.05$) are denoted by a star (*).

5.2.6 Retinal nerve fibre layer thickness

The retinal nerve fibre layer thickness for ARM and control groups is shown as a function of eccentricity in figure 5.2.6. The retinal nerve fibre layer increased in thickness with increasing eccentricity superiorly and inferiorly to the fovea, the greatest increase was seen towards the optic nerve head nasally, whilst the thickness temporally to the fovea was minimal reaching a peak at 6° eccentricity. The retinal nerve fibre layer was found to be significantly thinner for the ARM group at 4° and 8° superiorly and ($p<0.05$; independent t-test) but did not approach significance at any other locations.

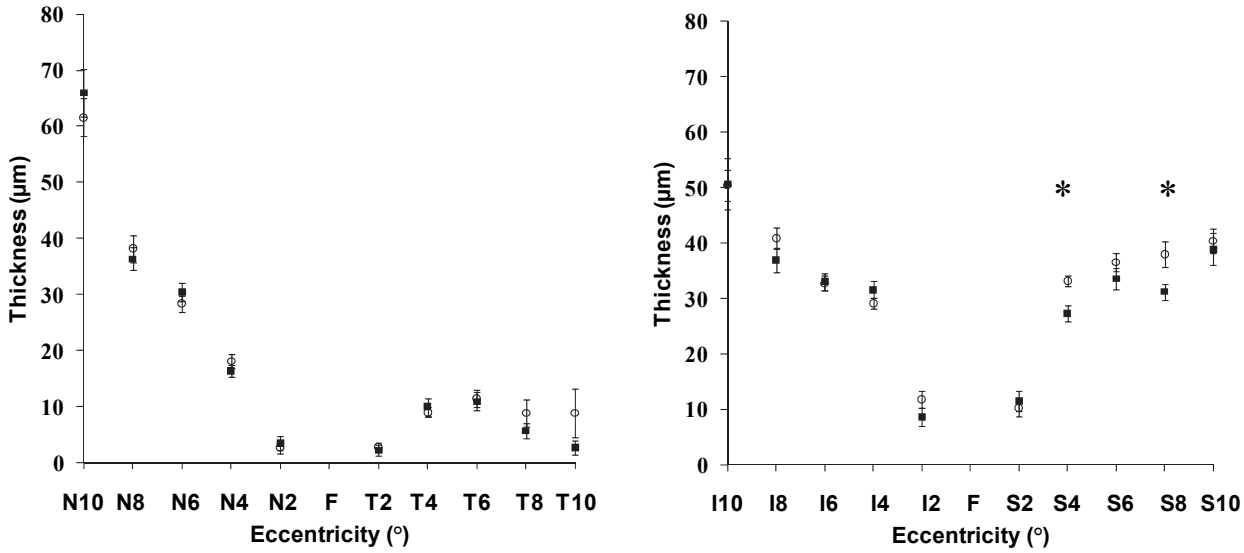

Figure 5.2.6: Retinal nerve fibre layer thickness for controls (open symbols) and participants with ARM (filled symbols). Error bars indicate standard error at each measurement location. Locations where the difference between groups was statistically significant (p<0.05) are denoted by a star (*).

5.2.7 Between group macular layer thickness

The effect of retinal or choroidal layer thickness differences across all measurement locations for each retinal or choroidal layer was assessed by two approaches. Firstly, a Two way between group analysis of variance, that considered the between group effect when of all thickness measurements at all locations are considered together. The second involved calculating a weighted average thickness for each retinal or choroidal layer assessed and assessing the statistical significance of any difference between groups identified.

5.2.7.1 Two way between groups analysis of variance

Two way between group (ARM and Control) analysis of variance identified significant differences for all retinal layers at the p<0.001 significance level. The Eta squared parameter, which represents size of effect, returned the highest value for the photoreceptor layer (0.061) and lowest for the nerve fibre layer (0.027). The choroidal measurements did not demonstrate a significant difference between groups (p>0.05).

OCT Parameter	Significance between groups	Eta squared
Retina	P<0.001	0.05
Photoreceptor layer	*P<0.001*	*0.061*
Bipolar cell layer	*P<0.001*	*0.047*
Ganglion cell layer	*P<0.001*	*0.049*
Nerve fibre layer	*P<0.001*	*0.027*
Choroid	P>0.05	-

Table 5.2.1: Two way between groups ANOVA comparing OCT layer thickness values at all measurement locations between the Control and ARM groups.

5.2.7.2 Weighted average layer thickness

The weighted average retinal thickness was marginally thinner for the ARM (263 ±52 µm) compared to the control group (269 ±29 µm) but was not found to be significantly different (p>0.2; Mann-Whitney U-test). Similarly none of the intra-retinal layers demonstrated a statistically significant difference between groups when the weighted average thicknesses were compared (see table 5.2.1). The weighted average choroidal thickness was shown to be greater in the ARM group (204 ±62 µm) compared to the controls (186 ±62 µm), again this difference was not statistically significant (p>0.3; independent t-test).

Layer	Group		p-value
	Control	ARM	
	Mean (SD)	Mean (SD)	
Retina[1]	269 (29)	263 (52)	0.230*
Choroid	186 (62)	204 (62)	0.328
Nerve fibre	31 (7)	28 (5)	0.082
Ganglion cell	63 (10)	68 (14)	0.285*
Bipolar cell[1]	55 (8)	54 (14)	0.275*
Photoreceptor[1]	121 (13)	120 (21)	0.800

1. corrected for age
*. non-parametric (Mann-Whitney U-test) statistical test applied

Table 5.2.2: Mean weighted average thickness values for 6 layer measurements. P-values for independent t-tests, or Mann-Whitney U-test for non-parametric data, carried out between groups are shown, no tests identified a significant difference between groups at the p<0.05 significance level.

5.2.8 Diagnostic ability

An analysis of the diagnostic potential was carried out for each thickness measurement where a statistical difference between groups was identified; the eleven qualifying measurements are shown in table 5.2.2. Receiver operating characteristics (ROC) curves were produced for each thickness measurement, with the retinal,

photoreceptor layer and bipolar cell layer ROC results shown in figure 5.2.7 and the ganglion cell and retinal nerve fibre layer ROC results shown in figure 5.2.8. The ROC curves were assessed for the overall diagnostic potential of each measurement by comparing the area under the curve (AUC). The AUC for the thickness measurements ranged from 0.642 for the photoreceptor layer at 2° nasal to 0.787 for the photoreceptor layer at 2° superior to the fovea.

Measured layer	Location	Optimal cut-off	Sensitivity	Specificity
Retinal thickness	Nasal 2°	284 µm	69%	59%
	Temporal 2°	265 µm	92%	59%
Photoreceptor layer thickness	Nasal 2°	148 µm	65%	55%
	Superior 2°	128 µm	92%	67%
	Superior 4°	125 µm	73%	76%
Bipolar cell layer thickness	Nasal 2°	57 µm	81%	59%
Ganglion cell layer thickness	Nasal 2°	74 µm	62%	64%
	Temporal 2°	68 µm	89%	65%
	Superior 2°	84 µm	62%	68%
Nerve fibre layer thickness	Superior 4°	31 µm	77%	68%
	Superior 8°	33 µm	58%	75%

Table 5.2.3: A summary of the 11 thickness measurements which best differentiated participants with ARM from healthy controls. The optimal cut off value for each measurement and the sensitivity and specificity of each are shown.

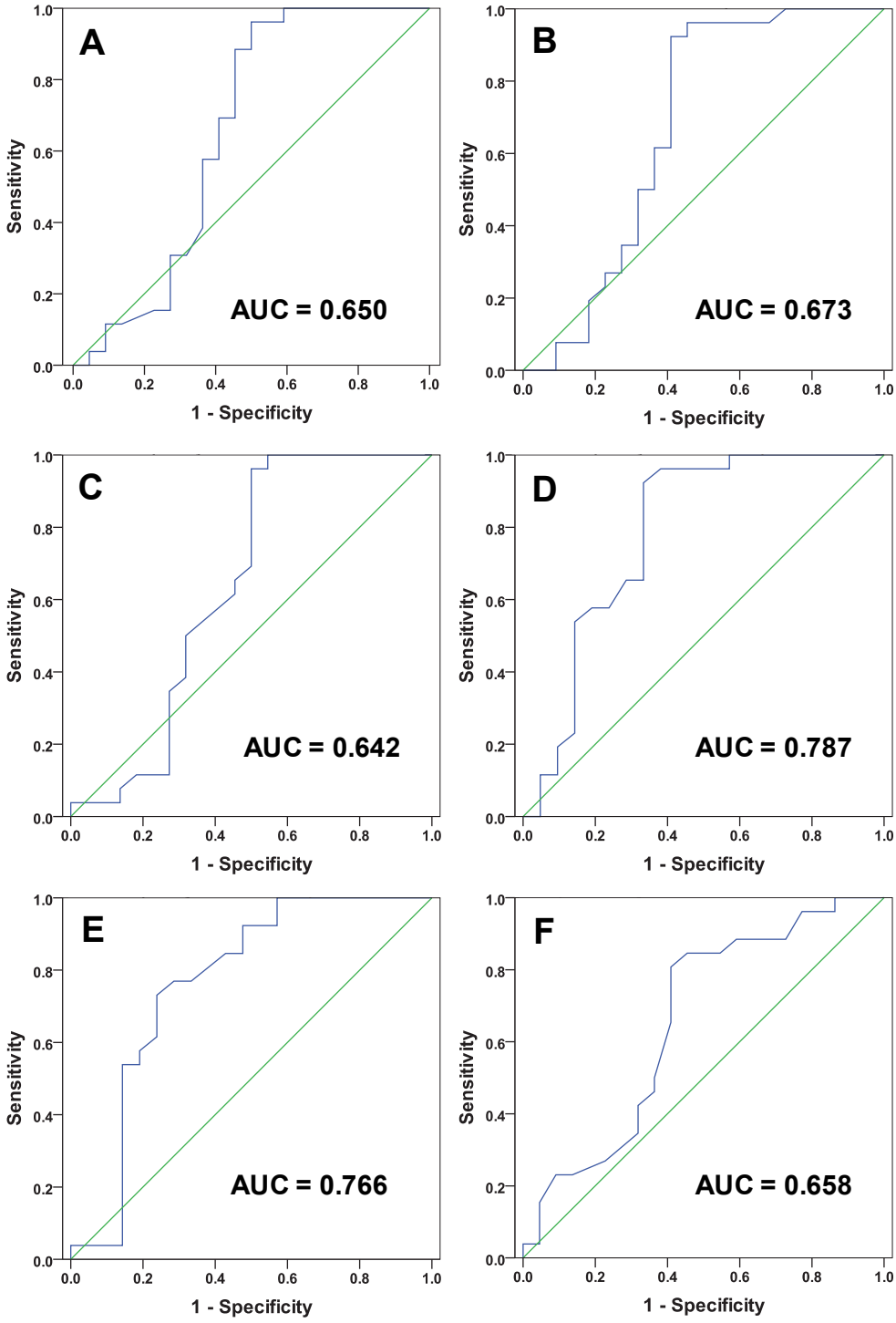

Figure 5.2.7: ROC curves assessing diagnostic potential for retinal, photoreceptor and bipolar cell layer thickness measurements at locations where a statistical difference between groups had been shown. Area under the curve (AUC) is shown for each ROC curve. (A) Retinal thickness Nasal 2°, (B) Retinal thickness Temporal 2°,(C) Photoreceptor layer thickness Nasal 2°, (D) Photoreceptor layer thickness Superior 2°, (E) Photoreceptor layer thickness Superior 4°, (F) Bipolar cell layer thickness Nasal 2°.

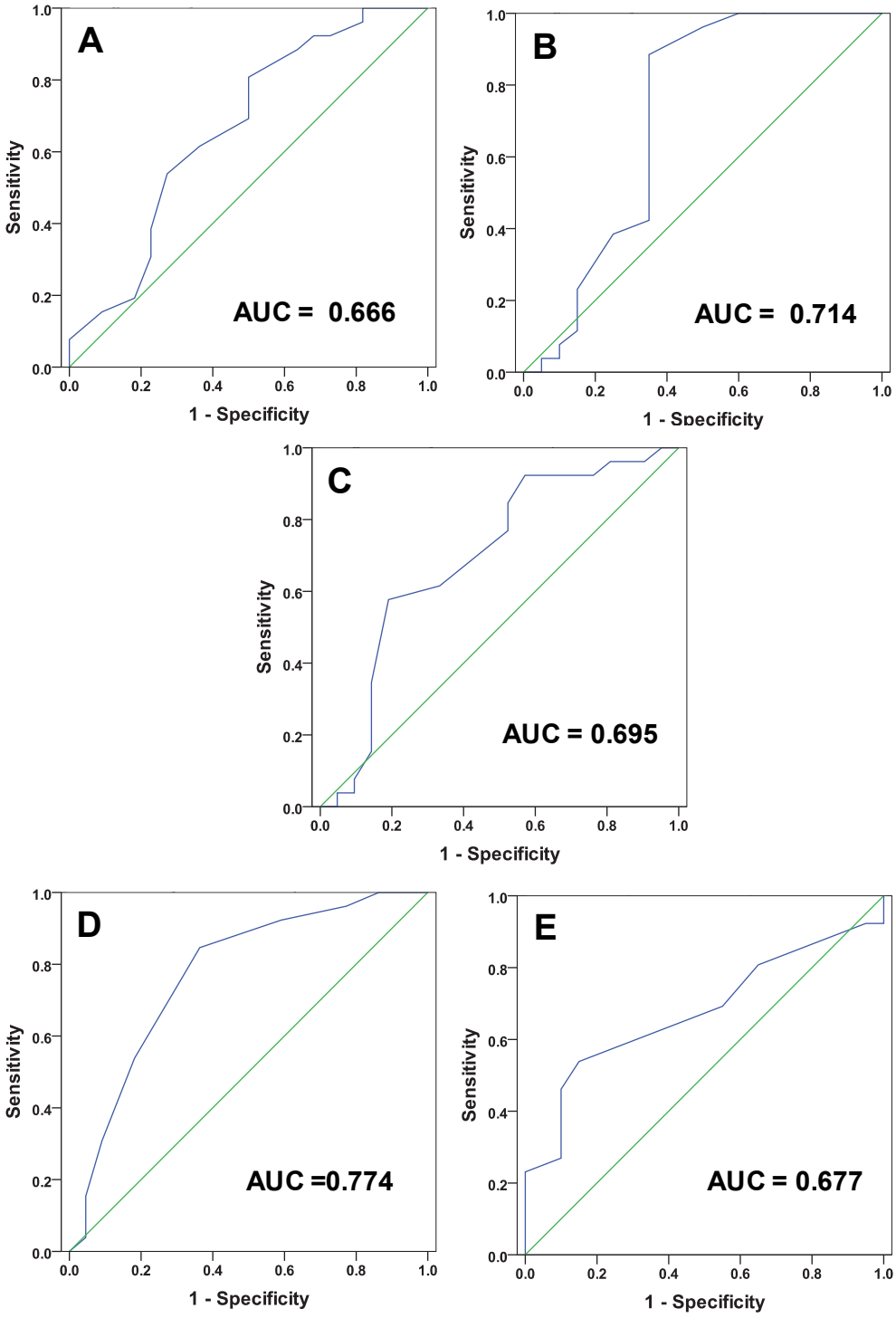

Figure 5.2.8: ROC curves assessing diagnostic potential for ganglion cell and nerve fibre layer thicknesses measurements at locations where a statistical difference between groups had been shown. Area under the curve (AUC) is shown for each ROC curve.(A)Ganglion cell layer thickness Nasal 2°, (B) Ganglion cell layer thickness Temporal 2°, (C) Ganglion cell layer thickness Superior 2°, (D) Nerve fibre layer thickness Superior 4°, (E) Nerve fibre layer thickness Superior 8°.

The optimal cut off value for differentiation between the control and ARM groups was determined based on the combination of greatest sensitivity and specificity. These values are shown in table 5.2.2. The total retinal thickness assessed at 2° nasally and temporally proved to have a reasonable sensitivity (69 and 92 % respectively) and poor specificity (59 % each) to ARM, this is reflective of the other OCT parameters (see table 5.2.2). The photoreceptor layer thickness at 2° superior to the fovea appears to have the best diagnostic potential with sensitivity and specificity of 92 % and 67 % respectively.

5.3 Discussion

This chapter intended to approach the data analysis using participants with ARM who were age and axial length matched to the controls, as was the case in the analysis described by Wood et al. (2011a). However, an alternative approach was adopted here whereby each individual thickness measurement was corrected for age and axial length where a relationship with those variables was found. Given that age-related losses of retinal cells may be heterogeneous across the macula, for example photoreceptor loss is reported to begin inferiorly and then spreads to cause greatest loss in an annular ring between 0.5 to 3 mm eccentricity (Curcio et al., 1993), these corrections were applied on a point by point basis.

Many recent studies have reported retinal thickness values (see Appendix F), for example, Legaretta et al. (2008) and Kakinoki et al. (2009) reported foveal retinal thickness in healthy individuals of 258.2 µm (± 23.5 µm) and 257.6µm (± 19.6 µm) respectively. These values are generally thicker than the 216 µm (± 32 µm) found in this thesis. However, previous studies used commercial OCT systems and reported thickness values based on the averages for the ETDRS grid sub-fields (Legarreta et al., 2008; Kakinoki et al., 2009; Cheng, Lam and Yap, 2010; Grover et al., 2010; Loduca et al., 2010). Therefore, the thickness at the foveal pit in this study cannot be directly compared to the average of the ETDRS central sub-field (radius 500 µm, ~2°). These values may be more directly comparable to the average of the 2° eccentricity measurements and foveal pit measurement, which for the control participants produced a value of 286.4 µm.

Loduca et al. (2010) measured the thickness of the photoreceptor outer segments and a layer corresponding to the outer nuclear layer and photoreceptor inner segments separately. The combined values of these two layers are comparable to the thickness of the photoreceptor layer measured in this study. They reported an average thickness within the central ETDRS sub-field (~2°) of 144 µm, the average of the 4 measurements at 2° for

control participants in this study was 148.5 µm. Other retinal locations have similar values, for example when comparing the thickness within the inner subfield (~5°) superior to the fovea, where a thickness of 117 µm was reported by Loduca et al. (2010) an equivalent location in this data set returned a measurement of 133 µm (location S4).

The bipolar cell layer in this study is equivalent to the sum of the inner nuclear layer and outer plexiform layer thickness measured by Loduca et al. (2010) using OCT images obtained from normal subjects. The thickness of the central ETDRS sub-field (~2°) of 61 µm, was of a similar magnitude to the average of the 4 measurements at 2° for control participants in this study (68.75 µm). The values reported by Loduca et al. (2010) also reflect the reduction in bipolar cell thickness with increasing eccentricity shown in these data.

The ganglion cell layer thickness values in normal participants reported by Loduca et al. (2010) was structurally correspondent to the ganglion cell layer described in this thesis. The values reported by Loduca et al. (2010) for the central ETDRS sub-field (~2°) of 56 µm were smaller than the 81µm (average of the 4 measurements at 2° for control participants) found in this study. However, the values reported by Loduca et al. (2010) for the extra-foveal thicknesses reached a peak within the inner subfield, before declining on the outer sub-fields, reflecting the same pattern as shown by these data (see figure 5.2.5).

The retinal nerve fibre layer thickness values in normal participants reported by Loduca et al. (2010) were again comparable to those found in this thesis, with similar thicknesses at the 2° location, and a similar pattern of increasing thickness with eccentricity, reaching a maximum adjacent to the optic nerve head, and a minimum temporally to the fovea (see figure 5.2.6).

Given the finding of a reduced retinal thickness in participants with ARM at the fovea, and adjacent parafovea locations, in Wood et al. (2011a) we would have expected to identify a statistically significant reduction in retinal thickness at the fovea and at all four 2° measurement locations. However, only two of these locations proved statistically significant (N2 and T2) between control and ARM groups. These findings could possibly be related to the methodology used, i.e. the 36° OCT scan imaged a wider visual angle than the published 20° data. This meant that the a-scan spacing was reduced accordingly, as both images comprised 512x512 a-scans, so the 36° images had a reduced transverse resolution in comparison to the 20° images (see figure 5.3.1). When the mean foveal thickness (average of vertical and horizontal b-scan data) is compared between the 20° and 36° images for the 16 control participants described in Wood et al. (2011a), there is

reasonable agreement with 95% confidence intervals of 14.85 to -19.86 µm. However, the variance of the 36° data with standard deviations of ± 33 µm and ±50 µm for control and ARM participants respectively at the fovea is greater than the ±18 µm and ±27 µm for the 20° images. These findings are also reflected in the variance of the thickness values obtained for the other locations measured.

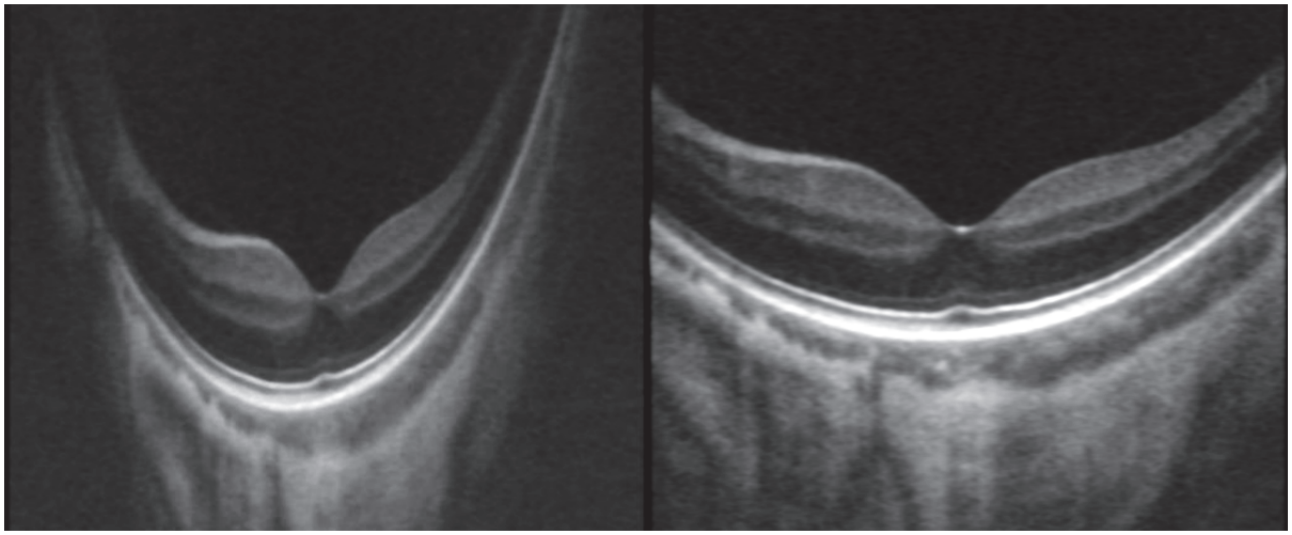

Figure 5.3.1: Comparison of two512x512 a-scan images obtained from the same eye but with a visual angle of 36° (left) and 20° (right).

In Wood et al. (2011a) the reductions in retinal thickness in the group of participants with ARM were hypothesised to be attributable to losses in the photoreceptor layer. The literature reports that photoreceptor loss occurs overlying drusen in early AMD (Kaluzny et al., 2009; Malamos et al., 2009; Schuman et al., 2009), whilst histology indicates photoreceptor loss (with a predilection for rods over cones) in non-exudative AMD, with the greatest photoreceptor loss occurring within the parafoveal/perifoveal region, equivalent to 1.5 to 10° from the foveal pit (Curcio et al., 1996). The statistically significant reduction in photoreceptor layer thickness at locations N2, S2 and S4, in this study, supports the hypothesis that localised loss of photoreceptors may be responsible for the reduction in overall retinal thickness associated with early AMD in this study and Wood et al. (2011a).

In addition to the reductions in photoreceptor layer thickness, significant reductions in the ganglion cell layer thickness at locations N2, T2 and S2 were found. These are also likely to contribute to the overall reductions in retinal thickness observed. This finding was not expected. Studies have shown reduced RGC density in advanced AMD (Medeiros and Curcio, 1997 ; 2001), however Medeiros et al. (2001) reported no significant reduction in

RGC density in 6 non-exudative (dry) AMD eyes when compared to normal participants (n=15). The finding of reductions in ganglion cell layer thickness could be reflective of a localised loss of retinal ganglion cells, possibly related to photoreceptor malfunction or loss within the outer retina. Further investigation should be conducted to confirm these findings given the lack of evidence for reductions in ganglion cell numbers at this stage of disease.

The two way between groups analysis of variance identified a significant reduction in thickness in the ARM groups for the retina and all intra-retinal layers across the locations measured. This again indicates that retinal thickness and the thickness of its component layers are affected in age-related maculopathy. Of particular interest was the eta squared parameters returned, where a bigger number represents a larger size of effect. Overall the retina returned an eta squared value of 0.05, however, when the component layers were analysed individually the photoreceptors demonstrated the largest effect (eta squared = 0.061) reducing for the intermediate layers (eta squared = 0.047 & 0.049) with the smallest values returned for the retinal nerve fibre layer (eta squared = 0.027). This indicates that the disease effect is greatest in the outer retina, although disease related changes in thickness are also present throughout the retina, reflecting the findings previously discussed for individual intra-retinal layers and locations.

Given that the majority of the statistically significant differences between the control and ARM groups were identified in close proximity to the fovea, this suggests and reinforces the widely held view that the central macula is particularly susceptible to age-related disease (Provis et al., 2005). The localised nature and lack or statistically significant changes in thickness across a wider range of retinal locations suggests that the ARM group studied in this thesis were at an early stage of disease progression.

Only a handful of studies have assessed choroidal thickness in healthy individuals using OCT imaging (Ikuno and Tano, 2009; Margolis and Spaide, 2009; Esmaeelpour et al., 2010; Ikuno et al., 2010; Manjunath et al., 2010; Wood et al., 2011a). A few of these have used a similar 1060 nm system (Esmaeelpour et al., 2010; Ikuno et al., 2010; Wood et al., 2011a). For example, Esmaeelpour et al. (2010) used a 1060 nm OCT to investigate the correlation between axial length and choroidal thickness in 34 healthy subjects (64 eyes) aged 19-80 years and found a mean central choroidal thickness of 315μm (SD 106μm), with the choroid thinnest in the nasal parafovea. This is reflected in other studies which found choroidal thickness to be greatest at the fovea, with a reduction in thickness with eccentricity reported to be greater nasally than temporally (Margolis and

Spaide, 2009; Ikuno et al., 2010; Manjunath et al., 2010; Wood et al., 2011a), a pattern which is reflected in the data within this thesis for both control and ARM participants.

The mean sub-foveal choroidal thickness reported has varied between studies from 272μm (± 81μm) (Manjunath et al., 2010), to 354nm (±111μm) (Ikuno et al., 2010) for normal participants. The 222 μm (±83μm) found in this thesis is lower, although the mean age of the control group is higher than the mean age than other studies (Ikuno et al., 2010; Manjunath et al., 2010) (see Appendix F for study details).

Evidence within the literature suggests that choroidal thickness may be affected by age, and this may explain the thinner choroidal thickness reported in this thesis (see section 5.2.2). In fact, a recent study investigating choroidal thickness in healthy individuals (n=31) that had a mean age of 64.6 years found a sub foveal thickness of 199.8 μm ±85.6, consistent with the findings reported here (Hirata et al., 2011). Margolis et al. (2009) who investigated choroidal thickness in vivo using OCT, suggested a reduction of 15.6 μm per decade using regression analysis in a study of 30 participants (mean age 50.4, range 19 to 85 years). Esmaeelpour et al. (2010) reported an age related thinning in myopic eyes, although this was not evident in emmetropic or hyperopic eyes. When assessed for age, the data within this thesis revealed no correlations with age for choroidal measurements at any location. However, it may be that we did not have a wide enough range of age data to demonstrate an effect on choroidal thickness. Another point to consider is that our 1060 nm OCT is different from other FD- OCT instruments that have measured choroidal thickness and there may be inherent differences across instruments.

The finding of no significant differences in choroidal thickness between control and ARM groups at any sub-macular location agrees with a histological study which reported no significant decrease in choroidal thickness compared to age matched controls, despite a significant decrease in choriocapillary density, in eyes with features of AMD (n=25) (Ramrattan et al., 1994). There is, however, evidence that choroidal thinning may occur in end-stage AMD (Sarks, 1976; McLeod et al., 2009). McLeod et al. (2009) examined the post-mortem choroid in 3 eyes with neovascular AMD, 5 with geographic atrophy, and 3 aged-matched control eyes; they identified a linear relationship between the loss of RPE and choriocapillaris in geographic atrophy, and a 50% reduction in choroidal vascular cross-sectional area in eyes with wet AMD, even in the absence of RPE atrophy. Additionally, Sarks (1976) conducted a histological study on eyes (n=378) from patients aged 43-97 years, with either a normal retinal appearance or some degree of AMD. They reported a thinning of the choroid, resulting in a ‘tigroid’ retinal appearance. The thinning

was associated with increasing age both in elderly patients classified as clinically normal and in those with all stages of AMD; however, it was particularly prevalent in those with advanced AMD.

In contrast to reports of age and AMD related choroidal thinning, it has also been suggested that “para-inflammation” within the choroid in response to ageing or age-related disease may result in choroidal thickening (Xu, Chen and Forrester, 2009), which may partially explain the increased thickness seen in the ARM group. However, this increased thickness was not significant at any location assessed.

The variability of the measurements and the sample size limited the minimum detectable difference between groups in this study. If we assume a power of 0.8, a significance level of 95 % and N=44 (22 per group), using the Altman nomogram for unpaired t-tests, then the smallest detectable differences between groups can be calculated: these values are shown in table 5.3.1. Smaller difference in means were found at many of the measurement locations assessed, however this study was not powered to determine if these were significant. It is therefore possible that disease effects exist at these locations, but as these differences are smaller in magnitude than one standard deviation of the OCT measurements, within the control population, it is unlikely that they are clinically detectable or diagnostically useful for ARM at this time. Future improvements in OCT imaging and analysis techniques may make smaller magnitude differences between groups detectable and therefore an investigation with a larger sample size may prove beneficial at a later date.

OCT parameter (layer thickness)	Assumed variance (1 standard deviation)	Smallest detectable difference
Retina	29 µm	23 µm
Photoreceptor	13 µm	10 µm
Bipolar cell	8 µm	6 µm
Ganglion cell	10 µm	8 µm
Nerve fiber	7 µm	6 µm
Choroid	62 µm	50 µm

Table 5.3.1: Smallest detectable difference between groups, assuming a power of 0.8, at the p=0.05 significance level for unpaired t-tests using the Altman Nomogram. Assumed variance (1 standard deviation) based on control group for each parameter, and equal size of groups (n=24 each; actually controls n=26 and ARM n=24).

Diagnostically the structural parameters assessed within this chapter provided a moderate ability to differentiate between ARM and healthy participants. However, the

nature and distribution of the measurement locations presents a difficulty when applying this clinically. Clinicians are unlikely to assess thickness at a specific location, such as 2° nasally when diagnosing a condition. Although the locations with statistically significant differences in retinal thickness between groups were predominately parafoveal, only some of the expected locations assessed produced significant findings. In part, significant differences between groups may have been masked by the increased variability of data here, compared to the measurements obtained using the 20°x20° images described in Wood et al. (2011a).

The diagnosis of ARM in this study was based on the retinal appearance of affected eyes, effectively an assessment of retinal structural changes, and this is currently considered the 'gold standard' method for the diagnosis of AMD (Klein et al., 1991; Bird et al., 1995; AREDS, 2001a). The development of a new clinical test for the purposes of diagnosis requires a variety of different attributes. An OCT based system would potentially offer a quick and non-invasive technique. A reasonable approach may be to assess mean retinal thickness over a region approximating the central 2°. However, given that not every retinal location provided a statistical difference, then this average measure is likely to be less sensitive to ARM related changes. Clark et al. (2011) evaluated retinal thickness measures using the Cirrus OCT (Carl Zeiss, Meditec Inc, CA) on 74 adults with a range of AMD from near normal to extensive geographic atrophy. Although differences were shown for the retinal thickness in central and paracentral subfields, confirming the findings in this study, those differences between almost normal participants and those with disease (equivalent to the ARM group in this study) were less than 20 μm in each case, and less than the standard deviations of the measurements.

It would appear that there are small measurable structural changes, which occur in ARM, predominantly in the parafoveal region. However, the magnitude and distribution of these changes combined with normal variation means that they are not an effective biomarker for the diagnosis of ARM.

Chapter 6: Retinal function

This chapter describes a study designed to evaluate the effect of ARM on retinal function using four focal ERG techniques. Section 1.5 described the four ERG techniques, three of which had previously been shown to have diagnostic potential for ARM (Binns and Margrain, 2007): the focal cone ERG and focal flicker ERG provided static measures of cone function, whilst the ERG photostress test provided a dynamic measure of cone adaptation. The fourth technique, the focal rod ERG (Binns and Margrain, 2006) provided a static measure of rod function. The sensitivity of the focal rod ERG to ARM has not previously been assessed, however there is psychophysical evidence of rod dysfunction in ARM (Owsley et al., 2000; Owsley et al., 2001; Owsley et al., 2007). Chapter 3 described a series of studies intended to improve the clinical utility and diagnostic potential of these four focal ERG techniques. The modified techniques developed are employed in this study.

The first aim of this chapter was to identify which ERG parameters were sensitive to ARM-related functional change. The second aim was to assess the diagnostic potential of each parameter, i.e. to determine which techniques had the best sensitivity and specificity to ARM, and to compare to the diagnostic potential of the OCT measures evaluated in chapter 5. Finally, these values provided the basis for a comparison of retinal structure to function described in chapter 7.

6.1 Methods (ERG protocols)

6.1.1 Participant preparation

Participants were prepared for ERG recording using the protocol described in section 3.1.1. Electrode impedance was also assessed prior to recording, if the impedance of any electrodes exceeded 7 kilo ohms (kΩ) the electrode was reattached following further skin preparation; high electrode or unequal impedance can result in excessive noise and therefore a reduced SNR.

6.1.2 Focal cone ERG

Four focal cone ERG traces were recorded and analysed using the methods previously described in section 3.1.3. The mean amplitudes and implicit times of the a and b waves were determined for each trace and then averaged for each participant.

6.1.3 Focal flicker ERG

Eight focal flicker ERG traces were recorded and analysed using the methods described in section 3.1.4. The mean amplitude and implicit time was determined for each trace and then averaged for each participant.

6.1.4 ERG photostress test

An ERG photostress test was recorded and analysed for each participant using the general methods described in section 3.1.5 however, the following paragraphs describe several adaptations made to the protocol.

Eight, rather than four, pre-bleach focal flicker ERGs (each consisting of 100 averaged responses) were recorded to provide a more robust baseline for ERG recovery. All participants were pre-adapted to the stimulus for a period of 5 minutes as experimental work demonstrated progressive changes in the amplitude and implicit time of the flicker ERG which appear to stabilise after 5 minutes of adaptation (see section 3.5). Post-bleach ERG recording began 10 seconds after the bleach and focal flicker ERGs were obtained at 20 s intervals thereafter for 5 minutes, each recording took approximately 5 seconds to complete (see figure 6.1.1).

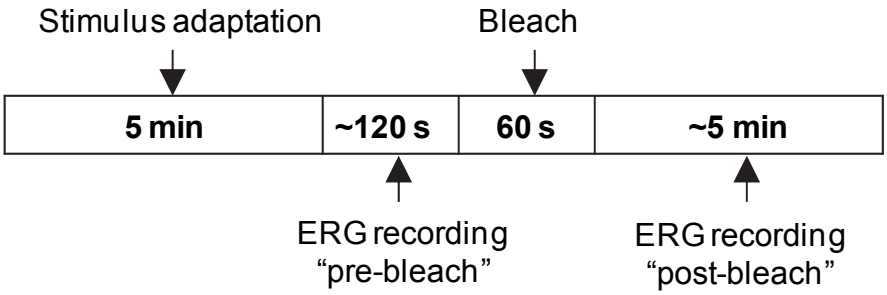

Figure 6.1.1: Timeline showing the recording process for the ERG photostress test with timings shown for each stage.

As the baseline amplitude of the focal flicker ERG can vary between individuals as a result of physiological differences (e.g. fundus pigmentation, scleral resistance or axial length) as well as disease (Fishman et al., 2005), all ERG photostress recovery curves are presented with the amplitude normalised to the pre-bleach baseline. For example, the recovery curves presented in figure 6.1.2 (curves A & B) have been reproduced with normalised amplitudes (curves C & D). This allows easier visual comparison of recovery rates.

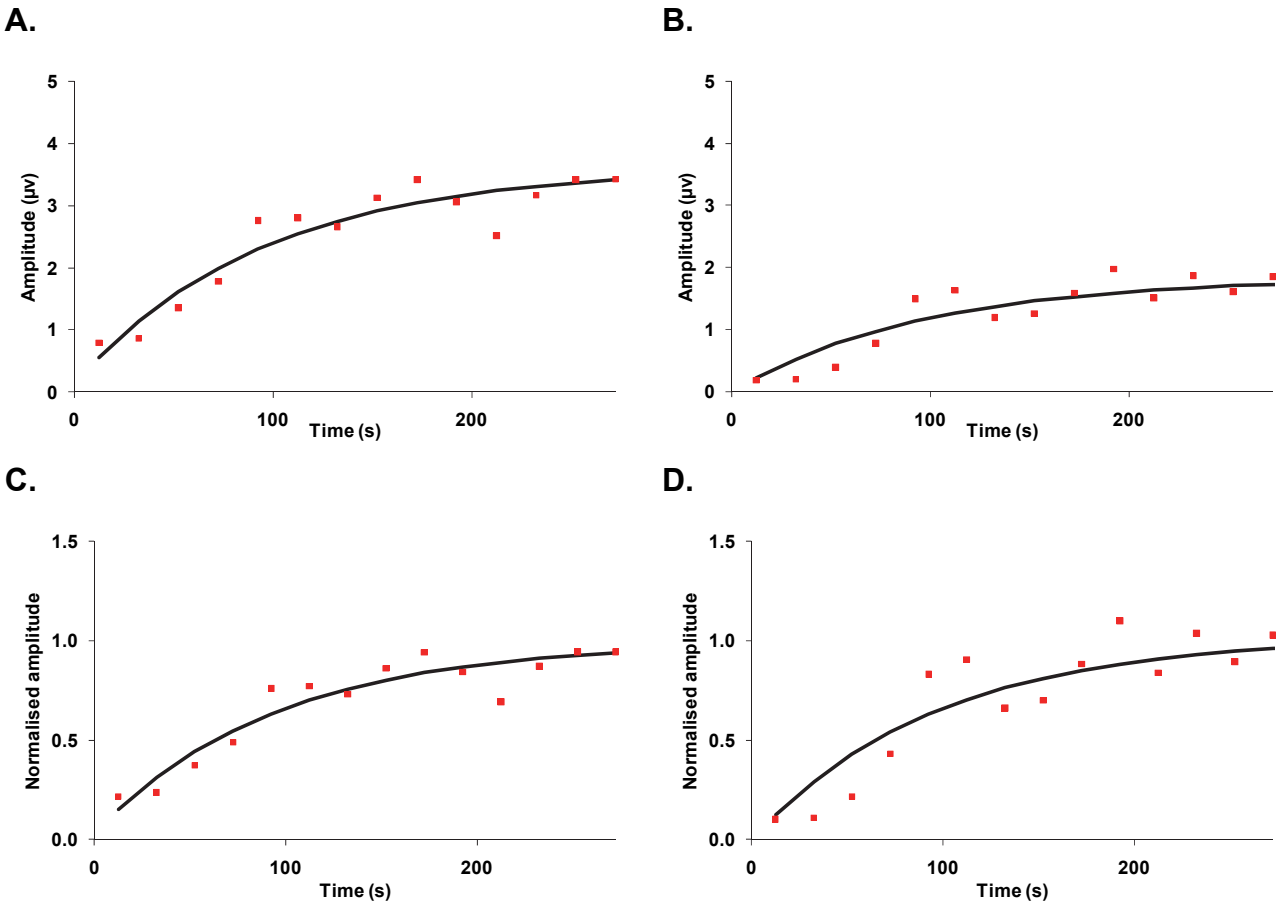

Figure 6.1.2: Top: Two recovery curves for the ERG photostress test from participants AW (A) and TM (B) with baseline amplitudes of 3.6µV and 1.8µV respectively. Bottom: The recovery curves for participants AW (C) and TM (D) have been reproduced with the amplitudes normalised to the pre-bleach baseline. The time constants of recovery were determined as 95 s and 96 s for participants AW and TM respectively.

To provide a more objective approach to identifying and removing outlying data points (e.g. those with a poor SNR) 95% confidence limits were calculated for the modelled data. These confidence limits were calculated based on the fit residuals i.e. the difference between the real amplitude value and the modelled value. The standard deviation of the post bleach recovery data residuals was calculated, this value was then multiplied by 1.96, and this value ± the modelled amplitude provided the confidence limits. These upper and lower confidence limits were then plotted on the recovery curves and used to assess the quality of each data point. Points lying outside these limits could be considered as outliers and were reassessed based on the following criteria:

- If the absolute amplitude of the data point exceeded twice the baseline amplitude then it was excluded.

- If the data point waveform did not have the biphasic appearance expected of a reliable focal flicker ERG (see figure 6.1.3), then the data point was excluded (see figure 6.1.4).

Datasets with any outliers removed were remodelled and the returned values for “a”, “B” and “τ” recorded.

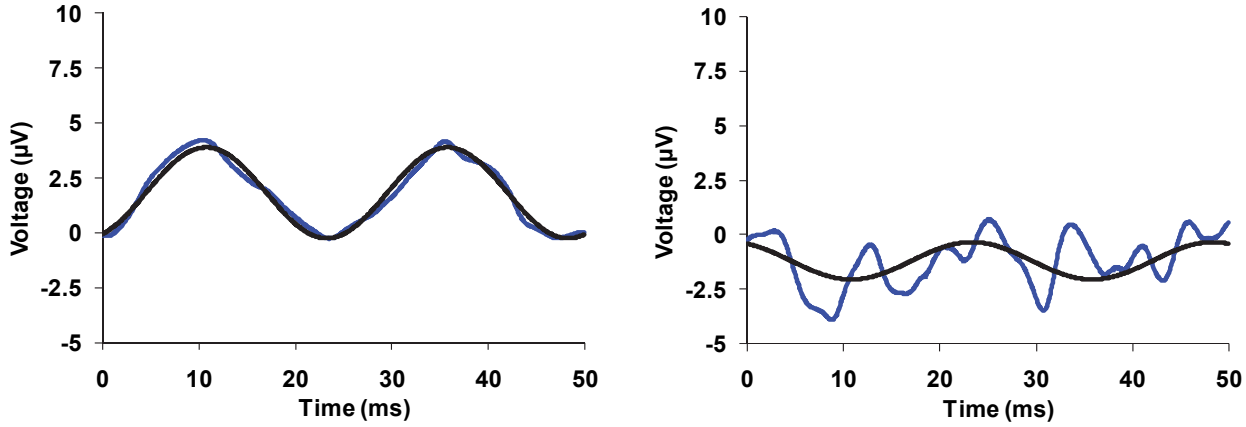

Figure 6.1.3: Focal flicker ERG traces showing the actual response prior to Fourier analysis (blue) and the isolated 1st harmonic (black) following Fourier analysis. A normal biphasic response is shown on the left, whilst a non-biphasic response (which would be excluded from data modelling) is shown on the right.

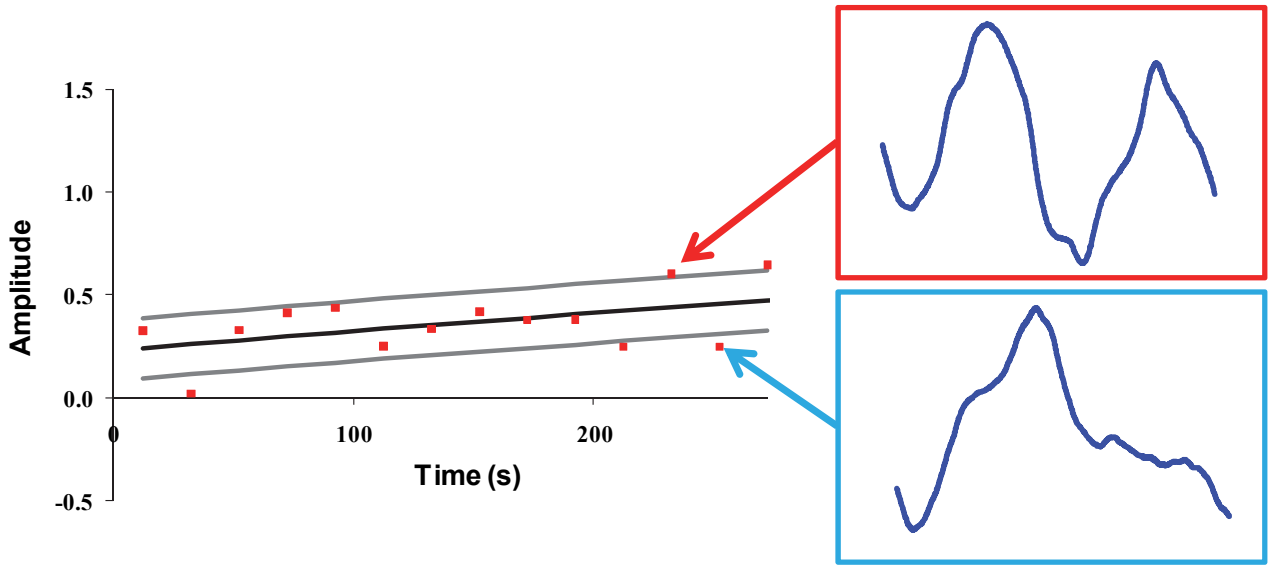

Figure 6.1.4: A modelled (black line) ERG photostress test recovery with 95% confidence intervals (grey lines). Example traces are shown for two data points, the first (Top; red box) lies within the confidence interval and shows the expected waveform, the second (Bottom; blue box) lies outside the confidence interval and does not demonstrate a biphasic waveform and was therefore removed from the analysis.

6.1.5 Focal rod ERG

The focal rod ERG protocol was adapted from that described in section 3.1.6, such that the response would be elicited to both a 20 and 500 scotopic td.s blue stimulus. The stimulus properties are given in table 6.1.1. A focal rod ERG was recorded for each stimulus, comprising ~75 averages per trace (recorded in blocks of 5 to minimise blink artefacts). Additional averaging was undertaken as required to maximise the SNR.

As these luminance levels have been shown to contain a cone contribution (see section 3.7.2), ERG recordings were repeated with the same stimulus presented against a constant rod suppressing green background of 1500 scotopic td.s, producing a cone response that could be subtracted to isolate the rod response of the focal rod ERG. These traces were analysed as described in section 3.1.6. In addition, the ratio between 20 td.s and 500 td.s response amplitudes was also calculated for both a and b wave for each participant.

Scotopic td.s	Photopic cd.m^{-2}	Duration (ms)
20	3	5
500	37.50	10

Table 6.1.1: Duration and luminance of focal stimulus used to elicit the 20 and 500 td.s focal rod ERG.

6.1.6 Data analysis

The ERG parameters for the control participants were assessed for any correlation with age and axial length because the control and ARM groups were not matched for these factors (see section 4.3.2). Normally distributed data (assessed using the Shapiro-Wilk test) were tested using the Pearson's correlations coefficient, whilst non-parametric data were assessed using the Spearman's rank correlation coefficient. Where a statistically significant correlation was identified ($p<0.05$) the parameters of both control and ARM groups were corrected based on the gradient of a linear regression analysis.

Once any corrections were made for age or axial length, the mean data of the two groups were compared with independent t-tests (if normally distributed according to the Shapiro-Wilk test), whilst non-normally distributed data were compared using the non-parametric Mann-Whitney U-test, a statistically significant difference was determined based on the $p<0.05$ (95%) confidence level. In cases where any ERG parameter was successfully recorded on less than 80% of participants, in either group, then non-

parametric statistical tests were applied. Statistical analysis was carried out using SPSS 19 software (IBM, Armonk NY).

Electroretinogram parameters that demonstrated statistical differences between groups were assessed for diagnostic potential by determining the area under ROC curve.

6.2 Results

Electroretinograms (ERG) were recorded from all 24 participants with ARM and 26 controls. The individual ERG response parameters for each participant and technique are shown in Appendix K; values where adjustment for age or axial length was made are indicated.

6.2.1 Focal cone ERG

The focal cone ERG was successfully recorded on all study participants (n=50). Figure 6.2.1 shows typical focal cone ERG responses recorded from 3 controls and 3 participants with ARM. Those recorded from individuals with ARM tended to be smaller and slower than those obtained from members of the control group. The ARM group (n=24) returned mean a and b wave amplitudes of -2.25 μV (±0.99) and 5.18 μV (±1.89) respectively. This was smaller than mean a and b wave amplitudes for the control group (n=26) of -2.58 μV (±0.82) and 5.95 μV (±1.54) respectively. However, the difference between groups did not reach statistical significance, with $p>0.1$ (independent t-tests) for both a and b wave amplitudes.

The mean focal cone ERG a and b wave implicit times were 25.5 ms (±1.58) and 47.4 ms (±3.27) respectively for the ARM group, and 24.5 ms (±2.19) and 44.6 ms (±2.21) for the control group. The difference between groups for b-wave implicit time was statistically significant ($p<0.001$; independent t-test) whilst the a-wave implicit time was approaching significance ($p<0.06$; independent t-test).

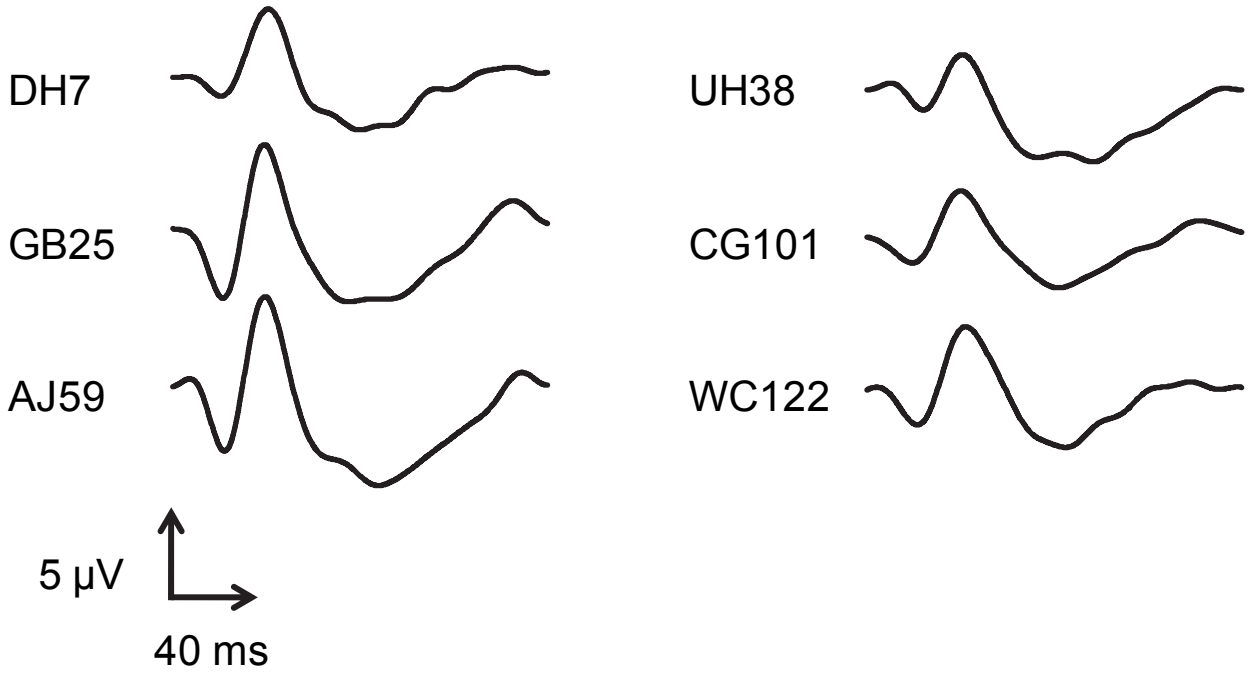

Figure 6.2.1: Example of typical Fourier analysed focal cone ERGs recorded from control (left) and ARM (right) participants.

6.2.2 Focal flicker ERG

The focal flicker ERG was successfully recorded in all controls (n=26) and 22 of the 24 participants with ARM. The focal flicker ERG traces were generally smaller and less well defined for the those with ARM compared to the control participants (see figure 6.2.2). The mean amplitude and implicit time for the control group was 2.2 µV (±0.75) and 10.8 ms (±0.88) respectively, this compared to the ARM group with a smaller amplitude of 1.94 µV (±1.15) and longer implicit time of 10.9 ms (±1.86). However, these differences were not significant for either the amplitude ($p>0.3$; independent t-test) or implicit time ($p>0.6$; independent t-test). There was considerable overlap between the data for the two groups, which may be attributable to the high variability of the ARM data for both amplitudes and implicit times compared to the control participants.

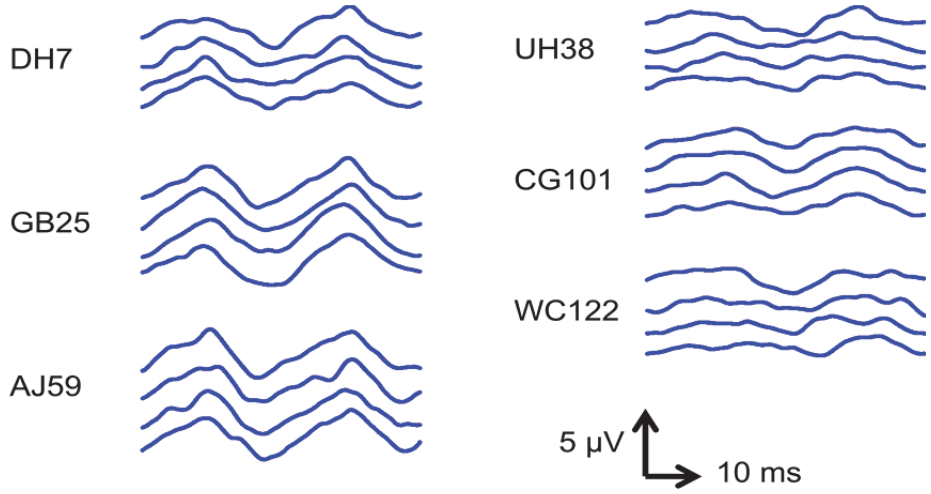

Figure 6.2.2: Example of typical focal flicker ERG responses for 3 controls (left) and 3 participants with ARM (right).

6.2.3 ERG photostress test

The ERG photostress test recoveries were successfully modelled (i.e. the Excel solver function (Microsoft, Redmond WA) was able to find a least squares solution for the data) for all control participants, but for only 15 of the 24 participants with ARM. Failure of the modelling resulted from the absence of ERG amplitude recovery in the ARM group (see figure 6.2.3 for sample data). Of the successfully modelled ERG photostress recoveries, the underlying focal flicker ERGs appeared to be smaller and more variable in appearance in participants with ARM, with less defined biphasic waveforms than in controls (see figure 6.2.4).

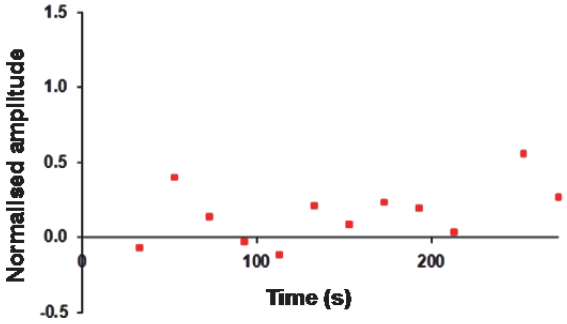

Figure 6.2.3: The ERG photostress test amplitude recovery in an ARM participant (JH108) that was not successfully modelled.

The control group produced a mean time constant of 159.7 s (±95.98) compared to a much longer mean of 250.3 (±181.95) for the ARM participants, this difference approached significance (p=0.09; independent t-test). However, the comparison of means

did not take into account the large proportion of participants with ARM who showed no recovery. When a non-parametric approach was undertaken, with test failures arbitrarily assigned a high time constant of recovery (1000 s), a median value of 161s was found for the control participants and 322s for the ARM participants, the difference between groups was highly significant ($p<0.001$). The individual amplitude recovery data are shown in the Appendix K, figure K.1.

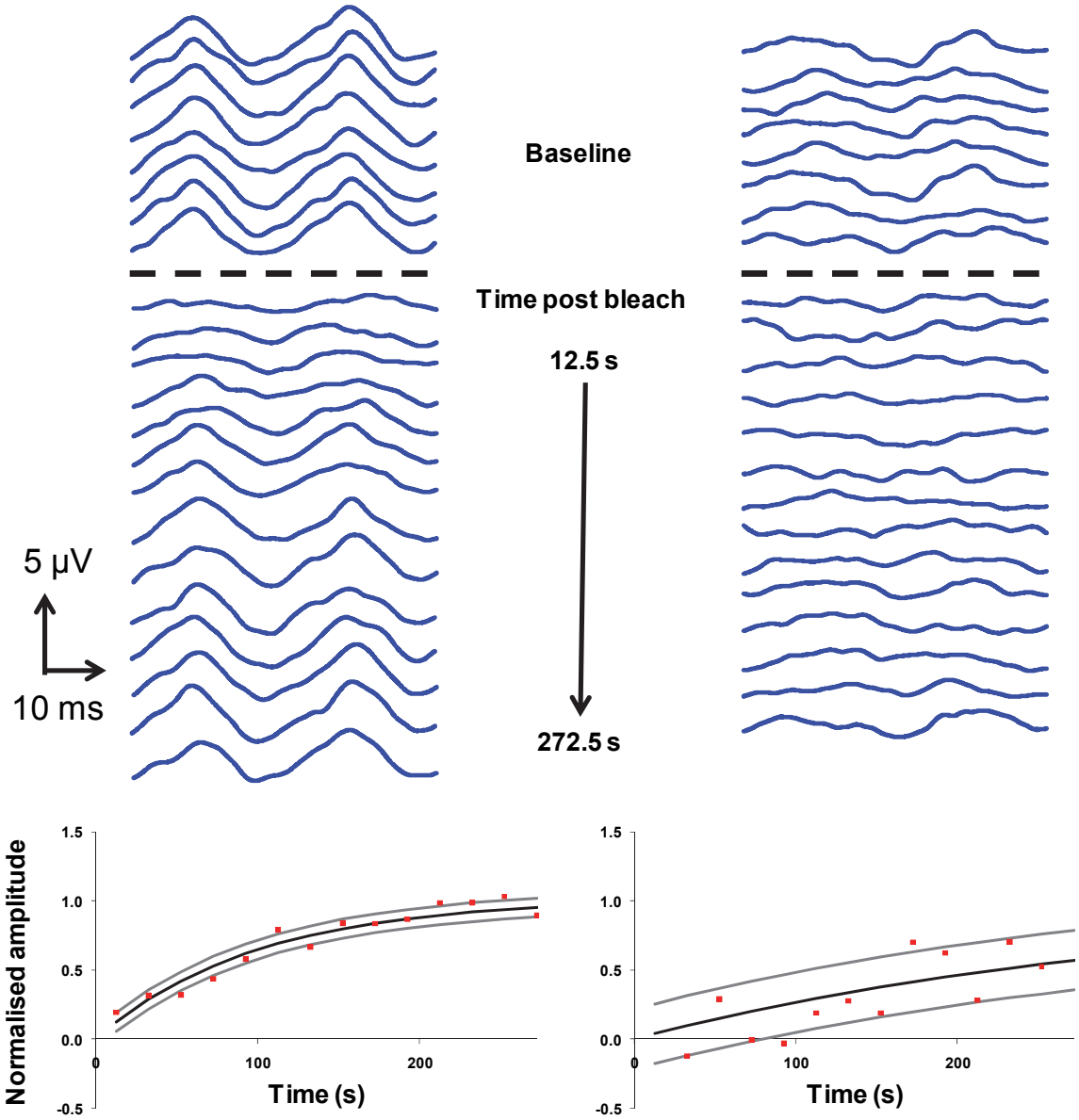

Figure 6.2.4: Top: Raw focal flicker ERG traces for healthy participant PF70 (left) and for ARM participant UH38 (right). Bottom: the ERG photostress test recoveries are shown for each participant. Red points indicate focal flicker ERG amplitudes; the recovery model is indicated by the black line and 95% confidence limits are shown as grey lines. Time constants were 98 s and 330 s respectively for participants PF70 (control) and UH38 (ARM).

6.2.4 Focal rod ERG

The focal rod ERG was successfully recorded using the 20 td.s stimulus from only 10 of 24 ARM participants, of which only 7 demonstrated a measureable a-wave, and only 18 of 26 control participants, of which only 10 had a measurable a-wave. In contrast, all but 2 participants (both with ARM) produced a measurable focal rod ERG in response to a 500 scotopic td.s stimulus, although a-waves were not measureable on all participants.

The focal rod ERGs recorded in response to the 20 td.s stimulus were generally smaller and less well defined than those for the brighter 500 td.s stimulus for both ARM and control participants (see figure 6.2.5 for example data from 3 control and 3 participants with ARM). For both the 20 td.s and 500 td.s stimuli the ARM participants produced less well defined responses, in addition they were generally smaller and demonstrated delayed time to peak compared to the equivalent responses from control participants.

The median a and b wave amplitudes (±Inter-quartile range) for the 20 scotopic td.s stimulus were of -0.98 µV (± 0.8) and 4.14 µV (±1.1) respectively for the control group. The ARM group produced median a and b wave amplitudes -1.35 µV (±1.4) and 3.5 µV (±2.3) respectively. No 20 td.s focal rod ERG a or b wave parameter (amplitude or implicit time) reached statistical significance when compared between groups.

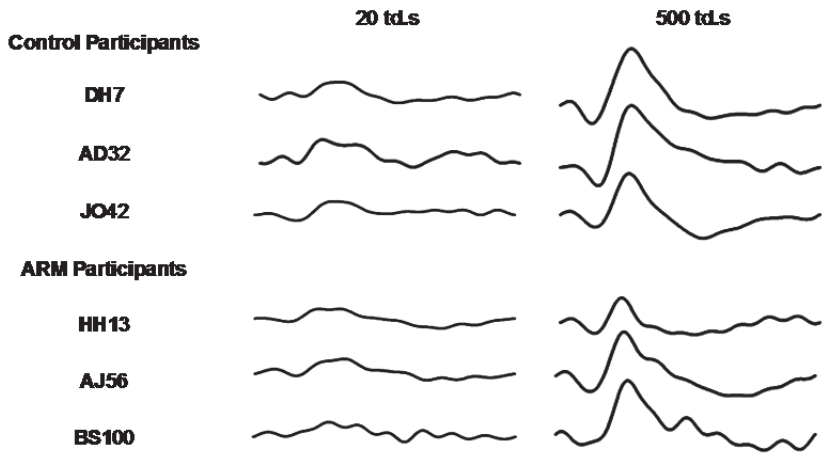

Figure 6.2.5: Example of typical Fourier analysed focal rod ERG responses for the 20 td.s and 500 td.s stimulus intensity recorded from 3 controls (Top) and 3 participants with ARM (bottom).

In contrast, the 500 td.s focal rod ERGs were larger, and a and b wave parameters successfully identified on a greater number of study participants. The b wave amplitudes

and implicit times were successfully measured on 100% of control, and 92% of ARM participants, the mean amplitudes were 11.9 μV (±4.78) and 8.8 μV (±3.69) respectively for the control group and the group with ARM. The b-wave amplitude was significantly larger in the controls than the ARM group ($p=0.017$; independent t-test). Furthermore, the mean b-wave implicit time was found to be longer in the ARM group, 57.1 ms (±5.86), compared to the control group at 53.9 ms (±4.90); this difference was again statistically significant ($p=0.046$; independent t-test). The a wave amplitudes and implicit times were successfully identified on fewer participants (see table 6.2.1), and therefore analysed using non-parametric statistics, however neither parameter was shown to be significantly different between groups (see table 6.2.1).

Given the small number of 20 td.s ERG parameters successfully measured, it was not viable to calculate and compare the ratio of response amplitudes at the two stimulus intensities.

6.2.5 Parameter summary

The group averaged results for the focal cone ERG, focal rod ERG, ERG photostress test and focal flicker ERG have been summarised in table 6.2.1.

Parameter	Group								p-value
	Control				ARM				
	Success	Median	Mean	±SD	Success	Median	Mean	±SD	
Focal cone ERG									
a-wave amplitude (μV)	100%	-2.6	-2.6	*0.8*	100%	*-2.1*	-2.2	*1.0*	0.197
a-wave implicit time (ms)	100%	24.2	24.5	*2.2*	100%	*25.5*	25.5	*1.6*	0.059
b-wave amplitude (μV)	100%	6.2	5.9	*1.5*	100%	*4.9*	5.2	*1.9*	0.120
b-wave implicit time (ms)	100%	43.8	44.6	*2.2*	100%	*46.9*	47.4	*3.3*	**0.001**
Focal rod ERG (20 td.s)									
a-wave amplitude (μV)	39%	*-1.0*	-1.0	*0.6*	29%	-1.3	-1.3	*0.9*	0.495*
a-wave implicit time (ms)	39%	*30.8*	30.4	*4.4*	29%	26.5	26.7	*5.1*	0.107*
b-wave amplitude (μV)	69%	*4.1*	4.3	*1.5*	42%	3.5	3.6	*1.7*	0.292*
b-wave implicit time (ms)	69%	*61.0*	60.1	*6.1*	42%	62.5	62.7	*6.2*	0.374*
Focal rod ERG (500 td.s)									
a-wave amplitude (μV)	92%	*-3.1*	-3.0	*1.1*	71%	-2.7	-2.7	*1.2*	0.316*
a-wave implicit time (ms)	92%	*27.0*	27.4	*2.7*	71%	28.5	28.9	*4.1*	0.630*
b-wave amplitude (μV)	100%	*12.8*	11.9	*4.8*	92%	8.7	8.8	*3.7*	**0.017**
b-wave implicit time (ms)	100%	*53.8*	53.9	*4.9*	92%	56.0	57.1	*5.9*	**0.046**
ERG photostress test									
time constant (s)	63%	*161*	160	*96*	100%	322	250	*182*	**<0.001***
Focal flicker ERG									
amplitude (μV)	100%	2.1	2.2	*0.7*	92%	*1.7*	1.9	*1.2*	0.361
Implicit time (ms)[1]	100%	10.9	10.7	*0.9*	92%	*10.8*	10.9	*1.9*	0.686

1. corrected for age
* non-parametric (Mann-Whitney U-test) statistical test applied

*Table 6.2.1: Mean and standard deviation for each ERG parameter assessed. P-values for independent t-tests (or Mann-Whitney U-test for non-parametric data) carried out between groups at each location are shown, with significant values (p<0.05) highlighted in **bold** type.*

6.2.6 Diagnostic ability

Four ERG parameters were shown to have a statistical difference between groups (see table 6.2.1). In addition, the focal cone ERG a-wave implicit time approached significance. These five parameters were believed to be the most promising diagnostic indicators for differentiating participants with ARM from healthy controls and therefore were assessed for diagnostic ability.

Receiver operating characteristic curves were produced (see figure 6.2.6) and assessed for each of the ERG parameters described in table 6.2.2. In the case of the ERG photostress test a failure to demonstrate a recovery within the recovery period was arbitrarily assigned a values of 1000s, which exceeded the longest time constant recorded from any individual, for the purposes of conducting the ROC analysis. The overall diagnostic potential for each parameter was then assessed by comparing the area under the curve (AUC) for each. The AUC for the ERG parameters ranged from 0.672 for the focal rod ERG (500 td.s) b-wave implicit time to 0.807 for the ERG photostress test time constant of photopigment regeneration. The ERG photostress test showed the best diagnostic potential when model failure was included as a predictor of ARM.

The ERG parameters were also assessed to determine the optimal cut off value for each which provided the best combination of sensitivity and specificity in differentiating between the control and ARM groups. These values are shown in table 6.2.2. The ERG photostress test provided the greatest sensitivity (75%) and specificity (81%) when a cut off of 192 s was applied. The focal rod ERG (500 td.s) proved to be the least diagnostic of the ERG parameters assessed, with b wave amplitude and implicit time sensitivities of 62 and 55 % respectively.

Test	Parameter	Optimal cut-off	Sensitivity	Specificity
Focal cone ERG	a-wave implicit time	24.63 ms	67%	65%
	b-wave implicit time	45.65 ms	71%	77%
Focal rod ERG (500 td.s)	b-wave amplitude	10.02 mV	62%	68%
	b-wave implicit time	55.75 ms	55%	77%
ERG photostress test	Time constant	192 s	75%	81%

Table 6.2.2: A summary of 5 ERG parameters which best differentiate participants with ARM from healthy controls. The optimal cut off value for each parameter and the respective sensitivity and specificity of each are shown.

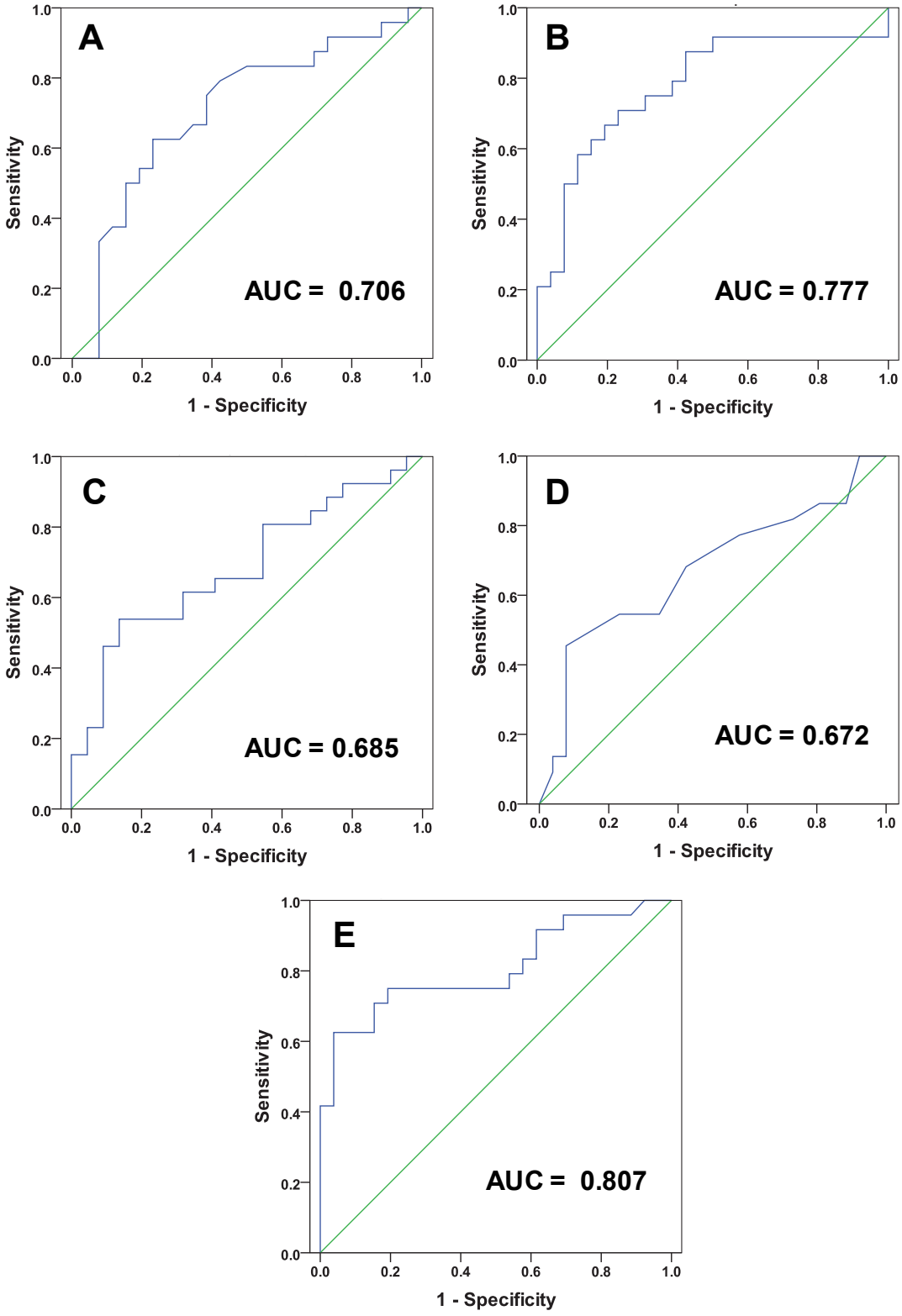

Figure 6.2.6: ROC curves assessing diagnostic potential for ERG parameters. Area under the curve (AUC) is shown for each ROC curve. (A) Focal cone ERG a-wave implicit time, (B) Focal cone ERG b-wave implicit time, (C) Focal rod ERG 500 td.s b-wave amplitude, (D) Focal rod ERG 500 td.s b-wave implicit time, (E) ERG photostress test time constant.

6.3 Discussion

This chapter describes the results of a number of electrophysiological tests in people with ARM. The tests used assessed the integrity of rod and cone pathways, as well as retinal adaptation. Both focal cone and rod ERGs showed abnormalities in ARM, but the ERG photostress test provided the best discrimination between groups, with 9 participants with ARM failing to show recovery that could be modelled within 5 minutes of the bleach, which has been shown to be an indicator of ARM (Binns and Margrain, 2007).

Scotopic visual function was assessed in this thesis using the focal rod ERG, this was done using both a bright (500 td.s) and dimmer (20 td.s) stimulus. A measurable response to the 20 td.s stimulus was not obtained from 20 of the participants, predominantly but not exclusively those with ARM. Ultimately, the greater proportion of immeasurable 20 td.s focal rod responses in this group may be attributable to the disease itself. Participants with widespread rod loss or dysfunction, known to be a feature of ARM (Curcio et al., 1993; Curcio et al., 1996; Owsley et al., 2001; Owsley et al., 2007), may produce smaller signals which become difficult to identify from the background noise. The lack of measurable signals in participants with ARM is not therefore surprising.

The 500 td.s focal rod ERG stimulus provided measurable results in a far greater proportion of participants; the brighter stimulus is likely to have contributed to this by evoking a larger amplitude response, which is measureable even in participants with dysfunction. As can be seen from the b-wave amplitude and implicit time of the response to the 500 td.s stimulus, there was both a reduction in the amplitude and delay in the implicit time for participants with ARM compared to controls. The finding of deficits in parameters of rod function which mediate scotopic vision was not unexpected; the literature contains widespread evidence of functional deficits in scotopic visual parameters in age-related macular disease (Eisner et al., 1991; Eisner et al., 1992; Steinmetz et al., 1993; Owsley et al., 2001; Haimovici et al., 2002; Owsley et al., 2007; Dimitrov et al., 2008) as well as histological evidence of macular rod loss (Curcio et al., 1993; Curcio et al., 1996).

Photopic visual function was assessed by 3 different techniques within this thesis, each eliciting a different type of electrophysiological response. The focal cone ERG however, was the only photopic technique to demonstrate a statistically significant difference between groups for a photopic ERG parameter. A significantly delayed b-wave implicit time was found in the group with ARM. In addition, although the a-wave implicit time was not found to be statistically different between groups, the p-value was

approaching significance. This is consistent with previously reported findings of delayed focal cone ERG a and b wave implicit times in participants with ARM (Binns and Margrain, 2007).The finding that implicit times but not amplitudes were significantly different between groups is likely to be due to greater variability of amplitudes than implicit times in ERG recordings (Hochstein, Molnar and Marmor, 2007; Mortlock et al., 2010). Binns and Margrain (2007) reported area under the ROC curve for the a and b wave implicit times of 0.74 and 0.77 respectively, which is comparable to the 0.71 and 0.78 respectively found in this thesis.

There is no evidence of widespread macular cone loss, in histological studies of ARM (Curcio et al., 1996), but cone dysfunction may be explained by histological evidence suggesting that the cones undergo morphological changes in ARM (Curcio, Owsley and Jackson, 2000). The impact of these morphological changes may therefore be reflected in reduced or delayed input to the bipolar cells, which is consequently detected as increased implicit times for the a and b wave in participants with ARM. Other studies have reported abnormal cone function in early AMD, including increased thresholds (Eisner et al., 1991; Owsley et al., 2000; Owsley et al., 2007), reduced colour vision (Eisner et al., 1991; Holz et al., 1995; Feigl et al., 2005b; Mitrut et al., 2010) and reduction in cone dominated ERGs (Sandberg and Gaudio, 1995; Sandberg et al., 1998; Binns and Margrain, 2007).

We could hypothesis that the focal flicker ERG parameters would be affected in ARM, given the effect of the AMD disease process on the mechanics of metabolic supply in the retina (Karwatowski et al., 1995; Moore et al., 1995; Guymer et al., 1999; Moore and Clover, 2001; Huang et al., 2008; Wang et al., 2009; Booij et al., 2010). Supply of metabolites and retinoid to the outer retina must be transported from the choriocapillaris via Bruch's membrane (Saari, 2000). The molecular deposition and thickening of Bruch's membrane (Ramrattan et al., 1994; Moore et al., 1995; Moore and Clover, 2001), choroidal blood flow abnormalities (Grunwald et al., 1998; Ciulla et al., 1999; Ciulla et al., 2002) and an increased oxygen diffusion distance (Stefansson et al., 2011) associated with AMD will hinder metabolic supply. The increased metabolic demand imposed by flicker stimuli (Kiryu et al., 1995) is likely to impose a further stress on the ability of the outer retina to maintain sufficient metabolic supply, this may be expected to impact on retinal function. The focal flicker ERGs from the participants with ARM displayed both a smaller amplitude and longer implicit time than the control group, however, these parameters were not found to be significantly different between groups. Other studies that have used the flicker ERG to assess participants with AMD have found a reduction in amplitude (Birch and Fish,

1988; Falsini et al., 1999b; Binns and Margrain, 2007) and prolonged implicit time (Sandberg et al., 1993; Binns and Margrain, 2007). Birch and Fish (1988), identified a relationship between age and flicker ERG amplitude, and adjusted the results for this factor (the same approach followed in this thesis), whilst the others used age matched groups to control for age effects (Sandberg et al., 1993; Falsini et al., 1999b; Binns and Margrain, 2007). The most likely explanation for the lack of significant difference between groups in this thesis is that participants in previous studies often had more advanced disease and therefore probably greater retinal dysfunction than the participants with ARM in this study. This suggests that changes in outer retinal function, which we would expect to be reflected in the focal flicker ERG (Remulla et al., 1995; Falsini et al., 2000; Binns and Margrain, 2005), may not manifest at this stage of disease, or at least not in all participants. The greater variability of the ARM group results may also reflect a heterogeneous distribution of functional abnormality in people with a similar gross retinal appearance.

The dynamics of photopigment regeneration are known to be affected in AMD (Owsley et al., 2001; Lamb and Pugh, 2004; Owsley et al., 2007), and the ERG photostress test has previously been shown to be sensitive to ARM (Binns and Margrain, 2007). The ERG photostress test recovery times in this thesis demonstrated a highly significant difference ($p<0.001$; Mann-Whitney U-test) between groups, whilst the median time constants for ARM and control groups of 161 s and 322 s, respectively, are very close to the 161 s for control and 328 s for ARM participants previously reported (Binns and Margrain, 2007).

The lack of measurable recovery within the measurement interval (~5 minutes) for 9 participants within ARM group is likely to be reflective of the disease status. Given that lengthened recovery time is expected in ARM, then failure of the ERG amplitude to recover within the measurement interval is likely to be indicative of the disease process. When absence of recovery is considered in addition to lengthened photostress recovery as a marker of disease, the ERG photostress test proves to be an effective diagnostic measure, demonstrated by the ROC analysis in this chapter. Previously, ROC analysis for the discrimination between ARM and control participants reported by Binns and Margrain (2007) produced an area under the curve of 0.74. In comparison, the ROC analysis carried out in section 6.2.6 found an AUC of 0.81 indicating an improved diagnostic potential. This improvement may be attributable to the modifications of the original protocol made in this thesis, in particularly the adoption of the Maxwellian view optical system to provide the

photobleach. The improved bleach delivery should have enabled a more consistent photopigment bleach to be achieved. The 75% sensitivity and 81% specificity found for this test, when a cut off of 192 s is used, indicates a good diagnostic ability for the detection of age-related macular degeneration, even at the early stage of disease (age-related maculopathy) investigated in this thesis.

Previously we had showed that the time constant of recovery determined by the ERG photostress test was affected by age (see section 3.6) (Wood et al., 2011b), but the data in this chapter did not demonstrate such a relationship. However, the findings of Wood et al.(2011b), and those of Coile and Baker (1992), demonstrated much greater variability in time constants of recovery in older participants. Therefore, given that the participants within this chapter represent an older and narrower age range then the inherent variability of data may have acted to mask any relationship.

Finally, table 6.3.1 shows the smallest detectable difference based on the power of this study for a selection of the ERG parameters assessed in this chapter. Accepting assumptions regarding the power (0.8) and variance (1 standard deviation) of the measures, the smallest detectable differences were smaller than the variance for each ERG parameter assessed. Although smaller difference in parameters may potentially exist between groups, diagnostically detecting difference smaller that the variance of the parameter concerned is unlikely to be of diagnostic value.

ERG parameter	Assumed standard deviation	Smallest detectable difference
Focal rod ERG (500 td.s)		
b-wave amplitude	4.78 μV	3.82 μV
b-wave implicit time	4.9 ms	3.92 ms
Focal cone ERG		
b-wave amplitude	1.54 μV	1.23 μV
b-wave implicit time	2.21 ms	1.77 ms
Focal flicker ERG		
amplitude	0.75 μV	0.60 μV
implicit time	0.88 ms	0.70 ms
ERG photostress test		
time constant	95.98 s	77 s

Table 6.3.1: Smallest detectable difference between groups, assuming a power of 0.8, at the p=0.05 significance level for unpaired t-tests using the Altman Nomogram. Assumed variance (1 standard deviation) based on control group for each parameter, and equal size of groups (n=24 each; actually controls n=26 and ARM n=24).

In conclusion, static measures of both cone and rod mediated ERGs were shown to be sensitive to ARM related changes at the retina, and provided moderate diagnostic

potential. However, the ERG photostress test demonstrated the best diagnostic ability of the parameters assessed, and would appear to support the findings of other studies that dynamic rather than static measures of retinal function are most sensitivity to age-related maculopathy (Owsley et al., 2001; Binns and Margrain, 2007).

Chapter 7: Relating retinal structure and function

This chapter investigates the relationship between the structural and functional measures described in chapters 5 and 6 respectively. The ERG represents a summed response of the neurones stimulated, in which particular parameters can be attributed to specific cellular origins (see section 1.5 for a comprehensive review). The nature of ERGs, as described, suggests that they may be proportionate to the cellular population and specific to particular retinal layers. OCT imaging offers the unique ability to visualise and quantify some of these intra-retinal layers (as discussed in section 1.4). It is therefore possible that a relationship between OCT retinal layer volumes and ERG functional parameters may exist, assuming the retinal layer volumes reflect the cellular population contained within. This relationship has not to our knowledge been explored in previous publications. In addition to OCT thickness, data was also collected on the presence of retinal features of ARM in this study cohort (see section 2.4). It has previously been shown that some ERG parameters are related to the severity of retinal features of ARM (Falsini et al., 1999b), although this has not been widely investigated to date.

The first aim of this chapter was to determine if retinal volume, assessed by manual segmentation of OCT images, was related to retinal function assessed using the ERG in the healthy retina. This was assessed in a layer-by-layer analysis of data from the control participants. The second aim was to determine if the retinal appearance, assessed by grading of features of ARM in retinal photographs, was related to any of the focal ERG parameters in participants with ARM.

7.1 The relationship between retinal and choroidal layer volumes and function

7.1.1 Methods

Volumes were calculated for each of the 6 retinal and choroidal layers measured in chapter 5; this was done by multiplying the weighted average thickness (corrected for age and axial length) for each layer by the area covered by a circle of 10° radius, equivalent to the stimulus size used in all the ERG techniques (20° diameter). Volumes were calculated for the 26 participants classified as normal.

The ERG parameters, as measured and corrected for age and axial length in chapter 6, and layer volumes were assessed for normality using the Sharpio-Wilk test. Analysis was then carried out to look for correlations between each ERG parameter and each of the 6 layer volumes, using either the Pearsons correlation coefficient or

Spearmans rank coefficient in the cases of parametric and non-parametric data respectively. Bonferroni correction for multiple tests was not applied to the statistical tests on this occasion, therefore the significance level was reduced to $p<0.01$ to mediate the effect of false positive results.

7.1.2 Results

All the ERG parameters were assessed for correlations with the 6 different structural parameters. No pair of parameters demonstrated a statistically significant correlations at the $p<0.01$ level. However, at the lower $p<0.05$ level four comparisons were identified, the focal rod ERG (500 td.s) a-wave amplitude correlated with the volume of the whole retina ($p=0.03$) and the ganglion cell layer ($p=0.03$), whilst the focal rod ERG (20 td.s) b-wave implicit time correlated with the retina ($p=0.02$) and retinal nerve fibre layer volumes ($p=0.04$). A linear regression analysis was carried out for each of these parameters and the relationships plotted are shown in figure 7.1.1. Each pair of parameters demonstrated low R^2 values ($R^2<0.3$; see figure 7.1.1) (Altman, 1991), suggesting that even where less conservative approach is applied (i.e. $p<0.05$), a relationship between structure and function it may only account for a small proportion of the total variance in volumes. Therefore it was concluded that no close association between retinal or choroidal layer volumes and ERG parameters of macular retinal function in normal participants exists.

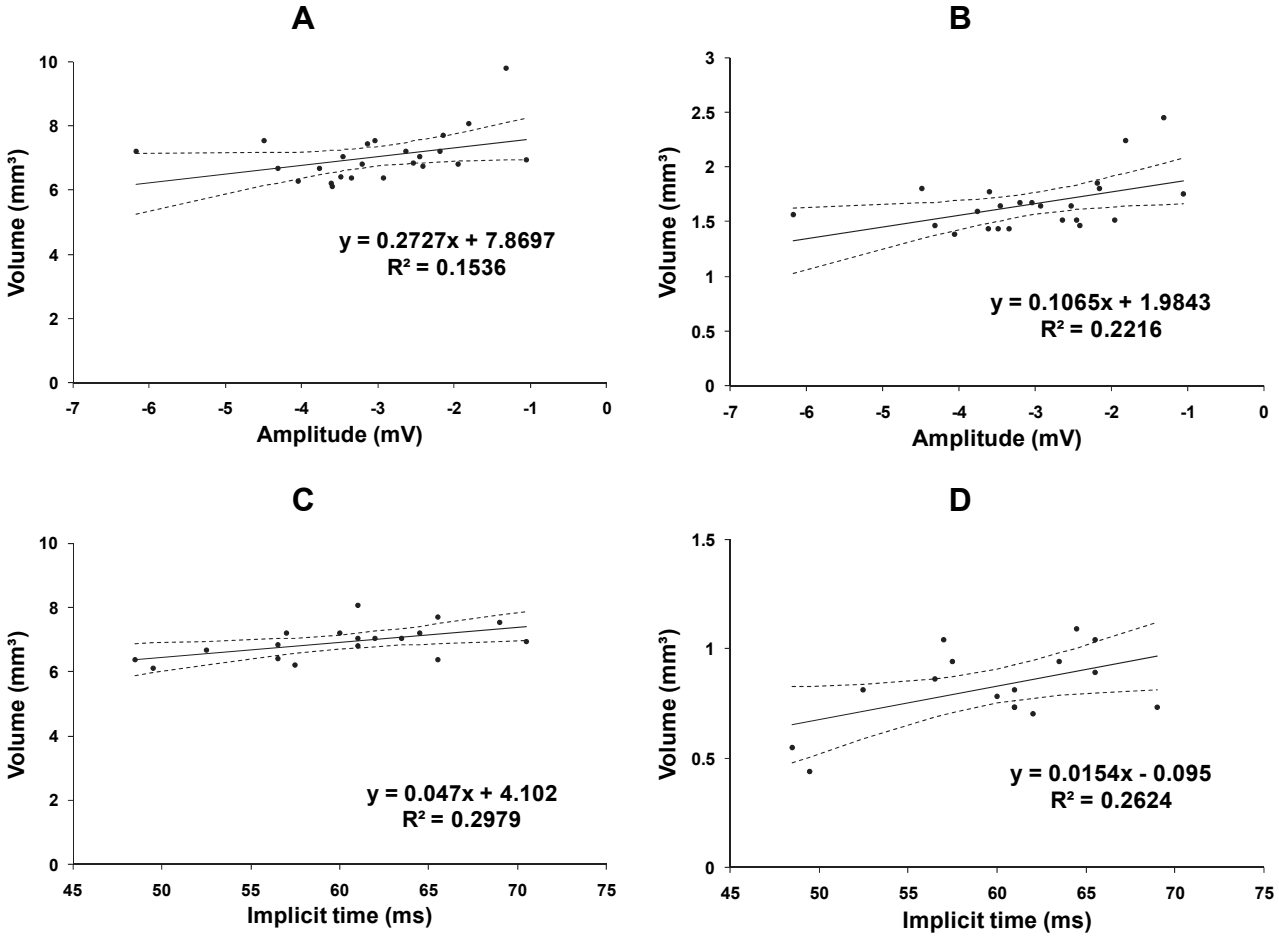

Figure 7.1.1: Linear regression analysis showing regression lines (bold) and 95 confidence intervals (dashed lines): A – Retinal volume plotted against focal rod ERG (500 td.s) a-wave amplitude. B – Ganglion cell layer volume plotted against focal rod ERG (500 td.s) a-wave amplitude. C – Retinal volume plotted against focal rod ERG (20 td.s) b-wave implicit time. D – Retinal nerve fibre layer volume plotted against focal rod ERG (20 td.s) b-wave implicit time.

7.2 The relationship between retinal appearance and function in participants with ARM

7.2.1 Methods

Retinal appearance (based on retinal photography) was graded according to the International Classification and Grading System for Age-Related Maculopathy (Bird et al., 1995) as described in section 2.4 for all 24 participants with ARM. These gradings were modified to reflect feature severity as described in table 7.2.1.

All of the ERG parameters, as measured in chapter 6, were assessed for correlations with each of the severity gradings using the Spearman rank correlation coefficient. Furthermore, ERG parameters were assessed for their ability to differentiate participants with wet AMD in the contralateral eye using independent t-tests. The purpose of this analysis was to identify any potential relationships between retinal features and retinal function in the participants with ARM. Correction for multiple tests was not applied to the statistical tests on this occasion, therefore a significance value of $p<0.01$ was applied to mediate the effect of false positives.

In addition independent t-tests, or Mann-Whitney u-tests for non-parametric data, were carried out to identify which retinal features were most closely associated with a wet contralateral eye.

Retinal feature as described in Bird et al. (1995)	Adapted categories
1.1 Drusen morphology, highest grade present	1) absent / questionable 2) hard drusen (<C_1, 125µm) 3) intermediate, soft drusen (>C_0,<C_1; >63µm, <125µm) 4) large, soft distinct drusen (>C_1, 125µm) 5) large, soft indistinct drusen (>C_1, 125µm) crystalline/calcified/glistening, semisolid or serogranular
1.2 Predominant drusen type	1) absent / questionable 2) hard drusen (<C_1, 125µm) 3) intermediate, soft drusen (>C_0,<C_1; >63µm, <125µm) 4) large, soft distinct drusen (>C_1, 125µm) 5) large, soft indistinct drusen (>C_1, 125µm) crystalline/calcified/glistening, semisolid or serogranular
1.3 Total number of drusen	1) absent / questionable 2) 1-9 3) 10-19 4) >20
1.4 Average drusen size	1) <C_0 (<63µm) 2) >C_0<C_1 (>63µm,< 125µm) 3) >C_l<C_2 (>125µm,<175µm) 4) >C_2<C_3 (>175µm,<250µm) 5) >C_3 (>250µm)
3.1 Hyperpigmentation	1) absent / questionable 2) present <C_0 (<63µm) 3) present >C_0 (>63µm)
3.2 Hypopigmentation	1) absent / questionable 2) present <C_0 (<63µm) 3) present >C_0 (>63µm)

Table 7.2.1: A summary of the retinal features used for the comparison with retinal function. The categories have been adapted and simplified from the original grading described by Bird et al. (1995) for the purposes of this analysis.

7.2.2 Results

Only the correlation between the Focal cone ERG a-wave implicit time and grade of hyperpigmentation was shown to be significant ($p<0.001$). Figure 7.2.1 shows a box and whisker plot for the relationship between focal cone ERG a-wave implicit time and grade of hyperpigmentation (1 to 3, in order of severity), which demonstrated a relationship at the $p<0.001$ significance level, it can be seen that delayed implicit times are strongly associated with hyperpigmentation grade severity.

Independent t-tests were carried out to identify which retinal features were most closely associated with a wet contralateral eye found the focal cone ERG b-wave implicit time ($p<0.01$) and the ERG photostress test time constant ($p<0.007$) to be sensitive measures. Figure 7.2.2 shows the focal cone ERG b-wave implicit time and ERG photostress test recovery time constant for participants grouped according to the status of the non-test eye, both parameters demonstrate delayed times for participants with wet AMD in the fellow eye. Four unsuccessful ERG photostress recoveries occurred in participants with wet AMD in the contralateral eye (out of 10), whilst 5 occurred in participants without wet AMD in the contralateral eye (out of 14). These participants were not included in the box and whisker diagram or the independent t-test. When these participants are incorporated and the recovering time allocated a value of 1000s, the adjusted medians for each group were 197s for contralateral eyes without wet AMD and 613 s for contralateral eyes with wet AMD.

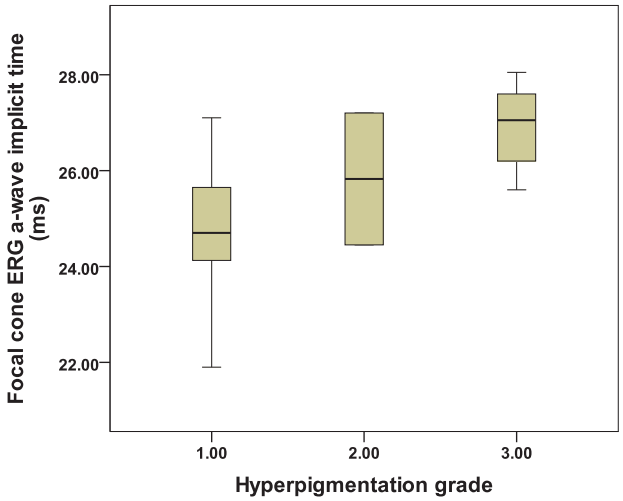

Figure 7.2.1: Box and whisker plots showing focal cone ERG b-wave implicit time for grading of hyperpigmentation as described in table 7.1.1. Medians (±Inter-quartile range) were 24.7 (±1.5) 25.8 (±1.4) and 27.1 (±1.4) ms respectively for hyperpigmentation grades 1, 2 and 3.

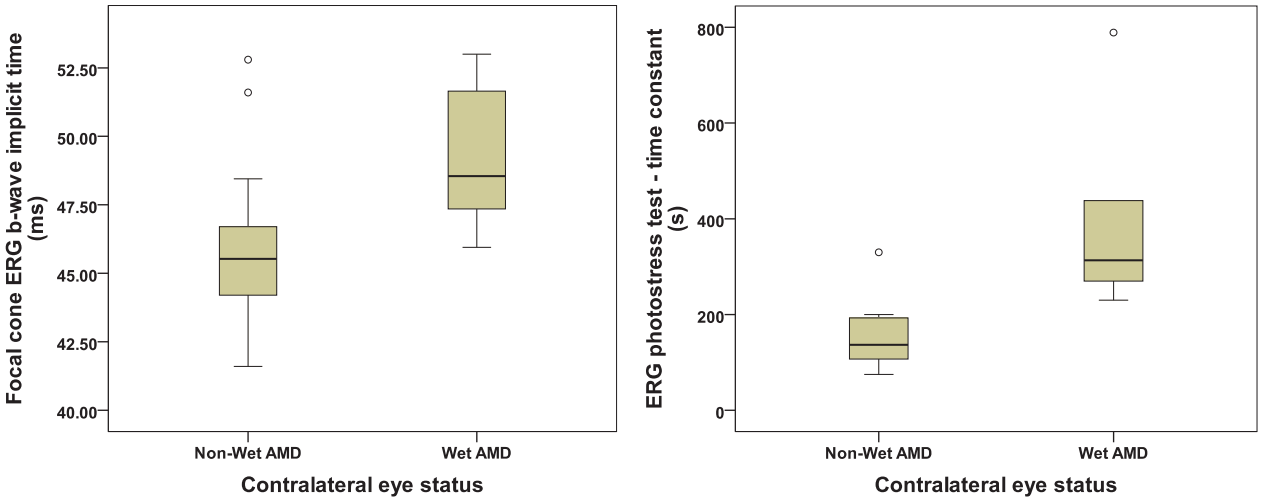

Figure 7.2.2: Box and whisker plots showing focal cone ERG b-wave implicit time and ERG photostress test time constants for wet and non-wet AMD contralateral eye status. Medians (±Inter-quartile range) were 45.5 (±2.4) and 48.6 (±3.9) ms for focal cone ERG b-wave implicit time for eyes without and with wet AMD in the contralateral eyes respectively. Medians ERG photostress recovery time constants were 137 (±86) and 313 (±126) ms for eyes without and with wet AMD in the contralateral eyes respectively

7.3 Discussion

The analysis in this chapter reveals that structural measures obtained through OCT are not interchangeable with functional tests using the ERG. There were no correlations between OCT derived structural and ERG based functional measures at the $p<0.01$ significance level, whilst those identified at the $p<0.05$ level were weak. Additionally, only one retinal features of ARM was found to be related to ERG based functional tests at the $p<0.01$ significance level. The scarcity of relationships may be surprising, given that there are significant differences in ERG parameters for those with and without ARM, it would seem logical that there should be a relationship with the grade of ARM (i.e. the more severe ARM equating with increased functional loss). However, two functional parameters were shown to be particularly effective in differentiating eyes where the fellow eye is categorised as wet AMD. This is relevant as a diagnosis of wet AMD in the fellow eye results in an increased risk of developing choroidal neovascularisation in a previously dry eye (Pieramici and Bressler, 1998; AREDS, 2001b). This suggests that ERG photostress test time constants and focal cone ERG b-wave implicit times may have prognostic value.

The analysis of the structural and functional data in the control participants involved conducting multiple correlations to identify statistically significant relationships; when this is done there is an increased risk with each additional test that a type 1 error will occur. In total, 90 correlation analyses were carried out. Without corrections for multiple testing we would expect ~4 type 1 errors to occur, at the p=0.05 significance level i.e. 4 comparisons would be found to be spuriously significant due to chance alone. The results in this study therefore appear to be consistent with that expectation. When the 4 statistically significant correlations are considered, with regard to the origin of the ERG parameters and composition of the retinal layers concerned, there is no obvious scientific rationale to support these relationships and the strength of the correlations is weak. This suggests that these findings may be spurious. It may have seemed prudent to apply a statistical approach that would limit the number of type 1 errors within the analysis, for example the Bonferroni correction (Altman, 1991; Curtin and Schulz, 1998); however, such a conservative methodology could have limited the ability to identify potential relationships between structural and functional parameters, thus an approach of reducing the significance level to $p<0.01$ was adopted.

We may have expected retinal function in healthy eyes to be related to the volume of the retinal, intra-retinal or choroid layers in which the functional processes originate and on which they depend. The ERG is a sum of the entire retinal response to a stimulus, of which individual components of the response are dominated by contributions attributed to particular cellular origins (Frishman, 2006). Change to the size and speed of a response can be expected from differences in spatial organisation and density and population of the various contributing cell types, in addition to localised or diffuse deficits within the cellular population stimulated. A reduction in the number of cells within the retina could therefore be expected to reduce the size of the response proportionately. However, it would appear that the relationship between the two is more complex.

Measures of thickness and volume have been shown to be poor indicators of retinal cell populations. A study of ageing and cell loss in rat retinas showed reductions in retinal thickness whilst the overall volume and density of cellular populations (GCL, INL, ONL) appeared not to be affected (Feng et al., 2007). Furthermore, Curcio et al. (1993) demonstrated a loss of ~30% in photoreceptor density with ageing in 27 donor retinas, however, the space vacated by deceased rod photoreceptors was filled by enlargement of remaining rod photoreceptor inner segments, suggesting that cellular loss within the retina may not be reflected in reduced volume. In addition, as an example of the potential

physiological differences in cell population and density within the normal population, the peak density of the cone photoreceptors in healthy donor eyes has been shown to vary between 96,000 and 281,000 cones per square millimetre (Curcio et al., 1987).

Evidence indicates that cone photoreceptors survive longer in AMD than their fellow rod photoreceptors, but these surviving cones appear to undergo morphological changes (Curcio et al., 1996; Curcio et al., 2000). A study of cone photoreceptor integrity in eyes with AMD demonstrated signs of misalignment and outer segment deterioration, even in early disease (Kanis et al., 2008). Microscopy also reveals abnormalities in the cone axons and opsin distribution related to ageing and AMD (Shelley et al., 2009). This suggests that the density of cell populations can remain relatively unaffected whilst being structurally and/or functionally compromised.

It is finally worth considering the methodology employed to determine the retinal volume. The technique employed manual measurements at up to 21 locations within a 20° diameter circle and these points were used to calculate an average thickness. The small number of points used relies on a relative uniformity of thickness across the retinal area sampled to produce an accurate measure. In some cases it was not always possible to obtain a thickness measurement at each location, further reducing the accuracy of the final volumes calculated. The overall macular volume for the normal participants was 7.00 ± 0.77 (SD) mm^3, and was of a comparable magnitude to the total macular thickness calculated using commercial software, which corresponds to the area within the outer ring of the ETDRS grid, for example 6.84 ±0.36 mm^3 in 219 healthy eyes assessed using an OCT 3 (Carl Zeiss, Meditec Inc, CA) (Sugita et al., 2008), or the normative range of 6.18 to 7.42 mm^3 provided with the Stratus OCT system (Carl Zeiss, Meditec Inc, CA). However, it would be expected that automated segmentation techniques produce more accurate values than the approach used in this thesis, as they can utilise many more data points within the image and therefore will better reflect localised variations in layer thickness. Improved measurement accuracy and greater numbers of participants (including higher age and prescription ranges) could potentially reveal a weak relationship between retinal, intra-retinal or choroidal layer volumes and ERG parameters of retinal function.

We can conclude that no strong relationship exists between the ERG parameters assessed and retinal, intra-retinal and choroidal layer volumes in healthy participants on the evidence that the relationship between layer volume or thickness and cellular population or cellular health within the retina is not strong.

In this thesis a number of clinical features of ARM were associated with ERG parameters, even at the early stage of disease investigated. The strongest association was found between extent of hyperpigmentation and delayed focal cone a-wave implicit time, a response which is dominated by photoreceptor activity. Given that pigmentary abnormalities are reflective of localised RPE dysfunction, and when we consider the extensive support which the RPE provides to normal photoreceptor function (see section 1.2.5 for an overview) it may be expected that disruption of the RPE would negatively affect aspects of photoreceptor function. Other studies have reported a relationship between focal pigmentary changes and visual function in ARM (Collins and Brown, 1989; Eisner et al., 1991; Cheng and Vingrys, 1993). Eisner et al. (1991) also found a relationship between cone function and focal hyperpigmentation, and demonstrated a decrease in absolute cone sensitivity, assessed psychophysically, in participants with pigmentary changes compared to other individuals with ARM. Focal hyperpigmentation was found to be associated with an increased risk of developing wet AMD in a study following 71 patients with bilateral drusen (Smiddy and Fine, 1984). Longitudinal data assessing the prognostic value of the focal cone ERG a-wave implicit time are not available.

A number of clinical features of ARM have been shown to be reflective of changes in retinal function (Collins and Brown, 1989; Eisner et al., 1991; Cheng and Vingrys, 1993; Midena et al., 1997; Falsini et al., 1999b). Midena et al. (1997) investigated central visual field sensitivity, contrast sensitivity, colour vision and photostress recovery on 47 participants with AMD and was able to show reduction in contrast sensitivity measures related to drusen confluence. In addition, a slower photostress was associated with increased extent of drusen, pigmentary changes and atrophy. Mean sensitivity of the central retina and colour vision were not found to be related to number of drusen, focal hyperpigmentation or atrophy, although the mean sensitivity approached significance for the presence of drusen confluence ($p<0.06$). Other studies have tended to grade retinal appearance, which may better reflect overall disease severity than individual retinal features (see table 7.2.1), for example Eisner et al. (1991) investigated retinal function in groups of ‘high’ and ‘low’ risk eyes, assessed by retinal appearance. Their study showed that abnormalities in colour matching and dark adaptation were greater in eyes with ‘high’ risk features, which included the presence of hyperpigmentation, drusen confluence or large (>250 μm diameter) and /or extensive drusen (predominantly >63 μm in diameter). In addition, ERG-based measures of retinal function have also been shown to be sensitive to

ARM, with Falsini et al. (1999b) finding a significant correlation between grading scores of increasing disease severity and reductions in focal flicker ERG amplitude.

A notable finding in this study was the strong association between fellow eyes of wet AMD and delayed focal cone ERG b-wave implicit times and lengthened ERG photostress test time constants of recovery. Sandberg, Miller and Gaudio (1993) also reported delayed implicit times in the 'good eye' of participants (n=67) with unilateral wet AMD. Remulla et al. (1995), who also investigated the fellow eyes of 67 patients with unilateral wet AMD, identified a relationship between choroidal perfusion defects and delayed implicit time in these patients. This suggests that delays in photoreceptor responses maybe linked to reduced vascular supply.

The finding that the time constant of recovery for the ERG photostress test is particularly prolonged in participants with unilateral wet AMD in the fellow eye agrees with a study by Sandberg and Gaudio (1995) who reported that 62% of participants (n=133) with unilateral wet AMD had delayed photostress recovery times in the fellow eye. Similarly, Sandberg et al. (Sandberg et al., 1998) carried out a longitudinal study to assess the characteristics of patients with unilateral wet AMD which conferred a high risk of progression to wet AMD in the fellow eye. They found that glare recovery time was an independent predictor of progression to wet AMD, which is consistent with the findings of this study that prolonged recovery is associated with high risk fellow eyes of participants with unilateral wet AMD. Prolonged recovery after bleach may be explained when we consider the retinal changes which are associated with an increased risk of progression to wet AMD. These changes include the presence of confluent drusen, choroidal perfusion defects and thickening of Bruch's membrane, all of which have been implicated as contributing factors for localised retinal hypoxia (Feigl, 2009; Stefansson et al., 2011). Hypoxia is a known stimulus for VEGF production (Aiello et al., 1995) and by extension increased risk of choroidal neovascularisation (wet AMD) and, hypoxia has also been shown to adversely affect dark adaptation (Vingrys and Garner, 1987; Brinchmann-Hansen and Myhre, 1989; Connolly and Hosking, 2006). As the ERG photostress test is a dynamic test of cone dark adaptation, the finding that it is particularly sensitive to eyes considered at higher risk of progression to wet AMD may implicate retinal hypoxia as the underlying mechanism.

In conclusion, there is no apparent relationship between retinal, intra-retinal and choroidal layer volumes and ERG-based measures of retinal function in healthy older adults, attributable to the predominant cellular components the retina. This suggests that

both functional and structural tests are useful in the assessment of retinal health, as each provides independent information. However, some of the functional parameters were found to be sensitive to the presence of wet AMD in the fellow eyes of participants with ARM.

Chapter 8: Conclusions and future work

The overall aim of this work was to investigate structural and functional changes in the early stages of AMD. Initially, Chapter 1 discussed the current literature regarding age-related macular degeneration, in particular the early stage of disease known as age-related maculopathy. Methods which have previously been used to assess retinal structural and function at the macula were discussed, specifically those which had been shown to be, or likely to be, sensitive to AMD-related changes. Previously identified relationships between measures of structure and function in AMD were also discussed. As a consequence, the following aims were identified: firstly, to determine and compare the diagnostic potential of structural measures, assessed by OCT imaging, and functional parameters, assessed using focal ERG techniques. Secondly, to determine if a relationship existed between these measures of retinal structure and function in healthy individuals and, finally, to determine if a relationship existed between retinal appearance and the focal ERG parameters in participants with ARM.

The investigation of retinal structure was carried out using a long wavelength (1060 nm) OCT system, which facilitated not only allowed retinal, but also choroidal imaging (Povazay et al., 2003; Povazay et al., 2007a). This was the first study to image the choroid using long wavelength OCT technology in people with ARM. Chapter 2 described the development of the analytical methods for assessing retinal and choroidal layer thickness from 1060 nm OCT images. This ultimately led to the adoption of a manual measurement technique, later applied in chapter 5.

Chapter 5 investigated retinal, choroidal and 4 intra-retinal layer thicknesses at 21 macular locations in participants with ARM and healthy controls. Retinal thickness was shown to be reduced at multiple locations assessed within the parafoveal region in participants with ARM, whilst the more peripheral macula was unaffected. This appears to be consistent with other OCT studies of participants with ARM that reported localised, but not diffuse or generalised, reductions in retinal thickness (Kaluzny et al., 2009; Malamos et al., 2009; Schuman et al., 2009). Individual retinal and intra-retinal thickness measurements showed moderate diagnostic ability, but given the point by point nature of the analysis used, it was not deemed a clinically useful approach. In contrast, choroidal thickness was shown to be unaffected in ARM.

Many ERG parameters are attributable to specific cellular origins within the retina (see section 1.5) (Frishman, 2006), and therefore were thought the most likely functional parameters to facilitate a direct comparison with the retinal layers measured by OCT

imaging. Function in this thesis was assessed using four focal ERG techniques, providing a localised assessment of retinal function at the macula. The ERG photostress test, focal flicker ERG and focal cone ERG had previously been shown to be sensitive to ARM (Binns and Margrain, 2007), whilst the focal rod ERG was expected to be sensitive given previous reports of abnormal rod function in ARM participants (Owsley et al., 2000; Owsley et al., 2001; Owsley et al., 2007). Chapter 3 described a series of studies intended to improve the clinical practicality and diagnostic ability of these tests, prior to their use in chapter 6. In particular an investigation into bleaching parameters strongly indicated the use of equilibrium bleaches, over photoflash bleaches, for the ERG photostress test; these findings resulted in a publication (Wood et al., 2011b).

Chapter 6 described a study that investigated the differences between the ERG results obtained from participants with ARM and controls; in particular the diagnostic potential of those parameters affected was determined. Parameters affected in ARM included the b-wave of the focal rod ERG b-wave amplitude and implicit time and the focal cone ERG b-wave implicit time. When compared to the OCT measurements (see chapter 5) ERG parameters showed better diagnostic capability as, although the range of area under the curves on ROC analysis were similar (0.672 to 0.807 for ERG parameters, and 0.642 to 0.787 for OCT), the ERG parameters provided better sensitivity and specificity for clinical cut off values. The ERG photostress test recovery time constant provided the best diagnostic ability of any single parameter assessed in this thesis, with an area under the ROC curve of 0.81. Furthermore, whilst OCT thickness measures at specific locations provided moderate diagnostic potential, it would not be clinically feasible to base a diagnostic approach on a single thickness measurement at an individual retinal location. In this study, the overall thickness of the layers across the macular region appeared to be only mildly affected by ARM. Further investigation of other aspects of macular and choroidal structure, e.g. integrity of layers, may yield more useful diagnostic information.

Chapter 7 describes the relationship between the OCT measures (structure) and ERG parameters (function) assessed. It was shown that retinal, intra-retinal and choroidal layer volumes were not strongly related to the ERG parameters assessed in normal participants. Although, some aspects of retinal appearance and function were shown to be related in ARM participants, in particular, extent of focal hyperpigmentation was significantly related to focal cone ERG a-wave implicit time ($p<0.001$), supporting previous reports of relationships between retinal appearance and function (Collins and Brown, 1989; Eisner et al., 1991; Cheng and Vingrys, 1993; Falsini et al., 1999b). However, of

potential clinical significance was the finding that the ERG photostress recovery time constant and focal cone ERG b-wave implicit time were prolonged in fellow eyes of participants with wet AMD, suggesting that these parameters may be sensitive to underlying retinal changes that precede progression to wet AMD.

Finally, it is important to consider that the diagnosis of ARM or AMD in this thesis was based on the retinal appearance of affected eyes; this is, in effect, the gold standard method for the diagnosis of AMD (Klein et al., 1991; Bird et al., 1995; AREDS, 2001a). At present no technique which utilises functional measures has been widely used as a diagnostic tool for ARM. The participants in this study were, therefore, allocated to control or ARM groups based on the grading of retinal photography and OCT images for clinical signs associated with AMD. The first point to consider when assessing the diagnostic potential of both the structural and functional parameters included in this thesis is that the sensitivity and specificity obtained were dependent upon the assumption that all participants were classified accurately at the outset. If functional or structural changes occur within the retina prior to observable clinical features then it is possible that participants designated as controls may have had sub-clinical disease, the true diagnostic value of the parameters evaluated may therefore be higher than those calculated in this study. A longitudinal study assessing the outcomes of participants in the ‘control’ group would provide the only means of retrospectively identifying those who would go on to develop ARM.

The potential limitations of this study include that the comparison of means for the parameters assessed was limited by the power of the statistical tests applied and the size of control and ARM groups, it is therefore possible that the smaller magnitude differences between groups could prove to be significant with further investigation. The manual measurement technique used to obtain thickness values from the OCT images was subjective in nature, and therefore open to error. The application of an automated segmentation technique may reduce the variability of results, due to increased averaging and objectivity, thus allowing smaller differences to be detected. Additionally, the reliance on fundoscopic grading for disease group allocation and lack of longitudinal follow up could potentially influence the assessment of diagnostic potential made for the different clinical parameters. Finally, a baseline assessment of smoking was not made; this could potentially have had a confounding effect on the clinical parameters assessed in this thesis.

In conclusion, both structural and functional changes were observed in people with ARM. These included parafoveal reductions in retinal thickness, delayed focal rod and cone ERG implicit times and delayed ERG photostress recovery. Diagnostically, ROC analysis suggests that ERG parameters provided better diagnostic potential than the OCT measures assessed. Additionally, prolonged ERG photostress test recoveries were implicated as a potential predictor of disease progression and shown to provide the best diagnostic potential for ARM. Measures of retinal, intra-retinal and choroidal thickness were not shown to be related to the ERG parameters assessed, this lack of any strong relationships between the focal ERG parameters and OCT layer measurements suggests that they represent independent biomarkers for ARM.

8.1 Future Work

Following on from chapter 6 it would be interesting to conduct a longitudinal study to investigate the effect of disease progression on the ERG parameters studied, in particular the predictive ability of the ERG photostress test for the progression to wet AMD. Similarly a longitudinal study would allow the identification of participants who may have had sub-clinical AMD at baseline, allowing refinement of the disease groups, leading to a better assessment of the diagnostic potential of the ERG parameters.

Chapter 5 identified a difference in the ganglion cell layer thickness between the control and ARM groups at 3 parafoveal locations, suggesting that the inner retina may also be affected in early ARM. As the PhNR has been shown to reflect the activity of RGC in the inner retina (Viswanathan et al., 1999), then future study of the PhNR elicited from focal stimuli in participants with ARM may reveal whether RGC activity is affected.

The work in chapter 5 relied upon a manual analysis technique to produce retinal, intra-retinal and choroidal thickness values at 21 retinal locations. In the future, analysis software should become available for the 1060 nm OCT system that would allow more conventional analysis based on automated segmentation, similar to that recently used by Loduca et al. (2010) to assess retinal and intra-retinal layer thicknesses in OCT images. Application of such techniques to the images collected in this thesis would allow more specific localisation of thickness differences, the construction of thickness maps and calculation of values in the ETDRS format. The application of such analytical techniques may allow for better measurement accuracy and improve the quality of thickness and volume measurements produced. In particular, thickness maps may reveal patterns of

retinal or intra-retinal layer loss characteristic of ARM in a similar way to rod photoreceptor loss identified in histology (Curcio et al., 1996).

Furthermore, recent OCT studies have related IS/OS junction abnormalities to acuity (Hayashi et al., 2009; Landa et al., 2011). This suggests that specific localised abnormalities in retinal structure may reflect retinal changes with functional consequences better than the macro measures of thickness and volume assessed in this thesis. A study investigating the microstructure abnormalities, such as changes to the IS/OS appearance in OCT images and relating them to ERG measures, may help identify whether specific structural changes affect the ERG waveform, and if so, to what extent.

Chapter 9: References

Adler D S, Ko T H, Konorev A K, Mamedov D S, Prokhorov V V, Fujimoto J J, and Yakubovich S D (2004) Broadband light source based on quantum-well superluminescent diodes for high-resolution optical coherence tomography. *IEEE J Quantum Electron* 34: 915-918.

Ahmed J, Braun R D, Dunn R, and Linsenmeier R A (1993) Oxygen distribution in the macaque retina. *Invest Ophthalmol Vis Sci* 34: 516-521.

Aiello L P, Northrup J M, Keyt B A, Takagi H, and Iwamoto M A (1995) Hypoxic regulation of vascular endothelial growth factor in retinal cells. *Arch Ophthalmol* 113: 1538-1544.

Aizawa S, Mitamura Y, Baba T, Hagiwara A, Ogata K, and Yamamoto S (2009) Correlation between visual function and photoreceptor inner/outer segment junction in patients with retinitis pigmentosa. *Eye* 23: 304-308.

Aldebasi Y H, Drasdo N, North R V, and Morgan J E (2001) The pattern electroretinogram (PERG) with contralateral corneal reference. *Ophthalmic Physiol Opt* 21: 243-246.

Alpern M, Ching C C, and Kitahara K (1983) The directional sensitivity of retinal rods. *J Physiol* 343: 577-592.

Altman D G (1991) *Practical statistics for medical research*. London: CRC Press.

Altunay H (2007) Fine structure of the retinal pigment epithelium, bruch's membrane and choriocapillaris in the camel. *Anat Histol Embryol* 36: 116-120.

Anderson D H, and Fisher S K (1976) The photoreceptors of diurnal squirrels: outer segment structure, disc shedding, and protein renewal. *J Ultrastruct Res* 55: 119-141.

Anderson D H, Mullins R F, Hageman G S, and Johnson L V (2002) A role for local inflammation in the formation of drusen in the aging eye. *Am J Ophthalmol* 134: 411-431.

Anger E M, Unterhuber A, Hermann B, Sattmann H, Schubert C, Morgan J E, Cowey A et al. (2004) Ultrahigh resolution optical coherence tomography of the monkey fovea. Identification of retinal sublayers by correlation with semithin histology sections. *Exp Eye Res* 78: 1117-1125.

Arden G B, Carter R M, Hogg C R, Powell D J, Ernst W J, Clover G M, Lyness A L et al. (1983) A modified ERG technique and the results obtained in X-linked retinitis pigmentosa. *Br J Ophthalmol* 67: 419-430.

AREDS (2000) The Age-Related Eye Disease Study: a clinical trial of zinc and antioxidants-Age-Related Eye Disease Study Report No. 2. *J Nutr* 130: 1516S-1519S.

AREDS (2001a) The age-related eye disease study system for classifying age-related macular degeneration from stereoscopic color fundus photographs: the age-related eye disease study report number 6. *Am J Ophthalmol* 132: 668-681.

AREDS (2001b) A randomized, placebo-controlled, clinical trial of high-dose supplementation with vitamins C and E, beta carotene, and zinc for age-related macular degeneration and vision loss: AREDS report no. 8. *Arch Ophthalmol* 119: 1417-1436.

Arichika S, Hangai M, and Yoshimura N (2010) Correlation between thickening of the inner and outer retina and visual acuity in patients with epiretinal membrane. *Retina* 30: 503-508.

Bach M, and Meigen T (1999) Do's and don'ts in Fourier analysis of steady-state potentials. *Doc Ophthalmol* 99: 69-82.

Baehr W, Wu S M, Bird A C, and Palczewski K (2003) The retinoid cycle and retina disease. *Vision Res* 43: 2957-2958.

Bailey I L, and Lovie J E (1976) New design principles for visual acuity letter charts. *Am J Optom Physiol Opt* 53: 740-745.

Bartlett H, Davies L N, and Eperjesi F (2004) Reliability, normative data, and the effect of age-related macular disease on the Eger Macular Stressometer photostress recovery time. *Ophthalmic Physiol Opt* 24: 594-599.

Bashshur Z F, Haddad Z A, Schakal A, Jaafar R F, Saab M, and Noureddin B N (2008) Intravitreal bevacizumab for treatment of neovascular age-related macular degeneration: a one-year prospective study. *Am J Ophthalmol* 145: 249-256.

Bauer P J (2002) The complex of cGMP-gated channel and Na+/Ca2+, K+ exchanger in rod photoreceptors. *Adv Exp Med Biol* 514: 253-274.

Bearse M A, and Sutter E E (1996) Imaging localized retinal dysfunction with the multifocal electroretinogram. *J Opt Soc Am A* 13: 634-640.

Beatty S, Koh H, Phil M, Henson D, and Boulton M (2000) The role of oxidative stress in the pathogenesis of age-related macular degeneration. *Surv Ophthalmol* 45: 115-134.

Beatty S, Murray I J, Henson D B, Carden D, Koh H, and Boulton M E (2001) Macular pigment and risk for age-related macular degeneration in subjects from a Northern European population. *Invest Ophthalmol Vis Sci* 42: 439-446.

Beirne R O, Hogg R E, Stevenson M R, Zlatkova M B, Chakravarthy U, and Anderson R S (2006) Severity staging by early features of age-related maculopathy exhibits weak relationships with functional deficits on SWS grating acuity. *Invest Ophthalmol Vis Sci* 47: 4624-4631.

Bennett A G, Rudnicka A R, and Edgar D F (1994) Improvements on Littmann's method of determining the size of retinal features by fundus photography. *Graefes Arch Clin Exp Ophthalmol* 232: 361-367.

Berman K, and Brodaty H (2006) Psychosocial effects of age-related macular degeneration. *Int Psychogeriatr* 18: 415-428.

Bhatnagar P, Spaide R F, Takahashi B S, Peragallo J H, Freund K B, Klancnik J M, Jr., Cooney M J et al. (2007) Ranibizumab for treatment of choroidal neovascularization secondary to age-related macular degeneration. *Retina* 27: 846-850.

Binns A M, and Margrain T H (2005) Evaluation of retinal function using the Dynamic Focal Cone ERG. *Ophthalmic Physiol Opt* 25: 492-500.

Binns A M, and Margrain T H (2006) Development of a technique for recording the focal rod ERG. *Ophthalmic Physiol Opt* 26: 71-79.

Binns A M, and Margrain T H (2007) Evaluating retinal function in age-related maculopathy with the ERG photostress test. *Invest Ophthalmol Vis Sci* 48: 2806-2813.

Birch D G, and Anderson J L (1992) Standardized full-field electroretinography. Normal values and their variation with age. *Arch Ophthalmol* 110: 1571-1576.

Birch D G, and Fish G E (1987) Rod ERGs in retinitis pigmentosa and cone-rod degeneration. *Invest Ophthalmol Vis Sci* 28: 140-150.

Birch D G, and Fish G E (1988) Focal cone electroretinograms: aging and macular disease. *Doc Ophthalmol* 69: 211-220.

Birch D G, Hood D C, Locke K G, Hoffman D R, and Tzekov R T (2002) Quantitative electroretinogram measures of phototransduction in cone and rod photoreceptors: normal aging, progression with disease, and test-retest variability. *Arch Ophthalmol* 120: 1045-1051.

Bird A C, Bressler N M, Bressler S B, Chisholm I H, Coscas G, Davis M D, de Jong P T V M et al. (1995) An international classification and grading system for age-related maculopathy and age-related macular degeneration. *Surv Ophthalmol* 39: 367-374.

Bird A C, and Marshall J (1986) Retinal-pigment epithelial detachments in the elderly. *Trans Ophthalmol Soc U K* 105: 674-682.

Bizheva K, Pflug R, Hermann B, Povazay B, Sattmann H, Qiu P, Anger E et al. (2006) Optophysiology: depth-resolved probing of retinal physiology with functional ultrahigh-resolution optical coherence tomography. *Proc Natl Acad Sci U S A* 103: 5066-5071.

Blair M P, Gupta M, Blair N P, and Shahidi M (2010) Association Between Retinal Thickness and Retinal Pigment Epithelium Elevation in Age-Related Macular Degeneration. *Ophthalmic Surg Lasers Imaging* 41: 175-181.

Bland J M, and Altman D G (1986) Statistical methods for assessing agreement between two methods of clinical measurement. *J Lancet* 1 (8476): 307-310.

Bland J M, and Altman D G (1995) Multiple significance tests: the Bonferroni method. *BMJ* 310: 170.

Bland J M, and Altman D G (1999) Measuring agreement in method comparison studies. *Stat Methods Med Res* 8: 135-160.

Booij J C, Baas D C, Beisekeeva J, Gorgels T G, and Bergen A A (2010) The dynamic nature of Bruch's membrane. *Prog Retin Eye Res* 29: 1-18.

Bowmaker J K, and Dartnall H J (1980) Visual pigments of rods and cones in a human retina. *J Physiol* 298: 501-511.

Bowman K J (1978) The effect of illuminance on colour discrimination in senile macular degeneration. *Mod Probl Ophthalmol* 19: 71-76.

Boycott B B, and Wassle H (1974) The morphological types of ganglion cells of the domestic cat's retina. *J Physiol* 240: 397-419.

Bressler N M, Silva J C, Bressler S B, Fine S L, and Green W R (1994) Clinicopathological correlation of drusen and retinal-pigment epithelial abnormalities in age-related macular degeneration. *Retina* 14: 130-142.

Bressler S B, Maguire M G, Bressler N M, and Fine S L (1990) Relationship of drusen and abnormalities of the retinal pigment epithelium to the prognosis of neovascular macular degeneration. The Macular Photocoagulation Study Group. *Arch Ophthalmol* 108: 1442-1447.

Breton M E, and Montzka D P (1992) Empiric limits of rod photocurrent component underlying a-wave response in the electroretinogram. *Doc Ophthalmol* 79: 337-361.

Brezinski M (2006) *Optical Coherence Tomography: Principles and Applications*. 1st ed. Academic Press.

Brigell M, Bach M, Barber C, Moskowitz A, and Robson J (2003) Guidelines for calibration of stimulus and recording parameters used in clinical electrophysiology of vision. *Doc Ophthalmol* 107: 185-193.

Brinchmann-Hansen O, and Myhre K (1989) The effect of hypoxia upon macular recovery time in normal humans. *Aviat Space Environ Med* 60: 1183-1186.

Brown B, and Lovie-Kitchin J (1987) Temporal function in age related maculopathy. *Clin Exp Optom* 70: 112-116.

Brown M, Marmor M, Vaegan, Zrenner E, Brigell M, and Bach M (2006) ISCEV Standard for Clinical Electro-oculography (EOG) 2006. *Doc Ophthalmol* 113: 205-212.

Bruce V, Green P R, and Georgeson M A (2003) *Visual Perception: Physiology, Psychology and Ecology*. 4th ed. Psychology Press.

BSI (2007) Ophthalmic Instruments - fundamental requirements and test methods. Part 2 - Light Hazard Protection. *British Standards Institute* BS EN 15004-2.

Bunce C, and Wormald R (2006) Leading causes of certification for blindness and partial sight in England & Wales. *BMC Public Health* 6: 58.

Bunt-Milam A H, Saari J C, Klock I B, and Garwin G G (1985) Zonulae adherentes pore size in the external limiting membrane of the rabbit retina. *Invest Ophthalmol Vis Sci* 26: 1377-1380.

Bush R A, and Sieving P A (1994) A proximal retinal component in the primate photopic ERG a-wave. *Invest Ophthalmol Vis Sci* 35: 635-645.

Bush R A, and Sieving P A (1996) Inner retinal contributions to the primate photopic fast flicker electroretinogram. *J Opt Soc Am A Opt Image Sci Vis* 13: 557-565.

Casswell A G, Kohen D, and Bird A C (1985) Retinal-pigment epithelial detachments in the elderly - classification and outcome. *Br J Ophthalmol* 69: 397-403.

Cervetto L, Lagnado L, Perry R J, Robinson D W, and McNaughton P A (1989) Extrusion of calcium from rod outer segments is driven by both sodium and potassium gradients. *Nature* 337: 740-743.

Chakravarthy U, Wong T Y, Fletcher A, Piault E, Evans C, Zlateva G, Buggage R et al. (2010) Clinical risk factors for age-related macular degeneration: a systematic review and meta-analysis. *BMC Ophthalmol* 10: In press.

Chauhan D S, and Marshall J (1999) The interpretation of optical coherence tomography images of the retina. *Invest Ophthalmol Vis Sci* 40: 2332-2342.

Chen C, Wu L, Wu D, Huang S, Wen F, Luo G, and Long S (2004) The local cone and rod system function in early age-related macular degeneration. *Doc Ophthalmol* 109: 1-8.

Chen C C, and Heller J (1977) Uptake of retinol and retinoic acid from serum retinol-binding protein by retinal pigment epithelial cells. *J Biol Chem* 252: 5216-5221.

Chen J, and Lee L (2007) Clinical applications and new developments of optical coherence tomography: an evidence-based review. *Clin Exp Optom* 90: 317-335.

Chen J C, Fitzke F W, Pauleikhoff D, and Bird A C (1992) Functional loss in age-related Bruch's membrane change with choroidal perfusion defect. *Invest Ophthalmol Vis Sci* 33: 334-340.

Chen Y L, Burnes D L, de Bruin M, Mujat M, and de Boer J F (2009) Three-dimensional pointwise comparison of human retinal optical property at 845 and 1060 nm using optical frequency domain imaging. *J Biomed Opt* 14.

Cheng A S, and Vingrys A J (1993) Visual losses in early age-related maculopathy. *Optom Vis Sci* 70: 89-96.

Cheng S C K, Lam C S Y, and Yap M K H (2010) Retinal thickness in myopic and non-myopic eyes. *Ophthalmic Physiol Opt* 30: 776-784.

Chiang A, and Regillo C D (2011) Preferred therapies for neovascular age-related macular degeneration. *Curr Opin Ophthalmol* 22: 199-204.

Chiti Z, North R V, Mortlock K E, and Drasdo N (2003) The S-cone electroretinogram: a comparison of techniques, normative data and age-related variation. *Ophthalmic Physiol Opt* 23: 370-376.

Chong E W T, Wong T Y, Kreis A J, Simpson J A, and Guymer R H (2007) Dietary antioxidants and primary prevention of age related macular degeneration: systematic review and meta-analysis. *Br Med J* 335: 755-759.

Chong N H V, Keonin J, Luthert P J, Frennesson C I, Weingeist D M, Wolf R L, Mullins R F et al. (2005) Decreased thickness and integrity of the macular elastic layer of Bruch's membrane correspond to the distribution of lesions associated with age-related macular degeneration. *Am J Pathol* 166: 241-251.

Choroidal Neovascularization Prevention Trial Research G (1998) Choroidal neovascularization in the choroidal neovascularization prevention trial. *Ophthalmology* 105: 1364-1372.

Choshi T, Matsumoto C S, and Nakatsuka K (2003) Rod-driven focal macular electroretinogram. *Jpn J Ophthalmol* 47: 356-361.

Chylack L T, Wolfe J K, Singer D M, Leske M C, Bullimore M A, Bailey I L, Friend J et al. (1993) The Lens Opacities Classification System-III. *Arch Ophthalmol* 111: 831-836.

Ciulla T A, Harris A, Chung H S, Danis R P, Kagemann L, McNulty L, Pratt L M et al. (1999) Color Doppler imaging discloses reduced ocular blood flow velocities in nonexudative age-related macular degeneration. *Am J Ophthalmol* 128: 75-80.

Ciulla T A, Harris A, Kagemann L, Danis R P, Pratt L M, Chung H S, Weinberger D et al. (2002) Choroidal perfusion perturbations in non-neovascular age related macular degeneration. *Br J Ophthalmol* 86: 209-213.

Clark M E, McGwin G, Jr., Neely D, Feist R, Mason J O, 3rd, Thomley M, White M F, Jr. et al. (2011) Association between retinal thickness measured by spectral-domain optical coherence tomography (OCT) and rod-mediated dark adaptation in non-exudative age-related maculopathy. *Br J Ophthalmol* 95: 1427-1432.

Coile D C, and Baker H D (1992) Foveal dark adaptation, photopigment regeneration, and aging. *Vis Neurosci* 8: 27-39.

Coleman H R, Chan C-C, Ferris Iii F L, and Chew E Y (2008) Age-related macular degeneration. *J Lancet* 372: 1835-1845.

Collins M, and Brown B (1989) Glare recovery and it's relation to other clinical findings in age related maculopathy. *Clin Vision Sci* 4: 155-163.

Colotto A, Falsini B, Salgarello T, Iarossi G, Galan M E, and Scullica L (2000) Photopic negative response of the human ERG: Losses associated with glaucomatous damage. *Invest Ophthalmol Vis Sci* 41: 2205-2211.

Connolly D M, and Hosking S L (2006) Aviation-related respiratory gas disturbances affect dark adaptation: a reappraisal. *Vision Res* 46: 1784-1793.

Copenhagen D R, and Jahr C E (1989) Release of endogenous excitatory amino acids from turtle photoreceptors. *Nature* 341: 536-539.

Csutak A, Lengyel I, Jonasson F, Leung I, Geirsdottir A, Xing W, and Peto T (2010) Agreement between image grading of conventional (45 degrees) and ultra wide-angle (200 degrees) digital images in the macula in the Reykjavik eye study. *Eye* 24: 1568-1575.

Curcio C A, Allen K A, Sloan K R, Lerea C L, Hurley J B, Klock I B, and Milam A H (1991) Distribution and morphology of human cone photoreceptors stained with anti-blue opsin. *J Comp Neurol* 312: 610-624.

Curcio C A, Medeiros N E, and Millican C L (1996) Photoreceptor loss in age-related macular degeneration. *Invest Ophthalmol Vis Sci* 37: 1236-1249.

Curcio C A, Millican C L, Allen K A, and Kalina R E (1993) Aging of the human photoreceptor mosaic: evidence for selective vulnerability of rods in central retina. *Invest Ophthalmol Vis Sci* 34: 3278-3296.

Curcio C A, Owsley C, and Jackson G R (2000) Spare the rods, save the cones in aging and age-related maculopathy. *Invest Ophthalmol Vis Sci* 41: 2015-2018.

Curcio C A, Sloan K R, Jr., Packer O, Hendrickson A E, and Kalina R E (1987) Distribution of cones in human and monkey retina: individual variability and radial asymmetry. *Science* 236: 579-582.

Curcio C A, Sloan K R, Kalina R E, and Hendrickson A E (1990) Human photoreceptor topography. *J Comp Neurol* 292: 497-523.

Curtin F, and Schulz P (1998) Multiple correlations and Bonferroni's correction. *Biol Psychiatry* 44: 775-777.

Dawson W W, Trick G L, and Litzkow C A (1979) Improved electrode for electroretinography. *Invest Ophthalmol Vis Sci* 18: 988-991.

Del Priore L V, Tezel T H, and Kaplan H J (2006) Maculoplasty for age-related macular degeneration: reengineering Bruch's membrane and the human macula. *Prog Retin Eye Res* 25: 539-562.

Delaey C, and Van De Voorde J (2000) Regulatory mechanisms in the retinal and choroidal circulation. *Ophthalmic Res* 32: 249-256.

Detry-Morel M, Zeyen T, Kestelyn P, Collignon J, Goethals M, and Belgian Glaucoma S (2004) Screening for glaucoma in a general population with the non-mydriatic fundus camera and the frequency doubling perimeter. *Eur J Ophthalmol* 14: 387-393.

Dimitrov P N, Guymer R H, Zele A J, Anderson A J, and Vingrys A J (2008) Measuring rod and cone dynamics in age-related maculopathy. *Invest Ophthalmol Vis Sci* 49: 55-65.

Donoso L A, Kim D, Frost A, Callahan A, and Hageman G (2006) The role of inflammation in the pathogenesis of age-related macular degeneration. *Surv Ophthalmol* 51: 137-152.

Donoso L A, Vrabec T, and Kuivaniemi H (2010) The Role of Complement Factor H in Age-related Macular Degeneration: A Review. *Surv Ophthalmol* 55: 227-246.

Dowling J E, and Wald G (1960) The biological function of vitamin A acid. *Proc Natl Acad Sci U S A* 46: 587-608.

Drasdo N, Aldebasi Y H, Chiti Z, Mortlock K E, Morgan J E, and North R V (2001) The s-cone PHNR and pattern ERG in primary open angle glaucoma. *Invest Ophthalmol Vis Sci* 42: 1266-1272.

Drasdo N, and Fowler C W (1974) Nonlinear projection of retinal image in a wide-angle schematic eye. *Br J Ophthalmol* 58: 709-714.

Drexler W (2004) Ultrahigh-resolution optical coherence tomography. *J Biomed Opt* 9: 47-74.

Drexler W, and Fujimoto J G (2008) State-of-the-art retinal optical coherence tomography. *Prog Retin Eye Res* 27: 45-88.

Drexler W, Sattmann H, Hermann B, Ko T H, Stur M, Unterhuber A, Scholda C et al. (2003) Enhanced visualization of macular pathology with the use of ultrahigh-resolution optical coherence tomography. *Arch Ophthalmol* 121: 695-706.

Eisner A, Fleming S A, Klein M L, and Mauldin W M (1987) Sensitivities in older eyes with good acuity: eyes whose fellow eye has exudative AMD. *Invest Ophthalmol Vis Sci* 28: 1832-1837.

Eisner A, Klein M L, Zilis J D, and Watkins M D (1992) Visual function and the subsequent development of exudative age-related macular degeneration. *Invest Ophthalmol Vis Sci* 33: 3091-3102.

Eisner A, Stoumbos V D, Klein M L, and Fleming S A (1991) Relations between fundus appearance and function. Eyes whose fellow eye has exudative age-related macular degeneration. *Invest Ophthalmol Vis Sci* 32: 8-20.

Elliott D B (2007) *Clinical Procedures in Primary Eye Care*. 3rd ed. Butterworth-Heinemann.

Elman M J, Fine S L, Murphy R P, Patz A, and Auer C (1986) The natural-history of serous retinal-pigment epithelium detachment in patients with age-related macular degeneration. *Ophthalmology* 93: 224-230.

Elsner A E, Burns S A, and Weiter J J (2002) Cone photopigment in older subjects: decreased optical density in early age-related macular degeneration. *J Opt Soc Am A Opt Image Sci Vis* 19: 215-222.

Esmaeelpour M, Povazay B, Hermann B, Hofer B, Kajic V, Kapoor K, Sheen N J L et al. (2010) Three-Dimensional 1060-nm OCT: Choroidal Thickness Maps in Normal Subjects and Improved Posterior Segment Visualization in Cataract Patients. *Invest Ophthalmol Vis Sci* 51: 5260-5266.

Evans J R (2001) Risk factors for age-related macular degeneration. *Prog Retin Eye Res* 20: 227-253.

Evans J R (2006) Antioxidant vitamin and mineral supplements for slowing the progression of age-related macular degeneration. *Cochrane Database Syst Rev*.

Fahle M, and Bach M (2006) Origins of the Visual Evoked Potential. In: Heckenlively, J R, and Arden, G B [eds.] *Principles and Practice of Clinical Electrophysiology of Vision*. Cambridge, MA: MIT Press, pp. 207-234.

Falkner C I, Leitich H, Frommlet F, Bauer P, and Binder S (2007) The end of submacular surgery for age-related macular degeneration? A meta-analysis. *Graefes Arch Clin Exp Ophthalmol* 245: 490-501.

Falsini B, Fadda A, Iarossi G, Piccardi M, Canu D, Minnella A, Serrao S et al. (2000) Retinal sensitivity to flicker modulation: reduced by early age-related maculopathy. *Invest Ophthalmol Vis Sci* 41: 1498-1506.

Falsini B, Iarossi G, Fadda A, Porrello G, Valentini P, Piccardi M, and Scullica L (1999a) The fundamental and second harmonic of the photopic flicker electroretinogram: temporal frequency-dependent abnormalities in retinitis pigmentosa. *Clin Neurophysiol* 110: 1554-1562.

Falsini B, Porciatti V, Fadda A, Merendino E, Iarossi G, and Cermola S (1995) The first and second harmonics of the macular flicker electroretinogram: differential effects of retinal diseases. *Doc Ophthalmol* 90: 157-167.

Falsini B, Serrao S, Fadda A, Iarossi G, Porrello G, Cocco F, and Merendino E (1999b) Focal electroretinograms and fundus appearance in nonexudative age-related macular degeneration. Quantitative relationship between retinal morphology and function. *Graefes Arch Clin Exp Ophthalmol* 237: 193-200.

Falsini B, Ziccardi L, Stifano G, Iarossi G, Merendino E, Minnella A M, Fadda A et al. (2007) Temporal response properties of the macular cone system: effect of normal aging and age-related maculopathy. *Invest Ophthalmol Vis Sci* 48: 4811-4817.

Farnsworth D (1943) The Farnsworth-Munsell 100-Hue and Dichotomous Tests for Color Vision. *J Opt Soc Am* 33: 568-574.

Feigl B (2009) Age-related maculopathy - linking aetiology and pathophysiological changes to the ischaemia hypothesis. *Prog Retin Eye Res* 28: 63-86.

Feigl B, Brown B, Lovie-Kitchin J, and Swann P (2005a) Cone- and rod-mediated multifocal electroretinogram in early age-related maculopathy. *Eye* 19: 431-441.

Feigl B, Brown B, Lovie-Kitchin J, and Swann P (2005b) Monitoring retinal function in early age-related maculopathy: visual performance after 1 year. *Eye* 19: 1169-1177.

Feigl B, Stewart I, and Brown B (2007) Experimental hypoxia in human eyes: implications for ischaemic disease. *Clin Neurophysiol* 118: 887-895.

Feigl B, Stewart I B, Brown B, and Zele A J (2008) Local neuroretinal function during acute hypoxia in healthy older people. *Invest Ophthalmol Vis Sci* 49: 807-813.

Feng L, Sun Z, Han H, Zhou Y, and Zhang M (2007) No age-related cell loss in three retinal nuclear layers of the Long-Evans rat. *Vis Neurosci* 24: 799-803.

Ferris F L, 3rd, Kassoff A, Bresnick G H, and Bailey I (1982) New visual acuity charts for clinical research. *Am J Ophthalmol* 94: 91-96.

Fesenko E E, Kolesnikov S S, and Lyubarsky A L (1985) Induction by cyclic GMP of cationic conductance in plasma membrane of retinal rod outer segment. *Nature* 313: 310-313.

Fishman G A, Chappelow A V, Anderson R J, Rotenstreich Y, and Derlacki D J (2005) Short-term inter-visit variability of ERG amplitudes in normal subjects and patients with retinitis pigmentosa. *Retina* 25: 1014-1021.

Forooghian F, Stetson P F, Meyer S A, Chew E Y, Wong W T, Cukras C, Meyerle C B et al. (2010) Relationship between photoreceptor outer segment length and visual acuity in diabetic macular edema. *Retina* 30: 63-70.

Frank R N, Amin R H, Eliott D, Puklin J E, and Abrams G W (1996) Basic fibroblast growth factor and vascular endothelial growth factor are present in epiretinal and choroidal neovascular membranes. *Am J Ophthalmol* 122: 393-403.

Freund P R, Watson J, Gilmour G S, Gaillard F, and Sauve Y (2011) Differential changes in retina function with normal aging in humans. *Doc Ophthalmol* 122: 177-190.

Friedburg C, Thomas M M, and Lamb T D (2001) Time course of the flash response of dark- and light-adapted human rod photoreceptors derived from the electroretinogram. *J Physiol* 534: 217-242.

Friedman E (2008) The pathogenesis of age-related macular degeneration. *Am J Ophthalmol* 146: 348-349.

Friedman E, Krupsky S, Lane A M, Oak S S, Friedman E S, Egan K, and Gragoudas E S (1995) Ocular blood flow velocity in age-related macular degeneration. *Ophthalmology* 102: 640-646.

Frishman L J (2006) Origins of the electroretinogram. In: Heckenlively, J R, and Arden, G B [eds.] *Principles and Practice of Clinical Electrophysiology of Vision*. Cambridge, MA: MIT Press, pp. 139-183.

Fryczkowski A W, and Sherman M D (1988) Scanning electron microscopy of human ocular vascular casts: the submacular choriocapillaris. *Acta Anatomica* 132: 265-269.

Fukuda Y, and Stone J (1974) Retinal distribution and central projections of Y-, X-, and W-cells of the cat's retina. *J Neurophysiol* 37: 749-772.

Fulton A B, and Rushton W A (1978) The human rod ERG: correlation with psychophysical responses in light and dark adaptation. *Vision Res* 18: 793-800.

Gaffney A J, Binns A M, and Margrain T H (2011) Topography of cone dark adaptation deficits in age-related maculopathy. *Optom Vis Sci* 88: 1080-1087.

Gass J D (1972) Drusen and disciform macular detachment and degeneration. *Trans Am Ophthalmol Soc* 70: 409-436.

Geller A M, Sieving P A, and Green D G (1992) Effect on grating identification of sampling with degenerate arrays. *J Opt Soc Am A* 9: 472-477.

Ghazi N G, Kirk T, Allam S, and Yan G (2009) Quantification of Error in Optical Coherence Tomography Central Macular Thickness Measurement in Wet Age-related Macular Degeneration. *Am J Ophthalmol* 148: 90-96.

Gloesmann M, Hermann B, Schubert C, Sattmann H, Ahnelt P K, and Drexler W (2003) Histologic correlation of pig retina radial stratification with ultrahigh-resolution optical coherence tomography. *Invest Ophthalmol Vis Sci* 44: 1696-1703.

Gonzalez-Fernandez F (2003) Interphotoreceptor retinoid-binding protein--an old gene for new eyes. *Vision Res* 43: 3021-3036.

Gouras P (1984) Colour Vision. *Prog Retin Eye Res* 3: 227-261.

Granit R (1933) The components of the retinal action potential in mammals and their relation to the discharge in the optic nerve. *J Physiol* 77: 207-239.

Green W R (1999) Histopathology of age-related macular degeneration. *Mol Vis* 5: 27.

Grover S, Murthy R K, Brar V S, and Chalam K V (2010) Comparison of Retinal Thickness in Normal Eyes Using Stratus and Spectralis Optical Coherence Tomography. *Invest Ophthalmol Vis Sci* 51: 2644-2647.

Grunwald J E, Hariprasad S M, and DuPont J (1998) Effect of aging on foveolar choroidal circulation. *Arch Ophthalmol* 116: 150-154.

Gurevich L, and Slaughter M M (1993) Comparison of the wave-forms of the on bipolar neuron and the b-wave of the electroretinogram. *Vision Res* 33: 2431-2435.

Guymer R, Luthert P, and Bird A (1999) Changes in Bruch's membrane and related structures with age. *Prog Retin Eye Res* 18: 59-90.

Hagins W A, Penn R D, and Yoshikami S (1970) Dark current and photocurrent in retinal rods. *Biophys J* 10: 380-412.

Haimovici R, Owens S L, Fitzke F W, and Bird A C (2002) Dark adaptation in age-related macular degeneration: relationship to the fellow eye. *Graefes Arch Clin Exp Ophthalmol* 240: 90-95.

Hare W A, and Ton H (2002) Effects of APB, PDA, and TTX on ERG responses recorded using both multifocal and conventional methods in monkey. *Doc Ophthalmol* 105: 189-222.

Hargrave P A, and McDowell J H (1992) Rhodopsin and phototransduction: a model system for G protein-linked receptors. *FASEB J* 6: 2323-2331.

Harris A, Chung H S, Ciulla T A, and Kagemann L (1999) Progress in measurement of ocular blood flow and relevance to our understanding of glaucoma and age-related macular degeneration. *Prog Retin Eye Res* 18: 669-687.

Hart W M (1987) The temporal responsiveness of vision. In: Moses, R A, and Hart, W M [eds.] *Adler's physiology of the eye. Clinical application*. St. Louis: The C. V. Mosby Company.

Hayashi H, Yamashiro K, Tsujikawa A, Ota M, Otani A, and Yoshimura N (2009) Association between foveal photoreceptor integrity and visual outcome in neovascular age-related macular degeneration. *Am J Ophthalmol* 148: 83-89.

Hecht S, Haig C, and Chase A M (1937) The influence of light adaptation on subsequent dark adaptation of the eye. *J Gen Physiol* 20: 831-850.

Hendrickson A E (2005) Organization of the Adult Primate Fovea. In: Penfold, P L, and Provis, J M [eds.] *Macular Degeneration*. Heidelburg: Springer, pp. 1-20.

Henson D (2000) *Visual Fields*. 2nd ed. Oxford: Butterworth-Heinemann.

Hermann B, Fernandez E J, Unterhuber A, Sattmann H, Fercher A F, Drexler W, Prieto P M et al. (2004) Adaptive-optics ultrahigh-resolution optical coherence tomography. *Opt Lett* 29: 2142-2144.

Hicks D, and Sahel J (1999) The implications of rod-dependent cone survival for basic and clinical research. *Invest Ophthalmol Vis Sci* 40: 3071-3074.

Hirata M, Tsujikawa A, Matsumoto A, Hangai M, Ooto S, Yamashiro K, Akiba M et al. (2011) Macular choroidal thickness and volume in normal subjects measured by swept-source optical coherence tomography. *Invest Ophthalmol Vis Sci* 52: 4971-4978.

Hochstein G D, Molnar F E, and Marmor M F (2007) Intrasession variability of the full-field ERG. *Doc Ophthalmol* 115: 77-83.

Hogg R, Curry E, Muldrew A, Winder J, Stevenson M, McClure M, and Chakravarthy U (2003) Identification of lesion components that influence visual function in age related macular degeneration. *Br J Ophthalmol* 87: 609-614.

Holder G E, Brigell M G, Hawlina M, Meigen T, Vaegan, and Bach M (2007) ISCEV standard for clinical pattern electroretinography--2007 update. *Doc Ophthalmol* 114: 111-116.

Hollins M, and Alpern M (1973) Dark adaptation and visual pigment regeneration in human cones. *J Gen Physiol* 62: 430-447.

Holopigian K, Greenstein V C, Seiple W, Hood D C, and Carr R E (2004) Rod and cone photoreceptor function in patients with cone dystrophy. *Invest Ophthalmol Vis Sci* 45: 275-281.

Holopigian K, Seiple W, Greenstein V, Kim D, and Carr R E (1997) Relative effects of aging and age-related macular degeneration on peripheral visual function. *Optom Vis Sci* 74: 152-159.

Holz F G, Bellman C, Staudt S, Schutt F, and Volcker H E (2001) Fundus autofluorescence and development of geographic atrophy in age-related macular degeneration. *Invest Ophthalmol Vis Sci* 42: 1051-1056.

Holz F G, Gross-Jendroska M, Eckstein A, Hogg C R, Arden G B, and Bird A C (1995) Colour contrast sensitivity in patients with age-related Bruch's membrane changes. *Ger J Ophthalmol* 4: 336-341.

Hood D, Bach M, Brigell M, Keating D, Kondo M, Lyons J, Marmor M et al. (2012) ISCEV standard for clinical multifocal electroretinography (mfERG) (2011 edition). *Doc Ophthalmol* 124: 1-13.

Hood D C, Bach M, Brigell M, Keating D, Kondo M, Lyons J S, and Palmowski-Wolfe A M (2008) ISCEV guidelines for clinical multifocal electroretinography (2007 edition). *Doc Ophthalmol* 116: 1-11.

Hood D C, and Birch D G (1990a) A quantitative measure of the electrical activity of human rod photoreceptors using electroretinography. *Vis Neurosci* 5: 379-387.

Hood D C, and Birch D G (1990b) The A-wave of the human electroretinogram and rod receptor function. *Invest Ophthalmol Vis Sci* 31: 2070-2081.

Hood D C, and Birch D G (1996) Assessing abnormal rod photoreceptor activity with the a-wave of the electroretinogram: applications and methods. *Doc Ophthalmol* 92: 253-267.

Hood D C, Holopigian K, Greenstein V, Seiple W, Li J, Sutter E E, and Carr R E (1998) Assessment of local retinal function in patients with retinitis pigmentosa using the multi-focal ERG technique. *Vision Res* 38: 163-179.

Hood D C, Shady S, and Birch D G (1994) Understanding changes in the b-wave of the ERG caused by heterogeneous receptor damage. *Invest Ophthalmol Vis Sci* 35: 2477-2488.

Huang D, Swanson E A, Lin C P, Schuman J S, Stinson W G, Chang W, Hee M R et al. (1991) Optical coherence tomography. *Science* 254: 1178-1181.

Huang J D, Curcio C A, and Johnson M (2008) Morphometric analysis of lipoprotein-like particle accumulation in aging human macular Bruch's membrane. *Invest Ophthalmol Vis Sci* 49: 2721-2727.

Huang Y J, Cideciyan A V, Papastergiou G I, Banin E, Semple-Rowland S L, Milam A H, and Jacobson S G (1998) Relation of optical coherence tomography to microanatomy in normal and rd chickens. *Invest Ophthalmol Vis Sci* 39: 2405-2416.

Hudspeth A J, and Yee A G (1973) The intercellular junctional complexes of retinal pigment epithelia. *Invest Ophthalmol* 12: 354-365.

Hutchinson A, McIntosh A, Peters J, O'Keeffe C, Khunti K, Baker R, and Booth A (2000) Effectiveness of screening and monitoring tests for diabetic retinopathy - a systematic review. *Diabet Med* 17: 495-506.

Ikuno Y, Kawaguchi K, Nouchi T, and Yasuno Y (2010) Choroidal Thickness in Healthy Japanese Subjects. *Invest Ophthalmol Vis Sci* 51: 2173-2176.

Ikuno Y, and Tano Y (2009) Retinal and Choroidal Biometry in Highly Myopic Eyes with Spectral-Domain Optical Coherence Tomography. *Invest Ophthalmol Vis Sci* 50: 3876-3880.

Iwama D, Tsujikawa A, Ojima Y, Nakanishi H, Yamashiro K, Tamura H, Ooto S et al. (2010) Relationship between retinal sensitivity and morphologic changes in eyes with confluent soft drusen. *Clin Experiment Ophthalmol* 38: 483-488.

Jackson G R, Owsley C, and McGwinJr G (1999) Aging and dark adaptation. *Vision Res* 39: 3975-3982.

Jaffe G J, and Caprioli J (2004) Optical coherence tomography to detect and manage retinal disease and glaucoma. *Am J Ophthalmol* 137: 156-169.

Jamison J A, Bush R A, Lei B, and Sieving P A (2001) Characterization of the rod photoresponse isolated from the dark-adapted primate ERG. *Vis Neurosci* 18: 445-455.

Joeres S, Tsong J W, Updike P G, Collins A T, Dustin L, Walsh A C, Romano P W et al. (2007) Reproducibility of quantitative optical coherence tomography subanalysis in neovascular age-related macular degeneration. *Invest Ophthalmol Vis Sci* 48: 4300-4307.

Johnson L V, Leitner W P, Staples M K, and Anderson D H (2001) Complement activation and inflammatory processes in drusen formation and age related macular degeneration. *Exp Eye Res* 73: 887-896.

Joseph D P, and Miller S S (1992) Alpha-1-adrenergic modulation of K and Cl transport in bovine retinal pigment epithelium. *J Gen Physiol* 99: 263-290.

Kakinoki M, Sawada O, Sawada T, Kawamura H, and Ohji M (2009) Comparison of Macular Thickness Between Cirrus HD-OCT and Stratus OCT. *Ophthalmic Surg Lasers Imaging* 40: 135-140.

Kalloniatis M, and Luu C (2005) *Psychophysics of Vision.* www.webvision.med.utah.edu Accessed: 30/01/2011

Kaluzny J J, Wojtkowski M, Sikorski B L, Szkulmowski M, Szkulmowska A, Bajraszewski T, Fujimoto J G et al. (2009) Analysis of the Outer Retina Reconstructed by High-Resolution, Three-Dimensional Spectral Domain Optical Coherence Tomography. *Ophthalmic Surg Lasers Imaging* 40: 102-108.

Kang S H, Hong S W, Im S K, Lee S H, and Ahn M D (2010) Effect of Myopia on the Thickness of the Retinal Nerve Fiber Layer Measured by Cirrus HD Optical Coherence Tomography. *Invest Ophthalmol Vis Sci* 51: 4075-4083.

Kanis M J, Wisse R P L, Berendschot T, van de Kraats J, and van Norren D (2008) Foveal cone-photoreceptor integrity in aging macula disorder. *Invest Ophthalmol Vis Sci* 49: 2077-2081.

Kanski J (2003) *Clinical Ophthalmology*. 5th ed. Oxford: Butterworth-Heinemann.

Karwatowski W S, Jeffries T E, Duance V C, Albon J, Bailey A J, and Easty D L (1995) Preparation of Bruch's membrane and analysis of the age-related changes in the structural collagens. *Br J Ophthalmol* 79: 944-952.

Karwoski C J, and Xu X J (1999) Current source-density analysis of light-evoked field potentials in rabbit retina. *Vis Neurosci* 16: 369-377.

Kashani A H, Keane P A, Dustin L, Walsh A C, and Sadda S R (2009) Quantitative Subanalysis of Intraretinal Cystoid Spaces and Outer Nuclear Layer using Optical Coherence Tomography in Neovascular Age-Related Macular Degeneration. *Invest Ophthalmol Vis Sci* 50: 3366-3373.

Keane P A, Liakopoulos S, Jivrajka R V, Chang K T, Alasil T, Walsh A C, and Sadda S R (2009) Evaluation of Optical Coherence Tomography Retinal Thickness Parameters for Use in Clinical Trials for Neovascular Age-Related Macular Degeneration. *Invest Ophthalmol Vis Sci* 50: 3378-3385.

Kennedy C J, Rakoczy P E, and Constable I J (1995) Lipofuscin of the retinal pigment epithelium: A review. *Eye* 9: 763-771.

Kernt M, Schaller U C, Stumpf C, Ulbig M W, Kampik A, and Neubauer A S (2010) Choroidal pigmented lesions imaged by ultra-wide-field scanning laser ophthalmoscopy with two laser wavelengths (Optomap). *Clin Ophthalmol* 4: 829-836.

Kirchhof B, and Ryan S J (1993) Differential permeance of retina and retinal-pigment epithelium to water - implications for retinal adhesion. *Int Ophthalmol* 17: 19-22.

Kiryu J, Asrani S, Shahidi M, Mori M, and Zeimer R (1995) Local response of the primate retinal microcirculation to increased metabolic demand induced by flicker. *Invest Ophthalmol Vis Sci* 36: 1240-1246.

Klaver C C W, van Leeuwen R, Vingerling J R, and de Jong P T V M (2004) Epidemiology of Age-Related Maculopathy: A review. In: Holz, F G, Pauleikhoff, D, Spaide, R F, and Bird, A C [eds.] *Age-related Macular Degeneration*. Heidelburg: Springer, pp. 1-17.

Klein R, Davis M D, Magli Y L, Segal P, Klein B E, and Hubbard L (1991) The Wisconsin age-related maculopathy grading system. *Ophthalmology* 98: 1128-1134.

Klein R, Klein B E, and Linton K L (1992) Prevalence of age-related maculopathy. The Beaver Dam Eye Study. *Ophthalmology* 99: 933-943.

Klein R, Klein B E, and Moss S E (1998) Relation of smoking to the incidence of age-related maculopathy. The Beaver Dam Eye Study. *Am J Epidemiol* 147: 103-110.

Klein R, Klein B E K, Jensen S C, and Meuer S M (1997) The five-year incidence and progression of age-related maculopathy - The Beaver Dam eye study. *Ophthalmology* 104: 7-21.

Klein R, Peto T, Bird A, and Vannewkirk M R (2004) The epidemiology of age-related macular degeneration. *Am J Ophthalmol* 137: 486-495.

Klein R, Wang Q, Klein B E, Moss S E, and Meuer S M (1995) The relationship of age-related maculopathy, cataract, and glaucoma to visual acuity. *Invest Ophthalmol Vis Sci* 36: 182-191.

Kleiner R C, Enger C, Alexander M F, and Fine S L (1988) Contrast sensitivity in age-related macular degeneration. *Arch Ophthalmol* 106: 55-57.

Knapp A G, and Schiller P H (1984) The contribution of on-bipolar cells to the electroretinogram of rabbits and monkeys - a study using 2-amino-4-phosphonobutyrate (APB). *Vision Res* 24: 1841-1846.

Ko T H, Adler D C, Fujimoto J G, Mamedov D, Prokhorov V, Shidlovski V, and Yakubovich S (2004) Ultrahigh resolution optical coherence tomography imaging with a broadband superluminescent diode light source. *Opt Express* 12: 2112-2119.

Ko T H, Fujimoto J G, Schuman J S, Paunescu L A, Kowalevicz A M, Hartl I, Drexler W et al. (2005) Comparison of ultrahigh- and standard-resolution optical coherence tomography for imaging macular pathology. *Ophthalmology* 112: 1922 e1921-1915.

Kolb H (2006) Functional organisation of the retina. In: Heckenlively, J R, and Arden, G B [eds.] *Principles and Practice of Clinical Electrophysiology of Vision*. Cambridge, MA: MIT Press, pp. 47-64.

Kolb H, and Famiglietti E V (1974) Rod and Cone Pathways in the Inner Plexiform Layer of Cat Retina. *Science* 186: 47-49.

Kolb H, Fernandez E, Schouten J, Ahnelt P, Linberg K A, and Fisher S K (1994) Are there three types of horizontal cell in the human retina? *J Comp Neurol* 343: 370-386.

Kolb H, Fernandez E J, and Nelson R (2003a) *Anatomy and Physiology of the retina.* www.webvision.med.utah.edu Accessed: 10/01/2011

Kolb H, Fernandez E J, and Nelson R (2003b) *Simple anatomy of the retina.* www.webvision.med.utah.edu Accessed: 05/01/2011

Kolb H, Linberg K A, and Fisher S K (1992) The neurons of the human retina: a Golgi study. *J Comp Neurol* 318: 147-187.

Kolb H, Nelson R, and Mariani A (1981) Amacrine cells, bipolar cells and ganglion cells of the cat retina: a Golgi study. *Vision Res* 21: 1081-1114.

Kondo M, and Sieving P A (2001) Primate photopic sine-wave flicker ERG: vector modeling analysis of component origins using glutamate analogs. *Invest Ophthalmol Vis Sci* 42: 305-312.

Kondo M, and Sieving P A (2002) Post-photoreceptoral activity dominates primate photopic 32-Hz ERG for sine-, square-, and pulsed stimuli. *Invest Ophthalmol Vis Sci* 43: 2500-2507.

Krebs I, Falkner-Radler C I, Hagen S, Haas P, Brannath W, Lie S, Ansari-Shahrezaei S et al. (2008) Quality of Threshold Algorithm in Age-related Macular Degeneration: Stratus versus Cirrus OCT. *Invest Ophthalmol Vis Sci* 50: 995-1000.

Lachica E A, and Casagrande V A (1993) The morphology of collicular and retinal axons ending on small relay (W-like) cells of the primate lateral geniculate nucleus. *Vis Neurosci* 10: 403-418.

Lamb T D, and Pugh E N, Jr. (2004) Dark adaptation and the retinoid cycle of vision. *Prog Retin Eye Res* 23: 307-380.

Landa G, Su E, Garcia P M, Seiple W H, and Rosen R B (2011) Inner segment-outer segment junctional layer integrity and corresponding retinal sensitivity in dry and wet forms of age-related macular degeneration. *Retina* 31: 364-370.

Lazic R, and Gabric N (2007) Verteporfin therapy and intravitreal bevacizumab combined and alone in choroidal neovascularization due to age-related macular degeneration. *Ophthalmology* 114: 1179-1185.

Legarreta J E, Gregori G, Punjabi O S, Knighton R W, Lalwani G A, and Puliafito C A (2008) Macular thickness measurements in normal eyes using spectral domain optical coherence tomography. *Ophthalmic Surg Lasers Imaging* 39: S43-S49.

Lei B, and Perlman I (1999) The contributions of voltage- and time-dependent potassium conductances to the electroretinogram in rabbits. *Vis Neurosci* 16: 743-754.

Leung C K, Cheng A C, Chong K K, Leung K S, Mohamed S, Lau C S, Cheung C Y et al. (2007) Optic disc measurements in myopia with optical coherence tomography and confocal scanning laser ophthalmoscopy. *Invest Ophthalmol Vis Sci* 48: 3178-3183.

Leventhal A G, Rodieck R W, and Dreher B (1981) Retinal ganglion cell classes in the Old World monkey: morphology and central projections. *Science* 213: 1139-1142.

Li J, Tso M O M, and Lam T T (2001) Reduced amplitude and delayed latency in foveal response of multifocal electroretinogram in early age related macular degeneration. *Br J Ophthalmol* 85: 287-290.

Littmann H (1982) [Determination of the real size of an object on the fundus of the living eye]. *Klin Monbl Augenheilkd* 180: 286-289.

Loduca A L, Zhang C, Zelkha R, and Shahidi M (2010) Thickness mapping of retinal layers by spectral-domain optical coherence tomography. *Am J Ophthalmol* 150: 849-855.

Loffler K U, and Lee W R (1986) Basal linear deposit in the human macula. *Graefes Arch Clin Exp Ophthalmol* 224: 493-501.

Lovasik J V (1983) An electrophysiological investigation of the macular photostress test. *Invest Ophthalmol Vis Sci* 24: 437-441.

Lovie-Kitchin J E (1988) Validity and reliability of visual acuity measurements. *Ophthalmic Physiol Opt* 8: 363-370.

Lundeen J S (2008) *Coherence (physics).* http://en.wikipedia.org/wiki/Coherence_(physics) Accessed: 16.07.2008

Luo D G, Xue T, and Yau K W (2008) How vision begins: an odyssey. *Proc Natl Acad Sci U S A* 105: 9855-9862.

Maguire M G (1999) Natural History. In: Berger, J W, Fine, S L, and Maguire, M G [eds.] *Age-related Macular Degeneration*. (1st edn.) St Louis, Missouri: Mosby Inc, pp. 17-30.

Maheshwary A S, Oster S F, Yuson R M, Cheng L, Mojana F, and Freeman W R (2010) The association between percent disruption of the photoreceptor inner segment-outer segment junction and visual acuity in diabetic macular edema. *Am J Ophthalmol* 150: 63-67.

Mahroo O A, and Lamb T D (2004) Recovery of the human photopic electroretinogram after bleaching exposures: estimation of pigment regeneration kinetics. *J Physiol* 554: 417-437.

Malamos P, Sacu S, Georgopoulos M, Kiss C, Pruente C, and Schmidt-Erfurth U (2009) Correlation of High-Definition Optical Coherence Tomography and Fluorescein Angiography Imaging in Neovascular Macular Degeneration. *Invest Ophthalmol Vis Sci* 50: 4926-4933.

Manjunath V, Taha M, Fujimoto J G, and Duker J S (2010) Choroidal Thickness in Normal Eyes Measured Using Cirrus HD Optical Coherence Tomography. *Am J Ophthalmol* 150: 325-329.

Mares-Perlman J A, Brady W E, Klein R, VandenLangenberg G M, Klein B E, and Palta M (1995) Dietary fat and age-related maculopathy. *Arch Ophthalmol* 113: 743-748.

Margolis R, and Spaide R F (2009) A Pilot Study of Enhanced Depth Imaging Optical Coherence Tomography of the Choroid in Normal Eyes. *Am J Ophthalmol* 147: 811-815.

Margrain T H, Boulton M, Marshall J, and Sliney D H (2004) Do blue light filters confer protection against age-related macular degeneration? *Prog Retin Eye Res* 23: 523-531.

Margrain T H, and Thomson D (2002) Sources of variability in the clinical photostress test. *Ophthalmic Physiol Opt* 22: 61-67.

Marmor M, and Zrenner E (2006) EOG standard. In: Heckenlively, J R, and Arden, G B [eds.] *Principles and Practice of Clinical Electrophysiology of Vision*. Cambridge, MA: MIT Press, pp. 289.

Marmor M F, Fulton A B, Holder G E, Miyake Y, Brigell M, and Bach M (2009) ISCEV Standard for full-field clinical electroretinography (2008 update). *Doc Ophthalmol* 118: 69-77.

Marmor M F, and Wolfensberger T J (1998) *The retinal pigment epithelium*. New York: Oxford University Press.

Martin D F, Maguire M G, Ying G S, Grunwald J E, Fine S L, Jaffe G J, and Grp C R (2011) Ranibizumab and Bevacizumab for Neovascular Age-Related Macular Degeneration The CATT Research Group. *N Engl J Med* 364: 1897-1908.

Massof R W, and Johnson M A (1981) Prereceptor light absorption in setters with neuronal ceroid lipofuscinosis. *Invest Ophthalmol Vis Sci* 20: 134-136.

Massof R W, Wu L, Finkelstein D, Perry C, Starr S J, and Johnson M A (1984) Properties of electroretinographic intensity-response functions in retinitis pigmentosa. *Doc Ophthalmol* 57: 279-296.

Mata N L, Moghrabi W N, Lee J S, Bui T V, Radu R A, Horwitz J, and Travis G H (2004) Rpe65 is a retinyl ester binding protein that presents insoluble substrate to the isomerase in retinal pigment epithelial cells. *J Biol Chem* 279: 635-643.

Mata N L, Radu R A, Clemmons R C, and Travis G H (2002) Isomerization and oxidation of vitamin a in cone-dominant retinas: a novel pathway for visual-pigment regeneration in daylight. *Neuron* 36: 69-80.

Mavrofrides E G, Villate N, Rosenfeld P J, and Puliafito C A (2004) Age-related macular degeneration. In: Schuman, J, Puliafito, C A, and Fujimoto, J G [eds.] *Optical Coherence Tomography of Ocular Diseases*. (2nd edn.) Thorofare, NJ: Slack Press, pp. 243-344.

Mayer M J, Dougherty R F, and Hu L T (1995) A covariance structure analysis of flicker sensitivity. *Vision Res* 35: 1575-1583.

Mayer M J, Ward B, Klein R, Talcott J B, Dougherty R F, and Glucs A (1994) Flicker sensitivity and fundus appearance in pre-exudative age-related maculopathy. *Invest Ophthalmol Vis Sci* 35: 1138-1149.

McLeod D S, Grebe R, Bhutto I, Merges C, Baba T, and Lutty G A (2009) Relationship between RPE and Choriocapillaris in Age-Related Macular Degeneration. *Invest Ophthalmol Vis Sci* 50: 4982-4991.

Medeiros N E, and Curcio C A (1997) Loss of neurons in the ganglion cell layer (GCL) of eyes with age-related maculopathy (ARM) and macular degeneration (AMD). *Invest Ophthalmol Vis Sci* 38: 443-443.

Medeiros N E, and Curcio C A (2001) Preservation of ganglion cell layer neurons in age-related macular degeneration. *Invest Ophthalmol Vis Sci* 42: 795-803.

Menke M N, and Feke G T (2005) Assessment of the effects of morphological changes related to age-related macular degeneration on optical coherence tomography retinal thickness measurements. *Ophthalmic Surg Lasers Imaging* 36: 310-314.

Mentzer A E, Eifler D M, Montiani-Ferreira F, Tuntivanich N, Forcier J Q, and Petersen-Jones S M (2005) Influence of recording electrode type and reference electrode position on the canine electroretinogram. *Doc Ophthalmol* 111: 95-106.

Miceli M V, Liles M R, and Newsome D A (1994) Evaluation of oxidative processes in human pigment epithelial cells associated with retinal outer segment phagocytosis. *Exp Cell Res* 214: 242-249.

Midena E, Degli Angeli C, Blarzino M C, Valenti M, and Segato T (1997) Macular function impairment in eyes with early age-related macular degeneration. *Invest Ophthalmol Vis Sci* 38: 469-477.

Midena E, Segato T, Blarzino M C, and Angeli C D (1994) Macular drusen and the sensitivity of the central visual field. *Doc Ophthalmol* 88: 179-185.

Miller R F, and Dowling J E (1970) Intracellular responses of the Muller (glial) cells of mudpuppy retina: their relation to b-wave of the electroretinogram. *J Neurophysiol* 33: 323-341.

Millodot M (2009) *Dictionary of Optometry and Visual Science*. 7th ed. New York: Butterworth-Heinemann.

Mitchell J, and Bradley C (2006) Quality of life in age-related macular degeneration: a review of the literature. *Health Qual Life Outcomes* 4: epub only.

Mitchell P, Korobelnik J F, Lanzetta P, Holz F G, Pruente C, Schmidt-Erfurth U, Tano Y et al. (2010) Ranibizumab (Lucentis) in neovascular age-related macular degeneration: evidence from clinical trials. *Br J Ophthalmol* 94: 2-13.

Mitchell P, Wang J J, Smith W, and Leeder S R (2002) Smoking and the 5-year incidence of age-related maculopathy - The Blue Mountains Eye Study. *Arch Ophthalmol* 120: 1357-1363.

Mitrut I, Verma A, Madill S, Smith R T, and Chong N V (2010) Color contrast and drusen area. *Ophthalmology* 117: 1280-1281.

Miyake Y, Horiguchi M, Ota I, and Shiroyama N (1987) Characteristic ERG-flicker anomaly in incomplete congenital stationary night blindness. *Invest Ophthalmol Vis Sci* 28: 1816-1823.

Miyake Y, Shiroyama N, Horiguchi M, and Ota I (1989) Asymmetry of focal ERG in human macular region. *Invest Ophthalmol Vis Sci* 30: 1743-1749.

Miyake Y, Shiroyama N, Ota I, and Horiguchi M (1988) Oscillatory potentials in electroretinograms of the human macular region. *Invest Ophthalmol Vis Sci* 29: 1631-1635.

Moore D J, and Clover G M (2001) The effect of age on the macromolecular permeability of human Bruch's membrane. *Invest Ophthalmol Vis Sci* 42: 2970-2975.

Moore D J, Hussain A A, and Marshall J (1995) Age-related variation in the hydraulic conductivity of Bruch's membrane. *Invest Ophthalmol Vis Sci* 36: 1290-1297.

Mortlock K E, Binns A M, Aldebasi Y H, and North R V (2010) Inter-subject, inter-ocular and inter-session repeatability of the photopic negative response of the electroretinogram recorded using DTL and skin electrodes. *Doc Ophthalmol* 121: 123-134.

Moutray T, Alarbi M, Mahon G, Stevenson M, and Chakravarthy U (2008) Relationships between clinical measures of visual function, fluorescein angiographic and optical coherence tomography features in patients with subfoveal choroidal neovascularisation. *Br J Ophthalmol* 92: 361-364.

MPSG (1993) Laser photocoagulation of subfoveal neovascular lesions of age-related macular degeneration. Updated findings from two clinical trials. Macular Photocoagulation Study Group. *Arch Ophthalmol* 111: 1200-1209.

MPSG (1994) Visual outcome after laser photocoagulation for subfoveal choroidal neovascularization secondary to age-related macular degeneration. The influence of initial

lesion size and initial visual acuity. Macular Photocoagulation Study Group. *Arch Ophthalmol* 112: 480-488.

MPSG (1996) Occult choroidal neovascularization. Influence on visual outcome in patients with age-related macular degeneration. *Arch Ophthalmol* 114: 400-412.

Murphy R P, Yeo J H, Green W R, and Patz A (1985) Dehiscences of the pigment epithelium. *Trans Am Ophthalmol Soc* 83: 63-81.

Naka K I (1969) Computer assisted analysis of S-potentials. *Biophys J* 9: 845-859.

Naka K I, and Rushton W A (1966a) S-potentials from colour units in the retina of fish (Cyprinidae). *J Physiol* 185: 536-555.

Naka K I, and Rushton W A (1966b) S-potentials from luminosity units in the retina of fish (Cyprinidae). *J Physiol* 185: 587-599.

Neelam K, Nolan J, Chakravarthy U, and Beatty S (2009) Psychophysical Function in Age-related Maculopathy. *Surv Ophthalmol* 54: 167-210.

Nelson R, and Connaughton V P (2003) *Bipolar cell pathways in the vertebrate retina.* www.webvision.med.utah.edu Accessed: 10/01/2011

Nelson R, Famiglietti E V, and Kolb H (1978) Intracellular staining reveals different levels of stratification for on- and off-center ganglion cells in cat retina. *J Neurophysiol* 41: 472-483.

Newman E A (1985) Membrane physiology of retinal glial (Müller) cells. *J Neurosci* 5: 2225-2239.

Newsom R S, McAlister J C, Saeed M, and McHugh J D (2001) Transpupillary thermotherapy (TTT) for the treatment of choroidal neovascularisation. *Br J Ophthalmol* 85: 173-178.

Newsome D A, and Negreiro M (2009) Reproducible measurement of macular light flash recovery time using a novel device can indicate the presence and worsening of macular diseases. *Curr Eye Res* 34: 162-170.

Nishihara H, Kondo M, Ishikawa K, Sugita T, Piao C-H, Nakamura Y, and Terasaki H (2008) Focal macular electroretinograms in eyes with wet type Age-related macular degeneration. *Invest Ophthalmol Vis Sci* 49: 3121-3125.

Noell W (1953) Studies on the electrophysiology and the metabolism of the retina. Randolph Field, Texas: United States Air Force School of Aerospace Medicine. pp. 1-122

Novotny H R, and Alvis D L (1961) A method of photographing fluorescence in circulating blood in human retina. *Circulation* 24: 82-86.

Nowak J Z (2006) Age-related macular degeneration (AMD): pathogenesis and therapy. *Pharmacol Rep* 58: 353-363.

Nozaki M, Raisler B J, Sakurai E, Sarma J V, Barnum S R, Lambris J D, Chen Y et al. (2006) Drusen complement components C3a and C5a promote choroidal neovascularization. *Proc Natl Acad Sci U S A* 103: 2328-2333.

Odom J V (2006) Amplifiers and Special Purpose Data Acquisition Systems. In: Heckenlively, J R, and Arden, G B [eds.] *Principles and Practice of Clinical Electrophysiology of Vision*. (2nd edn.) Cambridge, MA: MIT press, pp. 255-264.

Odom J V, Bach M, Brigell M, Holder G E, McCulloch D L, Tormene A P, and Vaegan (2010) ISCEV standard for clinical visual evoked potentials (2009 update). *Doc Ophthalmol* 120: 111-119.

Oster S F, Mojana F, Brar M, Yuson R M, Cheng L, and Freeman W R (2010) Disruption of the photoreceptor inner segment/outer segment layer on spectral domain-optical coherence tomography is a predictor of poor visual acuity in patients with epiretinal membranes. *Retina* 30: 713-718.

Osterberg G (1935) Topography of the layer of rods and cones in the human retina. *Acta Ophthalmol Suppl* 6: 1-103.

Owsley C (2003) Contrast sensitivity. *Ophthalmol Clin North Am* 16: 171-177.

Owsley C, Jackson G R, Cideciyan A V, Huang Y, Fine S L, Ho A C, Maguire M G et al. (2000) Psychophysical evidence for rod vulnerability in age-related macular degeneration. *Invest Ophthalmol Vis Sci* 41: 267-273.

Owsley C, Jackson G R, White M, Feist R, and Edwards D (2001) Delays in rod-mediated dark adaptation in early age-related maculopathy. *Ophthalmology* 108: 1196-1202.

Owsley C, McGwin Jr G, Jackson G R, Kallies K, and Clark M (2007) Cone- and Rod-Mediated Dark Adaptation Impairment in Age-Related Maculopathy. *Ophthalmology* 114: 1728-1735.

Owsley C, Sloane M E, Skalka H W, and Jackson C A (1990) A comparison of the regan low-contrast letter charts and contrast sensitivity testing in older patients. *Clin Vision Sci* 5: 325-334.

Pappuru R R, Ouyang Y, Nittala M G, Hemmati H D, Keane P A, Walsh A C, and Sadda S R (2011) Relationship between Outer Retinal Thickness Substructures and Visual Acuity in Eyes with Dry Age Related Macular Degeneration. *Invest Ophthalmol Vis Sci* 52: 6743-6748.

Parisi V (2001) Electrophysiological evaluation of the macular cone adaptation: VEP after photostress. *Doc Ophthalmol* 102: 251-262.

Pauleikhoff D, Hermans P, Holz F G, and Bird A (2004) Histopathology. In: Holz, F G, Pauleikhoff, D, Spaide, R F, and Bird, A C [eds.] *Age-related Macular Degeneration*. New York: Springer, pp. 48-64.

Paupoo A A, Mahroo O A, Friedburg C, and Lamb T D (2000) Human cone photoreceptor responses measured by the electroretinogram [correction of electoretinogram] a-wave during and after exposure to intense illumination. *J Physiol* 529 Pt 2: 469-482.

Peachey N S, Alexander K R, and Fishman G A (1987) Rod and cone system contributions to oscillatory potentials - an explanation for the conditioning flash effect. *Vision Res* 27: 859-866.

Peachey N S, Alexander K R, and Fishman G A (1989) The luminance-response function of the dark-adapted human electroretinogram. *Vision Res* 29: 263-270.

Peachey N S, Alexander K R, and Fishman G A (1991) Visual adaptation and the cone flicker electroretinogram. *Invest Ophthalmol Vis Sci* 32: 1517-1522.

Pelli D G, Robson J G, and Wilkins A J (1988) The design of a new letter chart for measuring contrast sensitivity. *Clin Vision Sci* 2: 187-199.

Penfold P L, Madigan M C, Gillies M C, and Provis J M (2001) Immunological and aetiological aspects of macular degeneration. *Prog Retin Eye Res* 20: 385-414.

Penn R D, and Hagins W A (1969) Signal transmission along retinal rods and origin of electroretinographic a-wave. *Nature* 223: 201-204.

Penn R D, and Hagins W A (1972) Kinetics of the photocurrent of retinal rods. *Biophys J* 12: 1073-1094.

Perry V H, and Cowey A (1981) The morphological correlates of X- and Y-like retinal ganglion cells in the retina of monkeys. *Exp Brain Res* 43: 226-228.

Perry V H, and Cowey A (1984) Retinal ganglion cells that project to the superior colliculus and pretectum in the macaque monkey. *Neuroscience* 12: 1125-1137.

Perry V H, Oehler R, and Cowey A (1984) Retinal ganglion cells that project to the dorsal lateral geniculate nucleus in the macaque monkey. *Neuroscience* 12: 1101-1123.

Phipps J A, Dang T M, Vingrys A J, and Guymer R H (2004) Flicker perimetry losses in age-related macular degeneration. *Invest Ophthalmol Vis Sci* 45: 3355-3360.

Phipps J A, Guymer R H, and Vingrys A J (2003) Loss of cone function in age-related maculopathy. *Invest Ophthalmol Vis Sci* 44: 2277-2283.

Piccardi M, Ziccardi L, Stifano G, Montrone L, Iarossi G, Minnella A, Fadda A et al. (2009) Regional cone-mediated dysfunction in age-related maculopathy evaluated by focal electroretinograms: relationship with retinal morphology and perimetric sensitivity. *Ophthalmic Res* 41: 194-202.

Pieramici D J, and Bressler S B (1998) Age-related macular degeneration and risk factors for the development of choroidal neovascularization in the fellow eye. *Curr Opin Ophthalmol* 9: 38-46.

Pieroni C G, Witkin A J, Ko T H, Fujimoto J G, Chan A, Schuman J S, Ishikawa H et al. (2006) Ultrahigh resolution optical coherence tomography in non-exudative age related macular degeneration. *Br J Ophthalmol* 90: 191-197.

Povazay B, Bizheva K, Hermann B, Unterhuber A, Sattmann H, Fercher A F, Drexler W et al. (2003) Enhanced visualization of choroidal vessels using ultrahigh resolution ophthalmic OCT at 1050 nm. *Opt Express* 11: 1980-1986.

Povazay B, Hermann B, Unterhuber A, Hofer B, Sattmann H, Zeiler F, Morgan J E et al. (2007a) Three-dimensional optical coherence tomography at 1050 nm versus 800 nm in retinal pathologies: enhanced performance and choroidal penetration in cataract patients. *J Biomed Opt* 12: epub only.

Povazay B, Hermann B, Unterhuber A, Hofer B, Sattmann H, Zeiler F, Morgan J E et al. (2007b) Three-dimensional optical coherence tomography at 1050 nm versus 800 nm in retinal pathologies: enhanced performance and choroidal penetration in cataract patients. *J Biomed Opt* 12: 041211.

Povazay B, Hofer B, Torti C, Hermann B, Tumlinson A R, Esmaeelpour M, Egan C A et al. (2009) Impact of enhanced resolution, speed and penetration on three-dimensional retinal optical coherence tomography. *Opt Express* 17: 4134-4150.

Provis J M, Diaz C M, and Dreher B (1998) Ontogeny of the primate fovea:a central issue in retinal development. *Prog Neurobiol* 54: 549-581.

Provis J M, Penfold P L, Cornish E E, Sandercoe T M, and Madigan M C (2005) Anatomy and development of the macula: specialisation and the vulnerability to macular degeneration. *Clin Exp Optom* 88: 269-281.

Ramrattan R S, van der Schaft T L, Mooy C M, de Bruijn W C, Mulder P G, and de Jong P T (1994) Morphometric analysis of Bruch's membrane, the choriocapillaris, and the choroid in aging. *Invest Ophthalmol Vis Sci* 35: 2857-2864.

Rasband W (1997) ImageJ. Bethesda, Maryland, USA: National Institutes of Health.

Redmond T M, Yu S, Lee E, Bok D, Hamasaki D, Chen N, Goletz P et al. (1998) Rpe65 is necessary for production of 11-cis-vitamin A in the retinal visual cycle. *Nat Genet* 20: 344-351.

Remulla J F, Gaudio A R, Miller S, and Sandberg M A (1995) Foveal electroretinograms and choroidal perfusion characteristics in fellow eyes of patients with unilateral neovascular age-related macular degeneration. *Br J Ophthalmol* 79: 558-561.

Riva C E, Cranstoun S D, Grunwald J E, and Petrig B L (1994) Choroidal blood flow in the foveal region of the human ocular fundus. *Invest Ophthalmol Vis Sci* 35: 4273-4281.

Robson J G, and Frishman L J (1995) Response linearity and kinetics of the cat retina - the bipolar cell component of the dark-adapted electroretinogram. *Vis Neurosci* 12: 837-850.

Rodieck R W (1972) Components of electroretinogram - reappraisal. *Vision Res* 12: 773-780.

Roecker E B, Pulos E, Bresnick G H, and Severns M (1992) Characterization of the electroretinographic scotopic B-wave amplitude in diabetic and normal subjects. *Invest Ophthalmol Vis Sci* 33: 1575-1583.

Roquet W, Roudot-Thoraval F, Coscas G, and Soubrane G (2004) Clinical features of drusenoid pigment epithelial detachment in age related macular degeneration. *Br J Ophthalmol* 88: 638-642.

Roth F, Bindewald A, and Holz F G (2004) Keypathophysiologic pathways in age-related macular disease. *Graefes Arch Clin Exp Ophthalmol* 242: 710-716.

Rovner B W, Casten R J, and Tasman W S (2002) Effect of depression on vision function in age-related macular degeneration. *Arch Ophthalmol* 120: 1041-1044.

Rushton W A H, and Henry G H (1968) Bleaching and regeneration of cone pigments in man. *Vision Res* 8: 617-631.

Saari J C (2000) Biochemistry of visual pigment regeneration: the Friedenwald lecture. *Invest Ophthalmol Vis Sci* 41: 337-348.

Sadda S R, Liakopoulos S, Keane P A, Ongchin S C, Msutta S, Chang K T, and Walsh A C (2010) Relationship between angiographic and optical coherence tomographic (OCT) parameters for quantifying choroidal neovascular lesions. *Graefes Arch Clin Exp Ophthalmol* 248: 175-184.

Sadda S R, Wu Z, Walsh A C, Richine L, Dougall J, Cortez R, and LaBree L D (2006) Errors in retinal thickness measurements obtained by optical coherence tomography. *Ophthalmology* 113: 285-293.

Sandberg M A, and Gaudio A R (1995) Slow photostress recovery and disease severity in age-related macular degeneration. *Retina* 15: 407-412.

Sandberg M A, Miller S, and Gaudio A R (1993) Foveal cone ERGs in fellow eyes of patients with unilateral neovascular age-related macular degeneration. *Invest Ophthalmol Vis Sci* 34: 3477-3480.

Sandberg M A, Pawlyk B S, and Berson E L (1996) Isolation of focal rod electroretinograms from the dark-adapted human eye. *Invest Ophthalmol Vis Sci* 37: 930-934.

Sandberg M A, Weiner A, Miller S, and Gaudio A R (1998) High-risk characteristics of fellow eyes of patients with unilateral neovascular age-related macular degeneration. *Ophthalmology* 105: 441-447.

Sangiovanni J P, Agron E, Meleth A D, Reed G F, Sperduto R D, Clemons T E, and Chew E Y (2009) Omega-3 Long-chain polyunsaturated fatty acid intake and 12-y incidence of neovascular age-related macular degeneration and central geographic atrophy: AREDS

report 30, a prospective cohort study from the Age-Related Eye Disease Study. *Am J Clin Nutr* 90: 1601-1607.

Sangiovanni J P, Chew E Y, Clemons T E, Ferris F L, 3rd, Gensler G, Lindblad A S, Milton R C et al. (2007) The relationship of dietary carotenoid and vitamin A, E, and C intake with age-related macular degeneration in a case-control study: AREDS Report No. 22. *Arch Ophthalmol* 125: 1225-1232.

Sarks J P, Sarks S H, and Killingsworth M C (1988) Evolution of geographic atrophy of the retinal pigment epithelium. *Eye* 2: 552-577.

Sarks S H (1976) Ageing and degeneration in the macular region: a clinico-pathological study. *Br J Ophthalmol* 60: 324-341.

Sarks S H (1980) Drusen and their relationship to senile macular degeneration. *Aust J Ophthalmol* 8: 117-130.

Sarks S H, Arnold J J, Killingsworth M C, and Sarks J P (1999) Early drusen formation in the normal and aging eye and their relation to age related maculopathy: a clinicopathological study. *Br J Ophthalmol* 83: 358-368.

Sarthy V P, Pignataro L, Pannicke T, Weick M, Reichenbach A, Harada T, Tanaka K et al. (2005) Glutamate transport by retinal Muller cells in glutamate/aspartate transporter-knockout mice. *Glia* 49: 184-196.

Schertler G F, Villa C, and Henderson R (1993) Projection structure of rhodopsin. *Nature* 362: 770-772.

Schmidt-Erfurth U, Leitgeb R A, Michels S, Povazay B, Sacu S, Hermann B, Ahlers C et al. (2005) Three-dimensional ultrahigh-resolution optical coherence tomography of macular diseases. *Invest Ophthalmol Vis Sci* 46: 3393-3402.

Schmitt J M (1999) Optical coherence tomography (OCT): A review. *IEEE J Sel Top Quantum Electron* 5: 1205-1215.

Schuchard R A (1993) Validitiy and interpretation of Amsler grid reports. *Arch Ophthalmol* 111: 776-780.

Schuman S G, Koreishi A F, Farsiu S, Jung S H, Izatt J A, and Toth C A (2009) Photoreceptor Layer Thinning over Drusen in Eyes with Age-Related Macular Degeneration Imaged In Vivo with Spectral-Domain Optical Coherence Tomography. *Ophthalmology* 116: 488-496.

Seddon J M, Ajani U A, Sperduto R D, Hiller R, Blair N, Burton T C, Farber M D et al. (1994) Dietary carotenoids, vitamins A, C, and E, and advanced age-related macular degeneration. Eye Disease Case-Control Study Group. *JAMA* 272: 1413-1420.

Seddon J M, Rosner B, Sperduto R D, Yannuzzi L, Haller J A, Blair N P, and Willett W (2001) Dietary fat and risk for advanced age-related macular degeneration. *Arch Ophthalmol* 119: 1191-1199.

Seiple W, Greenstein V, and Carr R (1989) Losses of temporal modulation sensitivity in retinal degenerations. *Br J Ophthalmol* 73: 440-447.

Severns M L, and Johnson M A (1993a) The care and fitting of Naka-Rushton functions to electroretinographic intensity-response data. *Doc Ophthalmol* 85: 135-150.

Severns M L, and Johnson M A (1993b) The variability of the b-wave of the electroretinogram with stimulus luminance. *Doc Ophthalmol* 84: 291-299.

Sharpe L T, Stockman A, and MacLeod D I (1989) Rod flicker perception: scotopic duality, phase lags and destructive interference. *Vision Res* 29: 1539-1559.

Shelley E J, Madigan M C, Natoli R, Penfold P L, and Provis J M (2009) Cone Degeneration in Aging and Age-Related Macular Degeneration. *Arch Ophthalmol* 127: 483-492.

Shiells R A, and Falk G (1999) Contribution of rod, on-bipolar, and horizontal cell light responses to the ERG of dogfish retina. *Vis Neurosci* 16: 503-511.

Shin H J, Chung H, and Kim H C (2011) Association between foveal microstructure and visual outcome in age-related macular degeneration. *Retina* 31: 1627-1636.

Sickel W (1972) Retinal metabolism in dark and light. In: Fuortes, M G F [ed.] *Handbook of Sensory Physiology.* Berlin: Springer-Verlag, pp. 667-727.

Sieving P A, Frishman L J, and Steinberg R H (1986) Scotopic threshold response of proximal retina in cat. *J Neurophysiol* 56: 1049-1061.

Simo R, Villarroel M, Corraliza L, Hernandez C, and Garcia-Ramirez M (2010) The retinal pigment epithelium: something more than a constituent of the blood-retinal barrier--implications for the pathogenesis of diabetic retinopathy. *J Biomed Biotechnol* 2010: epub only.

Skottun B C, Nordby K, and Magnussen S (1981) Photopic and scotopic flicker sensitivity of a rod monochromat. *Invest Ophthalmol Vis Sci* 21: 877-879.

Smiddy W E, and Fine S L (1984) Prognosis of patients with bilateral macular drusen. *Ophthalmology* 91: 271-277.

Snell R S, and Lemp M A (1998) *Clinical anatomy of the eye*. 2nd ed. London: Blackwell Science.

Soares A S, and LeBlanc R P (2006) Scanning Laser Tomograph. In: Huang, D, Kaiser, P K, Lowder, C Y, and Traboulsi, E I [eds.] *Retinal imaging*. Philadelphia: Mosby Elsevier, pp. 93-101.

Sperduto R D, Hiller R, Podgor M J, Palmberg P, Ferris F L, and Wentworth D (1986) Comparability of ophthalmic diagnoses by clinical and reading center examiners in the visual-acuity impairment survey pilot-study. *Am J Epidemiol* 124: 994-1003.

Stangos N, Voutas S, Topouzis F, and Karampatakis V (1995) Contrast sensitivity evaluation in eyes predisposed to age-related macular degeneration and presenting normal visual acuity. *Ophthalmologica* 209: 194-198.

Stefansson E, Geirsdottir A, and Sigurdsson H (2011) Metabolic physiology in age related macular degeneration. *Prog Retin Eye Res* 30: 72-80.

Steinmetz R L, Haimovici R, Jubb C, Fitzke F W, and Bird A C (1993) Symptomatic abnormalities of dark adaptation in patients with age-related Bruch's membrane change. *Br J Ophthalmol* 77: 549-554.

Stirling C E, and Lee A (1980) Ouabain 3H autoradiography of frog retina. *J Cell Biol* 85: 313-324.

Stockton R A, and Slaughter M M (1989) B-wave of the electroretinogram - a reflection of on bipolar cell-activity. *J Gen Physiol* 93: 101-122.

Stone J, and Fukuda Y (1974) Properties of cat retinal ganglion cells: a comparison of W-cells with X- and Y-cells. *J Neurophysiol* 37: 722-748.

Strauss O (2005) The retinal pigment epithelium in visual function. *Physiol Rev* 85: 845-881.

Stroud K A (1986) *Further Engineering Mathematics*. (3rd edn.) Basingstoke: Palgrave, pp. 953-964.

Sugita T, Kondo M, Piao C-H, Ito Y, and Terasaki H (2008) Correlation between Macular Volume and Focal Macular Electroretinogram in Patients with Retinitis Pigmentosa. *Invest Ophthalmol Vis Sci* 49: 3551-3558.

Sumita R (1961) The Fine Structure of Bruch's Membrane of the Human Choroid as Revealed by Electron Microscopy. *J Electron Microsc* 10: 111-118.

Sunness J S (1999) Geographic Atrophy. In: Berger, J W, Fine, S L, and Maguire, M G [eds.] *Age-related Macular Degeneration*. (1st edn.) St Louis, Missouri: Mosby Inc, pp. 155-166.

Sunness J S, Johnson M A, Massof R W, and Marcus S (1988) Retinal sensitivity over drusen and nondrusen areas. A study using fundus perimetry. *Arch Ophthalmol* 106: 1081-1084.

Sunness J S, Massof R W, Johnson M A, Finkelstein D, and Fine S L (1985) Peripheral retinal function in age-related macular degeneration. *Arch Ophthalmol* 103: 811-816.

Szmajda B A, Grunert U, and Martin P R (2008) Retinal ganglion cell inputs to the koniocellular pathway. *J Comp Neurol* 510: 251-268.

Taban M, Sharma S, Williams D R, Waheed N, and Kaiser P K (2009) Comparing Retinal Thickness Measurements Using Automated Fast Macular Thickness Map versus Six-Radial Line Scans with Manual Measurements. *Ophthalmology* 116: 964-970.

Tan J S, Mitchell P, Kifley A, Flood V, Smith W, and Wang J J (2007) Smoking and the long-term incidence of age-related macular degeneration: the Blue Mountains Eye Study. *Arch Ophthalmol* 125: 1089-1095.

Tan J S, Wang J J, Flood V, and Mitchell P (2009) Dietary fatty acids and the 10-year incidence of age-related macular degeneration: the Blue Mountains Eye Study. *Arch Ophthalmol* 127: 656-665.

Terasaki H, Ishikawa K, Niwa Y, Piao C H, Niwa T, Kondo M, Ito Y et al. (2004) Changes in focal macular ERGs after macular translocation surgery with 360 degrees retinotomy. *Invest Ophthalmol Vis Sci* 45: 567-573.

Terasaki H, Miyake Y, Niwa T, Ito Y, Suzuki T, Kikuchi M, and Kondo M (2002) Focal macular electroretinograms before and after removal of choroidal neovascular lesions. *Invest Ophthalmol Vis Sci* 43: 1540-1545.

Tolentino M J, Miller S, Gaudio A R, and Sandberg M A (1994) Visual field deficits in early age-related macular degeneration. *Vision Res* 34: 409-413.

Tomany S C, Cruickshanks K J, Klein R, Klein B E K, and Knudtson M D (2004) Sunlight and the 10-year incidence of age-related maculopathy - The Beaver Dam eye study. *Arch Ophthalmol* 122: 750-757.

Toth C A, Narayan D G, Boppart S A, Hee M R, Fujimoto J G, Birngruber R, Cain C P et al. (1997) A comparison of retinal morphology viewed by optical coherence tomography and by light microscopy. *Arch Ophthalmol* 115: 1425-1428.

UN (2005) World Population prospects: 2004 revision. Department of Economic and Social Affairs' Population Division, United Nations Organisation.

Unterhuber A, Povazay B, Hermann B, Sattmann H, Chavez-Pirson A, and Drexler W (2005) In vivo retinal optical coherence tomography at 1040 nm - enhanced penetration into the choroid. *Opt Express* 13: 3252-3258.

Van Cader T C (1978) History of ophthalmic photography. *J Ophth Photo* 1: 7-9.

van der Tweel L, and Estéves O (2006) Analytical Techniques. In: Heckenlively, J R, and Arden, G B [eds.] *Principles and Practice of Clinical Electrophysiology of Vision*. (2nd edn.) Cambridge, MA: MIT press, pp. 439-460.

Van Herick W, Shaffer R N, and Schwartz A (1969) Estimation of width of angle of anterior chamber. Incidence and significance of the narrow angle. *Am J Ophthalmol* 68: 626-629.

Van Velthoven M E, Faber D J, Verbraak F D, van Leeuwen T G, and de Smet M D (2007) Recent developments in optical coherence tomography for imaging the retina. *Prog Retin Eye Res* 26: 57-77.

Velten I M, Horn F K, Korth M, and Velten K (2001) The b-wave of the dark adapted flash electroretinogram in patients with advanced asymmetrical glaucoma and normal subjects. *Br J Ophthalmol* 85: 403-409.

Vingrys A J, and Garner L F (1987) The effect of a moderate level of hypoxia on human color vision. *Doc Ophthalmol* 66: 171-185.

Vingrys A J, and King-Smith P E (1988) A quantitative scoring technique for panel tests of color vision. *Invest Ophthalmol Vis Sci* 29: 50-63.

Virgili G, and Bini A (2007) Laser photocoagulation for neovascular age-related macular degeneration. *Cochrane Database Syst Rev*.

Viswanathan S, Frishman L J, and Robson J G (2002) Inner-retinal contributions to the photopic sinusoidal flicker electroretinogram of macaques: Macaque photopic sinusoidal flicker ERG. *Doc Ophthalmol* 105: 223-242.

Viswanathan S, Frishman L J, Robson J G, Harwerth R S, and Smith E L (1999) The photopic negative response of the macaque electroretinogram: Reduction by experimental glaucoma. *Invest Ophthalmol Vis Sci* 40: 1124-1136.

Viswanathan S, Frishman L J, Robson J G, and Walters J W (2001) The photopic negative response of the flash electroretinogram in primary open angle glaucoma. *Invest Ophthalmol Vis Sci* 42: 514-522.

Wakabayashi K, Gieser J, and Sieving P A (1988) Aspartate separation of the scotopic threshold response (STR) from the photoreceptor a-wave of the cat and monkey ERG. *Invest Ophthalmol Vis Sci* 29: 1615-1622.

Walter P, Widder R A, Luke C, Konigsfeld P, and Brunner R (1999) Electrophysiological abnormalities in age-related macular degeneration. *Graefes Arch Clin Exp Ophthalmol* 237: 962-968.

Wang J-S, and Kefalov V J (2011) The Cone-specific visual cycle. *Prog Retin Eye Res* 30: 115-128.

Wang L, Li C M, Rudolf M, Belyaeva O V, Chung B H, Messinger J D, Kedishvili N Y et al. (2009) Lipoprotein particles of intraocular origin in human Bruch membrane: an unusual lipid profile. *Invest Ophthalmol Vis Sci* 50: 870-877.

Webb R H, and Hughes G W (1981) Scanning laser ophthalmoscope. *IEEE Trans Biomed Eng* 28: 488-492.

Webb R H, Hughes G W, and Delori F C (1987) Confocal scanning laser ophthalmoscope. *Appl Opt* 26: 1492-1499.

Weiner A, and Sandberg M A (1991) Normal change in the foveal cone ERG with increasing duration of light exposure. *Invest Ophthalmol Vis Sci* 32: 2842-2845.

Weisinger H, Vingrys A, and Sinclair A (1996) Electrodiagnostic methods in vision Part1. Clinical application and measurement. *Clin Exp Optom* 79: 50-61.

Weleber R G (1981) The effect of age on human cone and rod ganzfeld electroretinograms. *Invest Ophthalmol Vis Sci* 20: 392-399.

Westheimer G (1966) The Maxwellian view. *Vision Res* 6: 669-682.

Wilden U, Wust E, Weyand I, and Kuhn H (1986) Rapid affinity purification of retinal arrestin (48 kDa protein) via its light-dependent binding to phosphorylated rhodopsin. *FEBS Lett* 207: 292-295.

Witkovsky P, Dudek F E, and Ripps H (1975) Slow PIII component of carp electroretinogram. *J Gen Physiol* 65: 119-134.

Witmer A N, Vrensen G F, Van Noorden C J, and Schlingemann R O (2003) Vascular endothelial growth factors and angiogenesis in eye disease. *Prog Retin Eye Res* 22: 1-29.

Wolffsohn J S, Anderson S J, Mitchell J, Woodcock A, Rubinstein M, Ffytche T, Browning A et al. (2006) Effect of age related macular degeneration on the Eger macular stressometer photostress recovery time. *Br J Ophthalmol* 90: 432-434.

Wood A, Binns A, Margrain T, Drexler W, Povazay B, Esmaeelpour M, and Sheen N (2011a) Retinal and choroidal thickness in early Age-related macular degeneration *Am J Ophthalmol*: In press.

Wood A, Margrain T, and Binns A (2011b) The effect of bleach duration and age on the ERG photostress test. *Graefes Arch Clin Exp Ophthalmol* 249: 1359-1365.

Wu Q, Blakeley L R, Cornwall M C, Crouch R K, Wiggert B N, and Koutalos Y (2007) Interphotoreceptor retinoid-binding protein is the physiologically relevant carrier that removes retinol from rod photoreceptor outer segments. *Biochemistry* 46: 8669-8679.

Wyszeki G, and Stiles W S (1982) *Colour Science: Concepts and methods, quantative data and formulae.* 2nd ed. New York: Wiley-Interscience.

Xu H, Chen M, and Forrester J V (2009) Para-inflammation in the aging retina. *Prog Retin Eye Res* 28: 348-368.

Xu X, and Karwoski C J (1994) Current source density analysis of retinal field potentials. II. Pharmacological analysis of the b-wave and M-wave. *J Neurophysiol* 72: 96-105.

Yamada Y, Ishibashi K, Bhutto I A, Tian J, Lutty G A, and Handa J T (2006) The expression of advanced glycation endproduct receptors in rpe cells associated with basal deposits in human maculas. *Exp Eye Res* 82: 840-848.

Yamaguchi Y, Otani T, and Kishi S (2000) Comparison of optical coherence tomography and retinal thickness analyser. *Rinsho Ganka* 54: 941-945.

Yau K W (1994) Phototransduction mechanism in retinal rods and cones. The Friedenwald Lecture. *Invest Ophthalmol Vis Sci* 35: 9-32.

Yonemura D, Kawasaki K, Shibata N, and Tanabe J (1974) Electroretinographic PIII component of human excised retina. *Jpn J Ophthalmol* 18: 322-333.

Young R W, and Bok D (1969) Participation of the retinal pigment epithelium in the rod outer segment renewal process. *J Cell Biol* 42: 392-403.

Yuda K, Inoue Y, Tomidokoro A, Tamaki Y, and Yanagi Y (2010) Nerve fiber layer thickness in exudative age-related macular degeneration in Japanese patients. *Graefes Arch Clin Exp Ophthalmol* 248: 353-359.

Zarbin M A (2004) Current concepts in the pathogenesis of age-related macular degeneration. *Arch Ophthalmol* 122: 598-614.

Zayit-Soudry S, Moroz I, and Loewenstein A (2007) Retinal pigment epithelial detachment. *Surv Ophthalmol* 52: 227-243.

Appendix A: Photobleach calculation

Calculating percentage of rhodopsin bleached

Rhodopsin bleaches in this thesis were calculated using the equation described by Thomas and Lamb (1999) (see equation A.1). Values reported and used by Thomas and Lamb (1999) included a bleaching constant of 10^7 Td.s (L_{Rh}) and a time constant of 420 s (τ_{Rh}) additionally by using Equation A.2 it was possible to calculate I_{Rh} as 23809 td. These values were used in this thesis to calculate rhodopsin bleaches, example calculations are shown below for both a short (photoflash) and long (equilibrium) duration rhodopsin bleach.

$$B = \frac{I}{I + I_{\mathrm{Rh}}} \left(1 - \exp\left(-\left(1 + \frac{I}{I_{\mathrm{Rh}}}\right) \frac{t}{\tau_{\mathrm{Rh}}}\right)\right),$$

Equation A.1: *Photobleach calculation from Thomas and Lamb (1999),* ***B*** *= percentage of rhodopsin photopigment bleached,* ***I*** *retinal illuminance,* ***t*** *exposure duration,* I_{Rh} *bleaching constant and* τ_{Rh} *time constant*

$$L_{Rh} = I_{Rh} . \tau_{Rh}$$

Equation A.2: *Where* I_{Rh} *is the light intensity at which half the rhodopsin is bleached,* L_{Rh} *is the rhodopsin bleaching constant and* τ_{Rh} *is the time constant of rhodopsin regeneration (Thomas and Lamb, 1999).*

Example calculations:

Mecablitz C-76 Flashunit “photoflash bleach”

t 6.6 ms

I 2.97E+09 Td

Irh 23809 Td

τrh 420 s

Lrh 1.00E+07 Td.s

Rhodopsin bleach (B) 86.2 %

Ganzfeld “equilibrium bleach”

t 120 s

I 3.98E+05 Td

Irh 23809 Td

τrh 420 s

Lrh 1.00E+07 Td.s

Rhodopsin bleach (B) 93.8 %

Calculating percentage of iodopsin bleached

Iodopsin bleaches in this thesis were calculated using the equation described by Paupoo et al. (2000) originally adapted from Equation A.1 as described by Thomas and Lamb (1999). Unlike rhodopsin bleaches, the time constant for iodopsin bleaches varies according to the bleach duration, with long duration equilibrium bleaches having a fixed time constant whereas shorter duration bleaches (<10 seconds duration) have a smaller time constant related to the bleach duration (Rushton and Henry, 1968; Hollins and Alpern, 1973). Hollins and Alpern (1973) reported a iodopsin time constant of 105 s for equilibrium (>10 second) bleaches, whilst shorter duration bleach (i.e. photoflash bleach) were shown to decrease with shorter bleach duration to a lower limit of 65 s. Hollins and Alpern (1973) also reported a bleaching constant ($\mathbf{I_p}$) of 30000 td for iodopsin. These values reported and used by Hollins and Alpern were used in this thesis to calculate iodopsin bleaches, for equilibrium (long duration) bleaches a time constant of 105s was used and a time constant of 65 s was used for (short duration) photoflash bleaches. Additionally, the bleaching constant ($\mathbf{L_p}$) was calculated, using Equation A.3, for each type of bleach, $\mathbf{L_p}$ = 3.15x10^6 td.s for an equilibrium (long duration) bleach ($\boldsymbol{\tau_p}$ = 105 s) and $\mathbf{L_p}$ = 1.92x10^6 td.s for a photoflash (short duration) bleach ($\boldsymbol{\tau_p}$ = 65 s). Below example calculations are shown below for both photoflash and equilibrium iodopsin bleaches.

$$B = \frac{I}{I + I_P}\left(1 - \exp\left(-\left(1 + \frac{I}{I_P}\right)\frac{t}{\tau_P}\right)\right)$$

Equation A.3: *Photobleach calculation from Paupoo et al. (2000),* ***B*** *= percentage of iodopsin photopigment bleached,* ***I*** *retinal illuminance,* ***t*** *exposure duration,* $\boldsymbol{I_p}$ *bleaching constant and* $\boldsymbol{\tau_p}$ *time constant.*

$$\mathbf{L_p = I_p . \tau_p}$$

Equation A.4: *The above was derived from Thomas and Lamb (1999) for Iodopsin. Where* I_p *is the light intensity at which half the iodopsin is bleached,* L_p *is the iodopsin bleaching constant and* τ_p *is the time constant of iodopsin regeneration.*

Example calculations:

Mecablitz C-76 Flashunit “photoflash bleach”

t 6.6 ms

I 1.19E+09 Td

Ip 30000 Td

τp 64 s

Lp 1.00E+07 Td.s

Iodopsin bleach (B) 98.4 %

Ganzfeld “equilibrium bleach”

t 120 s

I 1.59E+05 Td

Ip 30000 Td

τp 105 s

Lp 1.00E+07 Td.s

Iodopsin bleach (B) 84.1%

References

Hollins M, and Alpern M (1973) Dark adaptation and visual pigment regeneration in human cones. *J Gen Physiol* 62: 430-447.

Paupoo A A, Mahroo O A, Friedburg C, and Lamb T D (2000) Human cone photoreceptor responses measured by the electroretinogram [correction of electoretinogram] a-wave during and after exposure to intense illumination. *J Physiol* 529 Pt 2: 469-482.

Rushton W A H, and Henry G H (1968) Bleaching and regeneration of cone pigments in man. *Vision Res* 8: 617-631.

Thomas M M, and Lamb T D (1999) Light adaptation and dark adaptation of human rod photoreceptors measured from the a-wave of the electroretinogram. *J Physiol* 518 (Pt 2): 479-496.

Appendix B: Maxwellian view photobleach

The following appendix describes the calibration of the Maxwellian view optical system used in this thesis. Maxwellian viewing is the principle of imaging the light source directly into the pupil plane, rather than viewing it directly. Provided that the source is smaller than the pupil area, it can be assumed under these conditions that all the light from the source enters the pupil (Westheimer, 1966).

A Maxwellian view optical system was set up consisting of a super bright white LED and two 20D lenses. An eye piece was positioned such that the image of the source would be positioned at the pupil plane of the viewing eye. The retinal illuminance was calculated using the following equation (Westheimer, 1966) by measuring the illuminance of a perfectly diffusing surface at a set distance, illuminated by the Maxwellian view system.

Equation B.1: Retinal illuminance (td) = $10^7 B x^2 / r$

B = luminance of perfectly diffusing surface (mL)
r = reflectance of surface
x = distance from image plane to surface (m)

The photometer measurement was converted from $cd.m^{-2}$ to millilamberts (1mL is equal to $10/\pi$ cdm^{-2}).

Calibration

The Maxwellian view optical system was setup and the image projected onto a uniform surface (reflectance ~ 84.2%) at 0.185 m (x), the luminance of the surface was then measured at a range of voltages using a photometer (LS-110; Konica Minolta, Osaka, Japan). Retinal illuminance values were calculated using equation B.1.

Volts (v)	($cd.m^{-2}$)	(Log td.s)
2.5	0.09	4.06
3	0.70	4.95
4	2.59	5.52
5	4.16	5.73
6	6.18	5.90
9	10.66	6.13

Table B.1: Table showing the voltages, measured luminances and the calculated log trolands values for the source at each voltage.

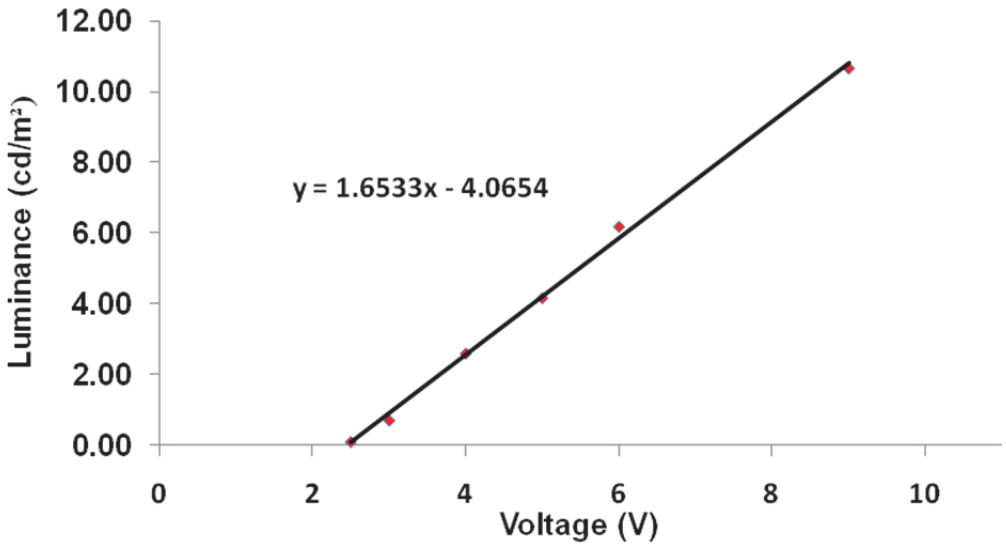

Figure B.1: Graph showing the relationship between illuminance and voltage for the maxwellian view optical system at a distance of 0.185 m, equation shown is that of the linear best fit of the data.

Photopigment Bleach (%)	(Log td.s)	(td.s)	Millilamberts (mL)	(cd.m^{-2})	Voltage (V)
95	5.76	570123.66	1.40	4.46	5.16
90	5.44	277887.50	0.68	2.18	3.78
80	**5.16**	**145657.56**	**0.36**	**1.14**	**3.15**
70	4.99	98420.65	0.24	0.77	2.93
60	4.85	70932.47	0.17	0.56	2.79
50	4.71	51811.67	0.13	0.41	2.70
40	4.57	37244.28	0.09	0.29	2.64
30	4.41	25518.99	0.06	0.20	2.58

Table B.2: Table showing the calculating of voltage requirement to obtain a range of photopigment bleaching using the maxwellian view optical system assuming a 60 second exposure. Retinal illuminance was calculated using equation B.1 and the final determination of voltage was achieved by applying the value to the equation of a straight line from figure B.1. The photopigment (iodopsin) bleach was calculated as described in Appendix A; the values for an 80% iodopsin photopigment bleach as required for the ERG photostress test are highlighted in bold.

References

Westheimer G (1966) The Maxwellian view. *Vision Res* 6: 669-682.

Appendix C: Photoflash calibration and safety

This appendix describes a series of calculations to demonstrate the compliance of the Metz Mecablitz C76 photoflash unit with the relevant safety regulations. The calibration of the unit is also described.

Prior to use, the safety of the photoflash needed to be demonstrated; the appropriate safety regulations are laid out in the British Standard BSEN 15004:2 (BSI, 2007) "*Ophthalmic Instruments - fundamental requirements and test methods Part 2 - Light Hazard Protection*". These standards are based upon the International Commission on Non-Ionizing Radiation Protection (ICNIRP, 1997) guidelines.

The ICNIRP guidelines provide spectral weightings and calculations for 3 primary types of exposure hazard:

- **Retinal thermal hazard** (380-1400 nm)
- **Blue-light photochemical hazard** (300-700 nm)
- **Infrared radiation hazards to the eye** (780-3000 nm) divided into, cornea & lens, retina and skin.

British Standards (BSI, 2007) annex C state that, if the output of a white light source is less than 1 $cd.m^{-2}$, then spectral data is not required when calculating the safe exposure limit. The Metz Mecablitz C76 output exceeds this value. The manufacturer kindly provided the spectral output distribution of the unit (see figure C.1), and the total radiometric output was obtained by the using a light meter (IL1700; International Light Inc., Newburyport, MA) with a SED033 detector. This allowed the radiometric output to be determined at 5 nm wavelength intervals.

The spectral irradiance (E_λ) was calculated by dividing the total light output measured using the light meter, by the known spectral distribution of the flash (see figure C.1). This information was then multiplied by a wavelength specific calibration factor (provided by International Light Inc., Newburyport, MA), for each wavelength to produce an irradiance output in Wcm^{-2}. The spectral radiance (L_λ) was also calculated for the flash by multiplying the spectral irradiance (E_λ) by the flash duration.

The calculated spectral irradiance and spectral radiance values were applied to the safety calculations identified in BSEN 15004:2 (BSI, 2007), utilising the specific spectral weightings within the guidelines. In order to confirm the safety of the photoflash, the safety calculations produced by the ICNIRP (1997) were also carried out. The individual calculations are shown below in figures C.2 to C.6; the symbols used are identified in table C.1.

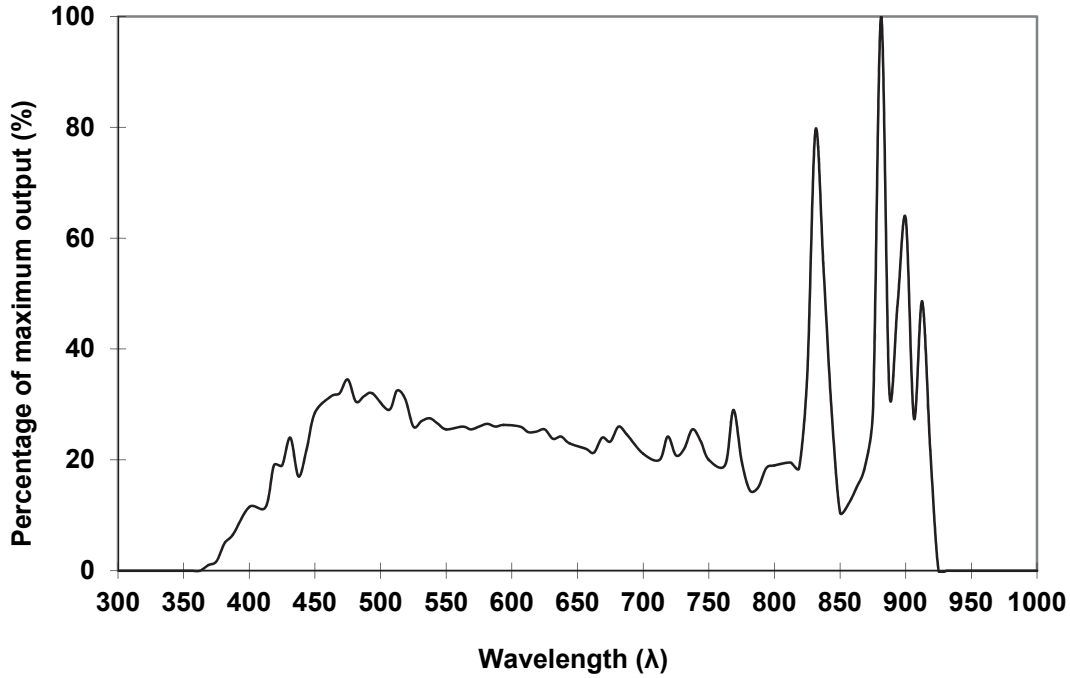

Figure C.1: "Spectral distribution of Mecablitz C76 Flash" as provided by Metz.

5.5.1.1	Weighted corneal and lenticular ultraviolet radiation radiant exposure, $H_{S\text{-}CL}$	250 to 400	$H_{S\text{-}CL} = \sum_{250}^{400} (E_\lambda \times t) \times S(\lambda) \times \Delta\lambda$	3 mJ/cm^2

Figure C.2: Corneal and lenticular ultraviolet radiation exposure limit (BSI, 2007)

a)	Weighted retinal visible and infrared radiation radiant exposure, $H_{VIR\text{-}R}$	380 to 1 400	$H_{VIR-R} = \sum_{380}^{1\,400} (E_\lambda \times \Delta t) \times R(\lambda) \times \Delta\lambda$	$\left(\frac{10}{d_r} t^{3/4}\right) \frac{J}{cm^2}$

Figure C.3: Visible and infrared radiation limit values (BSI, 2007)

5.5.2.2	Unweighted corneal and lenticular infrared radiation radiant exposure, $H_{IR\text{-}CL}$	770 to 2 500	$H_{IR-CL} = \sum_{770}^{2\,500} H_\lambda \times \Delta\lambda$	1,8 $t^{1/4}$ J/cm^2

Figure C.4: Corneal and lenticular infrared radiation exposure limit (BSI, 2007)

$$L_B \cdot t = \sum_{300}^{700} L_\lambda \cdot B(\lambda) \cdot t \cdot \Delta\lambda$$

$$\leq 100 \text{ J cm}^{-2} \text{ sr}^{-1} \text{ (effective)},$$

Figure C.5: Blue-light photochemical retinal hazard (300-700 nm)(ICNIRP, 1997)

$$\sum_{380}^{1,400} L_\lambda \cdot R(\lambda) \cdot \Delta\lambda < L_{\mathrm{HAZ}}.$$

$$L_{\mathrm{HAZ}} = 5/(\alpha \cdot t^{0.25}) (\mathrm{in\ W\ cm^{-2}\ sr^{-1}}).$$

Figure C.6: Retina infrared exposure limit (380-1400nm) (ICNIRP, 1997)

Symbol	Quantity	Unit
E_λ	Spectral irradiance	W/cm^2
L_λ	Spectral radiance	J/cm^2
$E_{S\text{-}CL}$	Weighted corneal and lenticular ultraviolet radiation irradiance	W/cm^2
$E_{VIR\text{-}R}$	Weighted retinal visible and infrared radiation thermal irradiance	W/cm^2
$H_{IR\text{-}CL}$	Unweighted corneal and lenticular infrared radiation radiant exposure	J/cm^2
L_{haz}	Limit for radiant exposure	
$L_B.t$	Limit for blue light photochemical exposure	
$S(\lambda)$	Ultraviolet radiation hazard weighting function	
$R(\lambda)$	Visible and infrared radiation thermal hazard weighting function	
$\Delta\lambda$	Summation interval	nm
α	Angular sub tense of light source	Maximum value 0.1 radians
d_r	Minimum retinal image diameter	If greater than 1.7mm use 1.7 If less then 0.03mm use 0.03
t	Exposure time	s

Table C.1: Symbols as used by light hazard protection calculation for BSI (BSI, 2007) and ICNIRP (ICNIRP, 1997) standards.

Flash calibration

To ensure that the photoflash bleached the correct amount of photopigment the consistency of the flash output was assessed. The luminance of the C-76 Mecablitz flash unit was measured using the IL1700 light meter for 27 consecutive discharges at maximum output. In addition, to determine if the flash intensity remained constant after a period of inactivity, similar to that which may occur in the laboratory during the study, the flash unit was stored for 7 days without recharging before a further 10 consecutive discharges were measured.

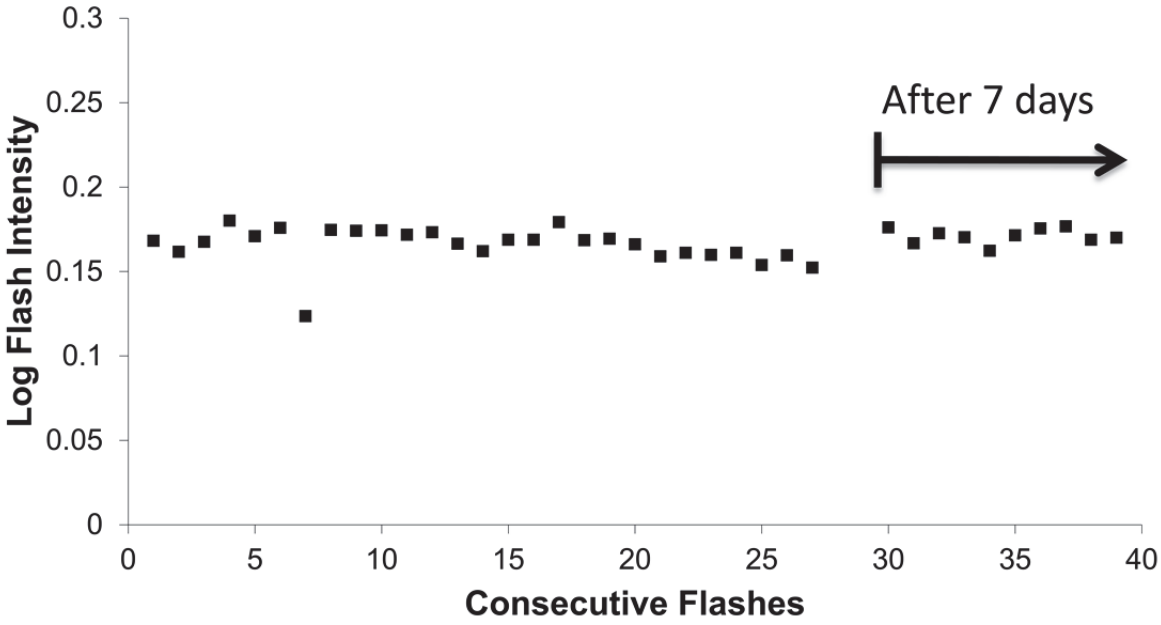

Figure C.7: A graph showing the log flash intensity for a series of consecutive photoflash discharges on two occasions separated by a 7 day interval without recharging the photoflash unit.

The results (see figure C.7) indicated that the flash output remain relatively constant between consecutive flashes and following a period of inactivity (up to 7 days). All measured flashes were within 0.1 log units of each other. The flash consistency was deemed satisfactory, given that no more than 4 consecutive discharges per patient visit were likely and that the unit was not left without recharging for a period greater than 1 week prior to a patient visit.

Reference

BSI (2007) Ophthalmic Instruments - fundamental requirements and test methods Part 2 - Light Hazard Protection. *British Standards Institute* BS EN 15004-2.

ICNIRP (1997) Guidelines on limits of exposure to broad-band incoherent optical radiation (0.38 to 3 microM). International Commission on Non-Ionizing Radiation Protection. *Health Phys* 73: 539-554.

Appendix D: ERG luminance calibration

The ERG techniques employed during this thesis required a variety of focal and background light stimuli. The protocols required specific luminance values; the following describes the luminance calculations for each of the stimuli employed in the final protocols and the calibration carried out over the period of data collection. After initial calibration the equipment was reassessed prior to periods of data collection and repeated at regular (approximately monthly) intervals within these periods. All luminance measurements were obtained using a photometer (LS-110; Konica Minolta, Osaka, Japan).

Photopic focal ERG stimuli

The photopic ERG techniques (Focal Cone ERG, Focal flicker ERG and ERG photostress test) utilised a focal ERG stimulus with a time averaged luminance of 30 $cd.m^{-2}$ presented at different temporal frequencies using a 50% duty cycle. The stimulus was calibrated with a constant (non-flickering) light to a luminance value of 60 $cd.m^{-2}$, with the photometer focused at the centre of the stimulus. Over the course of the data collection period a range of between 59.92 and 67.43 $cd.m^{-2}$ with a mean of 62.55 $cd.m^{-2}$ was measured from the stimuli (see table D).

Measurement date	Luminance $cd.m^{-2}$
Initial	**60.00**
08.01.2010	61.82
25.01.2010	60.32
10.02.2010	59.92
01.03.2010	68.47
23.04.2010	60.29
11.05.2010	61.17
02.06.2010	67.43
16.08.2010	65.62
24.09.2010	62.82
13.05.2011	60.54
09.06.2011	62.18
Mean	**62.55**
Standard deviation	**2.99**

Table D.1: Luminance of the focal stimuli for the photopic ERG techniques, the figure in bold indivated the initial calibration luminance.

Photopic suppressing background

The photopic ERG techniques (Focal Cone ERG, Focal flicker ERG and ERG photostress test) utilised a white light suppressing background which was luminance matched to the time averaged luminance (30 $cd.m^{-2}$) of the focal stimulus used. The background was calibrated for a point approximately 10 cm above the focal stimulus. Over the course of the data collection period a range of between 26.46 and 33.01 $cd.m^{-2}$ with a mean of 29.26 $cd.m^{-2}$ was measured for the photopic background (see table D.2).

Measurement date	Luminance $cd.m^{-2}$
Initial	**30.00**
08.01.2010	30.04
25.01.2010	29.36
10.02.2010	26.46
01.03.2010	27.00
23.04.2010	28.84
11.05.2010	28.17
02.06.2010	28.62
16.08.2010	29.49
24.09.2010	30.10
13.05.2011	29.98
09.06.2011	33.01
Mean	**29.26**
Standard deviation	**1.68**

Table D.2: Luminance of the suppressing background used for the photopic ERG techniques, the figure in bold indicate the initial calibration luminance.

Scotopic focal ERG stimuli

The focal rod ERG was recorded using both a low (20 scotopic td.s) and high (500 scotopic td.s) luminance focal stimulus. As the photometer measures in photopic $cd.m^{-2}$, the measurements were converted from photopic to scotopic units using the conversion factor of 26.66 for blue light (454 nm), taking account of the rod spectral sensitivity (Wyszeki and Stiles, 1982). Conversion to trolands assumed a dilated pupil (area = 50 mm^2). Therefore the constant photopic luminance of the stimuli for a flash duration of 5 and 10 ms respectively for the low and high luminance targets were calculated as follows:

Low Luminance

(20/50)/26.66 * (1000/5) = 3

Scotopic retinal illuminance = 20 scotopic td.s
Pupil diameter = 50 mm²
Conversion factor for 454 nm light = 26.66
Stimulus duration = 5 ms

High Luminance

(500/50)/26.66 * (1000/10) = 37.5

Scotopic retinal illuminance = 500 scotopic td.s
Pupil diameter = 50 mm²
Conversion factor for 454 nm light = 26.66
Stimulus duration = 5 ms

Measurement date	Low luminance stimuli cd.m²	High luminance stimuli cd.m²
Initial	**3.00**	**37.50**
08.01.2010	5.50	34.50
25.01.2010	3.83	29.50
10.02.2010	4.13	33.09
01.03.2010	3.06	31.17
23.04.2010	5.52	32.40
11.05.2010	3.34	32.26
02.06.2010	2.98	35.33
16.08.2010	2.94	32.14
24.09.2010	3.06	34.13
13.05.2011	3.44	34.03
09.06.2011	3.45	35.16
Mean	**3.69**	**33.43**
Standard deviation	**0.93**	**2.13**

Table D.3: Luminance of high and low luminace focal stimuli for the focal rod ERG, the figures in bold indicate the initial calibration luminace.

The scotopic focal stimuli were therefore calibrated to provide a constant output of 3 and 37.5 $cd.m^{-2}$ for the low and high luminance stimuli respectively. Over the course of the data collection period the low luminance target ranged between 2.94 and 5.52 $cd.m^{-2}$ with a mean of 3.69 $cd.m^{-2}$ whilst the high luminance target ranged between 29.50 and 37.50 $cd.m^{-2}$ with a mean of 33.43 $cd.m^{-2}$ (see table D.3). These means equate to scotopic values of 24.9 and 442.6 scotopic td.s for the low and high luminance stimuli respectively.

Scotopic suppressing background

The focal rod ERG technique, as described by Binns and Margain (Binns and Margrain, 2006), utilised a log 1.67 scotopic td.s green Ganzfeld surround. The equivalent photopic luminance was calculated to be 0.33 $cd.m^{-2}$, assuming a conversion factor from scotopic to photopic sensitivity for green light (525 nm) of 2.81(Wyszeki and Stiles, 1982). Conversion to trolands assumed a dilated pupil (area = 50 mm^2). Over the course of the data collection period a range of between 1.38 to 1.80 log scotopic td.s was measured, with a mean of 1.58 log scotopic td.s (see table D.4).

Measurement date	Luminance	
	$cd.m^{-2}$	log scotopic td.s
Initial	**0.33**	**1.67**
08.01.2010	0.45	1.80
25.01.2010	0.41	1.76
10.02.2010	0.21	1.47
01.03.2010	0.24	1.53
23.04.2010	0.23	1.51
11.05.2010	0.26	1.56
02.06.2010	0.17	1.38
16.08.2010	0.24	1.53
24.09.2010	0.21	1.47
13.05.2011	0.27	1.58
09.06.2011	0.38	1.73
Mean	**0.28**	**1.58**
Standard deviation	**0.09**	**0.13**

Table D.4: Scotopic suppressing background initial calibration (bold) and consecutive luminance measured during data collection.

Maxwellian view bleaching unit

The calibration for the Maxwellian view optical system has been previously described in Appendix B, these luminance measurements were obtained using the same methodology. Over the course of the data collection period the bleaching luminance ranged between 1.07 and 1.14 $cd.m^{-2}$, with a mean of 1.12 $cd.m^{-2}$ (see table D.5).

Measurement date	Luminance $cd.m^{-2}$
Initial	**1.14**
08.01.2010	1.09
25.01.2010	1.14
10.02.2010	1.12
01.03.2010	1.07
23.04.2010	1.12
11.05.2010	1.14
02.06.2010	1.09
16.08.2010	1.14
24.09.2010	1.12
13.05.2011	1.14
09.06.2011	1.12
Mean	**1.12**
Standard deviation	**0.02**

Table D.5: Luminance of the maxwellian view optical system as used for the ERG photostress test, the figure in bold indicates the initial calibration luminace.

References

Binns A M, and Margrain T H (2006) Development of a technique for recording the focal rod ERG. *Ophthalmic Physiol Opt* 26: 71-79.

Wyszeki G, and Stiles W S (1982) *Colour Science: Concepts and methods, quantative data and formulae.* 2nd Edition ed. New York: Wiley-Interscience.

Appendix E: Focal rod ERG intensity response data

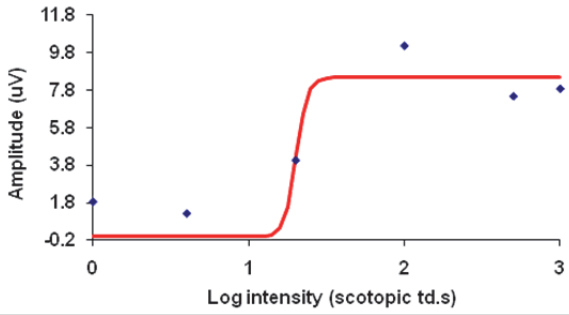

BA1 Rmax=8.51, n=34.89, LogK=1.30

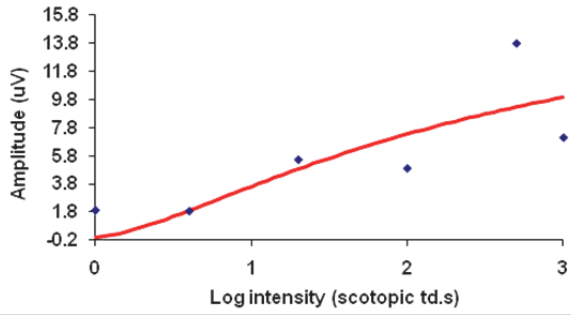

BA2 Rmax=17.42, n=1.48, LogK=2.47

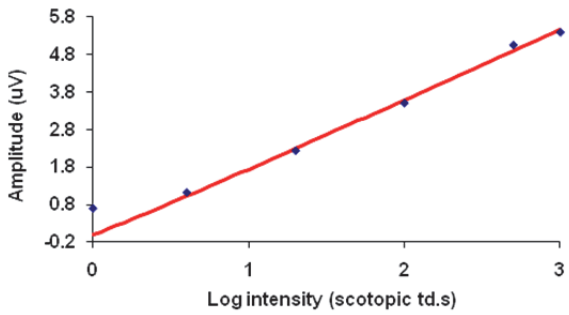

CB1 Rmax=999.11, n=1.05, LogK =432.28

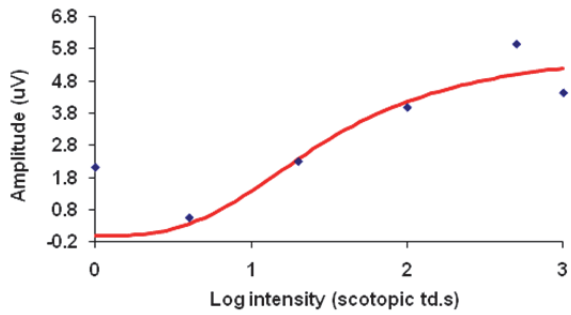

CB2 Rmax=5.80, n=3.02, LogK =1.47

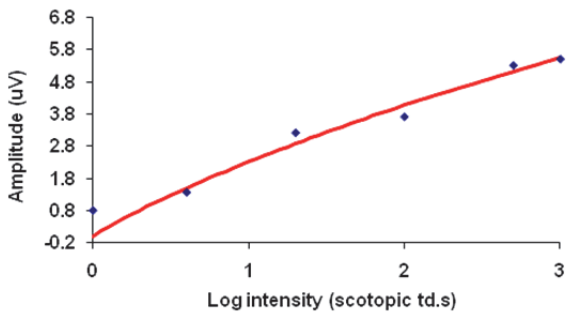

DF1 Rmax=28.01, n=0.91, LogK =13.84

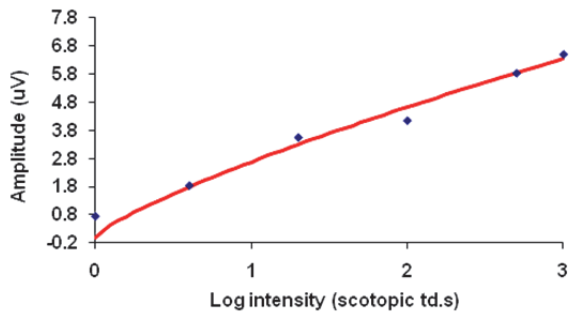

DF2 Rmax=206.86, n=0.80, LogK =224.95

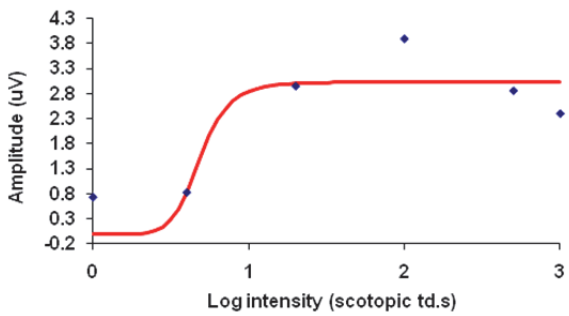

DFO1 Rmax=3.03, n=7.30, LogK =0.69

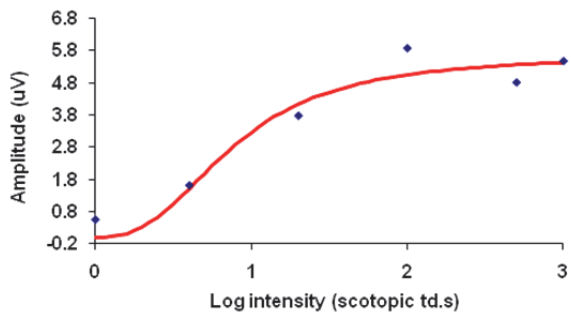

DFO2 Rmax=5.66, n=2.61, LogK =0.89

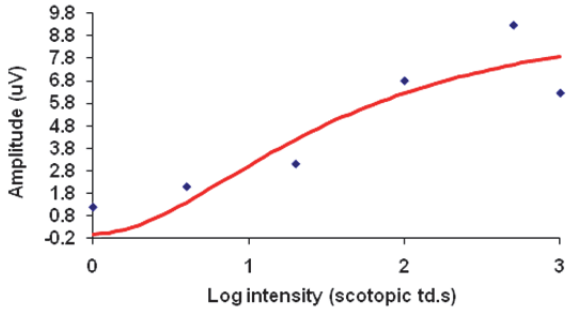

RE1 Rmax=10.19, n=1.91, LogK =1.57

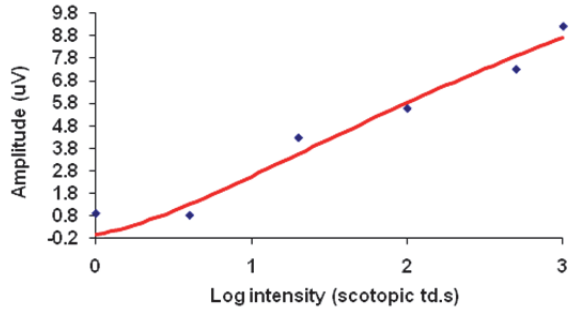

RE2 Rmax=24.55, n=1.41, LogK =4.57

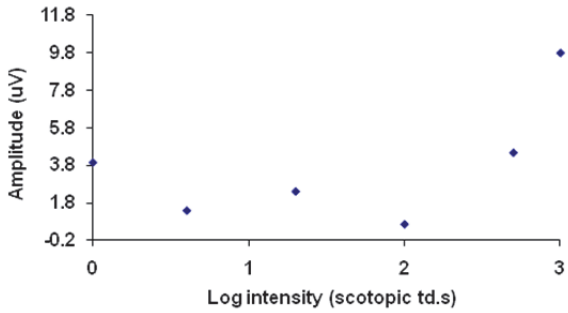

SA1 No Fit

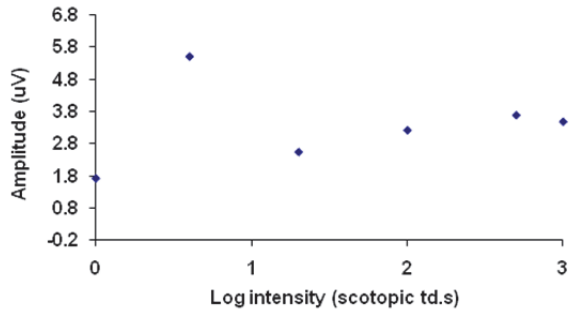

SA2 No Fit

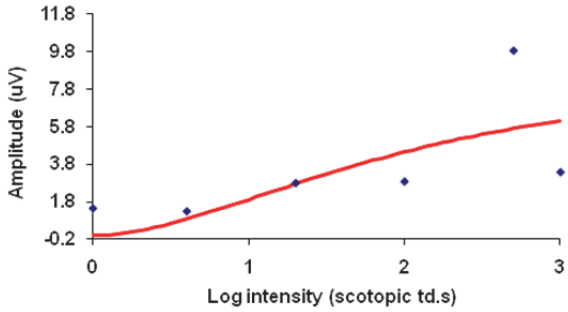

WBS1 Rmax=9.38, n=1.81, LogK =2.12

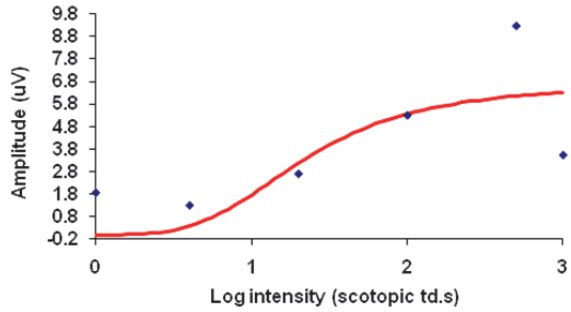

WBS2 Rmax=6.70, n=3.47, LogK =1.34

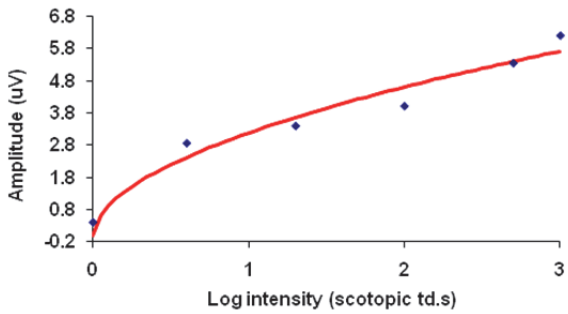

JF1 Rmax=436.17, n=0.54, LogK =9125.77

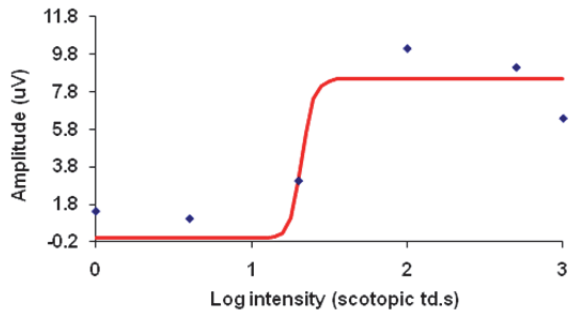

JF2 Rmax=8.50, n=34.07, LogK =1.32

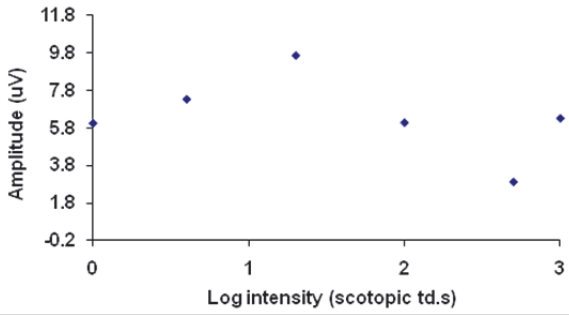

LB1 No Fit

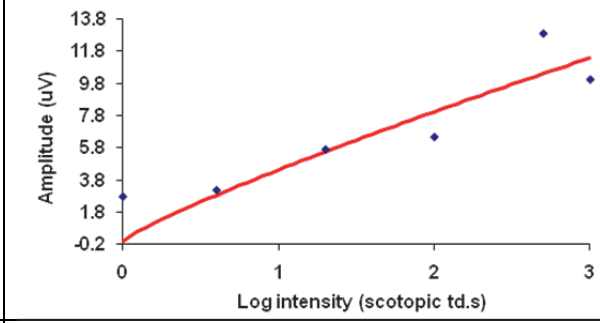

LB2 Rmax=1209.63, n=0.86, LogK =664.92

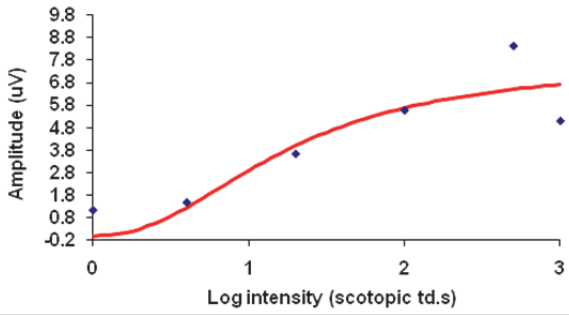

LD1 Rmax=7.69, n=2.22, LogK =1.25

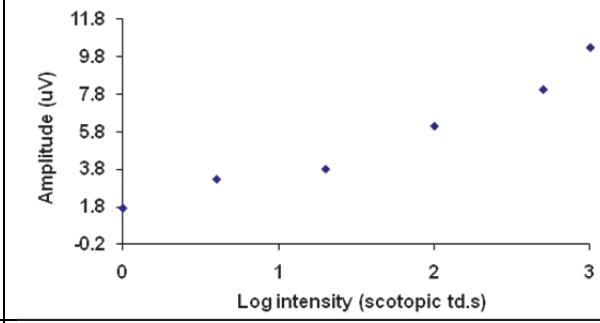

LD2 No Fit

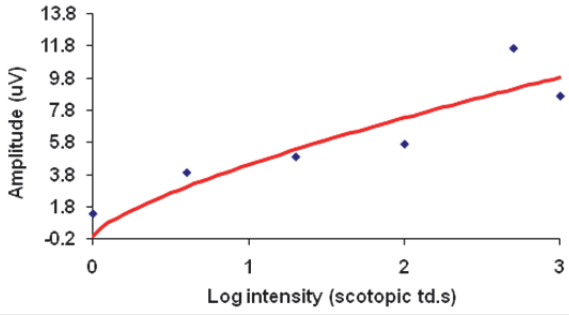

MF1 Rmax=1868.80, n=0.73, LogK =3888.17

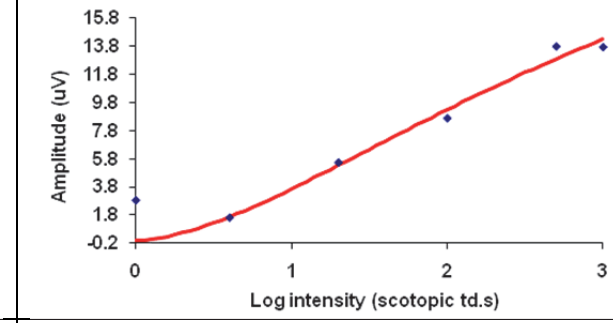

MF2 Rmax=32.12, n=1.67, LogK =3.43

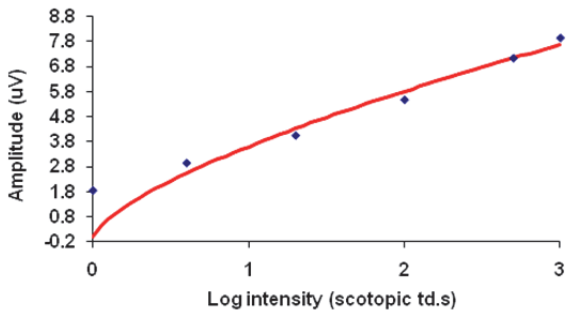

ND1 Rmax=610.83, n=0.69, LogK =1614.74

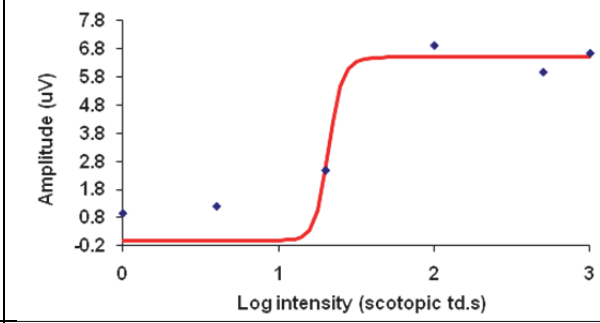

ND2 Rmax=6.50, n=29.12, LogK =1.32

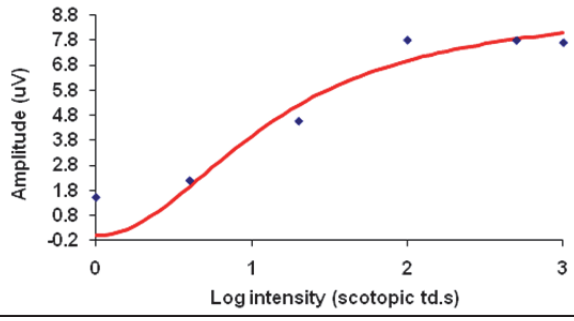

PF1 Rmax=9.20, n=2.05, LogK =1.14

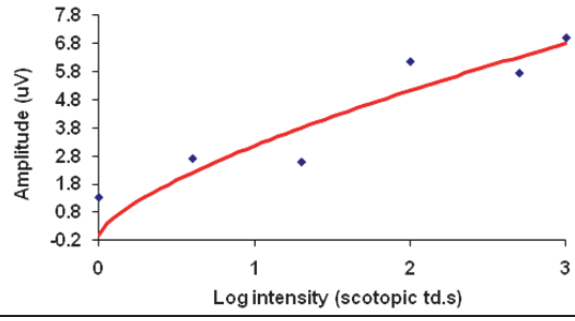

PF2 Rmax=352.57, n=0.71, LogK =776.29

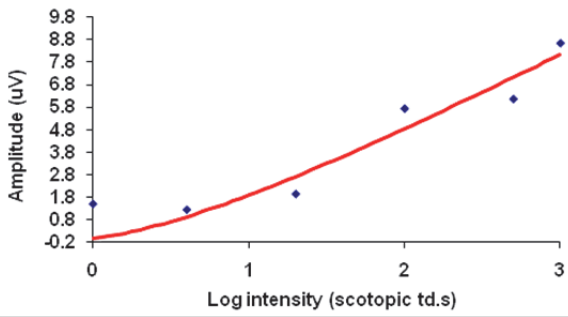

SD1 Rmax=67.18, n=1.42, LogK =12.17

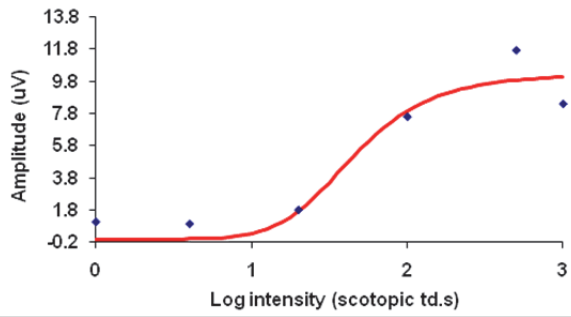

SD2 Rmax=10.27, n=6.58, LogK =1.66

Figure E.1: Intensity-response curves for focal rod ERG b-wave amplitudes (blue dots) at 6 stimulus intensities are shown. The 'Naka-Rushton' model (red line) was fitted to each dataset. Participant ID, and parameters R_{max}, n and LogK are shown below each curve.

Appendix F: OCT Literature - Retinal and Choroid thickness

<table>
<tr><th>Study & participant details</th><th>Measurement methodology</th><th>Reported values</th></tr>
<tr><td>Ikuno et al. (2009)

Myopic eyes (n=31), 51.7 ± 11.4 years (-6 to -23 D)</td><td>Cirrus HD-OCT
(Carl Zeiss Meditec, Inc.).

512 x 128 3D-scan

Manual measurement at fovea and at 4 eccentric locations (1.5 mm from fovea) using onboard software.

“Retinal thickness was defined as the vertical distance from the RPE (the outermost hyper-reflective line at the retina–choroidal interface) to the retinal surface.”

“Choroidal thickness was defined as the distance from the RPE line to the hyper-refractive line behind the large vessel layers of the choroid, presumed to be the choroid–sclera interface.”</td><td><u>Retinal Thickness</u>
Fovea 201.2 ± 40.6 µm
Temporal 290.1 ± 38.3 µm
Nasal 298.1 ± 30.8 µm
Superior 279.0 ± 41.1 µm
Inferior 286.9 ± 46.7 µm

<u>Choroidal Thickness</u>
Fovea 99.3 ± 58.8 µm
Temporal 123.8 ± 60.9 µm
Nasal 82.7 ± 35.8 µm
Superior 131.0 ± 59.1 µm
Inferior 105.2 ± 48.3 µm</td></tr>
<tr><td>Legaretta et al. (2008)

Normal eyes (n=50), 22 to 68 years.</td><td>Cirrus HD-OCT
(Carl Zeiss Meditec, Inc.)

200 x 200 3D-scan

Automated segmentation using onboard algorithm with output in ETDRS grid configuration.

“This algorithm detects the internal limiting membrane as the inner retinal boundary and the anterior surface of the retinal pigment epithelium as the outer retinal boundary.”

Stratus TD-OCT
(Carl Zeiss Meditec, Inc.)

Automated segmentation using onboard algorithm with output in ETDRS grid configuration for a subgroup of 13 participants.</td><td>
<table>
<tr><th>ETDRS Location</th><th>Cirrus</th><th>Stratus</th></tr>
<tr><td>Fovea (500 µm)</td><td>258.2 ± 23.5</td><td>212 ± 20</td></tr>
<tr><td>Inner ring (1.5 mm)</td><td></td><td></td></tr>
<tr><td>Superior</td><td>326.6 ± 18.9</td><td>255 ± 17</td></tr>
<tr><td>Inferior</td><td>326.0 ± 24.4</td><td>260 ± 15</td></tr>
<tr><td>Temporal</td><td>312.6 ± 17.1</td><td>251 ± 13</td></tr>
<tr><td>Nasal</td><td>328.6 ± 18.3</td><td>267 ± 16</td></tr>
<tr><td>Outer ring (3-mm)</td><td></td><td></td></tr>
<tr><td>Superior</td><td>282.5 ± 14.9</td><td>239 ± 16</td></tr>
<tr><td>Inferior</td><td>270.9 ± 13.9</td><td>210 ± 13</td></tr>
<tr><td>Temporal</td><td>266.3 ± 17.7</td><td>210 ± 14</td></tr>
<tr><td>Nasal</td><td>295.5 ± 17.0</td><td>246 ± 14</td></tr>
</table>
</td></tr>
</table>

<table>
<tr>
<td>Grover et al. (2010)

Normal eyes (n=36),
20 to 69 years.</td>
<td>Spectralis SD-OCT
(Heidelberg Engineering, Heidelberg, Germany)

Automated segmentation using onboard algorithm, output in ETDRS grid configuration.

Stratus TD-OCT
(Carl Zeiss Meditec, Inc.)

Automated segmentation using onboard algorithm with output in ETDRS grid configuration derived from 6 radial b-scans.</td>
<td>
<table>
<tr><th>ETDRS Location</th><th>Stratus</th><th>Spectralis</th></tr>
<tr><td>Fovea (500 µm)</td><td>202.3</td><td>271.4</td></tr>
<tr><td>Inner ring (1.5 mm)</td><td></td><td></td></tr>
<tr><td>Superior</td><td>270.8</td><td>343.3</td></tr>
<tr><td>Inferior</td><td>264.7</td><td>338.8</td></tr>
<tr><td>Temporal</td><td>255.7</td><td>326.8</td></tr>
<tr><td>Nasal</td><td>265.4</td><td>339.4</td></tr>
<tr><td>Outer ring (3-mm)</td><td></td><td></td></tr>
<tr><td>Superior</td><td>269.5</td><td>334.3</td></tr>
<tr><td>Inferior</td><td>268.9</td><td>330.8</td></tr>
<tr><td>Temporal</td><td>257.5</td><td>324.6</td></tr>
<tr><td>Nasal</td><td>277.4</td><td>344.8</td></tr>
</table>
</td>
</tr>
<tr>
<td rowspan="2">Kakinoki et al. (2009)

Normal eyes (n=50), 49.9 ±18 years.</td>
<td>Cirrus HD-OCT
(Carl Zeiss Meditec, Inc.)

200 x 200 3D-scan

Automated segmentation using onboard algorithm, output for macula (central subfield ETDRS grid) only.</td>
<td>Foveal (500µm)
257.6 ± 19.6 µm</td>
</tr>
<tr>
<td>Stratus TD-OCT
(Carl Zeiss Meditec, Inc.)

6 radial b-scans

Automated segmentation using onboard algorithm, output for macula (central subfield ETDRS grid) only.</td>
<td>Foveal (500µm)
197.2 ± 17.8 µm</td>
</tr>
</table>

<table>
<tr>
<td>Cheng et al. (2010)

Myopic (n=30; -6.00 to -13.63 DS, mean age 22.73) and non-myopic eyes (n=31; +2,75 to -0.50 DS, mean age 23.26)</td>
<td>Stratus TD-OCT
(Carl Zeiss Meditec, Inc.)

6 radial b-scans

Automated segmentation using onboard algorithm with output in ETDRS grid configuration derived from 6 radial b-scans.</td>
<td>
<table>
<tr><th>ETDRS Location</th><th>Normal</th><th>Myopic</th></tr>
<tr><td>Fovea</td><td>149 ± 11.80</td><td>162 ± 19.21</td></tr>
<tr><td>Fovea (500 µm)</td><td>191 ± 12.37</td><td>199 ± 17.27</td></tr>
<tr><td>Inner ring (1.5 mm)</td><td></td><td></td></tr>
<tr><td>Superior</td><td>280 ± 10.84</td><td>268 ± 12.83</td></tr>
<tr><td>Inferior</td><td>278 ± 9.65</td><td>267 ± 13.80</td></tr>
<tr><td>Temporal</td><td>264 ± 10.15</td><td>255 ± 14.04</td></tr>
<tr><td>Nasal</td><td>281 ± 9.63</td><td>271 ± 13.73</td></tr>
<tr><td>Outer ring (3-mm)</td><td></td><td></td></tr>
<tr><td>Superior</td><td>253 ± 11.79</td><td>236 ± 15.17</td></tr>
<tr><td>Inferior</td><td>242 ± 14.55</td><td>221 ± 14.03</td></tr>
<tr><td>Temporal</td><td>233 ± 9.29</td><td>215 ± 13.20</td></tr>
<tr><td>Nasal</td><td>269 ± 13.73</td><td>253 ± 16.59</td></tr>
</table>
</td>
</tr>
<tr>
<td>Ikuno et al. (2010)

Healthy eyes (n=86; 43 patients, mean age 39.4)</td>
<td>Prototype 1060 nm OCT

Manual measurement at fovea and at 4 eccentric locations (3 mm from fovea) using custom software.

“The vertical distance between the hyper-refractive RPE layer and the chorio-scleral interface was measured manually using a software calliper built into the custom-made OCT image viewer.”</td>
<td><u>Choroidal Thickness</u>
Fovea 354 ± 111 µm
Superior 364 ± 86 µm
Inferior 345 ± 108 µm
Nasal 227 ± 532 µm
Temporal 337 ± 102 µm</td>
</tr>
<tr>
<td>Spaide et al. (2009)

28 eyes (17 px)
80.6±7.3 yr</td>
<td>Spectralis SD-OCT
(Heidelberg Engineering, Heidelberg, Germany)

Images obtained using an enhanced depth imaging technique.</td>
<td>All eyes selected had a choroidal thickness of less than 125 µm</td>
</tr>
</table>

Loduca et al. (2010) Healthy eyes (n=15), 52 ± 6 years	Spectralis SD-OCT (Heidelberg Engineering, Heidelberg, Germany) 6 x 5 mm retinal area, comprising 19 b-scans Automated segmentation using customised algorithm with output in ETDRS grid configuration for each of 6 intra-retinal layers. Intra-retina layers measured are as follows: Layer 1 - Retinal nerve fibre layer Layer 2 - Ganglion cell layer & inner plexiform layer Layer 3 - Inner nuclear layer Layer 4 - Outer plexiform layer Layer 5 - Outer nuclear layer & photoreceptor inner segments Layer 6 - photoreceptor outer segments	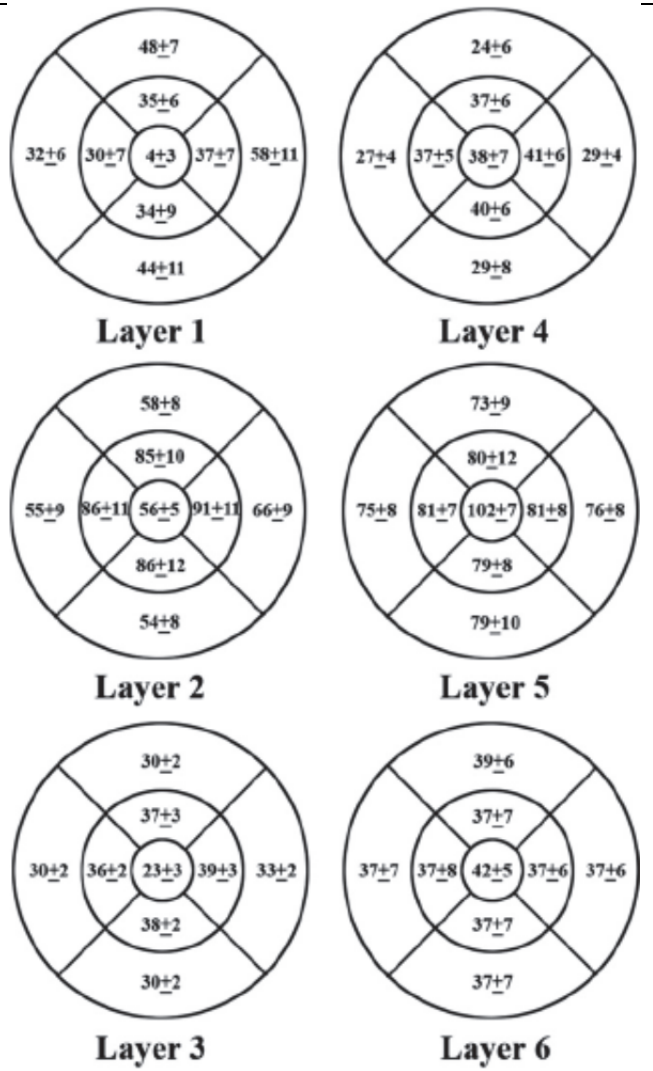 Image from Loduca et al. showing mean normal macular thickness for 6 intra-retinal layers and corresponding standard deviations shown in an ETDRS grid configuration

<table>
<tr>
<td>Manjunath et al. (2010)

Healthy eyes (n=34), mean age 51.1 years</td>
<td>Cirrus HD-OCT
(Carl Zeiss Meditec, Inc.)

1 x 4096 B-scan

Manual measurement at individual retinal locations using onboard software.

“2 independent observers measured choroidal thickness perpendicularly from the outer edge of the hyper-reflective RPE to the inner sclera”</td>
<td>
<table>
<tr><th>Location (mm from fovea)</th><th>Choroidal thickness (µm)</th></tr>
<tr><td>Temporal (2.5)</td><td>218</td></tr>
<tr><td>Temporal (2.0)</td><td>237</td></tr>
<tr><td>Temporal (1.5)</td><td>248</td></tr>
<tr><td>Temporal (1.0)</td><td>256</td></tr>
<tr><td>Temporal (0.5)</td><td>264</td></tr>
<tr><td>Fovea (0)</td><td>272</td></tr>
<tr><td>Nasal (0.5)</td><td>261</td></tr>
<tr><td>Nasal (1.0)</td><td>248</td></tr>
<tr><td>Nasal (1.5)</td><td>217</td></tr>
<tr><td>Nasal (2.0)</td><td>186</td></tr>
<tr><td>Nasal (2.5)</td><td>157</td></tr>
</table>
</td>
</tr>
<tr>
<td>Margolis et al. (2009)

Healthy eyes (n=54; 30 patients), mean age 50.4 years</td>
<td>Spectralis SD-OCT
(Heidelberg Engineering, Heidelberg, Germany)

Images obtained using an enhanced depth imaging technique with manual measurement at individual retinal locations using onboard software.

“The choroid was measured from the outer border of the retinal pigment epithelium to the inner scleral border”</td>
<td>
<table>
<tr><th>Location (mm from fovea)</th><th>Choroidal thickness (µm)</th></tr>
<tr><td>Temporal (3.0)</td><td>261</td></tr>
<tr><td>Temporal (2.5)</td><td>266</td></tr>
<tr><td>Temporal (2.0)</td><td>268</td></tr>
<tr><td>Temporal (1.5)</td><td>268</td></tr>
<tr><td>Temporal (1.0)</td><td>273</td></tr>
<tr><td>Temporal (0.5)</td><td>277</td></tr>
<tr><td>Fovea (0)</td><td>287</td></tr>
<tr><td>Nasal (0.5)</td><td>276</td></tr>
<tr><td>Nasal (1.0)</td><td>253</td></tr>
<tr><td>Nasal (1.5)</td><td>232</td></tr>
<tr><td>Nasal (2.0)</td><td>203</td></tr>
<tr><td>Nasal (2.5)</td><td>170</td></tr>
<tr><td>Nasal (3.0)</td><td>145</td></tr>
</table>
</td>
</tr>
</table>

<table>
<tr>
<td>Hirata et al. (2011)

Healthy eyes (n=31), mean age 64.6 ± 17.3 years</td>
<td>Swept source OCT at 1050 nm

512x128 3D scan

Images were obtained using a long wavelength OCT and the choroid was manually segmented producing thickness maps and ETDRS grid output. Manual calliper measurements were also obtained at the fovea, 1 mm and 2.25 mm eccentricities.

“The choroidal thickness was measured as the distance between the outer border of the hyper-reflective line, considered to be the RPE, and the chorioscleral border”</td>
<td>
<table>
<tr><th>Location (mm from fovea)</th><th>Choroidal thickness (µm)</th></tr>
<tr><td>Fovea (0)</td><td>199.8</td></tr>
<tr><td>Temporal (1.0)</td><td>201.6</td></tr>
<tr><td>Superior (1.0)</td><td>206.6</td></tr>
<tr><td>Nasal (1.0)</td><td>183.5</td></tr>
<tr><td>Inferior (1.0)</td><td>203.9</td></tr>
<tr><td>Temporal (2.25)</td><td>200.6</td></tr>
<tr><td>Superior (2.25)</td><td>229.3</td></tr>
<tr><td>Nasal (2.25)</td><td>139.6</td></tr>
<tr><td>Inferior (2.25)</td><td>190.4</td></tr>
</table>
</td>
</tr>
</table>

Table F.1: A comparison of OCT determined retinal and choroid thickness values from recent literature (2008 onwards).

References

Cheng S C K, Lam C S Y, and Yap M K H (2010) Retinal thickness in myopic and non-myopic eyes. *Ophthalmic and Physiological Optics* 30: 776-784.

Grover S, Murthy R K, Brar V S, and Chalam K V (2010) Comparison of Retinal Thickness in Normal Eyes Using Stratus and Spectralis Optical Coherence Tomography. *Investigative Ophthalmology & Visual Science* 51: 2644-2647.

Hirata M, Tsujikawa A, Matsumoto A, Hangai M, Ooto S, Yamashiro K, Akiba M et al. (2011) Macular choroidal thickness and volume in normal subjects measured by swept-source optical coherence tomography. *Invest Ophthalmol Vis Sci* 52: 4971-4978.

Ikuno Y, Kawaguchi K, Nouchi T, and Yasuno Y (2010) Choroidal Thickness in Healthy Japanese Subjects. *Investigative Ophthalmology & Visual Science* 51: 2173-2176.

Ikuno Y, and Tano Y (2009) Retinal and Choroidal Biometry in Highly Myopic Eyes with Spectral-Domain Optical Coherence Tomography. *Investigative Ophthalmology & Visual Science* 50: 3876-3880.

Kakinoki M, Sawada O, Sawada T, Kawamura H, and Ohji M (2009) Comparison of Macular Thickness Between Cirrus HD-OCT and Stratus OCT. *Ophthalmic Surgery Lasers & Imaging* 40: 135-140.

Legarreta J E, Gregori G, Punjabi O S, Knighton R W, Lalwani G A, and Puliafito C A (2008) Macular thickness measurements in normal eyes using spectral domain optical coherence tomography. *Ophthalmic Surgery Lasers & Imaging* 39: S43-S49.

Loduca A L, Zhang C, Zelkha R, and Shahidi M (2010) Thickness mapping of retinal layers by spectral-domain optical coherence tomography. *Am J Ophthalmol* 150: 849-855.

Manjunath V, Taha M, Fujimoto J G, and Duker J S (2010) Choroidal Thickness in Normal Eyes Measured Using Cirrus HD Optical Coherence Tomography. *Am J Ophthalmol*.

Margolis R, and Spaide R F (2009) A Pilot Study of Enhanced Depth Imaging Optical Coherence Tomography of the Choroid in Normal Eyes. *Am J Ophthalmol* 147: 811-815.

Spaide R F (2009) Age-related choroidal atrophy. *Am J Ophthalmol* 147: 801-810.

Appendix G:ERG Literature - AMD

Authors	Parameters investigated	Summary of main findings
Walter et al. (1999) 66 AMD (mean 70.5 ±7.7 years) -122 eyes 47 Control (mean 66.5 ±7.4 years) - 47 eyes	Full field rod and cone ERG a and b waves Flicker ERG (30 Hz) EOG OP's	• Photopic a and b wave amplitudes reduced. • Photopic a wave implicit times prolonged. • The scotopic b-wave amplitudes reduced. • OP2 reduced. • EOG dark trough, light peak and light rise reduced. *Additionally, geographic atrophy and PED resulted in specific changes to ERG implicit times.*
Binns and Margrain (2007) 31 ARM (mean 72.4 ±8 years) 27 Control (mean 71.7 ±7 years)	Focal cone ERG transient a and b wave Focal flicker ERG (41 Hz, 20° stimulus) ERG photostress test	• ERG photostress test recovery was slower in ARM ($P<0.002$, area under ROC curve 0.74). • Focal cone ERG implicit times increased (a-wave, $p<0.002$; b-wave, $p<0.001$). • Focal flicker ERG implicit time increased ($p<0.001$) and amplitude reduced ($p<0.003$).
Sunness et al. (1985) 21 AMD (57-80 years) 23 Control (19-50 years)	EOG (Arden ratio) Full field flicker ERG Full field rod ERG (intensity-response)	• EOG or Full field ERG parameters were unaffected and did not show an association with disease severity.
Biersdorf and Diller (1969) Control (mean 30 years) 14 AMD eyes (44 – 72 years)	Focal (4° stimulus) and full field b wave amplitude	• Focal ERG responses were abnormal in AMD
Holopigian et al. (1997) 10 ARM (mean 75 ±4.6 years) ~19 Control (23-81 years)	Full field rod and cone ERG a and b waves and OP Full field rod ERG (intensity response) Full field flicker ERG (30 Hz) EOG (Arden ratio)	• EOG unaffected • OP unaffected • Full field scotopic ERG parameters were abnormal in some patients. *Additionally age related changes were reported in scotopic and photopic ERG parameters.*
Birch and Fish (1988) 134 Macular disease eyes (49 AMD eyes) 100 Control eyes (5-79 years)	Focal flicker ERG (3° stimulus)	• Amplitude was correlated with age for foveal responses ($r= -0.91$; $p<0.001$). • In eyes with maculopathy responses were significantly reduced in 94% of eyes with 20/40 (6/12) or poorer acuity.
Sandberg et al. (1993) 73 Unilateral wet AMD (61-89 years)	Focal flicker ERG (42 Hz, 4° stimulus)	• Fellow eyes of wet AMD participants were on average normal in amplitude but implicit times were delayed. *Additionally, the implicit time was shown to increase, but*

28 Control (mean 69.7 ±1.3 years)		*amplitudes decrease, with ageing.*
Remulla et al. (1995) 67 Unilateral wet AMD (mean 72.1 ±0.8 years) 28 Control (mean 69.7 ±1.3 years)	Focal flicker ERG (42 Hz, 4° stimulus)	• Twenty eight (42%) of eyes with contralateral wet AMD had a choroidal perfusion defect. • In eye with choroidal perfusion defects ERG implicit times were 1 ms slower (p=0.0167) and were more likely to be delayed (p=0.0078) than in eyes with normal choroidal filling. *Additionally, ERG implicit time was positively related to the percentage area of macular drusen.*
***Sandberg et al. (1998)** 127 Unilateral wet AMD	Focal flicker ERG	• The interval to CNV development in participants was shown to be inversely related to the focal flicker ERG implicit time at baseline. *Participants were observed for up to 4.5 years from baseline.*
Falsini et al. (1999) 25 eyes with bilateral dry AMD (mean 66.2 ±7.3 years) 10 healthy eyes (67 ±4 years)	Focal flicker ERG (32 Hz, 9° stimulus)	• AMD group showed a reduction in the mean focal flicker ERG amplitude (57% loss, P<0.001), but not implicit time. *Additionally, ERG amplitudes were also negatively correlated with the Wisconsin grading score (r=-0.63, p<0.001) and the percentage area of pathological hyperfluorescence (r=-0.70, p<0.01).*
Falsini et al. (2000) 19 ARM (mean 67 ±7 years) 11 Control (mean 65 ±7 years)	Focal flicker ERG (41 Hz, 18° stimulus)	• Reductions in amplitude and delayed implicit times (phase).
Falsini et al. (2007) 13 Young (14-29 years) 9 Old (55-80 years) 18 ARM (22-80 years, VA >0.4)	Focal flicker ERG (3.7 to 52 Hz, 18° stimulus)	• Mean amplitudes were depressed in participants with ARM. *Additionally, the flicker ERG response was shown to be differentially affected at different temporal frequency by normal aging and in ARM.*
Li, Tso and Lam (2001) 15 ARM (mean 50.6 ±5.7 years) 20 Controls (mean 52.1 ±3.7 years)	Multifocal ERG	• No differences in the amplitudes and the latencies between the different retinal regions (nasal versus temporal and superior versus inferior). • Foveal amplitude reduced. • Latency prolonged.
Chen et al. (2004) 24 dry AMD (mean 66 years) 16 Control (mean 63 years)	Multifocal ERG (rod and cone)	• Cone summed N1 amplitude reduced (p<0.05). • Rod P1 and N1 amplitude reduced (central 2.5°; p<0.05).

Ladewig et al. (2003) 20 AMD (mean 70 ±9 years) 23 Control (mean 62 ±7 years)	Full field ERG rod, cone and mixed a and b waves Full field flicker ERG (30 Hz)	• Rod a wave amplitude reduced ($p<0.02$). • Mixed (rod and cone) a wave amplitude reduced ($p<0.02$). • Cone a wave amplitude reduced ($p<0.001$). • Flicker ERG amplitude reduced ($p<0.001$).
Piccardi et al. (2009) 26 ARM (58-82 years) 12 Control (67-82 years)	Central (4.5°) and paracentral (4.5-18°) focal flicker ERG (41 Hz)	• Central and paracentral reduction in amplitude ($p<0.01$). • Paracentral implicit time (phase) was delayed ($p<0.01$).
Feigl et al. (2005a) 17 ARM (mean 70 years) 16 Control (mean 68 years)	Multifocal ERG (rod and cone)	• The cone results showed no statistically significant difference. • The rod responses were delayed.
Feigl et al. (2005b) 13 ARM (mean 72 years) 13 Control (mean 70 years)	Multifocal ERG (rod and cone) at baseline and after 1 year.	• Rod-mediated responses were significantly delayed at baseline and after 1 year. • Cone- mediated responses were within the normal range at both visits. *Retinal changes were found in only two subjects (18%) between visits.*
Ronan et al. (2006) 52 AMD (mean 75.7 years) 16 Controls (mean 81.4 years)	Full field rod and cone ERG a and b waves Full field dark adapted bright flash ERG Full field flicker ERG (30 Hz)	• Full field photopic ERG b-wave reduced ($p=0.0296$). *This was a retrospective study.*

Table G.1: A summary of ERG studies involving participants with ARM or AMD, the any effects on measured ERG parameters attributable to disease have been highlighted. This table does not include intervention studies.

References

Biersdorf W R, and Diller D A (1969) Local electroretinogram in macular degeneration. *Am J Ophthalmol* 68: 296-303.

Binns A M, and Margrain T H (2007) Evaluating retinal function in age-related maculopathy with the ERG photostress test. *Ophthalmic Physiol Opt* 48: 2806-2813.

Birch D G, and Fish G E (1988) Focal cone electroretinograms: aging and macular disease. *Doc Ophthalmol* 69: 211-220.

Chen C, Wu L, Wu D, Huang S, Wen F, Luo G, and Long S (2004) The local cone and rod system function in early age-related macular degeneration. *Doc Ophthalmol* 109: 1-8.

Falsini B, Fadda A, Iarossi G, Piccardi M, Canu D, Minnella A, Serrao S et al. (2000) Retinal sensitivity to flicker modulation: reduced by early age-related maculopathy. *Invest Ophthalmol Vis Sci* 41: 1498-1506.

Falsini B, Serrao S, Fadda A, Iarossi G, Porrello G, Cocco F, and Merendino E (1999) Focal electroretinograms and fundus appearance in nonexudative age-related macular degeneration. Quantitative relationship between retinal morphology and function. *Graefes Arch Clin Exp Ophthalmol* 237: 193-200.

Falsini B, Ziccardi L, Stifano G, Iarossi G, Merendino E, Minnella A M, Fadda A et al. (2007) Temporal response properties of the macular cone system: effect of normal aging and age-related maculopathy. *Invest Ophthalmol Vis Sci* 48: 4811-4817.

Feigl B, Brown B, Lovie-Kitchin J, and Swann P (2005a) Cone- and rod-mediated multifocal electroretinogram in early age-related maculopathy. *Eye* 19: 431-441.

Feigl B, Brown B, Lovie-Kitchin J, and Swann P (2005b) Monitoring retinal function in early age-related maculopathy: visual performance after 1 year. *Eye* 19: 1169-1177.

Holopigian K, Seiple W, Greenstein V, Kim D, and Carr R E (1997) Relative effects of aging and age-related macular degeneration on peripheral visual function. *Optom Vis Sci* 74: 152-159.

Ladewig M, Kraus H, Foerster M H, and Kellner U (2003) Cone dysfunction in patients with late-onset cone dystrophy and age-related macular degeneration. *Archives of Ophthalmology* 121: 1557-1561.

Li J, Tso M O M, and Lam T T (2001) Reduced amplitude and delayed latency in foveal response of multifocal electroretinogram in early age related macular degeneration. *British Journal of Ophthalmology* 85: 287-290.

Piccardi M, Ziccardi L, Stifano G, Montrone L, Iarossi G, Minnella A, Fadda A et al. (2009) Regional cone-mediated dysfunction in age-related maculopathy evaluated by focal electroretinograms: relationship with retinal morphology and perimetric sensitivity. *Ophthalmic Res* 41: 194-202.

Remulla J F, Gaudio A R, Miller S, and Sandberg M A (1995) Foveal electroretinograms and choroidal perfusion characteristics in fellow eyes of patients with unilateral neovascular age-related macular degeneration. *Br J Ophthalmol* 79: 558-561.

Ronan S, Nusinowitz S, Swaroop A, and Heckenlively J R (2006) Senile panretinal cone dysfunction in age-related macular degeneration (AMD): a report of 52 amd patients compared to age-matched controls. *Trans Am Ophthalmol Soc* 104: 232-240.

Sandberg M A, Miller S, and Gaudio A R (1993) Foveal cone ERGs in fellow eyes of patients with unilateral neovascular age-related macular degeneration. *Invest Ophthalmol Vis Sci* 34: 3477-3480.

Sandberg M A, Weiner A, Miller S, and Gaudio A R (1998) High-risk characteristics of fellow eyes of patients with unilateral neovascular age-related macular degeneration. *Ophthalmology* 105: 441-447.

Sunness J S, Massof R W, Johnson M A, Finkelstein D, and Fine S L (1985) Peripheral retinal function in age-related macular degeneration. *Arch Ophthalmol* 103: 811-816.

Walter P, Widder R A, Luke C, Konigsfeld P, and Brunner R (1999) Electrophysiological abnormalities in age-related macular degeneration. *Graefes Arch Clin Exp Ophthalmol* 237: 962-968.

Appendix H: AMD Grading

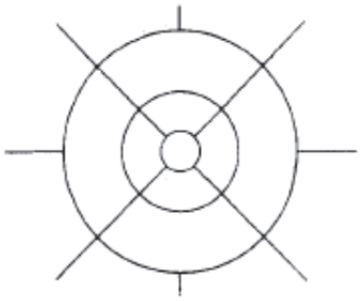

Figure H.1: Grid used to overlie macular retinal images for both International and AREDS grading systems, showing central, inner and outer zones, diameters are 1000, 3000 and 6000μm respectively. Image from Bird et al. (1995).

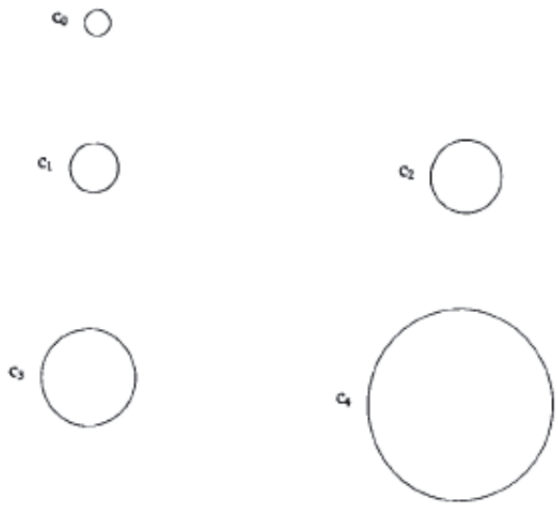

Figure H.2: Five circles of varying sized used with the International Classification System to grade lesion size. The approximate dimensions for a normal macula are as follows: C_0 63μm, C_1 125μm, C_2 175μm, C_3 250μm, C_4 500μm.

Grading feature	Equivalent diameter in Powerpoint
37° Diameter Image (10656μm)	141.92 mm
Outer zone 6000μm	79.91 mm
Inner zone 3000μm	39.95 mm
Central zone 1000μm	13.32 mm
C_0 63μm,	0.84 mm
C_1 125μm,	1.66 mm
C_2 175μm,	2.33 mm
C_3 250μm,	3.33 mm
C_4 500μm.	6.66 mm

Table H.1: Showing the conversion of retinal distances to scaled values for use with 37° retinal images undertaken for each grading features used with the International classification system (Bird et al., 1995).

TABLE 2

Grading of Drusen

1.1 Drusen morphology. Grade highest # present within outer circle.
0) absent
1) questionable
2) hard drusen (<C1, 125μm)
3) intermediate, soft drusen (>C0≤C1; >63μm ≤125μm)
4) large, soft distinct drusen (>C1, 125μm)
5) large, soft indistinct drusen (>C1, 125μm)
5a) crystalline/calcified/glistening
5b) semisolid
5c) serogranular
7) cannot grade, obscuring lesions
8) cannot grade, photo quality

1.2 Predominant drusen type within outer circle
0) absent
1) questionable
2) hard drusen (<C1, 125μm)
3) intermediate, soft drusen (>C0≤C1; >63μm ≤125μm)
4) large, soft distinct drusen (>C1, 125μm)
5) large, soft indistinct drusen (>C1, 125μm)
5a) crystalline/calcified/glistening
5b) semisolid
5c) serogranular
7) cannot grade, obscuring lesions
8) cannot grade, photo quality

1.3 Number of drusen
0) absent
1) questionable
2) 1-9
3) 10-19
4) ≥20
7) cannot grade, obscuring lesions
8) cannot grade, photo quality

1.4 Drusen size
1) $<C_0$ (<63μm)
2) $\geq C_0 < C_1$ (≥63μm, <125μm)
3) $\geq C_1 < C_2$ (≥125μm, <175μm)
4) $\geq C_2 < C_3$ (≥175μm, <250μm)
5) $\geq C_3$ (≥250μm)
7) cannot grade, obscuring lesions
8) cannot grade, photo quality

1.5 Main location of drusen. Drusen may not be central to indicated subfield, but may be more to periphery.
1) outside outer circle (mid-peripheral subfield)
2) in outer subfield
3) in middle subfield
4) in central subfield
4a) outside fovea (center point)
4b) in fovea
7) cannot grade, obscuring lesions
8) cannot grade, photo quality

1.6 Area covered by drusen in subfield 1.5
1) <10%
2) <25%
3) <50%
4) ≥50%
7) cannot grade, obscuring lesions
8) cannot grade, photo quality

TABLE 3

Hyperpigmentation and Hypopigmentation of the Retina

Hyperpigmentation
0) absent
1) questionable
2) present $<C_0$ (<63μm)
3) present $\geq C_0$ (≥63μm)
7) cannot grade, obscuring lesions
8) cannot grade, photo quality

Hypopigmentation
0) absent
1) questionable
2) present $<C_0$ (<63μm)
3) present $\geq C_0$ (≥63μm)
7) cannot grade, obscuring lesions
8) cannot grade, photo quality

Main location hyper/hypopigmentation. This may not be central to indicated subfield, but may be more to periphery. Choose most central location.
1) outside outer circle (mid-peripheral subfield)
2) in outer subfield
3) in middle subfield
4) in central subfield
4a) outside fovea (center point)
4b) in fovea
7) cannot grade, obscuring lesions
8) cannot grade, photo quality

Figure H.3: Drusen and retinal pigmentation grading criteria for the International classification system (Bird et al., 1995).

References

Bird A C, Bressler N M, Bressler S B, Chisholm I H, Coscas G, Davis M D, de Jong P T V M et al. (1995) An international classification and grading system for age-related maculopathy and age-related macular degeneration. *Survey of Ophthalmology* 39: 367-374.

Appendix I: Participant baseline data

Participant	Right eye												Left eye											
	Drusen						Pigmentation			Dry	Wet	Classification	Drusen						Pigmentation			Dry	Wet	Classification
	1.1	1.2	1.3	1.4	1.5	1.6	3.1	3.2	3.3				1.1	1.2	1.3	1.4	1.5	1.6	3.1	3.2	3.3			
DG24	2	2	2	2	3	1	3	1	3	N	N	ARM	0	0	0				0	0		N	N	Normal
UH38	5b	5b	2	5	2	1	0	2	2	N	N	ARM	5b	5b	3	5	2	1	0	0		N	N	ARM
MK48	5b	4	4	3	3	2	2	1	3	N	N	ARM	4	3	4	2	3	2	0	1		N	N	ARM
PJ45	3	2	2	2	3	1	0	0		N	N	ARM	0	0	0				0	0		N	N	Normal
JM83	4	2	2	4	2	1	0	0		N	N	ARM	5b	1	2	4	3	1	0	0		N	N	ARM
RJ95	1	1	1				1	1		N	Y	Wet	1	1	1				2	3	3	N	N	ARM
DR96	5b	5b	3	4	3	2	3	3	3	N	N	ARM	3	3	2	2	2	1	1	2	3	N	Y	Wet
TO97	0	0	0				3	1	2	N	Y	Wet	0	0	0				3	1	4a	N	N	ARM
BS100	5b	3	2	2	2	1	1	1		N	N	ARM	5b	5b	2	4	3	1	1	1	3	N	N	Wet
DN82	2	2	2	1	3	1	1	1		N	N	Normal	3	2	2	2	4a	1	2	1	3	N	N	ARM
DP103	1	1	1				1	3	4a	N	N	ARM	3	3	2	3	3	1	1	3	3	N	N	ARM
SJ90	1	1	1				1	3	2	N	Y	Wet	4	3	4	2	3	2	3	3	3	N	N	ARM
CG101	5b	3	4	2	2	1	1	1		N	N	ARM	3	3	2	2	2	1	0	1		N	N	ARM
SO107	5a	5b	4	5	3	3	3	3	3	N	Y	Wet	5b	5b	4	5	3	4	1	1		N	N	ARM
JH108	3	3	4	2	3	1	1	0		N	N	ARM	0	0	0				0	0		N	Y	Wet
AP109	0	0	0				3	1	3	N	N	ARM	0	0	0				3	1	3	N	N	ARM
PT139	3	2	2	2	2	1	1	1		N	N	ARM	5b	5b	2	3	2	1	1	2	2	N	N	ARM
MT125	3	3	3	2	4a	2	1	1		N	N	ARM	1	1	1				1	2	3	N	N	ARM
WC122	5b	3	3	2	2	1	1	3	2	N	N	ARM	5b	5b	3	3	2	1	1	2	2	N	N	Wet
JT99	8	8	8				3	1	3	N	N	ARM	1	1	1				3	3	3	N	Y	Wet
BS116	0	0	0				0	1		N	N	Normal	5b	2	2	1	4a	1	0	1		N	N	ARM
BC92	5b	5b	4	3	3	3	2	3	3	Y	Y	Wet	5c	4	4	4	3	4	1	3	3	N	N	ARM
PS115	1	1	1				0	1		N	N	Normal	2	2	2	1	3	1	1	2	3	N	N	ARM
SH93	3	3	2	3	3	1	3	3		N	Y	Wet	1	1	1				3	1	4a	N	N	ARM

Table I.1: ARM participant drusen and pigmentation grades for the International AMD Classification and Grading System (n=24).

Participant	Right eye												Left eye											
	Drusen						Pigmentation			Dry	Wet	Classification	Drusen						Pigmentation			Dry	Wet	Classification
	1.1	1.2	1.3	1.4	1.5	1.6	3.1	3.2	3.3				1.1	1.2	1.3	1.4	1.5	1.6	3.1	3.2	3.3			
DH8	0	0	0				0	0		N	N	Normal	0	0	0				0	0		N	N	Normal
DH7	0	0	0				0	0		N	N	Normal	0	0	0				0	0		N	N	Normal
DG20	0	0	0				0	0		N	N	Normal	0	0	0				0	0		N	N	Normal
RG27	0	0	0				0	0		N	N	Normal	1	1	1				0	0		N	N	Normal
GB25	0	0	0				0	0		N	N	Normal	0	0	0				0	0		N	N	Normal
MH31	1	1	1				0	0		N	N	Normal	0	0	0				0	0		N	N	Normal
AD32	0	0	0				0	0		N	N	Normal	0	0	0				0	0		N	N	Normal
JO42	2	2	3	1	4a	2	0	0		N	N	Normal	1	1	1				0	0		N	N	Normal
RE68	0	0	0				0	0		N	N	Normal	0	0	0				0	0		N	N	Normal
AJ59	2	2	2	1	4a	1	1	0		N	N	Normal	1	1	1				0	0		N	N	Normal
TK73	0	0	0				0	0		N	N	Normal	0	0	0				0	0		N	N	Normal
PF70	1	1	1				0	1		N	N	Normal	0	0	0				0	0		N	N	Normal
MK75	2	2	2	1	2	1	0	0		N	N	Normal	0	0	0				0	0		N	N	Normal
RJ77	1	1	1				0	0		N	N	Normal	1	1	1				0	0		N	N	Normal
CO87	0	0	0				0	0		N	N	Normal	0	0	0				0	0		N	N	Normal
AO88	1	1	1				0	1		N	N	Normal	0	0	0				0	0		N	N	Normal
DT131	0	0	0				0	1		N	N	Normal	0	0	0				0	0		N	N	Normal
PG26	0	0	0				0	0		N	N	Normal	0	0	0				0	0		N	N	Normal
EN112	0	0	0				0	0		N	N	Normal	0	0	0				0	0		N	N	Normal
AI46	1	1	1				0	1		N	N	Normal	0	0	0				0	0		N	N	Normal
BB80	0	0	0				0	0		N	N	Normal	0	0	0				0	0		N	N	Normal
HH13	0	0	0				0	0		N	N	Normal	0	0	0				0	0		N	N	Normal
AJ56	0	0	0				1	0		N	N	Normal	2	2	2	2	3	1	0	1		N	N	ARM
BA69	0	0	0				0	0		N	N	Normal	0	0	0				0	0		N	N	Normal
GJ65	0	0	0				0	0		N	N	Normal	0	0	0				0	0		N	N	Normal
DJ53	0	0	0				0	0		N	N	Normal	0	0	0				0	0		N	N	Normal

Table I.2: Control participant drusen and pigmentation grades for the International AMD Classification and Grading System (n=26).

Participant	Angle	Maj Rad	Min Rad	S-index	C-index
DG24	61.98	9.23	6.71	1.38	1.00
UH38	61.98	9.23	6.71	1.38	1.00
MK48	**84.75**	**20.36**	**6.74**	**3.02**	**2.20**
PJ45	61.98	9.23	6.71	1.38	1.00
JM83	61.98	9.23	6.71	1.38	1.00
RJ95	61.98	9.23	6.71	1.38	1.00
DR96	61.98	9.23	6.71	1.38	1.00
TO97	61.98	9.23	6.71	1.38	1.00
BS100	61.98	9.23	6.71	1.38	1.00
DN82	61.98	9.23	6.71	1.38	1.00
DP103	61.98	9.23	6.71	1.38	1.00
SJ90	**80.05**	**15.19**	**7.09**	**2.14**	**1.64**
CG101	61.98	9.23	6.71	1.38	1.00
SO107	61.98	9.23	6.71	1.38	1.00
JH108	**79.00**	**12.24**	**7.04**	**1.74**	**1.33**
AP109	61.98	9.23	6.71	1.38	1.00
PT139	61.98	9.23	6.71	1.38	1.00
MT125	61.98	9.23	6.71	1.38	1.00
WC122	**67.55**	**10.37**	**6.79**	**1.53**	**1.12**
JT99	**67.41**	**10.54**	**6.77**	**1.53**	**1.12**
BS116	61.98	9.23	6.71	1.38	1.00
BC92	**74.58**	**20.21**	**7.69**	**2.63**	**2.19**
PS115	**71.20**	**10.41**	**6.93**	**1.50**	**1.13**
SH93	61.98	9.23	6.71	1.38	1.00

Table I.3: D-15 colour vision results for ARM participants (n=24), 7 participants expressed defective colour vision (bold).

Participant	Angle	Maj Rad	Min Rad	S-index	C-index
DH8	61.98	9.23	6.71	1.38	1.00
DH7	61.98	9.23	6.71	1.38	1.00
DG20	61.98	9.23	6.71	1.38	1.00
RG27	61.98	9.23	6.71	1.38	1.00
GB25	61.98	9.23	6.71	1.38	1.00
MH31	61.98	9.23	6.71	1.38	1.00
AD32	61.98	9.23	6.71	1.38	1.00
JO42	61.98	9.23	6.71	1.38	1.00
RE68	61.98	9.23	6.71	1.38	1.00
AJ59	61.98	9.23	6.71	1.38	1.00
TK73	61.98	9.23	6.71	1.38	1.00
PF70	61.98	9.23	6.71	1.38	1.00
MK75	61.98	9.23	6.71	1.38	1.00
RJ77	61.98	9.23	6.71	1.38	1.00
CO87	61.98	9.23	6.71	1.38	1.00
AO88	61.98	9.23	6.71	1.38	1.00
DT131	61.98	9.23	6.71	1.38	1.00
PG26	61.98	9.23	6.71	1.38	1.00
EN112	**80.62**	**13.25**	**7.06**	**1.88**	**1.44**
AI46	61.98	9.23	6.71	1.38	1.00
BB80	61.98	9.23	6.71	1.38	1.00
HH13	61.98	9.23	6.71	1.38	1.00
AJ56	61.98	9.23	6.71	1.38	1.00
BA69	61.98	9.23	6.71	1.38	1.00
GJ65	61.98	9.23	6.71	1.38	1.00
DJ53	61.98	9.23	6.71	1.38	1.00

Table I.4: D-15 colour vision results for control participants (n=26), 1 participant expressed defective colour vision (bold).

Participant	DOB	Age	Gender	Test eye	VA	Axial Length	Refraction			LOCS III grading			
							Sph	Cyl	Axis	NC	NO	C	P
DG24	22/04/1953	56	M	R	-0.06	23.37	-0.25	-1.00	95	2.0	2.0	0.1	0.1
UH38	09/04/1936	73	F	L	0.04	23.72	1.50	-0.25	12	3.0	4.0	3.5	0.1
MK48	05/07/1939	70	F	L	0.10	23.60	2.75	-1.50	77	2.0	3.0	0.1	0.1
PJ45	03/06/1945	64	M	R	0.00	22.51	2.25	-0.50	102	2.0	2.0	0.1	0.1
JM83	06/08/1942	67	F	L	0.04	22.07	3.00	-1.25	86	3.5	3.5	2.0	0.1
RJ95	04/08/1945	64	M	L	0.02	23.30	0.00	-0.50	171	2.0	2.0	0.1	0.1
DR96	10/08/1931	78	M	R	0.28	21.64	3.00	-0.75	116	3.0	3.0	0.1	0.1
TO97	22/04/1937	72	M	L	0.36	24.26	3.00	-1.25	150	3.0	3.0	0.5	0.1
BS100	08/06/1930	79	F	R	0.10	23.46	4.00	-1.25	88	3.0	2.0	0.1	0.1
DN82	11/01/1930	80	M	L	0.02	23.79	3.50	-0.50	37	2.5	2.0	2.0	0.1
DP103	21/06/1951	58	M	L	0.04	23.76	0.25	-1.25	7	1.0	1.0	0.1	0.1
SJ90	13/12/1944	65	F	L	0.10	23.65	1.25	-1.00	175	2.0	2.0	0.1	0.1
CG101	30/09/1922	87	F	L	0.30	23.47	2.50	-1.00	30	IOL	IOL	IOL	IOL
SO107	15/08/1934	75	F	L	0.20	22.68	6.00	-2.75	160	3.0	2.5	2.0	0.1
JH108	28/11/1934	75	M	R	0.06	23.10	1.75			2.5	2.5	0.5	0.1
AP109	16/10/1930	79	F	L	-0.10	23.03	0.50	-0.50	81	IOL	IOL	IOL	IOL
PT139	28/01/1939	72	F	L	0.16	21.96	1.00	-2.00	78	3.0	3.0	0.1	0.1
MT125	24/04/1939	70	F	R	0.22	22.73	3.75	-0.50	90	1.0	1.0	0.1	0.1
WC122	06/07/1933	77	M	R	0.18	23.69	0.50	-1.00	97	2.0	2.5	2.0	0.1
JT99	23/08/1932	77	F	R	0.30	23.84	3.75	-2.75	95	IOL	IOL	IOL	IOL
BS116	08/12/1933	77	F	L	0.10	22.15	5.00	1.00	76	3.0	3.5	2.0	0.1
BC92	13/01/1922	88	F	L	0.12	23.06	1.75	-2.50	80	IOL	IOL	IOL	IOL
PS115	14/02/1929	82	M	L	-0.02	23.79	3.75	-1.00	86	2.0	1.0	0.1	0.1
SH93	03.09.1923	86	F	L	0.00	22.35	1.25	-1.75	77	IOL	IOL	IOL	IOL

Table I.5: Baseline characteristics for ARM participants (n=24).

Participant	DOB	Age	Gender	Test eye	VA	Axial Length	Refraction			LOCS III grading			
							Sph	Cyl	Axis	NC	NO	C	P
DH8	21/12/1938	70	M	R	0.02	24.28	1.00	-0.50	85	2.0	2.0	2.0	0.1
DH7	17/02/1946	63	M	R	0.24	23.34	2.00	-0.75	96	1.5	1.5	0.1	0.1
DG20	03/12/1932	76	M	R	0.22	23.36	4.50	-0.75	115	2.0	3.0	3.5	2.0
RG27	03/05/1933	76	M	L	0.06	23.29	2.00	-1.25	75	1.0	1.0	0.1	0.1
GB25	04/03/1943	66	F	L	0.28	24.25	0.75	-0.50	84	2.0	2.0	0.1	0.1
MH31	27/12/1942	66	M	L	-0.10	23.94	0.00	-0.50	158	2.0	2.5	0.1	0.1
AD32	14/01/1938	71	F	L	-0.02	23.27	0.25	-0.50	31	3.5	3.0	3.0	1.5
JO42	01/01/1947	62	M	L	-0.08	24.46	-1.75	-1.25	100	2.5	2.0	0.1	0.1
RE68	27/02/1946	63	M	R	0.10	24.97	-1.75	-0.75	140	3.0	3.0	0.1	0.1
AJ59	24/04/1949	60	M	R	-0.08	23.62	0.25	-0.50	93	3.0	3.0	0.1	0.1
TK73	22/02/1945	65	F	R	0.00	23.17	1.75	-0.25	114	2.0	3.0	0.1	0.1
PF70	18/10/1937	72	F	R	0.08	23.69	0.50	-0.75	92	1.0	1.0	0.1	0.1
MK75	25/05/1944	65	F	L	0.02	22.01	4.00	-1.50	78	2.50	2.50	0.10	0.10
RJ77	16/10/1949	60	M	R	-0.02	25.30	0.25			1.5	1.5	0.1	0.1
CO87	02/02/1937	73	M	R	0.10	23.66	1.75	-0.50	70	2.50	2.50	0.10	0.10
AO88	11/05/1938	71	M	L	0.10	22.47	2.00	-0.25	51	1.50	1.50	0.10	0.10
DT131	02/05/1936	74	F	R	0.08	23.12	2.75	-0.75	173	0.1	0.1	0.1	0.1
PG26	30/07/1949	60	M	L	-0.10	25.37	-3.00	-1.00	68	2.0	2.0	0.1	0.1
EN112	27/08/1923	87	M	R	0.26	23.87	1.25	-0.50	94	3.50	3.00	0.10	0.10
AI46	17/10/1934	75	M	L	0.04	25.49	-0.75	-1.50	84	2.0	2.5	0.1	0.1
BB80	22/02/1942	67	F	L	0.00	22.61	3.75	-0.50	150	2.0	2.5	2.5	0.1
HH13	21/04/1951	58	F	R	-0.04	23.31	1.25	-0.5	74	1	1	0.1	0.1
AJ56	25/02/1950	59	M	L	-0.10	22.47	2.25	-1.50	90	IOL	IOL	IOL	IOL
BA69	20/09/1952	57	M	L	-0.02	22.98	2.50	-0.50	67	2.50	2.50	0.10	0.50
GJ65	03/04/1950	59	M	R	-0.10	24.00	0.25			2.0	3.0	0.1	0.1
DJ53	04/03/1953	56	F	R	0.04	23.11		-0.50	73	2.0	2.0	0.1	0.1

Table I.6: Baseline characteristics for control participants (n=26).

Appendix J: OCT data

	Location																					
Participant	N10	N8[1]	N6[1]	N4[1]	N2[1]	F	T2[1]	T4[1]	T6[1]	T8[1]	T10	I10	I8[1]	I6[1]	I4[1]	I2[1]	F	S2[1]	S4[1]	S6[1]	S8[1]	S10
DH8	260	253	294	310	288	214	277	291	256	222	204	214	216	253	299	287	199	296	304	268	239	228
DH7	275	275	299	317	313	214	304	305	281	247	231	233	241	262	297	306	221	312	321	284	269	258
DG20	260	252	260	279	325	185	248	276	256	226	224	267	232	244	275	248	187	277	299	277	240	228
RG27	292	291	314	335	313	250	321	332	322	286	262	248	244	258	296	328	255	335	321	292	257	253
GB25	270	271	298	312	269	199	266	288	264	232	216	224	235	259	293	281	185	297	300	259	247	248
MH31	313	288	318	334	308	219	300	314	295	263	255	260	259	290	324	329	214	334	341	319	283	267
AD32	243	229	311	286	263	182	356	272	247	223	214		209	222	258	278	190	287	290	263	247	262
JO42	267	284	300	285	299	211	277	285	269	239	238		241	269	316	287	209	299	318	284	264	255
RE68		265	304	329	323	199	304	317	279	242	207	228	236	252	301	316	197	324	304	275	250	243
AJ59	238	266	305	322	280	185	290	302	278	243	207	219	240	266	305	298	182	288	307	285	265	250
TK73	228	251	286	303	271	182	268	299	280	231		226	242	275	309	263	187	294	314	266	253	243
PF70	233	215	289	288	260	209	273	290	264	226	219	204	204	242	276	295	209	283	295	249	221	228
MK75	253	275	296	293	269	209	263	275	261	251	219		261	263	285	278	202	275	300	278	263	243
RJ77	292	293	329	349	306	199	320	332	297	267	231	241	260	278	325	334	207	334	332	312	287	248
CO87	228	237	249	308	285	219	274	288	257	236	231	233	229	250	281	286	224	296	279	257	228	
AO88	236	234	255	293	278	199	273	287	249	223	209	216	216	232	268	275	197	280	280	246	223	211
DT131	391	393	414	425	365	279	352	355	399	358	340	384	370	394	417	376	272	389	422	398	360	374
PG26	277	286	293	319	328	211	312	298	263	221		221	243	263	296	315	241	322	307	288	268	250
EN112	345	329	356	369	348	316	335	363	323	276	294	296	286	322	371	368	309	354	357	328	319	326
AI46	289	235	254	289	291	214	287	290	256	227	221	204	205	229	277	298	209	266	306	243	234	224
BB80	265	266	290	305	266	199	269	284	259	240	221	243	237	266	291	281	192	306	308	288	262	262
HH13	245	285	316	339	343	267	331	352	347	315	284	238	259	282	326	348	248	344	343	304	279	258
AJ56	277	303	332	361	350	265	322	336	309	267	221		264	290	327	344	270	340	353	300	277	245
BA69	209	253	284	314	297	177	304	322	305	275	255	204	245	279	321	311	182	305	326	289	259	214
GJ65	272	288	320	341	333	211	314	319	289	255	209	236	269	282	312	329	216	321	319	290	272	226
DJ53	248	299	324	334	302	214	291	309	290	248	216	216	256	293	328	301	211	304	335	303	275	236
Mean	**268**	**274**	**303**	**321**	**303**	**217**	**297**	**307**	**284**	**252**	**234**	**239**	**246**	**270**	**307**	**306**	**216**	**310**	**319**	**286**	**263**	**251**
SD	39	36	34	32	30	33	28	26	35	32	33	39	32	34	33	32	32	29	29	32	29	34

Direction from Fovea: Foveal pit (F), Nasal (N), Temporal (T), Superior (S), Inferior (I)
Distance from Fovea: 2° (2), 4° (4), 6° (6), 8° (8) and 10° (10)
1.corrected for age 2.corrected for axial length

Table J.1: Retinal thickness results for control participants (n=26).

	Location																				
Participant	N10	N8[1]	N6[1]	N4[1]	N2[1]	F	T2[1]	T4[1]	T6[1]	T8[1]	T10	I10	I8[1]	I6[1]	I4[1]	I2[1]	F	S2[1]	S4[1]	S6[1]	S8[1]	S10
DG24	277	304	341	348	319	219	308	311	290	270	236	270	264	278	326	328	221	333	328	301	280	248
UH38		244	249	274	268	211	254	274	238	212	207		197	208	256	273	194	276	266	242	226	221
MK48	275	246	250	242	176	153	166	235	227	220	197		221	236	250	209	156	218	256	248	249	255
PJ45	289	302	321	329	313	214	294	318	289	267	238		251	280	326	309	216	322	324	304	277	260
JM83	265	274	290	293	232	175	237	271	254	237	226	238	235	264	286	257	173	259	296	279	252	248
RJ95	255	265	306	312	296	197	282	289	258	226	204	221	236	270	321	248	199	310	304	277	248	236
DR96	245	226	250	267	208	117	195	246	250	224	228	233	220	240	251	227	131	222	254	259	253	238
TO97	270	268	303	315	282	153	254	292	250	226	228	216	231	266	305	295	160	290	264	281	238	226
BS100	345	346	378	388	368	316	351	376	338	291	294	296	303	338	387	385	309	366	373	344	334	326
DN82	245	205	227	255	242	180	264	245	212	192	182	207	192	214	249	266	190	258	243	216	186	185
DP103	279	297	335	370	343	202	321	342	303	276	248	243	267	299	348	331	202	325	350	309	276	238
SJ90	224	239	252	252	262	175	253	270	246	226	209	226	227	236	258	273	185	258	261	249	229	231
CG101																						
SO107	241	242	266	264	245	190	248	266	227	206	207	221	212	251	269	255	190	259	260	245	222	238
JH108	248	242	273	291	240	180	226	292	261	245		260	234	263	296	262	170	273	304	255	234	238
AP109		205	223	233	201	194	196	220	200	174	187	214	182	199	212	212	199	226	235	211	193	
PT139	350	353	364	386	343	270	317	373	361	328	313	304	302	339	363	346	265	351	388	351	323	330
MT125	255	250	263	276	261	219	260	264	239	229	211	221	240	241	268	267	221	274	282	263		
WC122	338	335	357	383	354	289	372	384	357	323	306	345	334	351	372	387	292	377	392	368	325	321
JT99																						
BS116	394	411	423	422	337	277	360	401	391	360	333	350	366	400	416	372	267	387	424			
BC92		206	181	187	160	160	163	196	182	179	226		179	203	194	172	148	201	207	190	178	238
PS115	367	359	377	396	344	267	345	398	359	331	338	355	316	356	401	342	260	350	350	363	321	328
SH93		227	235	262	241	207	250	250	223	195	211	233	205	236	264	268	216	246	269	248	216	228
Mean	**287**	**275**	**294**	**307**	**274**	**207**	**269**	**296**	**271**	**247**	**240**	**259**	**246**	**271**	**301**	**286**	**207**	**290**	**301**	**276**	**253**	**254**
SD	50	57	62	63	60	50	60	60	58	52	48	50	50	55	61	58	47	55	58	50	46	41

Direction from Fovea: Foveal pit (F), Nasal (N), Temporal (T), Superior (S), Inferior (I)
Distance from Fovea: 2° (2), 4° (4), 6° (6), 8° (8) and 10° (10)
1.corrected for age 2.corrected for axial length

Table J.2: Retinal thickness results for ARM participants (n=22).

	Location																					
Participant	N10	N8[2]	N6	N4	N2[2]	F	T2	T4	T6	T8	T10	I10[2]	I8	I6	I4	I2	F	S2	S4	S6	S8[2]	S10[2]
DH8	114	168	243	248	250	231	219	236	211	202	170	159	187	199	207	231	245	233	219	216	236	191
DH7	146	192	236	224	227	207	245	279	262	238	233	166	202	199	170	180	190	221	284	292	207	217
DG20																						
RG27	92	102	141	180	205	216	199	199	156	153	114	147	165	170	168	207	224	211	207	204	193	200
GB25	80	127	160	190	220	231	231	214	194	177	158	182	185	199	216	221	250	265	241	277	290	275
MH31	68	56	58	80	114	114	104	119	104	129	117	127	136	124	102	126	114	73	95	112	139	150
AD32	134	187	228	309	295	284	168	284	279	275	265		190	221	228	267	296	309	318	311	256	229
JO42	53	68	61	114	94	100	122	129	122	124	122		124	117	104	104	112	124	122	109	116	107
RE68		76	87	109	160	134	143	134	132	131	122	141	112	126	122	136	136	119	112	109	156	139
AJ59	66	73	95	122	160	177	185	197	190	187	190	131	129	141	156	168	163	158	175	165	148	150
TK73	87	80	109	151	187	207	224	204	187	192		197	185	199	190	192	202	190	202	224	199	199
PF70	78	129	136	187	173	173	153	151	139	148	168	132	80	117	146	170	158	126	139	141	132	146
MK75	100	75	170	214	182	228	228	248	187	197	180		192	250	279	292	233	224	233	224	168	151
RJ77	66	192	219	299	362	323	306	318	313	279	241	225	221	258	255	316	345	345	338	309	322	355
CO87	146	168	255	243	265	282	272	287	262	250	253	181	238	311	294	292	214	211	148	134	132	
AO88	70	105	187	187	182	231	241	221	241	224	204	30	104	124	163	207	226	265	309	301	245	232
DT131	228	226	272	279	283	304	294	294	345	292	313	249	270	301	289	304	309	318	333	335	344	347
PG26	85	124	114	95	176	153	146	117	124	160		177	129	143	175	143	143	117	139	153	207	205
EN112	49	76	80	97	97	83	126	95	102	153	143	142	85	83	83	73	87	131	87	95	85	138
AI46	49	117	146	194	272	204	199	199	204	194	180	154	119	153	180	204	197	214	219	236	293	276
BB80	114	129	233	282	293	357	389	418	420	433	442	192	272	296	318	316	357	362	345	330	260	271
HH13	136	129	141	117	147	180	146	119	97	83	68	213	192	194	158	158	163	180	177	253	251	241
AJ56	134	119	170	182	194	238	226	214	202	197	187		214	236	241	255	231	204	221	243	206	222
BA69	156	161	190	190	200	243	241	214	182	143	100	158	194	185	204	219	243	243	248	243	223	227
GJ65	107	144	143	182	213	228	202	194	199	194	160	199	204	170	173	175	236	226	231	241	191	214
DJ53	107	127	262	357	385	467	474	464	399	391	343	349	382	442	474	457	450	433	399	389	317	303
Mean	**103**	**126**	**166**	**193**	**213**	**224**	**219**	**222**	**210**	**206**	**194**	**174**	**180**	**198**	**204**	**216**	**221**	**220**	**222**	**226**	**213**	**216**
SD	42	45	65	74	74	84	84	91	88	81	87	60	67	80	84	83	84	86	85	82	69	65

Direction from Fovea: Foveal pit (F), Nasal (N), Temporal (T), Superior (S), Inferior (I)
Distance from Fovea: 2° (2), 4° (4), 6° (6), 8° (8) and 10° (10)
1.corrected for age 2.corrected for axial length

Table J.3: Choroidal thickness results for control participants (n=25).

	Location																					
Participant	N10	N8[2]	N6	N4	N2[2]	F	T2	T4	T6	T8	T10	I10[2]	I8	I6	I4	I2	F	S2	S4	S6	S8[2]	S10[2]
DG24	107	121	197	245	254	265	260	236	219	219	199	113	194	192	194	221	238	287	299	296	278	268
UH38		79	117	153	171	202	202	185	175	151	163		117	119	148	177	219	228	250	250	239	217
MK48	51	58	95	114	126	129	143	141	131	136	131		63	97	78	119	122	143	139	136	133	136
PJ45	207	229	296	258	178	279	245	207	168	134	100		168	187	204	221	202	243	238	233	165	152
JM83	221	230	338	333	269	313	279	275	250	216	204	148	282	330	323	311	318	350	394	403	353	301
RJ95	170	280	301	316	269	292	318	270	194	187	197	300	311	323	294	306	287	241	265	313	285	304
DR96	117	101	175	231	140	207	156	146	131	163	170	111	207	224	250	265	265	241	282	260	144	177
TO97	173	191	275	350	409	416	362	306	328	304	294	301	304	313	340	352	377	318	323	267	300	321
BS100			104	180	187	214	219	204	214	221	216	121	146	202	258	250	267	245	199	170	155	
DN82	46	58	68	102	140	163	119	185	182	134	153	63	70	83	107	139	175	148	163	148	147	115
DP103	126	242	236	202	282	343	338	304	202	194	158	205	258	299	313	311	289	311	326	321	338	303
SJ90	73	72	90	117	130	148	153	165	168	146	134	140	139	141	136	146	146	148	146	143	147	157
CG101																						
SO107	117	85	139	146	123	148	143	148	175	202	194	115	139	126	148	146	151	156	163	194	180	225
JH108	90	83	136	165	164	204	180	151	204	209		191	199	241	221	231	209	170	151	165	120	130
AP109		132	141	173	162	216	194	187	192	214	211	135	182	190	180	185	209	209	199	214	178	
PT139	122	96	202	156	95	165	194	194	226	226	207	144	238	233	236	255	260	258	272	265	211	215
MT125	119	132	204	250	241	289	270	233	224	192	187	85	134	175	216	243	294	289	267	236		
WC122	236	289	321	323	340	357	367	326	316	323	311	319	333	357	377	362	367	389	374	365	367	370
JT99																						
BS116	197	201	272	335	299	389	391	367	328	316	296	200	262	284	301	333	389	357				
BC92		29	70	97	83	153	153	153	156	173	156		129	122	131	129	141	160	151	160	73	110
PS115	83	117	158	221	244	214	199	177	173	185	202	179	207	180	204	207	209	248	270	224	217	244
SH93		213	279	318	311							188	277	299	311	318	330	382	340			
Mean	**133**	**145**	**192**	**217**	**210**	**243**	**233**	**217**	**207**	**202**	**194**	**170**	**198**	**214**	**226**	**238**	**248**	**251**	**248**	**238**	**212**	**220**
SD	58	79	87	84	87	85	83	67	57	56	55	74	77	82	82	76	78	78	79	75	86	81

Direction from Fovea: Foveal pit (F), Nasal (N), Temporal (T), Superior (S), Inferior (I)
Distance from Fovea: 2° (2), 4° (4), 6° (6), 8° (8) and 10° (10)
1.corrected for age 2.corrected for axial length

Table J.4: Choroidal thickness results for ARM participants (n=22).

	Location																					
Participant	N10	N8[1]	N6[1]	N4[1]	N2[1]	F	T2	T4[1]	T6[1]	T8	T10	I10[1]	I8[1]	I6[1]	I4	I2[1]	F	S2[1]	S4[1]	S6	S8[1]	S10
DH8	104	113	107	129	144	214	156	133	122	112		98	101	94	124	134	199	136	126	131	113	117
DH7	114	125	136	138	158	214	163	142	136	114	112	116	115	115	126	133	221	131	135	126	129	126
DG20	102	97	109	122	224	185	134	112	108	114	109	89	90	95	107	110	187	126	120	119	103	107
RG27	114	117	131	146	149	250	163	119	125	117	122		104	115	136	144	255	116	127	117	115	119
GB25	90	98	127	142	135	199	117	120	108	104	97	90	90	93	87	93	185	142	122	112	107	
MH31	114	137	134	142	159	219	156	147	132	122			124	124	136	159	214	156	144	134	132	124
AD32		117	179	128	137	182	97	129	119	117	119			108	119	131	190	140	122	126	122	109
JO42		131	137	100	155	211	146	134	129	122			111	128	129	154	209	149	145	134	133	122
RE68		125	141	153	172	199	165	156	145	131			115	113	126	153	197	160	137	126	120	119
AJ59	90	104	123	137	154	185	146	132	117	102	97	85	93	96	83	110	182	133	116	107	108	92
TK73	87	109	124	131	154	182	151	146	138	122			106	118	124	150	187	143	135	124	120	112
PF70	95	101	131	117	130	209	141	118	130	107	102		94	109	119	110	209	136	126	117	107	
MK75	119	130	131	136	142	209	146	134	126	129	119		127	121	131	143	202	148	135	136	130	129
RJ77		109	147	154	174	199	173	156	142	112			113	118	124	135	207	150	140	124	130	
CO87		120	118	152	143	219	148	136	126	124	126	104	110	120	131	128	224	133	130	141		
AO88	95	105	113	128	147	199	168	136	111	87	100	107	92	105	109	123	197	130	120	114	105	107
DT131	139	158	170	173	167	279	221	210	193	173	168	132	160	156	41	156	272	187	170	185	161	146
PG26	87	123	130	144	161	211	134	127	122			104	106	118	117	125	241	133	138	129	127	119
EN112	129	132	155	159	190	316	204	165	143	134	134	108	115	121	158	183	309	172	148	153	139	143
AI46		115	108	126	136	214	153	128	123	119	124			109	122	118	209	144	128	122	116	119
BB80		119	126	133	140	199	143	131	111	112	107		116	121	114	126	192	133	124	122	121	117
HH13	124	135	143	156	192	267	177	164	146	131	129	121	122	125	129	157	248	155	139	122	134	126
AJ56	124	139	141	153	176	265	165	153	143	129	124		121	131	129	170	270	180	151	134	145	129
BA69	90	102	115	126	153	177	143	124	111	92	90	86	89	97	104	134	182	129	114	97	98	83
GJ65	112	125	144	148	171	211	151	145	138	124		120	116	117	124	146	216	148	141	122	118	
DJ53	114	115	140	152	162	214	129	143	139	122	100	116	117	117	122	147	211	150	139	129	128	124
Mean	**108**	**119**	**133**	**139**	**159**	**217**	**153**	**140**	**130**	**119**	**115**	**106**	**110**	**115**	**118**	**137**	**216**	**145**	**133**	**127**	**122**	**118**
SD	16	15	18	16	21	33	25	20	18	16	18	15	16	14	22	20	32	17	13	16	14	14

Direction from Fovea: Nasal (N), Temporal (T), Superior (S), Inferior (I)
Distance from Fovea: 2° (2), 4° (4), 6° (6), 8° (8) and 10° (10)
1.corrected for age 2.corrected for axial length

Table J.5: Photoreceptor layer thickness results for control participants (n=26).

	Location																					
Participant	N10	N8[1]	N6[1]	N4[1]	N2[1]	F	T2	T4[1]	T6[1]	T8	T10	I10[1]	I8[1]	I6[1]	I4	I2[1]	F	S2[1]	S4[1]	S6	S8[1]	S10
DG24	100	120	136	156	187	219	146	148	125	109	119		122	129	122	157	221	123	122	114	116	117
UH38				131	133	211	153	131	116	119	126				126	126	194	94	106	107	108	102
MK48			95	103	81	153		97	93	90	85				104	95	156	78	101	104	104	100
PJ45	119	117	130	139	153	214	139	133	120	117	124		124	122	129	139	216	135	131	124	114	119
JM83	102	116	121	133	147	175	139	121	114	107	102	94	96	102	109	136	173	136	121	117	114	122
RJ95	109	112	123	132	161	197	146	135	129	107	117	110	111	114	134	105	199	122	124	119	119	117
DR96	107	100	118	134	118	117	139	121	117	119			105	108	122	100	131	82	118	126	138	126
TO97		109	131	137	154	153	119	135	117	124	122	76	103	116	131	132	160	139	94	139	114	112
BS100				67	67	316	92	68	97	107	95		80	83	78	52	309	88	63	107		
DN82	92	81	79	78	75	180	151	101	93	114	102		76	72	90	80	190	84	104	104		
DP103		126	148	164	187	202	173	162	144	126	129	116	132	144	146	164	202	155	154	131	136	
SJ90		111	111	109	154	175	146	134	123	126	119		120	113	97	123	185	111	96	112	125	
CG101																						
SO107		120	115	126	129	190	160	130	102	114			98	111	124	140	190	140	128	129	101	
JH108	87	110	120	121	124	180	146	128	126	119			110	106	131	96	170	123	123	122	116	
AP109		106	100	111	116	194	134	112	102	102			89	95	112	106	199	115	102	109	98	
PT139	143	160	163	178	198	270	221	196	168	158	146	120	135	143	165	183	265	195	162	141	143	153
MT125	104	106	102	103	100	219	146	123	122	119			113	101	122	120	221	124	118	136		
WC122	151	145	156	172	190	289	231	178	158	163	151	127	116	128	156	201	292	161	167	173	158	153
JT99																						
BS116	158	171	178	191	193	277	165	149	153	151	148	148	150	160	175	184	267					
BC92		82	61	61	59	160		71	79	114			83	91	97	58	148	67	69	95	80	
PS115	165	159	169	180	202	267	224	158	156	160	146		142	155	168	165	260	126	107	165	146	146
SH93			113	129	121	207	175	123	105	126		90	102	108	129	129	216	108	122	129	111	
Mean	**120**	**119**	**123**	**130**	**139**	**207**	**157**	**130**	**121**	**122**	**122**	**110**	**110**	**115**	**126**	**127**	**207**	**119**	**116**	**124**	**119**	**124**
SD	27	25	29	35	44	50	34	30	23	19	20	23	20	23	25	39	47	31	26	19	19	19

Direction from Fovea: Nasal (N), Temporal (T), Superior (S), Inferior (I)
Distance from Fovea: 2° (2), 4° (4), 6° (6), 8° (8) and 10° (10)
1.corrected for age 2.corrected for axial length

Table J.6: Photoreceptor layer thickness results for ARM participants (n=22).

	Location																			
Participant	N10[1]	N8	N6[1]	N4[1]	N2[1]	T2	T4	T6	T8[1]	T10	I10[1]	I8[1]	I6	I4	I2	S2	S4[1]	S6	S8[1]	S10
DH8	41	46	75	67	66	53	61	46	45		44	45	68	68	73	66	61	49	44	41
DH7	48	53	59	66	75	51	63	51	57	49	43	47	63	58	73	78	65	61	53	49
DG20	35	61	49	57	42	63	66	63	47	44	36	49	58	63	68	61	61	58	38	44
RG27	40	63	104	67	57	75	87	66	59	53		44	51	75	80	114	75	70	51	29
GB25	71	68	74	64	59	73	73	73	54	46	44	53	75	97	97	58	73	49	54	
MH31	49	46	74	78	61	58	66	61	69			46	61	68	58	70	68	58	54	49
AD32		44	56	64	53	197	58	58	44	44			44	61	66	58	63	58	44	63
JO42		53	63	70	61	49	70	58	46			50	44	58	53	56	58	53	46	46
RE68		49	64	74	61	49	66	61	50			44	49	66	66	61	67	66	53	41
AJ59	50	63	76	69	65	61	70	61	58	44	47	49	66	95	90	78	71	66	55	49
TK73	48	51	61	67	47	41	53	53	43			47	51	58	51	68	66	44	40	36
PF70	45	39	57	61	47	68	73	51	48	51		31	51	58	75	68	63	56	38	
MK75	50	56	70	69	59	51	61	51	43	41		52	66	63	51	51	66	49	49	44
RJ77		63	66	76	68	46	66	51	60			44	49	66	83	78	59	61	50	
CO87		53	51	70	61	61	61	61	50	49	35	40	56	63	73	68	57	56		
AO88	40	49	47	62	60	49	61	56	88	51	28	39	44	58	70	68	58	53	41	44
DT131	94	102	93	103	99	61	61	75	73	75	83	80	112	233	112	92	103	87	64	63
PG26	43	56	61	71	73	73	70	49			52	47	51	66	80	87	64	44	42	36
EN112	60	90	70	94	86	85	90	85	58	70	42	56	83	109	90	73	65	85	66	66
AI46		53	48	56	67	70	63	34	48	44			49	66	87	70	56	49	27	39
BB80		63	63	65	58	53	63	61	61	51		36	61	68	61	70	63	53	41	46
HH13	56	56	72	76	62	46	66	63	67	51	30	54	56	66	75	78	75	63	48	39
AJ56	59	53	77	84	83	66	68	66	56	46		60	53	70	78	61	72	63	48	66
BA69	59	56	51	74	67	56	68	66	61	44	46	50	53	63	68	75	71	61	51	44
GJ65	47	51	63	70	73	63	70	53	54		41	43	61	58	66	63	60	46	50	
DJ53	56	56	77	80	63	61	66	56	50	58	52	58	61	58	58	58	66	73	52	39
Mean	**52**	**57**	**66**	**71**	**64**	**65**	**67**	**59**	**56**	**51**	**45**	**48**	**59**	**74**	**73**	**70**	**67**	**59**	**48**	**46**
SD	13	13	14	10	12	29	8	10	11	9	13	10	14	35	14	13	9	11	8	10

Direction from Fovea: Nasal (N), Temporal (T), Superior (S), Inferior (I)
Distance from Fovea: 2° (2), 4° (4), 6° (6), 8° (8) and 10° (10)
1.corrected for age 2.corrected for axial length

Table J.7: Bipolar cell layer thickness results for control participants (n=26).

	Location																		
Participant	N10[1]	N8	N6[1]	N4[1]	N2[1]	T2	T4	T6	T8[1]	T10	I10[1]	I8[1]	I6	I4	I2	S2	S4[1]	S6	S8[1]	S10
DG24	78	66	92	82	61	63	66	66	69	53		48	49	70	68	102	91	75	71	22
UH38				53	54	56	61	61	42	24				63	66	104	72	61	52	53
MK48			43	50	49		58	56	50	46				46	49	70	52	56	32	44
PJ45	57	63	72	75	67	68	70	63	56	44		38	56	63	63	78	67	63	57	41
JM83	60	61	55	58	46	46	63	56	53	49	41	43	61	61	53	56	65	56	46	34
RJ95	49	51	67	78	63	66	58	44	47	34	42	48	46	61	56	92	67	51	40	39
DR96	37	53	43	51	38	44	58	58	45			33	56	63	73	80	48	56	49	44
TO97		51	52	63	52	63	58	51	36	36	49	41	53	58	70	61	53	53	43	36
BS100				77	57	70	73	61	39	36		27	51	78	97	49	74	41		
DN82	36	49	45	73	73	51	53	53	26	34		24	51	80	95	68	47	44		
DP103		70	86	78	69	53	73	68	72	46	64	58	70	68	66	78	70	70	63	
SJ90		36	56	57	47	44	44	46	41	41		40	46	61	75	70	47	46	37	
CG101																				
SO107		44	55	56	43	44	44	56	33			26	49	61	58	53	69	53	44	
JH108	34	51	53	70	55	58	68	61	50			36	58	68	85	68	71	61	41	
AP109		39	34	45	38	41	53	46	27			32	49	46	49	46	49	46	37	
PT139	75	92	81	92	67	58	141	78	70	70	66	72	92	87	85	73	97	102	75	75
MT125	46	53	65	84	88	51	56	41	43			38	56	53	61	32	59	53		
WC122	55	80	79	90	68	66	87	78	65	61	62	82	97	100	85	102	92	78	65	53
JT99																				
BS116	65	90	69	66	68	114	117	102	85	90	59	73	92	92	80					
BC92		44	18	30	19		46	39	25			21	49	53	39	46	45	51	34	
PS115	55	75	59	81	53	66	109	87	82	85		58	78	102	100	124	101	100	57	68
SH93			16	53	50	49	53	56	27		11	25	53	66	70	61	53	51	30	
Mean	**54**	**59**	**57**	**67**	**56**	**59**	**69**	**60**	**49**	**50**	**49**	**43**	**61**	**68**	**70**	**72**	**66**	**60**	**49**	**46**
SD	14	17	21	16	15	16	25	15	18	19	18	18	16	16	17	23	17	16	13	15

Direction from Fovea: Nasal (N), Temporal (T), Superior (S), Inferior (I)
Distance from Fovea: 2° (2), 4° (4), 6° (6), 8° (8) and 10° (10)
1.corrected for age 2.corrected for axial length

Table J.8: Bipolar cell layer thickness results for ARM participants (n=22).

	Location																			
Participant	N10	N8	N6	N4	N2	T2	T4	T6[1]	T8[1]	T10[1+2]	I10	I8[1]	I6	I4	I2	S2	S4	S6	S8	S10
DH8	49	53	75	95	73	70	85	80	53		24	34	68	80	70	83	85	63	51	36
DH7	61	61	75	95	80	83	90	86	69	66	41	48	51	78	92	92	83	61	58	51
DG20	46	61	83	87	58	70	90	77	61	58	39	39	68	97	78	92	97	80	56	41
RG27	56	66	41	100	97	95	114	118	99	67		34	53	85	100	87	90	63	53	58
GB25	44	68	75	92	75	66	80	73	64	78	46	46	63	87	73	78	75	58	41	
MH31	68	63	73	92	87	85	97	98	74			46	73	87	112	95	83	87	66	46
AD32		53	56	78	73	70	73	54	52	48			46	58	70	75	75	56	53	49
JO42		46	70	87	83	73	75	77	72			48	61	87	75	92	80	58	51	46
RE68		53	73	87	78	83	95	74	61			43	53	78	83	87	63	49	41	49
AJ59	56	61	78	95	61	70	85	86	74	74	39	49	61	78	85	68	85	56	61	58
TK73	39	56	78	95	70	73	95	82	67			52	73	95	61	83	75	56	41	32
PF70	49	66	83	112	83	75	100	83	71	63		48	66	83	85	80	78	68	66	
MK75	46	53	68	73	68	63	73	77	74	57		47	53	68	78	75	75	63	56	44
RJ77		51	70	95	66	87	95	91	81			52	63	85	92	92	92	70	51	
CO87		46	58	70	80	78	83	62	56	52	32	43	56	68	75	83	70	49		
AO88	46	44	61	83	70	66	90	69	48	53	34	44	53	83	70	83	75	53	49	32
DT131	73	102	124	119	97	85	85	110	99	76	75	71	95	126	100	102	114	97	75	114
PG26	51	46	68	80	95	83	87	93			34	49	56	68	87	87	70	58	53	41
EN112	73	92	95	109	70	83	109	91	86	73	53	65	92	117	102	95	117	83	68	75
AI46		32	61	87	75	73	90	87	52	54			41	68	85	53	92	51	41	44
BB80		46	73	87	68	73	80	77	68	62		48	58	83	78	87	85	68	56	56
HH13	78	85	102	104	90	90	109	102	78	56	53	48	63	87	95	87	92	66	53	44
AJ56	56	63	90	100	83	75	102	87	82	57		55	73	85	80	85	92	58	56	32
BA69	61	73	109	102	78	85	109	94	74	51	39	56	80	97	102	97	102	78	56	44
GJ65	44	58	78	100	78	75	90	85	65		36	50	61	83	90	87	73	68	56	
DJ53	46	68	83	83	78	70	85	77	72	70	36	51	66	97	87	92	97	46	61	41
Mean	**55**	**60**	**77**	**93**	**77**	**77**	**91**	**84**	**70**	**62**	**42**	**48**	**63**	**85**	**85**	**85**	**85**	**64**	**55**	**49**
SD	11	15	17	12	10	8	11	14	13	9	12	8	13	15	12	10	13	13	9	18

Direction from Fovea: Nasal (N), Temporal (T), Superior (S), Inferior (I)
Distance from Fovea: 2° (2), 4° (4), 6° (6), 8° (8) and 10° (10)
1.corrected for age 2.corrected for axial length

Table J.9: Ganglion cell layer thickness results for control participants (n=26).

	Location																		
Participant	N10	N8	N6	N4	N2	T2	T4	T6[1]	T8[1]	T10[1+2]	I10	I8[1]	I6	I4	I2	S2	S4	S6	S8	S10
DG24	53	78	90	95	73	66	85	90	77	63		46	56	85	83	83	83	68	56	78
UH38				75	68	53	70	55	44	52				61	73	70	75	63	41	36
MK48			70	90	46		80	77	80	64				78	68	70	78	61	68	46
PJ45	51	70	95	100	83	83	102	92	78	61		57	70	95	90	95	100	80	73	61
JM83	61	68	87	85	39	53	80	77	73	75	36	55	63	90	68	68	85	70	66	46
RJ95	44	58	85	85	66	66	85	75	68	57	32	50	66	87	85	83	87	66	53	51
DR96	46	61	68	68	51	36	61	58	52			45	53	68	51	51	68	63	46	44
TO97		73	83	100	75	83	92	73	66	68	41	36	58	90	78	83	92	63	53	49
BS100				87	90	63	90	64	61	60		52	58	80	83	70	90	75		
DN82	41	49	63	87	73	78	78	54	40	35		37	66	78	80	85	73	61		
DP103		56	75	100	87	78	90	78	68	83	39	50	49	80	95	83	87	63	46	
SJ90		53	66	73	61	61	92	77	60	52		42	51	70	56	61	83	58	41	
CG101																				
SO107		56	70	68	73	61	92	58	49			54	68	78	63	56	53	56	46	
JH108	66	56	70	85	61	39	97	73	76			61	68	83	87	85	83	56	49	
AP109		53	70	66	46	46	56	50	46			23	49	61	56	53	58	51	36	
PT139	70	75	92	100	78	49	36	114	100	92	58	58	75	95	83	85	102	87	78	58
MT125	56	66	73	78	63	63	80	75	68			56	61	80	73	87	83	58		
WC122	80	85	95	104	95	97	100	95	82	74	73	87	92	95	95	100	102	85	68	61
JT99																				
BS116	97	112	148	148	75	92	124	127	118	84	61	89	119	143	117					
BC92		56	66	85	68		80	61	41			37	51	58	83	75	73	44	51	
PS115	58	90	100	114	87	87	112	100	82	79		53	102	112	90	104	104	73	78	56
SH93			75	73	68	66	75	51	43		34	38	66	75	73	73	83	75	51	
Mean	**60**	**68**	**82**	**89**	**69**	**66**	**84**	**76**	**67**	**67**	**47**	**51**	**67**	**84**	**79**	**77**	**83**	**66**	**56**	**53**
SD	16	16	19	19	15	17	19	20	20	15	15	16	18	18	15	14	13	11	13	11

Direction from Fovea: Nasal (N), Temporal (T), Superior (S), Inferior (I)
Distance from Fovea: 2° (2), 4° (4), 6° (6), 8° (8) and 10° (10)
1.corrected for age 2.corrected for axial length

Table J.10: Ganglion cell layer thickness results for ARM participants (n=22).

	Location																			
Participant	N10[2]	N8	N6[2]	N4	N2	T2	T4[1]	T6[1]	T8	T10	I10	I8	I6	I4[2]	I2	S2	S4	S6	S8	S10
DH8	46	44	34	19	5	5	13	9	12		39	34	27	32	12	12	34	32	32	34
DH7	63	32	31	17	0	0	8	8	7	10	41	32	29	28	5	10	36	29	27	32
DG20	68	44	21	15	0	0	13	12	5	5	80	51	32	27	0	0	27	39	46	36
RG27	75	56	38	24	10	7	16	17	12	12	66	58	49	20	12	19	34	61	41	46
GB25	53	36	20	15	0	10	14	9	10	0	44	44	27	18	17	19	29	39	44	41
MH31	77	41	36	22	1	0	5	5	0	0	61	41	32	31	0	12	46	39	32	49
AD32	34	19	21	17	0	0	14	17	10	0			29	30	15	15	32	32	29	41
JO42	49	49	26	27	0	0	3	2	0	0		32	32	30	0	0	32	29	32	41
RE68		34	22	15	12	0	0	0	0	0	41	34	34	21	12	15	34	27	34	34
AJ59	52	32	30	19	0	0	12	11	10	0	63	49	36	37	7	7	32	44	39	51
TK73	65	34	26	10	0	0	4	6	0	0	56	36	32	30	0	0	36	39	51	63
PF70	35	15	17	0	0	0	2	3	0	0	29	29	22	27	29	0	32	19	12	
MK75	75	34	33	15	0	0	7	6	5	0		34	22	24	5	0	22	27	27	27
RJ77	66	63	40	22	0	0	12	11	15	15	61	51	41	32	19	12	36	44	53	53
CO87		24	22	17	0	0	12	11	7	0	46	34	24	32	15	15	24	24	19	
AO88	73	41	39	22	0	0	2	15	0	0	36	39	34	30	15	0	29	34	29	29
DT131	87	39	29	32	0	0	3	23	15	15	75	56	39	33	15	10	39	44	63	51
PG26	66	53	28	22	0	10	10	0	0	0	46	41	32	27	17	12	32	44	41	53
EN112	48	36	33	12	0	5	8	11	0	0	44	44	46	29	10	19	39	49	53	41
AI46	88	44	30	22	12	7	13	14	10	0	36	36	39	34	15	0	34	39	53	22
BB80	66	39	33	19	0	0	10	10	0	0	41	36	27	29	17	15	36	46	44	44
HH13							9	32	39	58	53	36	29	28	15	22	32	36	39	49
AJ56	73	39	29	22	10		9	10				29	24	30	10	12	34	29	24	19
BA69	26	12	12	10			16	31	49	80	56	51	39	38			34	34	49	44
GJ65	72	46	35	22	12	10	9	10	12		56	61	36	31	22	19	41	39	44	36
DJ53	58	49	27	17		10	11	14	5		36	32	39	31			27	34	29	32
Mean	**62**	**38**	**28**	**18**	**3**	**3**	**9**	**12**	**9**	**9**	**50**	**41**	**33**	**29**	**12**	**10**	**33**	**37**	**38**	**40**
SD	16	12	7	6	5	4	5	8	12	20	13	9	7	5	7	8	5	9	12	11

Direction from Fovea: Nasal (N), Temporal (T), Superior (S), Inferior (I)
Distance from Fovea: 2° (2), 4° (4), 6° (6), 8° (8) and 10° (10)
1.corrected for age 2.corrected for axial length

Table J.11: Nerve fibre layer thickness results for control participants (n=26).

	Location																			
Participant	N10[2]	N8	N6[2]	N4	N2	T2	T4[1]	T6[1]	T8	T10	I10	I8	I6	I4[2]	I2	S2	S4	S6	S8	S10
DG24	66	29	26	12	0	12	8	6	15	12	104	49	34	27	12	22	27	22	32	32
UH38		27	14	17	12	5	15	8	7	0			17	19	15	10	17	24	27	29
MK48	83	51	42	0	0	0	1	2	0	0		34	36	29	0	0	27	34	46	66
PJ45	90	49	29	15	10	0	11	13	17	12		32	29	37	15	15	24	32	32	39
JM83	75	29	33	17	0	0	7	8	5	0	66	39	39	31	0	0	24	36	27	46
RJ95	63	41	33	17	7	0	9	8	5	0	44	27	41	35	0	12	24	36	34	29
DR96	82	24	27	17	0	0	12	21	10		41	34	34	27	12	12	27	36	24	24
TO97	47	41	34	17	0	0	9	10	0	0	36	49	44	35	19	10	27	36	29	29
BS100			30	19	7	0	12	14	0	0	51	34	29	35	12	10	22	32	32	36
DN82	53	41	39	19	19	12	20	17	12	0		51	39	29	22	24	27	34	32	
DP103	48	36	26	27	0	0	14	10	10	0	44	27	27	36	0	7	34	27	27	
SJ90	43	36	20	12	0	0	0	0	0	0	29	24	24	27	17	15	34	29	24	34
CG101																				
SO107	67	32	28	17	0	0	3	14	10	0	39	32	32	27	0	12	15	24	34	34
JH108	60	34	31	17	0	0	3	5	0	0	56	24	39	33	0	0	32	34	32	
AP109		19	20	15	0	0	5	7	0	0	39	34	19	21	12	15	32	29	27	
PT139	90	32	33	17	0	0	2	3	0	0	46	34	34	31	0	0	29	32	29	44
MT125	63	29	26	12	10	7	6	2	0			32	27	22	17	32	24	22		
WC122	35	36	27	19	0	0	23	30	15	12	58	46	44	44	15	17	36	53	39	53
JT99																				
BS116	91	49	33	19	0	10	16	13	7	0	56	51	39	31	0	12	19			
BC92		46	36	17	12							32	34	31	10	19	32	44	22	32
PS115	62	51	48	24	0	0	25	20	7	15		58	36	51	0	0	46	56	46	58
SH93		29	34	12	0	0	7	18	0	0	51	34	29	37	12	10	22	32	32	36
Mean	**66**	**36**	**30**	**16**	**4**	**2**	**10**	**11**	**6**	**3**	**51**	**37**	**33**	**32**	**9**	**11**	**27**	**34**	**31**	**39**
SD	17	9	8	5	6	4	7	7	6	5	18	10	7	7	8	8	7	9	6	12

Direction from Fovea: Nasal (N), Temporal (T), Superior (S), Inferior (I)
Distance from Fovea: 2° (2), 4° (4), 6° (6), 8° (8) and 10° (10)
1.corrected for age 2.corrected for axial length

Table J.12: Nerve fibre layer thickness results for ARM participants (n=22).

Appendix K: ERG data

	A-wave		B-wave	
Participant	Amplitude (μV)	Implicit time (ms)	Amplitude (μV)	Implicit time (ms)
DH8	-2.69	25.5	3.96	45.5
DH7	-1.65	24.2	4.97	45.0
DG20	-0.59	22.2	2.79	42.5
RG27	-2.61	24.5	7.67	45.1
GB25	-2.90	23.5	7.34	43.4
MH31	-3.54	24.8	6.97	43.4
AD32	-3.69	24.2	7.24	44.3
JO42	-1.83	25.3	4.97	45.3
RE68	-3.86	26.1	7.19	45.9
AJ59	-3.56	24.9	8.45	44.0
TK73	-2.43	23.4	7.01	42.8
PF70	-3.14	23.3	7.35	42.6
MK75	-1.15	17.8	4.84	42.9
RJ77	-1.92	26.4	4.76	47.0
CO87	-2.89	24.3	5.75	43.0
AO88	-4.29	30.1	3.55	51.5
DT131	-2.76	24.2	5.59	44.1
PG26	-2.69	23.1	6.45	42.7
EN112	-2.02	29.3	4.12	49.7
AI46	-2.22	24.1	6.96	46.1
BB80	-2.53	23.9	6.40	43.0
HH13	-2.41	24.1	4.21	43.3
AJ56	-2.57	24.1	4.95	43.4
BA69	-2.78	24.7	6.23	46.3
GJ65	-2.27	24.2	6.22	43.5
DJ53	-2.14	23.4	8.72	42.9
Mean	**-2.58**	**24.47**	**5.95**	**44.61**
SD	0.82	2.19	1.54	2.21

Table K.1: Focal cone ERG results for control participants (n=26).

	A-wave		B-wave	
Participant	Amplitude (μV)	Implicit time (ms)	Amplitude (μV)	Implicit time (ms)
DG24	-3.00	25.6	7.38	44.2
UH38	-1.80	27.1	3.56	46.2
MK48	-1.15	21.9	2.59	52.8
PJ45	-1.33	24.3	4.85	46.4
JM83	-3.35	24.0	6.43	41.6
RJ95	-1.53	24.4	3.37	46.7
DR96	-2.06	28.0	5.40	50.3
TO97	-4.08	27.4	6.29	48.1
BS100	-1.78	25.5	5.83	47.2
DN82	-1.33	27.2	2.53	51.6
DP103	-3.09	23.2	7.51	42.2
SJ90	-1.92	26.5	5.01	53.0
CG101	-1.47	24.3	3.67	45.7
SO107	-3.37	26.9	10.31	51.6
JH108	-0.12	24.2	4.80	45.9
AP109	-3.32	27.8	4.68	48.4
PT139	-2.15	25.8	4.87	43.7
MT125	-3.09	25.2	6.81	44.9
WC122	-1.61	26.4	4.40	47.8
JT99	-2.05	25.8	3.14	47.3
BS116	-2.71	25.2	5.96	45.3
BC92	-1.16	23.6	3.07	52.3
PS115	-2.60	24.7	4.10	44.2
SH93	-3.84	27.0	7.72	48.9
Mean	**-2.25**	**25.52**	**5.18**	**47.37**
SD	0.99	1.58	1.89	3.27

Table K.2: Focal cone ERG results for ARM participants (n=24).

	A-wave		B-wave	
Participant	Amplitude (μV)	Implicit time (ms)	Amplitude (μV)	Implicit time (ms)
DH8*			4.5	56.5
DH7*			3.3	62.0
DG20	-1.45	33.50	3.5	65.5
RG27*			4.8	57.0
GB25#				
MH31#				
AD32*			4.5	48.5
JO42	-1.22	32.50	4.2	61.0
RE68#				
AJ59	-0.43	29.50	3.9	56.5
TK73*			3.0	52.5
PF70	-0.29	26.00	7.7	49.5
MK75#				
RJ77 #				
CO87#				
AO88#				
DT131#				
PG26	-1.39	29.00	4.6	63.5
EN112			2.1	61.00
AI46*			4.0	57.5
BB80*			4.6	61.0
HH13	-0.70	26.50	2.7	65.50
AJ56	-0.53	32.00	3.5	69.00
BA69	-2.11	39.00	4.6	70.50
GJ65	-1.21	32.00	4.1	64.50
DJ53	-0.74	24.00	7.8	60.00
Mean	**-1.01**	**30.40**	**4.30**	**60.08**
SD	0.57	4.36	1.46	6.09

* No measureable a-wave
# No measurable waveform

Table K.3: 20 td.s focal rod ERG results for control participants (n=19).

	A-wave		B-wave	
Participant	Amplitude (μV)	Implicit time (ms)	Amplitude (μV)	Implicit time (ms)
DG24	-1.80	26.50	5.4	59.5
UH38	-0.39	21.00	2.3	55.0
MK48 #				
PJ45	-2.13	37.00	3.7	70.5
JM83	-1.35	23.00	3.7	54.5
RJ95*			1.8	63.5
DR96#				
TO97#				
BS100	-0.55	25.00	3.1	58.0
DN82#				
DP103	-2.55	27.50	6.5	70.5
SJ90 #				
CG101	-0.50	27.00	5.1	63.0
SO107#				
JH108 #				
AP109*			3.4	70.5
PT139#				
MT125 #				
WC122*			0.9	62.0
JT99 #				
BS116				
BC92#				
PS115#				
SH93#				
Mean	**-1.32**	**26.71**	**3.58**	**62.70**
SD	0.87	5.10	1.72	6.17

* No measureable a-wave
# No measurable waveform

Table K.4: 20 td.s focal rod ERG results for ARM participants (n=10).

	A-wave		B-wave	
Participant	Amplitude (μV)	Implicit time (ms)	Amplitude (μV)	Implicit time (ms)
DH8	-3.48	27.0	8.36	55.5
DH7	-3.46	24.5	13.02	55.0
DG20	-2.93	33.0	6.70	56.0
RG27	-2.18	27.5	15.03	54.5
GB25	-3.76	24.5	16.64	51.5
MH31	-4.49	27.0	19.17	54.5
AD32	-3.34	29.5	13.85	55.0
JO42	-2.45	27.0	9.38	53.5
RE68	-2.41	28.5	16.71	56.0
AJ59	-2.53	23.5	15.56	54.0
TK73	-4.31	27.5	13.77	52.0
PF70	-3.60	27.0	14.61	51.0
MK75	-1.95	31.0	15.03	70.5
RJ77	-3.13	27.0	18.92	54.0
CO87	-4.05	27.0	17.47	56.0
AO88*			3.67	41.0
DT131	-1.32	35.0	5.47	53.5
PG26*			8.25	49.5
EN112	-1.81	26.0	3.32	61.0
AI46	-3.61	24.0	12.67	53.0
BB80	-3.20	25.0	10.51	56.0
HH13	-2.15	26.5	6.38	47.5
AJ56	-3.04	26.5	10.47	53.0
BA69	-1.06	29.5	8.58	53.0
GJ65	-2.64	26.5	8.14	52.0
DJ53	-6.17	27.5	18.39	53.0
Mean	**-3.05**	**27.42**	**11.93**	**53.90**
SD	1.11	2.69	4.78	4.90

* No measureable a-wave
# No measurable waveform

Table K.5: 500 td.s focal rod ERG results for control participants (n=26).

	A-wave		B-wave	
Participant	Amplitude (μV)	Implicit time (ms)	Amplitude (μV)	Implicit time (ms)
DG24	-3.91	24.0	11.31	49.5
UH38	-2.67	29.5	8.78	56.0
MK48 #				
PJ45			7.70	59.0
JM83	-2.74	28.0	11.71	49.5
RJ95	-2.15	28.5	8.67	52.0
DR96*			3.23	58.0
TO97	-3.98	27.5	11.94	57.5
BS100	-1.82	20.5	11.14	56.0
DN82	-3.74	31.5	4.85	54.0
DP103	-4.95	27.0	15.76	54.5
SJ90	-1.36	37.0	6.92	59.5
CG101	-1.25	28.0	9.45	53.5
SO107	-3.25	36.5	13.22	65.5
JH108	-0.66	30.0	6.29	54.5
AP109	-1.88	33.0	8.66	60.0
PT139	-1.81	30.0	6.69	49.5
MT125	-1.83	25.0	17.10	59.0
WC122*			4.95	54.5
JT99 #				
BS116			3.48	70.5
BC92*			5.46	70.5
PS115	-2.87	27.00	7.56	53.0
SH93	-4.52	28.50	9.57	60.0
Mean	**-2.67**	**28.91**	**8.84**	**57.09**
SD	1.23	4.11	3.69	5.86

* No measureable a-wave
# No measurable waveform

Table K.6: 500 td.s focal rod ERG results for ARM participants (n=22).

Participant	Time constant (s)
DG24	137
UH38	330
MK48*	
PJ45	94
JM83	152
RJ95*	
DR96	313
TO97	438
BS100*	
DN82*	
DP103	107
SJ90*	
CG101	75
SO107	789
JH108*	
AP109*	
PT139	113
MT125	193
WC122	230
JT99	270
BS116	200
BC92*	
PS115*	
SH93	314
Mean	**250.34**
SD	181.95

* Model unable to find recovery

Table K.7: ERG photostress test results for ARM participants (n=15).

Participant	Time constant (s)
DH8	188
DH7	199
DG20	191
RG27	76
GB25	82
MH31	171
AD32	189
JO42	245
RE68	165
AJ59	95
TK73	84
PF70	98
MK75	268
RJ77	142
CO87	528
AO88	63
DT131	244
PG26	169
EN112	157
AI46	172
BB80	75
HH13	91
AJ56	78
BA69	70
GJ65	180
DJ53	132
Mean	**159.70**
SD	95.98

Table K.8: ERG photostress test results for control participants (n=26).

Participant	Amplitude (μV)	Implicit time (ms)[1]
DG24	4.83	13.0
UH38	1.02	11.6
MK48	1.46	10.1
PJ45	2.39	10.5
JM83	3.70	9.5
RJ95*		
DR96	1.61	12.7
TO97	1.87	12.4
BS100	0.71	5.2
DN82	0.69	10.2
DP103	3.72	11.6
SJ90*		
CG101	1.35	10.9
SO107	2.47	14.7
JH108	1.74	12.1
AP109	0.75	10.7
PT139	1.40	10.3
MT125	2.45	12.2
WC122	1.00	12.5
JT99	1.01	10.1
BS116	2.98	8.9
BC92	0.49	10.2
PS115	2.98	10.1
SH93	1.96	10.9
Mean	**1.94**	**10.93**
SD	1.15	1.86

* No measurable waveform

1. corrected for age

Table K.9: Focal flicker ERG results for ARM participants (n=22).

Participant	Amplitude (μV)	Implicit time (ms)[1]
DH8	1.94	10.8
DH7	1.99	11.2
DG20	2.25	9.6
RG27	2.32	12.1
GB25	3.05	11.0
MH31	1.11	11.7
AD32	1.85	9.9
JO42	1.71	11.2
RE68	1.69	12.1
AJ59	2.78	11.4
TK73	3.71	9.0
PF70	2.98	9.5
MK75	1.81	10.5
RJ77	1.28	11.6
CO87	3.05	9.8
AO88	1.40	11.0
DT131	1.43	9.7
PG26	2.26	11.0
EN112	1.17	12.0
AI46	3.14	10.9
BB80	1.44	10.9
HH13	2.64	10.9
AJ56	2.95	11.8
BA69	2.35	9.8
GJ65	1.36	9.8
DJ53	3.28	10.3
Mean	**2.19**	**10.75**
SD	0.75	0.88

* No measurable waveform

1. corrected for age

Table K.10: Focal flicker ERG results for control participants (n=26).

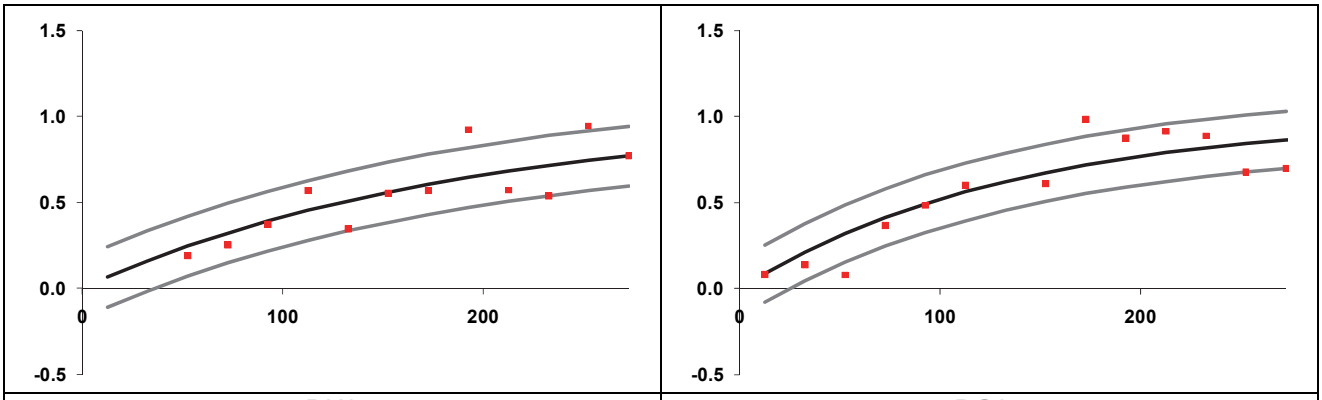

DH8

DG24

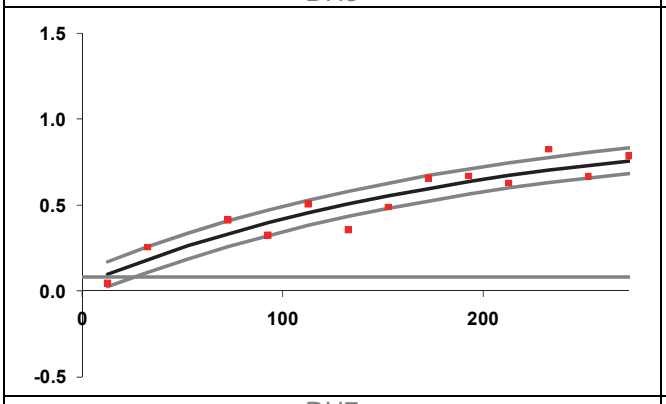

DH7

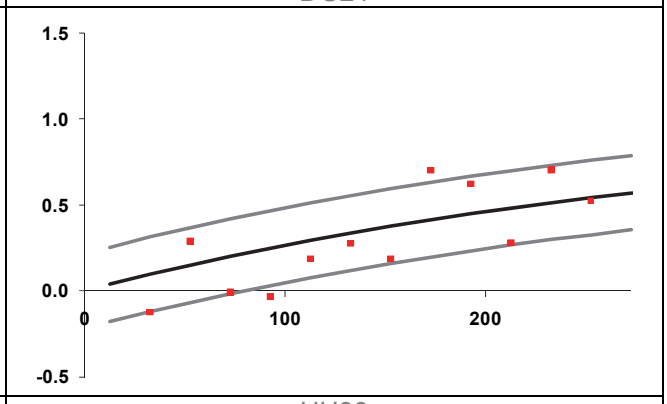

UH38

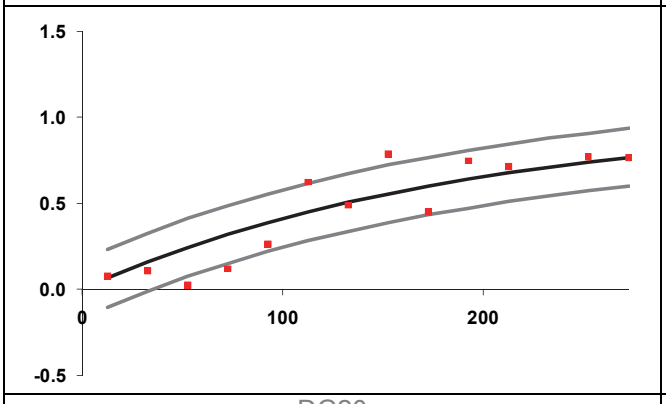

DG20

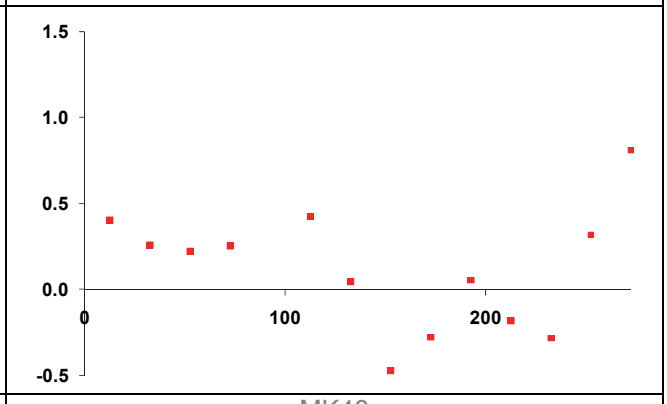

MK48

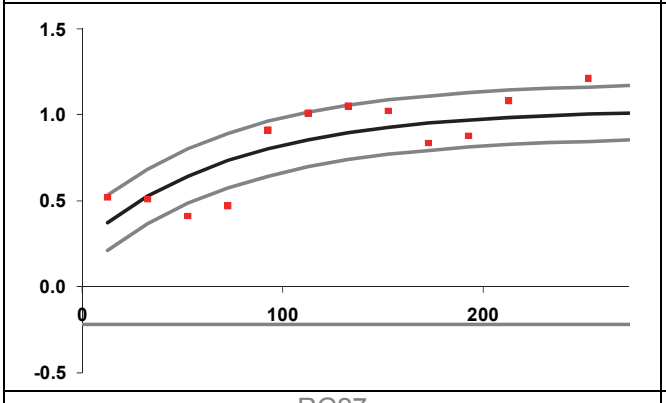

RG27

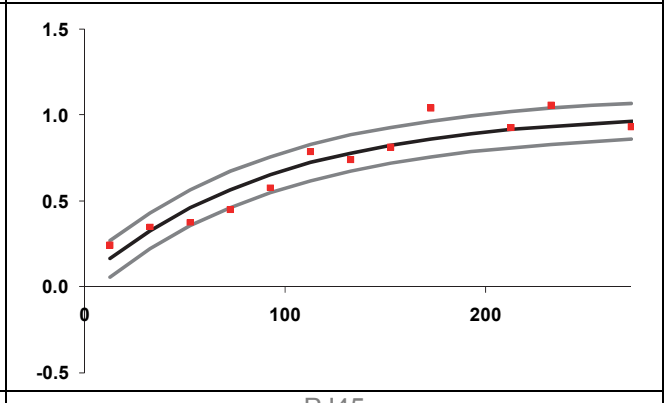

PJ45

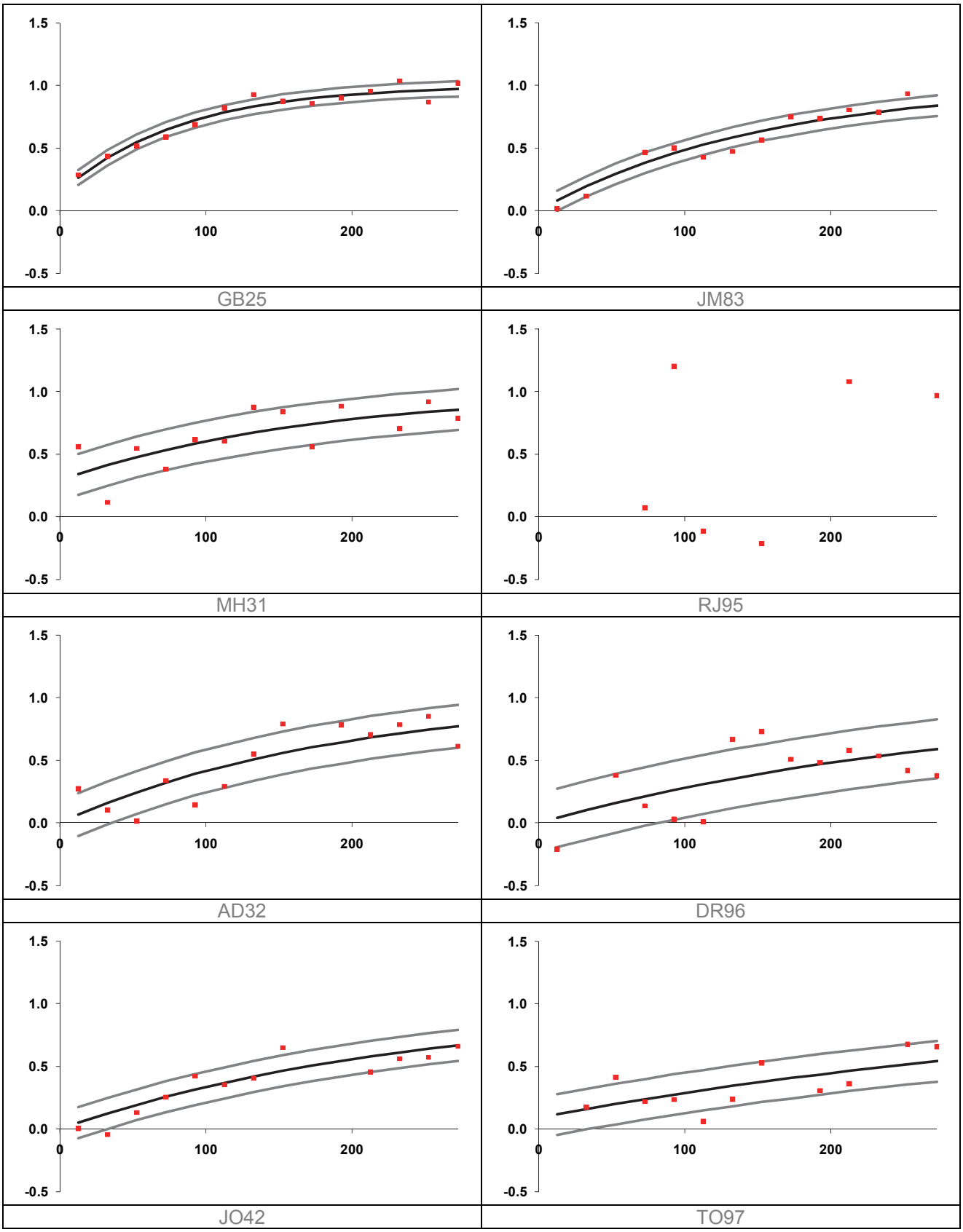
1.5
1.0
0.5
0.0
-0.5
0
100
200
GB25
JM83
MH31
RJ95
AD32
DR96
JO42
TO97

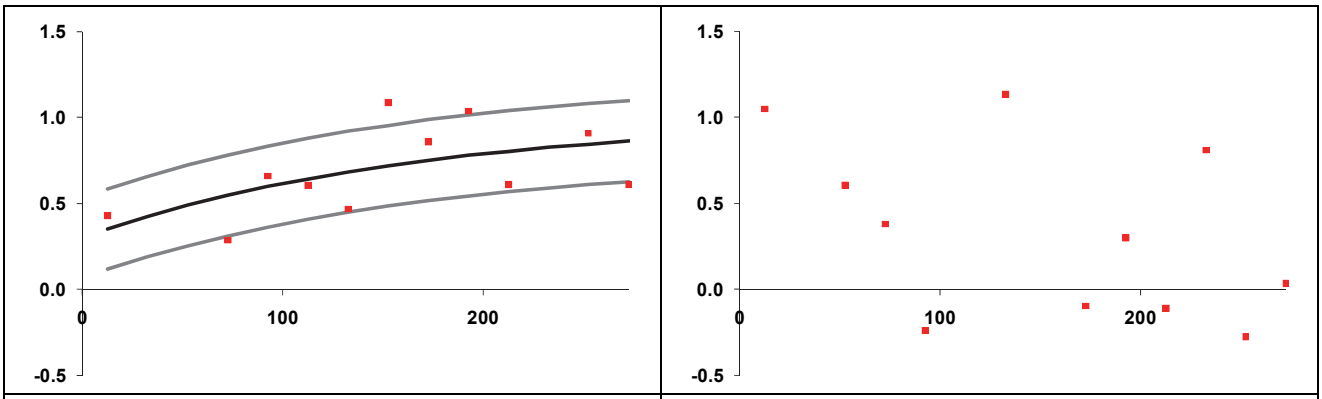

RE68

BS100

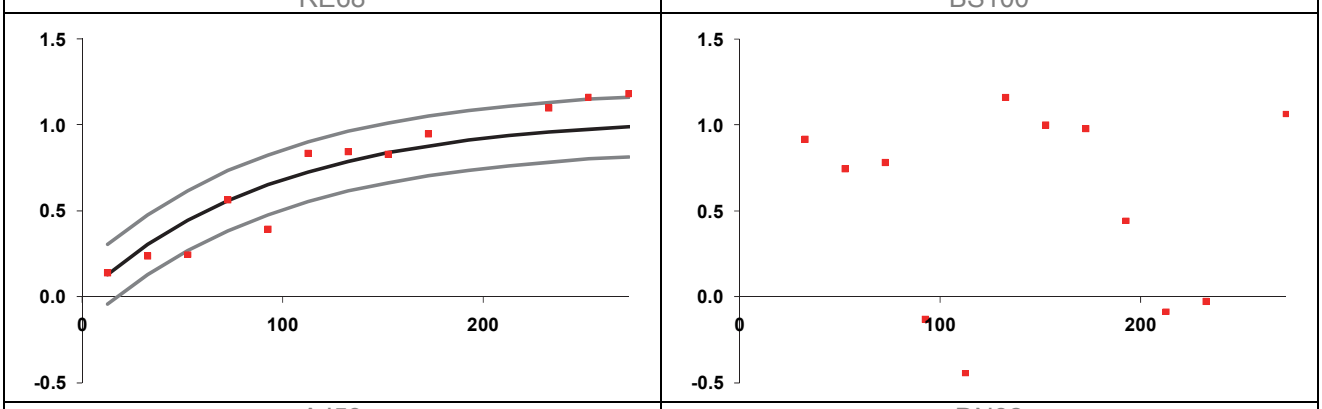

AJ59

DN82

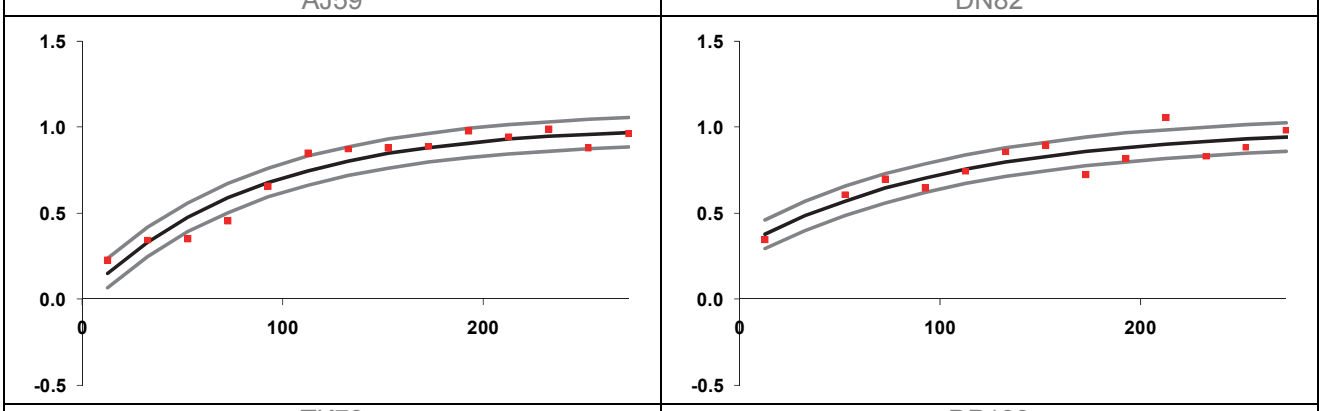

TK73

DP103

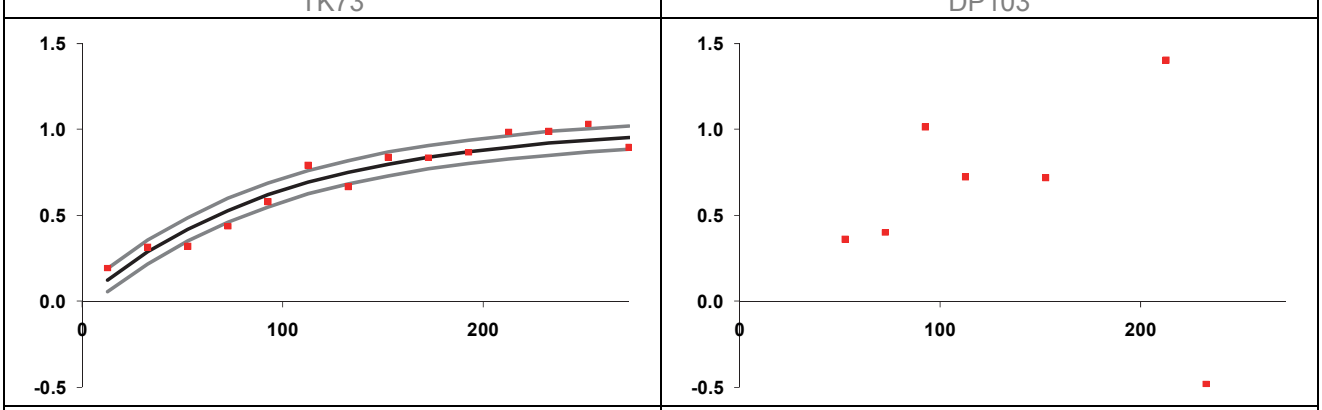

PF70

SJ90

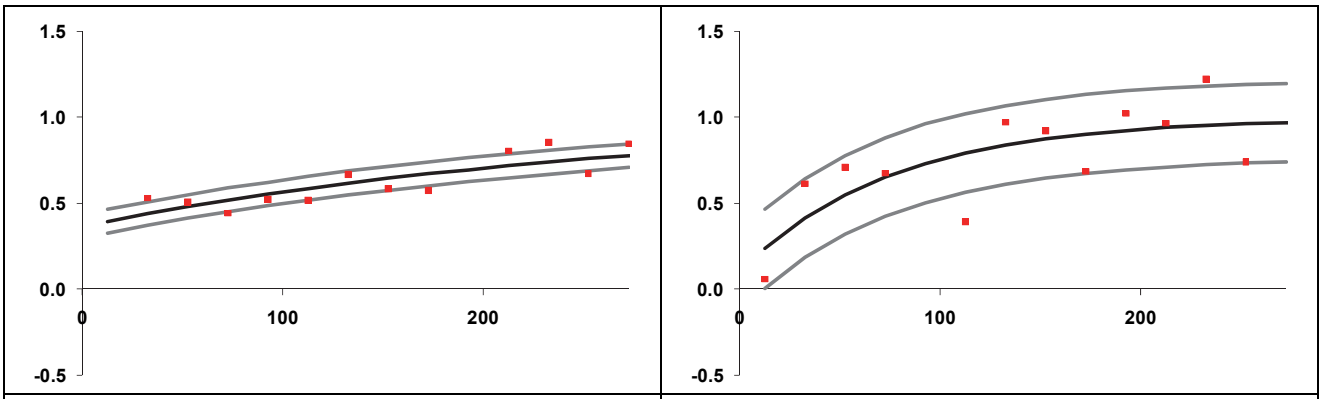

MK75

CG101

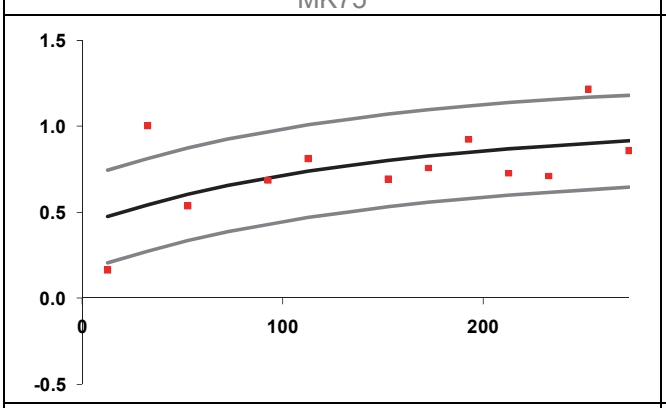

RJ77

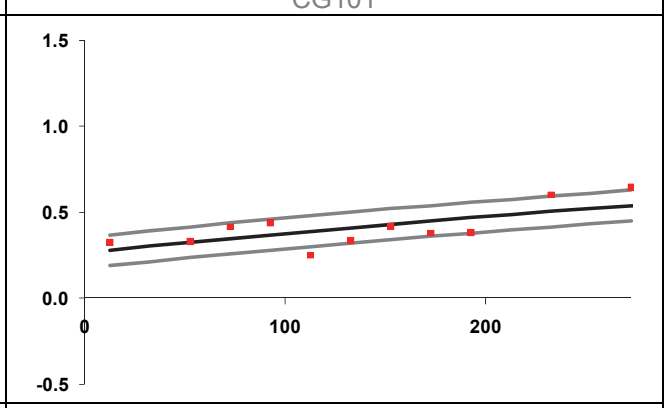

SO107

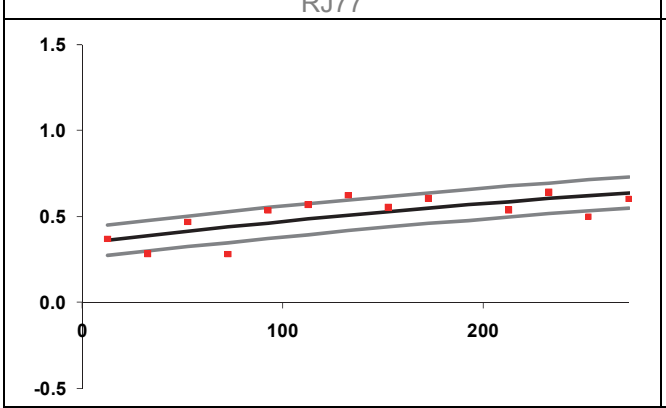

CO87

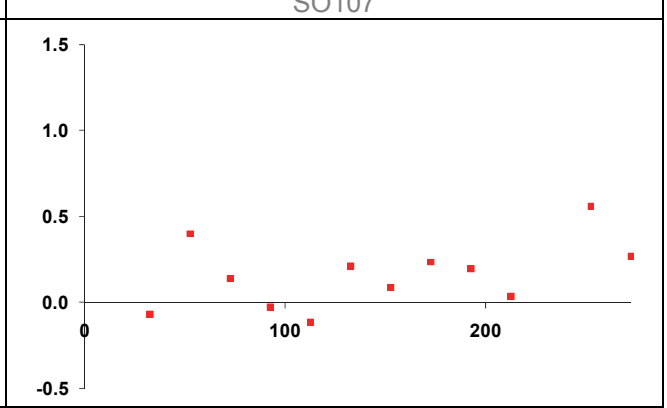

JH108

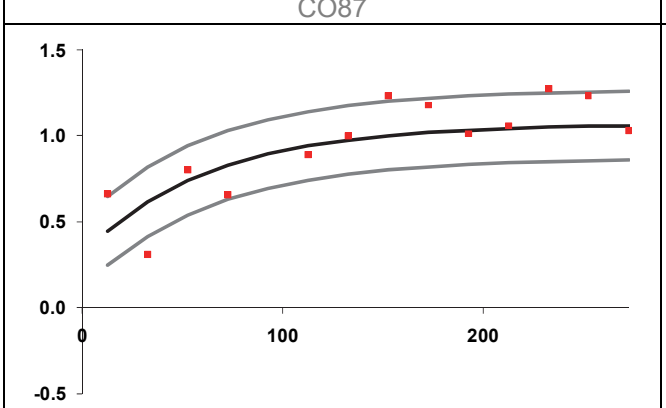

AO88

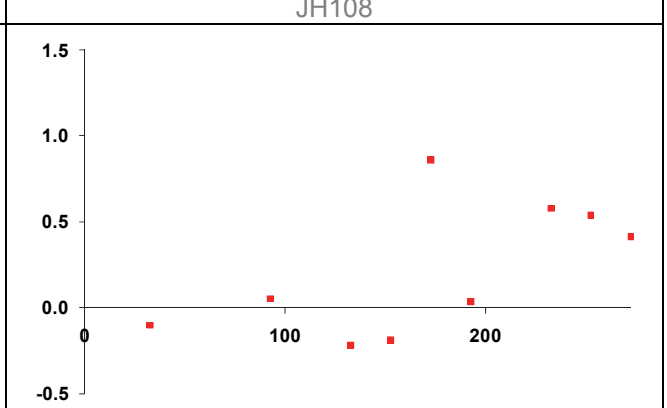

AP109

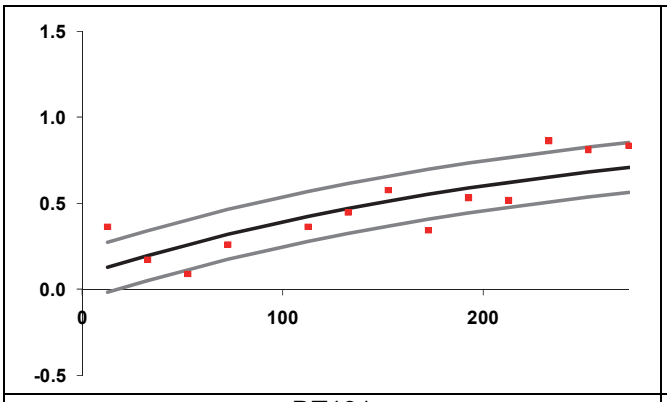

DT131

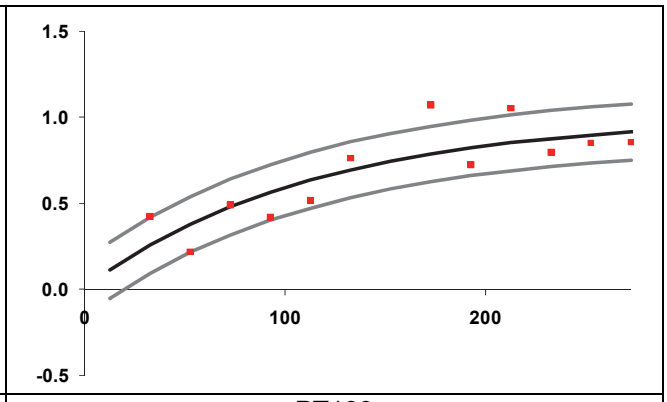

PT139

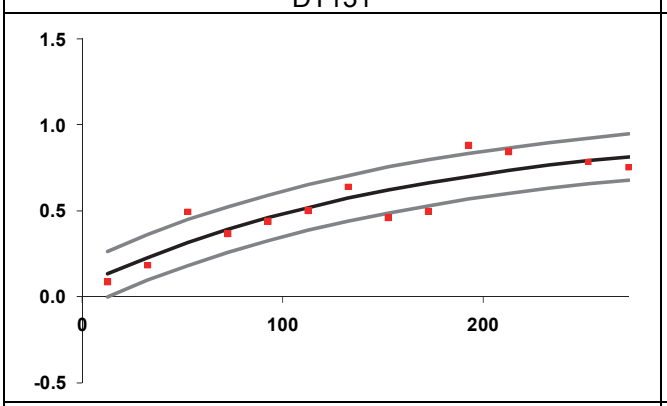

PG26

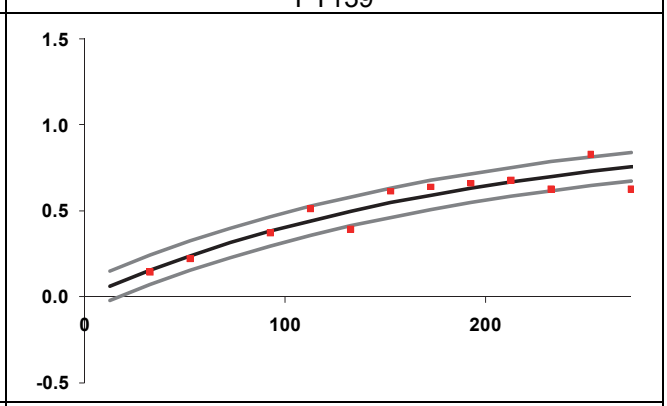

MT125

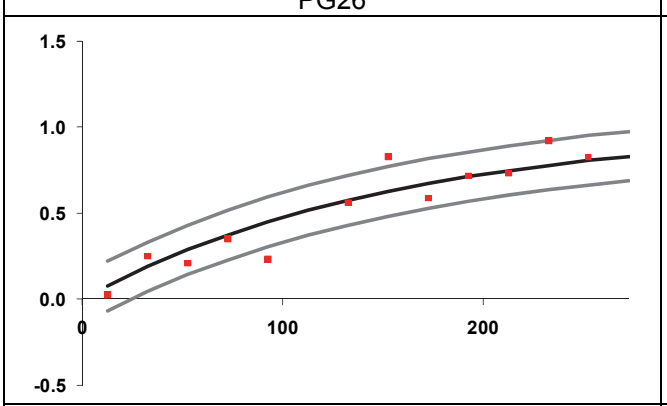

EN112

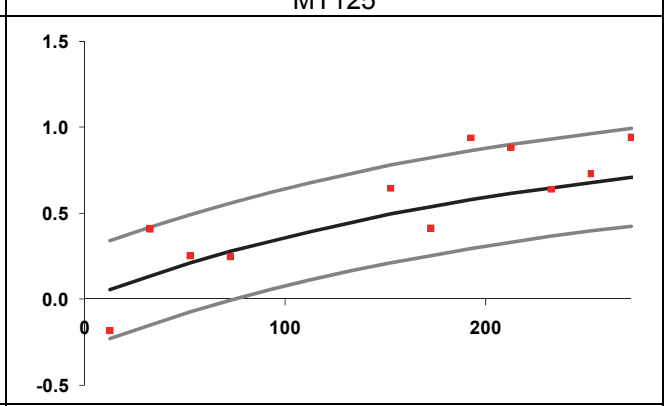

WC122

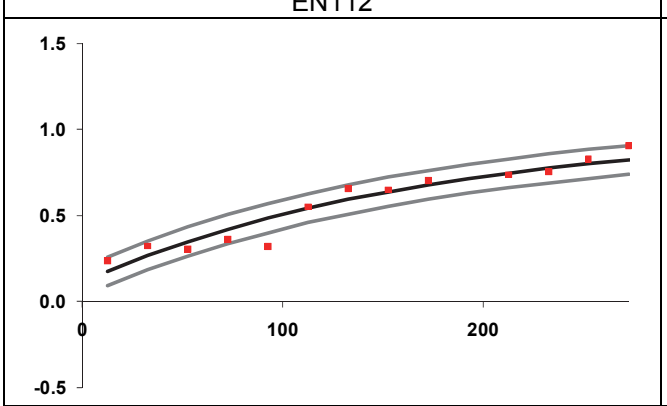

AI46

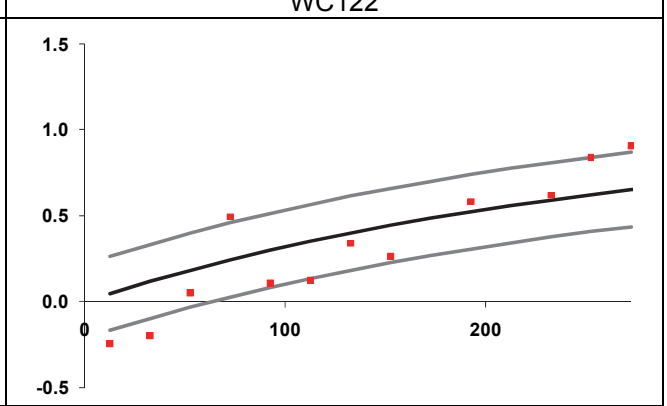

JT99

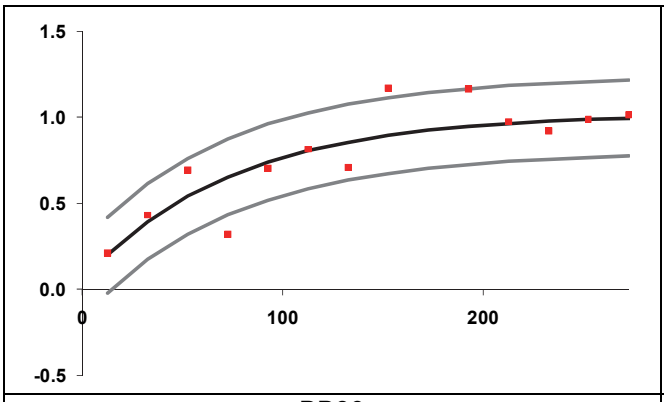

BB80

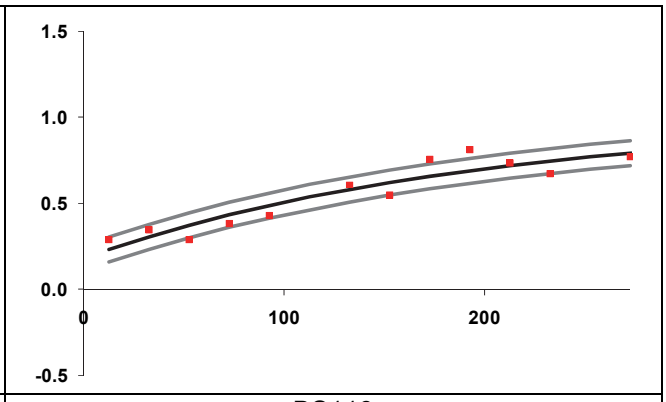

BS116

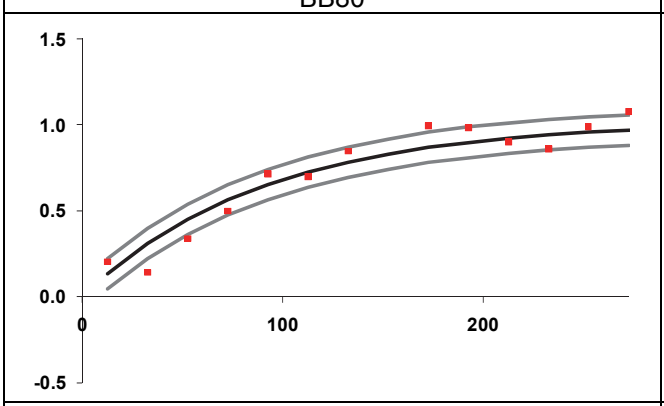

HH13

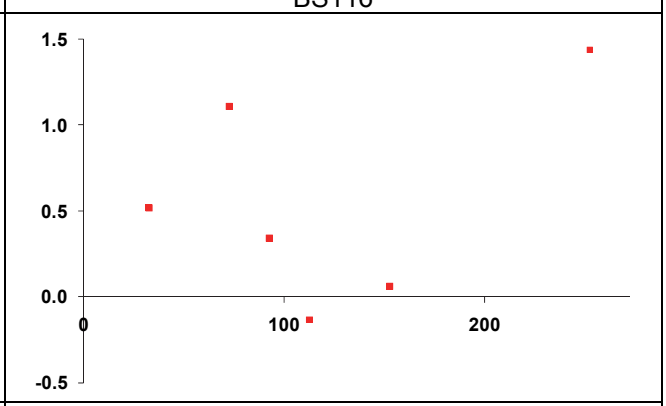

BC92

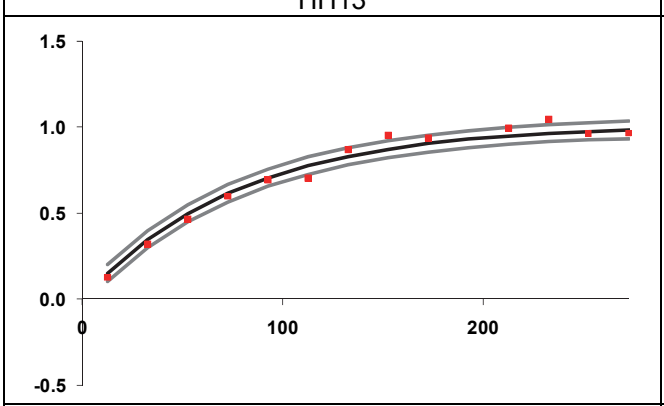

AJ56

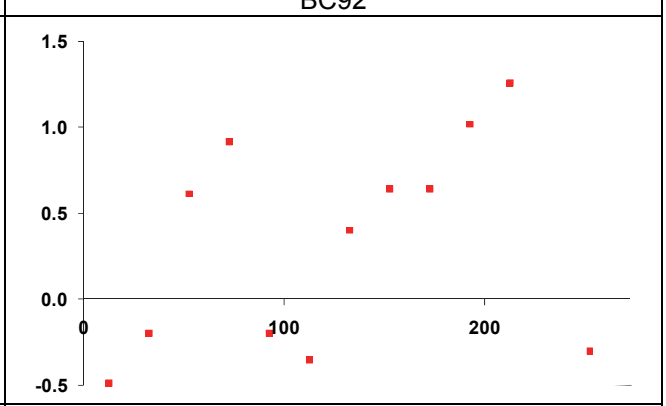

PS115

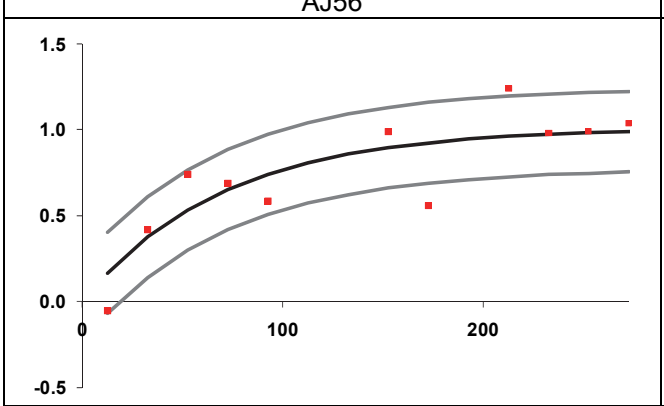

BA69

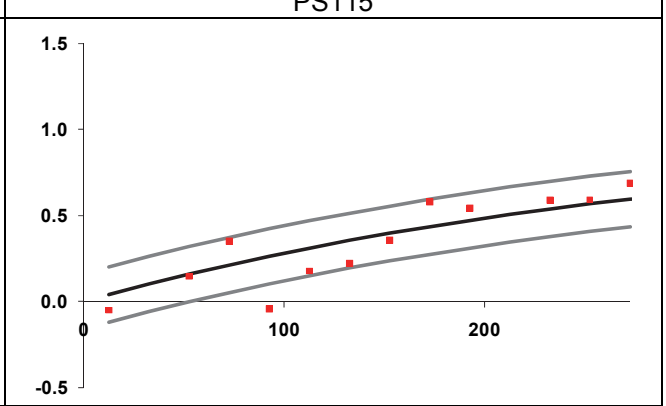

SH93

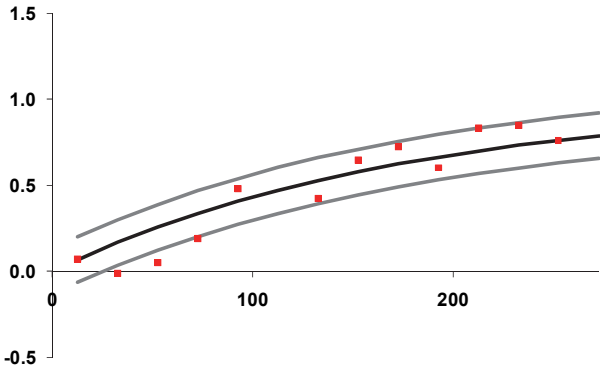

GJ65

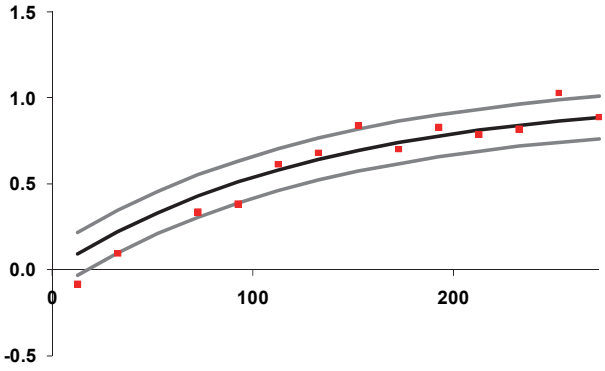

DJ53

Figure K.1: ERG photostress test recovery curves for control (n=26; Left) and ARM (n=24; Right) participants. X axis shows time in seconds, Y axis shows amplitude normalised to the pre-bleach amplitude (1). Amplitude recovery model is indicated by black line, with 95% confidence intervals indicated by grey lines.

Graefes Arch Clin Exp Ophthalmol (2011) 249:1359–1365
DOI 10.1007/s00417-011-1627-7

MISCELLANEOUS

Appendix L:
The effect of bleach duration and age on the ERG photostress test

Ashley Wood · Tom Margrain · Alison Binns

Received: 1 July 2010 / Revised: 11 January 2011 / Accepted: 13 January 2011 / Published online: 2 February 2011

Abstract
Background The ERG photostress test assesses the recovery of the focal 41 Hz ERG following exposure to a bright light that bleaches a significant proportion of photopigment. The aims of this study were: 1) to compare the repeatability of the ERG photostress test recovery time constant following long and short duration light exposure, and 2) to determine the effect of age on the ERG photostress test recovery time constant.
Methods Focal 41 Hz ERGs were recorded from 23 participants (age range 20–71 years) at 20-second intervals for 5 minutes following either a short-duration (photoflash) or long-duration (equilibrium) light exposure. After a 5-minute wash-out period, the procedure was repeated using the second bleach modality. The time constant of cone recovery was determined by fitting an exponential model to the amplitude recovery data. The whole procedure was repeated on a second occasion. The co-efficient of repeatability (CoR) was calculated for each bleaching technique. The relationship between the time constant of recovery and age was investigated (Pearson's correlation coefficient).
Results The time constant of recovery following an equilibrium bleach was more repeatable than recovery following a photoflash (CoR=85s and 184s respectively). Eight trials (from seven participants) failed to show a reduction in amplitude following the photoflash, suggesting that a blink or fixation loss had occurred. All participants were reliably light-adapted by the equilibrium bleach. For the equilibrium bleach data, the time constant of recovery increased with age at a rate of 27 seconds per decade.
Conclusions The equilibrium bleach was more reliable and repeatable than the photoflash. Increasing participant age was shown to result in a lengthening of the recovery time constant, of a magnitude comparable to previously published psychophysical data.

Keywords Electroretinogram, ERG · Cone adaptation · Repeatability · Age-related macular degeneration

Financial affiliations: This research was funded by the School of Optometry and Vision Sciences, Cardiff University.

The authors have control of all primary data, and agree to allow Graefe's Archive for Clinical and Experimental Ophthalmology to review their data on request.

A. Wood · T. Margrain · A. Binns (✉)
School of Optometry and Vision Sciences, Cardiff University,
Maindy Road,
Cathays, Cardiff CF24 4LU, UK
e-mail: BinnsAM@cf.ac.uk

Introduction

The electroretinogram (ERG) photostress test [1, 2] was developed as a dynamic test of outer retinal function, which assesses the recovery of the 41 Hz ERG amplitude, following exposure to a bright light. The technique is capable of differentiating patients with early age-related maculopathy (ARM) from healthy controls, even when VA remains near normal [2].

In dark adaptation and photostress studies, photopigment bleaching has been elicited in one of two ways. The first method typically involves the use of a photoflash unit which produces a very brief but intense flash of light [3–7]. The second method is to expose the retina to a less intense but longer duration light until equilibrium is reached between photopigment bleaching and regeneration [1, 2, 8–10]. The literature suggests that the kinetics of cone photopigment recovery are different in these two situations. Following an equilibrium bleach, the time constant of cone

recovery is not dependent on the percentage of photopigment bleached, whilst the recovery following a photoflash is prolonged with an increasing percentage of photopigment bleached [3]. For exposures that bleach the same amount of photopigment, the time constant of cone recovery is also shorter after exposure to a brief flash than after an equilibrium bleach [3]. Given that clinic time is at a premium, the use of a photoflash is an attractive alternative to the longer duration equilibrium bleach currently used with the ERG photostress test [2].

To investigate the potential utility of this approach, the first aim of this study was to compare the inter-session repeatability of ERG photostress test results obtained with equilibrium and photoflash bleaches. The psychophysically determined time constant of cone dark adaptation is known to be affected by age [4], with a reported increase of 0.21 minutes per decade. Therefore, the second aim of this study was to investigate the effect of age on the time constant of cone recovery as determined by the ERG photostress test with both bleaching techniques.

Material and methods

Participants

Twenty-three healthy participants, aged 20 to 71 years (mean age 43.5±17.6 years) were recruited for this study from staff, students and volunteers attending the Eye Clinic at the School of Optometry and Vision Sciences. All participants had a corrected visual acuity of 0.2 (LogMAR) or better, clear ocular media, normal retinal/optic disc appearance, no history of retinal or systemic disease, and were not taking medication known to affect retinal function. The study adhered to the tenets of the Declaration of Helsinki and was approved by the School of Optometry and Vision Sciences Research Ethics Committee. Each participant was given a full explanation of the procedures involved, and their written informed consent was obtained before participation in the study.

ERG recording

The earth electrode was a silver–silver chloride touchproof skin electrode (Viasys Healthcare Ltd., Warwick, UK) applied to the midfrontal position, whilst active and contralateral reference electrodes consisted of DTL fibres (Unimed Electrode Supplies, Surrey, UK) positioned in the lower fornix of both eyes. Contralateral corneal reference electrodes have been reported to provide larger ERG amplitude responses than traditional skin electrodes [5].

ERGs were recorded in response to a focal (20° diameter) amber stimulus (peak output 595nm, half height band width 17 nm) produced by a miniature Ganzfeld LED stimulator (CH Electronics, Kent, UK). The stimulator comprised an array of LEDs set behind a circular diffuser. The LEDs provided a square wave flicker stimulus at a frequency of 41 Hz (50% duty cycle, flash duration 12 ms) with a time-averaged luminance of 30 cd/m^2. The stimulus subtended 20° at the eye, when viewed from a distance of 14 cm, and was set within a luminance-matched Ganzfeld surround to suppress responses from the peripheral retina. Stimulus luminance was measured with a photometer (LS-110; Konica Minolta, Osaka, Japan).

An evoked potential monitoring system (Medelec Synergy EP; Oxford Instruments Medical, Surrey, UK) was used to record all ERGs in the course of this study. ERG responses were recorded monocularly, bandpass filtered (1 to 100 Hz) and digitally averaged. A 50 ms time base at a sampling rate of 20 KHz was used with one hundred sweeps (each consisting of two response cycles) averaged per trace. An artefact reject setting (50 μV) allowed the exclusion of traces contaminated by eye movements.

Bleaching techniques

The long duration ‘equilibrium’ bleach was provided by a tungsten halogen source which was presented to the subject within a Ganzfeld bowl. A central fixation cross was placed within the Ganzfeld bowl such that the bleaching source subtended 40° at the eye. The flickering amber stimulus was placed directly above this, allowing the subject to take up position for ERG recording quickly at cessation of the photobleach. Heat filters were in place, which reduced output of the bleaching light to below 5% between 800–900 nm so that excessive infra-red (IR) radiation did not reach the eye.

Using this apparatus the eye was light-adapted to a bright white background of 5.6 log td for a period of 2 minutes. The effective retinal illuminance was calculated as 5.2 log photopic td, when adjusted for the Stiles–Crawford effect, which bleached approximately 84% of the cone visual pigment [3].

The short duration “photoflash” bleach was provided by a Metz Mecablitz 76 MZ-5 flashgun (Metz-Werke GmbH & Co., Zirndorf, Germany), positioned such that this source also subtended 40° at the eye when centrally fixated. The eye was exposed to a bright white flash of 7.3 log td.s for a period of approximately 6.6 ms. The effective retinal illuminance, adjusted for the Stiles–Crawford effect, was calculated as 6.9 log photopic td.s, which bleached approximately 98% of the cone visual pigment [3, 6].

The time constant of cone recovery following an equilibrium bleach is independent of the percentage bleach achieved [3]. However following a ‘non-equilibrium’ short duration bleach of an equivalent level the time constant is

shorter [3, 7], and is variable, with the quickest recoveries following less intense bleaches [3]. Therefore, the maximum intensity bleach from the flash unit was used in this study, theoretically producing the longest recovery times over which to monitor the ERG recovery.

Heat filters were used to attenuate output to below 5% between 800-900 nm, so that excessive infra-red (IR) radiation did not reach the eye. Additionally a UV filter integrated within the flash gun eliminated wavelengths below 375 nm. All bleach luminance measurements were made using an IL1700 photometer (International Light Inc, Newburyport, MA, USA) and exposures were within the safety guidelines set out within BS EN 15004-2 [8].

General procedure

Both bleaching protocols were evaluated at the same recording session, and participants were randomly assigned to one of two groups determining whether the photoflash or equilibrium bleach was to be used first. The eye with better visual acuity was chosen for testing, with the left eye chosen as default in cases of equal acuity. The non-test eye was patched. Pupils were dilated with 1 drop of 1.0 % tropicamide prior to electrode attachment.

Prior to recording, a 5-minute period of adaptation to the flickering stimulus and surround was undertaken to avoid any flicker adaptation effects during the recording period. In order to prevent any residual bleach effect between tests, a 5-minute break was implemented. Initially four 41 Hz flicker ERG traces, each consisting of the average of 100 sweeps, were recorded to provide a baseline pre-bleach amplitude. This was followed by exposure of the eye to either the photoflash or equilibrium bleach. Upon completion of the bleach, the participants had 10 seconds to align themselves with the stimulus for the recording of the first trace; a total of 15 traces were then recorded at 20-second intervals over a 5-minute period. Each trace took approximately 5 seconds to record; however, the time required was extended if any blinks or other contamination occurred which led to trace rejection. This would normally leave 10 to 15 seconds between successive recordings for the participant to relax and blink. The entire protocol was repeated on a second occasion within 4 weeks of the first visit for every study participant. A sequential representation of the protocol undertaken at each visit is shown in Fig. 1.

Analysis

The amplitude of the fundamental frequency of each trace was determined by Fourier analysis using Excel 2003 (Microsoft. Redmond, WA, USA) and plotted as a function of time after cessation of the bleach. In order to limit the effect of any noise or contamination of individual traces, especially in those traces immediately post-bleach where the signal-to-noise ratio was low, the Fourier analysis for all post-bleach traces was phase-locked to the mean of the four pre-bleach traces. In this way, only 41 Hz signals which were the same phase as the pre-bleach signal were extracted.

The time constant of cone photopigment regeneration was determined by fitting Eq. 1 to the amplitude recovery data on a least squares fit basis, using the Solver function of Excel 2003 (Microsoft).

$$\text{Amplitude}\,(t) = a\,[1 - B^{*}\exp\,(-t/\tau)] \quad (1)$$

Where "t" is time after the photobleach in seconds, "a" is the pre-bleach amplitude, "B" is the proportion of photopigment bleached (where B=0 signifies 0% and B=1 signifies 100%) and "τ" is the time constant in seconds. "B" was constrained within the model to return a value of 0 or greater. Inter-session repeatability of the time constant of recovery was assessed by calculating the coefficient of repeatability (CoR) (determined as 1.96 x the standard deviation of differences between visits 1 and 2). The repeatability was also graphically demonstrated by plotting the difference in time constant between visits 1 and 2 against the mean time constant for both visits, a technique advocated by Bland and Altman [9]. The agreement between recovery time constants for long and short duration bleaches was also presented using this (Bland and Altman) approach [9].

The effect of age on the recovery time constant was also assessed. Recovery time constants for all participants were plotted as a function of age, with the gradient of the best fitting line indicating the change in time constant per decade of life. Pearson's correlation coefficient was calculated to determine whether this relationship was significant.

Results

Typical 41 Hz ERG traces for three participants aged 23, 44 and 60 are shown in Fig. 2. The initial four traces shown are the pre-bleach baseline and represent the expected waveform after a full recovery. The subsequent 15 traces were recorded at 20-second intervals following the bleach. The recovery in ERG amplitude post-bleach, towards the baseline level, is apparent in these participants for both bleaching modalities. The amplitude values plotted against time for these three participants are shown in Fig. 3. The amplitude recovery has been fitted with Eq. 1.

For the group of 23 participants, a total of 46 ERG photostress tests were recorded using the equilibrium bleach, and 46 were recorded using the photoflash bleach. From the trials conducted using the equilibrium bleach,

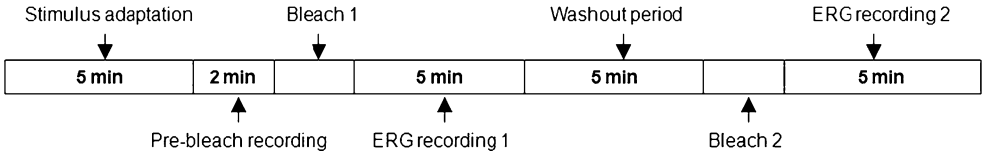

Fig. 1 The timeline showing the recording process for the ERG photostress tests. The bleach type for tests 1 and 2 was randomly selected prior to recording for each participant, and bleach duration was either 6.6 ms or 2 minutes

only one was excluded due to excessive recording noise; however, of the trials conducted using the photoflash, eight were excluded due to ineffective bleaching, i.e., the 'bleach' did not diminish the amplitude of the 41 Hz ERG and hence there was no recovery. Of the eight failed photoflash bleaches, one participant did not produce valid results on either visit. The mean time constants for the equilibrium (117±72s) and photoflash bleach (112 ± 58s) techniques were not significantly different (paired *t*-test; P=0.992).

Figure 4 describes the repeatability of each technique; the CoR was 85s (n=22) for the equilibrium bleach and 184s (n=16) for the photoflash bleach. The mean difference between visits was close to zero, indicating no bias between visits (see Fig. 4).

Figure 5 compares the mean time constant of recovery between the two techniques for the 15 participants where successful bleaches were achieved for both bleach techniques. There was no bias towards a longer time constant for either technique.

Figure 6 plots the time constant of recovery as a function of age for both techniques. For the equilibrium bleach data, the time constant (τ) of recovery increased by 27.6s per decade of life; this relationship was statistically significant (Pearson's correlation coefficient r=0.66, P=0.0008). There was also a subjectively evident increase in variability with older subjects. There was no significant relationship between age and time constant of recovery for the photoflash technique (Pearson's correlation coefficient, P=0.19).

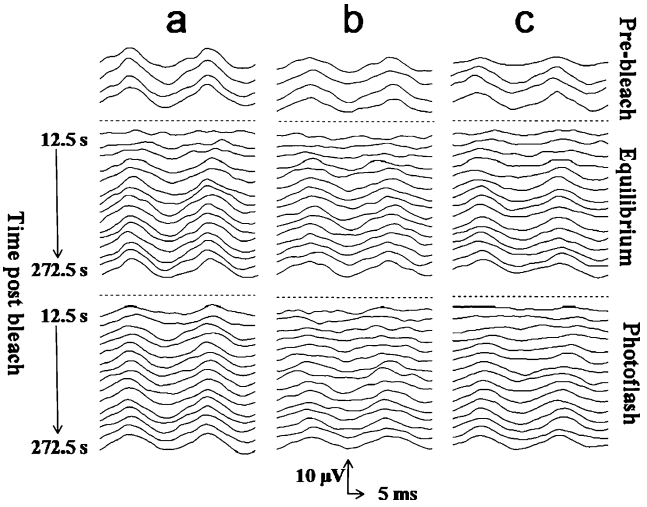

Fig. 2 Raw 41 Hz ERG traces for participants **a** (aged 23 years), **b** (aged 44 years) and **c** (aged 60 years). *Top panel* shows pre-bleach traces, *middle panel* shows traces following an equilibrium bleach, and the *bottom panel* shows the traces following a photoflash bleach

Discussion

The results provide compelling evidence for the retention of the equilibrium bleach as part of the ERG photostress test. The equilibrium bleach showed relatively good repeatability (CoR 85s) and was successfully recorded on 45 out of 46 occasions. The photoflash bleach, by comparison, was less repeatable (CoR 184s), and did not always provide an effective bleach.

Previously, we have shown that the ERG photostress test can differentiate those with early ARM from age-matched controls, demonstrating a mean difference of 106s in time constants between groups [2]. Given that the coefficient of repeatability for the photoflash technique (184s) is larger than the difference between those with and without disease (106s) [2], it is apparent that the sensitivity and specificity of the ERG photostress test would be compromised by switching to the photoflash bleaching method.

It is noteworthy that this assessment of the repeatability of the photoflash bleaching method only included data from 16 out of 23 subjects for whom a post-bleach recovery was available. The observation that the photoflash unit did not diminish the amplitude of the 41 Hz ERG in seven participants (eight trials) suggests that blinks or gross fixation losses must have coincided with the timing of the photoflash discharge. Given the number of bleach failures, additional bleaches would need to be administered to obtain satisfactory results. In a clinical situation, this would increase examination time, making the technique clinically nonviable. The instantaneous nature of the photoflash exposure may also have increased the potential for partial bleaches, due to inaccurate patient fixation and incomplete blinks, and this may have contributed to the relatively poor CoR of this technique.

In contrast, the equilibrium bleach allows 2 minutes to bleach the retina; therefore, transient fixation losses and blinking are unlikely to affect the photopigment bleach obtained. In addition, there is a theoretical basis for assuming that an equilibrium bleach may provide a better separation between individuals with ARM and age-matched

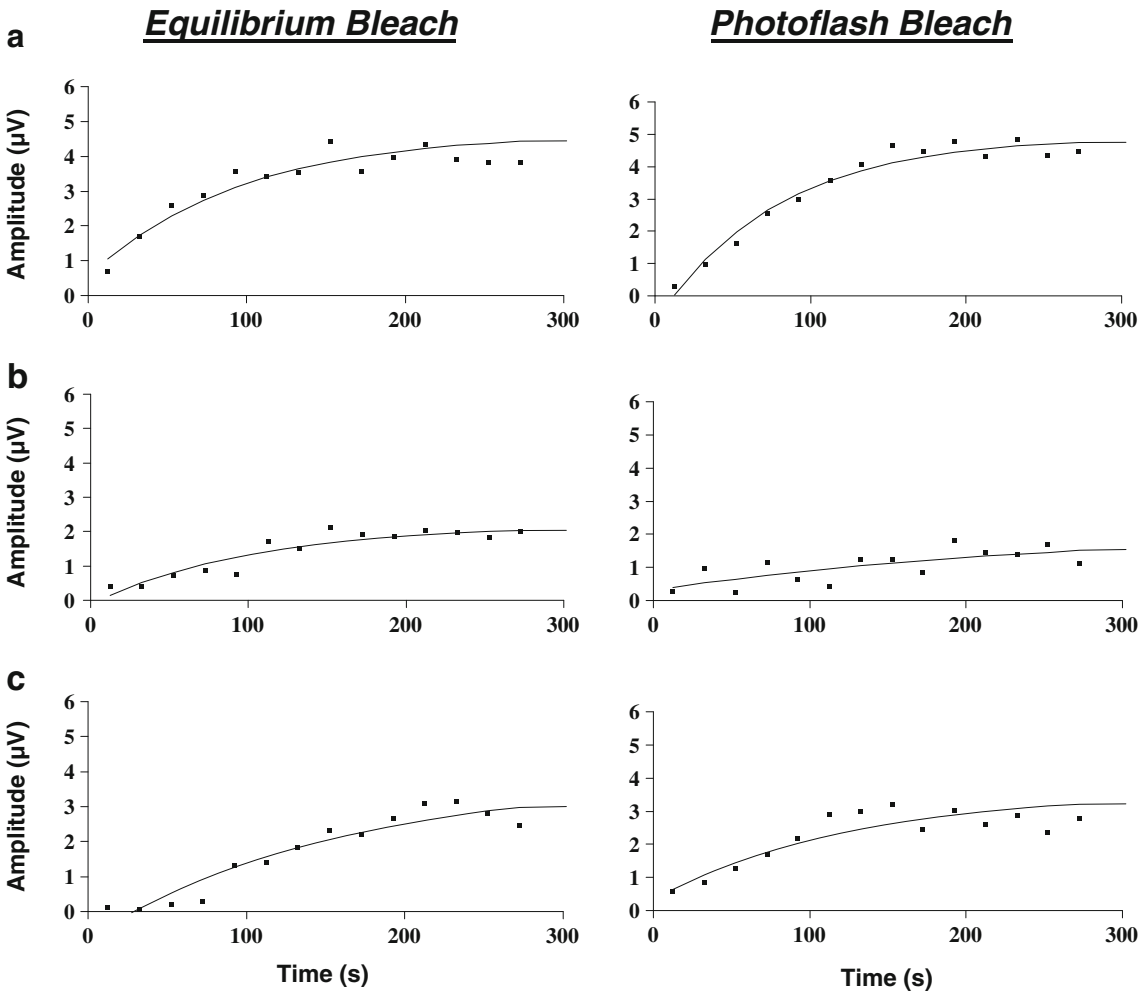

Fig. 3 ERG amplitudes for participants **a**, **b** and **c** plotted against time post-bleach, and best-fitting exponential model (Eq. 1) to recovery data following the equilibrium bleach (participant **a**; τ=95.6, participant **b**; τ=103.5, participant **c**; τ=157.8) and photoflash bleach (participant **a**; τ=77.8, participant **b**; τ=273.2, participant **c**; τ=127.5)

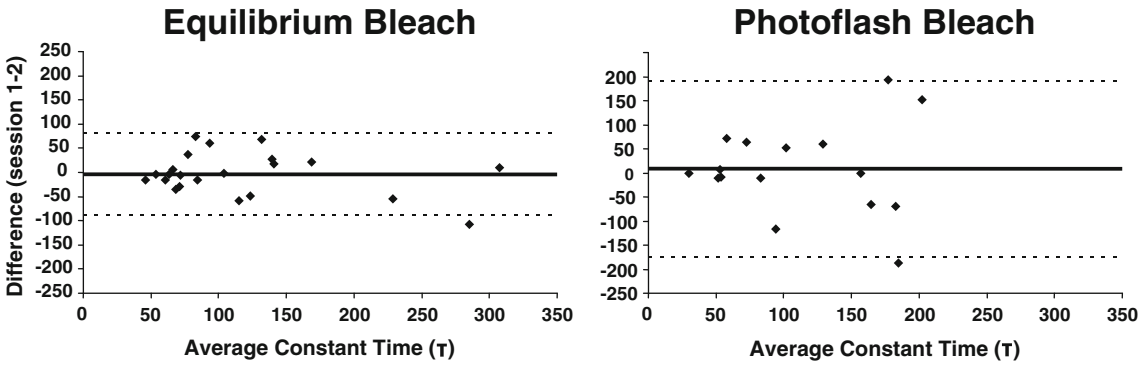

Fig. 4 Intersession difference plotted against intersession average, providing a graphical representation of intersession repeatability as advocated by Bland and Altman [9]. The *solid horizontal line* represents the mean difference between visits 1 and 2, whilst the *dotted lines* indicate the 95% limits of agreement; a narrower interval between these lines indicates better repeatability. The coefficients of repeatability (1.96 × SD of differences) for each technique were 85s (equilibrium) and 184s (photoflash). This does not include data from those participants who were excluded due to ineffective bleaching

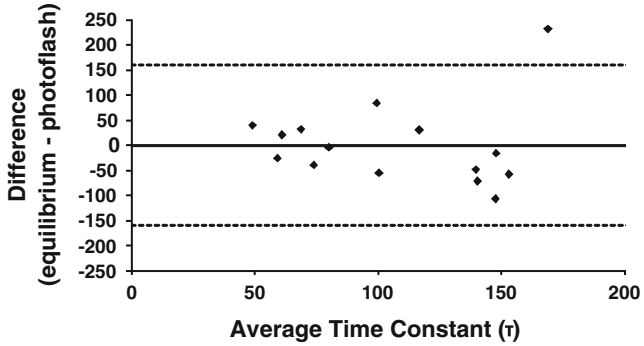

Fig. 5 Between technique differences in recovery time (mean short − mean long duration bleach) plotted as a function of average recovery time. The *solid horizontal line* represents the mean difference in recovery time constant, whilst the *dotted lines* indicate the 95% limits of agreement

controls than a photoflash bleach. The rod photoreceptors, when bleached, obtain the retinal required to regenerate photopigment from the RPE. As a result, the rate of photopigment regeneration within the rods is dependent on the health and function of the RPE and the diffusion of retinoids to the RPE from the choroidal circulation via Bruch's membrane [10]. The cone photoreceptors, however, are able to regenerate photopigment using a local store of retinoid derived from the Müller cells [11], and therefore do not necessarily have the same dependence on the health of the RPE, Bruch's membrane and choroidal circulation. Abnormal RPE/Bruch's function may have little or no effect on cone photopigment regeneration while this local retinoid store is present. Unlike photoflash bleaches, long-duration bleaches are likely to deplete local stores of 11-cis-retinal [7], placing greater emphasis on the role of the RPE in cone photopigment regeneration. Hence long-, but not short-duration bleaches may help elucidate functional delays in people with ARM.

It has been reported that the rate of dark adaptation decreases as we get older [12]. The effect of age on recovery time constant in this study produced an increase of 27 seconds per decade (0.45 minutes/decade), which was comparable to the findings of Coile & Baker [4] who showed an increase of 0.21 minutes per decade. Although the relationship between age and time constants in this study can be fitted using a single linear function, it is possible that a steeper rate of change above 55 years may be present, as suggested by Newsome et al. [13]. The increased variability in time constant with age makes this difficult to determine.

In agreement with our findings, Coile & Baker [4] also demonstrated a greater variability in the rate of adaptation of older participants compared to younger ones. The increased variability could suggest that those apparently normal individuals with prolonged time constants may be at risk of developing ARM. Currently, ARM is identified on the basis of fundus photography, but it is possible that significant changes occur in the function of the retina prior to the macroscopic changes, such as drusen and pigmentary alteration, becoming visible on ophthalmoscopic examination. Histological work by Sarks [14] identified changes to Bruch's membrane and the presence of basal linear deposits within the retina in eyes with a normal fundus appearance and often good visual acuity. Changes in the permeability of Bruch's membrane have been suggested to be the cause of delayed dark adaptation in ARM [15], so individuals with pre-clinical ARM might be expected to show abnormal time constants. Confounders such as media opacities could also be influencing the spread of data. The increase in lenticular changes with age would conceivably lead to more variability in retinal illumination, and therefore increase the variability of the results. However, this is unlikely as all those with marked lens opacities were excluded. Hollins and Alpern [3] showed that equilibrium bleaches at a range of intensities all produced the same time constants of recovery, making any difference in τ due to minor media opacities unlikely.

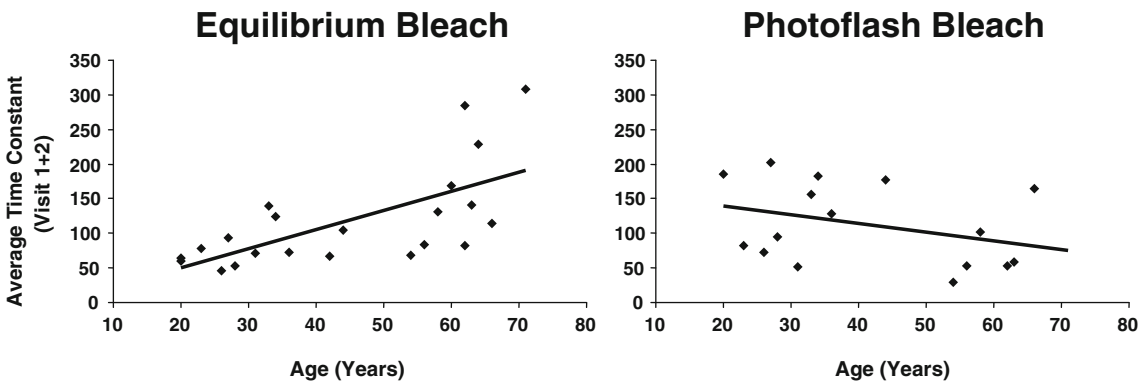

Fig. 6 The relationship between mean time constants (visits 1+2) and age for equilibrium and photoflash bleaches. A statistically significant correlation was identified for the equilibrium bleach (Pearson's correlation r=0.66, P=0.0008), whereas a non-significant negative correlation was found with the photoflash bleach (Pearson's correlation r=−0.34, P=0.19). This does not include data from those participants who were excluded due to ineffective bleaching

The photoflash data demonstrated a similar time constant to the equilibrium bleach technique. A shorter recovery may have been expected following the photoflash, had a similar proportion of photopigment been bleached for each technique [3]; however, given the higher percentage bleach provided by the photoflash, the lack of a significant difference in recovery time is not unexpected. Additionally, the photoflash technique did not demonstrate a significant relationship with age (see Fig. 6). This was attributed to the variability of the post-photoflash ERG data, particularly the traces recorded immediately post-bleach. Fitting Eq. 1 to noisy data will inevitably result in aberrant recovery times. This corresponds to participant-reported, and -observed, difficulty in avoiding blinks and eye movements for the initial ERG recordings after a photoflash, an observation not apparent following the equilibrium bleach.

Many studies have successfully used photoflash bleaches [16, 17], some of which report using techniques to hide or obscure the flash source [13, 18], potentially improving reliability of flash delivery by reducing anticipation. Most importantly, these studies assessed psychophysical responses, where the effects of blinking and eye movements following the flash exposure are likely to have a minimal impact on data quality and reliability, compared to the electrophysiological techniques used in this study.

In conclusion, the established equilibrium bleach technique was found to give good intersession repeatability, sufficient to be sensitive to ARM-related changes. The alternative photoflash bleaching technique, when applied with an ERG, was less repeatable and clinically unreliable. Finally, the time constant of recovery as determined using the equilibrium bleach was found to increase with age.

References

1. Binns AM, Margrain TH (2005) Evaluation of retinal function using the Dynamic Focal Cone ERG. Ophthalmic Physiol Opt 25:492–500
2. Binns AM, Margrain TH (2007) Evaluating retinal function in age-related maculopathy with the ERG photostress test. Ophthalmic Physiol Opt 48:2806–2813
3. Hollins M, Alpern M (1973) Dark adaptation and visual pigment regeneration in human cones. J Gen Physiol 62:430–447
4. Coile DC, Baker HD (1992) Foveal dark adaptation, photopigment regeneration, and aging. Vis Neurosci 8:27–39
5. Aldebasi YH, Drasdo N, North RV, Morgan JE (2001) The pattern electroretinogram (PERG) with contralateral corneal reference. Ophthalmic Physiol Opt 21:243–246
6. Paupoo AA, Mahroo OA, Friedburg C, Lamb TD (2000) Human cone photoreceptor responses measured by the electroretinogram [correction of electoretinogram] a-wave during and after exposure to intense illumination. J Physiol 529(Pt 2):469–482
7. Rushton WAH, Henry GH (1968) Bleaching and regeneration of cone pigments in man. Vision Res 8:617–631
8. BSI (2007) Ophthalmic Instruments — fundamental requirements and test methods. Part 2 — Light Hazard Protection. British Standards Institute BS EN 15004-2
9. Bland JM, Altman DG (1986) Statistical methods for assessing agreement between two methods of clinical measurement. Lancet 1:307–310
10. Lamb TD, Pugh EN Jr (2004) Dark adaptation and the retinoid cycle of vision. Prog Retin Eye Res 23:307–380
11. Mata NL, Radu RA, Clemmons RC, Travis GH (2002) Isomerization and oxidation of vitamin a in cone-dominant retinas: a novel pathway for visual-pigment regeneration in daylight. Neuron 36:69–80
12. Jackson GR, Owsley C, McGwinJr G (1999) Aging and dark adaptation. Vision Res 39:3975–3982
13. Newsome DA, Negreiro M (2009) Reproducible measurement of macular light flash recovery time using a novel device can indicate the presence and worsening of macular diseases. Curr Eye Res 34:162–170
14. Sarks SH (1976) Ageing and degeneration in the macular region: a clinico-pathological study. Br J Ophthalmol 60:324–341
15. Steinmetz RL, Haimovici R, Jubb C, Fitzke FW, Bird AC (1993) Symptomatic abnormalities of dark adaptation in patients with age-related Bruch's membrane change. Br J Ophthalmol 77:549–554
16. Owsley C, Jackson GR, White M, Feist R, Edwards D (2001) Delays in rod-mediated dark adaptation in early age-related maculopathy. Ophthalmology 108:1196–1202
17. Owsley C, McGwin G Jr, Jackson GR, Kallies K, Clark M (2007) Cone- and rod-mediated dark adaptation impairment in age-related maculopathy. Ophthalmology 114:1728–1735
18. Dimitrov PN, Guymer RH, Zele AJ, Anderson AJ, Vingrys AJ (2008) Measuring rod and cone dynamics in age-related maculopathy. Invest Ophthalmol Vis Sci 49:55–65

Appendix M:

Retinal and Choroidal Thickness in Early Age-Related Macular Degeneration

ASHLEY WOOD, ALISON BINNS, TOM MARGRAIN, WOLFGANG DREXLER, BORIS POVAŽAY, MARIEH ESMAEELPOUR, AND NIK SHEEN

• PURPOSE: To compare retinal thickness and choroidal thickness at increasing retinal eccentricity in individuals with early age-related macular degeneration (AMD) and in healthy controls using enhanced choroidal penetration, 3-dimensional optical coherence tomography at 1060 nm.

• DESIGN: Cross-sectional study.

• METHODS: Individuals with early AMD (n = 16; mean age, 71.6 ± 8.5 years) and a comparison group of healthy controls (n = 16; 67.6 ± 5.4 years) were recruited. Three-dimensional (20 degrees × 20 degrees) long-wavelength optical coherence tomography (1060 nm) images (approximately 8-μm axial resolution; 47 000 A scans/second, centered on the fovea) were obtained from all participants after pupil dilation. Retinal thickness was measured between the inner limiting membrane and the retinal pigment epithelium. Choroidal thickness was measured between the retinal pigment epithelium and the choroid–scleral interface. Thickness measurements were obtained subfoveally and at 0.5-mm intervals to a maximum of 2.0 mm nasally, temporally, superiorly, and inferiorly. The main outcome measures were retinal and choroidal thickness (measured in micrometers) at different eccentricities on vertical and horizontal meridians.

• RESULTS: Mean retinal thickness was reduced significantly in the group of participants with early AMD compared with the control group at multiple locations within 2.0 mm of the fovea. This difference was most significant at the fovea, where the mean retinal thickness of the early AMD group was 179 ± 27 μm and that of the control group was 202 ± 18 μm (P = .008). There was no significant difference in choroidal thickness between groups at any location.

• CONCLUSIONS: Retinal thickness is reduced in early AMD, but choroidal thickness seems to be unaffected by the early disease process. (Am J Ophthalmol 2011;xx: xxx. © 2011 by Elsevier Inc. All rights reserved.)

Accepted for publication May 18, 2011.

From the School of Optometry and Vision Sciences, Cardiff University, Cardiff, United Kingdom (A.W., A.B., T.M., W.D., B.P., M.E., N.S.).

Inquiries to Alison Binns, Optometry and Vision Sciences, Cardiff University, Cardiff CF24 4LU, United Kingdom; e-mail: binnsam@cardiff.ac.uk

AGE-RELATED MACULAR DEGENERATION (AMD) IS the leading cause of blindness in the United Kingdom, and is responsible for more people being registered as sight impaired or severely sight impaired than all other ocular conditions combined.[1] The prevalence of AMD is expected to increase globally between 2005 and 2050 because of a predicted 3-fold increase in the number of people older than 60 years.[2] AMD manifests either as choroidal neovascularization (wet AMD) or geographic atrophy (dry AMD), whereas early AMD, also known as age-related maculopathy, is characterized by soft drusen and focal pigmentary changes only.[3] Currently, treatment is available only for the wet (neovascular) type of AMD, usually in the form of antiangiogenic pharmacotherapy.[4] Although no treatment currently exists for dry AMD and early AMD, there is some evidence to suggest that nutritional supplements may slow the progression of the disease.[5] The ability to diagnose the onset of AMD accurately and to monitor disease progression is vital in the early identification of patients suitable for therapy and in evaluating the outcomes of the treatment.

Historically, the diagnosis and grading of AMD largely has been based on visual acuity and stereoscopic fundus photographs.[3] However in recent years, detailed analysis of retinal microstructure has become possible through optical coherence tomography (OCT), which offers an extra dimension to the evaluation of age-related macular disease.[6] OCT is a technique that uses the optical equivalent of the echo time delay in ultrasound to construct a cross-sectional image of the retina in vivo, analogous to a histologic section.

Frequency-domain (FD) OCT traditionally has used light sources with a bandwidth based at approximately 800 nm.[6] The limitation of this band of wavelengths is partly that ocular opacities can degrade the quality of the collected image (which is especially important in the assessment of elderly individuals), but also that the high level of scatter by retinal tissue and increased absorption by the retinal pigment epithelium (RPE) results in limited visualization of sub-RPE layers.[7–9] An alternative light source, with a bandwidth based at approximately 1060 nm, has been shown to allow deeper penetration into the choroidal tissue and better signal-to-noise ratio in the presence of media opacities.[7,9–11]

Although the longer-wavelength 1060-nm OCT is the first system that allows a reliable assessment of in vivo

0002-9394/$36.00
doi:10.1016/j.ajo.2011.05.021

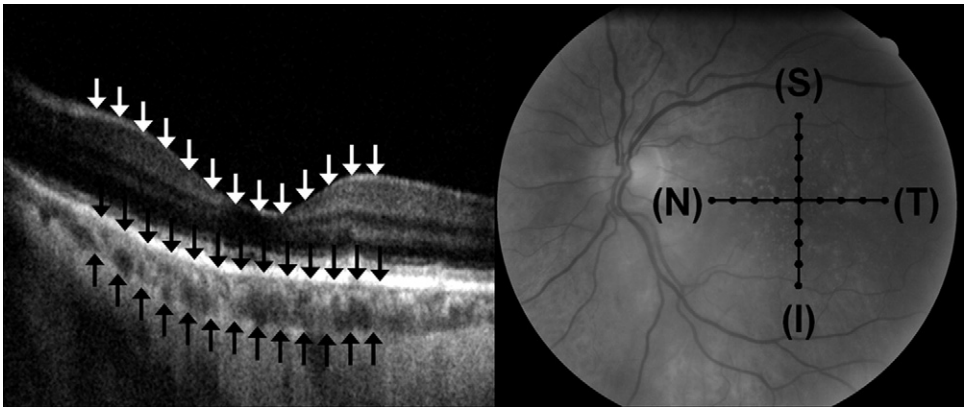

FIGURE 1. Optical coherence tomography (OCT) layer boundaries and measurement locations used in this study. (Left) Cross-sectional 1060-nm OCT B-scan, the superior row of arrows indicating the location of the inner limiting membrane (ILM), the middle row indicating the retinal pigmented epithelium (RPE), and the inferior row indicating the choroid–sclera boundary. These features were used to delineate the boundaries of the retina and choroid for thickness measurements. (Right) Fundus photograph with retinal locations overlaid (solid dots) at which each retinal and choroid thickness measurement was obtained. Retinal direction is indicated by S (superior), I (inferior), N (nasal), and T (temporal) as labeled.

choroidal thickness in all patients, it has been used to date only to assess outer retinal features and choroidal structure in patients with the neovascular form of AMD,[12] where the structural changes to the choroid–Bruch's membrane–RPE complex already are marked. There is substantial evidence to suggest that the dynamics of the choroidal circulation are affected earlier in the disease process (see Harris and associates for a review[13]), and histologic studies have found evidence of a difference in choroidal structure in eyes with early and advanced AMD compared with age-matched control eyes, such as reductions in choriocapillary density and choroidal thickness.[14–16] However, histologic evidence regarding choroidal thickness in AMD is mixed, with some evidence to suggest a reduction, particularly in the advanced stages of the disease,[15–16] whereas another study found no significant change in choroidal thickness, even in advanced AMD.[14]

The aim of this study was to use the 1060-nm enhanced choroidal penetration OCT to investigate retinal and choroidal thickness as a function of eccentricity in patients with early AMD (drusen or pigmentary changes only) as a means of determining the potential clinical value of the 1060-nm OCT in assessing early macular disease and of providing insight into the earliest structural changes occurring in AMD.

METHODS

• **PARTICIPANTS:** Control participants (n = 16) and those with early AMD (n = 16) were recruited for this study from among staff, students, and volunteers attending the eye clinic at the School of Optometry and Vision Sciences and the eye unit at the University Hospital of Wales. All participants had a corrected visual acuity (VA) of 0.3 logarithm of the minimal angle of resolution units (approximately 20/40) or better assessed using an Early Treatment Diabetic Retinopathy Study sight chart and a refractive error of less than ± 6 diopters. Participants were excluded if they had secondary retinal disease, significant cataract (Lens Opacities Classification System III grade 4 or more for any criteria[17]), or narrow iridocorneal angles (grade 1 or less assessed by Van Herick). Each participant was given a full explanation of the procedures involved, and their written informed consent was obtained before participation in the study.

Participants were categorized into either a control or early AMD group, depending on the assessment of 37-degree digital fundus images (CR-DGi nonmydriatic retinal camera; Canon Inc, Lake Success, New York, USA) and 20-degree 1060-nm OCT images. Images were assessed for AMD-related features located within a 6000μm diameter centered on the fovea. Definitions were based on the International and the Age-Related Eye Disease Study AMD classification systems.[3,18] Control participants exhibited no features associated with AMD, with any drusen present being less than 125 μm in diameter (hard drusen). Early AMD was defined as the presence of soft drusen (> 125 μm diameter), pigment changes, or drusenoid pigment epithelial detachment in the absence of any feature of advanced AMD (wet or dry) as defined by the Age-Related Eye Disease Study grading system.[18] Classification was carried out by on of the authors (A.W.) and was confirmed independently by 2 other authors (A.B. and T.M.). One drop of tropicamide 1.0% was instilled into both eyes of each participant, ensuring pupil dilation of at least 7 mm before obtaining fundus photographs and OCT images. Images were obtained from both eyes of all individuals to determine their AMD status. One eye was selected for analysis from each

TABLE 1. Clinical Features of Participants with Early Age-Related Macular Degeneration

Participant			Presence of Clinical Feature				
No.	Age (y)	Tested Eye	Drusen Diameter > 125 μm	Drusen No. > 10	Hyperpigmentation or Hypopigmentation	Drusenoid PED	Contralateral Eye Status[a]
1	56	R	N	N	Y	N	Normal
2	64	R	Y	N	N	N	Normal
3	80	L	Y	N	Y	N	Normal
4	79	L	N	N	Y	N	Early
5	70	L	Y	Y	N	N	Early
6	67	L	Y	N	N	N	Early
7	58	L	Y	N	Y	N	Early
8	87	L	Y	N	N	N	Early
9	73	L	Y	Y	N	N	Early
10	65	L	N	N	Y	N	Wet
11	74	L	N	N	Y	N	Wet
12	65	L	Y	Y	Y	N	Wet
13	75	R	Y	Y	N	N	Wet
14	78	R	Y	Y	Y	Y	Wet
15	79	R	Y	N	N	Y	Wet
16	75	L	Y	Y	N	Y	Wet

L = left eye; N = no; PED = pigment epithelial detachment; R = right eye; Y = yes.
[a]Early or wet denotes the subtype of age-related macular degeneration.

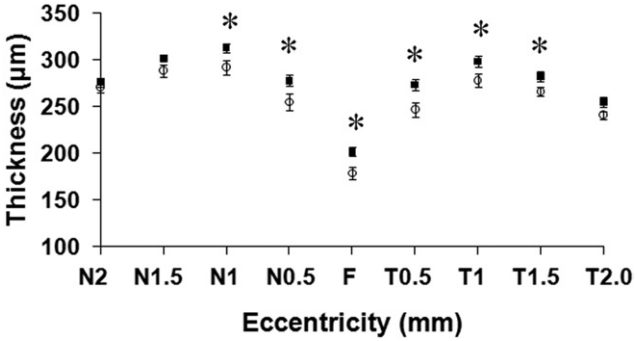

FIGURE 2. Graph showing retinal thickness in early age-related macular degeneration (AMD) along the horizontal meridian. Retinal thickness for normal (black squares) and early AMD (open circles) participants from (Left) 2 mm nasal to (Right) 2 mm temporal of the fovea. The asterisk (*) indicates retinal locations where a difference between groups is significant at the $P = .05$ level. Error bars indicate standard error at each point. Measurement locations identified as fovea (F), nasal (N), and temporal (T) with eccentricity of 0.5, 1.0, 1.5, or 2.0 mm.

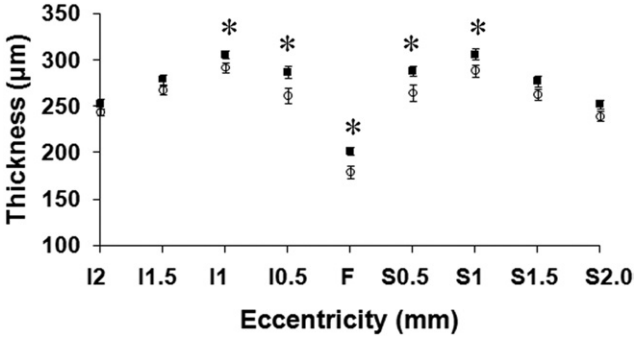

FIGURE 3. Graph showing retinal thickness in early age-related macular degeneration (AMD) along the vertical meridian. Retinal thickness for normal (black squares) and early AMD (open circles) participants from (Left) 2 mm inferior to (Right) 2 mm superior of the fovea. The asterisk (*) indicates retinal locations where a difference between groups is significant at the $P = .05$ level. Error bars indicate standard error at each point. Measurement locations identified as fovea (F), superior (S), or inferior (I) with eccentricity of 0.5, 1.0, 1.5, or 2.0 mm.

participant; this was the eye with a diagnosis of early AMD or, in the case of bilateral early AMD or controls, the eye with the better VA, with the left eye used as default.

• **IMAGING:** Three-dimensional OCT imaging at 1060 nm was performed with less than 2.5 mW at the cornea, below the maximum power limit for a 10-second exposure.[19,20] OCT volumes were acquired across a 20 × 20-degree (5.76 × 5.76-mm) field consisting of 512 × 512 A-scans obtained at a rate of 47 000 A-scans/second (approximately 8-7 μm axial resolution). OCT volumes were centered on the fovea, aligned by participant fixation. Axial length (cornea to RPE) measurements were acquired using optical biometry (IOL Master; Zeiss, Jena, Germany) for each eye by averaging 5 measurements.

TABLE 2. Mean Retinal Thickness Values at Each Location for Both the Control and Early Age-Related Macular Degeneration Groups

Location[a]	Control Retinal Thickness (μm) Mean	Control Retinal Thickness (μm) SD	Early AMD Retinal Thickness (μm) Mean	Early AMD Retinal Thickness (μm) SD	*t* Test[b] (*$P < .05$)
F	202	18	179	27	**.008**
T0.5	274	24	247	31	**.011**
T1.0	299	23	278	27	**.030**
T1.5	282	22	267	20	**.038**
T2.0	255	22	241	18	.055
N0.5	278	24	255	35	**.040**
N1.0	313	19	292	30	**.028**
N1.5	302	15	289	27	.092
N2.0	276	20	271	22	.480
S0.5	288	22	265	37	**.039**
S1.0	306	23	288	25	**.045**
S1.5	277	23	263	24	.090
S2.0	252	19	239	21	.083
I0.5	287	24	261	33	**.018**
I1.0	306	15	292	22	**.036**
I1.5	279	21	267	19	.104
I2.0	253	23	244	15	.205

AMD = age-related macular degeneration; SD = standard deviation.

[a]Measurement locations identified as fovea (F), nasal (N), temporal (T), superior (S), or inferior (I) with eccentricity of 0.5, 1.0, 1.5, or 2.0 mm.

[b]Independent *t* test; *P* values for differences between groups at each location are in boldface where a difference is significant at the $P = .05$ level.

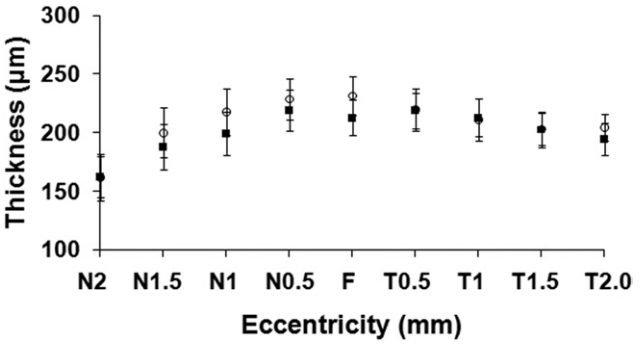

FIGURE 4. Graph showing choroidal thickness in early age-related macular degeneration (AMD) along the horizontal meridian. Choroidal thickness for normal (black squares) and early AMD (open circles) participants from (Left) 2 mm nasal to (Right) 2 mm temporal of the fovea. Error bars indicate standard error at each point. Measurement locations identified as fovea (F), nasal (N), and temporal (T) with eccentricity of 0.5, 1.0, 1.5, or 2.0 mm.

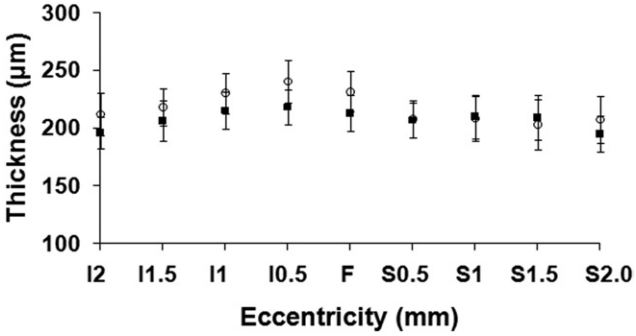

FIGURE 5. Graph showing choroidal thickness in early age-related macular degeneration (AMD) along the vertical meridian. Choroidal thickness for normal (black squares) and early AMD (open circles) participants from (Left) 2 mm inferior to (Right) 2 mm superior of the fovea. Error bars indicate standard error at each point. Measurement locations identified as fovea (F), superior (S), or inferior (I) with eccentricity of 0.5, 1.0, 1.5, or 2.0 mm.

TABLE 3. Mean Choroidal Thickness Values at Each Location for Both the Control and Early Age-Related Macular Degeneration Groups

Location[a]	Control Choroid Thickness (μm) Mean	Control Choroid Thickness (μm) SD	Early AMD Choroid Thickness (μm) Mean	Early AMD Choroid Thickness (μm) SD	*t* Test ($P < .05$)
F	213	63	231	70	.429
T0.5	219	60	220	72	.974
T1.0	213	65	211	71	.940
T1.5	203	62	203	54	.982
T2.0	195	54	204	47	.593
N0.5	219	71	229	71	.710
N1.0	199	74	218	80	.505
N1.5	188	77	200	85	.678
N2.0	162	70	162	80	1.000
S0.5	207	62	207	65	.973
S1.0	210	75	208	79	.952
S1.5	209	76	203	86	.830
S2.0	195	63	207	83	.640
I0.5	218	62	240	74	.360
I1.0	215	64	230	69	.529
I1.5	206	72	218	65	.624
I2.0	196	54	212	73	.487

AMD = age-related macular degeneration; SD = standard deviation.

[a]Measurement locations identified as fovea (F), nasal (N), temporal (T), superior (S), or inferior (I) with eccentricity of 0.5, 1.0, 1.5, or 2.0 mm.

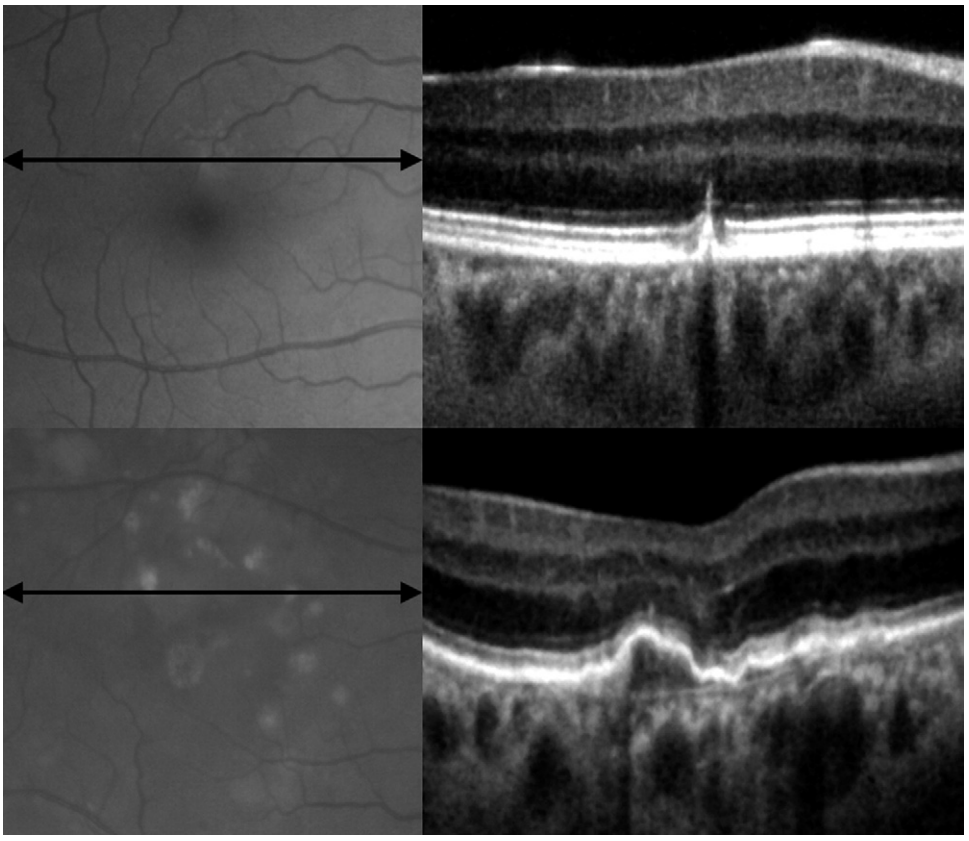

FIGURE 6. Retinal and optical coherence tomography (OCT) images for 2 study participants. Macular photographs and corresponding OCT sections (scan locations indicated by arrow) for (Top) Patient 1 and (Bottom) Patient 14. Patient 1: (Top left) photograph of localized pigmentary disturbance, with few drusen present; (Top right) OCT image of a drusen. Patient 14: (Bottom left) photograph of multiple large, soft druse, pigmentary disturbances, and drusenoid pigment epithelial detachments (PEDs); (Bottom right) OCT image of a drusenoid PED and soft drusen.

Image processing and analysis was undertaken using ImageJ software (ImageJ, Bethesda, Maryland, USA). Raw OCT images were enhanced digitally to improve the visibility of the retina and choroidal boundaries. Postprocessing procedures were carried out subjectively and included adjustments to brightness and contrast, B-scan registration, despeckling or noise removal, and application of Gaussian or convolving blur (ie, controlled blurring of the image between adjacent b-scans). Measurements were made using the caliper function in the axial plane of the images. The thickness represented by each pixel was calculated assuming a refractive index of 1.4.

Retinal thickness was measured from the most anterior hyperreflective line, which corresponds to the inner limiting membrane, to the center of the most posterior hyperreflective line, which corresponds to the RPE. Choroidal thickness was measured from the RPE to the choroid–sclera boundary. Thickness measurements were obtained for both the retina and the choroid at the fovea and then at 0.5-mm intervals to 2 mm nasally (N), temporally (T), superiorly (S), and inferiorly (I; see Figure 1). This produced thickness measurements at 17 individual retinal locations for each eye. At each location, the distribution of thickness measurements was checked for normality, and an independent *t* test was conducted between the control and early AMD groups.

Additionally, the fundus and OCT images were assessed subjectively; specifically, the participants regarded at the highest risk of progression to advanced AMD (i.e., those with drusenoid pigment epithelial detachment,[21] confluent drusen, or a fellow eye with advanced AMD[18]) were compared with those at lowest risk (ie, those with normal fellow eyes and none of the high-risk features listed above).

RESULTS

THE STUDY INVOLVED 32 PARTICIPANTS CONSISTING OF A control group (n = 16) and an early AMD group (n = 16). The control group (n = 16) had a mean age of 67.6 ± 5.4 years and a mean axial length of 23.7 ± 0.8 mm. The early AMD group (n = 16) had a mean age of 71.6 ± 8.5 years and a mean axial length of 23.2 ± 0.7 mm. The mean age (P = .12, independent *t* test) and axial length (P = .09, independent *t* test) of the 2 groups were not significantly

different. The clinical features of the participants with early AMD are shown in Table 1.

The mean retinal thickness for participants in the control and early AMD groups was plotted for each retinal location and is shown in Figure 2 for the horizontal meridian and in Figure 3 for the vertical meridian. The mean retinal thickness was found to be smallest at the fovea (F) for both groups, increasing with eccentricity in both vertical and horizontal meridians to reach a maximum at 1 mm, before declining with further increase in eccentricity. Central retinal thickness, measured at the fovea (F), was 202 ± 18 μm for the control group and 179 ± 27 μm for the early AMD group. This difference was significant ($P = .008$). Table 2 shows mean retinal thickness at each retinal location and the *P* value for the difference between the groups. The early AMD group was found to have significantly thinner retinal thickness values at the fovea and eccentricities to 1 mm, extending to 1.5 mm temporally.

Mean choroidal thickness was plotted for each retinal location measured along horizontal and vertical meridians (Figures 4 and 5). In the horizontal meridian, choroidal thickness was found to be greatest at the fovea (F), decreasing to a minimum nasally and showing a more modest reduction in thickness temporally. There was less variation in choroidal thickness in the vertical meridian. Central choroidal thickness, measured at the fovea (F), was 213 ± 63 μm for the control group and 231 ± 70 μm for the early AMD group. This difference was not significant ($P > .05$, independent *t* test). Table 3 shows mean choroidal thickness at each retinal location and the *P* value for the difference between each group. The difference between groups was not significant at any location for choroidal thickness.

OCT and macular photographs of those at most and least risk of progression to advanced AMD were compared subjectively to identify qualitative differences. Participant 1 (Figure 6) had a low risk of progression to advanced AMD,[22] whereas Participant 14 was at high risk of progression.[21] A common feature identified on the OCT images of both participants was a localized thinning of the photoreceptor layer overlying drusen or pigment epithelial detachments. This is exemplified in Figure 6, although the underlying choroidal thickness appears unaffected.

DISCUSSION

THIS STUDY USED ENHANCED CHOROIDAL PENETRATION (1060 nm) OCT to assess the thickness of the choroid in patients with early AMD. It was found that retinal thickness differed significantly at the fovea, and at a number of extrafoveal points, between individuals with early AMD and age-matched controls. However, there were no significant differences in choroidal thickness at any eccentricity assessed.

The one previous study that used a 1060-nm OCT system to evaluate the choroid in age-related macular disease recruited participants with the late neovascular form of AMD (n = 12).[12] Yasuno and associates compared images obtained using long-wavelength OCT with the standard 830-nm FD OCT in visualizing the morphologic features of structures beneath the RPE, such as choroidal neovascular membranes.[12] They found a general improvement in the image contrast of sub-RPE structures in most eyes, and in 3 eyes were able to see hyperreflective structures beneath the choroidal neovascular membranes not accessible using the 830-nm OCT. However, the study did not evaluate disease-related changes in the thickness of the choroid.

This study provides in vivo evidence that choroidal thickness may not be affected by early AMD. Histologic studies have been carried out to investigate the cross-sectional area and thickness of the choriocapillaris of donor eyes from individuals with early and advanced AMD.[14–16] Our data are in agreement with a study reporting a significant decrease in choriocapillary density in 25 eyes with features of AMD, but finding no significant decrease in the thickness of the choroid compared with age-matched controls.[14] Our data are also supported by a recent study by Chung and associates evaluating choroidal thickness in early AMD using the 870-nm OCT with an enhanced depth imaging technique.[23] They also found a small, but statistically nonsignificant, reduction in subfoveal choroidal thickness in the individuals with early AMD compared with age-matched controls.

However, there is evidence to suggest that choroidal thinning may occur in end-stage AMD.[15,16,23] McLeod and associates examined the postmortem choroid in 3 age-matched control eyes, 5 eyes with geographic atrophy, and 3 eyes with neovascular AMD and reported a linear relationship between the loss of RPE and choriocapillaris in geographic atrophy and a 50% reduction in choroidal vascular cross-sectional area in eyes with wet AMD, even in the absence of RPE atrophy.[15] Sarks carried out a histologic study on 378 eyes from patients 43 to 97 years of age who had either normal fundi or some degree of AMD.[16] He reported thinning of the choroid, resulting in a tigroid fundus appearance. Thinning was associated with increasing age both in older patients classified as clinically normal and in those with all stages of AMD, but it was particularly prevalent in those with advanced AMD. A significant reduction in in vivo subfoveal choroidal thickness also has been reported in individuals with exudative AMD in a study that used 870-nm enhanced depth imaging OCT.[23]

Although there is strong evidence for the occurrence of age-related thinning of the choroid[14,16,24] and for changes in choroidal perfusion in early AMD,[13,25,26] evidence for thinning of the choroid specific to early AMD is not apparent in the literature. Our findings suggest that any changes in the perfusion and blood flow dynamics of the

choriocapillaris associated with early AMD are independent of choroidal thickness.

Multiple studies have assessed choroidal thickness in healthy individuals using OCT[23,24,27–30]; however, only a few have used a 1060-nm system.[27,28] A recent study using 1060-nm OCT to investigate the correlation between axial length and choroidal thickness in 34 healthy subjects (64 eyes) 19 to 80 years of age found a mean central choroidal thickness of 315 μm (standard deviation [SD], 106 μm), with the choroid thinnest in the nasal parafovea.[27] Other studies also have found choroidal thickness to be greatest at the fovea, with a greater reduction in thickness with eccentricity reported nasally than temporally,[23,24,28,30] a pattern reflected in our findings from both controls and individuals with early AMD. The mean subfoveal choroidal thickness reported has varied between studies from 225 μm (SD, 53 μm)[23] to 354 μm (SD, 111 μm).[28] The control group used in our study was found to have a slightly lower mean subfoveal choroidal thickness of 213 μm (SD, 63 μm), which may reflect the greater mean age of the participants than in most previous studies.

A manual technique was used to identify the boundaries and to measure the retinal and choroidal thickness in this study. Although more time consuming than automated systems, there is evidence to suggest that manual measurement is more accurate, especially in the presence of disruption caused by diseases such as AMD.[31–33] Using this strategy, the mean retinal thickness was found to be lower in individuals with early AMD than in controls at all eccentricities; this reached statistical significance at the fovea and at extrafoveal locations up to 1 mm in eccentricity in all meridians.

Multiple comparisons were carried out in this study (17 retinal locations were evaluated). If these were unrelated variables, then one might expect the null hypothesis to be wrongly rejected in 1 comparison of 20 through chance alone (ie, multiple testing increases the risk of a type I error). However in this study, the retinal thickness measurements at different retinal locations were highly correlated (mean $r = 0.72$ across all retinal locations, Pearson correlation coefficient). When variables tested are correlated, the risk of a type I error decreases as the probability of the null hypothesis being rejected because of chance is not multiplicative of the probability of each individual comparison being found significant by chance alone.[34] However, even if a correction method such as that described by Sankoh and associates is used,[35] which factors in the correlation between variables, retinal thickness remains reduced significantly in individuals with early AMD at the fovea ($P = .019$), 0.5 mm inferiorly ($P = .039$), and 0.5 mm temporally ($P = .023$).

A number of studies have used OCT to evaluate retinal thickness in eyes with advanced dry or wet AMD,[36–40] but there is less evidence regarding retinal thickness assessed using OCT in early AMD.[41–43] One study using FD OCT on 17 eyes with early AMD and 17 healthy control eyes reported that photoreceptor layer thickness is reduced over drusen in eyes with early AMD, but that there is no evidence of a generalized reduction in thickness across the macular region.[43] Similarly, Kaluzny and associates used FD OCT to identify focal changes in retinal thickness in 24 eyes with soft drusen, localized to the position of the drusen.[41] They reported evidence of photoreceptor atrophy anterior to the drusen, but not diffusely present across the macula. Malamos and associates used FD OCT to evaluate macular changes in 12 individuals with early AMD, as well as 37 with choroidal neovascularization.[42] They also found that discrete thinning of the retina above underlying drusen was the only abnormality in retinal thickness in patients with early macular disease and that this was not sufficient to influence mean thicknesses of annuli centered on the fovea. This localized reduction in retinal thickness has been ascribed to the outer retina, with Schuman and associates finding inner retinal thickness to be almost unchanged over drusen.[43]

It is possible that the finding of a reduced retinal thickness in individuals with early AMD in our study reflects the photoreceptor degeneration reported to occur overlying drusen.[41–43] Although drusen areas were not targeted specifically for our measurements, subjective assessment of the images showed localized thinning of the photoreceptor layer overlying drusen and pigment epithelial detachment (Figure 6). Histologic findings from human donor eyes have suggested that a loss of photoreceptors (with a predilection for rods over cones) occurs in nonexudative AMD, which may explain such a reduction in retinal thickness.[44] The difference in retinal thickness between individuals with early AMD and age-matched controls in this study extended up to 1.5 mm (5.2 degrees) of eccentricity. Curcio and associates also reported that the location of greatest cell loss in age-related macular disease occurs within the parafovea and perifoveal region, from 1.5 to 10 degrees from fixation.[44] Further investigation of the individual intraretinal layer thicknesses and their relationship to clinical features in patients with early AMD may indicate the cause or location of the retinal thickness loss identified.

Legaretta and associates and Kakinoki and associates reported foveal retinal thickness in healthy subjects of 258.2 μm (SD, 23.5 μm) and 257.6 μm (SD, 19.6 μm), respectively, which is thicker than the 202 μm (SD, 18 μm) found in this study.[45,46] Both of these studies used the Cirrus OCT, which used the same retinal boundaries as this study but measured the foveal thickness as an average over 500 μm centered on the fovea, rather than at the foveola, as in this study.[45,46] The values found in this study are comparable with myopic foveal thickness measurements using a similar methodology to our own[29] and to minimum foveal thickness in normal eyes found using a Stratus OCT.[45–47]

Our overall approach to the analysis was conservative because we adopted an independent samples rather than a

paired approach, despite having matched our groups for age and axial length. Based on the standard deviation of the foveal thickness measurements and the sample size, the smallest difference between groups detectable in this study was 24.8 and 64.7 μm for retinal and choroidal thickness, respectively (with a power of 80% and a significance level of 0.05).[48] Intraobserver reliability previously was assessed for retinal and choroidal thickness measurements by one of the authors (A.W.) using the manual measurement technique used in this study. Using the Bland and Altman technique, the intraobserver coefficient of repeatability for measurement of foveal retinal thickness on 2 separate occasions was 18.9 μm for individuals with early AMD (n = 17) and 15.7 μm for healthy control participants (n = 24).[49] For choroidal thickness measurements, an intraobserver coefficient of repeatability of 58.7 and 35.6 μm was obtained for early AMD and control participants, respectively. This study therefore was powered to detect any difference that was greater than the measurement error of the technique.

Although a modest, but significant, reduction in retinal thickness in early AMD was shown, no significant change in choroidal thickness was found during this study. These findings suggest that measurement of choroidal thickness using OCT is not diagnostic for early age-related macular disease.

PUBLICATION OF THIS ARTICLE WAS SUPPORTED BY GRANT FP6-IST-NMP-2 STREPT (017128, NANOUB) FROM CARDIFF University, Cardiff, Wales; and Grant AP1110 from Action Medical Research (AMR), West Sussex, United Kingdom. The sponsor or funding organization had no role in the design or conduct of this research. The authors indicate no financial conflict of interest. Involved in Design of study (A.W., A.B., T.M., N.S., B.P., W.D.); Conduct of study (A.W., T.M., A.B., N.S.); Data collection (A.W.); Data analysis, management, and interpretation (A.W., T.M., N.S., A.B., M.E.); and Review and approval of manuscript (A.W., A.B., T.M., W.D., B.P., M.E., N.S.). The study adhered to the tenets of the Declaration of Helsinki, and institutional review board/ethics committee approval was obtained prospectively from the South East Wales Regional Ethics Committee & School of Optometry and Vision Sciences Research Ethics Committee. Informed consent was obtained from all participants.

REFERENCES

1. Bunce C, Wormald R. Leading causes of certification for blindness and partial sight in England & Wales. BMC Public Health 2006;6:58.
2. United Nations. World Population prospects: 2004 revision. New York: United Nations, 2005.
3. Bird AC, Bressler NM, Bressler SB, et al. An international classification and grading system for age-related maculopathy and age-related macular degeneration. The International ARM Epidemiological Study Group. Surv Ophthalmol 1995; 39(5):367–374.
4. Mitchell P, Korobelnik JF, Lanzetta P, et al. Ranibizumab (Lucentis) in neovascular age-related macular degeneration: evidence from clinical trials. Br J Ophthalmol 2010;94(1): 2–13.
5. AREDS. A randomized, placebo-controlled, clinical trial of high-dose supplementation with vitamins C and E, beta carotene, and zinc for age-related macular degeneration and vision loss: AREDS report no. 8. Arch Ophthalmol 2001; 119(10):1417–1436.
6. Drexler W, Fujimoto JG. State-of-the-art retinal optical coherence tomography. Prog Retin Eye Res 2008;27(1):45–88.
7. Povazay B, Hermann B, Unterhuber A, et al. Three-dimensional optical coherence tomography at 1050 nm versus 800 nm in retinal pathologies: enhanced performance and choroidal penetration in cataract patients. J Biomed Opt 2007; 12(4):041211.
8. Povazay B, Hofer B, Torti C, et al. Impact of enhanced resolution, speed and penetration on three-dimensional retinal optical coherence tomography. Opt Express 2009;17(5): 4134–4150.
9. Unterhuber A, Povazay B, Hermann B, Sattmann H, Chavez-Pirson A, Drexler W. In vivo retinal optical coherence tomography at 1040 nm-enhanced penetration into the choroid. Opt Express 2005;13(9):3252–3258.
10. Povazay B, Bizheva K, Hermann B, et al. Enhanced visualization of choroidal vessels using ultrahigh resolution ophthalmic OCT at 1050 nm. Opt Express 2003;11(17): 1980–1986.
11. Povazay B, Hermann B, Hofer B, et al. Wide-field optical coherence tomography of the choroid in vivo. Invest Ophthalmol Vis Sci 2009;50(4):1856–1863.
12. Yasuno Y, Miura M, Kawana K, et al. Visualization of sub-retinal pigment epithelium morphologies of exudative macular diseases by high-penetration optical coherence tomography. Invest Ophthalmol Vis Sci 2009;50(1):405–413.
13. Harris A, Chung HS, Ciulla TA, Kagemann L. Progress in measurement of ocular blood flow and relevance to our understanding of glaucoma and age-related macular degeneration. Prog Retin Eye Res 1999;18(5):669–687.
14. Ramrattan RS, van der Schaft TL, Mooy CM, de Bruijn WC, Mulder PG, de Jong PT. Morphometric analysis of Bruch's membrane, the choriocapillaris, and the choroid in aging. Invest Ophthalmol Vis Sci 1994;35(6):2857–2864.
15. McLeod DS, Grebe R, Bhutto I, Merges C, Baba T, Lutty GA. Relationship between RPE and choriocapillaris in age-related macular degeneration. Invest Ophthalmol Vis Sci 2009;50(10):4982–4991.
16. Sarks SH. Ageing and degeneration in the macular region: a clinico-pathological study. Br J Ophthalmol 1976;60(5): 324–341.
17. Chylack LT, Wolfe JK, Singer DM, et al. The Lens Opacities Classification System III. Arch Ophthalmol 1993;111(6): 831–836.
18. AREDS. The age-related eye disease study system for classifying age-related macular degeneration from stereoscopic color fundus photographs: the age-related eye disease study report number 6. Am J Ophthalmol 2001; 132(5):668–681.

19. ANSI. Safe Use of Lasers & Safe Use of Optical Fiber Communications American National Standards Institute—Z136 Committee. Orlando: The Laser Institute of America, 2000:168.
20. ICNIRP. Revision of guidelines on limits of exposure to laser radiation of wavelengths between 400 nm and 1.4 μm. International Commission on Non-Ionizing Radiation Protection. Health Phys 2000;79(4):431–440.
21. Roquet W, Roudot-Thoraval F, Coscas G, Soubrane G. Clinical features of drusenoid pigment epithelial detachment in age related macular degeneration. Br J Ophthalmol 2004; 88(5):638–642.
22. AREDS. A simplified severity scale for age-related macular degeneration—AREDS report no. 18. Arch Ophthalmol 2005;123(11):1570–1574.
23. Chung SE, Kang SW, Lee JH, Kim YT. Choroidal thickness in polypoidal choroidal vasculopathy and exudative age-related macular degeneration. Ophthalmology 2011;118(5): 840–845.
24. Margolis R, Spaide RF. A pilot study of enhanced depth imaging optical coherence tomography of the choroid in normal eyes. Am J Ophthalmol 2009;147(5):811–815.
25. Ciulla TA, Harris A, Chung HS, et al. Color Doppler imaging discloses reduced ocular blood flow velocities in nonexudative age-related macular degeneration. Am J Ophthalmol 1999;128(1):75–80.
26. Friedman E, Krupsky S, Lane AM, et al. Ocular blood flow velocity in age-related macular degeneration. Ophthalmology 1995;102(4):640–646.
27. Esmaeelpour M, Povazay B, Hermann B, et al. Three-dimensional 1060-nm OCT: choroidal thickness maps in normal subjects and improved posterior segment visualization in cataract patients. Invest Ophthalmol Vis Sci 2010; 51(10):5260–5266.
28. Ikuno Y, Kawaguchi K, Nouchi T, Yasuno Y. Choroidal thickness in healthy Japanese subjects. Invest Ophthalmol Vis Sci 2010;51(4):2173–2176.
29. Ikuno Y, Tano Y. Retinal and choroidal biometry in highly myopic eyes with spectral-domain optical coherence tomography. Invest Ophthalmol Vis Sci 2009;50(8):3876–3880.
30. Manjunath V, Taha M, Fujimoto JG, Duker JS. Choroidal thickness in normal eyes measured using Cirrus HD optical coherence tomography. Am J Ophthalmol 2010;150(3):325–329.
31. Taban M, Williams D, Smith SD, Kaiser PK. Assessing the reliability of automated OCT retinal thickness measurements in patients with choroidal neovascularization due to age-related macular degeneration. Ophthalmic Surg Lasers Imaging 2010;41(2):166–174.
32. Menke MN, Feke GT. Assessment of the effects of morphological changes related to age-related macular degeneration on optical coherence tomography retinal thickness measurements. Ophthalmic Surg Lasers Imaging 2005;36(4):310–314.
33. Ghazi NG, Kirk T, Allam S, Yan G. Quantification of error in optical coherence tomography central macular thickness measurement in wet age-related macular degeneration. Am J Ophthalmol 2009;148(1):90–96.
34. Bland JM, Altman DG. Multiple significance tests: the Bonferroni method. BMJ 1995;310(6973):170.
35. Sankoh AJ, Huque MF, Dubey SD. Some comments on frequently used multiple endpoint adjustment methods in clinical trials. Stat Med 1997;16(22):2529–2542.
36. Blair MP, Gupta M, Blair NP, Shahidi M. Association between retinal thickness and retinal pigment epithelium elevation in age-related macular degeneration. Ophthalmic Surg Lasers Imaging 2010;41(2):175–181.
37. Kashani AH, Keane PA, Dustin L, Walsh AC, Sadda SR. Quantitative subanalysis of cystoid spaces and outer nuclear layer using optical coherence tomography in age-related macular degeneration. Invest Ophthalmol Vis Sci 2009; 50(7):3366–3373.
38. Yamaguchi Y, Otani T, Kishi S. Comparison of optical coherence tomography and retinal thickness analyser. Rinsho Ganka 2000;54(5):941–945.
39. Yuda K, Inoue Y, Tomidokoro A, Tamaki Y, Yanagi Y. Nerve fiber layer thickness in exudative age-related macular degeneration in Japanese patients. Graefes Arch Clin Exp Ophthalmol 2010;248(3):353–359.
40. Joeres S, Tsong JW, Updike PG, et al. Reproducibility of quantitative optical coherence tomography subanalysis in neovascular age-related macular degeneration. Invest Ophthalmol Vis Sci 2007;48(9):4300–4307.
41. Kaluzny JJ, Wojtkowski M, Sikorski BL, et al. Analysis of the outer retina reconstructed by high-resolution, three-dimensional spectral domain optical coherence tomography. Ophthalmic Surg Lasers Imaging 2009;40(2):102–108.
42. Malamos P, Sacu S, Georgopoulos M, Kiss C, Pruente C, Schmidt-Erfurth U. Correlation of high-definition optical coherence tomography and fluorescein angiography imaging in neovascular macular degeneration. Invest Ophthalmol Vis Sci 2009;50(10):4926–4933.
43. Schuman SG, Koreishi AF, Farsiu S, Jung SH, Izatt JA, Toth CA. Photoreceptor layer thinning over drusen in eyes with age-related macular degeneration imaged in vivo with spectral-domain optical coherence tomography. Ophthalmology 2009;116(3):488–496.
44. Curcio CA, Medeiros NE, Millican CL. Photoreceptor loss in age-related macular degeneration. Invest Ophthalmol Vis Sci 1996;37(7):1236–1249.
45. Legarreta JE, Gregori G, Punjabi OS, Knighton RW, Lalwani GA, Puliafito CA. Macular thickness measurements in normal eyes using spectral domain optical coherence tomography. Ophthalmic Surg Lasers Imaging 2008;39(4):S43–S49.
46. Kakinoki M, Sawada O, Sawada T, Kawamura H, Ohji M. Comparison of macular thickness between Cirrus HD-OCT and Stratus OCT. Ophthalmic Surg Lasers Imaging 2009; 40(2):135–140.
47. Cheng SCK, Lam CSY, Yap MKH. Retinal thickness in myopic and non-myopic eyes. Ophthalmic Physiol Opt 2010;30(6):776–784.
48. Altman DG. Practical statistics for medical research. London: Chapman & Hall, 1991:1–611.
49. Bland JM, Altman DG. Statistical methods for assessing agreement between two methods of clinical measurement. Lancet 1986;1(8476):307–310.